

**Structural, microstructural, magnetic and hyperfine
characterization of some Zn-based nano and
microstructured ferrite systems with application potential**

**THESIS SUBMITTED FOR THE DEGREE OF
DOCTOR OF PHILOSOPHY (SCIENCE)
JADAVPUR UNIVERSITY
2023**



By
KOYEL SARKAR
DEPARTMENT OF PHYSICS, JADAVPUR UNIVERSITY
KOLKATA- 700032, INDIA

জাদবপুর বিশ্ববিদ্যালয়
কলকাতা-৭০০ ০৩২, ভারত



JADAVPUR UNIVERSITY
KOLKATA-700032, INDIA

FACULTY OF SCIENCE : DEPARTMENT OF PHYSICS

Dr. Sanjay Kumar
Professor
Department of Physics
Email: kumar_dsa@yahoo.com, sanjay.kumar@jadavpuruniversity.in

Ref No.: 16/23
Date: 09.10.2023

CERTIFICATE FROM THE SUPERVISOR

This is to certify that the thesis entitled 'Structural, microstructural, magnetic and hyperfine characterization of some Zn-based nano and microstructured ferrite systems with application potential' submitted by Koyel Sarkar (Registration no.: SOPHY1216916, Index no.: 16-16 Phys./25) for the award of Ph.D (Science) degree of Jadavpur University, is a record of a bonafide research work carried out by her under the supervision of Prof. Sanjay Kumar, Department of Physics, Jadavpur University, Kolkata-700032. Neither this thesis nor any part of it has been submitted for any degree/diploma or any other academic award anywhere before.

Sanjay Kumar 09.10.2023

(Signature of the Supervisor with official seal)



Dr. SANJAY KUMAR
Professor
Department of Physics
Jadavpur University
Kolkata - 700032, India

যাদবপুর বিশ্ববিদ্যালয়
কলকাতা-৭০০০৩২, ভারত



JADAVPUR UNIVERSITY
KOLKATA-700032, INDIA

FACULTY OF SCIENCE : DEPARTMENT OF PHYSICS

Dr. Sanjay Kumar

Professor

Department of Physics

Email: kumar_dsa@yahoo.com, sanjay.kumar@jadavpuruniversity.in

Ref No.: 17/23

Date: 09.10.2023

Certificate of similarity check for plagiarism verification

This is to certify that the plagiarism checking for this thesis authored by Koyel Sarkar has been performed using professional plagiarism prevention software iThenticate. According to the report generated by iThenticate there is 09 % similarity in this thesis, which is in category 'Level 0' (minor similarities) as per 'Promotion of Academic Integrity and Prevention of Plagiarism in Higher Education Institutions Regulations, 2018' of University Grant Commission (UGC) of India. All sentences written/rewritten by providing proper references (treated as quoted work), references (bibliography), table of contents, preface, acknowledgements, generic terms used in the subject area of the present thesis, a common knowledge or coincidental terms up to 12 (twelve) consecutive words (as prescribed in the above said UGC Regulation up to 14 (fourteen) terms for such common knowledge or coincidental terms can be excluded) and own works of the candidate published in peer reviewed journals (Journal of magnetism and magnetic material, 487 (2019) 165303-1 – 165303-11; Physica B: Condensed Matter, 583 (2020) 412015-1 – 412015-12; DAE SSPS Proceedings (2021) 198–199; these papers are attached in the Appendix of the thesis) are excluded from similarity checking. It is certified that the present thesis submitted by Koyel Sarkar is plagiarism free and she has followed standard norms of academic integrity and scientific ethics.

Sanjay Kumar
09.10.2023

(Signature of the Supervisor)

Kalyan Kr. Chattopadhyay
09.10.23

(Signature of the Head, Department of Physics)



Dr. SANJAY KUMAR
Professor
Department of Physics
Jadavpur University
Kolkata - 700032, India



Prof. Kalyan Kr. Chattopadhyay
Professor and Head
Department of Physics
Jadavpur University
Kolkata - 700 032

Declaration

I hereby declare that the work embodied in the present thesis titled 'Structural, microstructural, magnetic and hyperfine characterization of some Zn-based nano and microstructured ferrite systems with application potential' has been carried out by me in the Department of Physics, Jadavpur University, Kolkata-700032, India. Neither this thesis nor any part of it has been submitted for any degree elsewhere.

Date: 09.10.2023

Koyel Sarkar
(KOYEL SARKAR)

Research Scholar
Department of Physics
Jadavpur University
Kolkata- 700032, India

Dedicated to my parents....

Acknowledgement

First of all, I am sincerely thankful to God for providing me the strength to pursue this research work and leading me to its successful completion.

I express my profound gratitude to my supervisor Professor Sanjay Kumar, Department of Physics, Jadavpur University for his constant direction, constructive criticism and inspiration in pursuing the whole investigation of the present research. Words are always insufficient to express his working capacities and unending enthusiasm for scientific rigorousness for innovative investigations.

I am very grateful to Prof. Sukhen Das, Prof. Kalyan Kumar Chattopadhyay, Prof. Argha Deb, Dr. Partha Pratim Ray, Dr. Pabitra Kumar Paul, Dr. Sanat Karmakar of Department of Physics and Prof. Saurabh Das, Prof. Umesh Chandra Halder, Prof. Debajyoti Ghosal of Department of Chemistry, Jadavpur University, Kolkata.

I am thankful to Dr. V. R. Reddy (Scientist-G, UGC-DAE CSR, Indore) for low temperature and in-field Mössbauer spectroscopy measurement, Dr. Chandan Kumar Ghosh (School of Material Science and Nanotechnology, Jadavpur University) and Dr. Swarupananda Bhattacharjee for photocatalytic measurements. I would like to thank Dr. Papri Dasgupta (Saha Institute of Nuclear Physics) for different measurements. I would like to thank the FIST and PURSE program of Jadavpur University for providing us with the instrumental facilities. I am very thankful to UGC, Govt. of India for providing the NET-JRF fellowship.

I am immensely grateful to my senior lab mates Dr. Subhrajyoti Dey, Dr. Sumit Majumder, Dr. Rituparna Mondal, Dr. Sanjay Kumar Dey, Dr. Soumen Singha, Smt. Arpita Barua and Mr. Soumen Goswami for their guidance and support throughout my research. I would also like to thank my juniors Ms. Moosilee Dutta, Mr. Nirmal Mondal, Mr. Bhaskar Khanra and Mr. Sujaudhin Gaji.

I am thankful to my teacher Shri Utpal Kumar Paul who has been a great source of inspiration to me for studying Physics and pursuing scientific research in the field.

I am also thankful to Dr. Kajal Kumar Mukherjee, Director (Geophysics Division), Geological Survey of India for his constant support and encouragement to carry out the research work.

I am thankful to my friend Souma Saha, who has been a constant source of help and support throughout this journey. I would also like to thank my friends Dr. Prosenjit Biswas, Dr. Sumit Das and Lt. Rajdeep Paul.

Finally, I would like to express my deepest gratitude towards my parents for their constant encouragement and blessings.

Koyel Sarkar

Preface

This thesis focusses on synthesis, characterization, thorough study of the magnetic and hyperfine properties along with exploration of application potential of some Zn based nano and micro ferrite systems. Ferrite nanoparticles are among the most important magnetic materials that have fascinated the scientific community not only with their interesting magnetic features but also their widespread application in various fields. The magnetic properties of these nanoparticles are governed by two key factors viz., finite size effects and surface effects. The most studied finite size effect is superparamagnetism in which individual nanoparticles act as giant paramagnetic atom with rapid response to applied magnetic field and almost negligible hysteresis. These features make them suitable candidates in the field of biomedical application. However, these nanoparticles are associated with unavoidable issues like agglomeration and chemical instability which limit their application. Some of the surface effects include presence of surface canted spins, spin-glass like behaviour, increase in surface anisotropy and exchange bias effect due to presence of uncompensated spins. Ferrite nanoparticles displaying exchange bias phenomenon are in huge demand in the fields of permanent magnets, recording media and spintronics. So, it is seeming that the need of the hour is to explore ways to retain the discrete features beneficial for various fields alongside overcoming the factors limiting their extensive usage. In this regard, emphasis has been laid on the study of evolution of magnetic properties with doping of different concentrations of cobalt in nanosized Zn ferrite systems and manufacture of microstructures by self-assembly of Co-Zn ferrite nanoparticles.

Chapter-1 delves into the background and genesis of the present work. This chapter also includes some elementary aspects of nanomagnetism. Furthermore, the evolution in the intrinsic magnetic properties of different mixed Co-Zn ferrites and their utility in the fields of magnetic recording, catalysis and photocatalysis have also been dealt with.

Chapter-2 describes synthesis procedures like co-precipitation method, high energy ball milling method and solvothermal method adopted in the thesis. Characterization techniques viz., powder X-ray diffraction (PXRD), scanning electron microscopy (SEM), high resolution transmission electron microscopy (HRTEM), Energy-dispersive x-ray spectroscopy (EDX), X-ray photoelectron spectroscopy (XPS), UV-Vis and diffuse reflectance spectroscopy (DRS), photoluminescence (PL) spectroscopy, dynamic light scattering (DLS), zeta potential, dc magnetic, Mössbauer spectroscopy along with catalytic and photocatalytic studies are also discussed in detail.

Chapter-3 reports a detailed study on the effects of mechanical activation caused by high energy ball milling on the structural, magnetic and hyperfine properties of nanosized $\text{Co}_{0.5}\text{Zn}_{0.5}\text{Fe}_2\text{O}_4$ having three different particle sizes 63 (M1), 25 (M2) and 17 nm (M3) synthesized by chemical coprecipitation method. The theory of magnetic domains has been exploited to explicate the trend in coercivity. The effects of mechanical activation on cation redistribution and magnetic property of M2 have been investigated by infield Mössbauer spectroscopic measurements and verified by theoretical analysis of experimental results of Rietveld refinement of powder x-ray diffraction data in conjugation with dc magnetic study. The sample M2 may be used to design magnetic coding and sensing devices as it is capable of encoding, preserving and recalling binary numbers through magnetic field change.

Chapter-4 deals with the comparison of the structural, morphological, magnetic and hyperfine properties of ZnFe_2O_4 solid (ZFMS) and hollow (ZFMH) microspheres synthesized by simple solvothermal technique. ZFMS, formed by self-assembly of nanoparticles, displays superparamagnetic character predominantly along with collective magnetic excitations at room temperature. ZFMH exhibits single crystal like dotted selected area electron diffraction pattern and is magnetically well-ordered at room temperature. Interestingly, ZFMH displays Verwey transition in magnetization versus temperature studies. Moreover, cation vacancy is also evident in ZFMH from XPS and Mössbauer spectroscopic measurements.

Chapter-5 focusses on the electrochemical study of nanosized $\text{Co}_{0.5}\text{Zn}_{0.5}\text{Fe}_2\text{O}_4$ synthesized by hydrothermal method. The sample exhibits pseudocapacitive behaviour and can act as a supercapacitor.

Chapter-6 reports that the particle size, cation redistribution, surface spin disorder and strain induced anisotropy play a pivotal role in shaping the magnetic and hyperfine properties of nanosized $\text{Co}_{0.8}\text{Zn}_{0.2}\text{Fe}_2\text{O}_4$ samples with different particle size viz., 23 nm (CZ1), 34 nm (CZ2) and 42 nm (CZ3) prepared by coprecipitation method followed by high energy ball milling and subsequent thermal treatment. A reliable way of estimating cation distribution through infield Mössbauer spectroscopic study and dc magnetization measurement in conjugation has been shown in this chapter. Sample CZ1 exhibits exchange bias effect. All three samples display excellent catalytic activity in the multicomponent reaction for the synthesis of coumarin-3-carboxamide.

Chapter-7 deals with the structural, magnetic, hyperfine and optical properties of $\text{Co}_{0.5}\text{Zn}_{0.5}\text{Fe}_2\text{O}_4$ microspheres synthesised by template-free solvothermal technique. It has been shown that microspheres are mostly monodisperse and formed by self-assembly of

$\text{Co}_{0.5}\text{Zn}_{0.5}\text{Fe}_2\text{O}_4$ nanoparticles. The microspheres possess both direct and indirect transition and are having positive surface charge. They are ferrimagnetic in nature. Moreover, the sample acts as an efficient catalyst in the degradation of Congo Red dye even under visible light conditions. The photocatalytic study suggests that the sample can be suitably used as an efficient, magnetically separable, recyclable photocatalyst for removal of Congo Red from aqueous solution.

Chapter-8 presents the conclusion drawn from the research work included in this thesis and the future scope and prospect of the present work.

Date:

Koyel Sarkar 09.10.2023

(KOYEL SARKAR)
Department of Physics
Jadavpur University
Kolkata 700032

Contents

	Page No.
Preface	i – iv
Chapter 1: Introduction	01 – 47
1.1. Background and genesis of the problem	01
1.2. Basics of magnetism	16
1.3. Magnetic dynamics in nano-regime	18
1.3.1. Concept of anisotropy energy in nanomagnets	18
1.3.2. Superparamagnetism	21
1.3.3 Interparticle Interaction and Spin Glass Behavior	22
1.3.4. Collective Magnetic State	23
1.4. Application prospects of Zn based ferrites	25
1.4.1. Memory or Ageing Effect	25
1.4.2. Catalysis	26
1.4.3. Photocatalysis	27
1.5. Scope of the work	29
<i>References</i>	31
Chapter 2: Experimental methods	48 – 69
2.1. Synthesis techniques	48
2.1.1. Co-precipitation method	48
2.1.2. High energy ball milling method	49
2.1.3. Solvothermal/Hydrothermal	49
2.2. Characterization techniques	49
2.2.1. Powder x-ray diffraction (PXRD) study	50
2.2.2. Electron microscopic study	52
2.2.2.1. FESEM study	52
2.2.2.2. TEM study	53

2.2.3. Energy-dispersive x-ray spectroscopic study	55
2.2.4. Fourier-transform infrared spectroscopic study	56
2.2.5. UV–vis spectroscopic study	57
2.2.6. Photoluminescence spectroscopic study	58
2.2.7. Dynamic light scattering and Zeta potential study	58
2.2.8. dc magnetic study	59
2.2.8. Mössbauer spectroscopic study	60
2.2.9. Electrochemical performance study	62
2.2.9. Photocatalytic study	64
<i>References</i>	66
Chapter 3: Presence of mixed magnetic phase in mechanically milled nanosized $\text{Co}_{0.5}\text{Zn}_{0.5}\text{Fe}_2\text{O}_4$: A study on structural, magnetic and hyperfine properties	70 – 112
3.1. Introduction	70
3.2. Experimental	73
3.3. Results	74
3.3.1. Structural characterization	74
3.3.2. Electron microscopic investigation	78
3.3.3. Magnetic and hyperfine study	81
3.3.4. Study of memory effect	89
3.4. Discussion	91
3.5. Conclusion	100
<i>References</i>	102
Chapter 4: Cation vacancy and magnetic properties of ZnFe_2O_4 microspheres	113 – 148
4.1. Introduction	113
4.2. Experimental	116
4.2.1. Materials	116
4.2.2. Synthesis procedure	116
4.2.3. Characterization	117
4.3. Results	117

4.3.1. Structural and morphological characterization	117
4.3.2. X-ray photoelectron spectroscopic study	122
4.3.3. Magnetic and hyperfine study	126
4.4. Discussion	134
4.5. Conclusion	138
<i>References</i>	140

Chapter 5: Electrochemical Study of Nanosized $\text{Co}_{0.5}\text{Zn}_{0.5}\text{Fe}_2\text{O}_4$ Synthesized by Hydrothermal Method

149 – 168

5.1. Introduction	149
5.2. Experimental and method	151
5.2.1. Sample synthesis	151
5.2.2. Characterization	152
5.2.3. Electrode preparation for electrochemical study	153
5.3. Results	153
5.3.1. Structural and microstructural characterization	153
5.3.2. Study of Optical Properties	157
5.3.3. Magnetic Study	158
5.3.4. Electrochemical performance study	160
5.4. Conclusion	161
<i>References</i>	163

Chapter 6: Influences of morphology, cation distribution and surface spin canting on magnetic and hyperfine properties of mechanically activated and subsequently heat treated nanosized $\text{Co}_{0.8}\text{Zn}_{0.2}\text{Fe}_2\text{O}_4$ exhibiting excellent catalytic activity

169 – 219

6.1. Introduction	169
6.2. Experimental	174
6.2.1. Synthesis of $\text{Co}_{0.8}\text{Zn}_{0.2}\text{Fe}_2\text{O}_4$ nanoparticles and characterization techniques	174
6.2.2. Reaction methodology for the synthesis of coumarin-3-carboxamide using CZ1, CZ2 and CZ3 NPs as catalyst	176

6.3. Results	176
6.3.1. Structural and morphological study	176
6.3.2. Magnetic and hyperfine study	182
6.3.3. Study of catalytic activity of $\text{Co}_{0.8}\text{Zn}_{0.2}\text{Fe}_2\text{O}_4$ nanoparticles	195
6.3.3.1. Catalysis reaction	195
6.3.3.2. Reusability of the catalyst	202
6.4. Discussion	205
6.5. Conclusion	210
<i>References</i>	213
Chapter 7: Study on structural, magnetic, hyperfine, optical properties and dye-degradation of self-assembled $\text{Co}_{0.5}\text{Zn}_{0.5}\text{Fe}_2\text{O}_4$ microspheres	220 – 258
7.1. Introduction	214
7.2. Experimental Methods	224
7.2.1. Synthesis Procedure of $\text{Co}_{0.5}\text{Zn}_{0.5}\text{Fe}_2\text{O}_4$ Microspheres	224
7.2.2. Characterization techniques	225
7.2.3. Photocatalytic experiment	225
7.3. Results	226
7.3.1. Structural, microstructural and morphological study	226
7.3.2. Uv-vis and PL study	231
7.3.3. DLS and Zeta potential study	232
7.3.4. FTIR study	234
7.3.5. Magnetic and hyperfine study	236
7.3.6. Photocatalytic Study	241
7.3.6.1. Critical Catalyst study	241
7.3.6.2. Dark degradation study	241
7.3.6.3. Photo degradation study	243
7.3.6.4. Degradation kinetics study	244
7.3.6.4. Resuability test	245
7.4. Discussion	247
7.5. Conclusion	250

<i>References</i>	251
Chapter 8: Conclusion and future scope of the work	259 – 266
8.1. Conclusion -----	259
8.2. Future scope of the work -----	264
List of publications	
Seminar, Symposium, Conferences and Awards	
Appendix: Reprints of the published papers related to the thesis	



Chapter 1

Introduction



1.1 Background and genesis of the problem

In this era of nanoscience and nanotechnologies, newer scientific revelations are taking place almost every day to make human life easier. The prefix ‘nano’ refers to a Greek etonym nanos meaning ‘dwarf’. Simply, nanoscience refers to the study of matter on the nano regime ($\sim 10^{-9}$ m), while nanotechnology utilizes the principles of nanoscience to develop devices [1]. Fig. 1 shows the size variation of nanomaterials. The National Nanotechnology Initiative (NNI) in the United States defines Nanotechnology as “a science, engineering, and technology conducted at the nanoscale (1 to 100 nm), where unique phenomena enable novel applications in a wide range of fields, from chemistry, physics and biology, to medicine, engineering and electronics” [2]. This definition suggests the presence of two conditions for nanotechnology: The first is a topic of scale i.e., nanotechnology deals with the control of shape and size of matter at nanometer scale and the second topic has to do with novelty i.e., nanotechnology nurtures the properties at nanoscale to its advantage as per the industrial need and demand [3]. The Nobel laureate Richard P. Feynman, referred to as the father of nanotechnology, made the hypothesis “Why can’t we write the entire 24 volumes of the Encyclopedia Britannica on the head of a pin?” during his famous lecture entitled “There’s Plenty of Room at the Bottom” at the California Institute of Technology (Caltech) in 1959 [4]. Norio Taniguchi, a Japanese scientist first defined the term “nanotechnology” in 1974 as follows: “nanotechnology mainly consists of the processing of separation, consolidation, and deformation of materials by one atom or one molecule” [5].

The Romans have been known to use nanoparticles in fourth century AD, one of the most interesting examples of nanotechnology in the ancient world [6]. For example, the Lycurgus cup (Fig.2(a)), oldest example of dichroic glass, represents one of the most wonderful accomplishments in ancient glass industry [7]. Dichroic glass portrays two dissimilar types of glass, which alters color in certain lighting conditions [8]. The observed

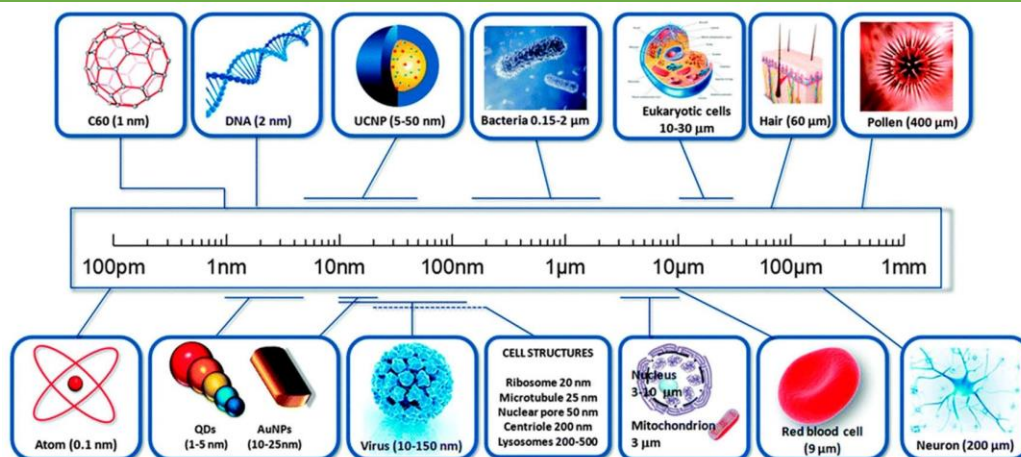


Fig. 1 Size variation of nanomaterials [6]

dichroism can be attributed to the existence of nanoparticles. X-ray studies divulged that this dichroic glass comprises of silver-gold nanoparticles along with some amount of copper dispersed in a glass matrix [7,9]. These nanoparticle composites produce different color combinations depending on their size and scattering effect [7,9]. Such effects have also been observed in late medieval church windows (Fig. 2(a)) and can be attributed to the blend of silver-gold nanoparticles into the glass [6]. The Renaissance pottery was created by Italians during 16th century by employing nanoparticles [10]. Sir Michael Faraday explored the unique optical and electronic properties of colloidal suspensions of “Ruby” gold by synthesizing and examining their characteristics [11]. He demonstrated the conditions under which gold nanoparticles produce different-colored solutions [11].



Fig. 2 (a) Lycurgus cup and (b) Medieval church windows

There was slow progress in the field of nanotechnology since Feynman conceived the ideas of nanoscience within science fraternity until 1981 when physicists Gerd Binnig and Heinrich Rohrer discovered Scanning Tunneling Microscope at IBM Zurich Research Laboratory [12,13]. After sometime, in 1990, Don Eigler and his colleagues used Scanning Tunneling Microscope to tune thirty-five single xenon atoms on a nickel surface and shaped the letters of IBM logo [14]. The invention of Scanning Tunneling Microscope revolutionized the field of nanoscience and further led to the development of the atomic force microscope and scanning probe microscopes [15,16]. In the subsequent times, nanoscience and nanotechnology advanced in the field of computer science to decrease the size of a normal computer from the size of a room size to portable laptops. Miniaturization of complex electrical circuits down to nanoscale level led to significant improvements in mobile phone technology and other modern electronic devices of day-to-day uses. One of the most fascinating areas of application of nanoscience is biomedical field [17]. During recent times, nanotechnological revelations in biology related fields such as diagnosis, drug delivery, and molecular imaging are being thoroughly researched and have delivered exceptional results [17]. Such examples of “nanopharmaceuticals” comprise nanomaterials for drug delivery and nanoparticles with antimicrobial activities or hierarchical nanostructures used as markers detection like nanobiochips, nanoelectrodes, or nanobiosensors [18]. Extraordinary improvements have also been made in the field of nano-oncology by developing the efficiency of conventional chemotherapy drugs for a series of destructive human cancers [19,20]. These progresses have been accomplished by aiming the tumor site with several functional nanoparticles [19,20]. Even more recently, there have been through studies on nanomaterials for usage in both ex vivo and in vivo purposes in biotechnology and biomedicine, respectively. These applications take benefit of the fact that the saturation magnetization and coercivity can be modified at the nanoregime. This tuning can be achieved

via size, shape and surface modification, and also by the addition of surfactants on the magnetic nanoparticles that can be guided or modulated by external magnetic fields [21]. In present times, technological developments have led to utilization of magnetic nanoparticles to design permanent magnets in large-scale applications, such as electrical vehicles and wind turbines based on the concept of “exchange-spring nanocomposite magnet” [21]. Fig. 3 shows the development in nanoscience and nanotechnology.

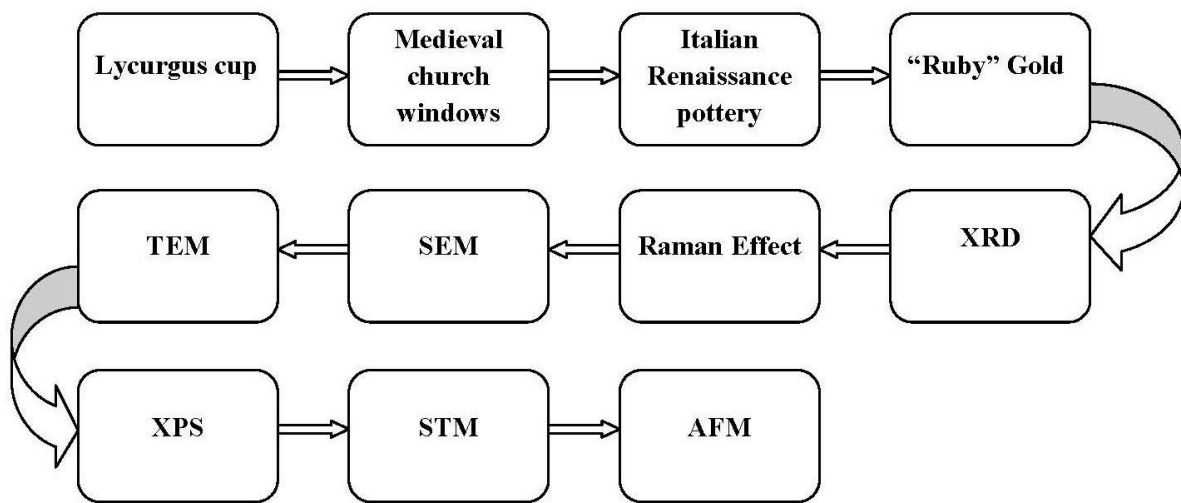


Fig. 3 Development in nanoscience and nanotechnology

Magnetic nanoparticles are of great significance for the scientific community owing to their applicability in a plethora of disciplines, including magnetic fluids, catalysis, biomedicine, magnetic resonance imaging, magnetic data storage, and environmental refurbishment [22-30]. In most of the envisioned nanotechnological applications like nanoscale electronics, magnetic separation techniques and magnetic resonance imaging, to name a few; the nanoparticles perform best when they are below a critical size [31]. Magnetic nanoparticles possess single domain below the critical volume of domain wall formation, resulting in large magnetic moments per unit volume i.e., displays superparamagnetic behavior. Such individual entities act like a giant paramagnetic atom exhibiting negligible remanence and almost zero coercivity at room temperature [31]. These properties are beneficial in various technological fields and can be tuned as per the requirement of the

applications. Moreover, these processes can be studied using simple theoretical models involving their responses in the presence of external magnetic fields [21]. Rising new nanotechnologies surround around combination of magnetic and electrical properties of the nanoparticles, which display multifunctional properties and are under through investigation. It is likely that in terms of applications as sensors and magnetic memory devices, magnetic nanocomposites and multilayered materials will be in the forefront [21]. It may be noted that these magnetic nanomaterials have garnered a lot of interest due to their noteworthy elementary properties that render them fit for assorted technological applications [31].

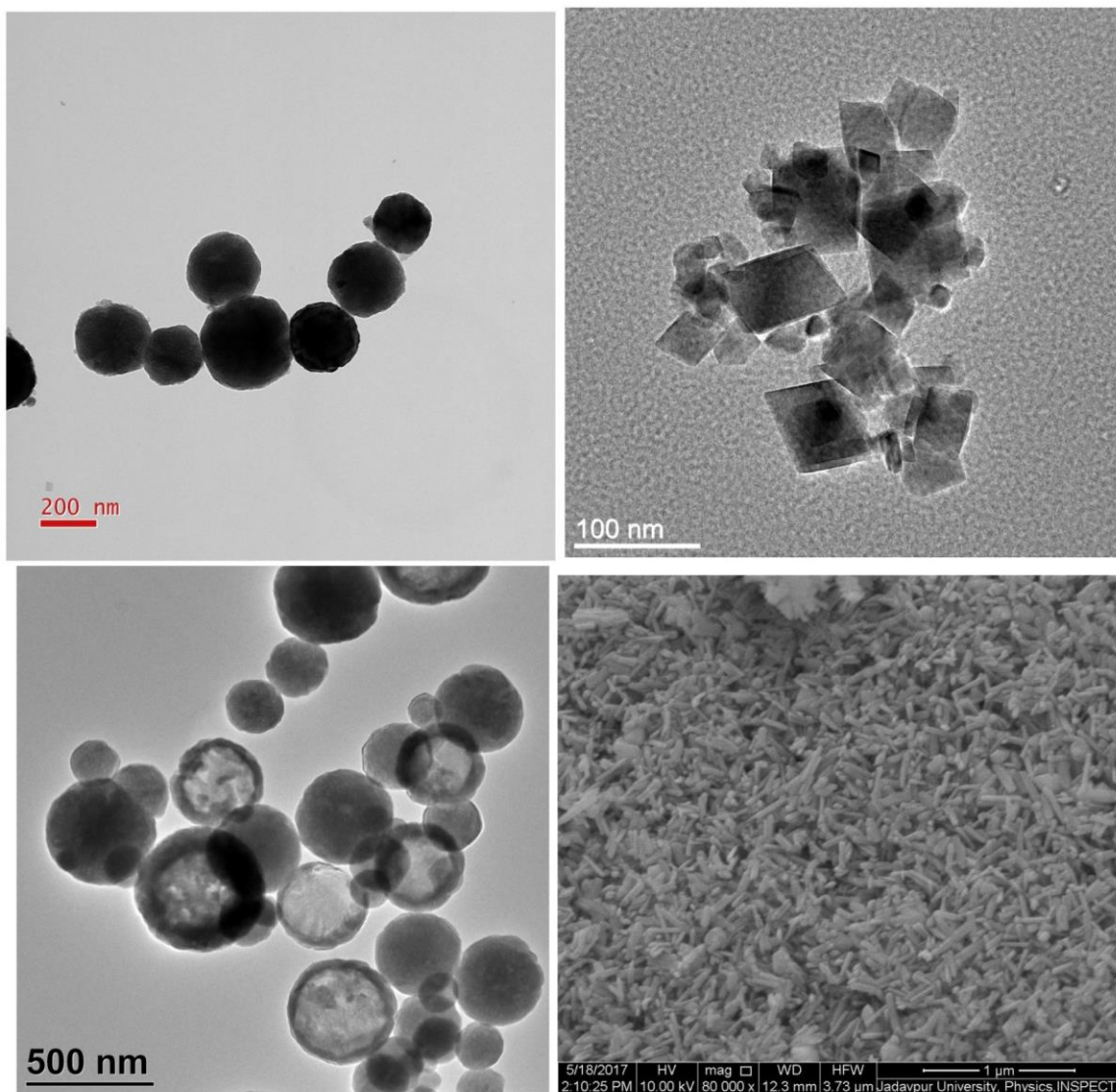


Fig.4 Different types of nano/micro structures

In case of magnetic data storage device fabrication, entry of a small amount of magnetic nanoparticles into the system may increase the storage density largely [32]. Nanosized magnetic particles are prospective candidates to be used in magnetic resonance imaging as contrast agents, biosensors, supercapacitors, electronic devices (radio frequency transformer cores, microwave absorber, filters, choke etc.), ferrofluids, magnetic refrigerants, high performance permanent magnets and also in biology and medical applications such as cancer therapy, drug-targeting, hyperthermia etc. [33 - 42]. These magnetic nanoparticles are highly useful in biological application such as bacteria detection, protein purification, toxin decorporation etc. [43 – 45]. Soft magnetic materials such as Sendust alloys, Fe-Co-/Fe-Ni-based alloys, iron/low-carbon steel, soft ferrites, Fe-Si steels etc. are ideal for power management, microelectronics and sensing devices owing to their high permeability and low-loss properties [46]. Magnetic nanomaterials having complex morphology such as nanotubes, nanorods, nanowires etc. [47 – 49] are widely used in nanotechnological devices, tunable microfluid channels with magnetic control, magnetized nano-tips for magnetic force microscopes etc. [50 – 52]. Nowadays, efforts have been made to develop and understand the characteristics of iron based magnetic nanoparticles by improving their applicability in various field as they exhibit remarkable enhancement in their magnetic properties compared to other types of magnetic nanomaterials [53, 54]. Apart from above mentioned common applications these iron based magnetic nanomaterials are widely used in therapeutic and clinical diagnostic applications as well [55, 56].

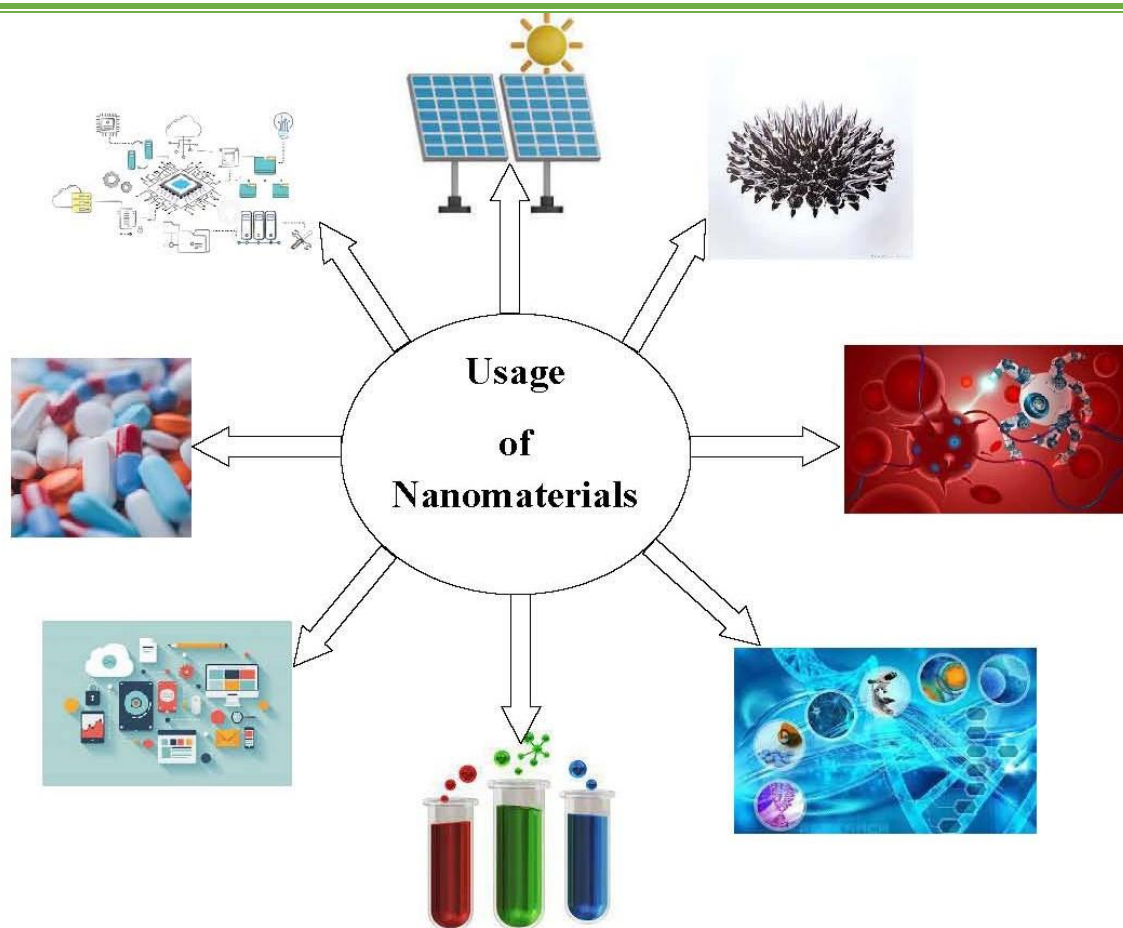


Fig.5 Application of nanoscience and nanotechnology [6]

In spite of having a long list of interesting applications and widespread applicability, these nanoparticles unfortunately suffer from a problem of inherent instability over longer periods of time [31]. As a result of this, the nanoparticles tend to form aggregates in order to minimize their surface to volume energy. Moreover, bare metallic nanoparticles get easily oxidized in air due to their high chemical activity, thus leading to loss of magnetic property and dispersibility. Moreover, surface effects can render these nanoparticles less magnetic with respect to their bulk [31]. These surface effects involve different mechanisms such as the presence of a magnetically dead layer on the particles surface, the occurrence of canted spins on the surface, or appearance of a spin-glass-like behavior in the system of canted spins [31]. To stabilize the surface of the bare magnetic nanoparticles against possible deterioration of their properties with subsequent time, methods of enveloping their surface with organic

species like surfactants or polymers, inorganic layer like silica or carbon, or noble metal coatings like gold are undertaken either during or after the synthesis process. It may be noted that these shielding shells not only stabilize the nanoparticles, but render them multifunctionality. For example, organic ligands employed to stabilize the surface of magnetic nanoparticles have been found to influence their magnetic properties by modifying the anisotropy energy barrier and magnetic moment of the metal atoms located at the nanoparticle surface [57]. Cobalt colloidal particles stabilized with organic ligands have displayed a large anisotropy energy value in contrary of reduced magnetic moment [57]. Moreover, a coat of silica has been found to obstruct diffusion of chemicals from inside of the nanoparticles to outside, thus, lowering the lethal effect of nanoparticles towards biological cells [58]. Apart from this, silica coating on nanoparticles also display enhanced optical properties [59]. Depending on the nature of coating and the bonding between the nanoparticle and the coating material, variation in magnetic properties has been observed [60]. For example, gold-coated cobalt nanoparticles have displayed lower magnetic anisotropy energy values as compared to uncoated particles, whereas iron nanoparticles with gold coating has shown enhancement in anisotropy energy, a consequence of alloy formation with the gold [57]. Coating of magnetic nature on a magnetic nanoparticle typically has a striking influence on the magnetic properties. The interactions among the two different magnetic phases result in exchange bias effect most commonly [61]. Furthermore, self-assembly of nanomaterials to fabricate hierarchical nanostructures is another way of stabilizing the intrinsic instability of magnetic nanoparticles alongwith development of functional nanomaterials [62]. These structures have found widespread applicability in the fields of nanotechnology, imaging techniques, biosensors, biomedicine etc. [62]. Self-assembly process can be achieved by using a nanostructured surface (template) or external fields (field-directed or field-assisted assembly) [63]. Self-assembled nanostructures have

excelled as facile and efficient materials in the field of development of novel drug delivery systems (DDSs) [16].

Ferrite nanomaterials are one of the most fascinating members of the domain of magnetic nanomaterials not only due to their importance from the view point of fundamental science but also due to their extensive application in a variety technological fields ranging from biomedical to hardware industry [64]. Ferrites can be categorized further into spinels, garnets and hexaferrites, but our arena of discussion in the thesis shall be limited to spinel ferrites only. The spinel ferrite structure MFe_2O_4 has a cubic close-packed arrangement of oxygen atoms with M^{2+} and Fe^{3+} at two different crystallographic sites viz., tetrahedral (A) and octahedral [B] sites. Due to difference in coordination of the metal atoms with oxygen ions at the two sublattice of the spinel structure, there is an inherent asymmetry between two sites. There are eight (A) sites and 16 [B] sites in the spinel lattice. Depending on the occupations of cations in the two sites, the spinel ferrites are further subdivided into normal, inverse and mixed ferrites, respectively [65]:

(i) The structure having only M^{2+} cations in the tetrahedral (A) site and Fe^{3+} ions in the octahedral [B] site are referred to as normal spinel.

(ii) The structure having only Fe^{3+} ions in the tetrahedral (A) site and both M^{2+} cations and Fe^{3+} ions simultaneously in the octahedral [B] site are referred to as inverse spinel.

(iii) Typically, the distribution of M^{2+} and Fe^{3+} ions among the (A) and [B] sites are random and thus referred to as mixed spinel.

Classically, spinel ferrites are ferrimagnetically ordered. The spins at (A) and [B] sites are aligned antiparallel to one another. But due to difference in the number of sites, a net moment of spins arises resulting in ferrimagnetic ordering for the crystal. The choice of metal ions and their distribution between the (A) and [B] sites allows a tunable magnetic system [66].

Nanostructured spinel ferrites display fascinating magnetic properties like superparamagnetism, spin-glass like behavior, collective magnetic state and spin canting effect [64-73]. The magnetic properties of nanosized spinel ferrites are strongly reliant on the shape, size, purity, stability, size distribution, morphology, surface spin alignment and cation distribution among (A) and [B] sites of the spinel lattice. Furthermore, the synthesis procedure adopted is of utmost importance in determining the magnetic characteristics. Thus, choice of appropriate synthesis technique is of tremendous importance for tuning magnetic quality in order to produce superior quality samples with enhanced physical properties and industrially applicable features. Generally, the synthesis procedures of these nanoparticles are mainly classified into two sub-categories i.e. 'bottom-up' and 'top-down' process [6,70]. In case of nanostructured ferrites, coprecipitation, thermal decomposition, self-assembly process viz., hydrothermal and solvothermal methods are most frequently used 'bottom-up' synthesis techniques while 'top-down' synthesis methods include mechanical milling technique and pulsed laser ablation [6,70]. Fig. 6 shows the two basic synthesis approaches.

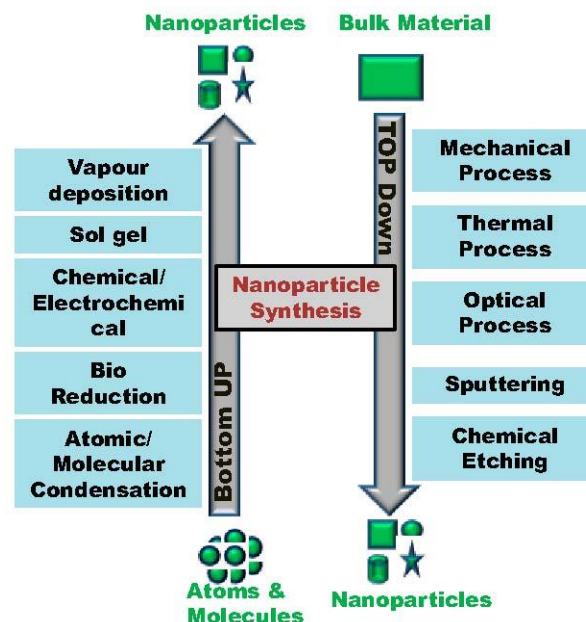


Fig.6. Bottom-up and top-down synthesis approach [6]

The particle size, shape and morphology can be controlled with the help of suitable synthesis route and adjustment of reaction parameters, thus, indirectly shaping the magnetic properties of the nanometric ferrites [75 – 78]. The self-assembly processes like hydrothermal/solvothermal methods have been employed to synthesize self-assembled hierarchical spinel ferrite nano- and micro – structures of controllable size and morphologies [79-81]. Self-assembly of these magnetic nanoparticles into distinct hierarchical structures is an important condition for achieving eventual control over their properties and to realize their multifunctionality [81]. In contrast to nonmagnetic nanoparticles, magnetic particles have dipolar forces, which are directional in nature and thus, provide facile control over self-assembly and directed assembly strategies. The collective physical properties of these self-assembled structures, having size closer to that of protein molecules, are promising for future biomedical applications [82]. Moreover, it is anticipated that these magnetic nano- and microstructure assemblies shall find significant usage in high density information storage with extremely high areal density and spintronic devices as well. A pre-requisite for these applications is a higher degree of control and large scale uniformity of these structures, which needs development of specialized synthesis techniques.

Nanosized ferrites typically display superparamagnetic behavior along with moderate saturation magnetization and they are magnetically guidable, separable and removable as they can react to the change in external magnetic fields very promptly. Additionally, they can be easily dispersed in a liquid medium and will not get agglomerated if the interparticle interactions are weak [83 – 87]. These make them suitable candidates in the fields of biomedicine, drug delivery, biosensing, catalysis, photocatalysis, wastewater treatment, ferrofluids and supercapacitor etc. [88 - 95]. In case of biomedical applications such as, in magnetic resonance imaging (MRI), cancer treatment etc, it has been observed that the spinel ferrites need to be in superparamagnetic state at room temperature [96]. Superparamagnetic

nanoparticles of ferrites can flip the direction of their spin in response to the external alternating magnetic field and as a result magnetic energy is converted into thermal energy that make ferrite nanoparticles useful in hyperthermia technique advantageous for killing of cancer cells [97, 98]. It may be noted that decrease in magnetization with the reduction of size and intrinsic unstable spontaneous magnetization strictly restricts their application in magnetic storage devices. Upon reduction of size of ferromagnetic or ferrimagnetic materials below a critical limit the magnetic anisotropy energy responsible for holding the magnetization in a particular direction becomes comparable to or less than the thermal energy of the system and the magnetic moment of such particles starts flipping randomly which in turn leads to superparamagnetism. Superparamagnetic nanoparticles do not show any hysteresis above blocking temperature. Moreover, ferrite nanoparticles exhibit spin canting effect which reduces the magnetization of these systems further. However, lowering of magnetization due to surface spin canting and unstable spontaneous magnetization at room temperature owing to the superparamagnetic character severely limit the applications of nanosized ferrite systems in the field of magnetic recording media. For application in recording media, high saturation magnetization and presence of coercivity at room temperature along with stability of magnetization are key requirements [67, 99 - 101]. The possible solution to the aforementioned problem is to beat superparamagnetism by enhancement of anisotropy energy and counteracting the affect of spin canting by tuning the cation distribution favourably. Another solution can be to overshadow the superparamagnetic character and spin canting effect by assembling of the nanoparticles into desirables structures with high saturation magnetization and coercivity.

It has been reported that the unfavorable effects of superparamagnetism and spin canting can be overcome by enhancing the anisotropy energy and judiciously readjusting the cations within the spinel ferrites in appropriate manner, respectively [67,69,71,72,102-106].

Recently, efforts have been made to achieve this goal. It has been found that the nanosized $\text{Co}_{0.2}\text{Zn}_{0.8}\text{Fe}_2\text{O}_4$ [73] ferrites synthesized by high energy ball milling method exhibit much better magnetization, magnetic order, magnetic ordering temperature and coercivity compared to their nanometric counterparts synthesized by conventional chemical routes. The history dependent magnetic property (memory phenomenon) in the dc magnetic measurement has been observed in these types of Co-Zn ferrites due to their broad distribution of particle size and the strong interparticle interaction [67, 73]. Nanosized $\text{Co}_{0.3}\text{Zn}_{0.7}\text{Fe}_2\text{O}_4$ synthesized by chemical coprecipitation method followed by high energy ball milling values has shown substantially higher values of magnetic parameters as compared to its counterparts synthesized by conventional chemical methods [107]. It has been shown that nanosized $\text{Ni}_{0.5}\text{Zn}_{0.5}\text{Fe}_2\text{O}_4$ prepared by high energy ball milling with different milling parameters exhibits lowering of magnetic ordering temperature [69]. Single spinel phase $\text{Co}_{1-\chi}\text{Zn}_{\chi}\text{Fe}_2\text{O}_{4+\gamma}$ synthesized by coprecipitation followed by thermal treatment has shown controlled modification of size resulting in applicability of this sample for magnetic fluid hyperthermia in a self-controlled regime [108]. Moreover, efforts have been made to synthesize submicron sized ferrites with high saturation magnetization through formation of hierarchical self-assembled and monodispersed solid and hollow microspheres of ferrites composed of superparamagnetic nanoparticles. These microspheres have been found to be highly interesting because they not only enhance the overall magnetization but also preserve the superparamagnetic character of the constituent nanoparticles. It has been observed the morphologies, crystallite sizes, magnetic properties of self-assembled ferrite microspheres were strongly affected by modification in the reaction conditions [79,82,109-117]. Manganese and zinc ferrite microspheres display superparamagnetic behavior while the cobalt and nickel microspheres show ferrimagnetic behavior [112]. It is supposed these structures can be considered as promising materials for drug loading and magnetically drug

delivery systems [112]. Yu et al., have proposed that self-assembled mesoporous cobalt and nickel ferrite spherical clusters have the prospective to be utilized in various applications, including catalysis, sensors, drug delivery, and rechargeable lithium batteries [115].

Recently, zinc ferrites have also received great interest due to their widespread application potential in fields of magnetic and electromagnetic devices, photocatalysis, solar cells etc. [86]. For example, ZnFe_2O_4 nanoparticles can be used as colorimetric biosensors for the recognition of urine glucose due to its intrinsic peroxidase-like activity of the nanoparticles [86]. ZnFe_2O_4 nanorods displayed a good photocatalytic sensing toward the disintegration of methylene blue dye [118]. ZnFe_2O_4 nanospheres exhibited excellent acetone sensing capability [119]. Hollow ZnFe_2O_4 nanospheres exhibited higher saturation magnetization and coercivity as compared to zinc ferrite nanosheets [120]. Moreover, the electromagnetic and consequently microwave adsorption properties of hollow ZnFe_2O_4 nanospheres are appreciable [120]. Zn-Doped Fe_3O_4 Hollow Nanospheres have proved to be an excellent material for high-frequency and biomedical applications [121]. Generally, zinc ferrite exhibits normal spinel structure with structural formula i.e., the tetrahedral (A) site does not contain Fe^{3+} ions. As a result, the oxygen mediated intersublattice super exchange interaction is not effectual here and zinc ferrite behaves ferrimagnetically only below 9 K (Néel temperature) [65]. However, some nanosized zinc ferrites exhibit ferrimagnetic coupling between tetrahedral (A) and octahedral [B] sites due to migration of Fe^{3+} ions from [B] to (A) sites [65]. This cation redistribution promotes enhancement of saturation magnetization and ordering temperature of nanosized zinc ferrites compared to its bulk counterparts [65]. It has been reported that submicron sized ZnFe_2O_4 clusters display superparamagnetic properties with a relative large saturation magnetization value.

In the last few decades, researchers have strongly emphasized on the synthesis and study of cobalt-zinc ferrite nanoparticles and their heterostructures as well because of their

extensive applications encompassing a wide variety of technological and industrial fields [122-124]. Zinc substituted cobalt ferrites are a class of magnetic nanomaterials, which have exhibit high value of permeability, low power losses, permittivity, saturation magnetization, coercivity, resistivity, and other favorable properties that make them suitable candidates for applications in various fields [125-135]. These ferrites are also used in biomedical areas such as magnetic resonance imaging and cancer treatments [137-140]. In the field of electronics, zinc substituted cobalt ferrites are used to make transducers, transformers, biosensors, and sensors [141-143]. In addition to these beneficial features, they are also found in our day-to-day electronic and electrical appliances as well [144-147]. The properties of these soft ferrites are highly tunable as per their application just by choice of appropriate synthesis procedure [122]. As a result, there is a persistent progression within the shape and size control of these ferrites. Additionally, efforts are being made to control the morphological and physical properties of these ferrites by applying various methods of synthesis like co-precipitation process [148], sol-gel method [149], conventional ceramic method [150], citrate precursor method [151], hydrothermal [152], auto-combustion [153], solid-state reaction method [154], and microemulsion [155]. Owing to the engrossing features of Co-Zn ferrites amidst the group of mixed ferrites, the research commune has focused their attention in their studies.

In this backdrop, the study of structural, microstructural, magnetic and hyperfine properties of some Zn-based nano- and micro- ferrites appears to be interesting in understanding the principles underlying the complex magnetic phenomena displayed by such systems along with examination of their application possibilities. This thesis focuses on the comprehensive study of the structural, microstructural, optical, magnetic and hyperfine properties of the $\text{Co}_{0.5}\text{Zn}_{0.5}\text{Fe}_2\text{O}_4$, $\text{Co}_{0.8}\text{Zn}_{0.2}\text{Fe}_2\text{O}_4$ nanoparticles and $\text{Co}_{0.5}\text{Zn}_{0.5}\text{Fe}_2\text{O}_4$, ZnFe_2O_4 solid and hollow microspheres with the aim to analyze the fundamental mechanisms behind the phenomena of superparamagnetism, spin glass-like behavior and collective

magnetic excitations in these samples, elucidate the influence of morphology and spin canting on their magnetic behavior and explore their applications as magnetic memory, catalyst and photocatalyst.

Nanostructured ferrite systems exhibit many unique magnetic features such as superparamagnetism, magnetic anisotropy, interparticle interactions, spin glass like behavior, spin canting effect, collective magnetic state etc. Before discussing the aforementioned phenomena of ferrite nanomagnets, it would be prudent to discuss the basic aspects of magnetism in brief. Furthermore, some works carried out on the areas of magnetic storage devices, catalysis and photocatalysis using Zn based ferrites have also been discussed as the application potential of the samples given in this thesis have been explored in these areas.

1.2. Basics of magnetism

Magnetism is one of the oldest regimes of physics. In the year 1600, Dr. William Gilbert hypothesized that the earth itself is a large magnet after thorough and systematic study. Subsequently, a number of historical contributions have helped to outline the modern science of magnetism. In recent times, any phenomenon related to magnetism finds its root at atomic level and the underlined mechanism is governed by the quantum mechanical phenomenon. After conducting a series of experiments, scientists divided different materials in following categories [65,156-158]:

- a) Diamagnetic materials are those that reduce the density of magnetic line of forces while exposed in an external field and results in negative susceptibility. It is a very weak effect in which the externally applied magnetic field lessens the effective current of the electronic orbit and thus produces a magnetic moment opposite in the direction of the external field.
- b) Paramagnetic materials display very feeble magnetization under the action of an external magnetic field. In these materials, the atoms have incomplete atomic shell

resulting in a permanent magnetic moment. So, the magnetic moments have a strong tendency to align themselves along the direction of the applied external magnetic field. However, the thermal energy tries to interrupt the alignment of the moments towards the field direction and the thermal fluctuation leads to only partial alignment in the field direction giving rise to small positive value of magnetic susceptibility.

- c) Ferromagnetic materials possess spontaneous magnetization even in the absence of an external magnetic field. The spontaneous magnetization persists only below the ferromagnetic transition temperature or Curie temperature and above it the magnetic moments get randomly oriented due to thermal fluctuations resulting in destruction of magnetic ordering within the sample. The magnetization of these materials increases with the increase in external magnetic field upto a certain value called the saturation magnetization above which there is no change in magnetization with further increase in field value. The relationship of magnetization and externally applied field is non-linear, i.e., ferromagnetic materials display hysteresis behavior. The residual magnetization that persists even after the field is switched off called the remnant magnetization. Coercivity of the sample is the magnitude of field required to be applied along the direction opposite to easy direction of magnetization to bring the magnetization of the sample to zero. According to the high and low coercivity magnetic materials are classified into hard and soft magnetic materials, respectively. The shape of the hysteresis loop along with the values of coercivity and saturation magnetization is a subject of interest from technological application view point.
- d) Antiferromagnetic materials have two sub-lattices in a unit cell whose magnetizations are equal and opposite in direction necessary for the maintaining minimum energy state. Thus, the neighboring moments balances each other which results in zero net magnetization. The temperature above which the saturation magnetization of

antiferromagnetic materials disappears i.e., thermal energy precludes spin moment alignment, is the Néel temperature of the system.

- e) Ferrimagnetic materials are a special case of antiferromagnetic materials in which two sub-lattices in a unit cell have different atomic arrangement (tetrahedral and octahedral) as a result of which a net magnetization persists. In ferrites the interaction between the (A) and [B] site cation is oxygen mediated and is called superexchange interaction.

1.3. Magnetic dynamics in nano-regime

1.3.1 Concept of anisotropy energy in nanomagnets

The magnetic properties of a material and their application potential in technological fields revolve around the concepts behind the factors controlling the field dependence of magnetization of these substances. Among all the factors, magnetic anisotropy portrays a significant role in governing the shape of the hysteresis loop and is utilized, very often, in the fabrication of most magnetic materials of industrial importance. Simply speaking, “anisotropy” in nanomagnets refers to the directional dependence of their magnetic properties. Anisotropy energy of ferromagnetic crystal acts in such a way that it is easy to magnetize the sample along certain definite crystallographic axes, which consequently are known as the easy axis of magnetization; while the directions along which it is most difficult to magnetize the sample are called hard direction of magnetization [157,159]. There are mainly four different kind of magnetic anisotropy:

1. Magnetocrystalline anisotropy

Magnetocrystalline anisotropy depends on the spin-orbit coupling and strongly influenced by the geometry of the crystal [156]. The most common types of crystal anisotropy are uniaxial anisotropy for hexagonal crystals and cubic anisotropy for the cubic crystals. The uniaxial anisotropy energy is given by the expression:

$$E = K_1 V \sin^2 \theta + K_2 V \sin^4 \theta + \dots$$

where K_1 and K_2 are the anisotropy constants, V is the particle volume and θ is the angle between the symmetry axis and magnetization [65]. In reference to ferromagnetic materials, K_1 is significantly higher than the subsequent higher order terms and so only the first term of the energy expression is considered in maximum cases. Consequently, the uniaxial anisotropy energy for single domain particle is given by

$$E = KV \sin^2 \theta$$

here K is termed as effective anisotropy constant. This expression indicates the presence of two local energy minima separated by energy KV .

In case of the system with cubic symmetry, the anisotropy energy can be expressed with the help of direction cosines ($\alpha_1, \alpha_2, \alpha_3$):

$$E = K_1 V (\alpha_1^2 \alpha_2^2 + \alpha_2^2 \alpha_3^2 + \alpha_3^2 \alpha_1^2) + K_2 V \alpha_1^2 \alpha_2^2 \alpha_3^2$$

Where, $\alpha_1 = \sin\theta \cos\phi$, $\alpha_2 = \sin\theta \sin\phi$ and $\alpha_3 = \cos\theta$ with θ and ϕ being the polar and azimuthal angles, respectively. The value of anisotropy energy generally lies between 10^2 to 10^7 Jm^{-3} . The value of anisotropy energy is lower in case of crystals having high symmetry and higher for crystals with lower symmetry [156].

2. Shape anisotropy:

The shape of the nanoparticles is a factor behind arousal of anisotropy in them. Ideally, a perfectly spherical single domain particle doesnot possess any shape anisotropy as the demagnetization factors are isotropic in all direction. However, it is easier to magnetize a non-spherical particle along a long axis rather than a shorter one as the demagnetizing field is comparatively smaller in the longer direction. A detailed discussion concerning the shape anisotropy can be found in the original article proposed by Stoner and Wohlfarth [160]. For a particle with uniaxial anisotropy along the z axis the shape anisotropy energy density can be expressed by a simple formula

$$K_s = \frac{1}{2} \mu_0 M_s^2 (N_x - N_z)$$

Where N_x and N_z are the demagnetization factors along the equatorial and the polar axis, respectively.

3. Surface anisotropy:

In a fine particle system, surface to volume ratio is very high, resulting in significantly higher magnetic contribution from the surface as compared to the bulk of the same particle. The main origin of surface anisotropy is the breach of symmetry and decline of nearest neighbor coordination in the surface region. With the reduction in particle size, the magnetic contribution from the surface regions becomes more prominent and thus, the surface anisotropy energy plays a crucial role in shaping the magnetic character of the sample. In case of nanoparticles, surface anisotropy energy presides over the magnetocrystalline and magnetostatic energy. The surface anisotropy energy for cubic symmetry is given by [161]

$$E = K_s \cos^2 \theta$$

where θ is the angle between the direction of magnetic moment and normal to the surface. The value of K_s depends upon the magnetostriction constants λ_{100} and λ_{111} and is of the order of magnitude 0.1 to 1 erg/cm² [162]. Surface anisotropy can be studied with the help of Mössbauer spectroscopy.

4. Stress anisotropy:

There is a change in the dimensions of a substance when exposed to a magnetic field, and this effect is called magnetostriction [65]. The anisotropy arising due to magnetostrictive effect is known as stress anisotropy. Stress alone can give rise to an axis of magnetization [65]. Therefore, in the presence of stress, anisotropy must be taken into consideration, along with any other anisotropy that is present. The stress anisotropy energy can be written as,

$$E_s = K_\sigma \sin^2 \theta$$

where K_σ is the stress anisotropy constant and θ is the angle between spontaneous magnetization and applied stress σ [65]. Stress anisotropy energy adopts a key responsibility in modifying the nanoscale magnetic properties of material and its effect is well-pronounced in mechanically activated magnetic nanoparticles.

1.3.2 Superparamagnetism

In an ensemble of uniaxial, single-domain nanoparticles, the anisotropy energy density can be written as:

$$E = K \sin^2 \theta$$

where K is the anisotropy constant and θ is the angle between spontaneous magnetization and the direction of easy axis [65]. For a particle of volume V , an energy barrier $\Delta E = KV$ needs to be overcome in order to reverse its magnetization. Practically, any material possesses fluctuations of thermal energy constantly occurring on a microscopic scale. In 1949, Professor Néel pointed out that below a particular size ΔE becomes extremely small such that energy fluctuations can surmount the anisotropy forces and spontaneously flip the direction of magnetization of those particles, even in the absence of an applied field. If a field is applied, then the external field will try to align the moments, while thermal energy will tend to misalign them. This resembles the behavior of a normal paramagnetic system, but with a noteworthy exception. The magnetic moment of such systems in the presence of a magnetic field is exceptionally high and such a behavior is termed as *superparamagnetism*.

Although superparamagnetism is usually observed in ultra-fine particles, the magnetic properties get strongly modified if the particle sizes are too small such that most of the atoms lie on the surface. In that case, relaxation of the magnetic moment takes place but it would be apt to apply the superparamagnetic model. So there exists a specific range of the particle sizes within which magnetic nanoparticles display superparamagnetism.

The magnetic behaviour displayed by the fine particles also depends on the window time (τ_m) of the experimental technique. When $\tau_m \gg \tau$, the relaxation appears so fast that no time average of the magnetization orientation is recorded. In this case the magnetic moment of the particle maintains thermal equilibrium distribution of orientations akin to Langevin paramagnet but with a notable distinction that magnetic moment of the particle $\sim 10^5$ times the atomic moment and the assembly of particles behaves like a paramagnetic material. On the other hand when $\tau_m \ll \tau$, the relaxation appears so slow (blocked state), with respect to the particular experimental method, the ensemble of particles behaves like an ordered magnetic state. Transition from superparamagnetic to ordered (quasi-static) magnetic state occurs with lowering of temperature. The blocking temperature, separating these two states, is defined as the temperature at which $\tau_m = \tau$. The blocking temperature with respect to a distinct experimental method depends on the particle size. As particle size increases the blocking temperature also increases. Moreover for a particular superparamagnetic sample, the blocking temperature also depends on the window time of the experimental technique and increases with decreasing window time.

1.3.3. Interparticle Interaction and Spin Glass Behavior

The interparticle interactions are inevitable in an assembly of magnetic nanoparticles. Most common interactions present in an assembly of magnetic nanoparticles are dipole-dipole interaction, exchange and superexchange interactions [65]. They are strongly influenced by the volume concentration and can be lessened by doping non-magnetic substances [163]. Magnetic dipolar interactions are omnipresent [164]. For a metallic nanocomposite matrix, RKKY interactions take place. In case of an insulating matrix, superexchange interaction can survive by relying on the type of bonding at the particle–matrix boundary. The superexchange interactions are long-ranged, whereas the exchange interactions exist up to short distance. In ferrite systems, the superexchange interactions are

mediated via oxygen anion. The determination of the interaction effects on the overall magnetic behavior of an assemblage of nanoparticles is extremely complex [162] because there are many factors at play. The disordered arrangements of particles with volume distributions and thermal fluctuations further team up the complication of the problem.

The immediate effect of particle-particle interaction is the alteration of the anisotropy energy barrier. Another probable effect of the interactions is a complete change of regime in which the magnetic properties are no longer relevant to superparamagnetism [165]. Some studies have established the inception of spin glass behaviour [166-168] at low temperatures when the magnetic dynamics is primarily governed by random dipolar interactions. Thus, it is clear that the idealistic situation of non-interacting superparamagnetic ensemble of fine particles may not be stringently applicable when we consider a real sample. Thus, in the presence of interactions (both dipolar and exchange), it is very difficult to define the individual anisotropy energy barrier for each particle. As a result, a possibility of spin-glass like behavior may exist at low temperature.

1.3.4. Collective Magnetic State

In an assembly of non-interacting magnetic nanoparticles, each particle has its own energy barrier (E_B) and a distinct blocking temperature T_B . It may be noted that T_B is always lower than the Curie temperature T_C for any system. The energy barriers of individual are no longer distinct in the presence of interparticle interactions. The superparamagnetic model can still be applied to such systems if the dynamics of the magnetic moment ‘ m ’ is governed by its own E_B , certainly tuned by the interactions. A changeover towards a collective magnetic state [169-172] will take place if it is difficult to define E_B individually for the particles. Then a mean energy barrier of the nanoparticle assembly (E_{ass}) with multiple minima in the phase space will arise. For different experimental techniques, the T_B can be either shift upwards (shorter τ) or downwards (larger τ). If T_B increases with interactions [173-175],

paramagnetic, superparamagnetic, blocked and collective states will appear with increase in temperature. In the blocked state, the magnetic ordering cannot be ferromagnetic as the arrangement of particle magnetic moments is disordered. However, a transition from superparamagnetic state to ferromagnetic state is expected [176,177] when the exchange type interactions are present and the local anisotropy is insignificant with respect to the interactions. The concept of superparamagnetic and collective states of magnetic nanoparticles is explained by Dormann et. al., [159]. According to them, at low temperature, the crystal lattice is disordered and the anisotropy is at random. In this condition, the anisotropy energy barrier for each individual particle becomes trivial and spin relaxation is presided by the anisotropy of the assembly resulting in collective state at low temperature.

Although the transition from the superparamagnetic to the collective state has been discussed, the evaluation of the properties of the collective state is quite challenging. Principally the experiments on fine particle assemblages have usually been carried out with zero-field cooled magnetization (M_{ZFC}) and Mössbauer spectroscopy. However for M_{ZFC} , τ is not uniquely known and for Mössbauer spectroscopy there is difficulty in determining T_B due to the lack of a unique line shape model for particles experiencing superparamagnetic relaxation. In addition, the two τ values are different. Furthermore, the assessment of the effects of interparticle interactions and particle size distribution add to the complexities. In spite of these shortcomings, there is a general agreement that the collective state has spin glass- like behaviour because of the arbitrary nature of the interactions. In many cases the term cluster glass [178,179] has been used, though the properties have been analyzed on the superparamagnetic model. Finally it might be said that magnetic nanoparticles show a progressive inhomogenous freezing (or blocking) via a thermally activated process, which might lead to a collective state at low temperatures.

1.4. Application prospects of Zn based ferrites

In recent past, nano and micro- ferrites have drawn considerable interest due to their potential technological application in magnetic storage devices, magnetic resonance imaging, drug delivery, hyperthermia, catalysis, ferrofluids, photocatalytic degradation of toxic dyes, environmental remediation etc. [31,180-185]. Based on the works on this thesis, the memory effect, catalysis and photocatalytic activity of nano/micro sized Zn based ferrites have been discussed.

1.4.1. Memory or Ageing Effect

The single domain magnetic nanoparticle assemblages display a astonishing phenomenon of history-dependent magnetic memory which can be recorded through dc magnetization versus temperature experiment [186,188-190]. In this study, the system is gradually cooled down from a high temperature, in presence of an external magnetic field. The magnetization of the system is measured as a function of temperature. The cooling is stalled as temperature is reached half way and the field is turned off for few hours before being reinstated. As the system is again heated from a temperature lower than the earlier one, then wiggles are observed in magnetization data at those temperatures where H was turned off, thus, recording a memory of the temperature changes. Such behaviour can be explained in two ways. Firstly, it can be ascribed to the aging phenomena accompanied by memory effects [186]. This elucidation cores on the frustration of the magnetic moments of the particles caused by dipole-dipole interactions resulting in deep energy vales arresting the system for extended times [187]. An alternate source for this memory effect can be accredited to broad distribution of particle size [188-190]. The polydispersive nature of the particle volume leads to a widespread distribution of blocking temperatures. The memory effect i.e., wiggles at all temperature steps arise as the system is halted at those temperatures, which lie within blocking temperatures of different sized particles.

1.4.2. Catalysis

In recent years, eco-friendly catalyst materials and benign solvents have engrossed the attention of scientific community owing to green chemistry view point and thus lead towards advancement of sustainable measures [191,192]. In connection to this aspect, nanocatalysts have materialized as of the most important sustainable resources pertaining to their good catalytic activity modulated by their small size, large surface area, selectivity, recovery and reusability [192-194]. Furthermore, the magnetic nanoparticles have appeared as a great player in the field of nanocatalysts citing their magnetic properties and the simplicity of recouping and recycling of the catalysts after reaction completion [195-201]. Thus, the loss of catalyst related to traditional filtration and centrifugation methods can be avoided and thus supports the principles of green chemistry [202]. In particular, catalysis by nanoparticles of transition metal elements such as Cu, Fe, Ni etc. has garnered huge interest due to their large surface area and unique thermal, chemical, electronic, magnetic and optical properties [203-207]. The environmentally benign Ni-NiO nanoparticles have shown fascinating catalytic activities [208]. Ferrite nanoparticles have emerged as excellent photocatalysts in the chemical reactions like C-C coupling [209], reduction [209], oxidation [209] and multicomponent reactions [210] mainly due to their eco-friendly nature, ease of access and price affordability. Current studies have revealed that composites with mixed ferrites are talented catalysts for electrocatalytic reactions concerning numerous redox reactions [209]. Nansized CoFe_2O_4 proved to be an effective catalyst in a Knoevenagel condensation reaction of assorted aldehydes [211]. CoFe_2O_4 nanocrystals catalyzed aerobic oxidation of cyclohexane to cyclohexanol or cyclohexanone under solvent-free conditions [212]. Iron and iron-cobalt oxide nanoparticles catalyzed breaking down of methanol into H_2 and CO was [213]. Zinc ferrite nanoparticles showed high efficiency and selectivity towards synthesis of chalcones by means of Claisen—Schmidt condensation reaction [214].

NiFe₂O₄ nanoparticles acted as an excellent catalyst in the Knoevenagel condensation of aldehydes and methylene compounds under mild conditions [215]. These features make the spinel ferrites beneficial from industrial, economical and environmental point of views. In the present thesis, we have reported the synthesis of coumarin-3-carboxamide via multicomponent reaction with the help of nanosized Co_{0.8}Zn_{0.2}Fe₂O₄ as an indispensable catalyst.

1.4.3. Photocatalysis

Photocatalysis comprises two types of applications broadly: (i) degradation of organic pollutant or dyes from different water bodies [216] and (ii) light energy conversion corresponding to water splitting [217,218]. Spinel ferrite nano and micro- ferrites are in the limelight owing to their ability to eliminate pollutants from wastewater through photodegradation process. For this process, ferrites are used as photocatalysts directly or by grouping with semiconducting materials and in presence of oxidants such as H₂O₂ [90,219]. Dyes are one the major pollutants comprised of organic compounds and are dumped by industries in water bodies causing environmental pollution. These pollutant dyes can be removed from water by their photocatalytic degradation [220-225]. The organic compounds forming major ingredients in these pollutants can be degraded to CO₂ and water through photocatalytic reactions without generation of additional waste or byproducts [220]. There are series of chemical reactions in photocatalysis procedure that also affect its surrounding nature [220,226]. These reactions take place between the catalysts and the medium in the presence of irradiation ranging from ultraviolet to visible light. This irradiation causes excitation of atoms of photocatalysts such that electrons can jump from valence band to conduction band, leaving equal number of holes at the valence band. These electron hole pairs accelerate further oxidation and reduction process involved in photocatalytic reactions which produces radical oxygen species [227]. These radicals can degrade the organic

compounds of the dyes and may convert them into CO₂, water, and other gaseous chemicals without any formation of byproducts. Moreover, electron hole pairs can originate hydrogen gas through several chemical reactions that may be utilized as an energy resource [228]. Schematic diagram of photocatalytic mechanism depicted in Figure 4. The photocatalysis process can be efficient when the following factors come into account, which are the power of the irradiation [229], the choice of catalyst material [230], the chemical [231] and physical [232] nature of the medium. Moreover, photocatalysts should have large surface area [233] and good optical properties such that photocatalysts with proper band gap energy can be a good absorber to absorb radiation sufficiently [234]. It should be noted that photocatalytic activity can be monitored with the addition of dopants or metal ions [235].

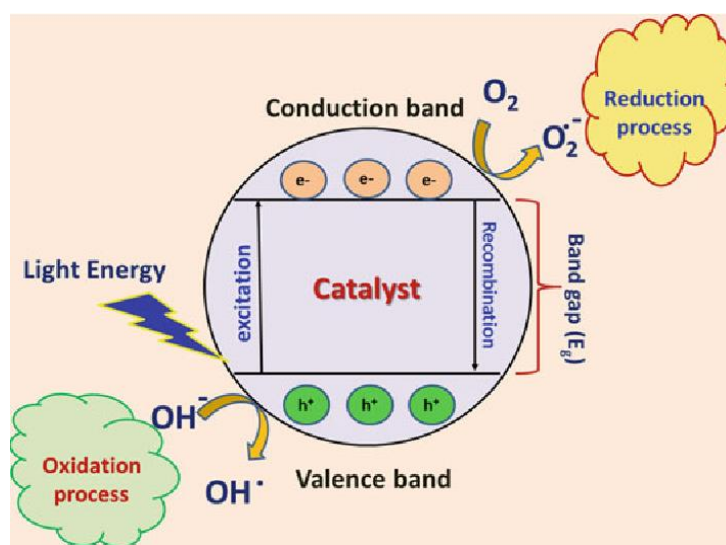


Figure 4. Schematic diagram of photocatalytic mechanism [165].

Spinel ferrites have excelled as photocatalysts because transition metal produces ions in the octahedral [B] sites that exchange with the tetrahedral (A) sites of spinel structure to improve their photocatalytic activity [226]. Moreover, spinel ferrite composite with polymers and oxides boosts the photocatalytic activity as well as enhances their chemical stability in basic and acidic medium [236-239]. The spinel ferrites are desirable for the degradation of pollutants in water under visible light irradiation through photocatalytic reactions as they

have appropriate band gap energy for absorption of visible light [240-244]. Although ZnFe_2O_4 are widely used in photocatalytic activity under visible light irradiation, but poor quantum efficiency of ZnFe_2O_4 reduces its photocatalytic performance significantly [245]. It has been observed that the photocatalytic activity of ZnFe_2O_4 under visible light can be increased by modulating its cation distribution through doping of Co^{2+} ions in proper stoichiometry. It may be note that Co substituted zinc ferrite either possess narrow energy band gap compared to that of zinc ferrite or may have metastable states within the energy band gap, which shifts the absorption band towards visible region. Thus, $\text{Co}_{1-x}\text{Zn}_x\text{Fe}_2\text{O}_4$ exhibits excellent photocatalytic performance under visible light irradiation [246]. In the present thesis, we have reported the photocatalytic activity of $\text{Co}_{0.5}\text{Zn}_{0.5}\text{Fe}_2\text{O}_4$ microspheres synthesized by solvothermal method for the degradation of Congo Red under dark, visible and UV light irradiation.

1.5. Scope of the work

The subject matter of the current thesis is to (i) study the structural, microstructural, optical, magnetic and hyperfine properties of $\text{Co}_{0.5}\text{Zn}_{0.5}\text{Fe}_2\text{O}_4$, $\text{Co}_{0.8}\text{Zn}_{0.2}\text{Fe}_2\text{O}_4$, nanoparticles and, ZnFe_2O_4 solid and hollow, $\text{Co}_{0.5}\text{Zn}_{0.5}\text{Fe}_2\text{O}_4$ microspheres, (ii) study the factors that led to the arousal of magnetic features like superparamagnetism, spin glass like behavior and collective magnetic state in relation to the above mentioned samples, (iii) investigate the application potential of these samples in the field of magnetic storage device and catalysis, (iv) enhance the industrial applicability of the nanosized ferrites by overcoming their innate superparamagnetic relaxation by development of magnetic ordering in the systems, (v) avert spin canting and increase saturation magnetization by regulating the cation distribution and forming microspheres by self-assembly of the corresponding nanoparticles. The scopes of the thesis are as follows:

- (i) Synthesis of nanosized $\text{Co}_{0.5}\text{Zn}_{0.5}\text{Fe}_2\text{O}_4$ by coprecipitation method followed by high energy ball milling and hydrothermal method, $\text{Co}_{0.8}\text{Zn}_{0.2}\text{Fe}_2\text{O}_4$ nanoparticles by coprecipitation method followed by high energy ball milling and thermal treatment, ZnFe_2O_4 solid and hollow microspheres, and $\text{Co}_{0.5}\text{Zn}_{0.5}\text{Fe}_2\text{O}_4$ microspheres by solvothermal method.
- (ii) Structural, microstructural, optical, magnetic and hyperfine characterization of the above mentioned samples by using powder x-ray diffraction (PXRD), Electron microscopic (FESEM, TEM, HRTEM,), Fourier transform infrared spectroscopic (FTIR), UV-Vis, UV-vis diffuse reflectance spectroscopic (DRS), DLS and Zeta-potential, photoluminescence (PL), dc magnetic and Mössbauer spectroscopic measurement techniques.
- (iii) To study the effects of mechanical activation caused by high energy ball milling on the structural, magnetic and hyperfine properties of nanosized $\text{Co}_{0.5}\text{Zn}_{0.5}\text{Fe}_2\text{O}_4$.
- (iv) In-depth study on morphology dependent magnetic properties of ZnFe_2O_4 solid and hollow microspheres.
- (v) To examine the possibility of using the $\text{Co}_{0.5}\text{Zn}_{0.5}\text{Fe}_2\text{O}_4$ nanoparticles for storing, generating and retrieving binary bit pattern by utilizing the dc memory protocol.
- (vi) To examine the capacitive behavior of nanosized $\text{Co}_{0.5}\text{Zn}_{0.5}\text{Fe}_2\text{O}_4$ through electrochemical study.
- (vii) To inspect the catalytic efficiency of nanosized $\text{Co}_{0.8}\text{Zn}_{0.2}\text{Fe}_2\text{O}_4$ in synthesizing coumarin-3-carboxamide through multicomponent reaction.
- (viii) To investigate the photocatalytic activity of $\text{Co}_{0.5}\text{Zn}_{0.5}\text{Fe}_2\text{O}_4$ microspheres for the removal of dye under dark, visible and UV light irradiation.

References

1. G. Mansoori, F. Soelaiman, *ASTMInt.* 2 (2005) 1–22.
2. National Nanotechnology Initiative (NNI). Available online: www.nano.gov.
3. F. Allhoff, *Nanoethics* 1 (2007) 185–210.
4. R.P. Feynman, *Eng. Sci.* 1960, 23, 22–36.
5. N. Taniguchi, C. Arakawa, T. Kobayashi, Tokyo, Japan, 26–29 August 1974.
6. S. Bayda, Md. Adeel, T. Tuccinardi, M. Cordani, F. Rizzolio, *Molecules* 25 (2020) 112.
7. I. Freestone, N. Meeks, M. Sax, C. Higgitt, *Gold Bull.* 2007, 40, 270–277.
8. D.J. Barber, I.C. Freestone, *Archaeometry* 1990, 32, 33–45.
9. F.E. Wagner, S. Haslbeck, L. Stievano, S. Calogero, Q.A. Pankhurst, K.P. Martinek, *Nature* 2000, 407, 691–692.
10. C.P. Poole, F.J. Owens, John Wiley & Sons: New York, NY, USA, 2003.
11. M. Faraday, *Philos. Trans. R. Soc. Lond.* 1857, 147, 145–181.
12. G. Binnig, H. Rohrer, C. Gerber, E. Weibel, *Appl. Phys. Lett.* 40 (1982) 178.
13. G. Binnig, H. Rohrer, C. Gerber, E. Weibel, *Phys. Rev. Lett.* 49 (1982) 57–61.
14. D.M. Eigler, E.K. Schweizer, *Nature* 1990, 344, 524–526.
15. G. Binnig, C.F. Quate, C. Gerber, *Phys. Rev. Lett.* 56 (1986) 930–933.
16. G. Binnig, U.S. Patent 4724318A, 16 October 1990.
17. C. Kinnear, C. T.L. Moore, L. Rodriguez-Lorenzo, B. Rothen-Rutishauser, A. Petri-Fink, *Chem. Rev.* 117 (2017) 11476–11521.
18. V. Weissig, T.K. Pettinger, N. Murdock, *Int. J. Nanomed.* 9 (2014) 4357–4373.
19. P.Y. Lee, K.K.Y. Wong, *Curr. Drug Deliv.* 8 (2011) 245–253.
20. Y. Yuan, Z. Gu, C. Yao, D. Luo, D. Yang, *Small* 15 (2019) 1900172.
21. Georgia C. Papaefthymiou, Taylor & Francis Group, LLC 2022.

22. S. Chikazumi, S. Taketomi, M. Ukita, M. Mizukami, H. Miyajima, M. Setogawa, Y. Kurihara, J. Magn. Mater. 1987, 65, 245.
23. A.-H. Lu, W. Schmidt, N. Matoussevitch, H. BPnnermann, B. Spliethoff, B. Tesche, E. Bill, W. Kiefer, F. SchVth, Angew. Chem. 2004, 116, 4403; Angew. Chem. Int. Ed. 2004, 43, 4303.
24. S. C. Tsang, V. Caps, I. Paraskevas, D. Chadwick, D. Thompsett, Angew. Chem. 2004, 116, 5763; Angew. Chem. Int. Ed. 2004, 43, 5645.
25. A. K. Gupta, M. Gupta, Biomaterials 2005, 26, 3995.
26. S. Mornet, S. Vasseur, F. Grasset, P. Verveka, G. Goglio, A. Demourgues, J. Portier, E. Pollert, E. Duguet, Prog. Solid State Chem. 2006, 34, 237.
27. Z. Li, L. Wei, M. Y. Gao, H. Lei, Adv. Mater. 2005, 17, 1001.
28. T. Hyeon, Chem. Commun. 2003, 927.
29. D. W. Elliott, W.-X. Zhang, Environ. Sci. Technol. 2001, 35, 4922.
30. M. Takafuji, S. Ide, H. Ihara, Z. Xu, Chem. Mater. 2004, 16, 1977.
31. An-Hui Lu, E. L. Salabas, F. Schüth, Angew. Chem. Int. Ed. 46 (2007) 1222 – 1244.
32. A. Moser, K. Takano, D. T. Margulies, M. Albrecht, Y. Sonobe, Y. Ikeda, S. Sun and E. Fullerton, J. Phys. D: Appl. Phys. 35 (2002) 157 – 167.
33. J. Gao, H. Gu and B. Xu, *Acc. Chem. Res.* 42 (2009) 1097 – 1107.
34. J. Jiménez, R. Sheparovych, M. Pita, A. N. García, E. Dominguez, S. Minko and E. Katz, *J. Phys. Chem. C* 112 (2008) 7337-7344.
35. M. Elrouby, A. M. Abdel-Mawgoud and R. Abd El-Rahman, *J. Mol. Struct.* 1147 (2017) 84-95.
36. D. Zhang, J. Cheng, X. Yang, B. Zhao and M. Cao, *J. Mater. Sci.* 49 (2014) 7221-7230.
37. L. G. Petrescu, M. C. Petrescu, V. Ioniță, E. Cazacu and C. D. Constantinescu, *Materials* **12** (2019) 3173-1 – 3173-12.

38. V. Socoliuc, D. Peddis, V. I. Petrenko, M. V. Avdeev, D. Susan-Resiga, T. Szabó, R. Turcu, E. Tombácz and L. Vékás, *Magnetochemistry* 6 (2020) 2-1 – 2-36.
39. J. A. Nelson, L. H. Bennett and M. J. Wagner, *J. Am. Chem. Soc.* 124 (2002) 2979-2983.
40. W. Andrä, U. Häfeli, R. Hergt and R. Misri, *Handbook of Magnetism and Advanced Magnetic Materials* (Novel Materials 4 (2007) 2536–22568, John Wiley & Sons, Chichester, UK).
41. C. C. Berry and A. S. G. Curtis, *J. Phys. D: Appl. Phys.* 36 (2003) R198–R206.
42. P. Tartaj, M. del Puerto Morales, S. Veintemillas-Verdaguer, T. González-Carreño and C. J. Serna, *J. Phys. D: Appl. Phys.* 36 (2003) R182–R197.
43. A. H. Lu, E. L. Salabas and F. Schüth, *Angew. Chem. Int. Ed.* 46 (2007) 1222 – 1244.
44. I. Percin, V. Karakoc, S. Akgol, E. Aksoz and A. Denizli, *Mater. Sci. Eng. C* 32 (2012) 1133–1140.
45. U. Häfeli, W. Schütt, J. Teller, M. Zborowski, (Scientific and Clinical Applications of Magnetic Carriers, Plenum Press: New York, NY, USA, 2010)
46. A. Inoue, F. Kong, *Soft magnetic materials*, 2020.
47. Z. Liu, D. Zhang, S. Han, C. Li, B. Lei, W. Lu, J. Fang, C. Zhou, *J. Am. Chem. Soc.* 127 (2005) 6–7.
48. A. Ramzannezhad, P. Gill and A. Bahari, *BioNanoMaterials* 18 (2017) 3-4.
49. A. Fert and L. Piraux, *J. Magn. Magn. Mater.* 200 (1999) 338 – 358.
50. X. C. Sun, Y.H. Huang and D.E. Nikles, *Int. J. Nanotechnol.* 1 (2004) 328–346.
51. W. Wicke, A. Ahmadzadeh, V. Jamali, H. Unterweger, C. Alexiou and R. Schober, *IEEE Trans. Nanobiosci.* 18 (2019) 156–169.
52. A. Hendrych, R. Kubínek and A.V. Zhukov (Modern Research and Educational Topics in Microscopy, Formatex: Badajoz, Spain, 2007)

-
53. S. Riaz, S. Naseem, and X. Han, *2015 IEEE International Magnetics Conference (INTERMAG)*, Beijing, pp. 1-1, 2015.
54. A. Monsalve, J. Vicente, A. Grippin and J. Dobson, *IEEE Magn. Lett.* 8 (2017) 1–5.
55. N. Ahmed, H. Fessi and A. Elaissari, *Drug Discov. Today* 17 (2012) 928–934.
56. D. Ho, X. Sun and S. Sun, *Accounts Chem. Res.* 44 (2011) 875–882.
57. P. M. Paulus, H. BPnnemann, A. M. van der Kraan, F. Luis, J. Sinzig, L. J. de Jongh, *Eur. Phys. J. D* 9 (1999) 501.
58. H.-J. Zhang, H.-M. Xiong, Q.-G. Ren, Y.-Y. Xia, J.-L. Kong, *J. Mater. Chem.*, 22 (2012) 13159.
59. M. M. Shirolkar, R. Das, T. Maity, P. Poddar, S. Kulkarni, *J. Phys. Chem. C*, 116 (2012) 19503.
60. S. Majumder, S. Dey, K. Bagani, S. K. Dey, S. Banerjee, S. Kumar, *Dalton Trans.* 44 (2015) 7190.
61. J. Nogués, J. Sort, V. Langlais, V. Skumryev, S. Suriñach, J. S. Muñoz, M. D. Baró, *Phys. Rep.* 422 (2005) 65.
62. S. Yadav, A. Kumar Sharma, P. Kumar, *Front. Bioeng. Biotechnol.* 8 (2020) 1 – 24.
63. S. Singamaneni, V. N. Bliznyuk, C. Binek, E.Y. Tsybal, *J. Mater. Chem.*, 21 (2011) 16819.
64. Karla R. Sanchez-Lievanos, James L. Stair, and Kathryn E. Knowles, *Inorg. Chem.* 60 (2021) 4291–4305.
65. B. D. Cullity and C. D. Graham, *Introduction To Magnetic Materials*, John Wiley & Sons, Inc., Hoboken, New Jersey (2009).
66. F. G. da Silva, J. Depeyrot, A. F. C. Campos, R. Aquino, D. Fiorani and D. Peddis, *J. Nanosci. Nanotechnol.* 19 (2019) 4888–4902.
-

67. S. Dey, S. K. Dey, K. Bagani, S. Majumder, A. Roychowdhury, S. Banerjee, V. R. Reddy and S. Kumar, *Appl. Phys. Lett.* 105 (2014) 063110-1 – 063110-4.
68. S. Dey, S. K. Dey, S. Majumder, A. Poddar, P. Dasgupta, S. Banerjee, S. Kumar, *Physica B* 448 (2014) 247–252.
69. S. Dey, S.K. Dey, B. Ghosh, V.R. Reddy, S. Kumar, Structural, microstructural, *Mater. Chem. Phys.* 138 (2013) 833–842.
70. R. N. Bhowmik and R. Ranganathan, *J. Mater. Sci.* 37 (2002) 4391 – 4398.
71. S. Dey, S. K. Dey, B. Ghosh, P. Dasgupta, A. Poddar, V.R. Reddy, S. Kumar, *J. Appl. Phys.* 114 (2013) 093901-1–093901-12.
72. B. Ghosh, S. Kumar, A. Poddar, C. Mazumdar, S. Banerjee, V.R. Reddy, A. Gupta, *J. Appl. Phys.* 108 (2010) 034307-1–034307-8.
73. S. Chakraverty, B. Ghosh, S. Kumar and A. Frydman, *Appl. Phys. Lett.* 88 (2006) 042501-1 – 042501-3.
74. K. K. Kefeni, T. A. M. Msagati and B. B. Mamba, *Mater Sci Eng B* 215 (2017) 37–55.
75. Y. Liu, J. jun Li, F. fei Min, J. bo Zhu, M. xu Zhang, *J. Magn. Magn.Mater.* 354 (2014) 295–298.
76. O. F. Odio and E. Reguera, *Nanostructured spinel ferrites: Synthesis, functionalization, nanomagnetism and environmental applications* (Magnetic Spinels-Synthesis, Properties and Applications, pp. 185-216, 2017).
77. S. F. Shaikh, M. Ubaidullah, R. S. Mane and A. M. Al-Enizi, *Types, Synthesis methods and applications of ferrites Spinel* (Ferrite Nanostructures for Energy Storage Devices, pp. 51-82, 2020).
78. W. S. Galvão, D. Neto, R. M. Freire and P. B. Fechine, *Solid State Phenom.* 241 (2016) 139-176).
-

-
79. Jianping Ge, Yongxing Hu, Maurizio Biasini, Ward P. Beyermann, and Yadong Yin, *Angew. Chem.* 119 (2007) 4420–4423.
80. Yao-Ming Hao, Shi-Yun Lou, Shao-Min Zhou, Rui-Jian Yuan, Gong-Yu Zhu and Ning Li, *Nanoscale Res. Lett.* 7 (2012) 100.
81. S. Singamaneni, V. N. Bliznyuk, C. Binek and E. Y. Tsymbal, *J. Mater. Chem.* 21 (2011) 16819.
82. H. Deng, X. Li, Q. Peng, X. Wang, J. Chen, and Y. Li, *Angew. Chem. Int. Ed.* 44 (2005) 2782–2785.
83. N. Bao, L. Shen, Y-H A. Wang, J. Ma, D. Mazumdar and A. Gupta, *J. Am. Chem. Soc.* 131 (2009) 12900–12901.
84. H. L. Yuan, Y. Q. Wang, S. M. Zhou, L. S. Liu, X. L. Chen, S. Y. Lou, R. J. Yuan, Y. M. Hao and N. Li, *Nanoscale Res Lett.* 5 (2010) 1817 – 1821.
85. K. R. Lee, S. Kim, D. H. Kang, J. I. Lee, Y. J. Lee, W. S. Kim, D-H. Cho, H. B. Lim, J. Kim and N. H. Hur, *Chem Mater.* 20 (2008) 6738 – 6742.
86. P. Guo, L. Cui, Y. Wang, M. Lv, B. Wang and X. S. Zhao, *Langmuir* 29 (2013) 8997–9003.
87. C. Pereira, A. M. Pereira, C. Fernandes, M. Rocha, R. Mendes, M. P. Fernández-García, A. Guedes, P. B. Tavares, J-M. Grenèche, J. P. Araújo and C. Freire, *Chem. Mater.* 24 (2012) 1496–1504.
88. K. K. Kefeni, T. A. Msagati, T. T. Nkambule and B. B. Mamba, *Mater. Sci. Eng.* 107 (2020) 110314-1 – 110314-19.
89. M. Amiri, M. S. Niasari and A. Akbari, *Adv. Colloid Interface Sci.* 265 (2019) 29–44.
90. T. A.P. R. Santos, *Trend. Anal. Chem.* 62 (2014) 28–36.
91. Y. Xin, X. Fu-bing, L. Hong-wei, W. Feng, C. Di-zhao, W. Zhao-yang, *Electrochim. Acta* 109 (2013) 750–755.
-

-
92. K. K. Kefeni and B. B. Mamba, *Sustainable Materials and Technologies* 23 (2020) e00140-1 – e00140-18.
93. L. George, C. Viji, M. Maheen and E. M. Mohammed, *Mater. Res. Express* 7 (2020) 015014-1 – 015014-17.
94. K. K. Kefeni, B. B. Mamba and T. A. Msagati, *Sep. Purif. Technol.* 188 (2017) 399-422.
95. B. Bhujun, M. T. Tan and A. S. Shanmugam, *Results Phys* 7 (2017) 345–353.
96. W. S. Galvão, D. M. A. Neto, R. M. Freire and P. B. A. Fechine, *Solid State Phenom.* 241 (2016) 139-176.
97. A. Hanini, K. Kacem, J. Gavard, H. Abdelmelek and S. Ammar, (*Handbook of Nanomaterials for Industrial Applications*, Elsevier, pp. 638-661, 2018).
98. M. S. A. Darwish, H. Kim, H. Lee, C. Ryu, J. Y. Lee and J. Yoon, *Nanomaterials* 9 (2019) 1176-1 – 1176-22.
99. V. Skumryev, S. Stoyanov, Y. Zhang, G. Hadjipanayis, D. Givord, and J. Nogues, *Nature* 423 (2003) 850 – 853.
100. L. Wu, A.M. Garcia, Q. Li and S. Sun, *Chem. Rev.* 116 (2016) 10473–10512.
101. C. Upadhyay, H.C. Verma and S. Anand, *J. Appl. Phys.* 95 (2004) 5746–5751.
102. R. N. Bhowmik, R. Ranganathan, S. Sarkar, C. Bansal, and R. Nagarajan, *Phys. Rev. B* 68 (2003) 134433.
103. S. Urcia-Romero, O. Perales-Perez, O. N. C. Uwakweh, C. Osorio, and H. A. Radovan, *J. Appl. Phys.* 109 (2011) 07B512.
104. N. Ponpandian, A. Narayanasamy, C.N. Chinnasamy, N. Sivakumar, J. M. Greneche, K. Chattopadhyay, K. Shinoda, B. Jeyadevan, and K. Tohji, *Appl. Phys. Lett.* 86 (2005) 192510-1 192510-3.
105. B.H. Liu, J. Ding, Z.L. Dong, C.B. Boothroyd, J.H. Yin, J.B. Yi, *Phys. Rev. B* 74 (2006) 184427.
-

106. V. Sepelák, S. Wißmann, K.D. Becker, *J. Magn. Magn. Mater.* 203 (1999) 135 – 137.
107. R. Mondal, S. Dey, K. Sarkar, P. Dasgupta, S. Kumar, *Mater. Res. Bull.* 102 (2018) 160–171.
108. M. Veverka, P. Veverka, Z. Jiráček, O. Kaman, K. Knížek, M. Maryško, E. Pollert and K. Závěta, *J. Magn. Magn. Mater.* 322 (2010) 2386–2389.
109. D. Yu, X. Sun, J. Zou, Z. Wang, F. Wang, and K. Tang, *J. Phys. Chem. B* 110 (2006) 21667-21671.
110. P. Hu, L. Yu, A. Zuo, C. Guo, and F. Yuan, *J. Phys. Chem. C* 113 (2009) 900–906.
111. B. Yong Yu and Seung-Yeop Kwak, *J. Mater. Chem.* 20 (2010) 8320–8328.
112. M. Penchal Reddy, A.M.A. Mohamed, *Microporous and Mesoporous Mater.* 215 (2015) 37 – 45.
113. P. Reddy Matli, X. Zhou, D. Shiyu, Q. Huang, *Int Nano Lett* 5 (2015) 53–59.
114. Q. Zhang, M. Zhu, Q. Zhang, Y. Li, H. Wang, *J. Magn. Magn. Mater.* 321 (2009) 3203–3206.
115. B. Yong Yu and Seung-Yeop Kwak, *Dalton Trans.* 40 (2011) 9989.
116. S. Rajesh Kumar, M. Manivel Raja, D. Mangalaraj, C. Viswanathan, N. Ponpandian, *Mater. Lett.* 110 (2013) 98–101.
117. D. Nagpal, V. Gajraj, A. Kumar, K.I. Gnanasekar, C.R. Mariappan, *Physica B* 630 (2022) 413679.
118. Z. G. Jia, D.P. Ren, Y.C. Liang, R.S. Zhu, *Mater. Lett.* 65 (2011) 3116 – 3119.
119. X. Zhou, J. Liu, C. Wang, P. Sun, X. Hu, X. Li, K. Shimanoe, N. Yamazoe, G. Lu, *Sens. Actuators B: Chem.* 206 (2015) 577–583.
120. A. Yan, X. Liu, R. Yi, R. Shi, N. Zhang, and G. Qiu, *J. Phys. Chem. C* 112 (2008) 8558–8563.
121. P. Saha, R. Rakshit, M. Alam, and K. Mandal, *Phys. Rev. Appl.* 11, (2019) 024059.

-
122. P. A. Vinosha, A. Manikandan, A. Sherley Judith Ceicilia, A. Dinesh, G. Francisco Nirmala, A. Christy Preetha, Y. Slimani, M.A. Almessiere, A. Baykal, B. Xavier, *Ceram. Int.* 47 (2021) 10512–10535.
123. R. Sagayaraj, S. Aravazhi, G. Chandrasekaran, *Int. Nano Lett.* 11 (2021) 307–319.
124. M. Dhiman, R. Sharma, V. Kumar, S. Singhal, *Ceram. Int.* 42 (2016) 12594 – 12605.
125. Xiaogu Huang, Jing Zhang, Shaorong Xiao, Guosheng Chen, *J. Am. Ceram. Soc* 97 (2014) 1363–1366.
126. M.H. Yousefi, S. Manouchehri, A. Arab, M. Mozaffari, Gh R. Amiri, J. Amighian, *Mater. Res. Bull* 45 (2010) 1792–1795.
127. T. Mariam, I.N. Esha, M.N. Khan, S. Choudhury, K.H. Maria, *J. Ceram. Process. Res* 21 (2020) 442–449.
128. G. Sathishkumar, C. Venkataraju, K. Sivakumar, *Mater. Sci. Appl* 1 (2010) 19–24.
129. Jerome J. Green, Frank Sandy, A catalog of low power loss parameters and high power thresholds for partially magnetized ferrites.", *IEEE Trans. Microw. Theor. Tech* 22 (1974) 645–651.
130. V. Mamelì, A. Musinu, Andrea Ardu, Guido Ennas, D. Peddis, D. Niznansky, C. Sangregorio, C. Innocenti, Nguyen Tk Thanh, C. Cannas, *Nanoscale* 8 (2016) 10124–10137.
131. B. Gillot, F. Jemmali, *Phys. Status Solidi* 76 (1983) 601–608.
132. B. Ünal, A. Baykal, *J. Supercond. Nov. Magnetism* 27 (2014) 469–479.
133. E. Kumar, R. Ranjith, T. Jayaprakash, A. Kumar, S. Kumar, *J. Phys. Chem. Solid* 74 (2013) 110–114.
134. M. Ben Ali, K. El Maalam, H. El Moussaoui, O. Mounkachi, M. Hamedoun, R. Masrour, E.K. Hlil, A. Benyoussef, *J. Magn. Magn Mater* 398 (2016) 20–25.
135. X. Huang, J. Zhang, S. Xiao, G. Chen, *J. Am. Ceram.Soc* 97 (2014) 1363–1366.
-

136. N. A. Algarou, Y. Slimani, M.A. Almessiere, A. Sadaqat, A.V. Trukhanov, M. A. Gondal, A.S. Hakeem, S.V. Trukhanov, M.G. Vakhitov, D.S. Klygach, A. Manikandan, A. Baykal, *Nanomaterials* 10 (2020) 2134.
137. N.A. Algarou, Y. Slimani, M.A. Almessiere, A. Baykal, S. Guner, A. Manikandan, I. Ercan, *J. Magn. Magn Mater.* 499 (2020) 166308.
138. B.M. Berkovsky, V. F. Medvedev, M. S. Krakov, *Magnetic Fluids: Engineering Applications*, 1993, 243–243.
139. V. Pilati, G. Rafael Cabreira, G. Guilherme, C. Priscilla, F. G. Silva, F. L. Paula, R. Perzynski, G. F. Goya, R. Aquino, J. Depeyrot, *J. Phys. Chem. C* 122 (2018) 3028–3038.
140. S. Amiri, H. Shokrollahi, *Mater. Sci. Eng. C* 33 (2013) 1–8.
141. C. Galup-Montoro, M. C. Schneider, Itamar JB. Loss, *IEEE J. Solid State Circ* 29 (1994) 1094–1101.
142. E.W. Gorter, *Nature* 165 (4203) (1950) 798–800.
143. John Comyn (Ed.), *Polymer Permeability*, Springer Science & Business Media, 2012.
144. P.I. Slick, "Ferrites for Non-microwave applications." *Ferromagnetic Materials: A Handbook on the Properties of Magnetically Ordered Substances*, 1980, pp. 189–241.
145. A. Mary Jacintha, A. Manikandan, K. Chinnaraj, S. Arul Antony, P. Neeraja, *J. Nanosci. Nanotechnol* 15 (2015) 9732–9740.
146. L. Svensson, K. Frogner, P. Jeppsson, T. Cedell, M. Andersson, *J. Magn. Magn Mater* 324 (18) (2012) 2717–2722.
147. E. Mazarío, P. Herrasti, M. P. Morales, N. Menéndez, *Nanotechnology* 23 (2012) 355708.
148. P. Annie Vinosha, A. Manikandan, R. Ragu, Y. Slimani, A. Baykal, Belina Xavier, *J. Alloys Compd* 13 (2020) 157517.

149. A. Manikandan, M. Durka, S. Arul Antony, J. Supercond. Nov. Magnetism 27 (2014) 2841–2857.
150. Ali Ghasemi, Mohammad Mousavinia, Ceram. Int 40 (2014) 2825–2834.
151. I. Soibam, S. Phanjoubam, C. Prakash, J. Alloys Compd 475 (2009) 328–331.
152. A. Manikandan, L. John Kennedy, M. Bououdina, J. Judith Vijaya, J. Magn. Magn Mater 349 (2014) 249–258.
153. A.V. Raut, R.S. Barkule, D.R. Shengule, K.M. Jadhav, J. Magn. Magn. Mater. 358 (2014) 87–92.
154. A. Hassadee, T. Jutarosaga, W. Onreabroy, Procedia Engineering 32 (2012) 597–602.
155. Daliya S. Mathew, Ruey-Shin Juang, Chem. Eng. J 129 (2007) 51–65.
156. S. Chikazumi, Physics of Ferromagnetism, 2nd ed., (Oxford University Press, Oxford, 1997).
157. C. Kittel, Reviews of Modern Physics, 21, (1949).
158. Jan Smit, eds, Magnetic properties of materials, (Inter University Electronics Series, vol. 13, McGraw Hill, 1971).
159. J. L. Dormann, D. Feorani and E. Tronc, Adv. Chem. Phys., vol. XVIII, Edited by I. Prigogine and S. A. Rice, John Wiley & Sons, (1997).
160. E. C. Stoner and E. P. Wohlfarth, Philos. Trans. Roy. Soc. (London, A240, 599) (Reprinted in 1991 in IEEE Trans. Magnetism, 27, 3475).
161. L. Néel, J. Phys. Radium, 15, 225 (1954).
162. J. L. Dormann and D. Feorani, eds., Magnetic Properties of Fine Particles, (North-Holland, Amsterdam, 1992).
163. B. Huke and M. Lucke, Rep. Prog. Phys, 67, 1731, (2004).
164. S. Morup and E. Tronc, Phys. Rev. Lett, 72, 3278, (1994).
165. M. F. Hansen and S. Morup, Phys. Rev. Lett, 90, 059705, (2003).
-

166. T. Jonsson, J. Mattson, C. Djuberg, F. A. Khan, P. Nordblad and P. Svedlindh, *Phys. Rev. Lett.*, **72**, 4138, (1995).
167. T. Jonsson, P. Nordblad and P. Svedlinch, *Phys. Rev. B*, **57**, 497, (1998).
168. P. Jonsson, M. F. Hansen and P. Nordblad, *Phys. Rev. B*, **61**, 1261, (2000).
169. M. Guzman, J. L. Delplancke, G. J. Long, J. Delwiche, M. J. H. Franksin and F. Granjean, *J. Appl. Phys.*, **92**, 2634, (2002).
170. X. Batlle and A. Labarta, *J. Phys. D* **35** (2002) R15.
171. W. Luo, S. R. Nagel, T. F. Rosenbaum R. E. Rosenweig, *Phys. Rev. Lett.* **67** (1991) 2121.
172. C. Cannas, M. F. Casula, G. Concas, A. Corrias, D. Gatteschi, A. Falqui, A. Musinu, C. Sangregorio and G. Spano, *J. Mater. Chem.* **11** (2001) 3180.
173. J. L. Dormann, R. Cherkaoui, L. Spinu, M. Noques, L. Lucari, F. D’orazio, D. Fiorani, A. Garcia, E. Tronc and J. P. Jolivet, *J. Magn. Mater.* **187** (1998) L139.
174. J. Zhnag, C. Boyd and W. Luo, *Phys. Lett.*, **77** (1996) 390.
175. V. Vincent, Y. Yuan, J. Hamman, H. Hurdequint and F. J. Guevara, *J. Magn. Mater.*, **161** (1996) 209.
176. S. Morup, *J. Magn. Mater.*, **37** (1983) 39.
177. S. Morup, M. B. Madsen, J. Franck, J. Villadsen and C. J. W. Koch, *J. Magn. Mater.*, **49** (1983) 163.
178. P. Didukh, A. S. Waniewska, *J. Magn. Mater.* **254**, 407, (2003).
179. M. Vettrano, X. He, M. Trudeau and D. M. Antonelli, *J. Mater. Chem.* **11**, 1755, (2001).
180. N. A. Frey, S. Peng, K. Cheng and S. Sun, *Chem. Soc. Rev.* **38** (2009) 2532–2542.
-

181. T. Neuberger, B. Schöpf, H. Hofmann, M. Hofmann and B.von Rechenberg, J. Magn. Mater. 293 (2005) 483-496.
182. A. T. Nguyen, L. T. M. Nguyen, C. K. Nguyen, T. Truong and N. T. S. Phan, ChemCatChem 6 (2014) 815 – 823.
183. S. T. Fardood, Z. Golfar and A. Ramazani, J Mater Sci: Mater Electron. 28 (2017) 17002–17008.
184. L. Wu, A. Mendoza-Garcia, Q. Li and S. Sun, Chem. Rev. 116 (2016) 10473–10512.
185. L. H. Reddy, J. L. Arias, J. Nicolas and P. Couvreur, Chem. Rev. 112 (2012) 5818 – 5878.
186. Y. Sun, M. B. Salamon, K. Garnier and R. S. Averback, Phys. Rev. Lett. 91 (2003) 167206.
187. A. P. Young, Spin Glasses and Random Fields, World Scientific, Singapore, (1987).
188. S. Chakraverty, M. Bandyopadhyay, S. Chatterjee, S. Dattagupta, A. Frydman, S. Sengupta and P. A. Sreeram, Phys. Rev. B 71 (2005) 054401.
189. R. K. Zheng and X. X. Zhang, e-print cond-mat/040336. (Archive)
190. M. Sasaki, P. E. Jonsson, H. Takayama and P. Nordblad, Phys. Rev. Lett. 93 (2004) 139701.
191. M. B. Gawande, P. S. Branco, R. S. Varma, Chem. Soc. Rev., 2013, 42, 3371–3393.
192. B. Karami, S. J. Hoseini, K. Eskandari, A. Ghasemi, H. Nasrabadi, Catal. Sci. Technol., 2 (2012) 331–338.
193. R. J. White, R. Luque, V. L. Budarin, J. H. Clark, D. J. MacQuarrie, Chem. Soc. Rev., 38 (2008) 481–494.
194. M. B. Gawande, A. K. Rath, P. S. Branco, T. M. Potewar, A. Velhinho, I. D. Nogueira, RSC Adv. 3 (2013) 3611–3617.
195. I. P. Beletskaya and A. V. Cheprakov, Chem. Rev. 100 (2000) 3009.
-

196. D. Astruc, F. Lu and J. R. Aranzaes, *Angew. Chem. Int. Ed.* 44 (2005) 7852-7872; *Angew. Chem.* 117 (2005) 8062.
197. R. Ghosh Chaudhuri and S. Paria, *Chem. Rev.* 112 (2012) 2373.
198. C. Ramarao, S. V. Ley, S. C. Smith, I. M. Shirley and N. De Almeida, *Chem. Commun.* 1132 (2002).
199. F. Alonso, P. Riente and M. Yus, *Acc. Chem. Res.* 44 (2011) 379.
200. D. Kundu, T Chatterjee and B. C. Ranu, *Adv. Synth. Catal.* 355 (2013) 2285.
201. D. L. Huber, *Small* 1 (2005) 482.
202. T. Yoshihara, Y. Yamaguchi, M. Hosaka, T. Takeuchi and S. Tobita, *Angew. Chem. Int. Ed.* 51 (2012) 4148.
203. R. Ghosh Chaudhuri and S. Paria, *Chem. Rev.* 112 (2012) 2373.
204. H. Morimoto, R. Fujiwara, Y. Shimizu, K. Morisaki and T. Ohshima, *Org. Lett.* 16 (2014) 2018.
205. B. M. Trost, *Angew. Chem. Int. Ed.* 34 (1995) 259.
206. V. Nair, A. U. Vinod, C. Rajesh, *J. Org. Chem.* 66 (2001) 4427.
207. B. B. Touré and D.-G. Hall, *Chem. Rev.* 109 (2009) 4439.
208. J. Park, E. Kang, S. Ukson, H. M. Park, M. K. Lee, J. Kim, K. W. Kim, J.-H. Noh, J.-H. Park, C. J. Boe, J.-G. Park and T. Hyeon, *Adv. Mater.* 17 (2005) 429.
209. M. Amiri, K. Eskandari, M. Salavati-Niasari, *Adv. Colloid Interface Sci.* 271 (2019) 101982.
210. A. R. Liandi, A. H. Cahyana, A. J. Fadillah Kusumah, A. Lupitasari, D. Naufal Alfariza, R. Nuraini, R. Wulan Sari, F. Citra Kusumasari, *Case Stud. Environ.* 7 (2023) 100303.
211. K. K. Senapati, C. Borgohain, P. Phukan, *J. Mol. Catal. A Chem.* 339 (2011) 24–31.
212. J. Tong, L. Bo, Z. Li, Z. Lei, C. Xia, *J. Mol. Catal. A Chem.* 307 (2009) 58–63.
-

213. E. Manova, T. Tsoncheva, C. Estournès, D. Paneva, K. Tenchev, I. Mitov, et al., *Appl. Catal. A Gen.* 300 (2006) 170–180.
214. R. M. Borade, S.B Somvanshi, S.B Kale, R. P. Pawar and K. M. Jadhav, *Mater. Res. Express* 7 (2020) 016116.
215. Q. Li, X. Wang, Y. Yu, Y. Chen, L. Dai, *72* (2016) 8358-8363.
216. N. K. Gupta, Y. Ghaffari, S. Kim, J. Bae, K. S. Kim and M. Saifuddin, *Sci. Rep.* 10 (2020) 1-11.
217. B. Ren, Y. Huang, C. Han, M. N. Nadagouda and D. D. Dionysiou, *Ferrites as photocatalysts for water splitting and degradation of contaminants (Ferrites and Ferrates: Chemistry and Applications in Sustainable Energy and Environmental Remediation, American Chemical Society, pp. 79-112, 2016).*
218. P. A. Mangrulkar, V. Polshettiwar, N. K. Labhsetwar, R. S. Varma and Sadhana S. Rayal, *Nanoscale*, 4 (2012) 5202-5209.
219. E. Casbeer, V. K. Sharma and X. Z. Li, *Sep. Purif. Technol.* 87 (2012) 1–14.
220. S. Maria, N. Jeghan and M. Kang, *Mater Res Bull* 91 (2017) 108–113.
221. C. Caia, Z. Zhang, J. Liu, N. Shan, H. Zhang and D. D. Dionysiou, *Appl. Catal. B Environ.* 182 (2016) 456–468.
222. J. Feng, Y. Hou, X. Wang, W. Quan, J. Zhang, Y. Wang and L. Li, *J. Alloy. Compd.* 681 (2016) 157–166.
223. N. Ain, W. Shaheen, B. Bashir, N. M. Abdelsalam, M. F. Warsi, M. A. Khan and M. Shahid, *Ceram. Int.* 42 (2016) 12401–12408.
224. Z. Li, J. Ai, M. Ge, *J. Env. Chem. Eng* 5 (2017) 1394–1403.
225. M. Ge, W. Liu, X. R. Hu and Z. L. Li, *J. Phys. Chem. Solids.* 109 (2017) 1–8.

226. T. Tatarchuk, B. Al-Najar, M. Bououdina and M. A. A. Ahmed, Catalytic and photocatalytic properties of oxide spinels (Handbook of Ecomaterials, Springer, Cham, 2019).
227. W. Joa, S. Kumar, M. A. Isaacs, A. F. Lee and S. Karthikeyan, Appl. Catal. B Environ. 201 (2017) 159–168.
228. Y. Zhang, X. Zhou, F. Zhang, T. Tian, Y. Ding and H. Gao, J. Catal. 352 (2017) 246–255.
229. H. Li, Y. Liu, J. Tang and Y. Deng, Solid. State. Sci. 58 (2016) 14–21.
230. P. Liu, H. He, G. Wei, X. Liang, F. Qi, F. Tan, W. Tan, J. Zhu and R. Zhu, Appl. Catal. B Environ. 182 (2016) 476–484.
231. H. Y. Zhu, R. Jiang, Y. Q. Fu, R. R. Li, J. Yao and S. T. Jiang, Appl. Surf. Sci. 369 (2016) 1–10.
232. Y. Xu, J. Aia and H. Zhang, J. Hazard. Mater. 309 (2016) 87–96.
233. M. Mousavi and A. Habibi-Yangjeh, Adv. Powder. Technol. 28 (2017) 1540–1553.
234. F. K. Butt, C. Cao, Q. Wan, P. Li, F. Idrees, M. Tahir, W. S. Khan, Z. Ali, M. J. M. Zapata, M. Safdar and X. Qu, Int. J. Hydrogen. Energ. 39 (2014) 7842–7851.
235. L. Gan, L. Xu and K. Qian, Mater. Des. 109 (2016) 354–360.
236. A. H. Mady, M. L. Baynosa, D. Tuma and J. J. Shim, Appl. Catal. B Environ. 203 (2017) 416–427.
237. N. Ain, W. Shaheen, B. Bashir, N. M. Abdelsalam, M. F. Warsi, M. A. Khan and M. Shahid, Ceram. Int. 42 (2016) 12401–12408.
238. Z. Li, J. Ai and M. Ge, J. Env. Chem. Eng. 5 (2017) 1394–1403.
239. P. Guo, G. Zhang, J. Yu, H. Li and X.S. Zhao, Colloids Surf. A Physicochem. Eng. Asp. 395 (2012) 168–174.

240. C. Liang, H. Liu, J. Zhou, X. Peng and H. Zhang, *J. Chem.* 2015 (2015) 791829-1 – 791829-8.
241. P. Mishra, S. Patnaik and K. Parida, *Catal. Sci. Technol.*, 9 (2019) 916-941.
- [188] H. Yang, J. Yana, Z. Lu, X. Cheng and Y. Tang, *J. Alloys Compd.* 476 (2009) 715–719.
242. A. Sutka, M. Millers, M. Vanags, U. Joost, M. Maiorov, V. Kisand, R. Pärna and I. Juhnevica, *Res. Chem. Intermed.* 41 (2015) 9439-9449.
243. A. Silambarasu, A. Manikandan and K. Balakrishnan, *J. Supercond. Nov. Magn.* 30 (2017) 2631-2640.
244. Y. O. López, H. M. Vázquez, J. S. Gutiérrez, V. G. Velderrain, A. L. Ortiz and V. Collins Martínez, (2015). *Journal of Nanomaterials*, 2015.
245. S. W. Cao, Y. J. Zhu, G. F. Cheng, Y. H. Huang, *J. Hazard. Mater.* 171 (2009) 431.
246. G. Fan, J. Tong and F. Li, *Ind. Eng. Chem. Res.* 51 (2012) 13639–13647.



Chapter 2

Experimental Methods



2.1 Synthesis techniques

Nano/micro structured spinel ferrites have attracted profound attention of the scientific community pertaining to their basic magnetic characteristics which can be regulated in accordance with the industrial need by employing different techniques for their synthesis [1–5]. It is well-known that variation in synthesis procedures can alter the composition, morphology and cation distribution of the ferrites [6,7]. So, emphasis has been laid to develop various types of synthesis procedures which led to the generation of multifunctional nano/micro structured spinel ferrites interestingly [7]. Combination of two or more conventional synthesis methods to produce such ferrites have resulted in fascinating magnetic features along with widespread applicability in diverse fields such as magnetic storage systems, magnetic fluids, microwave absorbers, catalysts, supercapacitors, sensors and biomedical [6 –10]. This section includes discussion on some low-cost, facile and eco-friendly synthesis techniques whose various combinations have been used for synthesis of our samples.

2.1.1 Co-precipitation method

Co-precipitation method is the one of the most facile, cheap, time-saving technique involving mild synthetic conditions to synthesize nanosized spinel ferrites [11 – 13]. The morphology of so formed ferrites can be governed by altering the experimental conditions, but it cannot be controlled well in terms of particle size and size distribution [14,15]. So, the precipitated product is subjected to heat treatment to achieve good crystallinity and better control in particle size. In this thesis, we have synthesized nanosized $\text{Co}_{0.5}\text{Zn}_{0.5}\text{Fe}_2\text{O}_4$ and $\text{Co}_{0.8}\text{Zn}_{0.2}\text{Fe}_2\text{O}_4$ using conventional co-precipitation method, which were further subjected other methods to obtain desirable products.

2.1.2. High energy ball milling method

High energy ball milling method is an easy, economic and top-down method to synthesize iron oxide nanoparticles. This method has been able to reduce the particle size very successfully [15 – 18]. Additionally, it has led to development of interesting magnetic features in the ball-milled nanoparticles owing to modification in their surface features and cation distribution [19-22]. Moreover, ball milling introduces strain anisotropy and defects into the system resulting in novel magnetic properties [15-22]. In this thesis, we have synthesized nanosized $\text{Co}_{0.5}\text{Zn}_{0.5}\text{Fe}_2\text{O}_4$ and $\text{Co}_{0.8}\text{Zn}_{0.2}\text{Fe}_2\text{O}_4$ by subjecting their respective bulk counterparts (produced by conventional co-precipitation method) to ball milling.

2.1.3. Solvothermal/Hydrothermal method

Solvothermal/Hydrothermal method is a surfactant-assisted chemical method that involves a novel way to develop size- and shape-tailored magnetic nanocrystals by carefully regulating the growth processes in liquid media [23,24]. These methods may be either single-step or more complex multiple-step solution-phase routes [25 – 27]. The particle size distribution, shape, morphology and crystallinity of spinel ferrites can be modified by adjusting the reaction time, temperature, type and amount of precursors, surfactants and metal ions [28 – 31]. Polymeric surfactants are used as binding agents in this process. Solvothermal/Hydrothermal technique is a simple, environment-friendly and one-pot reaction procedure to create nano/micro structured spinel ferrites which do not involve any thermal treatment. In this thesis, ZnFe_2O_4 solid and hollow microspheres (solvothermal) and nanosized $\text{Co}_{0.5}\text{Zn}_{0.5}\text{Fe}_2\text{O}_4$ (hydrothermal) have been synthesized by these techniques.

2.2. Characterization techniques

This section highlights the instrumental techniques that have been utilized to characterize the samples. Theory, working principle of the instruments and the method of

analysis have been discussed here. We have characterized our sample by using the following techniques.

- (i) Powder x-ray diffraction (PXRD) study
- (ii) Electron microscopic study
- (iii) Energy-dispersive x-ray spectroscopic (EDX) study
- (iv) X-ray photoelectron spectroscopy (XPS) study
- (v) UV–vis spectroscopic study
- (vi) Photoluminescence (PL) study
- (vii) DLS and Zeta potential
- (viii) dc magnetic study
- (ix) Mössbauer spectroscopic study
- (x) Electrochemical study and
- (xi) Photocatalytic activity study

2.2.1. Powder x-ray diffraction study

The powder x-ray diffraction (PXRD) pattern of the samples present in this thesis was recorded at room temperature by using a Bruker D8 Advance diffractometer using Cu-K α ($\lambda=1.54184$ Å) radiation over the 2θ range of 20-80°. The voltage and current of the x-ray generator were set at 35 kV and 35 mA, respectively. The counting time and step size were set at 5 s/step and 0.0199°, respectively.

DICVOL06 and TREOR90 of Fullprof2k package were utilized for indexing the PXRD pattern [32,33]. FINDSPACE of EXPO2009 package was used to ascertain the space group of the samples through the statistical analysis of their PXRD data [34,35]. Moreover, we have used two Rietveld based software packages viz., MAUD2.33 (Material Analysis Using Diffraction) [36] and GSAS (General Structure Analysis System) [37] with EXPGUI (graphical user interface) interface [38] to determine the structural, microstructural

parameters along with the phase- purity and bonding framework of the samples. In MAUD2.33, the initial positions of metal ions at tetrahedral (A) and octahedral [B] sites and O atoms were stated through their Wyckoff positions 8(b), 16(c), and 32(e), respectively. Moreover, the occupancies of the constituent elements and oxygen (O) obtained from in-field Mössbauer spectroscopic study, were provided as initial input parameters for the Rietveld refinement of PXRD data using MAUD2.33. Finally, we got refined values of structural (lattice parameter and atomic coordinates) and microstructural parameters (crystallite size, microstrain, density etc.) as well as quantitative abundance of different phases after successful refinement of PXRD pattern of the samples.

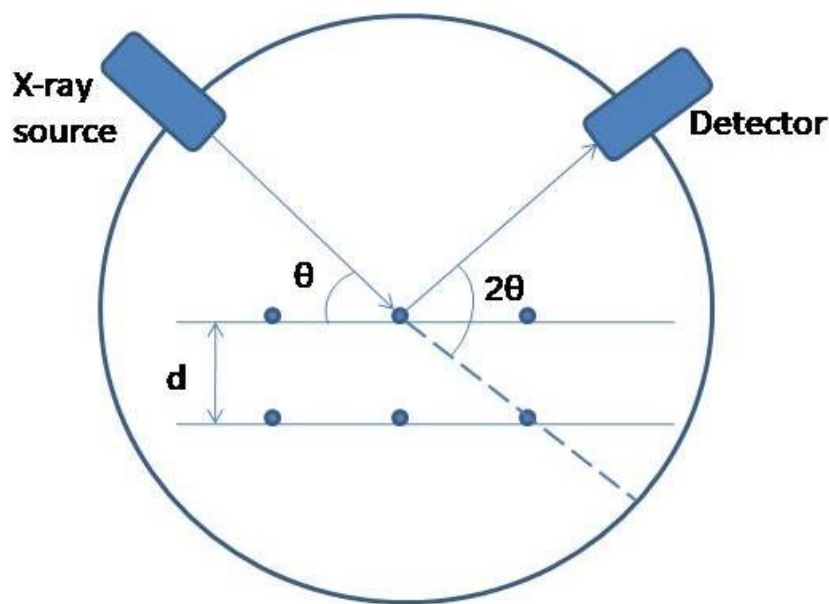


Fig.1. Simple diagram showing X-ray diffraction

On the other hand, GSAS program with EXPGUI interface is a trustworthy software package to process the lattice parameters, profile parameters, background coefficients and position coordinates of oxygen atom. In this software, the background can be refined by using shifted Chebyshev function of first kind with 36 points. Moreover, the generalized spherical

harmonic model was utilized to correct the preferred orientation in the final stage of refinement. There are 63 parameters i.e., 36 background points, 15 profile parameters, 3 coordinates, 1 lattice parameter and 7 orientation distribution functions that can be refined to get best fitting of observed PXRD pattern with that of calculated one.

2.2.2 Electron microscopic study

In this thesis, two types of electron microscopic techniques have been used. First one is Field Emission Scanning Electron Microscopic (FESEM) technique and the second one is High Resolution Transmission Electron Microscopic (HRTEM) technique. These techniques helped to gather the information about morphology and crystallographic orientation of the samples.

2.2.2.1 FESEM study

The FESEM morphographs have been captured by FEI INSPECT F50 FESEM equipment. This instrument consists of 1) electron optical column, 2) specimen chamber, 3) electron dispersive spectroscopy (EDS) detector, 4) back scatter detector (BSD), 5) monitors and 6) computers. The narrow probing electron beams are produced at both low and high energy density from field-emission cathode in the electron gun of the microscope. The electron beam is directed onto the specimen by accelerating in a field gradient through electromagnetic lenses. The bombardment of beam onto the surface of the sample produces several interactions that result in emission of electrons or photons from the surface. The FESEM instrument mainly produces morphographs from the intensity comparison of the secondary electrons generated after bombardment to that of the primary electron beam. As electrons in FESEM instrument interact with the surface layers of the sample, it can yield many important information like 1) topography: the features and textures of surface, 2) morphology: the shape, size and arrangement of particles that construct the sample, 3)

composition: constituent elements and compounds which comprise the samples and 4) crystallographic information [39,40].

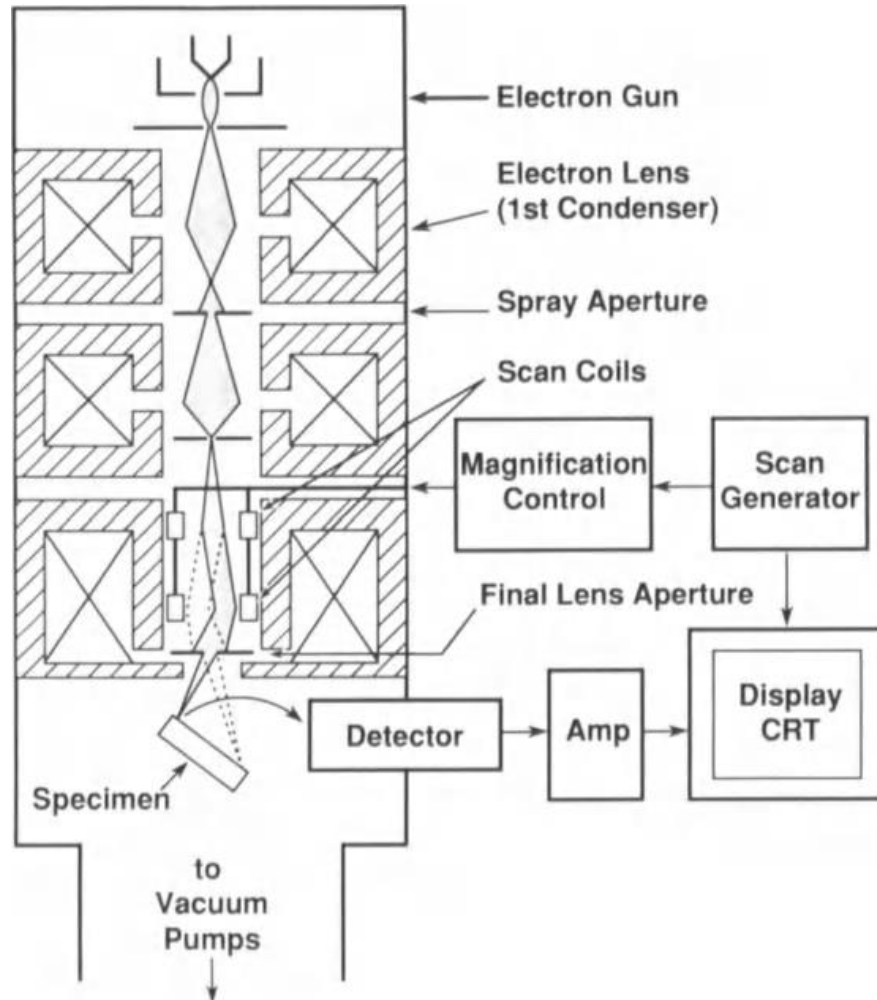


Fig.2. Schematic diagram of Field Emission Scanning Electron Microscope (FESEM) [40]

2.2.2.2 TEM study

(a) Sample preparation for TEM: It is well known that most of the magnetic nanoparticles have a tendency to form agglomerates. So, it becomes difficult to properly record the HRTEM images of magnetic nanoparticles. To get rid of this difficulty we have taken a special measure to break the agglomerates prior to the HRTEM study. To disperse the agglomerates, small amount of sample was primarily disseminated in ethyl alcohol by dynamic ultrasonication. After that Cu-grid with C coating was positioned at a spin coating

unit spinning at 400 rpm and a drop of sample was discharged on the grid. It will be apparent from the TEM micrograph that agglomeration could be sufficiently prevented.

(b) Working principle: The transmission electron images, lattice peripheries and selected area electron diffraction pattern of the present samples have been recorded by JEOL2100 HRTEM equipment. The instrument comprises of: 1) electron gun, 2) condenser aperture, 3) objective aperture, 4) intermediate aperture, 5) specimen port, 6) objective lens, 7) diffraction lens, 8) intermediate lens, 9) projector lenses, 10) binoculars, 11) fluorescent screen, 12) monitors and 13) computers. The working of the instruments is as follows: a) the electron beam interacts and passes through the specimen, b) the electrons are discharged from electron source and confined by two condenser lenses, c) the electrons then pass through the condenser aperture and hit the sample surface, d) brightness of the samples are controlled by the condenser lenses, e) the transmitted beams consisting elastically scattered electrons pass through the objective lens, f) apertures are used to choose these elastically scattered electrons that will form the image with the help of objective lens and g) these beams pass through intermediated lenses and projector lens, respectively. Intermediated lenses control the magnification of the image that is shown in Fig.3. We obtain different type of electrons after bombardment on the specimen. Thus, different types of images are obtained in TEM instrument by using different type of apertures and lenses. If diffracted beam is selected, dark field images can be obtained. On the other hand, bright field images can be formed by selecting unscattered beam. When a sample is subjected to a parallel beam and an aperture is used to select the area (few hundred of nanometers) from which the diffraction pattern is to be recorded, a selected area electron diffraction (SAED) pattern is formed [41,42]. SAED pattern can be either spot patterns corresponding to single crystal diffraction or ring patterns due to multiple crystal with variable orientation of powder samples. SAED images are required for determination of growth directions, structural intergrowth, phase identification

etc. TEM images are useful to determine the shape, size, order of the particles, arrangement of atoms of the samples, imperfections in crystalline structure etc.

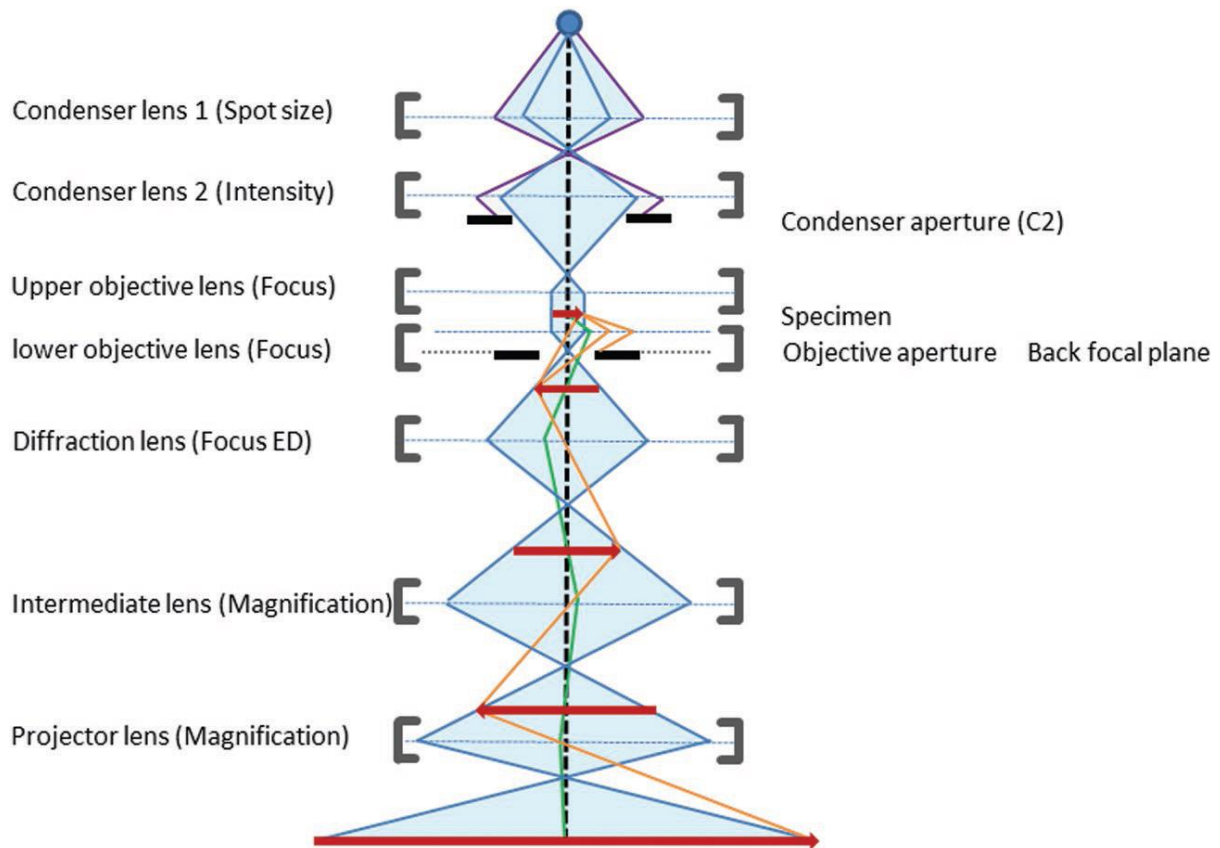


Fig.3. Schematic diagram of a transmission electron microscope [43].

2.2.3. Energy-dispersive x-ray spectroscopic study

The BRUKER EDS (Energy-dispersive x-ray spectroscopy) system used for analysing the identity of the constituent elements of the present samples is attached to the JEOL2100 HRTEM equipment. In EDS technique, x-rays are emitted from the sample when electron beam interacts with the atoms at the surface of the samples. X-ray energy indicates the characteristics of the elements from which it is emitted. The machine records the comparative abundance of x-rays emitted by different elements against their respective energy. The elemental composition of the sampled volume is assessed by the x-ray energy spectrum versus counts plot.

2.2.4. X-ray photoelectron spectroscopic study

XPS (X-ray photoelectron spectroscopy) is a quantifiable spectroscopic technique that records the elemental composition, experiential formula, chemical and electronic nature of the elements that occur inside a material. XPS spectra are attained by exposing a substance to X-rays while concurrently recording the kinetic energy and quantity of electrons that outflow from the top layer of the substance under observation. In this method, photon energy is absorbed by the surface electron inhabiting the core level. So, the energy distribution of emitted electrons would resemble the energy level variations of the electronic states in the sample under examination. The ejected photoelectrons are accumulated by the energy electron analyzer producing the spectrum. XPS was performed for samples ZnFe_2O_4 solid and hollow microspheres using XPS (Omicron Multiprobe Electron Microscopy System) with monochromatic Al $K\alpha$ x-ray source (1486.7 eV, model: XM 500). The data were analysed using the XPSPEAK 4.1 software. The photoelectron peaks under consideration were subjected to Shirley background subtraction and peak fitting with Gaussian-Lorentzian shaped profiles.

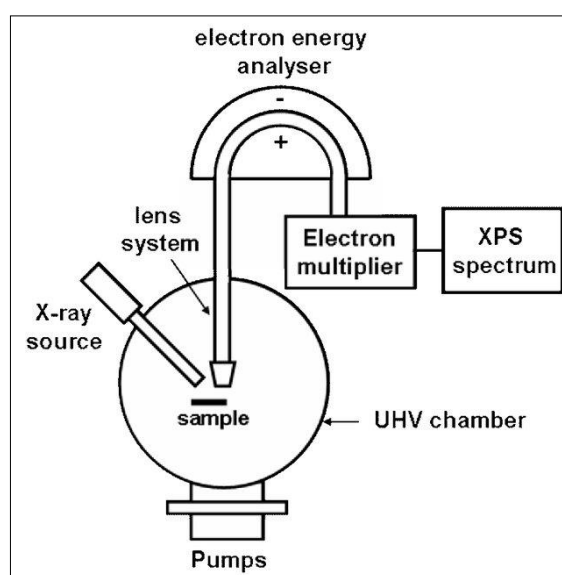


Fig.4. Schematic diagram of an XPS instrument [44].

2.2.5. Ultraviolet-Visible spectroscopic study

UV-vis spectroscopy is widely utilized to quantitatively characterize material's optical property especially band-gap property. In this process sample is exposed with ultraviolet and visible electromagnetic waves and the captivated energy is measured through the absorption spectrum [45]. Fig.5 shows the components of a typical spectrometer. Firstly, a light beam from a source (visible or ultraviolet) is segregated into its constituent wavelengths using a prism or diffraction grating. Further, the separated monochromatic beams are split into two equisized intensity beams using a half-mirrored device. The sample beam moves through a small clear vessel (cuvette) comprising a mixture of the composite under observation in a

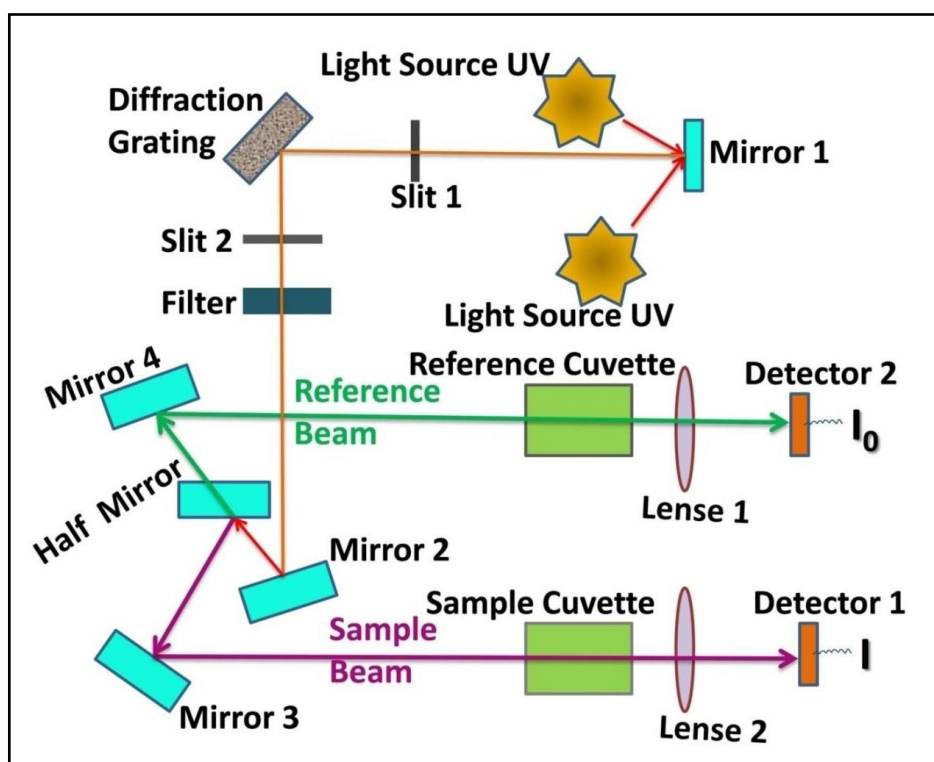


Fig.5. Parts comprising a typical spectrometer [46]

clear solvent. Whereas the reference beam moves through an alike cuvette holding only the solvent. The resulting intensities of these beams are then recorded by electron detectors and studied. The absorption peak's width for a nanoparticle spectrum firmly relies on the

chemical structure and the particle size. JASCO V-630 spectrophotometer has been used to characterize our samples.

2.2.6. Photoluminescence spectroscopic study

Photoluminescence (PL) spectroscopy is a non-touch, non-damaging method and it delivers information on electrical and optical properties of semiconductor materials. In this method, light is focused onto a substance, which absorb light energy by photoexcitation process. Subsequently, photo-excited electrons rise to a upper electronic state, and then release the extra energy in the form of photons to attain least energy state. This process of emission of light, or luminescence through the emission of photoelectrons is called photoluminescence (PL). In the process of photoluminescence, laser beam is directed on the sample, which absorb it and later emit light at wavelengths reliant on the chemical structure. The orientation of the sample is so maintained that the reflected light beam and the photoluminescence emission proliferate in dissimilar directions. The emanated light is focused through a fibre optic cable and finally into a spectrometer. It is prudent to place a filter in front of the fibre cable to eliminate any unwanted laser light. The photoluminescence spectrum specifies the comparative intensities of light of diverse wavelengths incoming the detector. The photoluminescence (PL) spectra of our samples have been recorded by using a JASCO FP-6700 spectrophotometer.

2.2.7. Dynamic light scattering and Zeta potential study

Zeta potential and particle size distribution were determined using a Zetasizer Nano ZS (Malvern Instruments, UK). A 2 mW He-Ne Laser of wavelength 633 nm was attached with the instrument and was used to irradiate the samples under observation. A throwaway zeta cuvette was utilized for particle size and zeta potential measurements. In dynamic light scattering (DLS) technique, the digital signal processing correlator was illuminated with back scattered light at an angle of 173° . The intensity versus intensity auto-correlation entity was

recorded and was utilized to estimate the average size by means of the Stokes-Einstein relation $a = \frac{kT}{6\pi\eta D}$, D is the diffusion constant and kT is the thermal energy [47,48]. The particle size distribution was attained via three consecutive measurements. The electrophoretic mobility was employed to measure Zeta potential through laser Doppler velocimetry by means of Helmholtz-Smoluchowski function

$$\zeta = 3 \frac{3\mu\eta}{2\epsilon f(\kappa a)} \quad (1)$$

Where, η and ϵ are the coefficient of viscosity and the permittivity of the aqueous medium, respectively. $f(\kappa a)$ is the Henry function which relies on the inverse Debye length (κ) and the radius (a) of the particle. In Smoluchowski calculation, the extreme value of the function $f(\kappa a) = 1.5$ subject to condition that particles are in aqueous media [47,48]. When the particles are dispersed in a non-aqueous media, $f(\kappa a) = 1$ (Huckel approximation). We have utilized $f(\kappa a) = 1.5$ value for our current study to compute zeta potential from calculated electrophoretic mobility. The average value of zeta potential was attained by means of three consecutive measurements with 10-100 runs in every measurement.

2.2.8. dc magnetic study

dc magnetic measurement of the present samples was carried by using both superconducting quantum interference device magnetometer (Quantum Design SVSM, USA) and a Cryogenic make vibrating sample magnetometer (VSM). The dc magnetization (M) versus temperature (T) curve was obtained by considering the zero-field cool (ZFC) and field cool (FC) protocol. On the other hand, dc magnetization as a function of magnetic field (M versus H) was recorded under ZFC mode at different temperatures.

(a) ZFC-FC protocol: This protocol, in general, gives us the information of the energy barriers of the magnetic systems and performed as mentioned below: For obtaining the ZFC magnetization curve, the substance is primarily cooled in absence of field from a high temperature possibly above the blocking temperature (T_B) of the system to a low temperature

upto 5- 10 K. Then the sample is subjected to a magnetic field and the magnetization versus temperature data is measured in the heating cycle. The same process is repeated for FC magnetization but only difference is that the sample is cooled under the influence of constant magnetic field and data is noted in the heating cycle with field on. In the ZFC and FC measurements, the external field which the sample is subjected to should be lower than the anisotropy field to assure that the ZFC-FC curve displays the inherent distribution of the energy barriers [49].

(b) Working principal of VSM: Faraday's law of induction. VSM consists of the following units: 1) One powerful electromagnet (magnetic field ~ 7 T), 2) Two pickup coils (Reference coil and detection coil) and 3) sample holder made of nonmagnetic material. To produce a signal equivalent to the magnetic moment, the sample is set to vibrate by velocity transducer in a slowly varying applied field. The variation of magnetic flux due to the sample vibration is sensed by the pick-up coils. Voltages that generate at two different set of coils, is measured and the difference of voltages is proportional to the magnetic moment of the sample.

2.2.9. Mössbauer spectroscopic study

Mössbauer spectroscopic study is connected to the extraction of information on the hyperfine interaction, which generates when the energies of nuclear state are perturbed by the electrons around the nucleus. In the thesis, the hyperfine properties of iron containing samples have been investigated by Mössbauer spectroscopic study. Mössbauer effect is nothing but the phenomena of recoilless emission and resonance absorption of γ rays [50]. It provides local information of a system having fast relaxation time, by detecting its magnetic ordering with the small characteristics experimental time ($\tau_m = 10^{-9}$ s). There are three hyperfine interactions viz., isomer shift, electric quadrupole splitting, and hyperfine magnetic field associated with Mössbauer effect, which are the most useful measurable quantities for the characterization of

materials in Mössbauer spectroscopic study. There are 40 elements (Ni, Sn, Ge, Ru, Sm, Eu etc.) in periodic table that exhibit Mössbauer effect with 100 nuclear transitions. However, the study of Mössbauer effect in ^{57}Fe is more convenient due to its narrow natural linewidth (4.6×10^{-9} s) and 14.41 KeV γ ray emission.

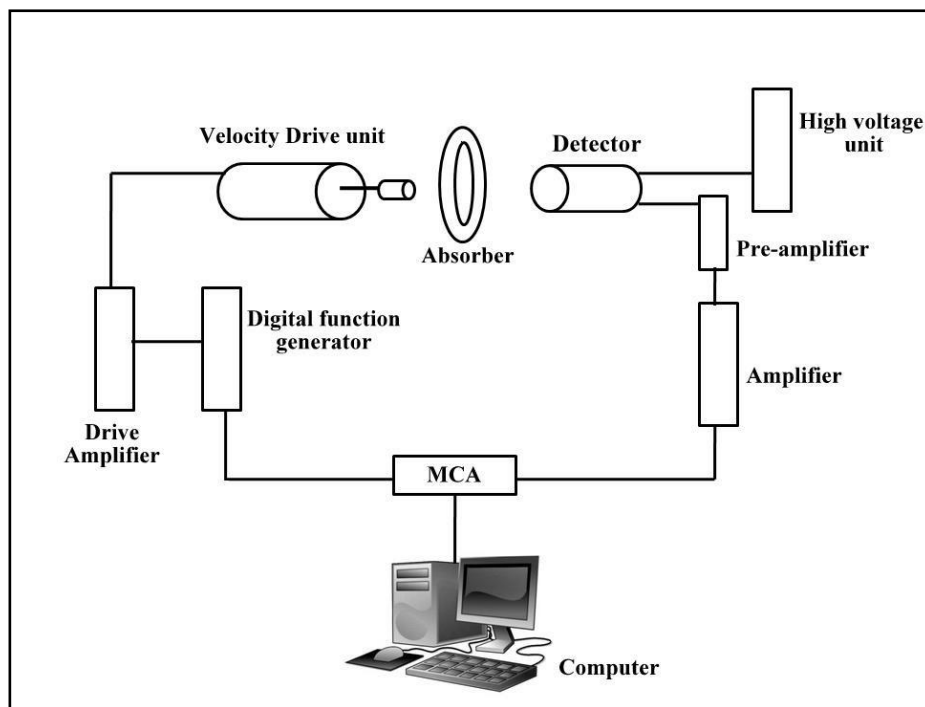


Fig.6. Block diagram of Mössbauer spectrometer

The block diagram of Mössbauer spectrometer is shown in Fig.6. The major parts in the experimental arrangement of Mössbauer spectrometer are consisted with the following: 1) Mössbauer radioactive source for γ ray emission, 2) an absorber, 3) a drive unit, 4) gamma ray detector and 5) data acquisition system. ^{57}Co in Rh matrix has been used as Mossbauer source as it has narrow line width and high recoil free fraction. Absorbers for Mössbauer spectroscopic study have been made by spreading uniformly the sample taken in powder form over $\sim 1 \text{ cm}^2$ area. The main three parts of drive unit (model CMTE 250) are a function generator, a drive amplifier and a Mössbauer velocity transducer (MVT). The source is mounted on the transducer that is made up of moving coil in a constant magnetic field and oscillates according to the drive current coming from amplifier. The detector is nothing but a sealed proportional counter, which is

attached with a low noise active filter amplifier and a pre-amplifier. The output of amplifier has been sent to the Multi-Channel Analyzer (MCA). However, the energy of 14.4 KeV γ ray is selected by a Single Channel analyzer (SCA), lower-level discriminator (LLD) and upper-level discriminator (ULD) in pulse height analysis (PHA) mode of MCA. Moreover, MCA generates clock pulses that synchronize the MVT and MCA. The single spectrum has been produced by folding the full spectrum around the center point during the analysis.

A constant acceleration drive (CMTE-250) with a 10 mCi ^{57}Co source was used to record Mössbauer spectra of the samples at room temperature in transmission geometry. The low temperature (5/10 K) Mössbauer spectra of the samples were carried out with JANIS SVT-400 MOSS cryostat system. In presence of an external magnetic field of 5 T applied parallel to the γ -ray direction, the Mössbauer spectra of the samples were acquired at low temperature (5/10 K) by using a superconducting magnet (JANIS SuperOptiMag) and a 40 mCi ^{57}Co source. The natural iron sample was used for the calibration of the Mössbauer spectrometer. The fitting of the Mössbauer spectra was performed by using the Recoil program [35]. In the thesis, the Mössbauer spectra were fitted by using the Lorentzian site analysis and Voigt based site analysis methods of Recoil program.

2.2.10 Electrochemical performance study

Electrochemistry deals with the chemical reactions that take place through means of electron transfer at the interface of an electrode and an ionic conductor i.e. electrolyte. Electricity is produced by transfer of electrons from one element to another through a reaction known as redox (oxidation-reduction) reaction. Most used setup in electrochemical performance study is that of three electrode cells. The three electrodes are working electrode, reference electrode and auxiliary or counter electrode. These three electrodes are connected to an instrument (potentiostat) that monitors the potential of the working electrode relative to the reference electrode and measures the resulting current passing between the working electrode and counter electrode. The tip of reference electrode is located as close to the

working electrode as possible to minimize the solution (electrolyte) resistance [52]. A typical three electrodes electrochemical cell has been used in the thesis work where, counter electrode is a wire-constructed platinum and reference electrode is the saturated calomel electrode that has a known potential. The electrolyte consists of a high concentrated solution of an ionized salt as well as electroactive species, which has been used as medium between the electrodes in the cell. In the present thesis, the cyclic voltammetry technique has been used to understand the kinetic and catalytic performance of an electrode. The details of this technique is discussed below briefly.

Cyclic voltammetry (CV) is a vital and powerful technique that is used to examine the redox processes in molecular species. During the experiment, an external potential ramp applied by the potentiostat is employed to the working electrode. This potential ramp changes progressively and returns to the initial potential by reversing the scan (Fig.7). In this manner, a triangular potential waveform is generated by scanning the potential between the switching potentials linearly with time in acyclic manner. The following equation is $E = E_i \pm vt$ (+ ve for cathodic and – ve for anodic sweep), where E = potential at time t , E_i = initial potential and v = scanning potential or sweep rate of potential.

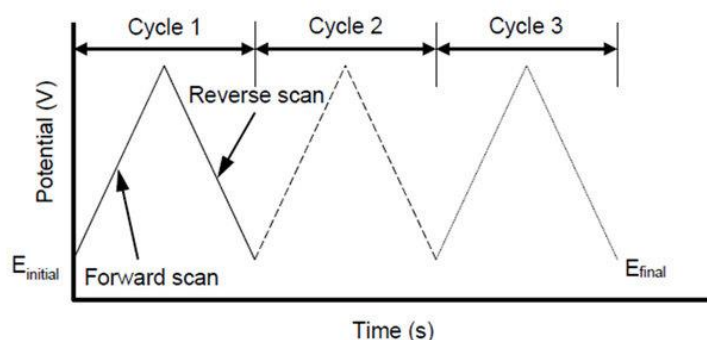


Fig.7. Triangular potential waveform applied to the working electrode [53]

A typical cyclic voltammogram (CV) curve where resulting current is monitored as a function of externally applied sweep potential is presented in Fig.8. In the diagram, the anodic current (i_{pa}) is produced when the scanning potential at working electrode becomes

more positive than that of redox couple present in the solution (greater than anodic peak potential E_{pa}); oxidation may occur in the corresponding species by transferring electrons from the solution to the electrode. On the other hand, when the working electrode potential in the return scan is more negative than the reduction potential of redox couple (greater than cathodic peak potential E_{pc}), reduction takes place by sweeping away electrons from the electrode to yield cathodic (i_{pc}) current. The anodic and cathodic currents are positive and negative, respectively, according to the IUPAC convention. The relationship among the potential of the electrochemical cell (E), standard reduction potential of the redox couple (E^0) and the concentration of the oxidized (Ox) and reduced (Red) analyte in the system are described by the Nernst equation at equilibrium [54].

$$E = E^0 + \frac{RT}{nF} \ln \frac{[Ox]}{[Red]}$$

where, R = molar gas constant ($8.3144 \text{ J Mol}^{-1} \text{ K}^{-1}$), T = absolute temperature (K), n = number of electrons transferred, F = Faraday constant. Moreover, in cyclic voltammetry, electrochemical reactions can be performed either by reversible or irreversible process.

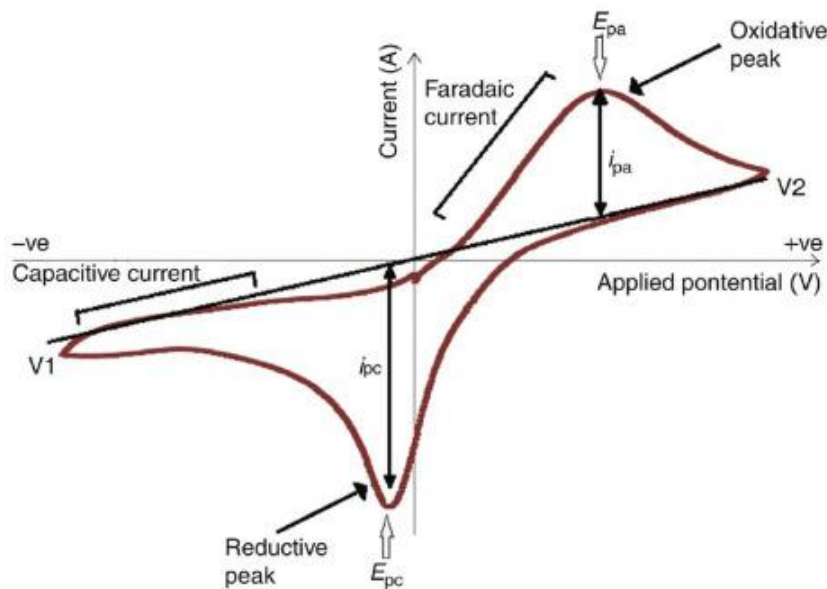


Fig.8. Cyclic voltammogram (CV) curve [55]

2.2.11. Photocatalytic activity study

In the thesis, $\text{Co}_{0.5}\text{Zn}_{0.5}\text{Fe}_2\text{O}_4$ microspheres were used as catalyst to remove pollutant dye (Congo Red) under dark and light conditions. For this work, a stock mixture was made by putting 15 mg of Congo Red (CR) into 1 L of distilled water. Further, the degradation experiment using photocatalysis was carried out by putting essential amount of catalyst into 20 ml of pollutant dye stock mixture stored in a glass vessel and subjecting the solution to different dark and light conditions. The process of photocatalytic degradation was supervised by capturing UV-Vis absorption spectra of the substance attained after magnetic separation with the help of JASCOV650 spectrophotometer. Fig. 9 shows the general mechanism of photocatalytic effect.

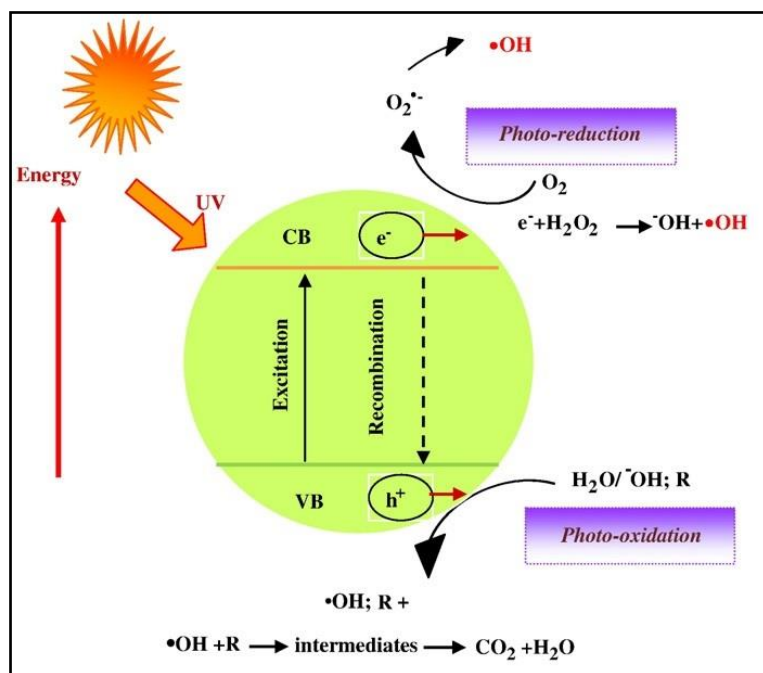


Fig.9. General mechanism of photocatalytic effect [56].

References

1. O. F. Odio and E. Reguera, *Magnetic Spinels: Synthesis, Properties and Applications*, (2017) 185-216.
2. T. Tatarchuk, M. Bououdina, J. J. Vijaya and L. J. Kennedy, *Nanophysics, Nanomaterials, Interface Studies, and Applications (NANO 2016)*, Springer Proceedings in Physics 195 (2016) 305-325.
3. A. S. Molakeri, S. Kalyane and A.B. Kulkarni, *Int. J Self-Propag. High-Temp. Synth.* 27 (2018) 44–50.
4. D. S. Mathew and R. Juang, *Chem. Eng. J* 129 (2007) 51–65.
5. D. Carta, M. F. Casula and A. Falqui, *J. Phys. Chem. C* 113 (2009) 8606– 8615.
6. An-Hui Lu, E. L. Salabas, and Ferdi Schüth, *Angew. Chem. Int. Ed.* 2007, 46, 1222 – 1244
7. S. K. Sharma, *Complex Magnetic Nanostructures*, Springer, Switzerland, 2017
8. L. Wu, A. Mendoza-Garcia, Q. Li and S. Sun, *Chem. Rev.* 116 (2016) 10473–10512.
9. S. Laurent, D. Forge, M. Port, A. Roch, C. Robic, L. V. Elst and R. N. Muller, *Chem. Rev.* 108 (2008) 2064–2110.
10. M. Kumar, H. S. Dosanjh, J. Singh, K. Monir and H. Singh, *Environ. Sci.: Water Res. Technol.* 6 (2020) 491- 514.
11. A. S. Albuquerque, M. V. Tolentino, J. D. Ardisson, F. C. Moura, R.de Mendonça and W. A. Macedo, *Ceram. Int.* 38 (2012) 2225 – 2231.
12. L. Yang, Y. Zhang, X. Liu, X. Jiang, Z. Zhang, T. Zhang and L. Zhang, *Chem. Eng.* 246 (2014) 88-96.
13. P. Roonasi and A. Y. Nezhad, *Mater. Chem. Phys.* 172 (2016) 143-149.
14. M. C. Mascolo, Y. Pei and T. A. Ring, *Materials* 6 (2013) 5549-5567.
15. S. Dey, S. K. Dey, B. Ghosh, V. R. Reddy and S. Kumar, *Mater. Chem. Phys.* 138 (2013) 833 – 842.

-
16. B. Ghosh, S. Kumar, A. Poddar, C. Mazumdar, S. Banerjee, V. R. Reddy and A. Gupta, J. Appl. Phys. 108 (2010) 034307.
 17. C. Suryanarayana, Prog. Mater Sci. 46 (2001) 1.
 18. C. Suryanarayana, Rev. Adv. Mater. Sci. 18 (2008) 203.
 19. C. N. Chinnasamy, A. Narayanasamy, N. Ponpandian, K. Chattopadhyay, H. Guertel, and J.M. Grenèche, J. Phys.: Condens. Matter 12, (2000) 7795.
 20. V. Šepelák, I. Bergmann, A. Feldhoff, P. Heitjans, F. Krumeich, D. Menzel, F.J. Litterst, S.J. Campbell, K.D. Becker, J. Phys. Chem. C 111 (2007) 5026.
 21. R.N. Bhowmik, R. Ranganathan, R. Nagarajan, B. Ghosh, S. Kumar, Phys. Rev. B 72 (2005) 094405; B. H. Liu and J. Ding, Appl. Phys. Lett. 88 (2006) 042506.
 22. N. Ponpandian, A. Narayanasamy, C. N. Chinnasamy, N. Sivakumar, J. M. Grenèche, K. Chattopadhyay, K. Shinoda, B. Jeyadevan and K. Tohji, Appl. Phys. Lett. 86 (2005) 192510; S. Chkoundali, S. Ammar, N. Jouini, F. Fievet, P. Molinie, M. Danot, F. Villain and J. M. Grenèche, J. Phys.: Condens. Matter 16 (2004) 4357.
 23. H. Deng, X. Li, Q. Peng, X. Wang, J. Chen, Y. Li, Angew. Chem. Int. Ed. 44 (2005) 2782–2785.
 24. M. Penchal Reddy, A.M.A. Mohamed, Micropor Mesopor Mat 215 (2015) 37-45.
 25. S. Fan, X. Li, L. Zeng, M. Zhang, Z. Yin, T. Lian and A. Chen, ACS Appl. Mater. Interfaces 10 (2018) 35919–35931.
 26. B. Y. Yu and S-Y Kwak, Dalton Trans. 40 (2011) 9989.
 27. S. Wang, X. Gao, J. Yang, Z. Zhu, H. Zhang and Y. Wang, RSC Adv. 4 (2014) 57967.
 28. H. Deng, X. Li, Q. Peng, X. Wang, J. Chen, and Y. Li, Angew. Chem. Int. Ed. 44 (2005) 2782–2785.
 29. W. Wu, S. Yang, J. Pan, L. Sun, J. Zhou, Z. Dai and C. Jiang, Cryst. Eng. Comm. 16 (2014) 5566-5572.
-


30. K. M. Jensen, H. L. Andersen, C. Tyrsted, E. D. Bøjesen, A. C. Dippel, N. Lock, S. J. L. Billinge, B. B. Iversen and M. Christensen, *Acs Nano* 8 (2014) 10704-10714.
31. S. Ge, X. Shi, K. Sun, C. Li, C. Uher, J. R. Baker Jr, M. M. B. Holl and B. G. Orr, *J. Phys. Chem. C* 113 (2009) 13593–13599.
32. P. E. Werner, L. Eriksson and M. J. Westdahl, *J. Appl. Crystallogr.* 18 (1985) 367 – 370.
33. A. Boultif, and D. Louër, *J. Appl. Crystallogr.* 37 (2004) 724 – 731.
34. A. Altomare, C. Giacovazzo, A. Guagliardi, A. G. G. Moliterni, R. Rizzi and E. J. Werner, *J. Appl. Crystallogr.* 33 (2000) 1180 – 1186.
35. A. Altomare, R. Caliendo, M. Camalli, C. Cuocci, C. Giacovazzo, A. G. G. Moliterni and R. Rizzi, *J. Appl. Crystallogr.* 37 (2004) 1025 – 1028.
36. L. Lutterotti, MAUDWEB, Version 1.9992, 2004 (<http://www.ing.unitn.it/~luttero/maud>, 2004).
37. A. C. Larson and R. B. Von Dreele, General Structure Analysis System (GSAS) (Los Alamos National Laboratory Report LAUR, 86 – 748, 2000).
38. B. H. Toby, *J. Appl. Crystallogr.* 34 (2001) 210 – 213.
39. D. McMullan, *Scanning* 17 (2006) 175–185.
40. J. I. Goldstein and D. E. Newbury, *Scanning Electron Microscopy and X-Ray Microanalysis*, (1992 1981 Plenum Press, New York).
41. R. F. Egerton, *Physical Principles of Electron Microscopy, An Introduction to TEM, SEM, and AEM* (Springer, pp. 57 – 119, 2005)
42. David B. Williams and C. Barry Carter, *Transmission Electron Microscopy* (Springer Science Business Media, LLC 1996, 2009)
43. Linda E. Franken, K. Grünwald, E. J. Boekema, and Marc C. A. Stuart, *Small* 16 (2020) 1906198.

-
44. D. Regonini, Anodised TiO₂ Nanotubes: Synthesis, Growth Mechanism and Thermal Stability (2008) University of Bath
 45. A. D. Skoog, J. F. Holler, R. S. Crouch, Principles of Instrumental Analysis (6th ed.). Belmont, CA: Thomson Brooks/Cole. pp. (2007) 169–173.
 46. S. Majumder, Synthesis, characterization and exploring application potential of some iron oxide and gold based functional nano and micro structures (2019) Jadavpur University.
 47. A. Halder, A. Sannigrahi, N. De, K. Chattopadhyay and S. Karmakar, Langmuir 36 (2020) 3522–3530.
 48. P. Maity, B. Saha, G.S. Kumar, S. Karmakar, BBA-Biomembranes 1858 (2016) 706-714.
 49. Y. Liu, D.J. Sellmyer, D. Shindo, Handbook of Advanced Magnetic Materials (2006 Tsinghua University Press Springer)
 50. G. K. Wertheim, Mössbauer Effect, Principles and Applications (Academic Press, New York, 1964).
 51. Y. Sun, M. B. Salamon, K. Garnier and R. S. Averbach, Phys. Rev. Lett. 91 (2003) 167206.
 52. C. G. Zoski, *Handbook of electrochemistry* (Elsevier, 2006).
 53. Chi-yuen Hui, Chi-wai Kan, Chee-leung Mak and Kam-hong Chau, Processes 7 (2019) 922.
 54. N. Elgrishi, K. J. Rountree, B. D. McCarthy, E. S. Rountree, T. T. Eisenhart, and J. L. Dempsey, *J. Chem. Educ.* **95** (2018)197-206.
 55. Md. Asyadi Azam, M. Mupit, Carbon Nanomaterials-Based Sensors (2022) 15-28.
 56. S. Ahmed, M.G. Rasul, Wayne N. Martens, R. Brown, M.A. Hashib, Desalination 261 (2010) 3 – 18.



Chapter 3

*Presence of mixed magnetic phase in
mechanically milled nanosized
 $\text{Co}_{0.5}\text{Zn}_{0.5}\text{Fe}_2\text{O}_4$: A study on structural,
magnetic and hyperfine properties*



3.1. Introduction

In recent times, nanosized spinel ferrites are in the limelight not only because of their application in hyperthermia [1], drug delivery [2], magnetic storage devices [3], sensors (electrochemical and gas sensing) [4-5], high frequency electronic devices [6] along with their use as contrast agent in magnetic resonance imaging [8] and active component in ferrofluid technology [9] but also pertaining to their distinctive physicochemical features as compared to their bulk counterparts [10,11]. The arousal of extraordinary properties in these spinel ferrites when reduced to nanoscale is due to increase in the surface to volume ratio, spin canting at the surface, cation redistribution between two interstitial sites of the spinel lattice and finite size effect [12,13]. On curbing down to the nanometric regime, stunning magnetic behaviors like superparamagnetism, high saturation magnetization, spin glass like freezing and several unique electrical properties like high electrical resistivity and high permeability crop up [11, 14-18]. These properties have shown variations following the synthesis procedure adopted, composition, size and shape of the fabricated nanoparticles [3, 19-24]. So, tailoring of these parameters can enable us to control the properties of the nanosized ferrites and render them suitable for various technological applications.

Nanosized $\text{Co}_{1-x}\text{Zn}_x\text{Fe}_2\text{O}_4$ ferrites have been studied comprehensively in recent years due to their phenomenal magnetic, electrical and photocatalytic properties [13,18,19-22,25-27]. Bulk ZnFe_2O_4 is a non-toxic and soft-magnetic normal spinel whereas bulk CoFe_2O_4 is a comparatively toxic and hard-magnetic inverse spinel [28]. Replacement of Co ions by Zn ions through proper synthesis procedure produces non-toxic nanosized $\text{Co}_{1-x}\text{Zn}_x\text{Fe}_2\text{O}_4$ ferrites and helps in optimizing their magnetic behavior, which leads to development of diverse magnetic orders owing to variation in sublattice exchange interactions within the spinel lattice [12,13,20-22,29]. Doping of non-magnetic Zn^{2+} ions in nanometric CoFe_2O_4 at a ratio of $X = 0.5$ gives rise to maximum value of saturation magnetization due to increase in

inter-sublattice A-O-B (J_{AB}) exchange interactions between tetrahedral (A) site and octahedral [B] site of the spinel lattice[30-33]. Above this ratio ($X > 0.5$), magnetization starts to decrease due to movement of Fe^{3+} ions from [B] site to (A) site in lieu of Zn^{2+} ions which preferentially occupy (A) site when $X < 0.5$. As per literature review, magnetization of nanometric $Co_{1-x}Zn_xFe_2O_4$ increases systematically in the region $0.1 \leq X \leq 0.5$ [34]. For $X > 0.5$, non-magnetic Zn^{2+} ions tends to occupy octahedral [B] site which results in weakening of the long range J_{AB} interactions and strengthening of the short range B-O-B (J_{BB}) and A-O-A (J_{AA}) interactions, simultaneously [34]. Thus, thorough investigation of magnetic properties of $Co_{0.5}Zn_{0.5}Fe_2O_4$ appears to be promising.

According to literature survey, most of the studies on nanosized $Co_{1-x}Zn_xFe_2O_4$ ferrites till date involve investigation of structural, magnetic and electrical properties of entire series of this system [20-22,29,31-33,35-37]. Very few groups have studied the properties of a particular composition of $Co_{1-x}Zn_xFe_2O_4$ in detail and some of them have come out with exceptional results, which otherwise get overshadowed when studied in series. Presence of nanosized magnetic clusters in an infinite magnetic framework, cluster-paramagnetic phase, cluster glass phase, mixed magnetic phase, non-collinear spin structure and superparamagnetic clusters have been recognized in nanosized $Co_{0.2}Zn_{0.8}Fe_2O_4$, $Co_{0.3}Zn_{0.7}Fe_2O_4$, $Co_{0.4}Zn_{0.6}Fe_2O_4$, $Co_{0.5}Zn_{0.5}Fe_2O_4$ and $Co_{0.6}Zn_{0.4}Fe_2O_4$ ferrites [34, 38-43]. The nanometric $Co_{0.5}Zn_{0.5}Fe_2O_4$ has attracted special attention due to rare presence of mixed magnetic phase in this system [34,43].

The synthesis procedure of nanosized spinel ferrites is of particular importance in determining their properties and their effectiveness in technological applications [19,25-27]. In this regard, chemical coprecipitation method has emerged as an efficient synthesis technique because of low-cost precursors, moderate preparation time, modest heating and large-scale production of nanometric ferrites, all of which are industrially important

[19,21,22,36,37,44]. But, these nanometric ferrites are vulnerable to reduction of magnetization and magnetic ordering temperature due to the undesirable effects of surface spin canting and superparamagnetism related to finite size effect [45-49]. Heat treatment can increase magnetization and blocking temperature of nanosized ferrites [22, 50] but is associated with the drawback of increase in particle size [46]. Interestingly, nanosized ferrites have displayed enhancement in magnetic parameters on mechanical milling due to cation rearrangement among the two interstitial sites of spinel lattice and escalation of stress anisotropy energy induced by the mechanical strain generated in the process [3,12,13,45,46,51,52]. So, synthesis of nanosized spinel ferrites by chemical coprecipitation method followed by mechanical treatment through high energy ball milling seems to be an appropriate technique to produce nanosized spinel ferrites of superior magnetic quality without compromising on the industrial demand of miniaturization.

In this background, we have employed the method of chemical coprecipitation to synthesize nanosized $\text{Co}_{0.5}\text{Zn}_{0.5}\text{Fe}_2\text{O}_4$ and ball milled it for duration of three, six and nine hours to obtain samples M1, M2 and M3, respectively, with the aim to examine the changes that have arisen in the structural, microstructural, magnetic and hyperfine properties of the samples as they undergo milling for different duration. The structural and microstructural characteristics have been inspected through powder x-ray diffraction and transmission electron microscopic techniques. The infield and without field Mössbauer spectroscopic technique along with dc magnetic measurements have been utilized to delve into the variations that have emerged in magnetic and hyperfine properties of the samples. Moreover, the dependence of magnetic properties on the structural changes induced by high energy ball milling has been investigated thoroughly on sample M2.

3.2. Experimental

$\text{Co}_{0.5}\text{Zn}_{0.5}\text{Fe}_2\text{O}_4$ nanoparticles were synthesized by chemical coprecipitation method followed by ball milling for three, six and nine hours to obtain samples M1 (~ 63 nm), M2 (~ 25 nm) and M3 (~ 17 nm). All Sigma-Aldrich made (purity more than 99.99%) reagents viz., $\text{CoCl}_2 \cdot 6\text{H}_2\text{O}$, $\text{ZnSO}_4 \cdot 7\text{H}_2\text{O}$ and $\text{Fe}(\text{NO}_3)_3 \cdot 9\text{H}_2\text{O}$ (precursors of the reaction) were taken in proper stoichiometric ratio and mixed in distilled water following addition of 10 M NaOH solution to attain a pH of ~12 under constant stirring. Afterward, the solution was continuously stirred for 9-10 hours and then the precipitate was washed in ethanol and collected by centrifugation. This precipitate was sintered at 700°C for 8 hours to obtain fine black powder. Further, this powder was annealed at 1000°C for 12 hours to attain better crystallinity. The so obtained sample shows average particle size of ~ 90 nm (Fig. 1). In general, the particle size of Co-Zn ferrites obtained from coprecipitation method ranges around 10-20 nm [12,13,22,53], but in the present case the average particle size is much larger due to the heat treatment of the sample obtained from coprecipitation method. The heat-treated sample was ball milled in a Fritsch Planetary Mono Mill Pulverisette 6 ball mill at a rotational speed of 330 rpm with ball to mass ratio 20:1 using tungsten carbide balls and vials. The detailed procedure followed for synthesis of the samples and the methodologies of ball milling experiment are also presented in our previous work [47]. Bruker D8 Advanced diffractometer, FEI Inspect F50 FESEM, JEOL 2100 HRTEM equipped with Bruker EDS system, Wissel made Mössbauer spectrometer equipped with Janis SuperOptimag superconducting magnet and Superconducting quantum interference device (SQUID) magnetometer (Quantum Design, SVSM, USA) were used for structural, morphological, hyperfine and magnetic characterization of the samples, respectively, by adopting standard measurement protocol illustrated in our earlier work [13]. The Mössbauer data of the samples were analyzed by Recoil program [54].

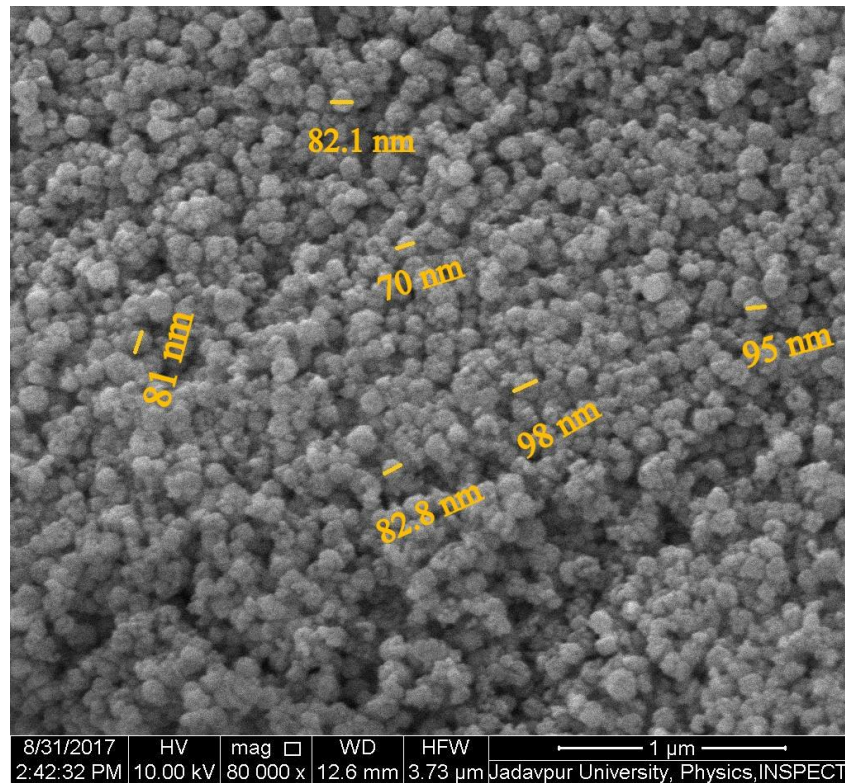


Fig.1 FESEM image of the sample obtained after coprecipitation followed by heat treatment

3.3. Results

3.3.1. Structural characterization

The observed reflections in the powder x-ray diffraction (PXRD) patterns of M1, M2 and M3 are in good conformity with the miller indices of cubic spinel structure of $Fd\bar{3}m$ space group and match well with JCPDS ICDD card numbers 22-1086 and 82-1049 for Co and Zn ferrite, respectively. The PXRD patterns of the samples M1, M2 and M3 have been indexed by Rietveld based software packages Fullprof2k [55,56]. MAUD2.33 package [57] has been used to analyze the phase purity and determine the microstructural parameters of the samples as this software can determine quantitative abundance of different phases in a composite (multiphase) material by structural refinement along with meaningful extraction of microstructural parameters by peak shift and broadening analysis of PXRD profile [58]

whereas most of the Rietveld programs (Fullprof, EXPO etc.) are not capable of implementing this procedure. The outcomes are summarized in Fig. 2 and Table 1.

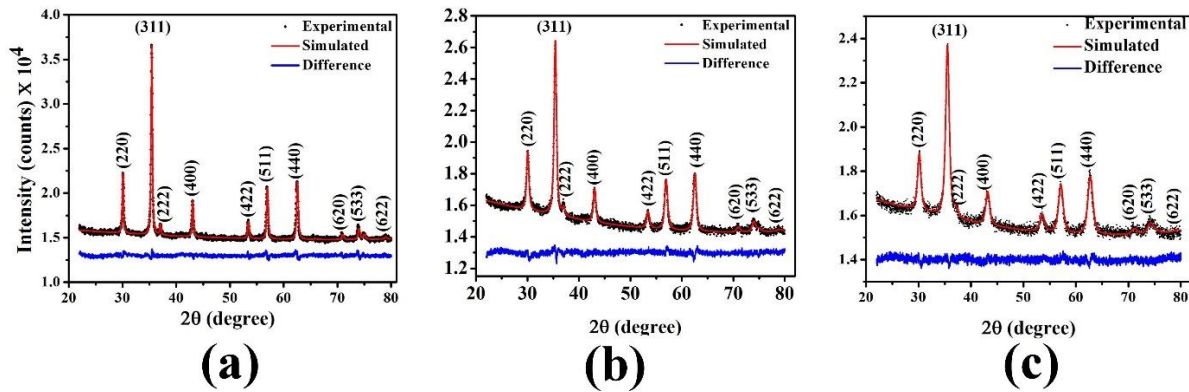


Fig. 2 PXRD pattern of the sample (a) M1, (b) M2 and (c) M3 obtained after MAUD analysis. The experimental data and the simulated pattern are represented by black dots and continuous red line, respectively. The difference between the experimental and simulated curve is plotted at the bottom with continuous blue line

Table 1 Crystal data and refinement parameters of the M1, M2, M3 obtained from MAUD

Parameters	M1	M2	M3
Crystal System	cubic	cubic	cubic
Space group	Fd-3m	Fd-3m	Fd-3m
Crystallite size (nm)	63.39	25.05	16.83
Microstrain	8.16×10^{-4}	1.97×10^{-3}	3.75×10^{-3}
Lattice parameter ($a(\text{\AA})$)	8.395	8.391	8.375
Density (g cm^{-3})	5.269	5.263	5.306
R_{wp}	0.016	0.010	0.009
R_{exp}	0.010	0.008	0.007
GOF	1.24	1.24	1.24

Further, GSAS software [59] has been used for extracting precise information on crystal structure of the samples taking into account the standard methodology reported earlier [3,13] and the results are presented in Fig. 3, Fig. 4 and Table 2,3. For Rietveld refinement by GSAS software, the initial positions of tetrahedral (A) site metal ions, octahedral [B] site

metal ions, and O atoms have been assigned in the special Wyckoff positions 8(b), 16(c), and 32(e), respectively, and refinement was carried out for the position coordinates of the oxygen atom, lattice parameters, background coefficients, cation occupancies and profile parameters. In the final stages of refinement, the preferred orientation correction was performed using the generalized spherical harmonic (order 14) model. The refinement of 63 parameters viz., 3 coordinates, 1 lattice parameter, 36 background points, 15 profile parameters, 7 orientation distribution function coefficients and 1 scale factor were performed. The experimentally recorded PXRD patterns of the samples are in good agreement with the corresponding simulated patterns. The values of lattice parameter obtained for M1, M2 and M3 are in good agreement with those for nanometric Co-Zn ferrites reported earlier [19,29,30,31,32,34,51]. This clearly discards the possibility of presence of any probable impurity phase in the samples. The results of fitting reveal that the samples are single phase nanometric spinel ferrites of $Fd\bar{3}m$ symmetry. The structural formula of M1, M2 and M3 are $(\text{Zn}^{2+}_{0.5}\text{Fe}^{3+}_{0.5})_{\text{A}}[\text{Co}^{2+}_{0.5}\text{Fe}^{3+}_{1.5}]_{\text{B}}\text{O}_4$, $(\text{Zn}^{2+}_{0.48}\text{Fe}^{3+}_{0.52})_{\text{A}}[\text{Co}^{2+}_{0.5}\text{Fe}^{3+}_{1.5}]_{\text{B}}\text{O}_4$, $(\text{Zn}^{2+}_{0.46}\text{Fe}^{3+}_{0.54})_{\text{A}}[\text{Co}^{2+}_{0.5}\text{Zn}^{2+}_{0.04}\text{Fe}^{3+}_{1.46}]_{\text{B}}\text{O}_4$, respectively. It may be noted that in our attempt to fit the PXRD data by placing Co^{2+} ions at (A) site, the values of refinement parameters (R_p , R_{wp} , and GOF) turned out to be undesirable. Thus, Co^{2+} ions have probably not occupied (A) site of the spinel lattice.

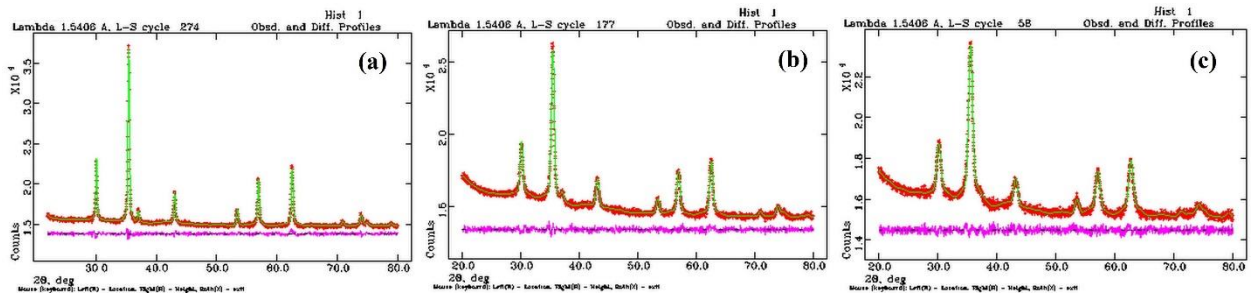


Fig.3. Indexed powder PXRD pattern of the sample (red dots) and the simulated Rietveld refinement plot (continuous green line) obtained by fitting the experimental powder PXRD pattern using GSAS program. The respective residue is plotted at the bottom (pink line).

Table 1 Structural and microstructural parameters along with metal-oxygen (M-O) bond angles and bond lengths of M1, M2 and M3 obtained from Rietveld analysis of PXRD pattern of the sample by GSAS program

Parameters	M1	M2	M3
Formula weight	475.7	475.7	475.7
Crystal System	F d -3 m	F d -3 m	F d -3 m
Lattice parameter (Å)	8.396(2)	8.390 (6)	8.378(10)
Density (g cm ⁻³)	5.338	5.331	5.373
Volume (Å ³)	591.89(4)	592.76 (13)	588.12(2)
Metal-Oxygen bond length (Å)	1.835 (A-site)	1.836 (A-site)	1.831 (A-site)
	2.089 (B-site)	2.090 (B-site)	2.085 (B-site)
Metal-Oxygen bond angle (Å)	109.47° (A-site)	109.47° (A-site)	109.47° (A-site)
	89.45° (B-site)	89.45° (B-site)	89.45° (B-site)

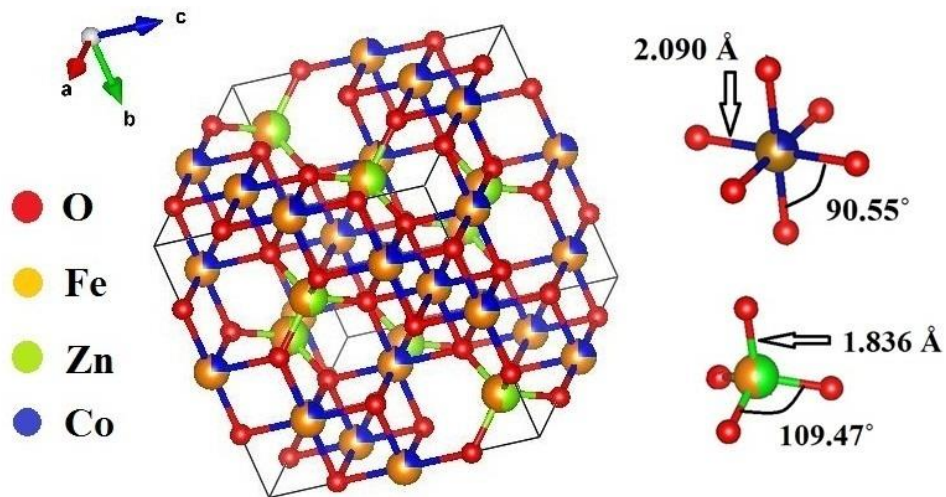


Fig. 4 Unit cell of the sample M2 showing tetrahedral (A) site and octahedral [B] site bond angles and bond lengths

Table 2 Fractional coordinates and occupancy of different ions obtained from the Rietveld refinement of PXRD pattern of M2 by GSAS program

Ions	x	y	z	Occupancy (± 0.003)
Zn (A)	0.125000	0.125000	0.125000	0.4800
Fe (A)	0.125000	0.125000	0.125000	0.5200
Co (B)	0.500000	0.500000	0.500000	0.2500
Zn (B)	0.500000	0.500000	0.500000	0.0100
Fe (B)	0.500000	0.500000	0.500000	0.7400
O	0.251194 (3)	0.251194 (3)	0.251194 (3)	1.0000

5.3.2. Electron microscopic investigation

Transmission electron microscopic (TEM) images representing the distribution of particle size in M1, M2 and M3 (Fig.5) reveal that the constituent particles in all three samples are of variable shape and size along with a strong tendency of aggregate formation, which increases with the diminution of particle size and vary following the sequence $M3 > M2 > M1$. Such agglomeration is a common trait in case of ferrites because of strong interparticle interaction [60]. All the three samples exhibit clear lattice fringes in their high-resolution TEM micrograph (Fig. 5). The distribution of particle size for M1, M2 and M3 has been examined by taking diameters (considering particles as nearly spherical) of nearly hundred nanoparticles into consideration and represented in the form of histograms. The polydispersive nature of the samples is clear from their respective histograms. The fitting of histograms with the log normal function (Fig. 6) yields average particle sizes of M1, M2 and M3 as ~ 63 , 25 and 17 nm with values of standard deviation (σ) as 0.15, 0.24 and 0.08, respectively. The value of ' σ ' quantifies the amount of dispersion in data values and so in the present case gives an idea about the polydispersity of the samples, which is directly related to the blocking temperature distribution.

The presence of bright distinct rings in the selected area diffraction (SAED) pattern of sample M2 (Fig. 7) and matching of 'd' values obtained from PXRD study with those obtained by evaluating the SAED pattern together with assure about the crystallinity of the nanoparticles. The EDX survey spectrum of M2 (Fig. 8) in the energy range of 0 to 16 keV displays only peaks for the constituent elements (Co, Zn and Fe) with no signature of any impurity phase. The ratio of Co, Zn and Fe is 16.14:16.16:64.71, which assure that the sample is in appropriate stoichiometry.

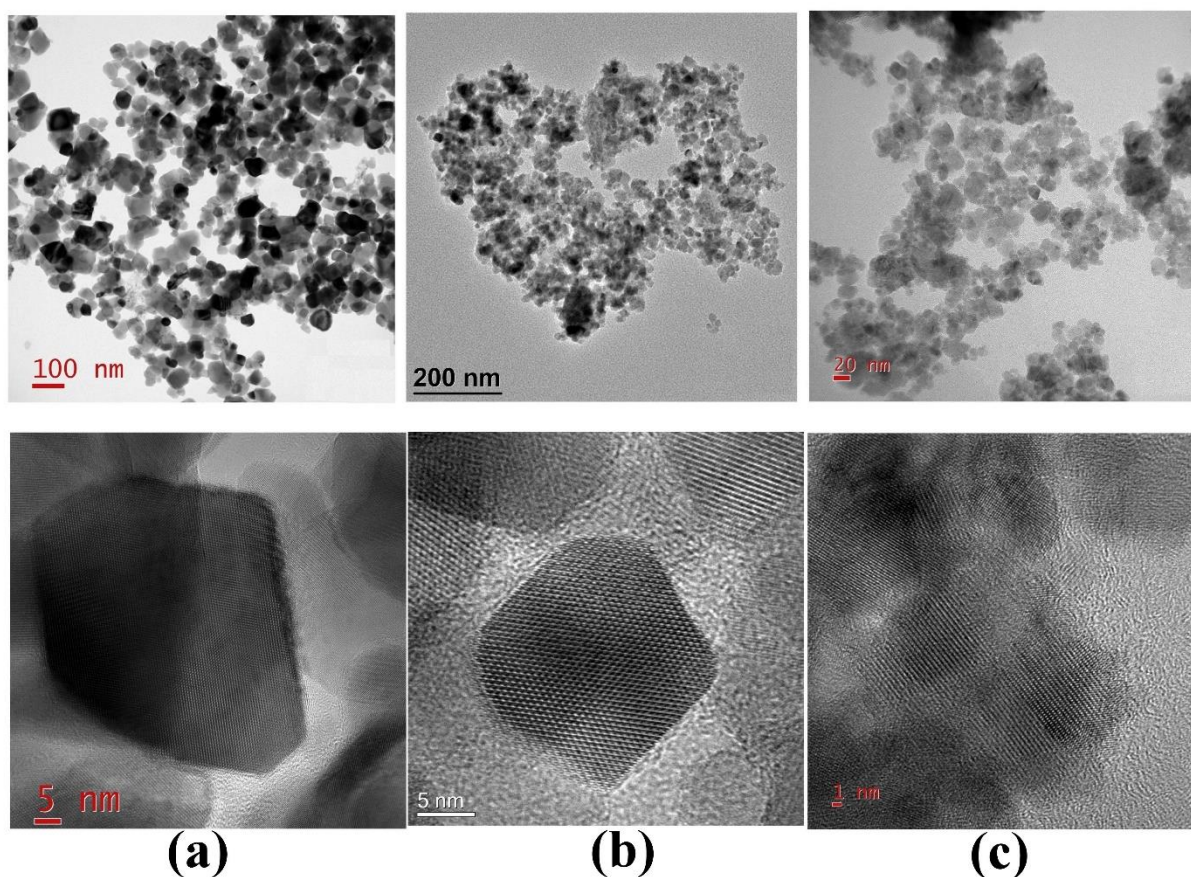


Fig. 5. TEM micrographs showing particle distribution and lattice fringes of (a) M1 (b) M2 (c) M3

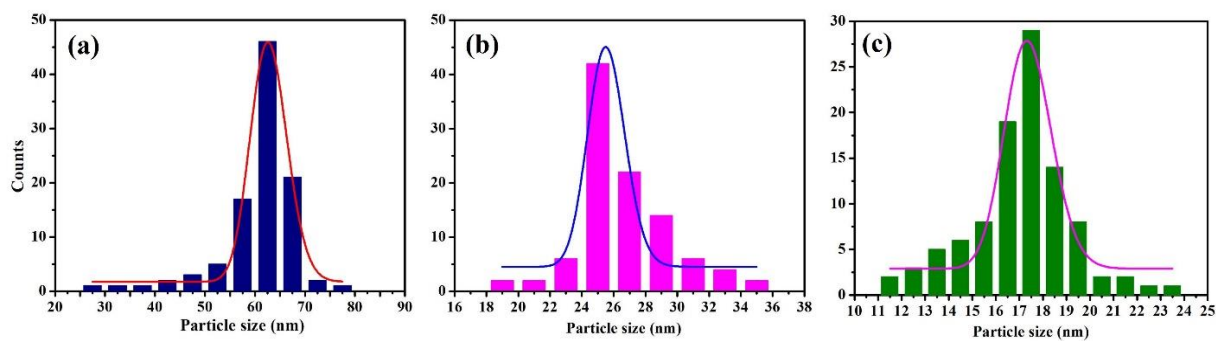


Fig. 6 Particle size histograms of (a) M1 (b) M2 (c) M3

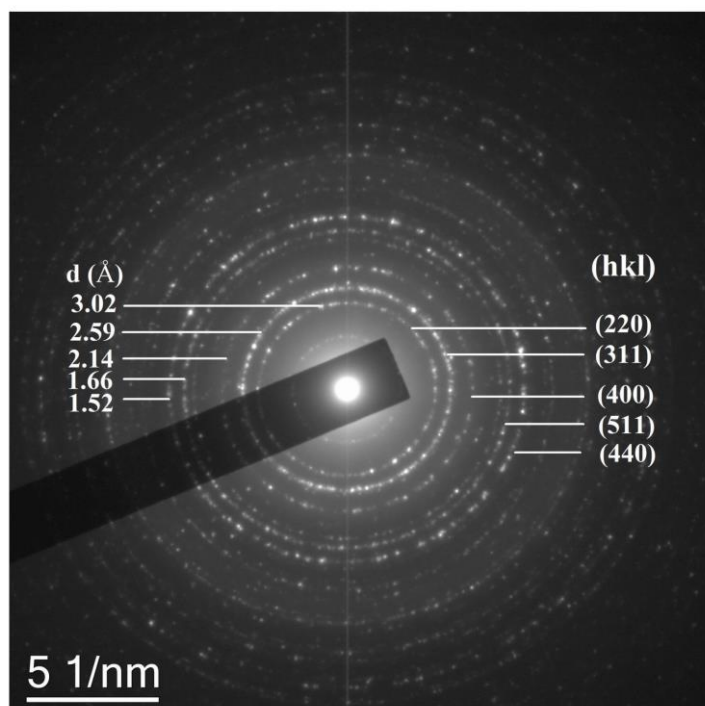


Fig. 7 SAED pattern of M2

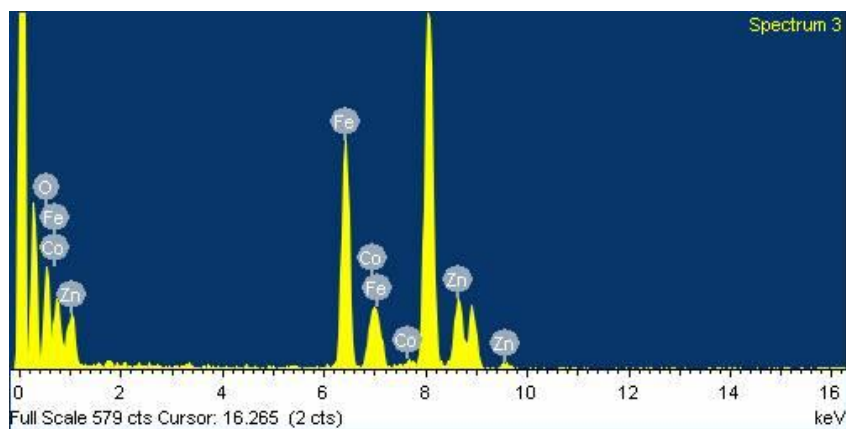


Fig. 8 EDX spectrum of M2

3.3.3. Magnetic and hyperfine study

The curves of zero field cooled (ZFC) and field cooled (FC) magnetization versus temperature (range of 5 – 350 K) of samples M1 (Fig. 9(a)), M2 (Fig.9(b)) and M3 (Fig.9(c)) under an external applied magnetic field of 100 Oe primarily exhibiting phase transition from superparamagnetic to magnetically well-ordered state with the decrease in temperature are shown in Fig. 9. It is well known that the distribution of blocking temperatures is closely related to the anisotropy energy barrier distribution of the system and thus, with the particle size distribution [61]. If the particle size distribution is uniform, the half-width of the ZFC versus temperature (T) curve is expected to be narrower [61]. The TEM study indicates the polydisperse nature of all three samples which in turn resulted in an increase in the half-width of the ZFC vs T curve. In such case, the maximum of the ZFC curve (T_{\max}) corresponds to the blocking of particles with average volume [62, 63] and can be written as $T_{\max} = \beta T_B$ [64], where β is proportionality constant that depends on the type of size distribution and T_B is defined as the temperature at which 50% of the nanoparticles are in blocked state and rest 50% are in superparamagnetic state. To account for the polydisperse nature of the samples, it would be better to determine T_B from the derivative of the difference in ZFC magnetization (M_{ZFC}) and FC magnetization (M_{FC}) with respect to temperature [22, 61]. We have plotted the $(d(M_{\text{ZFC}} - M_{\text{FC}}))/dT$ versus T curve (Fig. 10) and estimated the value of T_B for each sample. The values of T_{\max} , T_B and T_{irr} (temperature corresponding to the blocking of the largest particle) are enlisted in Table 4. The values of β for all three samples lies in the range 1.5-2.5 as should be for a nanoparticle assembly following log-normal distribution [65]. Further, the variations in values of T_B , T_{\max} and T_{irr} i.e., $T_B < T_{\max} < T_{\text{irr}}$ points out that the samples are polydisperse, thus, corroborating with the TEM study.

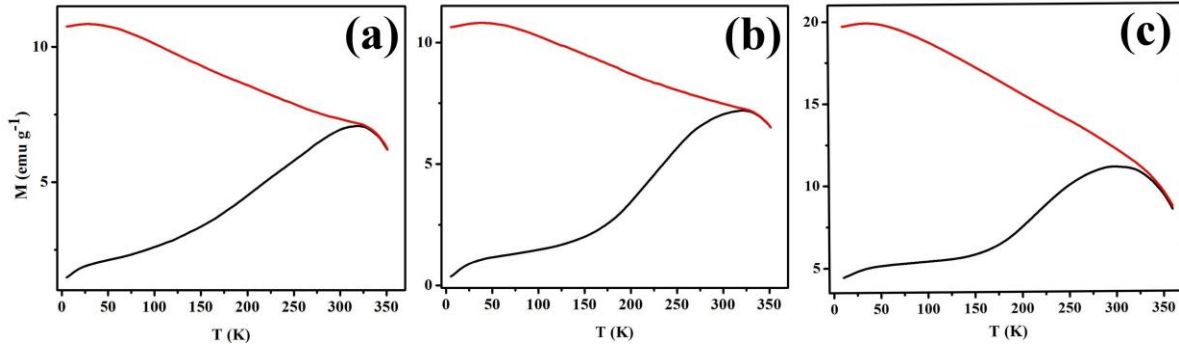


Fig.9 ZFC-FC magnetization curves of (a) M1 (b) M2 and (c) M3 at 100 Oe. The FC and ZFC magnetization is represented by red and the black lines, respectively.

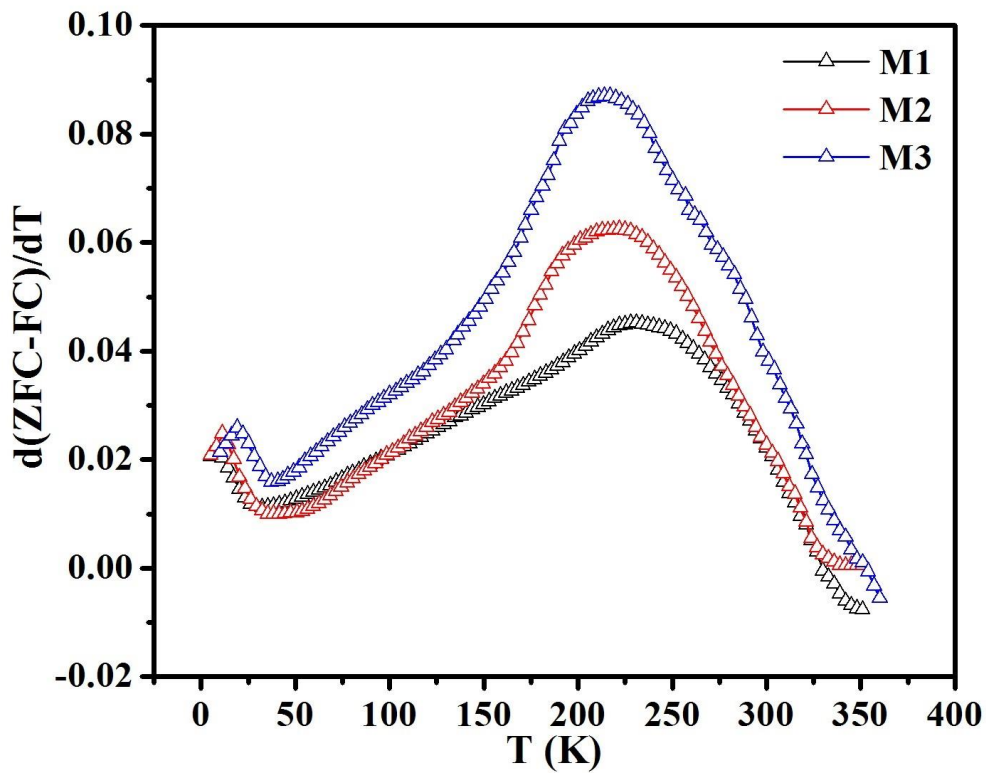


Fig. 10 $d(\text{ZFC-FC})/dT$ versus T curves for M1, M2 and M3

A second phase change transpires at about 50 K which is seen as a cusp in the ZFC curves of all the samples suggesting a spin glass like random freezing of moments resulting from strong magnetic interaction within the constituent particles of the samples [15,16,66]. This temperature is usually termed as the freezing temperature (T_f) of the system. In order to gain insight of the observed phase transition at low temperature, we have plotted the dM_{ZFC}/dT versus T curves for all three samples. The dM_{ZFC}/dT versus T curves for M1, M2

and M3 (Fig. 11) exhibit a maximum at ~ 20 K and the change in derivative begins at ~ 50 K which marks the inception of spin glass like behavior in their ZFC curve. Further, it is expected that FC curve will increase monotonically with reduction in temperature due to decreasing thermal fluctuations for typical superparamagnetic system [60]. But in this case, the FC curves of all three samples exhibit a slow fall in magnetization on decreasing the temperature below T_f of the ZFC curve. Usually if there is a combined interplay of interparticle interactions and spin glass like freezing, a flat region develops in the FC curve at very low temperatures. So, this unexpected behavior in magnetization of the FC curve below 50 K, in the present case, can be due to the random freezing of canted surface spin arrangement in the sample reinforced due to higher non-magnetic Zn^{2+} concentration in it, which can be further confirmed from in-field Mössbauer spectroscopic study.

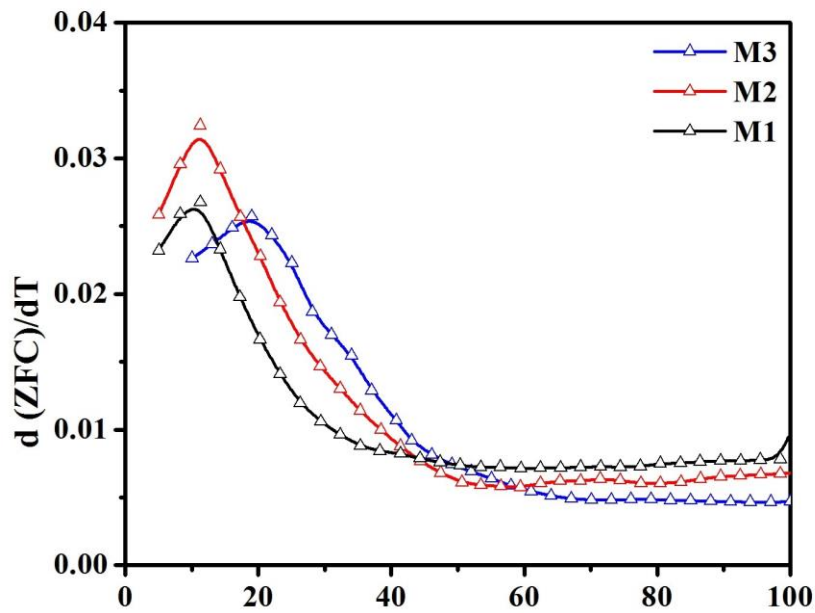


Fig. 11 $d(\text{ZFC})/dT$ versus T curves for M1, M2 and M3

We have further performed M-H (variation of magnetization with field change) loop measurements to validate the findings of ZFC-FC study. The M-H loops of M1, M2 and M3 at 300 and 10 K in the field range -1 to +1 T are shown in Fig. 12. M1 and M2 exhibit a small hysteresis in their M-H loops at room temperature but M3 does not. So, M3 is mostly

superparamagnetic but M1 and M2 clearly exhibit mixed magnetic phases. However, all the three samples exhibit clear hysteresis loops at 10 K. The values of saturation magnetization (M_{SAT}) at 300 and 10 K for the three samples have been estimated by plotting M versus $1/H$ curve using the law of approach to saturation. The values of M_{SAT} and coercivity (H_C) are provided in Table 4. The steep increase in the values of M_{SAT} and H_C at low temperature suggest development of magnetic ordering with the decrease in temperature, which may be due to freezing of surface canted spins.

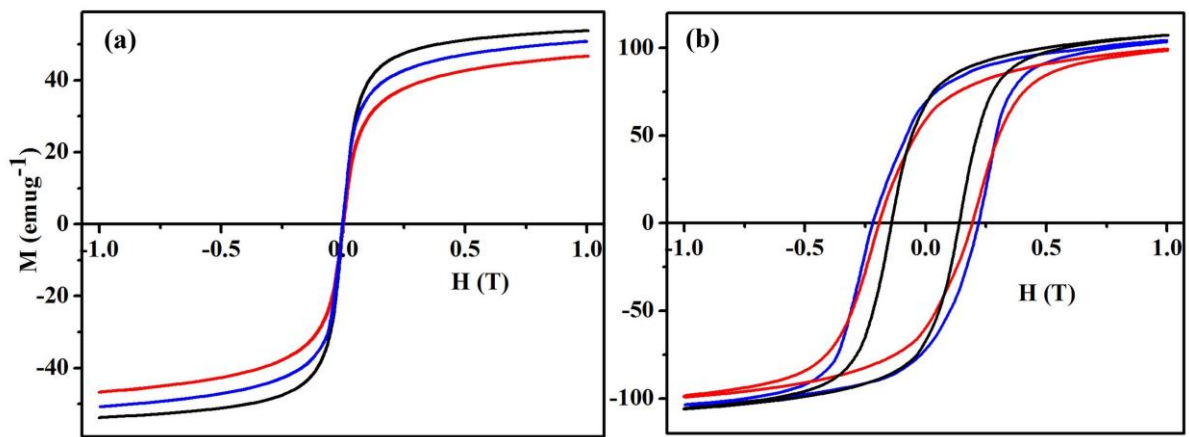


Fig.12 M-H (hysteresis) loop of M1 (black line), M2 (blue line) and M3 (red line) at (a) 300 and (b) 10 K shown between ± 1 T.

Table 4 Values of crystallite size obtained from PXRD, particle size obtained from TEM, blocking temperature (T_B), temperature corresponding to the maximum in ZFC curve (T_{max}), irreversibility temperature (T_{irr}), saturation magnetization (M_{SAT}) and coercivity (H_C)

Sl. No	Sample	Crystallite size (nm)	Particle size (nm)	T_B	T_{max}	T_{irr}	M_{SAT} (emu g ⁻¹)	H_C (Oe)
1.	M1	63	63	220	330	348	56.8 (300 K) 115.68 (10 K)	30 (300 K) 1395 (10 K)
2.	M2	25	25	210	318	345	55.3 (300 K) 113.84 (10 K)	20 (300 K) 2190 (10 K)
3.	M3	17	17	204	310	340	51.5 (300 K) 109.65 (10 K)	0 (300 K) 1950 (10 K)

^{57}Fe Mössbauer spectroscopy has been employed to determine the valency of iron ions and probe the hyperfine interactions to further delve into the observations arrived from the dc magnetic studies. The room temperature (300 K) Mössbauer data of M1, M2 and M3 have been analyzed by Recoil program [54] and the fitted spectra are presented in Fig. 13. The values of hyperfine parameters are listed in Table 5. The values of isomer shift (IS) indicate presence of only Fe^{3+} ions in all three samples [3,12,13,45,46]. M1 exhibits a clear hyperfine sextet (76.9%) and a feeble doublet (23.1%). In the spectrum of M2, a less intense sextet (69.9%) as compared to M1 along with a superparamagnetic doublet (30.1%) has been found. M3 displays a prominent doublet (49.73%) along with a poorly defined sextet (50.26%) in its room temperature Mössbauer spectrum. The intensity of the hyperfine sextet gradually diminishes with decreasing particle size. The doublet has large line width while the sextet is diffused in nature (Fig. 13). The pattern of evolution of the Mössbauer spectra with increase of particle size can be elucidated by the theory of superparamagnetic relaxations [14,15,28,60,66]. The dependence of the relaxation time (τ) of superparamagnetic nanoparticles on particle volume (V), temperature (T) and anisotropy energy constant (K) is given by Neel- Brown equation $\tau = \tau(0)\exp\left(\frac{KV}{kT}\right)$ [28] (k is the Boltzmann constant), which suggests that τ decreases with the reduction in particle size. If $\tau \ll \text{time of measurement } (\tau_m)$, total moment during the time of measurement becomes zero giving rise to a doublet [60]. On the contrary for $\tau \gg \tau_m$, a narrow hyperfine split sextet emerges [60]. But, the presence of an admixture of a relaxed sextet with a superparamagnetic doublet for all three samples indicates that the samples consist of both superparamagnetic ($\tau \ll \tau_m$) and magnetically well-ordered ($\tau \gg \tau_m$) particles. The results of dc magnetic measurements and room temperature Mössbauer spectroscopic measurements, together with, suggest that at room temperature

particles in all the samples exhibit mixed magnetic state composed of superparamagnetic and magnetically ordered phases.

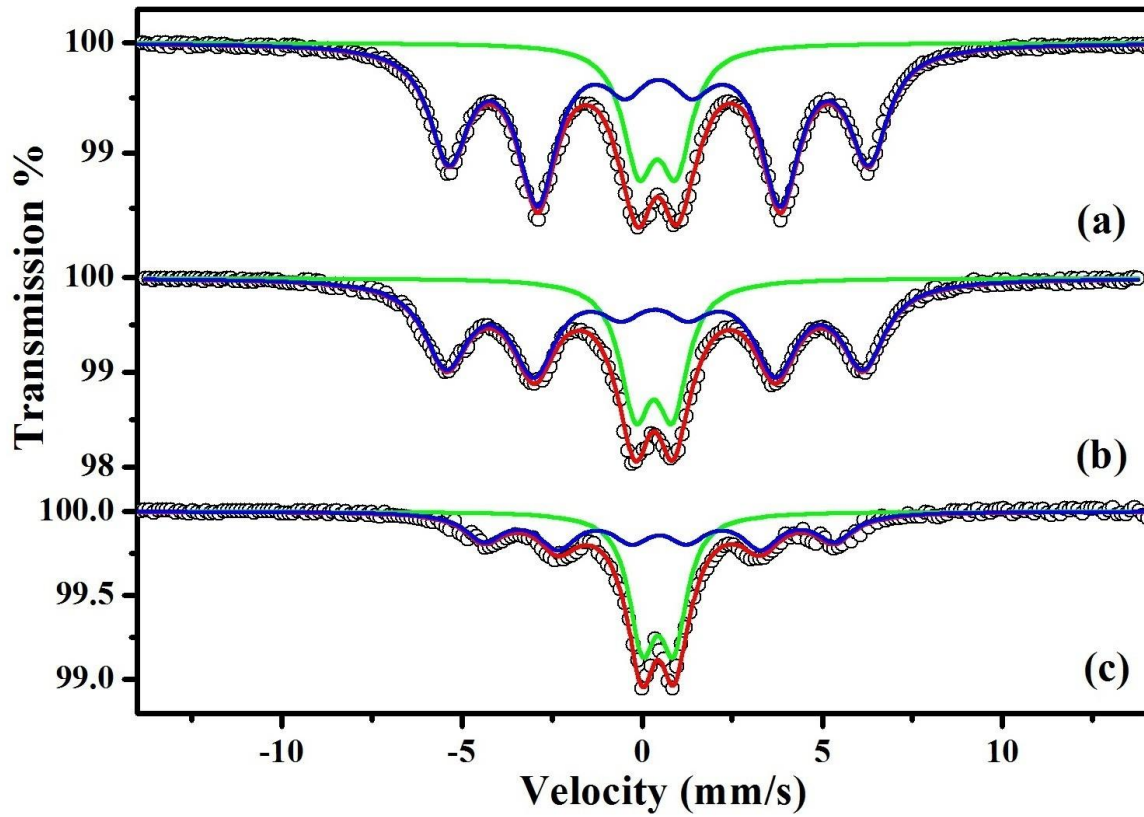


Fig.13 Mössbauer spectrum of (a) M1, (b) M2 and (c) M3 at 300 K

Table 5 Hyperfine parameters obtained by fitting the Mössbauer spectra of M1, M2 and M3 at 300 K

Sample	Spectra	IS (± 0.02) (mm s ⁻¹)	QS (± 0.07) (mm s ⁻¹)	HMF (± 0.1) (T)	Width (± 0.03) (mm s ⁻¹)	Area (± 0.3) (%)
M1	Sextet	0.45	0.0	38.33	0.6	75.25
	Doublet	0.40	1.0	-	0.5	24.74
M2	Sextet	0.36	0.0	36.0	0.7	69.93
	Doublet	0.30	1.0	-	0.5	30.06
M3	Sextet	0.45	0.0	30.0	0.6	50.26
	Doublet	0.42	1.0	-	0.4	49.73

Low temperature (5 K) in-field and without field Mössbauer spectroscopic data have been recorded to determine the spin configuration of M2, estimate the ratio of Fe^{3+} ions at (A) and [B] sites of the spinel lattice and explicate the magnetic behavior of M2 thoroughly. The in-field Mössbauer spectrum was recorded in presence of 5 T magnetic field applied parallel to the γ -ray direction. The ferrimagnetic nature of M2 can be affirmed from the appearance of a split in the 1st and the 6th line of the in-field Mössbauer spectrum of the sample [3,12,13,45-47,60]. Further, the occurrence of 2nd and 5th lines in the in-field Mössbauer spectrum of M2 clearly suggests the presence of canted spins in the sample [3,12,13,45-47,60]. Although two-component fitting is capable of extracting the information on the global canting of the system but it is unable to extort the local hyperfine character embedded in the Mössbauer spectrum [3,12]. So, the in-field Mössbauer spectrum recorded at 5 K has been fitted by four sextets using “Lorentzian site analysis” of Recoil program to acquire quantitative information on the distribution of cations and spin canting effect at the core and surface regions of the sample [12]. The refined values of the hyperfine parameters and the precise values of canting angles have been depicted in Table 6. The pair of sextets with lower hyperfine field (HMF), higher isomer shift (IS) and higher canting angles corresponds to the canted surface region. The core is also not perfectly aligned and possesses canted spins. The simulated and experimental spectra corroborate with each other (Fig. 14) and the values of refinement parameters are good enough. Presence of only Fe^{3+} ions in the sample can be asserted from the values of IS [28]. The proportion of the intensity of the sextets corresponding to (A) and [B] site of M2 for both core and shell is 0.35 which is greater than its bulk counterpart with equilibrium cation distribution (0.33). This suggests that the sample is chemically homogeneous and Fe^{3+} ions have migrated from [B] site to (A) site in M2. The ratio of Fe^{3+} at (A) and [B] sites obtained from the in-field Mössbauer spectrum corroborates with the one obtained from Rietveld refinement of PXRD pattern. Thus, the

four-component fitting assuming the core-shell model in case of M2 is capable of divulging the hyperfine character of the system accurately.

The without field Mössbauer spectrum of M2 at 5 K has been fitted with “Lorentzian profile” using four sextets by restricting the ratio of iron ions in (A) and [B] sites to that obtained from the infield spectrum to verify the results acquired from infield Mössbauer measurements [3,13]. The experimentally obtained and fitted spectra have matched with an excellent concord (Fig. 14). Presence of a well-defined sextet in the without field Mössbauer spectrum of M2 suggests that superparamagnetic relaxation has completely vanished at 5 K [3,13]. Table 6 contains the fitted values of hyperfine parameters of both the without field and infield Mössbauer study, and they agree very well with each other. Thus, taking into account the outcomes of the room temperature Mössbauer study, infield and without field Mössbauer spectrum of M2 at 5 K and dc magnetic measurements, it can be inferred that particles in M2 possess core-shell structure with a slightly canted core surrounded by a disordered shell and they exhibit superparamagnetic behavior at room temperature owing to their nanometric size.

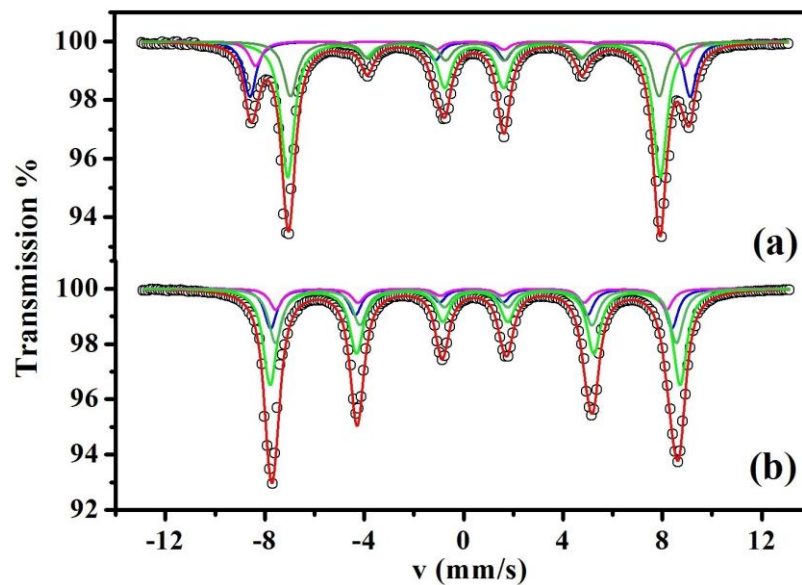


Fig.14 Mössbauer spectra of M2 at (a) 5 K with 5 T external magnetic field and (c) 5 K fitted by Lorentzian site analysis method of the Recoil program

Table 6 Values of zero field and infield Mössbauer parameters of the sample at 5K determined by Lorentzian profile fitting

Temperature /Field	Site	Width (mm s ⁻¹)	IS (mm s ⁻¹)	2ε (mm s ⁻¹)	B _{eff} ^a (T)	B _{hf} (T)	A ₂₃	θ ^b (degree)	Area (%)
5 K/ 5 T	[Fe ³⁺ _A] _C	0.28	0.31	-	54.94	50.07 ^c	0.1	12.75	17.9
	[Fe ³⁺ _A] _C	0.31	0.47	-	46.5	51.17 ^c	0.3	21.93	50.69
	[Fe ³⁺ _A] _S	0.28	0.30	-	53.5	48.76 ^c	0.2	17.97	8.14
	[Fe ³⁺ _A] _S	0.31	0.50	-	46.0	50.06 ^c	0.9	37.31	23.25
5 K/ 0 T	[Fe ³⁺ _A] _C	0.28	0.31	-	-	50.07	-	-	17.55
	[Fe ³⁺ _A] _C	0.31	0.47	-	-	51.17	-	-	46.80
	[Fe ³⁺ _A] _S	0.28	0.30	-	-	48.76	-	-	9.29
	[Fe ³⁺ _A] _S	0.31	0.50	-	-	50.06	-	-	26.33

‘C’ denotes the core region and ‘S’ denotes the shell region

^aObserved HMF (BHF) is the vector sum of the internal HMF and the external applied magnetic field.

^bThe average canting angle estimated from the ratio of the intensities of lines 2 and 3 from each subspectra, I₂/ I₃ (A₂₃) according to $\theta = \arccos[(4- I_2/ I_3) / (4+ I_2/ I_3)]^{1/2}$. Where I₂/ I₃=A₂₃.

^cEstimated according to the relationship of B_{eff}, B_{hf} and applied field.

3.3.4. Study of memory effect

From literature survey, it is well-established that magnetic nanoparticles can keep a track of field changes in their dc magnetization measurement as a function of temperature [67-70]. The origin of this effect can be accredited to the presence of either spin glass like state in the system or due to broad particle size distribution in the nanoparticle assembly [67,68]. In the present case, all the three samples consist of both superparamagnetic (single domain) and magnetically well-ordered (multidomain) particles with broad size distribution. Further, the constituent particles in all three samples possess strong interparticle interactions which result in spin glass like phase at low temperature. Thus, it can be predicted that the samples under investigation may exhibit memory effect in both low and high temperature regions.

In order to testify the above argument, we have carried out a memory protocol experiment on sample M2 following the procedure described herein. At first, the magnetization versus temperature ($M(T)$) data of M2 was recorded as the sample underwent cooling from 300 K to 250 K with application of 100 Oe external magnetic field. Then, the field was switched off after 250 K temperature was attained and the system was held in this state for one hour. Post that, the 100 Oe field was reinstated and $M(T)$ data was recorded for temperature decrease from 250 to 70 K. The field was raised to 200 Oe after the system reached 70 K and kept in this condition for one hour. Thereafter, the field was reduced to 100 Oe and $M(T)$ data was recorded from 70 to 25 K under 100 Oe field. The field was turned off and the system was arrested in this state for one hour. Again, 100 Oe field was restored and $M(T)$ data was taken from 25 to 5 K. After reaching 5 K, the system was heated from 5 to 300 K under 100 Oe magnetic field and $M(T)$ data was recorded. Both cooling and heating rates were fixed at 2 K/min throughout the experiment. Fig. 15 depicts the outcomes of the memory experiment. It clearly reveals that the system remembers the changes made in the values of applied magnetic field during the experiment and can track such changes, thus displaying “memory effect”. So, it seems that the nanoparticle assembly can encode a rapid rise or fall in the applied field during cooling process which can be successfully decoded in the heating cycle.

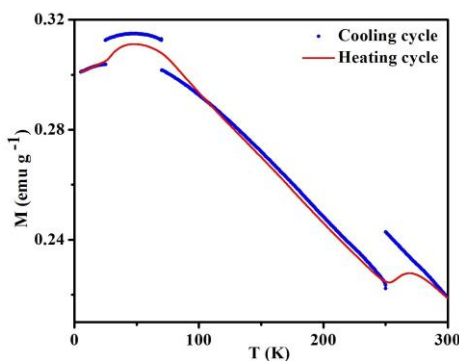


Fig.15 Memory effect in the dc magnetization of M2 (red line and blue dots represent the magnetization data for the heating and the cooling cycles, respectively).

3.4. Discussions

The results of Rietveld refinement of the PXRD pattern of M1, M2 and M3 using MAUD2.33 has revealed that all three samples are single phase nanometric spinel ferrite possessing $Fd\bar{3}m$ symmetry having chemical composition $\text{Co}_{0.5}\text{Zn}_{0.5}\text{Fe}_2\text{O}_4$. It is possible to estimate the value of lattice parameter (a_{es}) of $\text{Co}_{0.5}\text{Zn}_{0.5}\text{Fe}_2\text{O}_4$ system by taking the weighted average of the lattice parameters of pure CoFe_2O_4 and ZnFe_2O_4 i.e., using the relation $a_{\text{es}} = 0.5 a_1 + 0.5 a_2$, where $a_1 = 8.391 \text{ \AA}$ and $a_2 = 8.440 \text{ \AA}$ are the lattice parameters of CoFe_2O_4 (JCPDS ICDD card no. 22-1086) and ZnFe_2O_4 (JCPDS ICDD card no. 82-1049), respectively. The obtained value of a_{es} is $\sim 8.41 \text{ \AA}$, which is in good agreement with those of the present samples. The values of microstrain (Table 1) vary in the order $\text{M3 (63 nm)} > \text{M2 (25 nm)} > \text{M1 (17 nm)}$ i.e., microstrain increases upon increase in milling time which is a common phenomenon in mechanically milled ferrites [3]. In the present case, the values of lattice parameter (Table 1 and Table 2) change following the sequence $\text{M3} < \text{M2} < \text{M1}$ i.e., decreases with the increase in milling time. It is well known that mechanical milling promotes changes in structural and microstructural properties due to cation redistribution which, in turn, affect the magnetic properties of these compounds [3,12,13,45,46,51,52]. In this light, we have studied the effects of mechanical activation through ball milling on bonding properties, cation distribution and size reduction of all three samples. In this regard, we have calculated the theoretical values of lattice parameter (a), tetrahedral (d_{AO}) and octahedral (d_{BO}) bond lengths, and oxygen positional parameter (u) using the formulae described in detail in following works [3,29,71-75] taking into consideration the Shannon effective ionic radii [76] and compared those values with the ones obtained experimentally. All the calculations have been executed using the cation distribution obtained collectively from the Rietveld refinement of PXRD data and infield Mössbauer spectroscopy. The experimental results and theoretical calculations are in consonance (Table 7). This validates

that the outcomes of analysis of the PXRD data are reliable and the cation distribution of M2 is trustworthy. As can be seen from Table 7, the values of ‘a’ for all three samples are slightly reduced in comparison to bulk $\text{Co}_{0.5}\text{Zn}_{0.5}\text{Fe}_2\text{O}_4$. Further, the values of d_{AO} have reduced and d_{BO} increased in all three cases in contrast to bulk. It is a well-known fact that by comparing the value of u , one can map out the possibility of cation migration in spinel ferrites [71]. We have also observed that the value of u for the bulk $\text{Co}_{0.5}\text{Zn}_{0.5}\text{Fe}_2\text{O}_4$ is different from all three samples indicating cation redistribution as has been estimated from infield Mössbauer spectroscopic study. So, we can conclude that, in the present case, structural parameters have changed noticeably upon scaling down to nanometric size as a result of incorporation of mechanical strain by ball milling.

Table 7 Experimental and theoretical values of the structural parameters of nanosized $\text{Co}_{0.5}\text{Zn}_{0.5}\text{Fe}_2\text{O}_4$ and reported values of bulk $\text{Co}_{0.5}\text{Zn}_{0.5}\text{Fe}_2\text{O}_4$

Structural parameters	Nanosized Co _{0.5} Zn _{0.5} Fe ₂ O ₄						Bulk
	Experimental value (Å)			Theoretical value (Å)			Co _{0.5} Zn _{0.5} Fe ₂ O ₄
	M1	M2	M3	M1	M2	M3	(Å)
Lattice parameter (a)	8.396	8.400	8.378	8.399	8.3987	8.397	8.4208 [77]
A-O bond length (d _{AO})	1.835	1.836	1.831	1.905	1.903	1.900	1.954 ^a
B-O bond length (d _{BO})	2.089	2.090	2.085	2.05	2.051	2.052	2.032 ^a
A-site ionic radii (r _{AO})	0.475	0.476	0.471	0.545	0.543	0.541	-
B-site ionic radii (r _{BO})	0.709	0.710	0.705	0.67	0.671	0.672	-
Oxygen positional parameter	0.3762	0.3762	0.3762	0.3809	0.3808		0.384 [77]
(u)					0.3807		

^aCalculated using the formulae of (d_{AO}) and (d_{BO}) [29] using the values of ‘a’ and ‘u’ for bulk $\text{Co}_{0.5}\text{Zn}_{0.5}\text{Fe}_2\text{O}_4$

Furthermore, we have calculated the theoretical value of magnetic moment per formula unit (m) adopting the procedure described in our earlier works [3,13]. Since the cation distribution for both core and shell of M2 is $(\text{Zn}^{2+}_{0.48}\text{Fe}^{3+}_{0.52})_{\text{A}}[\text{Co}^{2+}_{0.5}\text{Zn}^{2+}_{0.02}\text{Fe}^{3+}_{1.48}]_{\text{B}}\text{O}_4$, we have calculated the theoretical value of m using this formula and taking canting angles from Table 6. The values of the magnetic moment for the core region (m_{CR}) and surface region (m_{SR}) are 5.72 and 4.606 μ_{B} , respectively. From the results of Mössbauer spectroscopic study, it has been found that the core and the shell regions cover 68.6 % and 31.4 % of the total volume of each particle, respectively. Considering this fact, we have calculated the value of m of the sample using the formula $m = 0.686 \times m_{\text{CR}} + 0.314 \times m_{\text{SR}}$ and obtained value of m is 5.37 μ_{B} . The experimental value of m for M2 in Bohr magneton (μ_{B}) obtained by using M-H data at 10 K is 5.32 μ_{B} . The experimental and theoretical values of ‘ m ’ are very close to each other which indicate that the structural formula used for the calculation of magnetic moments has been precisely determined and the particles in the sample possess almost ferrimagnetically aligned core with small canting along with magnetically disordered shell.

The results of TEM, dc magnetic and Mössbauer studies together with bring about following main issues about all three samples: (i) existence of mixed magnetic phases at room temperature, (ii) presence of overall ferrimagnetic ordering along with surface spin canting, and (iii) random spin glass like freezing of magnetic moments at low temperature. The possible reasons for such observations have been discussed thoroughly with supporting references in the rest part of this text. The morphological study of M1, M2 and M3 using TEM indicates that constituent particles of all three samples have variable shape and size, possess interparticle interactions and surface disorder. These features have induced two different phase transitions in the ZFC versus T curves of M1, M2 and M3; transition from superparamagnetic to blocked state below blocking temperature (T_{B}) and a random spin glass

like freezing below T_f ($< T_B$). According to the outcomes of Mössbauer spectroscopic studies at room temperature (~ 300 K), majority of the particles in the milled samples are in superparamagnetic state (single domain) and a small fraction (multi domain) exhibit collective magnetic excitations. Further, due to the presence of strong interparticle interactions within the samples, the particles in the samples undergo transition from collective state to spin glass like state, which has been indicated by the appearance of a sharp cusp in the ZFC versus T curve [66]. Hence, the observed behaviour of the ZFC versus T curves is a result of a complex combination of individual blocking phenomena, interparticle interaction and collective freezing of magnetic moments.

Further, the low temperature in-field Mössbauer spectroscopic studies also bring forth the core-shell structure of the nanoparticles in M2 with a core having slightly canted spins surrounded by a shell with disordered spin alignment. The effect of these disordered spins at the surface gets more prominent below a certain particle size when the surface to volume ratio is high. Thus, for the nanoparticle assembly in M2, these disordered surface spins get randomly frozen as the temperature is lowered and it has been manifested by fall in magnetization of the FC curve at very low temperatures. Thus, the dc magnetic and in-field Mössbauer studies together suggest that the freezing of disordered spins of the core-shell structure is responsible for the unexpected and topical magnetic behavior of the FC curves of the present samples at low temperature.

The constituent particles of all three samples M1, M2 and M3 are polydisperse in nature as has been observed from TEM analysis. Further, the room temperature Mössbauer spectra of all three samples possess an admixture of a superparamagnetic doublet and a diffused sextet. So, it is clear that all the samples consist of both single domain and multi domain particles. It is well known that for uniaxial single domain particles, anisotropy energy constant (K) can be calculated using the formula $KV = 25 k_B T_B$, where V is the particle

volume, k_B is the Boltzmann constant and T_B is the blocking temperature of the particle. So, in the present case, it will not be appropriate to use the above formula for calculation of K . But still then, we have used the above formula and found the values of K for M1, M2 and M3 as 3.07×10^2 , 4.4×10^3 , 1.41×10^4 J/m³, which are unusually small as compared to other nanosized Co-Zn systems [13,53,79]. So, we have employed a formula for the calculation of K , which does not take the particle size of the samples into consideration; instead the values of M_{SAT} , H_C and density of the nanoparticles (ρ) are used and can be written as $K = \mu_0 M_{SAT} \frac{H_a}{2} \rho$, where H_a is the anisotropy field and $\frac{H_a}{2}$ corresponds to the maximum value of H_C [79]. The values of K obtained using this formula are 8.6×10^4 , 1.3×10^5 , 1.1×10^5 J/m³ for M1, M2 and M3, respectively. The calculations have been done taking into consideration the estimated values of M_{SAT} and H_C provided in Table 4, and values of ρ present in Table 2. These values of K for M1, M2 and M3 are very close to that of pure cobalt ferrite ($\sim 2 \times 10^5$ J/m³). It can be clearly seen that there is a difference of almost two orders in the values of K for M1 and M2 obtained using formulae $KV = 25 k_B T_B$ and $K = \mu_0 M_{SAT} \frac{H_a}{2} \rho$ as both consist of mainly multi domain particles, whereas for M1 the difference is of one order as most of the constituent particles of M1 are single domain (superparamagnetic). Thus, the values of K obtained using $K = \mu_0 M_{SAT} \frac{H_a}{2} \rho$ formula is trustworthy. All the three samples exhibit high values of K due to enhancement of both magnetocrystalline and strain induced anisotropy caused by mechanical strain produced through high energy ball milling [13]. We have compared the lattice parameter of the present samples with bulk $Co_{0.5}Zn_{0.5}Fe_2O_4$ in Table 7 and observed that there is a contraction in lattice parameter for the present samples. This contraction has contributed to the increase in magnetocrystalline anisotropy energy. Further, an increase in microstrain with increasing milling time has been observed for the present samples. Thus, strain induced anisotropy and magnetocrystalline anisotropy together have lead to the enhancement of K .

The values of M_{SAT} of M1, M2 and M3, both at 300 and 10 K, falls off gradually with the decrement in particle size i.e., $M1 (63 \text{ nm}) > M2 (25 \text{ nm}) > M3 (17 \text{ nm})$. This reduction can be ascribed to the occurrence of spin canting at the nanoparticle surface introduced by high energy ball milling resulting in magnetic disorder [3,12,13,60]. With the minimization in particle size upon mechanical milling, surface effects become more prominent and thus, canted spins at the surface can cause a reduction in effective magnetization of the system [64,80]. Table 8 compares the values of room temperature (300 K) magnetic parameters like M_{SAT} and H_C for nanosized $Co_{0.5}Zn_{0.5}Fe_2O_4$ ferrites synthesized by different techniques with that of the present samples. It suggests that the value of M_{SAT} of $Co_{0.5}Zn_{0.5}Fe_2O_4$ ferrite depends upon the synthesis procedure and particle size. Further, the values of M_{SAT} of the present samples M1, M2 and M3 at 10 K, $Co_{0.5}Zn_{0.5}Fe_2O_4$ synthesized by coprecipitation followed by heat treatment with particle size 15 and 22 nm at 4.5 K [22] and $Co_{0.5}Zn_{0.5}Fe_2O_4$ synthesized by low temperature solution combustion method having particle size 12 nm at 20 K [32] are 115.68, 113.84, 109.65, 112.5, 125 and 100 emu g^{-1} , respectively. There is a sheer rise in the values of M_{SAT} at low temperature (10 K) as compared to room temperature (300 K). This behavior has been detected in ferrimagnetic nanoparticles and assigned to the freezing of surface spins [58,64,80,81].

Samples M1 and M2 exhibit small coercivity at room temperature (300 K) but M3 does not as it is almost purely superparamagnetic possessing very few larger sized particles as has been predicted from room temperature Mössbauer spectroscopic study. The small coercivity at 300 K displayed by M1 and M2 are due to increased magnetocrystalline anisotropy of the samples caused by ball milling [12]. At 10 K, the coercive field varies following the order $M2 > M3 > M1$. Waje et al., and Iqbal et al., have obtained similar changes in coercivity (H_C) beyond a certain particle size [18, 86]. This pattern of variation in H_C can be explained from the magnetic domain theory as has been illustrated in our earlier work [3].

Although for strongly interacting particles, it is problematic to obtain parameters related to non-interacting independent particles, we have calculated the critical diameter (D_C) of a particle approximately by using the formula $D_C = 9E_p/2\pi M_s$, where $E_p = \sqrt{\frac{2k_B T_C K}{a}}$ is the energy density of the magnetic domain wall and M_s is the saturation magnetization, considering it to be nearly spherical [3]. We have first estimated the value of E_p by taking Boltzmann constant k_B , magnetocrystalline anisotropy $K = 1.1 \times 10^5 \text{ J/m}^3$, lattice constant $a = 8.40 \text{ \AA}$, saturation magnetization $M_s = 647.17 \text{ Gauss}$ and Curie temperature $T_C = 420 \text{ K}$ as has been obtained from Veverka et al., considering the fact that sample M3 has particle size nearly equal to one of their samples having same chemical composition [22]. The calculated value of D_C for nanosized $\text{Co}_{0.5}\text{Zn}_{0.5}\text{Fe}_2\text{O}_4$ is $\sim 27 \text{ nm}$. Thus, particles in M1 (63 nm) are multi domain whereas M2 (25 nm) and M3 (17 nm) can be considered as single domain. Among three samples, the particle size of M2 is closest to the value of D_C . It is well known that the value of H_C increases with the decrement in particle size in multi domain region then attains a maximum value at D_C and again decreases in single domain regime with diminution of particle size [11, 88]. In the present case, the highest value of H_C has been obtained for M2 which consists of particles with diameter closer to the critical diameter while value of H_C decreases for both M3 with particle size much smaller than D_C and M1 with particle size larger than D_C . In larger particles, reversal of magnetization occurs by magnetic domain wall motion, whereas in a fine particle, entire spin needs to be rotated for magnetization reversal [3]. It is easier to rotate the domain wall in comparison to rotation of all the spins [11, 88]. Thus, higher value of H_C for M2 and M3 as compared to M1 is justified.

Table 8 Table for comparison of room temperature (300 K) magnetic parameters of nanosized $\text{Co}_{0.5}\text{Zn}_{0.5}\text{Fe}_2\text{O}_4$ ferrite synthesized by various procedures

Sl.No	Synthesis procedure	Particle size (nm)	Magnetisation M_s (emu g^{-1})	Coercivity H_c (Oe)	Reference
1.	Co-precipitation followed by heat treatment	7	-	>250	[22]
		15	-	250	
		22	-	<250	
2.	Wet chemical coprecipitation	7.26	75.80208	0	[29]
3.	Sol-gel auto combustion	29.01	90.13	176.24	[30]
4.	Coprecipitation	51	82	75.4	[31]
5.	Low temperature solution combustion	12	~ 63	~ 100	[32]
6.	Microwave combustion	45.81	65.20	66.36	[33]
7.	Chemical coprecipitation method	9.8	49.55	22	[34]
8.	Starch-assisted sol-gel auto-combustion method and ball milled	75.7	76.70	73.56	[51]
9.	Sol-gel auto-combustion method and ball milled	69.4	82.47	196.31	[52]
		21.68	21.38	9.56	
		18.99	61.38	79.7	
10.	Coprecipitation	5.8	15.5	-	[82]
11.	Precipitation Combustion	17.0	14.7	10	[83]
		24.0	3.65	50	
12.	Sol-gel Hydrothermal	23.1	73.6	314	[84]
		11.2	56.7	1464	
13.	High-temperature thermal decomposition	9.4	78.7	21	[85]
14.	Chemical coprecipitation	21	19.32	96.88	[86]
15.	Microwave combustion	35.68	73.80	~300	[87]
16.	Chemical coprecipitation Followed by high energy ball milling for				Present samples
		3 hours (M1)	56.8	30	
		6 hours (M2)	55.3	20	
		9 hours (M3)	51.5	0	

The superposition of a doublet and a sextet in the room temperature Mössbauer spectrum of all three samples suggest that some of the particles are very small and single domain in nature, hence, they exhibit superparamagnetic behavior while rest of the particles are larger in size and they display ferrimagnetic behavior. It infers that the particles in the

samples are not monodispersed. The outcomes of the low temperature (5 K) Mössbauer spectroscopic study (both in-field and without field) reveal that M2 constitutes of particles having ferrimagnetic phase and no signature of relaxation is visible at this temperature. However, the sample exhibits spin canting. On contrary, the dc magnetization study on M2 indicates presence of a cluster glass like state in the sample below 50 K which apparently disproves the results of Mössbauer spectroscopic study performed at 5K. This disparity between the two measurements can be accounted by considering the fact that Mössbauer spectroscopy probes the local fluctuations of hyperfine magnetic field whereas dc magnetization records the effective magnetic moment of the sample as a whole [66]. The presence of both (A) and [B] site sextets in the Mössbauer spectra of M2 at 5 K reveals that M2 is either ferrimagnetic in nature or there are regions (clusters) inside the particles of M2 which are in ferrimagnetic state. Thus, considering the results of Mössbauer spectroscopic study and dc magnetic measurements together, it can be concluded that there are ferrimagnetically ordered clusters inside the grains of the sample and with decreasing temperature the interplay between opposing sublattice interactions and frustrations result in freezing of local magnetic moment of these clusters in random orientation and the system en masse stabilizes in a spin glass like state [66].

The sample M2 has exhibited excellent memory effect in its dc magnetization measurements in both high temperature and low temperature regimes. The presence of strong interactions within the nanoparticle assembly and polydispersive nature of the sample have together given rise to the memory effect in M2. The presence of a stable spin glass phase in the sample is responsible for the origin of memory effect at low temperature region. The ensemble of nanoparticles can memorize the field change in its cooling cycle and can recall it accurately during the heating cycle. Hence, binary numbers 0 and 1 can be coded by defining ‘H decrease’ as “0” and ‘H increase’ as “1” in the cooling cycle of the dc magnetization

measurement and decoded if heating is done under constant magnetic field keeping both heating and cooling rates same.

3.5. Conclusion

The structural, microstructural, magnetic and hyperfine properties of nanosized $\text{Co}_{0.5}\text{Zn}_{0.5}\text{Fe}_2\text{O}_4$ having three different particle sizes have been carefully examined by PXRD, HRTEM, dc magnetic and Mössbauer spectroscopic techniques. The particle size from PXRD and crystallite size from TEM studies match well with each other revealing that M1, M2 and M3 are well-crystalline in nature. All the three samples have a wide distribution in particle size and possess strong interparticle interactions. The dc magnetic and room temperature Mössbauer spectroscopic studies together reveal that M1, M2 and M3 exhibit mixed magnetic behavior possessing both superparamagnetic and magnetically well-ordered phases at room temperature along with spin glass like freezing at low temperature invoked by the strong interparticle interactions within the ensemble of nanoparticles and random freezing of disordered surface spins at low temperature. The values of saturation magnetization of the samples are slightly lower than its equivalents due to presence of spin canting caused by milling. The values of coercivity at 10 K are much higher than at room temperature indicating absence of any relaxations within the samples at 10 K. The cation distribution of M2 obtained using infield Mössbauer spectroscopic and PXRD studies has been testified by a trustworthy method of comparison of the experimentally obtained value of magnetic moment per formula unit with that of its theoretically calculated value. The sample M2 can keep a memory of field changes in its dc magnetic measurements, i.e., displays “memory effect” and may be technologically applicable for fabrication of sensors capable of detecting field changes and in encoding and decoding binary numbers. In summary, we can conclude that the magnetic structure of nanosized ferrites can be moderated suitably through mechanical activation to

produce samples which can meet industrial demand of manufacturing miniature devices having superior magnetic quality.

References

1. Ç.E. Demirci, P.K. Manna, Y. Wroczynskyj, S. Aktürk, J. van Lierop, Lanthanum ion substituted cobalt ferrite nanoparticles and their hyperthermia efficiency, *J. Magn. Magn. Mater.* 458 (2018) 253–260. DOI: <https://doi.org/10.1016/j.jmmm.2018.03.024>
2. L. Khanna, N.K. Verma, S.K. Tripathi, Burgeoning tool of biomedical applications – Superparamagnetic nanoparticles, *J Alloys Compd* 752 (2018) 332-353. DOI: <https://doi.org/10.1016/j.jallcom.2018.04.093>
3. R. Mondal, S. Dey, S. Majumder, A. Poddar, P. Dasgupta, S. Kumar, Study on magnetic and hyperfine properties of mechanically milled $\text{Ni}_{0.4}\text{Zn}_{0.6}\text{Fe}_2\text{O}_4$ nanoparticles, *J. Magn. Magn. Mater.* 448 (2018) 135–145. DOI: <http://dx.doi.org/10.1016/j.jmmm.2017.07.031>
4. S. Majumder, B. Saha, S. Dey, R. Mondal, S. Kumar, S. Banerjee, A highly sensitive non-enzymatic hydrogen peroxide and hydrazine electrochemical sensor based on 3D micro-snowflake architectures of $\alpha\text{-Fe}_2\text{O}_3$, *RSC Adv.* 6 (2016) 59907. DOI: 10.1039/c6ra10470c
5. P. Guo, L. Cui, Y.Wang, M. Lv, B.Wang, X. S. Zhao, Facile Synthesis of ZnFe_2O_4 Nanoparticles with Tunable Magnetic and Sensing Properties, *Langmuir* 29 (2013) 8997–9003. DOI: dx.doi.org/10.1021/la401627x
6. A. B. Gadkari, T. J. Shinde, P. N. Vasambekar, Ferrite Gas Sensors, *IEEE SENS J* 11 (2011) 849. DOI: 10.1109/JSEN.2010.2068285
7. R. Sharma, P. Thakur, M.Kumar, P. Sharma, V. Sharma, Nanomaterials for high frequency device and photocatalytic applications: Mg-Zn-Ni ferrites, *J Alloys Compd* 746 (2018) 532-539. DOI: <https://doi.org/10.1016/j.jallcom.2018.02.287>
8. D. Lam Tran, V. Hong Le, H. Linh Pham, T. My Nhung Hoang, T. Quy Nguyen, T. Tai Luong, P. Thu Ha, X. Phuc Nguyen, Biomedical and environmental applications of magnetic nanoparticles, *Adv. Nat. Sci.: Nanosci. Nanotechnol.* 1 (2010) 045013 (5pp). DOI:10.1088/2043-6262/1/4/045013

-
9. S. Mornet, S. Vasseur, F. Grasset, E. Duguet, Magnetic nanoparticle design for medical diagnosis and therapy, *J. Mater. Chem.* 14 (2004) 2161 – 2175. DOI: 10.1039/b402025a
 10. L.Wu, A. Mendoza-Garcia, Q. Li, S. Sun, Organic Phase Syntheses of Magnetic Nanoparticles and Their Applications, *Chem. Rev.* 116 (2016) 10473–10512. DOI: 10.1021/acs.chemrev.5b00687
 11. An-Hui Lu, E. L. Salabas, F. Schüth, Magnetic Nanoparticles: Synthesis, Protection, Functionalization, and Application, *Angew. Chem. Int. Ed.* 46 (2007) 1222 – 1244. DOI: 10.1002/anie.200602866
 12. S. Dey, R. Mondal, S. K. Dey, S. Majumder, P. Dasgupta, A. Poddar, V. R. Reddy, S. Kumar, Tuning magnetization, blocking temperature, cation distribution of nanosized $\text{Co}_{0.2}\text{Zn}_{0.8}\text{Fe}_2\text{O}_4$ by mechanical activation, *J. Appl. Phys.* 118 (2015) 103905. DOI: <http://dx.doi.org/10.1063/1.4930801>
 13. R. Mondal, S. Dey, K. Sarkar, P. Dasgupta, S. Kumar, Influence of high energy ball milling on structural parameters, cation distribution and magnetic enhancement of nanosized $\text{Co}_{0.3}\text{Zn}_{0.7}\text{Fe}_2\text{O}_4$, *Mater. Res. Bull.* 102 (2018) 160–171. DOI: <https://doi.org/10.1016/j.materresbull.2018.02.016>
 14. G. Balaji, N.S. Gajbhiye, G. Wilde, J. Weissmüller, Magnetic properties of MnFe_2O_4 nanoparticles, *J. Magn. Magn. Mater.* 242–245 (2002) 617–620.
 15. R.D. Zysler, D. Fiorani, A.M. Testa, Investigation of magnetic properties of interacting Fe_2O_3 nanoparticles, *J. Magn. Magn. Mater.* 224 (2001) 5-11.
 16. J.L. Dormann, R. Cherkaoui, L. Spinu, M. Noguès, F. Lucari, F. D’Orazio, D. Fiorani, A. Garcia, E. Tronc, J.P. Jolivet, From pure superparamagnetic regime to glass collective state of magnetic moments in $\gamma\text{-Fe}_2\text{O}_3$ nanoparticle assemblies, *J. Magn. Magn. Mater.* 187 (1998) L139-L144.
-

17. A. N. Hapishah, M. Hashim, M. M. Syazwan, I. R. Idza, N. Rodziah, I. Ismayadi, Phase, microstructure and magnetic evaluation in yttrium iron garnet (YIG) synthesized via mechanical alloying, *J Mater Sci: Mater Electron* 28 (2017) 15270–15278. DOI 10.1007/s10854-017-7407-3
18. S. B. Waje, M. Hashim, W. D. Wan Yusoff, Z. Abbas, Sintering temperature dependence of room temperature magnetic and dielectric properties of $\text{Co}_{0.5}\text{Zn}_{0.5}\text{Fe}_2\text{O}_4$ prepared using mechanically alloyed nanoparticles, *J. Magn. Magn. Mater.* 322 (2010) 686–691. DOI:10.1016/j.jmmm.2009.10.041
19. Yi-Wei Liu, Jing Zhang, Lu-Shun Gu, Li-Xi Wang, Qi-Tu Zhang, Preparation and electromagnetic properties of nanosized $\text{Co}_{0.5}\text{Zn}_{0.5}\text{Fe}_2\text{O}_4$ ferrite, *Rare Met.* DOI 10.1007/s12598-015-0670-7.
20. V. Mamei, A. Musinu, A. Ardu, G. Ennas, D. Peddis, D. Niznansky, C. Sangregorio, C. Innocenti, Nguyen T. K. Thanh, C. Cannas, Studying the effect of Zn-substitution on the magnetic and hyperthermic properties of cobalt ferrite nanoparticles, *Nanoscale*, 8 (2016) 10124. DOI: 10.1039/c6nr01303a
21. M. Schmidt, H. L. Andersen, C. Granados-Miralles, M. Saura-Múzquiz, M. Stingaciu, M. Christensen, Tuning the size and magnetic properties of $\text{Zn}_x\text{Co}_{1-x}\text{Fe}_2\text{O}_4$ nanocrystallites, *Dalton Trans.* 45 (2016) 6439. DOI: 10.1039/c5dt04701c
22. M. Veverka, P. Veverka, Z. Jiráček, O. Kaman, K. Knížek, M. Maryško, E. Pollert, K. Závěta, Synthesis and magnetic properties of $\text{Co}_{1-x}\text{Zn}_x\text{Fe}_2\text{O}_{4+\gamma}$ nanoparticles as materials for magnetic fluid hyperthermia, *J. Magn. Magn. Mater.* 322 (2010) 2386–2389. DOI:10.1016/j.jmmm.2010.02.042
23. M. Penchal Reddy, A.M.A. Mohamed, One-pot solvothermal synthesis and performance of mesoporous magnetic ferrite MFe_2O_4 nanospheres, *Microporous Mesoporous Mater.* 215 (2015) 37 - 45. DOI: <http://dx.doi.org/10.1016/j.micromeso.2015.05.024>
-

-
24. Z. Jia, D. Ren, R. Zhu, Synthesis, characterization and magnetic properties of CoFe_2O_4 nanorods, *Mater. Lett.* 66 (2012) 128–131. DOI: 10.1016/j.matlet.2011.08.056
25. R. A. Bohara, N. D. Thorat, A. K. Chaurasia, S. H. Pawar, Cancer cell extinction through a magnetic fluid hyperthermia treatment produced by superparamagnetic Co–Zn ferrite nanoparticles, *RSC Adv.* 5 (2015) 47225. DOI: 10.1039/c5ra04553c
26. X. Huang, J. Zhang, W. Wang, T. Sang, B. Song, H. Zhu, W. Rao, C. Wong, Effect of pH value on electromagnetic loss properties of Co–Zn ferrite prepared via coprecipitation method, *J. Magn. Magn. Mater.* 405 (2016) 36–41. DOI: <http://dx.doi.org/10.1016/j.jmmm.2015.12.051>
27. M. Sundararajan, V. Sailaja, L. John Kennedy, J. Judith Vijaya, Photocatalytic degradation of rhodamine B under visible light using nanostructured zinc doped cobalt ferrite: Kinetics and mechanism, *Ceram. Int.* 43 (2017) 540–548. DOI: 10.1016/j.ceramint.2016.09.191
28. B.D. Cullity, *Introduction to Magnetic Materials*, Addison-Wesley, New York, 1972.
29. D. S. Nikam, S. V. Jadhav, V. M. Khot, R. A. Bohara, C. K. Hong, S. S. Malib, S. H. Pawar, Cation distribution, structural, morphological and magnetic properties of $\text{Co}_{1-x}\text{Zn}_x\text{Fe}_2\text{O}_4$ ($x = 0-1$) nanoparticles, *RSC Adv.* 5 (2015) 2338. DOI: 10.1039/c4ra08342c
30. A. Ramakrishna, N. Murali, Tulu Wegayehu Mammo, K. Samatha, V. Veeraiah, Structural and DC electrical resistivity, magnetic properties of $\text{Co}_{0.5}\text{M}_{0.5}\text{Fe}_2\text{O}_4$ ($\text{M} = \text{Ni}, \text{Zn}$, and Mg) ferrite nanoparticles, *Physica B: Condensed Matter* 534 (2018) 134–140. DOI: 10.1016/j.physb.2018.01.033
31. T.R. Tatarchuk, N.D. Paliychuk, M. Bououdina, B. Al-Najar, M. Pacia, W. Macyk, A. Shyichuk, Effect of cobalt substitution on structural, elastic, magnetic and optical properties of zinc ferrite nanoparticles, *J Alloys Compd* 731 (2018) 1256–1266. DOI: 10.1016/j.jallcom.2017.10.103
-

-
32. D. M. Jnaneshwara, D. N. Avadhani, B. D. Prasad, B. M. Nagabhushana, H. Nagabhushana, S.C. Sharma, S.C. Prashantha, C. Shivakumara, Effect of zinc substitution on the nanocobalt ferrite powders for nanoelectronic devices, *J Alloys Compd* 587 (2014) 50–58. DOI: 10.1016/j.jallcom.2013.10.146
33. A. Manikandan, L. John Kennedy, M. Bououdina, J. Judith Vijaya, Synthesis, optical and magnetic properties of pure and Co-doped ZnFe_2O_4 nanoparticles by microwave combustion method, *J. Magn. Magn. Mater.* 349 (2014) 249–258. DOI: 10.1016/j.jmmm.2013.09.013
34. I. Sharifi, H. Shokrollahi, Nanostructural, magnetic and Mössbauer studies of nanosized $\text{Co}_{1-x}\text{Zn}_x\text{Fe}_2\text{O}_4$ synthesized by co-precipitation, *J. Magn. Magn. Mater.* 324 (2012) 2397–2403. DOI: 10.1016/j.jmmm.2012.03.008
35. G. Barrera, M. Coisson, F. Celegato, S. Raghuvanshi, F. Mazaleyrat, S.N. Kane, P. Tiberto, Cation distribution effect on static and dynamic magnetic properties of $\text{Co}_{1-x}\text{Zn}_x\text{Fe}_2\text{O}_4$ ferrite powders, *J. Magn. Magn. Mater.* 456 (2018) 372–380. DOI: 10.1016/j.jmmm.2018.02.072
36. P. Coppola, F. G. da Silva, G. Gomide, F. L. O. Paula, A. F. C. Campos, R. Perzynski, C. Kern, J. Depeyrot, R. Aquino, Hydrothermal synthesis of mixed zinc–cobalt ferrite nanoparticles: structural and magnetic properties, *J Nanopart Res* 18 (2016) 138. DOI 10.1007/s11051-016-3430-1
37. T.R. Tatarchuk, M. Bououdina, N.D. Paliychuk, I.P. Yaremiy, V.V. Moklyak, Structural characterization and antistructure modeling of cobalt substituted zinc ferrites, *J Alloys Compd* 694 (2017) 777–791. DOI: 10.1016/j.jallcom.2016.10.067
38. R.N. Bhowmik, R. Ranganathan, Anomaly in cluster glass behaviour of $\text{Co}_{0.2}\text{Zn}_{0.8}\text{Fe}_2\text{O}_4$ spinel oxide, *J. Magn. Magn. Mater.* 248 (2002) 101–111.
39. H. Parmar, P. Acharya, R.V. Upadhyay, V. Siruguri, S. Rayaprol, Low temperature magnetic ground state in bulk $\text{Co}_{0.3}\text{Zn}_{0.7}\text{Fe}_2\text{O}_4$ spinel ferrite system: Neutron diffraction,
-

magnetization and ac-susceptibility studies, *Solid State Commun.* 153 (2013) 60–65. DOI: 10.1016/j.ssc.2012.09.021

40. R.V. Upadhyay, H. Parmar, P. Acharya, A. Banerjee, Progressive freezing of finite cluster in locally canted spin $\text{Co}_{0.3}\text{Zn}_{0.7}\text{Fe}_2\text{O}_4$ spinel ferrite system, *Solid State Commun.* 163 (2013) 50–54. DOI: 10.1016/j.ssc.2013.02.020

41. G. A. Petitt, D. W. Forester, Mossbauer Study of Cobalt-Zinc Ferrites, *Phys. Rev. B* 4 (1971) 11.

42. S. Dey, A. Roy, J. Ghose, R. N. Bhowmik, R. Ranganathan, Size dependent magnetic phase of nanocrystalline $\text{Co}_{0.2}\text{Zn}_{0.8}\text{Fe}_2\text{O}_4$, *J. Appl. Phys.* 90 (2001) 4138. DOI: 10.1063/1.1401798

43. I. Sharifi, H. Shokrollahi, Structural, Magnetic and Mössbauer evaluation of Mn substituted Co–Zn ferrite nanoparticles synthesized by co-precipitation, *J. Magn. Magn. Mater.* 334 (2013) 36–40. DOI: 10.1016/j.jmmm.2013.01.021

44. W. Sacchi Peternele, V. Monge Fuentes, M. Luiza Fascineli, J. Rodrigues da Silva, R. Carvalho Silva, Ca. Madeira Lucci, R. Bentes de Azevedo, Experimental Investigation of the Coprecipitation Method: An Approach to Obtain Magnetite and Maghemite Nanoparticles with Improved Properties, *J Nanomater.* DOI: 10.1155/2014/682985.

45. S. Dey, S. K. Dey, B. Ghosh, P. Dasgupta, A. Poddar, V. R. Reddy, S. Kumar, Role of inhomogeneous cation distribution in magnetic enhancement of nanosized $\text{Ni}_{0.35}\text{Zn}_{0.65}\text{Fe}_2\text{O}_4$: A structural, magnetic, and hyperfine study, *J. Appl. Phys.* 114 (2013) 093901. DOI: 10.1063/1.4819809

46. S. Dey, S. K. Dey, K. Bagani, S. Majumder, A. Roychowdhury, S. Banerjee, V. R. Reddy, D. Das, S. Kumar, Overcoming inherent magnetic instability, preventing spin canting and magnetic coding in an assembly of ferrimagnetic nanoparticles, *Appl. Phys. Lett.* 105 (2014) 063110. DOI: 10.1063/1.4893028

-
47. S. Dey, S.K. Dey, S. Majumder, A. Poddar, P. Dasgupta, S. Banerjee, S. Kumar, Superparamagnetic behavior of nanosized $\text{Co}_{0.2}\text{Zn}_{0.8}\text{Fe}_2\text{O}_4$ synthesized by a flow rate controlled chemical coprecipitation method, *Physica B* 448 (2014) 247–252. DOI: 10.1016/j.physb.2014.03.073
48. R. N. Bhowmik, R. Ranganathan, R. Nagarajan, Biswatosh Ghosh, S. Kumar, Role of strain-induced anisotropy on magnetic enhancement in mechanically alloyed $\text{Co}_{0.2}\text{Zn}_{0.8}\text{Fe}_2\text{O}_4$ nanoparticle, *Phys. Rev. B* 72 (2005) 094405. DOI: 10.1103/PhysRevB.72.094405
49. R. N. Bhowmik, R. Ranganathan, Magnetic enhancement of $\text{Co}_{0.2}\text{Zn}_{0.8}\text{Fe}_2\text{O}_4$ spinel oxide by mechanical milling, *Phys. Rev. B* 68 (2003) 134433. DOI: 10.1103/PhysRevB.68.134433
50. S. Dey, A. Roy, J. Ghose, R. N. Bhowmik, R. Ranganathan, Size dependent magnetic phase of nanocrystalline $\text{Co}_{0.2}\text{Zn}_{0.8}\text{Fe}_2\text{O}_4$, *J. Appl. Phys.* 90 (2001) 4138. DOI: 10.1063/1.1401798
51. R. Singh Yadav, I. Kuřitka, J. Havlica, M. Hnatko, C. Alexander, J. Masilko, L. Kalina, M. Hajdúchová, J. Rusnak, V. Enev, Structural, magnetic, elastic, dielectric and electrical properties of hotpress sintered $\text{Co}_{1-x}\text{Zn}_x\text{Fe}_2\text{O}_4$ ($x = 0.0, 0.5$) spinel ferrite nanoparticles, *J. Magn. Magn. Mater.* 447 (2018) 48–57. DOI: 10.1016/j.jmmm.2017.09.033
52. R. Singh Yadav, J. Havlica, M. Hnatko, P. Šajgalík, C. Alexander, M. Palou, E. Bartoníčková, M. Boháč, F. Frajkorová, J. Masilko, M. Zmrzlý, L. Kalina, M. Hajdúchová, V. Enev, Magnetic properties of $\text{Co}_{1-x}\text{Zn}_x\text{Fe}_2\text{O}_4$ spinel ferrite nanoparticles synthesized by starch-assisted sol–gel auto combustion method and its ball milling, *J. Magn. Magn. Mater.* 378 (2015) 190–199. DOI: 10.1016/j.jmmm.2014.11.027
53. C. Gómez-Polo, V. Recarte, L. Cervera, J.J. Beato-López, J. López-García, J.A. Rodríguez-Velamazán, M.D. Ugarte, E.C. Mendonça, J.G.S. Duque, Tailoring the structural and magnetic properties of Co-Zn nanosized ferrites for hyperthermia applications, *J. Magn. Magn. Mater.* 465 (2018) 211–219. DOI: 10.1016/j.jmmm.2018.05.051
-

-
54. K. Lagarec, D. G. Rancourt, Recoil-Mössbauer Spectral Analysis Software for Window, University of Ottawa Press. Ottawa, 1998.
55. A. Boultif, D. Louer, Powder pattern indexing with the dichotomy method, *J. Appl. Crystallogr.* 37 (2004) 724 – 731.
56. P. E. Werner, L. Eriksson, M. J. Westdahl, TREOR, a semi-exhaustive trial-and-error powder indexing program for all symmetries, *J. Appl. Crystallogr.* 18 (1985) 367 – 370.
57. L. Lutterotti, MAUDWEB, Version 1.9992 (2004).
58. D. Balzar, N. C. Popa, Analyzing Microstructure By Rietveld Refinement, *The Rigaku Journal* 22 (2015) 16-25.
59. B. H. Toby, EXPGUI, a graphical user interface for GSAS, *J. Appl. Crystallogr.* 34 (2001) 210 – 213.
60. S. Dey, S.K. Dey, B. Ghosh, V.R. Reddy, S. Kumar, Structural, microstructural, magnetic and hyperfine characterization of nanosized $\text{Ni}_{0.5}\text{Zn}_{0.5}\text{Fe}_2\text{O}_4$ synthesized by high energy ball-milling method, *Mater. Chem. Phys.* 138 (2013) 833-842. DOI: 10.1016/j.matchemphys.2012.12.067
61. J.J. Lu, H. Y. Deng, H. L. Huang, Thermal relaxation of interacting fine magnetic particles-field-cooled and zero-field-cooled magnetization variation, *J. Magn. Magn. Mater.* 209 (2000) 37-41.
62. A.H. Morrish, *The Principles of Magnetism*, John Wiley & Sons: New York 1965.
63. L. Nèel, *Ann. Geophys.* 5 (1949) 99.
64. D. Peddis, M. V. Mansilla, S. Mørup, C. Cannas, A. Musinu, G. Piccaluga, F. D’Orazio, F. Lucari, D. Fiorani, Spin-Canting and Magnetic Anisotropy in Ultrasmall CoFe_2O_4 Nanoparticles, *J. Phys. Chem. B* 112 (2008) 8507–8513.
65. J.L. Gittleman, B. Abels, S. Bozowski, *Phys. Rev. B* 9 (1974) 3891.
-

66. B. Ghosh, S. Kumar, A. Poddar, C. Mazumdar, S. Banerjee, V. R. Reddy, A. Gupta, Spin glasslike behavior and magnetic enhancement in nanosized Ni–Zn ferrite system, *J. Appl. Phys.* 108 (2010) 034307. DOI: 10.1063/1.3456174
67. S. Chakraverty, B. Ghosh, S. Kumar, A. Frydman, Magnetic coding in systems of nanomagnetic particles, *Appl. Phys. Lett.* 88 (2006) 042501. DOI: 10.1063/1.2166203
68. Y. Sun, M. B. Salamon, K. Garnier, R. S. Averback, Memory Effects in an Interacting Magnetic Nanoparticle System, *Phys. Rev. Lett.* 91 (2003) 167206 DOI: 10.1103/PhysRevLett.91.167206
69. M. Sasaki, P. E. Jönsson, H. Takayama, H. Mamiya, Aging and memory effects in superparamagnets and superspin glasses, *Phys. Rev. B* 71 (2005) 104405. DOI: 10.1103/PhysRevB.71.104405
70. M. Östh, D. Hérisson, P. Nordblad, J. A. De Toro, J. M. Riveiro, Ageing and memory effects in a mechanically alloyed nanoparticle system, *J. Magn. Magn. Mater.* 313 (2007) 373. DOI:10.1016/j.jmmm.2007.02.006
71. M. Satalkar, S. N. Kane, On the study of Structural properties and Cation distribution of $\text{Zn}_{0.75-x}\text{Ni}_x\text{Mg}_{0.15}\text{Cu}_{0.1}\text{Fe}_2\text{O}_4$ nano ferrite: Effect of Ni addition, *Journal of Physics: Conference Series* 755 (2016) 012050-1 – 012050-10. DOI:10.1088/1742-6596/755/1/012050
72. O. M. Hemeda, Structural and Magnetic Properties of $\text{Co}_{0.6}\text{Zn}_{0.4}\text{Mn}_x\text{Fe}_{2-x}\text{O}_4$, *Turk J Phys* 28 (2004) 121 – 132.
73. S. P. Dalawai, T. J. Shinde, A. B. Gadkari, P. N. Vasambekar, Structural properties of Cd- Co ferrites, *Bull. Mater. Sci.* 36 (2013) 919 – 922.
74. J.A. Gomes, M.H. Sousa, F.A. Tourinho, J. Mestnik-Filho, R. Itri, J. Depeyrot, Rietveld structure refinement of the cation distribution in ferrite fine particles studied by X-ray powder diffraction, *J. Magn. Magn. Mater.* 289 (2005) 184–187. DOI:10.1016/j.jmmm.2004.11.053
-


75. L. Kumar, P. Kumar, A. Narayan, M. Kar, Rietveld analysis of XRD patterns of different sizes of nanocrystalline cobalt ferrite, *Int Nano Lett.* 3 (2013) 8. DOI:10.1186/2228-5326-3-8
76. R.D. Shannon, Revised effective ionic radii and systematic studies of interatomic distances in halides and chalcogenides, *Acta Crystallogr. A.* 32 (1976) 751 – 767.
77. D.N. Bhosale, S.S. Suryavanshi, S.R. Sawant, A.M. Sankpal, S.V. Kakatkar, S.A. Patil, B.V. Khasbardar, Bulk magnetic studies on $\text{Co}_x\text{Zn}_{1-x}\text{Fe}_2\text{O}_4$ substituted with Al and Gd_2O_3 , *J. Magn. Magn. Mater.* 124 (1993) 298–300.
78. M Veverka, Z Jiráček, O Kaman, K Knížek, M Maryško, E Pollert, K Závěta, A Lančok, M Dlouhá, S Vratislav, Distribution of cations in nanosize and bulk Co-Zn ferrites, *Nanotechnology* 22 (2011) 345701-1 – 345701-7. DOI:10.1088/0957-4484/22/34/345701
79. V. Pilati, R. C. Gomes, G. Gomide, P. Coppola, F. G. Silva, F. L. O. Paula, R. Perzynski, G. F. Goya, R. Aquino, J. Depeyrot, Core/Shell Nanoparticles of Non-Stoichiometric Zn–Mn and Zn–Co Ferrites as Thermosensitive Heat Sources for Magnetic Fluid Hyperthermia, *J. Phys. Chem. C* 122 (2018) 3028–3038. DOI: 10.1021/acs.jpcc.7b11014
80. R. Aquino, J. Depeyrot, M. H Sousa, F. A. Tourinho, E. Dubois, R. Perzynski, Magnetization temperature dependence and freezing of surface spins in magnetic fluids based on ferrite nanoparticles, *Phys. Rev. B* 72 (2005) 184435. DOI: 10.1103/PhysRevB.72.184435
81. E. De Biasi, R.D. Zysler, C.A. Ramos, H. Romero, Magnetization enhancement at low temperature due to surface ordering in Fe–Ni–B amorphous nanoparticles, *Physica B* 320 (2002) 203–205.
82. H. Bhargava, K.T. Vasudevan, N. Lakshmi, K. Venugopalan, Bulk Magnetic Properties Of Nanosized Spinel Ferrites, *Int J Res Eng Technol* 05 (2016) 401-404.
83. H. Fakhr Nabavi, M. Aliofkhazraei, M. Hasanpoor, Combustion and Coprecipitation Synthesis of Co–Zn Ferrite Nanoparticles: Comparison of Structure and Magnetic Properties, *Int. J. Appl. Ceram. Technol.*, 13 [6] (2016) 1112–1118. DOI:10.1111/ijac.12580
-

84. H. Y. He, Comparison study on magnetic property of $\text{Co}_{0.5}\text{Zn}_{0.5}\text{Fe}_2\text{O}_4$ powders by template-assisted sol–gel and hydrothermal methods, *J Mater Sci: Mater Electron* 23 (2012) 995–1000. DOI 10.1007/s10854-011-0535-2
85. S. Lee, C. Sung Kim, Thermal Properties of $\text{Co}_{0.5}\text{Zn}_{0.5}\text{Fe}_2\text{O}_4$ Nanoparticles for Hyperthermia Applications, *J Korean Phys Soc.* 66 (2015) 104 – 107. DOI: 10.3938/jkps.66.104
86. J. Iqbal, M. Rajpoot, T. Jan, I. Ahmad, Annealing Induced Enhancement in Magnetic Properties of $\text{Co}_{0.5}\text{Zn}_{0.5}\text{Fe}_2\text{O}_4$ Nanoparticles, *J Supercond Nov Magn* 27 (2014) 1743–1749. DOI 10.1007/s10948-014-2505-4
87. M. Sundararajan, L. John Kennedy, J. Judith Vijaya, Synthesis and Characterization of Cobalt Substituted Zinc Ferrite Nanoparticles by Microwave Combustion Method, *J. Nanosci. Nanotechnol.* 15 (2015) 6719–6728. DOI:10.1166/jnn.2015.10347
88. C. Kittel, Physical theory of ferromagnetic domains, *Rev. Mod. Phys.* 21 (1949) 541-583.



Chapter 4

Cation vacancy and magnetic properties of ZnFe_2O_4 microspheres



4.1. Introduction

In recent times, the fabrication of self-assembled heterostructured magnetic materials have attracted immense attention of material scientists as their properties can be potentially tuned by building increasingly complex structures [1] leading to interesting functional features and wide variety of applications as well [1,2]. Fabrication of assembly of nanoparticles to form microspheres in the size range of protein molecules has extensive applications in the field of drug delivery [3-6]. Superparamagnetic ferrite nanoparticles display good dispersibility in solvent [7, 8] as interparticle interactions within the nanoparticles is weak and thus, they do not agglomerate. These characteristics render them apposite for biomedical applications [9,10]. But low magnetization resulting from finite size effect and spin canting hinders their application potential in many areas [11,12]. In order to attain high saturation magnetization while retaining the superparamagnetic character of the nanoparticles, a novel way of fabricating self-assembled heterostructures has been developed [1,2,13]. Among these heterostructures, microspheres have displayed highest value of saturation magnetization [14]. Further, self-assembled ferrite microspheres generally possess smooth and highly porous surface [15,16]. So, it seems obvious that nanoparticle-assembled ferrite microspheres will fare very well in magnetically guided site-specific drug delivery, magnetic hyperthermia and catalysis [17]. Apart from their application potential, these ferrite microspheres give rise to astonishing magnetic behavior like enhanced saturation magnetization and reduced coercive field at low temperature compared to those of their constituent nanoparticles [17-19]. These magnetic properties are very interesting from scientific view point and at the same time crucial for application in various fields. Since the microspheres are formed by self-assembly of nanoparticles, modulations of size and shape in the nanoscale regime can direct the evolution of their magnetic properties in unexpected ways [20,21]. These modulations can be controlled by tuning different parameters of synthesis

procedure of the nanocrystals. So, in order to obtain function specific nano/micro structures, choice of proper synthesis procedure is very important.

ZnFe_2O_4 is an important member of the ferrite family owing to its fascinating magnetic, electrical, electrochemical and sensing properties [22-31]. Although electrochemical and sensing properties of ZnFe_2O_4 nano and microstructures have been explored in great detail [27,30,32,33], there are only few studies on its magnetic behavior [15,16,23,24,26,29,34-37]. Among them, Guo et al., have showed that ZnFe_2O_4 solid microspheres (diameter ~ 450 nm) composed of small nanosheets synthesized by solvothermal method exhibit superparamagnetic behavior [23], Rahimi et al., have found that ZnFe_2O_4 hollow nanospheres (diameter ~ 127 nm) synthesized by solvothermal method using ultrasonic waves show ferromagnetic behavior [26], Xu et al., have observed antiferromagnetic behavior in the ZnFe_2O_4 hollow spheres (diameter ranging from 70-100 nm) synthesized by surfactant assisted hydrothermal approach [34], Guo et al., have obtained weak ferromagnetic character in solvothermally synthesized ZnFe_2O_4 solid and hollow colloidal nanocrystal assemblies (diameter ranging from 100-300 nm) [35], Chen et al., have synthesized ZnFe_2O_4 nanocubes (mean edge length ~ 50 nm) by simple hydrothermal technique and found them to be ferromagnetic with enhanced saturation magnetization and coercivity [36], Kmita et al., have synthesized ZnFe_2O_4 nanorods (mean length ~ 20 nm and thickness ~ 5 nm) by coprecipitation method and found them to be superparamagnetic [37]. From these studies, we can conclude that morphology and synthesis procedure are responsible in determining the magnetic behavior of the materials. Moreover, the observed diversity in the magnetic behavior of ZnFe_2O_4 motivates us to explore its magnetic behavior in more detail.

It is well known that the magnetic properties of ferrites are strongly dependent on the distribution of cations among tetrahedral (A) and octahedral [B] sites of the spinel lattice

[38]. Different synthesis procedures give rise to different morphologies causing cation redistribution among these two sites and consequently, magnetic properties get altered [39-41]. Surfactant-assisted chemical methods have paved a novel way to develop size- and shape-tailored magnetic nanocrystals by carefully regulating the growth processes in liquid media [15,16]. These methods may be either single-step or more complex multiple-step solution-phase routes. The former is convenient, cheaper, and non-time consuming while the latter is only advantageous for obtaining better size distribution [17]. In the literature, study on the structural, magnetic, electrical and electrochemical properties of solid and hollow microspheres of Fe_3O_4 synthesized by solvothermal method at 200°C using $\text{NaAc}+\text{PEG}$ and NH_4Ac , respectively, [15,42], CoFe_2O_4 synthesized by solvothermal method at 200°C using $\text{NaAc}+\text{PEG}$ and urea+oleylamine, respectively, [15,43], NiFe_2O_4 synthesized by solvothermal method at 180°C using $\text{NaAc}+\text{PEG}$ and at 200°C using NH_4Ac , respectively, [16,44], MnFe_2O_4 synthesized by solvothermal method at 180°C using $\text{NaAc}+\text{PEG}$ and $\text{NH}_4\text{Ac}+\text{PEG}$, respectively, [15,16,45], MgFe_2O_4 synthesized by solvothermal method at 180°C using $\text{NaAc}+\text{PEG}$ and at 200°C using urea+PEG, respectively, [46,47] and ZnFe_2O_4 synthesized by solvothermal method at 200°C and 180°C using $\text{NaAc}+\text{PEG}$, respectively, [15,48] have been found. Thus, it is apparent that one-step solvothermal method has emerged as an efficient technique to synthesize monodisperse spherical magnetic microspheres with large surface area, high magnetic saturation and good dispersive property in liquid media. Hence, it would be feasible to use this technique in developing ferrite microspheres with desirable properties.

In this backdrop, we have synthesized solid and hollow microspheres of ZnFe_2O_4 by one-step solvothermal method with the endeavor to thoroughly study their magnetic properties. The phase of the samples has been characterized by powder x-ray diffraction. The morphology, elemental composition and valance state of the constituent elements have been

investigated by field emission scanning electron microscopic, transmission electron microscopic, energy dispersive x-ray spectroscopic and X-ray photoelectron spectroscopic techniques. The dc magnetic and Mössbauer spectroscopic techniques have been employed to probe the magnetic and hyperfine properties of the microspheres.

4.2. Experimental

4.2.1. Materials

Analytical grade $\text{FeCl}_3 \cdot 6\text{H}_2\text{O}$, $\text{ZnSO}_4 \cdot 7\text{H}_2\text{O}$, anhydrous ZnCl_2 , $\text{NaAc} \cdot 3\text{H}_2\text{O}$, NH_4Ac and PEG-4000 were purchased from Sigma Aldrich and used without further purification. Ethylene glycol (EG) procured from Merck India (99.9 %) was used as the solvent.

4.2.2. Synthesis procedures

In the preparation of ZnFe_2O_4 solid microspheres (ZFMS), 5 mmol $\text{FeCl}_3 \cdot 6\text{H}_2\text{O}$ and 2.5 mmol $\text{ZnSO}_4 \cdot 7\text{H}_2\text{O}$ (precursors of the reaction) were mixed in 40 ml of EG under continuous magnetic stirring. After that 3.6 g $\text{NaAc} \cdot 3\text{H}_2\text{O}$ (stabilization agent) and 1 g PEG-4000 (structure-directing agent) were added into this mixture. The entire mixture was stirred for 5-6 hrs at room temperature following which it was transferred in a 100 ml Teflon pot. The pot was enclosed in a stainless-steel autoclave and solvothermally heated in an oven for 20 hrs at 180°C . The oven was allowed to cool naturally to room temperature after which the so obtained precipitate was washed several times by ethanol and deionized water in an ultracentrifuge. The resulting product was dried in a vacuum oven at 60°C for 6 hrs and finally a fine black coloured powder was obtained.

Similarly, ZnFe_2O_4 hollow microspheres (ZFMH) were synthesized by mixing 5 mmol $\text{FeCl}_3 \cdot 6\text{H}_2\text{O}$ and 2.5 mmol anhydrous ZnCl_2 (precursors of the reaction) in 40 ml of EG under continuous magnetic stirring. Then 50 mmol of NH_4Ac was added to the solution and the mixture was stirred for 5-6 hrs. After that, the mixture was autoclaved at 170°C for 17 hrs in an oven. The black precipitate obtained from the above procedure was washed several

times with ethanol and deionized water, and collected by centrifugation. The so obtained product was vacuum dried at 60 °C for 6 hrs. The final sample was a fine black powder.

4.2.3. Characterization

Structural and microstructural studies on the as-synthesized samples were carried out using powder x-ray diffraction (PXRD), field emission scanning electron microscopic (FESEM) and transmission electron microscopic (TEM) techniques. XRD measurements were performed using a Bruker D8 Advanced diffractometer with Cu K α irradiation in the 2 θ range of 20-80°. FESEM micrographs were recorded in a FEI INSPECT F50 system. TEM micrographs along with elemental study were collected using a JEOL 2100 HRTEM equipped with Bruker EDS system. X-ray photoelectron spectroscopy (XPS) was performed using XPS, Omicron, serial no 0571. Magnetic measurements viz., magnetization versus temperature (in zero-field cooling and field cooling modes) and variation of magnetization with field (hysteresis loops) were performed using a Cryogenic make vibrating sample magnetometer. The room temperature (300 K) and low temperature (5 K) Mössbauer spectra of both the samples were recorded in transmission geometry with constant acceleration drive (CMTE-250) using a 10 mCi ^{57}Co source. JANIS SVT-400 MOSS cryostat system was employed to obtain the 5 K Mössbauer spectrum. The 5 K Mössbauer spectrum in presence of a 5 T external magnetic field applied parallel to the γ -ray direction was recorded in presence of a superconducting magnet (JANIS SuperOptiMag) and a 40 mCi ^{57}Co source. Calibration of the Mössbauer spectrometer was done using a natural iron sample.

4.3. Results

4.3.1. Structural and morphological study

The PXRD patterns of ZFMS and ZFMH are shown in Fig. 1. The peak positions of both the samples are consistent with those of the cubic spinel structure of ZnFe_2O_4 nanoparticles (ICDD card no: 82-1049). The patterns have been indexed by TREOR90 of Fullprof2k package [49]. The space group has been determined using FINDSPACE of

EXPO2009 package [50]. The peaks of ZFMS are slightly broader as compared to ZFMH indicating that the crystallite size of the former is smaller. The patterns have been fitted by

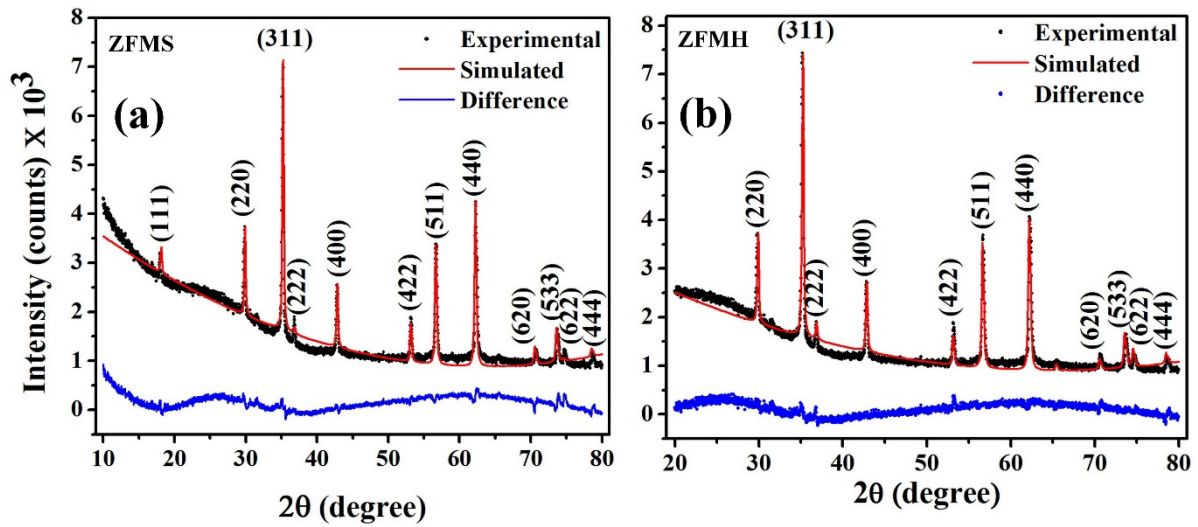


Fig.1. Indexed powder PXRD pattern of (a) ZFMS and (b) ZFMH (black dots) and the simulated Rietveld refinement plot (continuous red line) obtained by fitting the experimental powder PXRD pattern using MAUD2.33 software. The respective residue is plotted at the bottom (blue line).

Table 1. Crystal data and refinement parameters of ZFMS and ZFMH obtained from MAUD2.33

Parameters	ZFMS	ZFMH
Crystal System	cubic	cubic
Space group	$Fd\bar{3}m$	$Fd\bar{3}m$
Crystallite size (nm)	25	80
Microstrain	8.27×10^{-4}	2.76×10^{-4}
Lattice parameter ($a(\text{\AA})$)	8.487	8.432
Density (g cm^{-3})	5.098	5.198
R_{wp}	1.97	1.95
R_{exp}	1.41	1.42
GOF	1.29	1.10

Rietveld based MAUD2.33 software [51] from which the crystallite size of ZFMS and ZFMH has been deduced as ~ 25 nm and 80 nm, respectively. The experimental and simulated patterns are in well accord. The values of refinement, structural and microstructural

parameters have been enlisted in Table 1. Thus, both ZFMS and ZFMH have crystallized in $Fd\bar{3}m$ space group of cubic spinel lattice and devoid of any additional impurity phases.

The FESEM micrograph (Fig. 2 (a)) of ZFMS displays microspheres of average diameter ~ 314 nm, which have been formed by self-assembly of nanoparticles. The spheres are almost uniformly sized and their surface is slightly rough due to the aggregation of nanoparticles. In the FESEM micrograph of ZFMH, the spheres are almost regular in size with some broken spheres confirming their hollow interior (Fig. 2 (b)). In contrast to ZFMS, the surface of ZFMH is smooth due to continuous overlapping of subsequent layers of smaller nanoparticles during their formation following Kirkendall effect [52].

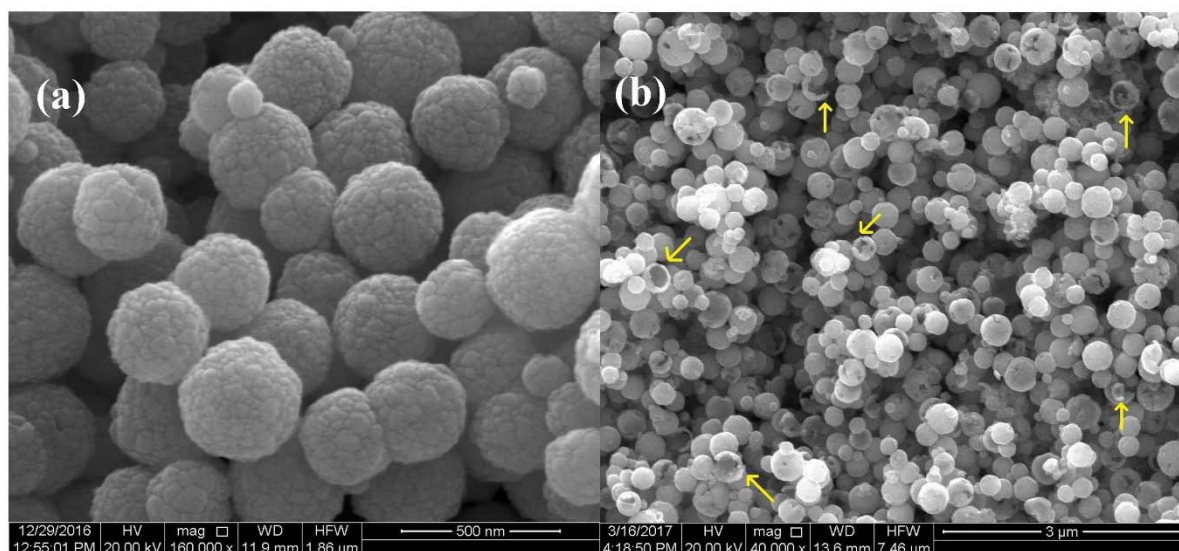


Fig.2. FESEM micrographs showing particle distribution of (a) ZFMS and (b) ZFMH (some of the broken hollow spheres have been marked by yellow arrows).

The morphology of ZFMS and ZFMH has been further investigated by TEM study. The average diameter of ZFMS as has been obtained from the TEM micrograph (Fig. 3 (a)) is ~ 310 nm. The spheres seen in the TEM micrograph of ZFMS are almost completely dark with clear sign of agglomeration as presented in the inset of (Fig. 3 (a)). The sharp contrast between the outer black margin and the bright center of the microspheres in the TEM micrograph of ZFMH (Fig. 3 (b)) confirms hollow structure formation. Typical TEM image

of a single hollow microsphere has been presented in the inset of Fig. 3 (b). It is clear that the shell of the hollow microspheres is smooth. Although some of the individual particles can be identified in the hollow region but their boundaries are not distinct. So, it is not possible to estimate the appropriate particle size of individual nanoparticles which have aggregated to form the spheres. The average diameter and shell thickness of ZFMH are ~ 375 and 50 nm, respectively.

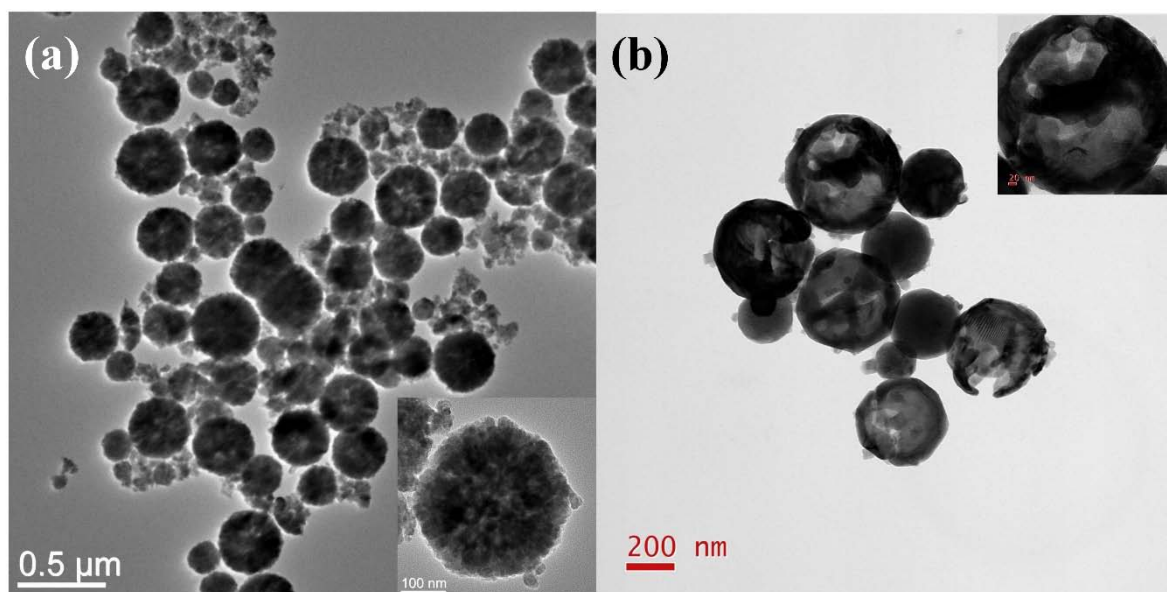


Fig.3. TEM micrographs showing particle distribution of (a) ZFMS and (b) ZFMH along with single particle at the inset of respective picture.

The selected area electron diffraction (SAED) pattern of ZFMS (Fig.4) shows some bright rings composed of evenly distributed bright spots indicating polycrystalline nature of the sample. The equally spaced bright spots in the SAED pattern of ZFMH (Fig.5(a)) arise from the clear lattice fringes and suggest good crystalline character of the sample.

The SAED patterns of both the samples have been fitted by CrysTBox software [53]. The crystallographic ‘d’ values obtained from SAED for both the samples are in good agreement with those obtained from PXRD study.

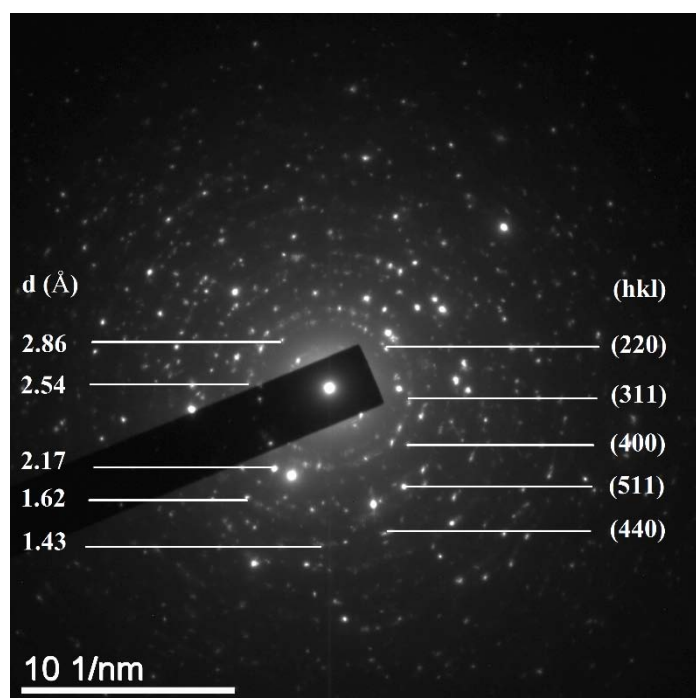


Fig. 4. SAED pattern of ZFMS

The energy dispersive x-ray (EDAX) spectra of both ZFMH (Fig.5(b)) and ZFMS (Fig.6) suggest presence of Fe, Zn and O atoms only with no signature of any contamination. The metal cations Fe and Zn are in the ratio $\sim 26:12$ in ZFMS, which shows that ZFMS is in proper stoichiometry. The atomic ratio of Fe:Zn is $\sim 45:0.8$, indicating that ZFMH is nonstoichiometric in nature.

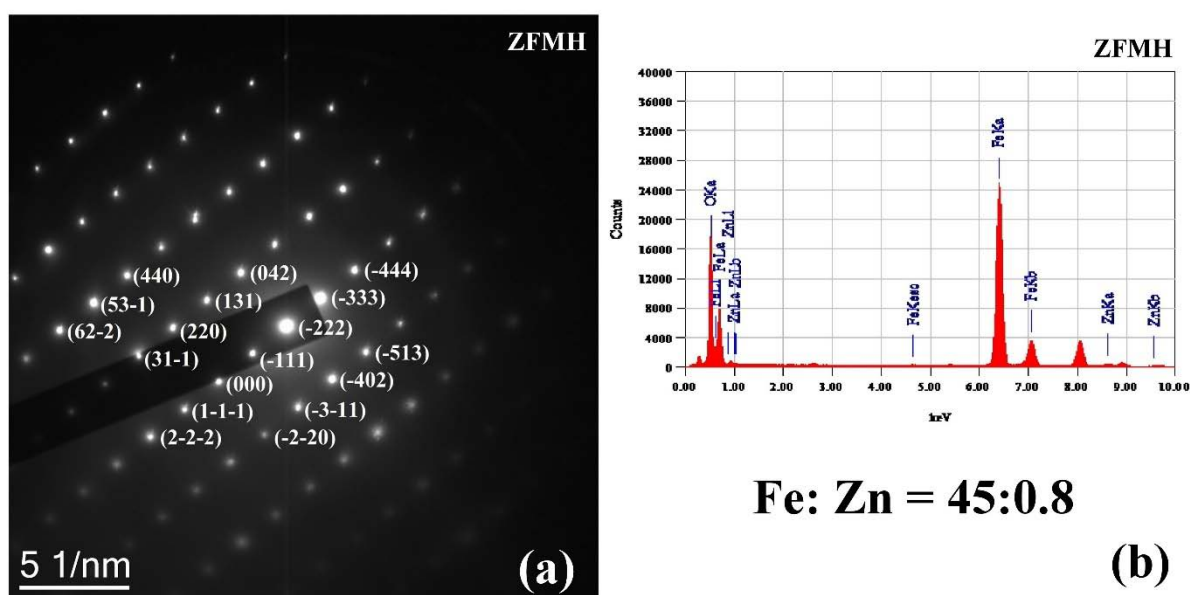


Fig.5. (a) Indexed SAED pattern and (b) EDAX analysis of ZFMH

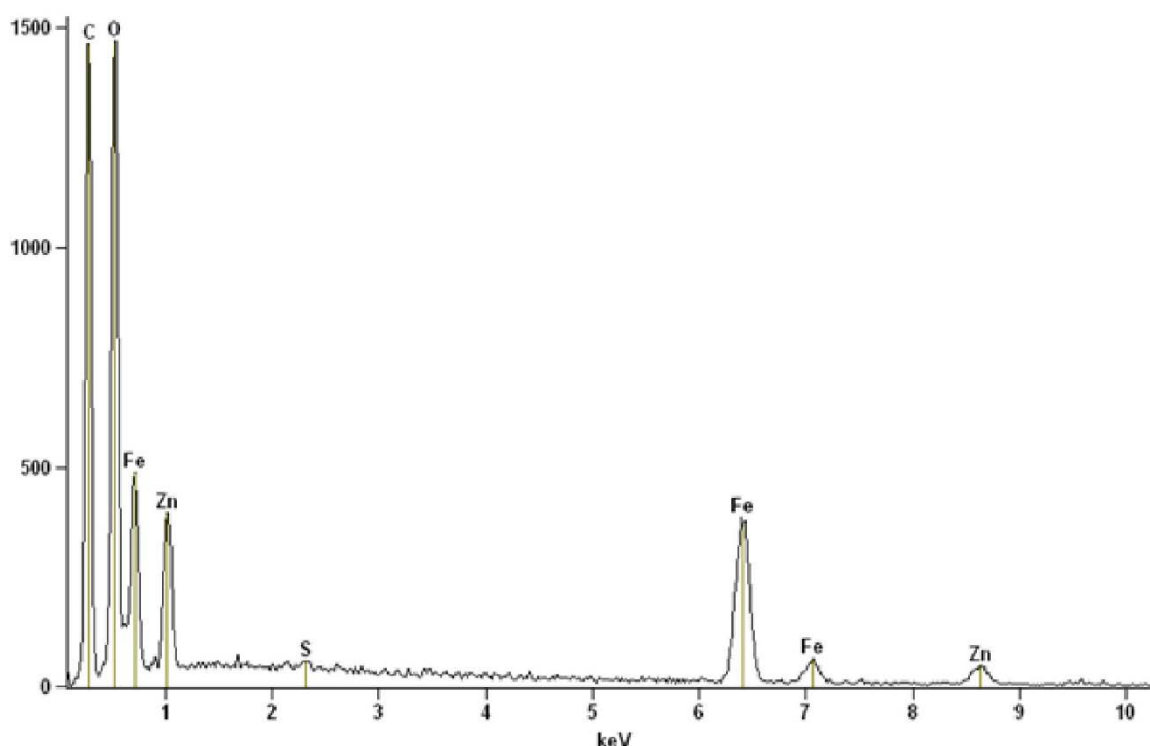


Fig.6. EDAX spectrum of ZFMS

4.3.2. X-ray photoelectron spectroscopic study

The x-ray photoelectron spectroscopy (XPS) is a widely used technique for characterizing ferrites [54 - 58]. We have recorded the XPS spectra of ZFMS and ZFMH to probe the chemical composition and valance state of the constituent elements of the samples. Figs.7 (a) and (b) show the XPS survey spectra of ZFMS and ZFMH, respectively. The adventitious C 1s peak in these spectra has been observed as the specimen for XPS study is prepared by pasting sample powder over a carbon coated adhesive tape. Peaks due to O 1s, Fe 2p_{3/2} and Fe 2p_{1/2} are observed in the survey spectra of both ZFMS and ZFMH. However, the peaks corresponding to Zn 2p_{3/2} and Zn 2p_{1/2} states are observed only in case of ZFMS. Thus, the absence of the peaks pertaining to Zn 2p states in the survey spectrum of ZFMH indicates that the sample may be devoid of Zn.

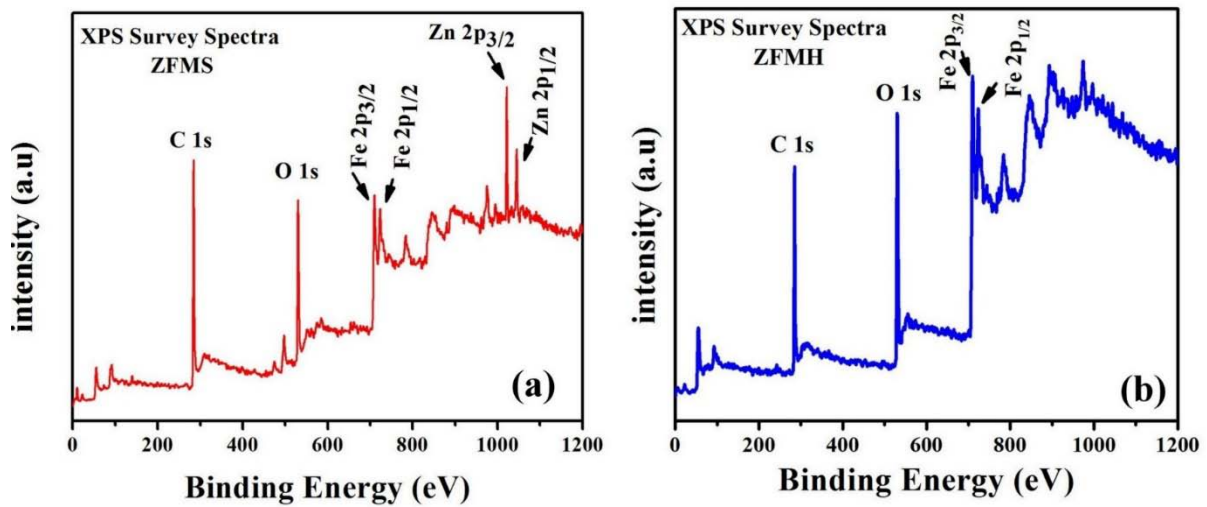


Fig.7. XPS survey spectra of (a) ZFMS and (b) ZFMH.

The high-resolution Fe 2p spectra of ZFMS and ZFMH are presented in Fig. 8 (a). In the Fe 2p XPS spectra, two peaks with binding energies (BEs) 710.1 eV and 723.5 eV for ZFMS and 709.7 eV and 722.8 eV for ZFMH can be attributed to Fe 2p_{3/2} and Fe 2p_{1/2}, respectively. Thus, Fe 2p peaks of ZFMH have been slightly shifted toward lower BEs with respect to ZFMS and this indicates towards the possibility of presence of Fe²⁺ ions in ZFMH [59]. The high-resolution Fe 2p_{3/2} XPS spectra of ZFMS and ZFMH (Figs. 8 (b) and (c)) are deconvoluted into two and three sub-peaks, respectively. The peaks at 709.2 and 710.9 eV (Fig. 6 (b)) can be assigned to Fe³⁺ (A) and [B] sites of ZnFe₂O₄, respectively. The area ratio corresponding to peaks due to Fe³⁺ ions at (A) and [B] sites (Fe³⁺_A : Fe³⁺_B) is 1:2.56. The peak at 707.9 eV for ZFMH (Fig.8 (c)) can be assigned to the Fe²⁺ 2p_{3/2} peak at (B) site [60] while The peaks located at 709.2 and 710.4 eV correspond to Fe³⁺ (A) and [B] sites, respectively [54,55]. The area ratio of the peaks corresponding to Fe²⁺ and Fe³⁺ ions (Fe²⁺: Fe³⁺) is 1:8 whereas, the area ratio Fe³⁺_A : Fe³⁺_B ratio is 1:1.25. Moreover, Fe 3p peaks in XPS spectra of ZFMS and ZFMH (Fig.8 (d)) are found at the BEs of 55.3 and 54.8 eV, respectively. The high-resolution Zn 2p XPS spectrum of ZFMS consist of two peaks which can be allocated to Zn 2p_{3/2} and Zn 2p_{1/2} states.

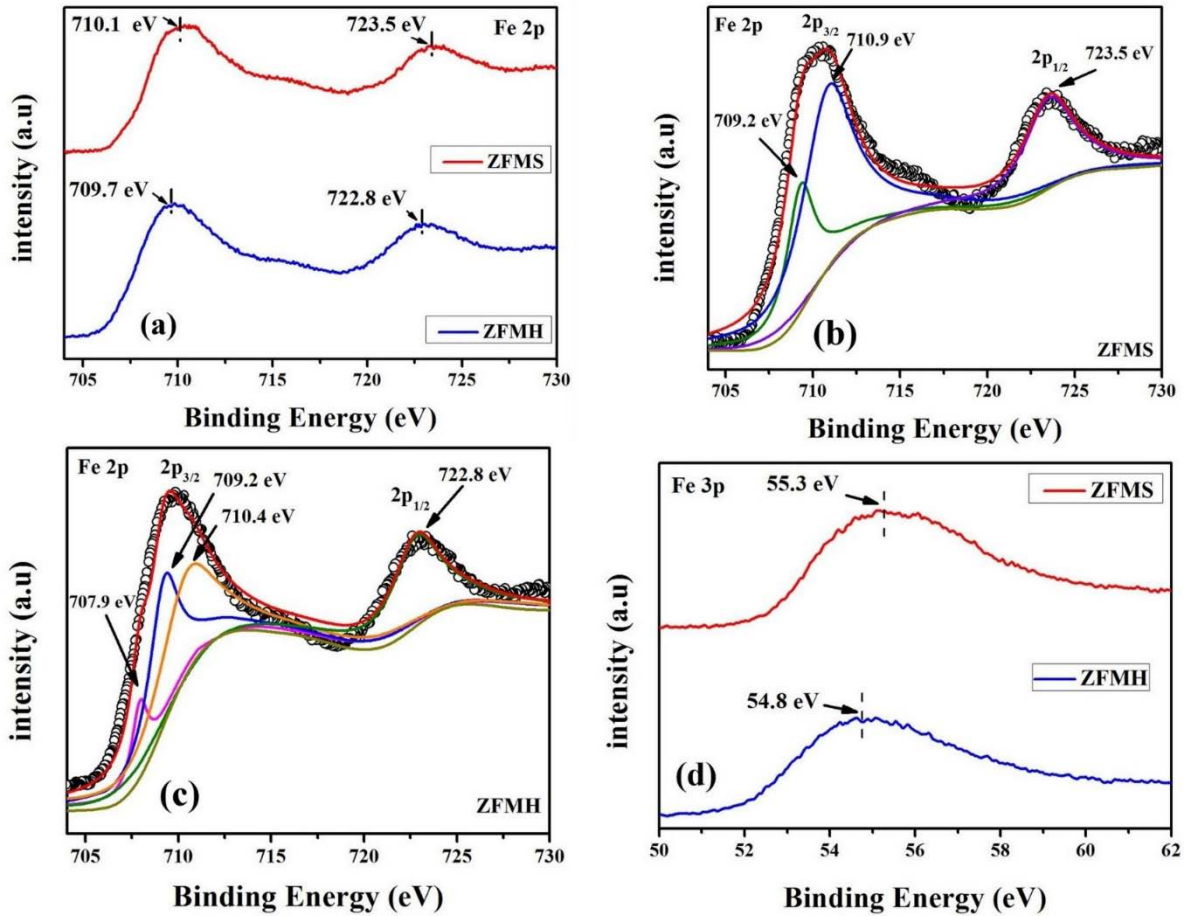


Fig.8. Core level XPS spectrum corresponding to the (a) Fe 2p peak of ZFMS and ZFMH, (b) fitted Fe 2p peak of ZFMS, (c) fitted Fe 2p peak of ZFMH and (d) Fe 3p peak of ZFMS and ZFMH.

The Zn 2p_{3/2} peak for ZFMS (Fig.9 (a)) is fitted with two sub-peaks centered at 1021.7 and 1022.3 eV assigned for Zn²⁺ at (A) and [B] sites, respectively. The area ratio of the peaks corresponding to Zn²⁺ at (A) and [B] sites ($Zn^{2+}_A - Zn^{2+}_B$) of ZnFe₂O₄ is 1:1.26. The peak at BE 1045.1 eV can be assigned to Zn 2p_{1/2} state [56]. In the high-resolution Zn 2p XPS spectrum of ZFMH (Fig. 9 (b)) two insignificant peaks due to Zn 2p_{3/2} and Zn 2p_{1/2} are noticed, which suggests that trace amount of Zn in +2 oxidation state is present in ZFMH. The O 1s XPS spectra of ZFMS and ZFMH are shown in Figs. 10 (a) and (b). The broad and asymmetric peak in O 1s XPS spectrum of ZFMS is deconvoluted into three sub-peaks whereas O 1s XPS spectrum of ZFMH is fitted with two sub-peaks. It may be noted that in

ZFMS both metallic iron and zinc are present. Hence, the signature of oxygen containing Zn and Fe species is expected in O 1s XPS spectrum of ZFMS. Further, the area ratio of the peaks located at 530.1 and 530.6 eV is 1:1.9, which is close to the ratio of Zn^{2+} and Fe^{3+} (1:2) in ZFMS.

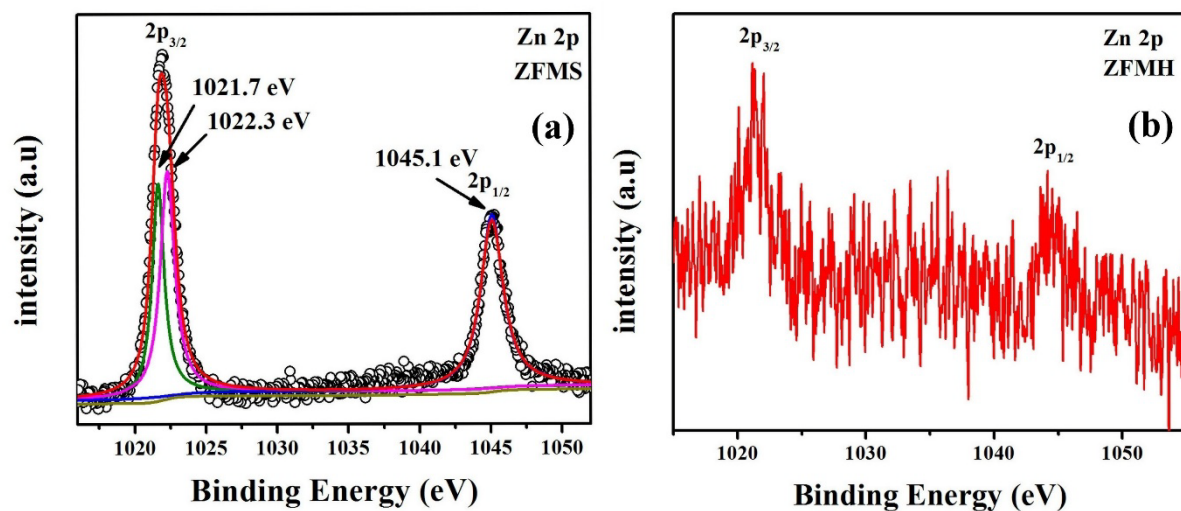


Fig.9. Core level XPS spectrum corresponding to the Zn 2p peak of (a) ZFMS and (b) ZFMH.

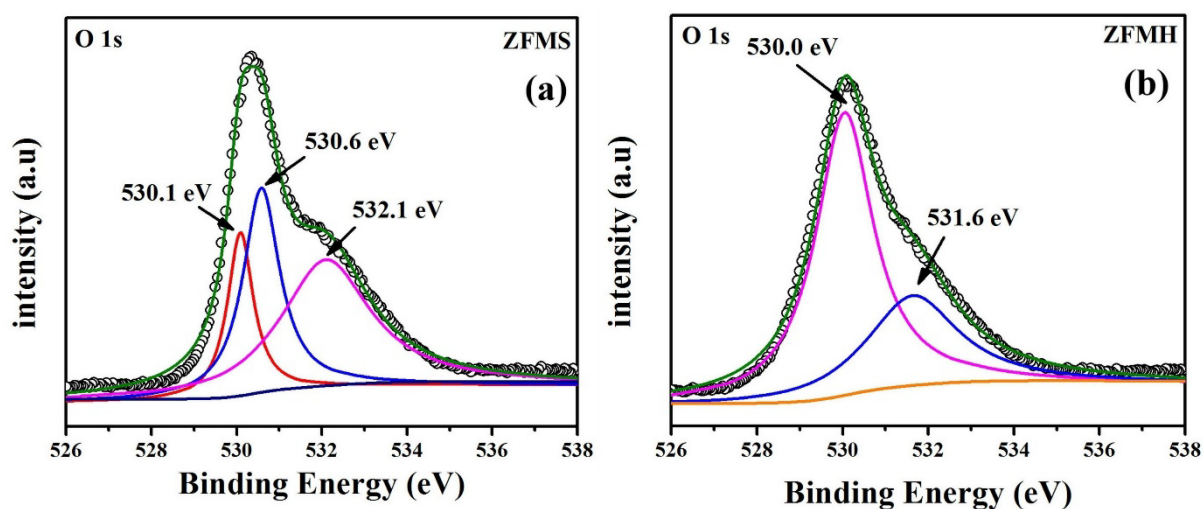


Fig.10. Core level XPS spectrum corresponding to the O 1s peak of (a) ZFMS and (b) ZFMH.

Thus, the peaks at BEs 530.1 and 530.6 eV can be assigned to O^{2-} ions in Zn-O, Fe-O frameworks of $ZnFe_2O_4$, respectively. Only a single peak located at 530 eV is observed in the O 1s XPS spectra of ZFMH which can be assigned to O^{2-} in Fe-O framework. No peak due to O^{2-} ions in Zn-O framework has been observed in O 1s XPS spectrum of ZFMH as only a trace amount of Zn^{2+} is present in this sample. The peaks with BEs 532.1 eV for ZFMS and 531.6 eV for ZFMH can be assigned to the surface absorbed oxygen containing species (possibly water molecules). [55,57,58].

4.3.3. Magnetic and hyperfine study

Figs.11 (a) and (b) show the thermal dependence of magnetization for ZFMS and ZFMH at a field of 100 Oe. The magnetic moment of the zero-field cooled (ZFC) curve of ZFMS remains almost constant between 300 to 200 K, below which it decreases gradually with decreasing temperature upto 25 K; under 25 K the moment falls sharply indicating a spin glass like random freezing [41]. The field cooled (FC) curve follows the trend of a typical superparamagnetic substance [61] and increases simultaneously with decreasing temperature; further below 25 K it becomes almost constant. The ZFC and FC curves do not coincide up to 300 K (highest measurement temperature).

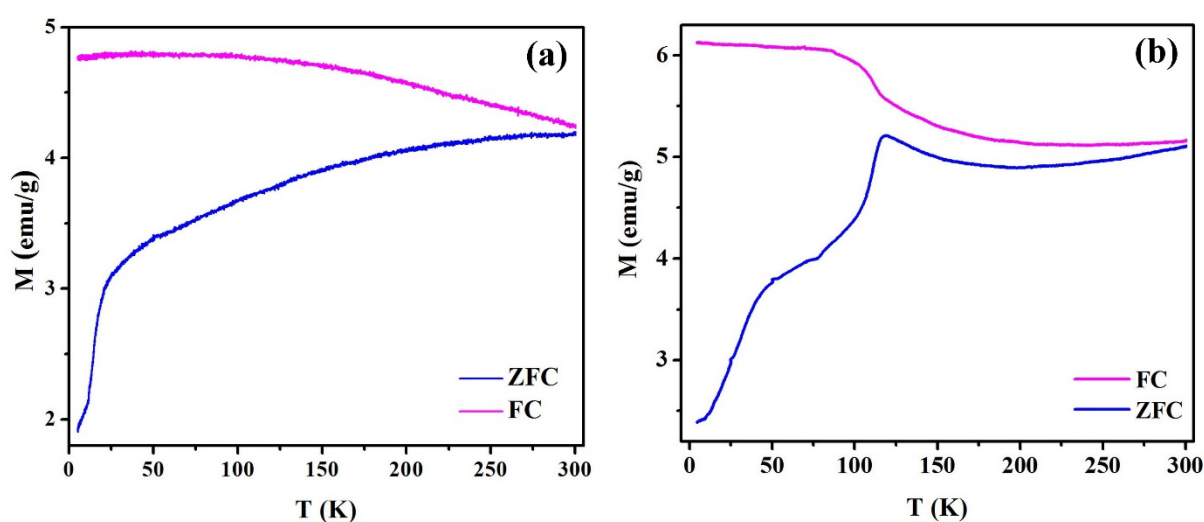


Fig.11. ZFC-FC magnetization curves of (a) ZFMS and (b) ZFMH at 100 Oe. The FC and ZFC magnetization are represented by pink and the blue lines, respectively.

The temperature dependence of magnetization for ZFMS suggests that the nanoparticles constituting the microsphere are superparamagnetic in nature and they possess a broad particle size distribution which results in a wide range of blocking temperatures. But due to aggregate formation, their magnetic behavior has been overshadowed and thus, they exhibit collective magnetic excitations at room temperature, which can be further confirmed from Mössbauer spectroscopy. Further, due to the randomness in distribution of anisotropy energy, spins freeze randomly with the decrease in temperature and lead to the formation of spin glasslike state [62]. The ZFC and FC curves of ZFMH display a completely different behavior from ZFMS. The ZFC and FC curves are slightly bifurcated from 300 K with almost no temperature dependence upto 150 K. The ZFC curve exhibits a distinct peak at ~ 120 K and at the same temperature; the FC magnetization curve takes a sudden leap after which it tends to be constant. Below 120 K, the magnetic moment of ZFC curve decreases sharply with decreasing temperature, while FC curve remains almost constant with negligible dependence on temperature. This behavior of the ZFC-FC curves is reminiscent of the Verway transition [63].

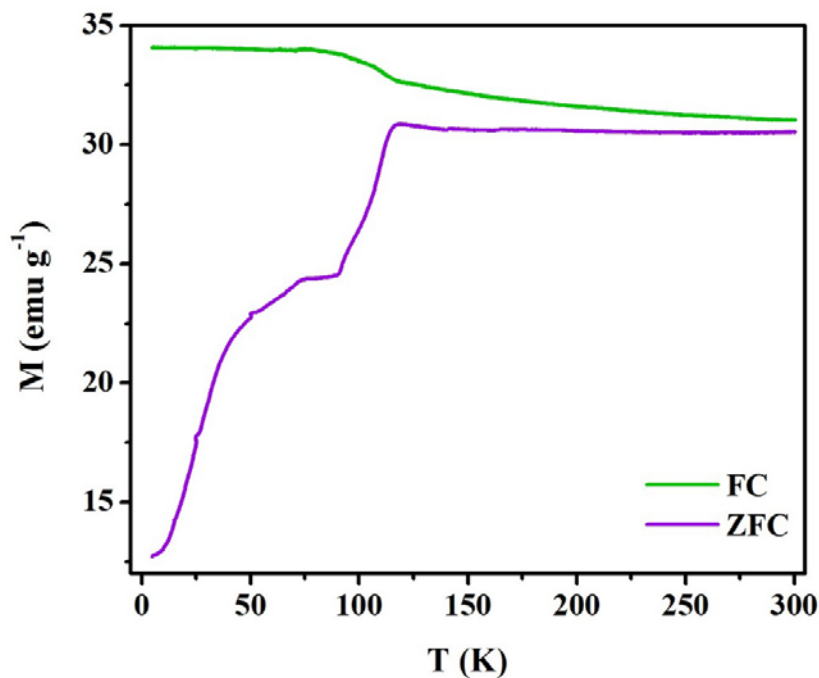


Fig.12. ZFC-FC curves of ZFMH at 500 Oe

Some of the works on MFe_2O_4 ($M = Mn^{2+}, Zn^{2+}, Co^{2+}, Ni^{2+}$ etc.) have ruled out the occurrence of Verway transition in them [64,65]. But, in the present case, we have found a signature of Verway transition in the ZFC-FC curves of ZFMH at 100 Oe. We have also recorded the ZFC-FC curves of ZFMH at 500 Oe (Fig.12) and found similar trend as in 100 Oe curves, which reinforces the proposition of Verway transition in the present case.

We have further recorded the curves of field dependence on magnetization (M-H) at 300, 100 and 10 K in the field range of ± 1 T for both ZFMS and ZFMH (Fig. 13). The M-H loop for ZFMS does not show any hysteresis (H_C) at 300 K supporting its superparamagnetic behavior. The 100 K M-H loop shows slight coercivity and high saturation magnetization (M_{SAT}) as compared to 300 K M-H curve indicating development of magnetic ordering at this temperature. The M-H curve for ZFMH shows small value of H_C at 300 K suggesting presence of magnetic ordering at this temperature. The values of M_{SAT} for ZFMS and ZFMH have been estimated by using the law of approach to saturation.

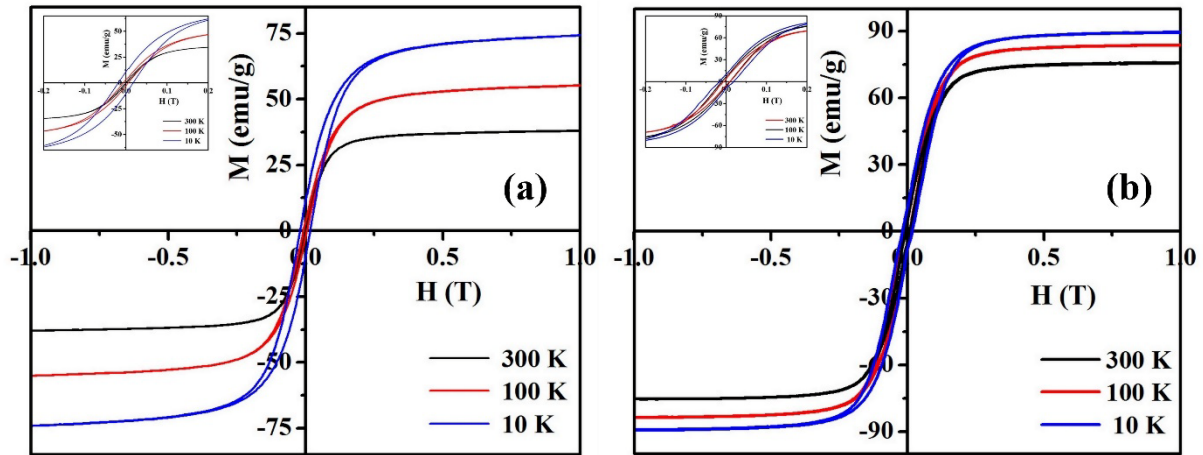


Fig. 13. M-H (hysteresis) loop of (a) ZFMS and (b) ZFMH at 300 (black line), 100 K (red line) and 10 K (blue line) shown between ± 1 T.

The values of M_{SAT} and H_C are presented in Table 2. We have compared the values of saturation magnetization at 300 K of the present samples with that of other $ZnFe_2O_4$ solid and hollow microspheres available in literature, and enlisted them in Table 3. It seems that

reaction parameters strongly influence the formation of microspheres and consequently their magnetic properties.

Table 2 Values of saturation magnetization (M_{SAT}) and coercivity (H_C) for ZFMS and ZFMH

Sample	Temperature (K)	M_{SAT} (emu/g)	H_C (Oe)
ZFMS	300	41.5	0
	100	64.0	55
	10	85.7	170
ZFMH	300	77.0	90
	100	84.5	100
	10	90.75	190

Table 3 Comparison of the room temperature (300 K) saturation magnetization M_{SAT} values of $ZnFe_2O_4$ microspheres with literature values

Sl No.	Synthesis procedure	Type of microsphere	Surfactant, reaction temperature ($^{\circ}C$) & time (hours)	Diameter of microsphere (nm)	M_{SAT} (emu/g)	Reference
1.	Solvothermal	solid	NaAc+PEG, 200 & 8-72	200-800	60	[15]
2.	Solvothermal	solid	NaAc, 200 & 12	450 (with particle sizes) 11.6 nm 16.2 nm 20.5 nm	49.5 53.8 61.3	[23]
3.	Solvothermal	hollow	NaAc+PEG, 180 & 16	100-210	32	[16]
4.	Solvothermal	hollow	NH_4Ac , 170-200 & 24-48	200-450	80.2	[24]
5.	Solvothermal	hollow	NH_4Ac , 210 & 48	127	76.2	[26]
6.	Solvothermal	hollow	PEG-600, 200 & 24	400	83.4	[29]
7.	Hydrothermal	hollow	SDS+ TMAOH, 180 & 48	70-100	47.7	[34]
8.	Solvothermal	solid	NaAc+PEG, 180 & 20	314	41.5	ZFMS (present study)
9.	Solvothermal	hollow	NH_4Ac , 170 & 17	375	77	ZFMH (present study)

The room temperature (300 K) Mössbauer spectra (Figs.14 (a) and (b)) show a strong superparamagnetic doublet along with diffused sextets for ZFMS and well-defined sextet with a clearly splitted left most line for ZFMH. Both the spectra have been fitted with “Lorentzian site analysis” of Recoil program [66]. The 300 K Mössbauer spectrum of ZFMS has been fitted with a doublet and two sextets whereas that of ZFMH has been fitted with two sextets. The fitting of both the samples is good enough and the values of hyperfine parameters are trustworthy. The results have been summarized in Table 4. The doublet is a signature of superparamagnetic character of the nanoparticles constituting ZFMS, whereas the diffused sextets are a result of collective magnetic excitation caused by nanoparticle aggregation. ZFMS has been formed by self-assembly of nanoparticles of variable size and assorted shape. So, ZFMS consist of both superparamagnetic and magnetically well-ordered particles, which give rise to an admixture of a doublet and two diffused sextets. The doublet is predominant indicating that most of the constituent particles are superparamagnetic. The ZFC-FC study has also given clear indication in regard of superparamagnetic character of the constituent particles. But, due to variation in the size of the nanoparticles, there is a wide range of distribution in blocking temperature. Since ZFMH is nonstoichiometric with very few Zn^{2+} ions and has shown Verway transition in its ZFC-FC study, so we have fitted the 300 K Mössbauer spectrum of ZFMH with two sextets; one pertaining to the Fe^{3+} ions at tetrahedral site and the other to Fe ions which generally exhibit an exchange of type $\text{Fe}^{2+} \leftrightarrow \text{Fe}^{3+}$ [67]. The values of hyperfine magnetic field (HMF) obtained from fitting for (A) and [B] sites are 57.58 and 51.39 T, respectively. The higher HMF value for (A) site corresponds to the contribution from about half of the Fe^{3+} ions present in the sample and the lower value of HMF for [B] site comes from Fe ions involving $\text{Fe}^{2+} \leftrightarrow \text{Fe}^{3+}$ exchange [67]. The presence of clear sextet in the Mössbauer spectrum of ZFMH suggests that the sample is magnetically well ordered at this temperature, which also corroborates the ZFC-FC study.

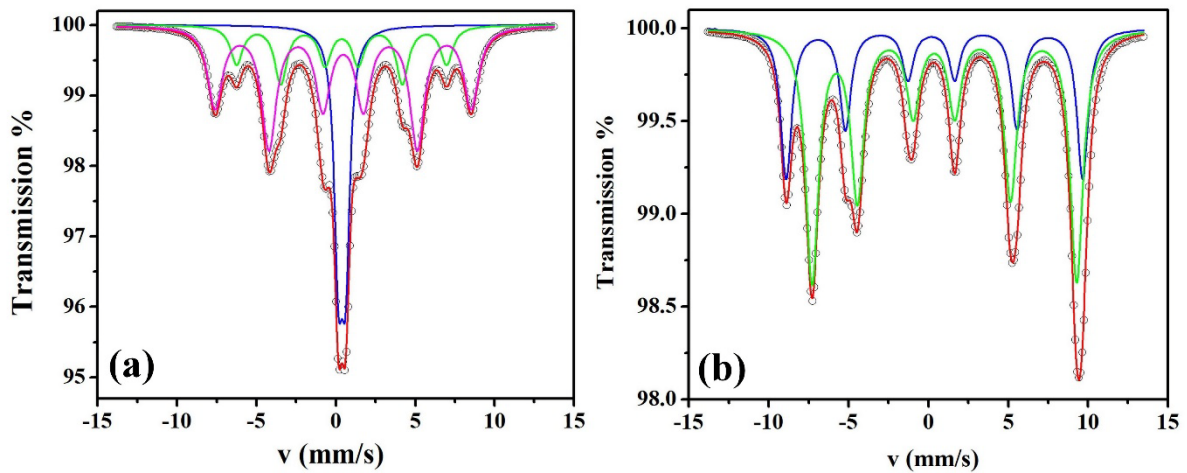


Fig.14. Mössbauer spectrum of (a) ZFMS and (b) ZFMH at 300 K

Table 4 Hyperfine parameters obtained by fitting the Mössbauer spectra of ZFMS and ZFMH at 300 K

Sample	Spectra	Site	IS (± 0.02) (mm s ⁻¹)	QS (± 0.07) (mm s ⁻¹)	HMF (± 0.1) (T)	Width (± 0.03) (mm s ⁻¹)	Area (± 0.3) (%)
ZFMS	Sextet	[Fe ³⁺ _A]	0.37	0.0	41.0	0.45	21.36
		[Fe ³⁺ _B]	0.47	0.0	50.0	0.55	54.76
	Doublet	-	0.39	0.45	-	0.30	23.87
ZFMH	Sextet	[Fe ³⁺ _A]	0.29	0.10	57.58	0.40	33.33
		[Fe _B]	0.69	0.33	51.39	0.48	66.67

Fig.15 presents the simulated and experimental infield and without field Mössbauer spectrum of ZFMS (Fig.15 (a) & (b)) and ZFMH (Fig.15 (c) & (d)). The splitted 1st and 6th lines in infield spectrum of both ZFMS and ZFMH are a signature of their ferrimagnetic character [40,61,62]. The existence of 2nd and 5th lines in the infield spectrum of ZFMS is clear indicator of presence of spin canting in the sample [40,68,69]. We have fitted the infield spectra with two sextets by using “Lorentzian site analysis” of Recoil program and tried to

obtain the precise values of canting angles along with other hyperfine parameters. The results have been summarized in Table 5. The values of isomer shift (IS) assure about the presence of only Fe^{3+} ions in the sample [40,68,69]. The goodness of the fitting suggests that the two-component fitting is capable of divulging the hyperfine character of this system precisely. The ratio of Fe^{3+} ions in (A) to [B] site ($\text{Fe}^{3+}_A/\text{Fe}^{3+}_B$) of ZFMS is 0.39, whereas in ideal case no Fe^{3+} ion should have been present in tetrahedral (A) site. This affirms that Fe^{3+} ions have migrated from [B] to (A) site in ZFMS.

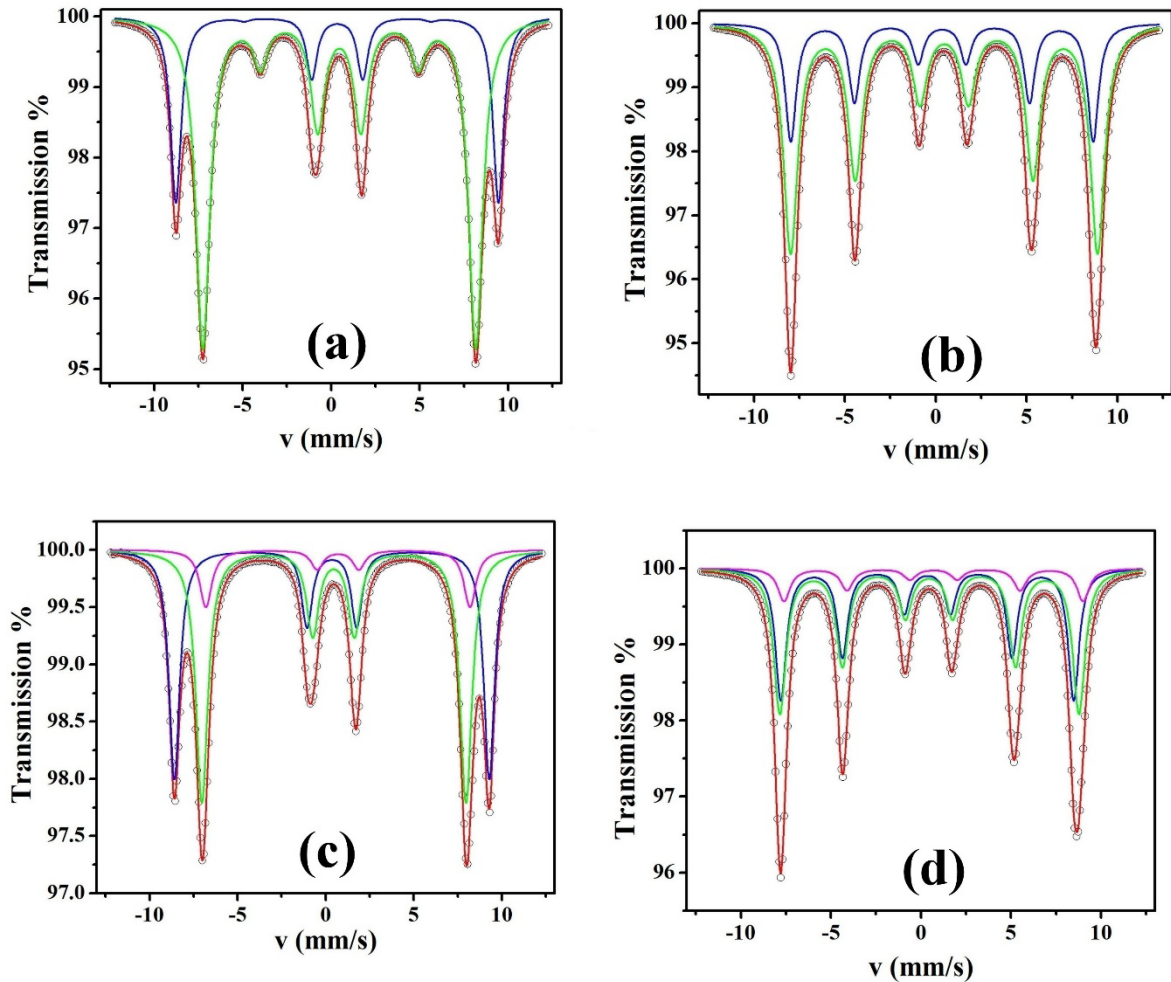


Fig.15. Fitted Mössbauer spectra of ZFMS at (a) 5 K with 5 T external magnetic field, (b) 5 K without field and ZFMH at (c) 5 K under 5 T external magnetic field, (d) 5 K without field by using Lorentzian site analysis method of the Recoil program.

Table 5 Values of zero field and infield Mössbauer parameters of the sample at 5 K determined by Lorentzian profile fitting.

Sample	Temperature	Site	Width	IS	2ε	B _{eff} ^a	B _{hf}	A ₂₃	θ ^b	Area
	/Field		(mm s ⁻¹)	(mm s ⁻¹)	(mm s ⁻¹)	(T)	(T)		(Degree)	(%)
			(±0.03)	(±0.03)	(±0.03)	(±0.14)	(±0.14)		(±0.02)	(±0.2)
ZFMS	5 K /5T	[Fe ³⁺ _A]	0.35	0.35	0.00	56.5	51.57	0.05	9.04	28.12
		[Fe ³⁺ _B]	0.47	0.47	0.00	47.8	52.35	0.41	25.54	71.87
	5 K /0 T	[Fe ³⁺ _A]	0.35	0.35	0.00	-	51.57	-	-	28.12
		[Fe ³⁺ _B]	0.47	0.47	0.00	-	52.35	-	-	71.87
ZFMH	5 K /5T	[Fe ³⁺ _A]	0.35	0.36	0.00	55.44	50.43	0.0	0.0	39.50
		[Fe ³⁺ _B]	0.40	0.47	0.01	46.50	51.50	0.0	0.0	49.35
		[Fe ²⁺ _B]	0.40	0.70	0.00	46.50	51.50	0.0	0.0	11.11
	5 K /0 T	[Fe ³⁺ _A]	0.35	0.36	0.00	-	50.43	-	-	39.50
		[Fe ³⁺ _B]	0.40	0.47	0.01	-	51.50	-	-	49.35
		[Fe ²⁺ _B]	0.40	0.70	0.00	-	51.50	-	-	11.11

^aObserved HMF (BHF) is the vector sum of the internal HMF and the external applied magnetic field.

^bThe average canting angle estimated from the ratio of the intensities of lines 2 and 3 from each subspectra, I₂/ I₃ (A₂₃) according to $\theta = \arccos[(4- I_2/ I_3) / (4+ I_2/ I_3)]^{1/2}$. Where I₂/ I₃=A₂₃.

^cEstimated according to the relationship of B_{eff}, B_{hf} and applied field.

So, as per the ratio of Fe³⁺_A/Fe³⁺_B obtained from infield spectrum, we propose a cation distribution for ZFMS as: (Zn_{0.44}Fe_{0.56})[Zn_{0.56}Fe_{1.44}]O₄. The infield Mössbauer spectrum of ZFMH discards the presence of spin canting in the sample. We have found from EDS study that ZFMH is nonstoichiometric in nature and it has also shown Verway transition in its ZFC-FC curves. It is well known that the latter is only possible if both Fe²⁺ and Fe³⁺ ions are simultaneously present at [B] site of the spinel lattice [70,71]. So, we have fitted the infield

Mössbauer spectrum of ZFMH by three sextets, where 1st and 2nd correspond to Fe³⁺ ions at (A) and [B] site, and 3rd to the Fe²⁺ ions at [B] site. The goodness of fitting and the values of isomer shift obtained from the fitting suggest that our proposition of presence of both Fe²⁺ and Fe³⁺ ions in the [B] site is correct. The values of hyperfine parameters have been included in Table 5. The proportion of intensity of Fe²⁺ ions in [B] site and the value of Fe³⁺_A/Fe³⁺_B obtained from the infield Mössbauer spectrum suggest that there is a vacancy of cations in the [B] site. So to account for the nonstoichiometry of ZFMH and the speculated cation vacancy at [B] site, we have deduced the following possible cation distribution for ZFMH from the ratio of intensities of Fe³⁺ at (A) to [B] sites and Fe²⁺ to Fe³⁺ ions in the infield Mössbauer spectrum: (Fe³⁺_xZn²⁺_{1-x})[Fe²⁺_{1-3Z}Fe³⁺_{1+2Z}Φ_Z]O₄, where Φ corresponds to vacancies that have appeared in the lattice to account for charge balance [72]. The formula can be written as: (Fe³⁺_{0.925}Zn²⁺_{0.075})[Fe²⁺_{0.31}Fe³⁺_{1.46}Φ_{0.23}]O₄. The ratio of Fe:Zn from the so obtained cation distribution is in good agreement with the ratio of the same estimated from EDS study. Further, the Verway transition in ZFMH can now be clearly asserted to the possible charge orbital ordering established due to the simultaneous presence of Fe²⁺ and Fe³⁺ ions in the [B] site.

4.4. Discussion

The structural and morphological characterization through PXRD, FESEM and TEM reveals following facts about ZFMS and ZFMH. ZFMS of diameter ~ 314 nm are composed of particles of crystallite size ~ 25 nm. They have crystallized in cubic spinel phase with lattice parameter ~ 8.487 Å. ZFMH has a hollow interior and an outer shell formed by continuous overlapping of layers of nanoparticles whose boundaries are indistinguishable. The smallest region of regular crystalline structure in ZFMH is of ~ 80 nm and it has also crystallized in cubic spinel phase. The value of lattice parameter for ZFMH is ~ 8.432 Å. The lattice parameter for bulk ZnFe₂O₄ is ~ 8.440 Å (ICDD card no: 82-1049). So, the lattice

parameters of ZFMS and ZFMH are in good agreement with that of bulk ZnFe_2O_4 , which suggests that the results of PXRD analysis are reliable. We have found that the crystallite size of ZFMH is quite large and clear boundaries of single particles are not separable in the TEM micrographs. Further, each bright single spot in the SAED pattern corresponds to a single large crystallite. The clear hyperfine split sextets in the 300 K Mössbauer spectrum of ZFMH also clearly indicates that the particles constituting it are larger in size, bear excellent crystalline character and consequently, are magnetically well-ordered.

The cation distribution proposed for ZFMS and ZFMH on the basis of valance state and the occupancy of iron ions at tetrahedral (A) and octahedral [B] sites of ZnFe_2O_4 obtained from the results of Mössbauer spectroscopic study can be verified by taking into account the valance state and ratio of metal ions determined through XPS study. In case of ZFMS, the value of $\text{Fe}^{3+}_\text{A}/\text{Fe}^{3+}_\text{B}$ determined from Mössbauer spectroscopic study is 0.39, which is same as that obtained from XPS study. Further, for ZFMS, the area ratio of Zn^{2+} at (A) and [B] sites ($\text{Zn}^{2+}_\text{A}/\text{Zn}^{2+}_\text{B}$) is 0.79 while the value of the same for cation distribution proposed for ZFMS on the basis of Mössbauer spectroscopic study is 0.786. Thus, the results of Mössbauer spectroscopic and XPS studies corroborate with each other and together with confirm that the cation distribution for ZFMS is $(\text{Zn}_{0.44}\text{Fe}_{0.56})[\text{Zn}_{0.56}\text{Fe}_{1.44}]\text{O}_4$. It may be noted that in ZnFe_2O_4 Zn^{2+} ions preferably occupy the (A) site [24]. However, in this case the Zn^{2+} ions have migrated from (A) to [B] sites by replacing equal amount of Fe^{3+} ions of [B] sites and pushing them to the (A) sites. Now, the cation distribution $(\text{Fe}^{3+}_{0.925}\text{Zn}^{2+}_{0.075})[\text{Fe}^{2+}_{0.31}\text{Fe}^{3+}_{1.46}\Phi_{0.23}]\text{O}_4$ for ZFMH has been determined using the ratio of $\text{Fe}^{3+}_\text{A}/\text{Fe}^{3+}_\text{B}$ and $\text{Fe}^{2+}/\text{Fe}^{3+}$ as obtained from Mössbauer spectroscopic study keeping in mind the charge balance condition. Again, both XPS and Mössbauer spectroscopic studies confirm the presence of Fe^{2+} ion in [B] sites of ZFMH. According to the Mössbauer spectroscopic study the values of $\text{Fe}^{3+}_\text{A}/\text{Fe}^{3+}_\text{B}$ and $\text{Fe}^{2+}/\text{Fe}^{3+}$ for ZFMH are 0.81 and 0.125, respectively,

while the corresponding values obtained from the analysis of Fe 2p_{3/2} XPS spectra are 0.80 and 0.125, respectively. Thus, the results of Mössbauer and XPS studies match well for ZFMH. The XPS study also indicates that very small amount of Zn is present in ZFMH. According to EDS study the ratio of Fe:Zn is ~ 45:0.8. Thus, ZFMH should be nonstoichiometric in nature and cation vacancy is inhabitable in it to maintain charge balance. Therefore, the perfect matching of occupancy of Fe³⁺ and Fe²⁺ ions at tetrahedral (A) and octahedral [B] sites for ZFMH suggest that the proposed cation distribution is correct and there is cation vacancy in this sample.

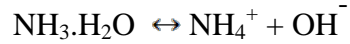
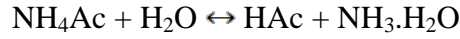
In order to test the accuracy of the cation distribution of ZFMS and ZFMH deduced from infield Mössbauer spectroscopic studies, we have calculated the theoretical value of magnetic moment per formula unit using the same and compared them with their experimental values obtained from dc magnetic studies. The theoretical magnetic moment per formula unit (m_{th}) of ferrites can be written as $m_{th} = m_B \cos \theta_B - m_A \cos \theta_A$ where, m_B and m_A are the magnetic moments associated with [B] and (A) sublattice of the spinel structure, respectively, θ_A and θ_B are the (A) and [B] site canting angles, respectively. Taking into consideration the values of θ_A and θ_B for ZFMS, we have found the value of m_{th} as 3.73 μ_B . The experimental magnetic moment per formula unit (m_{exp}) obtained from the value of M_{SAT} of 10 K M-H curve is 3.70 μ_B . The value of m_{th} and m_{exp} for ZFMH are 3.915 and 3.917 μ_B , respectively. The values of m_{th} and m_{exp} for both ZFMS and ZFMH are in excellent agreement. So, the deduced cation distribution of both ZFMS and ZFMH are trustworthy.

The dc magnetic measurements and Mössbauer spectroscopic studies give rise to some interesting magnetic phenomena such as superparamagnetism, spin glasslike freezing and collective magnetic excitations in ZFMS while most importantly Verwey transition in ZFMH. ZFMS have been formed by aggregation of nanoparticles of assorted shape and sizes. As a result, they display broad superparamagnetic hump in their ZFC curve at higher

temperatures with a distribution of blocking temperatures. On lowering the temperature, the spins freeze in random orientations due to competing sublattice interactions along with frustrations and the entire system stabilizes in a spin glasslike state. The room temperature Mössbauer spectroscopic studies of ZFMS reveal mixed magnetic phase possessing a superparamagnetic doublet along with diffused sextets. This result complies with the dc magnetic observations that the sample consists of nanoparticles with a broad particle size distribution consisting both superparamagnetic and magnetically well-ordered particles. There is an anomaly between the results of low temperature Mössbauer spectroscopic studies and the dc magnetic measurement. The 5 K zero field and in-field Mössbauer spectrum assure ferrimagnetic ordering within the sample whereas ZFC curve displays spin glasslike behavior at about same temperature. The difference arises from the fact that Mössbauer spectroscopy probes fluctuations of magnetic moment in the locality of Fe^{3+} ions whereas dc magnetic study records the magnetization as a whole.

ZFMH displays Verway transition in its dc magnetic studies. It is well known that Verway transition has been observed in magnetite at ~ 124 K [70,71]. Below this temperature, a first-order metal insulator transition takes place as a result of charge ordering between Fe^{3+} and Fe^{2+} ions at [B] site of the spinel lattice [70]. From literature survey, it is apparent that Verway transition is very prone to impurities and disappears with a little perturbation [73]. So, it is one of the most intriguing topics to researchers. Recently, Yeo et al., have found Verway transition in Gd doped magnetite nanoparticles and suggested that charge- orbital ordering has mainly instigated the transition [74]. In the present case, we have found from EDS study that ZFMH is nonstoichiometric in nature with very few Zn^{2+} ions in the system. The XPS study also corroborates this fact. From the results of XPS and low temperature Mössbauer spectroscopic studies we have found that apart from Fe^{3+} ions, Fe^{2+} ions are also present in ZFMH. These Fe^{2+} ions are the product of redox reaction of ethylene

glycol (solvent) and Fe^{3+} ions [75]. Further, NH_4Ac was used as hollowing agent in the synthesis of ZFMH. NH_4Ac is a weak-acid–weak-base salt that can be hydrolysed at high temperature in the presence of a trace amount of water coming from $\text{FeCl}_3 \cdot 6\text{H}_2\text{O}$ as follows:



Zinc has a tendency to form a very stable zinc amine complex. It seems that the Zn^{2+} ions at (A) site may have been replaced by Fe^{3+} ions from [B] site of the spinel lattice. Those misplaced Zn^{2+} ions have not migrated to [B] site following their strong chemical affinity towards (A) site; instead they may have formed the amine complex and remained in the solution, which was separated out during ultracentrifugation. As a result, a vacancy of Zn^{2+} ions has occurred in the lattice. Moreover, Verway transition is also sensitive to the nature of surface atoms [74] and no surface spin canting has been observed for ZFMH from its in-field Mössbauer spectroscopic study. Thus, it seems that presence of considerable amount of Fe^{2+} ions at [B] site in addition to Fe^{3+} ions resulting in charge-orbital ordering and absence of any surface spin canting leading to more symmetric coordination have together contributed to the occurrence of Verway transition in ZFMH.

4.5. Conclusion

The ZnFe_2O_4 solid and hollow microspheres, which have been synthesized by one-step solvothermal technique, display unique magnetic and hyperfine properties. The presence of collective magnetic excitations in the solid microspheres has been attributed to its nanoparticle self-assembled structure, which possesses both superparamagnetic and magnetically well-ordered particles. The appearance of Verway transition in the hollow microspheres has been mostly instigated by the charge orbital ordering between Fe^{3+} and Fe^{2+} ions in the [B] site of the spinel lattice. Presence of spin canting has been detected in the solid microspheres from its low temperature in-field Mössbauer spectroscopic studies, whereas a

possible cation vacancy along with existence of Fe^{2+} ions at [B] site of the spinel lattice has been found in the hollow microspheres. The cation distribution of both the microspheres has been testified by comparing the theoretical and experimental values of magnetic moment per formula unit and found to be reliable.

References

1. M. A. Boles, M. Engel, D. V. Talapin, Self-Assembly of Colloidal Nanocrystals: From Intricate Structures to Functional Materials, *Chem. Rev.* 116 (2016) 11220–11289.
2. S. Singamaneni, V. N. Bliznyuk, C. Binek, E.Y. Tsymbal, Magnetic nanoparticles: recent advances in synthesis, self-assembly and applications, *J. Mater. Chem.* 21 (2011) 16819.
3. M. Rad-Malekshahi, L. Lempink, M. Amidi, W. E. Hennink, E. Mastrobattista, Biomedical Applications of Self-Assembling Peptides, *Bioconjugate Chem.* 27 (2016) 3–18.
4. K. M. Z. Hossain, U. Patel, I. Ahmed, Development of microspheres for biomedical applications: a review, *Prog Biomater* 4 (2015) 1–19.
5. R. Mellors, I. Benzeval, R. Eisenthal, J. Hubble, Preparation of self-assembled microspheres and their potential for drug delivery, *Pharm Dev Technol* 15(1) (2010) 105–111.
6. L. Zhang, J. M. Chan, F. X. Gu, June-Wha Rhee, A. Z. Wang, A. F. Radovic-Moreno, F. Alexis, R. Langer, O. C. Farokhzad, Self-Assembled LipidPolymer Hybrid Nanoparticles: A Robust Drug Delivery Platform, *ACS Nano* 2 (2008) 1696–1702.
7. B. I. Kharisov, H. V. Rasika Dias, O. V. Kharissova, A. Vázquez, Y. Peña and I. Gómez, Solubilization, dispersion and stabilization of magnetic nanoparticles in water and non-aqueous solvents: recent trends, *RSC Adv.* 4 (2014) 45354–45381.
8. C. Pereira, A. M. Pereira, C. Fernandes, M. Rocha, R. Mendes, M. P. Fernández-García, A. Guedes, P. B. Tavares, J-M Grenèche, J. P. Araújo, and C. Freire, Superparamagnetic MFe_2O_4 ($M = Fe, Co, Mn$) Nanoparticles: Tuning the Particle Size and Magnetic Properties through a Novel One-Step Coprecipitation Route, *Chem. Mater.* 24 (2012) 1496–1504.
9. T. Neuberger, B. Pfaff, H. Hofmann, M. Hofmann, B. von Rechenberg, Superparamagnetic nanoparticles for biomedical applications: Possibilities and limitations of a new drug delivery system, *J. Magn. Mater* 293 (2005) 483–496.

-
10. D.K. Kim, Y. Zhang, W. Voit, K.V. Rao, J. Kehr, B. Bjelke, M. Muhammed, Superparamagnetic Iron Oxide Nanoparticles For Bio-Medical Applications, *Scripta Mater.* 44 (2001) 1713–1717.
 11. N. Bao, L. Shen, Yu-Hsiang A. Wang, J. Ma, D. Mazumdar, A. Gupta, Controlled Growth of Monodisperse Self-Supported Superparamagnetic Nanostructures of Spherical and Rod-Like CoFe_2O_4 Nanocrystals, *J. Am. Chem. Soc.* 131 (2009) 12900–12901.
 12. H. L. Yuan, Y. Q. Wang, S. M. Zhou, L.S. Liu, X. L. Chen, S. Y. Lou, R. J. Yuan, Y. M. Hao, N. Li, Low-Temperature Preparation of Superparamagnetic CoFe_2O_4 Microspheres with High Saturation Magnetization, *Nanoscale Res Lett* 5 (2010) 1817–1821.
 13. R. Mondal, K. Sarkar, S. Dey, D. Majumdar, S. K. Bhattacharya, P. Sen, S. Kumar, Magnetic, Pseudocapacitive, and H_2O_2 -Electrosensing Properties of Self-Assembled Superparamagnetic $\text{Co}_{0.3}\text{Zn}_{0.7}\text{Fe}_2\text{O}_4$ with Enhanced Saturation Magnetization, *ACS Omega* 4 (2019) 12632–12646.
 14. S. Majumder, S. Dey, K. Bagani, S. K. Dey, S. Banerjee, S. Kumar, A comparative study on the structural, optical and magnetic properties of Fe_3O_4 and $\text{Fe}_3\text{O}_4@\text{SiO}_2$ core-shell microspheres along with an assessment of their potentiality as electrochemical double layer capacitors, *Dalton Trans.* 44 (2015) 7190.
 15. H. Deng, X. Li, Q. Peng, X. Wang, J. Chen, Y. Li, Monodisperse Magnetic Single-Crystal Ferrite Microspheres *Angew. Chem. Int. Ed.* 44 (2005) 2782–2785.
 16. M. Penchal Reddy, A.M.A. Mohamed, One-pot solvothermal synthesis and performance of mesoporous magnetic ferrite MFe_2O_4 nanospheres, *Micropor Mesopor Mat* 215 (2015) 37–45.
 17. A. Kostopoulou, A. Lappas, Colloidal magnetic nanocrystal clusters: variable length-scale interaction mechanisms, synergetic functionalities and technological advantages *Nanotechnol Rev* 4(6) (2015) 595–624.
-

18. A. Kostopoulou, K. Brintakis, M. Vasilakaki, K. N. Trohidou, A. P. Douvalis, A. Lascialfari, L. Manna, A. Lappas, Assembly-mediated interplay of dipolar interactions and surface spin disorder in colloidal maghemite nanoclusters, *Nanoscale* 6 (2014) 3764.
19. L. Lartigue, P. Hugounenq, D. Alloyeau, S. P. Clarke, M. Levy, J-C Bacri, R. Bazzi, D. F. Brougham, C. Wilhelm, F. Gazeau, Cooperative Organization in Iron Oxide Multi-Core Nanoparticles Potentiates Their Efficiency as Heating Mediators and MRI Contrast Agents, *ACS Nano*, 6 (2012) 10935–10949.
20. G. F. Goya, T. S. Berquó, F. C. Fonseca, M. P. Morales, Static and dynamic magnetic properties of spherical magnetite nanoparticles *J. Appl. Phys.* 94 (2003) 3520.
21. A. Espinosa, A. Muñoz-Noval, M. García-Hernández, A. Serrano, J. Jiménez de la , A. Figuerola, A. Quarta, T. Pellegrino, C. Wilhelm, M. A. García, Magnetic properties of iron oxide nanoparticles prepared by seeded-growth route *J Nanopart Res* 15 (2013) 1514.
22. C. Yao, Q. Zeng, G. F. Goya, T. Torres, J. Liu, H. Wu, M. Ge, Y. Zeng, Y. Wang, J. Z. Jiang, ZnFe_2O_4 Nanocrystals: Synthesis and Magnetic Properties, *J. Phys. Chem. C* 111 (2007) 12274-12278.
23. P. Guo, L. Cui, Y. Wang, M. Lv, B. Wang, X. S. Zhao, Facile Synthesis of ZnFe_2O_4 Nanoparticles with Tunable Magnetic and Sensing Properties, *Langmuir* 29 (2013) 8997–9003.
24. A. Yan, X. Liu, R. Yi, R. Shi, N. Zhang, G. Qiu, Selective Synthesis and Properties of Monodisperse Zn Ferrite Hollow Nanospheres and Nanosheets, *J. Phys. Chem. C* 112 (2008) 8558–8563.
25. Z. Li, X. Lai, H. Wang, D. Mao, C. Xing, D. Wang, General Synthesis of Homogeneous Hollow Core-Shell Ferrite Microspheres, *J. Phys. Chem. C* 113 (2009) 2792–2797.

26. R. Rahimi, H. Kerdari, M. Rabbani, M. Shafiee, Synthesis, characterization and adsorbing properties of hollow Zn-Fe₂O₄ nanospheres on removal of Congo red from aqueous solution, *Desalination* 280 (2011) 412–418.
27. Meng Yu, Ying Huang, Ke Wang, Xiaopeng Han, Mingyue Wang, Yade Zhu, Liu Liu, Complete hollow ZnFe₂O₄ nanospheres with huge internal space synthesized by a simple solvothermal method as anode for lithium ion batteries, *App. Surf. Sci.* 462 (2018) 955–962.
28. D. Yang, K. Wei, Q. Liu, Y. Yang, X. Guo, H. Rong, M-L Cheng, G. Wang, Folic acid functionalized magnetic ZnFe₂O₄ hollow microsphere core/mesoporous silica shell composite particles: Synthesis and application in drug release, *Mater. Sci. Eng. C* 33 (2013) 2879–2884.
29. W. Jiang, Z. Cao, R. Gu, X. Ye, C. Jiang, X. Gong, A simple route to synthesize ZnFe₂O₄ hollow spheres and their magnetorheological characteristics, *Smart Mater. Struct.* 18 (2009) 125013.
30. Y. Qu, D. Zhang, X. Wang, H. Qiu, T. Zhang, M. Zhang, G. Tian, H. Yue, S. Feng, G. Chen, Porous ZnFe₂O₄ nanospheres as anode materials for Li-ion battery with high performance, *J Alloy Compd* 721 (2017) 697–704.
31. X. Zhou, J. Liu, C. Wang, P. Sun, X. Hu, X. Li, K. Shimanoe, N. Yamazoe, G. Lu, Highly sensitive acetone gas sensor based on porous ZnFe₂O₄ nanospheres, *Sensor Actuat B* 206 (2015) 577–583.
32. X. Guo, X. Lu, X. Fang, Y. Mao, Z. Wang, L. Chen, X. Xu, H. Yang, Y. Liu, A facile bubble-assisted synthesis of porous Zn ferrite hollow microsphere and their excellent performance as an anode in lithium ion battery, *Electrochem. commun.* 12 (2010) 847–850.
33. L. Yao, X. Hou, S. Hu, Q. Ru, X. Tang, L. Zhao, D. Sun, Lithium storage in hollow spherical ZnFe₂O₄ as anode materials for lithium ion batteries, *J Solid State Electrochem* 17 (2013) 2055–2060.

-
34. X-J. Xu, L-H Zhou, Q-G Zhai, C-Z Lu, Synthesis, Properties, and Formation Mechanism of Zinc Ferrite Hollow Spheres J. Am. Ceram. Soc. 90 (2007) 1959–1962.
35. P. Guo, M. Lv, G. Han, C. Wen, Q. Wang, H. Li, X. S. Zhao, Solvothermal Synthesis of Hierarchical Colloidal Nanocrystal Assemblies of ZnFe_2O_4 and Their Application in Water Treatment, Materials 9 (2016) 806.
36. Z. P. Chen, W. Q. Fang, B. Zhang, H. G. Yang, High-yield synthesis and magnetic properties of ZnFe_2O_4 single crystal nanocubes in aqueous solution, J Alloy Compd 550 (2013) 348–352.
37. A. Kmita, D. Lachowicz, J. Żukrowski, M. Gajewska, W. Szczerba, J. Kuciakowski, S. Zapotoczny, M. Sikora, One-Step Synthesis of Long Term Stable Superparamagnetic Colloid of Zinc Ferrite Nanorods in Water, Materials 12 (2019) 1048.
38. B. D. Cullity, C. D. Graham, Introduction to Magnetic Materials IEEE Press (2009).
39. S. Dey, S. K. Dey, B. Ghosh, P. Dasgupta, A. Poddar, V. R. Reddy, S. Kumar, Role of inhomogeneous cation distribution in magnetic enhancement of nanosized $\text{Ni}_{0.35}\text{Zn}_{0.65}\text{Fe}_2\text{O}_4$: A structural, magnetic, and hyperfine study, J. Appl. Phys. 114 (2013) 093901.
40. S. Dey, R. Mondal, S. K. Dey, S. Majumder, P. Dasgupta, A. Poddar, V. R. Reddy, S. Kumar, Tuning magnetization, blocking temperature, cation distribution of nanosized $\text{Co}_{0.2}\text{Zn}_{0.8}\text{Fe}_2\text{O}_4$ by mechanical activation, J. Appl. Phys. 118 (2015) 103905.
41. B. Ghosh, S. Kumar, A. Poddar, C. Mazumdar, S. Banerjee, V. R. Reddy, A. Gupta, Spin glasslike behavior and magnetic enhancement in nanosized Ni–Zn ferrite system, J. Appl. Phys. 108 (2010) 034307.
42. P. Hu, L. Yu, A. Zuo, C. Guo, F. Yuan, Fabrication of Monodisperse Magnetite Hollow Spheres, J. Phys. Chem. C 113 (2009) 900–906.
43. Y. Wang, D. Su1, A. Ung, J-ho Ahn, G. Wang, Hollow CoFe_2O_4 nanospheres as a high capacity anode material for lithium ion batteries, Nanotechnology 23 (2012) 055402 (6pp).
-

44. D. Mandal, M. Alam, K. Mandal, NiFe_2O_4 nano-hollow spheres with improved magnetic and dielectric properties *Physica B* 554 (2019) 51–56.
45. W. Zhang, X. Hou, Z. Lin, L. Yao, X. Wang, Y. Gao, S. Hu, Hollow microspheres and nanoparticles MnFe_2O_4 as superior anode materials for lithium ion batteries *J Mater Sci: Mater Electron* 26 (2015) 9535–9545.
46. M. P. Reddy, X. B. Zhou, Q. Huang, R. R. Reddy, Synthesis and Characterization of Ultrafine and Porous Structure of Magnesium Ferrite Nanospheres, *Int J Nano Stud Technol.* 3(6) (2014) 72-77.
47. Y. Yin, N. Huo, W. Liu, Z. Shi, Q. Wang, Y. Ding, J. Zhang, S. Yang, Hollow spheres of MgFe_2O_4 as anode material for lithium-ion batteries, *Scripta Mater* 110 (2016) 92–95.
48. M. P. Reddy, X. Zhou, D. Shiyu, Q. Huang, Fabrication, characterization, and magnetic behavior of porous ZnFe_2O_4 hollow microspheres, *Int Nano Lett* 5 (2015) 53–59.
49. P. E. Werner, L. Eriksson, M. Westdahl, TREOR, A semi-exhaustive trial-and-error powder indexing program for all symmetries, *J. Appl. Cryst.* 18 (1985) 367-370.
50. A. Altomare, R. Caliandro, M. Camalli, C. Cuocci, I. da Silva, C. Giacovazzo, A. Grazia G. Moliterni, R. Spagna, Space-group determination from powder diffraction data: a probabilistic approach, *J. Appl. Cryst.* 37 (2004) 957–966.
51. L. Lutterotti, MAUDWEB, Version 1.9992 (2004).
52. Y. Yin, R. M. Rioux, C. K. Erdonmez, S. Hughes, G. A. Somorjai, A. Paul Alivisatos, Formation of Hollow Nanocrystals Through the Nanoscale Kirkendall Effect, *Science* 304 (2004) 711-714.
53. M. Klinger, More features, more tools, more CrysTBox, *J. Appl. Cryst.* 50 (2017) 1226–1234.
54. M. Wen, Q. Li and Y. Li, Magnetic, electronic and structural properties of $\text{Zn}_x\text{Fe}_{3-x}\text{O}_4$, *J Electron Spectros Relat Phenomena* 153 (2006) 65–70.
-

-
55. Z. P. Chen, W. Q. Fang, B. Zhang and H. G. Yang, High-yield synthesis and magnetic properties of ZnFe_2O_4 single crystal nanocubes in aqueous solution, *J. Alloys Compd.* 550 (2013) 348–352.
56. J. Wu, N. Li, J. Xu, Y. Jiang, Z-G. Ye, Z. Xie and L. Zheng, Partially inverse spinel ZnFe_2O_4 with high saturation magnetization via a molten salt route, *Appl. Phys. Lett.* 99 (2011) 202505.
57. S. Majumder, M. Sardar, B. Satpati, S. Kumar and S. Banerjee, Magnetization enhancement of Fe_3O_4 by attaching onto graphene oxide: an interfacial effect, *J. Phys. Chem. C* 122 (2018) 21356-21365.
58. M. Wang, Z. Ai and L. Zhang, Generalized preparation of porous nanocrystalline ZnFe_2O_4 superstructures from zinc ferrioxalate precursor and its superparamagnetic property, *J. Phys. Chem. C* 112 (2008) 13163–13170.
59. G. Chen, J. J. Peng, C. Song, F. Zeng, F. Pan, Interplay between chemical state, electric properties, and ferromagnetism in Fe-doped ZnO films, *J. Appl. Phys.* 113 (2013) 104503.
60. J.F. Moulder, W.E. Stickle, P.E. Sobol and K.D. Bomben, *Handbook of X-ray Photoelectron Spectroscopy*, Perkin Elmer Corporation (1992).
61. S. Dey, S. K. Dey, B. Ghosh, V.R. Reddy, S. Kumar, Structural, microstructural, magnetic and hyperfine characterization of nanosized $\text{Ni}_{0.5}\text{Zn}_{0.5}\text{Fe}_2\text{O}_4$ synthesized by high energy ball-milling method, *Mater. Chem. Phys.* 138 (2013) 833-842.
62. J. L. Dormann, D. Fiorani, E. Tronc, *Magnetic relaxation in fine-particle Systems*, *Advances in Chemical Physics*, John Wiley & Sons (1997).
63. A. Mitra, J. Mohapatra, S. S. Meena, C. V. Tomy, M. Aslam, Verwey Transition in Ultrasmall-Sized Octahedral Fe_3O_4 Nanoparticles, *J. Phys. Chem. C* 118 (2014) 19356–19362.
-


-
64. J. Liu, Y. Bin, M. Matsuo, Magnetic Behavior of Zn-Doped Fe_3O_4 Nanoparticles Estimated in Terms of Crystal Domain Size, *J. Phys. Chem. C* 116 (2012) 134–143.
65. F. L. Deepak, M. Bañobre-López, E. Carbó-Argibay, M. Fátima Cerqueira, Y. Piñeiro-Redondo, J. Rivas, C. M. Thompson, S. Kamali, C. Rodríguez-Abreu, K. Kovnir, Y. V. Kolen'ko, A Systematic Study of the Structural and Magnetic Properties of Mn-, Co-, and Ni-Doped Colloidal Magnetite Nanoparticles, *J. Phys. Chem. C* 119 (2015) 11947–11957.
66. K. Lagarec, D.G. Rancourt, Recoil-Mössbauer Spectral Analysis Software for Window, University of Ottawa Press, Ottawa (1998).
67. R. Bauminger, S. G. Cohen, A. Marinov, S. Oper, K. Segal, Study of the Low-Temperature Transition in Magnetite and the Internal Fields Acting on Iron Nuclei in Some Spinel Ferrites, Using Mossbauer Absorption, *Phys Rev* 122 (1961) 1447-1450.
68. K. Sarkar, R. Mondal, S. Dey, S. Majumder, S. Kumar, Presence of mixed magnetic phase in mechanically milled nanosized $\text{Co}_{0.5}\text{Zn}_{0.5}\text{Fe}_2\text{O}_4$: A study on structural, magnetic and hyperfine properties, *J. Magn. Magn. Mater.* 487 (2019) 165303.
69. R. Mondal, S. Dey, K. Sarkar, P. Dasgupta, S. Kumar, Influence of high energy ball milling on structural parameters, cation distribution and magnetic enhancement of nanosized $\text{Co}_{0.3}\text{Zn}_{0.7}\text{Fe}_2\text{O}_4$, *Mater. Res. Bull.* 102 (2018) 160–171.
70. E. J. W. Verway, Electronic conduction of Magnetite (Fe_3O_4) and its Transition Point at Low Temperatures, *Nature* 144 (1939) 327-328.
71. Mark S. Senn, Jon P. Wright, J. Paul Attfield, Charge order and three-site distortions in the Verwey structure of magnetite, *Nature* 481 (2012) 173-176.
72. C. A. Gorski, M. M. Scherer, Determination of nanoparticulate magnetite stoichiometry by Mössbauer spectroscopy, acidic dissolution, and powder X-ray diffraction: A critical review, *American Mineralogist* 95 (2010) 1017–1026.
-

73. V. A. M. Brabers, F. Walz, H. Kronmüller, The formation mechanism of iron oxide nanoparticles within the microwave-assisted solvothermal synthesis and its correlation with the structural and magnetic properties, *Phys Rev B* 58 (1998) 14163-14166.
74. S. Yeo, H. Choi, C. S. Kim, G. T. Lee, J. H. Seo, H. J. Chad, J. C. Park, Survival of Verwey transition in gadolinium-doped ultrasmall magnetite nanoparticles, *Nanoscale* 9 (2017) 13976–75.
- Z. Kozakova, I. Kuritka, N. E. Kazantseva, V. Babayan, M. Pastorek, M. Machovsky, P. Bazant, P. Saha, The formation mechanism of iron oxide nanoparticles within the microwave-assisted solvothermal synthesis and its correlation with the structural and magnetic properties, *Dalton Trans.* 44 (2015) 21099.



Chapter 5

Electrochemical Study of Nanosized $\text{Co}_{0.5}\text{Zn}_{0.5}\text{Fe}_2\text{O}_4$ Synthesized by Hydrothermal Method



5.1. Introduction

Nanocrystalline magnetic materials have gained significant attention partially owing to their extraordinary physicochemical features in contrast to their bulk phase and primarily due to their multipurpose applications. [1-4]. Bulk ferrites possess equilibrium cation distribution whereas cation redistribution takes place in their nanosized counterparts [5-7]. Apart from this, the finite size effect and surface spin canting reduce the magnetization of nanometric ferrites significantly compared to their bulk phases [7]. The properties of nanometric ferrites are immensely influenced by their morphology, cation distribution and surface spin disorder. Efforts are being made to tune these features of nanosized ferrites by choosing synthesis technique cautiously [2,8]. Mechanically activated nanosized ferrites like Co-Zn, Ni-Zn, Mn-Zn etc., displaying high saturation magnetization and high coercivity at room temperature have evolved as promising candidates for applications in magnetic storage device [9-11]. In contrary, the nanostructured superparamagnetic ferrites viz., Fe_3O_4 , CoFe_2O_4 , ZnFe_2O_4 , MnFe_2O_4 , NiFe_2O_4 , CuFe_2O_4 etc., prepared by chemical method displaying moderate saturation magnetization and no coercivity at room temperature are preferred for catalysis, photocatalytic degradation of dyes and removal of heavy metals from polluted water discharged by industries due to their high surface to volume ratio, presence of active site, stability, reusability and ease of separation simply with the help of magnetic field [12,13-17].

In particular, CoFe_2O_4 with inverse spinel structure exhibits many interesting physical properties like high coercivity [18,19], high magnetic anisotropy [18], moderate saturation magnetization [19], high chemical stability [20] and electrical conductivity [21]. On the other side, ZnFe_2O_4 is antiferromagnetic in bulk [22] and shows ferrimagnetic nature in nanometric domain and in the form of thin films [23,24]. Substitution of non-magnetic Zn^{2+} ions in nanosized CoFe_2O_4 is expected to modify the exchange interactions in tetrahedral (A) and

octahedral [B] sites of the spinel lattice and accordingly modify magnetic properties of the so formed mixed Co-Zn ferrites [25,26]. According to literature, the properties of mixed $\text{Co}_{1-x}\text{Zn}_x\text{Fe}_2\text{O}_4$ ferrite series with $x = 0 - 1$ prepared by chemical method have been investigated in abundance [25-34]. Nanometric $\text{Co}_{0.2}\text{Zn}_{0.8}\text{Fe}_2\text{O}_4$, $\text{Co}_{0.3}\text{Zn}_{0.7}\text{Fe}_2\text{O}_4$, $\text{Co}_{0.4}\text{Zn}_{0.6}\text{Fe}_2\text{O}_4$, $\text{Co}_{0.5}\text{Zn}_{0.5}\text{Fe}_2\text{O}_4$ and $\text{Co}_{0.6}\text{Zn}_{0.4}\text{Fe}_2\text{O}_4$ ferrites have shown presence of magnetic clusters in an infinite magnetic framework, cluster-paramagnetic phase, cluster glass phase, dual magnetic phase, non-collinear spin structure and superparamagnetic clusters [35-41]. Doping of nonmagnetic Zn^{2+} ions in nanometric CoFe_2O_4 at a ratio of $X=0.5$ results in highest value of saturation magnetization due to increase in inter-sublattice A-O-B (JAB) exchange interactions between tetrahedral (A) site and octahedral [B] site of the spinel lattice [42-45]. Nanosized $\text{Co}_{0.5}\text{Zn}_{0.5}\text{Fe}_2\text{O}_4$ has been found to be an optimum composition displaying superior magnetic properties in the series of [46]. Nanometric $\text{Co}_x\text{Zn}_{1-x}\text{Fe}_2\text{O}_4$ has shown maximum saturation magnetization value for the as-prepared sample at $x = 0.5$ [47]. Nanosized $\text{Co}_{0.5}\text{Zn}_{0.5}\text{Fe}_2\text{O}_4$ ferrite has proved to be potentially used as an excellent microwave absorber in the C-band [48].

In the fast-growing world, development of energy storage devices is gaining special attention in order to sustainably harness the depleting energy resources. Supercapacitors are usually subdivided into two classes on the basis of their energy storage process [49]. One is electrochemical double layer capacitor (EDLC) in which energy storage takes place via electrostatic accretion of charges and second one is pseudocapacitor that stores energy by the process of redox reaction [49,50]. Although EDLCs deliver high power density and brilliant life cycle, their ability to store energy is limited following finite separation between the electrode and electrolytes [49,50]. In contrary, pseudocapacitors possess higher specific capacitance and energy density as compared to EDLCs, thus proving themselves beneficial in manufacture of superior quality energy storage devices [49,50]. RuO_2 is a typical

pseudocapacitor displaying high pseudocapacitive performance but comes with the shortcoming of high price [49-54]. Thus, it is the concern of the scientific community to manufacture some low-cost alternative to RuO_2 . To cater to the demands of the industry, attempts are being made to investigate the pseudocapacitive performance of some other transition metal oxides [55 – 60]. Unfortunately, many of them have shown low capacitance and cycling stability that render them useless in production of a good quality energy storage device [49]. In this context, nanostructured oxide materials have appeared as a panacea owing to their higher capacitance following high surface area and short ion transfer pathway [49]. Nanosized ferrites are appearing as potential candidates for supercapacitor application owing to their high surface to volume ratio, low price, environmental benignity, and large abundance [49, 55-66]. There is a plethora of reports on the electrochemical performance of pure ferrites [49,55-66]. But, electrochemical properties of mixed ferrites have not been explored abundantly.

In this background, we have synthesized nanosized $\text{Co}_{0.5}\text{Zn}_{0.5}\text{Fe}_2\text{O}_4$ by simple hydrothermal method and characterized them using powder x-ray diffraction, field emission scanning electron microscopic, transmission electron microscopic and UV-vis diffuse reflectance spectroscopic techniques. Moreover, we have investigated the electrochemical properties of nanosized $\text{Co}_{0.5}\text{Zn}_{0.5}\text{Fe}_2\text{O}_4$ and accessed their application as a supercapacitor.

5.2. Experimental

5.2.1. Sample synthesis

The nanosized $\text{Co}_{0.5}\text{Zn}_{0.5}\text{Fe}_2\text{O}_4$ (CZ5050) has been synthesized by hydrothermal method maintaining proper stoichiometric ratio and using reagents procured from Sigma Aldrich (purity 99.99 %). 5 mmol $\text{CoCl}_2 \cdot 6\text{H}_2\text{O}$, 5 mmol $\text{ZnCl}_2 \cdot 4\text{H}_2\text{O}$ and 10 mmol $\text{FeCl}_3 \cdot 6\text{H}_2\text{O}$ were dispersed in 80 ml distilled water in a glass beaker under constant stirring. Subsequently, 5.4 g $\text{CH}_3\text{COONa} \cdot 3\text{H}_2\text{O}$ (NaAc) was put in the above mixture. Further, the

concoction was maintained under continuous stirring at room conditions for sixty min to acquire a standardized dark brown mixture. Subsequently the mixture was immediately shifted to a Teflon-lined stainless-steel autoclave and the system was thermally treated at 180 °C for 18 h. Next this system was permitted to return to room temperature on its own. After that the produce was accumulated by centrifugation, cleaned for several times with deionized water and ethanol. Lastly, the so-obtained precipitate was desiccated at 60 °C for 10 h to attain a black powder.

5.2.2. Characterization

The powder X-ray diffraction (PXRD) pattern of the sample has been attained by a Bruker D8 Advanced Diffractometer using $\text{CuK}\alpha$ ($\lambda = 1.54184 \text{ \AA}$) radiation. For this, the X-ray generator was fixed at 40 kV and 40 mA. The diffraction images were attained at normal conditions (25°C) with step size 0.01991 and a counting time of 3s/step over the range of $2\theta=20^\circ\text{--}80^\circ$. The particle size and morphology of the sample were examined by field emission scanning and high-resolution transmission electron microscopic techniques (FESEM, Inspect F50 and HRTEM, Jeol 2100). Before subjecting the sample to TEM investigation, it was methodically crumpled in a mortar, disseminated in ethyl alcohol, set on a Cu-grid by means of spin-coater and desiccated in vacuum. The dc magnetization as a function of temperature and versus magnetic field was recorded using vibrating sample magnetometer (Cryogenics made). The $M(T)$ data were attained under zero field cooled (ZFC) and field cooled (FC) mode, respectively. The substance was cooled from 300 to 10 K without external magnetic field in zero field cooled mode and in the existence of magnetic field for field cooled mode. In the temperature range of 10 to 300 K, $M(T)$ data were attained in the presence of external magnetic field. In the field cooled mode, same field value was maintained while the cooling and measurement. The hysteresis loop data were attained at 300, 100 and 10 K were recorded under ZFC mode. The diffuse reflectance spectroscopy

(DRS) spectrum of the sample was attained using a PerkinElmer UV–vis spectrometer (Lambda 35).

5.2.3. Electrode preparation for electrochemical study

The working electrode for cyclic voltametric measurements has been prepared by following method. Firstly, a graphite rod with geometrical area 0.14 cm^2 has been cleaned carefully in deionized water through ultrasonication. Further the prepared rod has been draped by Teflon sheet while the ends of the rod were kept open. Later, the specimen has been put in deionized water and Nafion mixture through ultrasonication to get a hydra solution of required concentration. $10\text{ }\mu\text{L}$ of the as-prepared solution has been dispensed over the curved level exterior of the graphite rod and finally desiccated at room temperature for one night. The cyclic voltametric measurements have been performed using a potentiostat instrument (Digi-ivy, model No. DY2300) in 1 M and 0.1 M NaOH aqueous solution at $25\text{ }^\circ\text{C}$ taking a conventional three electrode system comprising of a working electrode, a saturated calomel electrode as the reference electrode and a Pt wire as counter electrode.

5.3. Results and Discussion

5.3.1. Structural and microstructural characterization

The primary goal of structural investigation is to ascertain the structural features like atomic coordinates, lattice parameters, etc., as well as microstructural parameters viz., crystallite size, microstrain etc. of the present sample. Moreover, it also aims to evaluate the possibility of any impurity phases present within the sample. The PXRD pattern of CZ5050 is presented in Fig. 1. The data has been refined using MAUD2.33 package [67] as it is capable of determining the structural, microstructural properties and quantifiable phases of the compound substances with a high level of accuracy. The values of structural, microstructural and refinement parameters are presented in Table 1. A significant broadening accompanied by decrease in the intensity of the Bragg peaks of the sample is suggestive of nano size,

structural non-uniformity, amorphous phase of the particle surface along with high microstrain within the lattice planes of the sample. The pattern has been labelled by TREOR90 of Fullprof.2k package [68]. Further, this labelling of lattice planes was crosschecked by DICVOL06 of Fullprof.2k package [69] and NTREOR of EXPO2009 package [70]. Both the results are in conformity. The space group has been found by utilizing FINDSPACE of EXPO2009 package through statistical study of the powder diffraction pattern [71]. The results ascertain that the sample has crystallized in $Fd\bar{3}m$ space group. Moreover, the Miller indices and the space group determined by the above stated Rietveld refinement technique are in conformity with JCPDS data base (JCPDS card no 89-1012 and 22-1086 for $ZnFe_2O_4$ and $CoFe_2O_4$). So, it is clear that the sample is a pure cubic spinel ferrite with $Fd\bar{3}m$ symmetry.

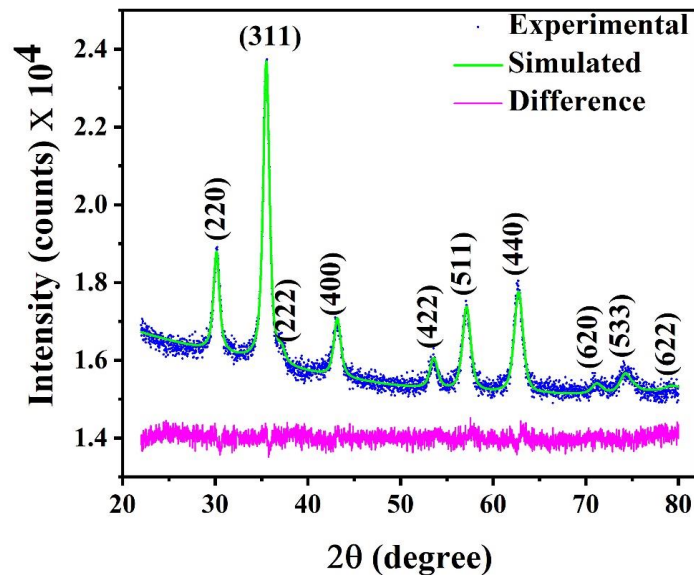


Fig. 1. PXRD pattern of CZ5050

Table 1. Crystal data and refinement parameters

Parameters	CZ5050
Crystallite size (nm)	17
Microstrain	3.76×10^{-3}
Lattice parameter ($a(\text{\AA})$)	8.372
Density (g cm^{-3})	5.304
R_{wp}	0.008
R_{exp}	0.005
GOF	1.21

The FESEM image of CZ5050 is shown in Fig. 2. It is clear that the samples are non-spherical in shape, possess size distribution and have an inclination towards agglomerate formation. The TEM micrograph of the sample showing particle size distribution is shown in Fig. 3. It is well-known that nanometric ferrites have an affinity of agglomeration. So, in order to disperse the particles properly, a small of the sample was first spread in ethanol through strong ultrasonication. Further, the Cu-grid was positioned on a spin coating unit spinning at 400 rpm and the sample was dropped on the grid. It is apparent from Fig.3 that we have succeeded in our attempt to avoid the agglomeration. An overview of TEM images suggests that single particles size ranges from 15-23 nm in size with average particle ~ 19 nm. In accordance with XRD measurement, the average crystallite size is ~ 17 nm. The amorphousness at the particle surface is well-explained by these results. The constituent particles are non-spherical in shape and possess a size distribution. The presence of bright distinct rings in the selected area diffraction (SAED) pattern of the sample (Fig.4) assures about the good crystallinity of the nanoparticles.

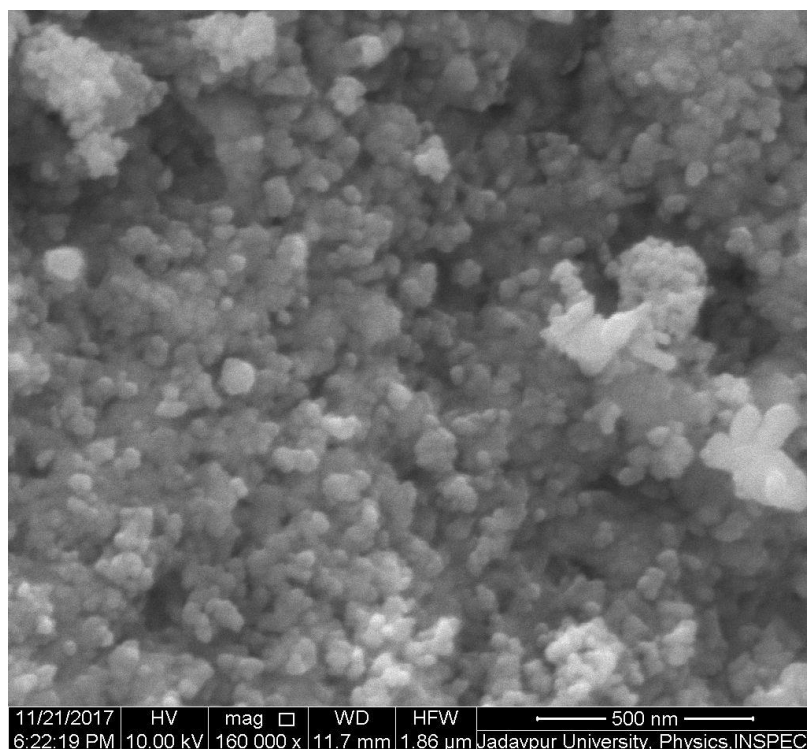


Fig. 2. FESEM micrograph of CZ5050

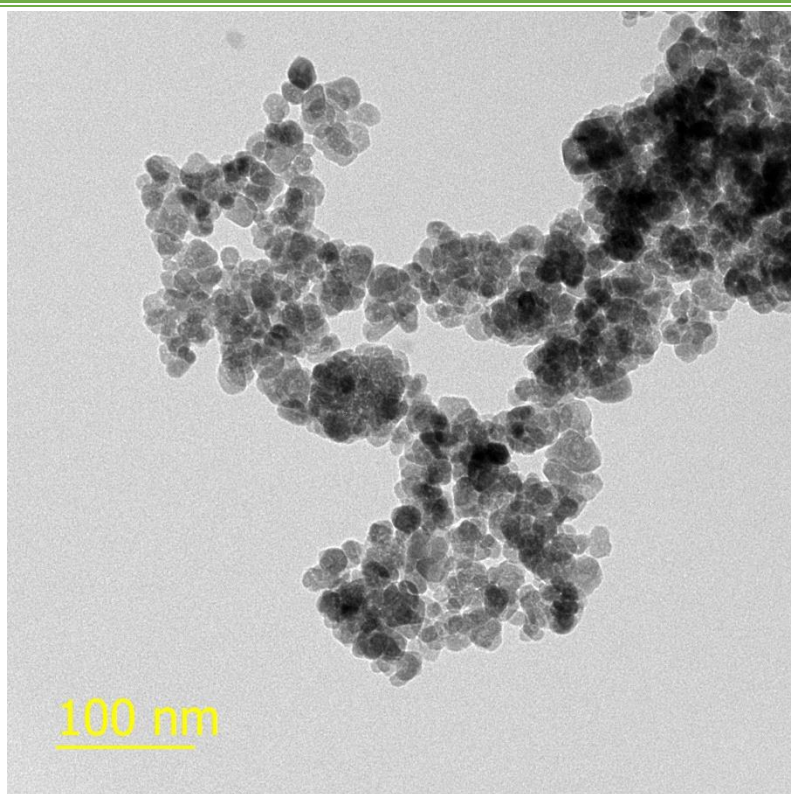


Fig. 3. TEM micrograph of CZ5050

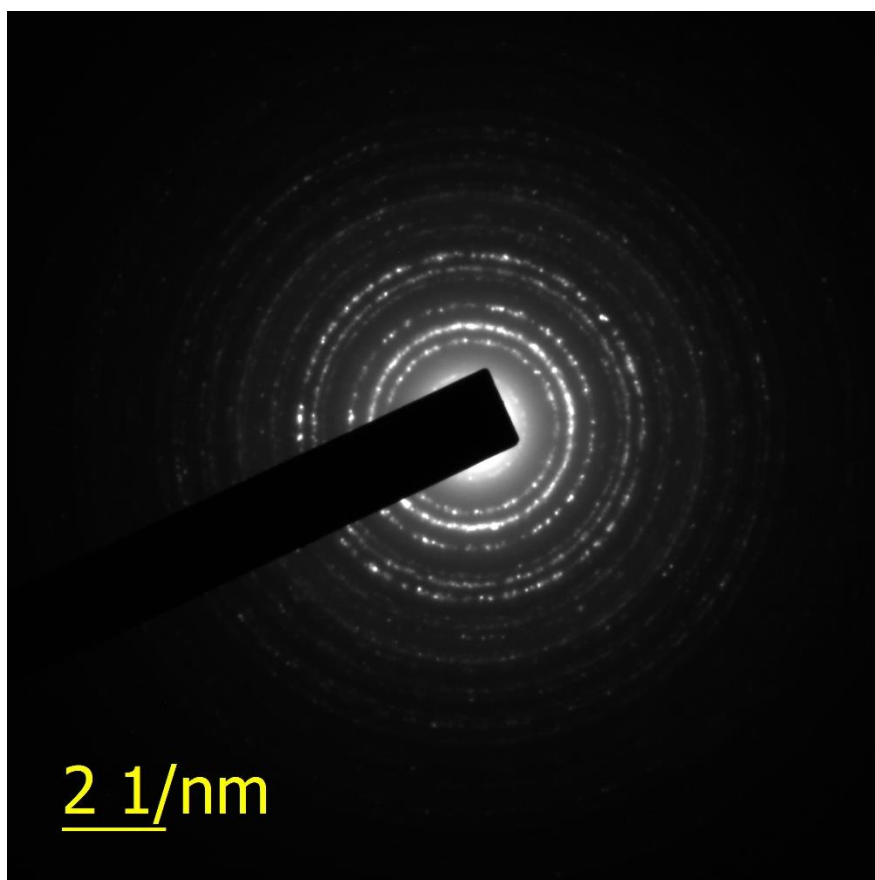


Fig. 4. SAED pattern of CZ5050

5.3.2. Study of Optical Properties

The knowledge of optical absorption property of a compound gives an idea of its electronic structural characteristics and is a crucial factor in determining its applicability in surface related fields like catalysis and electrochemistry. In this approach, UV-vis diffuse reflectance spectroscopy (UV-vis DRS) is a fast, low-priced and non-damaging method for analysis of optical property of solid compounds [72]. The UV-vis DRS spectrum of CZ5050 is shown in Fig. 5. It displays a broad absorption edge at around 705 nm. The band gap of CZ5050 is 1.75 eV (shown in inset of Fig.5), as estimated from the intercept of the $(\alpha h\nu)^2$ versus $h\nu$ plot (Kubelka–Munk plot), where α is the absorption coefficient [73]. The value of bandgap of the present sample is lower when compared to other nanosized CZ5050 [74]. This may be due to presence of lower unoccupied energy levels in the present sample. This is in contrast to the normal quantum confinement phenomenon according to which there is increase in bandgap at nanoregime.

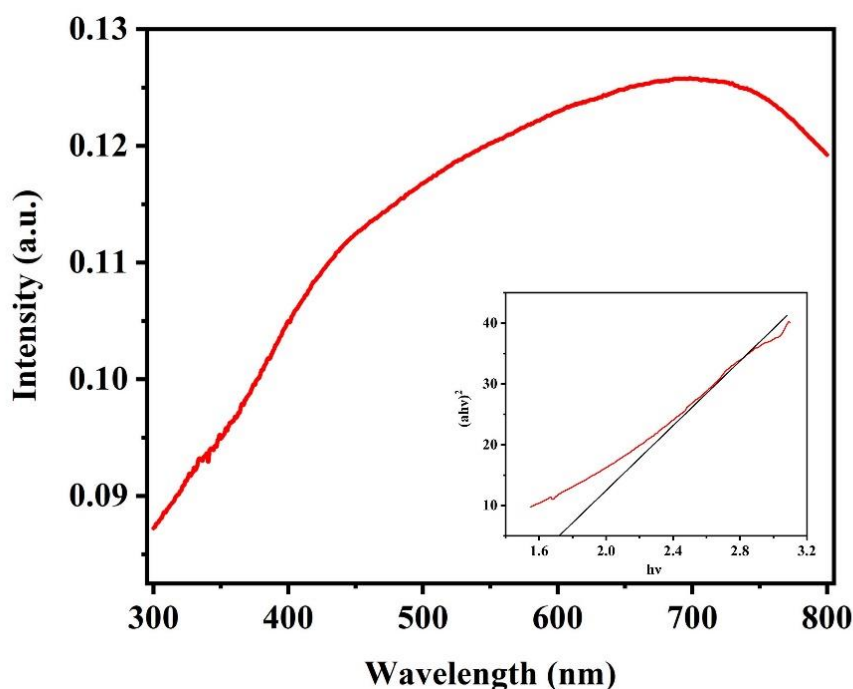


Fig. 5. UV-DRS spectrum of CZ5050 and $(\alpha h\nu)^2$ versus $h\nu$ plot (inset)

5.3.3. Magnetic study

The magnetization versus temperature (M-T) measurements in zero field cooled (ZFC) and field cooled (FC) modes have been carried out to ascertain the magnetic character of the sample. The ZFC-FC curves of CZ5050 in the temperature range of 10 – 380 K at 100 Oe external magnetic field are presented in Fig.6. The FC magnetization curve decreases slowly up to a certain temperature (280 K), then remains constant upto 150 K below which, it slightly increases in value upto 10 K. Such behavior of FC magnetization curve is a consequence of finite-size effects which are induced by dipolar and interparticle interactions [75]. The ZFC data exhibits a gradual decrease in magnetization with the decreasing temperature from 300 to 100 K, below which it becomes almost constant upto 10 K. This behavior indicates anisotropy energy induced loss of long-range ferrimagnetic ordering in the sample. The bifurcation observed in the ZFC-FC curves owing to minimization of Helmholtz free energy of the system is considerably less in the present sample. This may be attributed to the surface effect in nanosized particles that require very large value of magnetic field to overcome it [75]. There is absence of any superparamagnetic hump even upto 380 K. It states that the sample is magnetically ordered at room temperature.

In order to testify the findings of M-T studies, we have performed the hysteresis loop study of the sample. The magnetization versus fields (M-H) curves of the sample at 300 (at ± 1 T), 100 (± 5 T) and 10 K (± 5 T) are presented in Fig.7. The values of saturation magnetization (M_{SAT}) at 300, 100 and 10 K are 63.2, 77.4 and 78.4 emu g⁻¹, respectively. The M_{SAT} value for CZ5050 (63.53 emu g⁻¹) is less than that of the bulk CoFe₂O₄ (80 emu/g). This reduction in M_{SAT} can be accredited to the surface spin disorder at the nanoparticle surface [76]. The M_{SAT} values at 100 and 10 K have not increased significantly as compared to that at 300 K. The parameter of M_{SAT} is directly influenced by the internal spin structure i.e., a ordered core surrounded by a disordered shell owing to either spin canting or surface

anisotropy [77]. In addition to spin canting and effective anisotropy energy, interparticle interactions among the nanoparticle assemblage play a pivotal role in controlling the magnetic parameters in nano regime. The value of coercivity (H_C) at 300, 100 and 10 K are 740, 7900 and 13300 Oe, respectively. The value of H_C of the present sample at 10 K is remarkably high as compared to that of bulk CoFe_2O_4 (~ 5 kOe at 5 K) [78]. The H_C of any magnetic material at nanoregime is determined by the effective anisotropy of the system. The anisotropy energy is further influenced by the size, shape, spin structure and the nature of interactions existing in the nanoparticle ensemble. In the present case, the effective anisotropy and consequently the H_C is the overall result of the surface anisotropy and dipolar interactions present in the sample. The kinks in the M-H curves at 100 and 10 K are due to spin reorientation. moreover, such a bend may also be attributed to the domain-wall pinning occurring at applied field change. Since no impurity phases are present in the sample, the possibility of exchange between the hard and soft magnetic phases can be neglected. This reorientation is more dominant at 10 K as compared to 300 K.

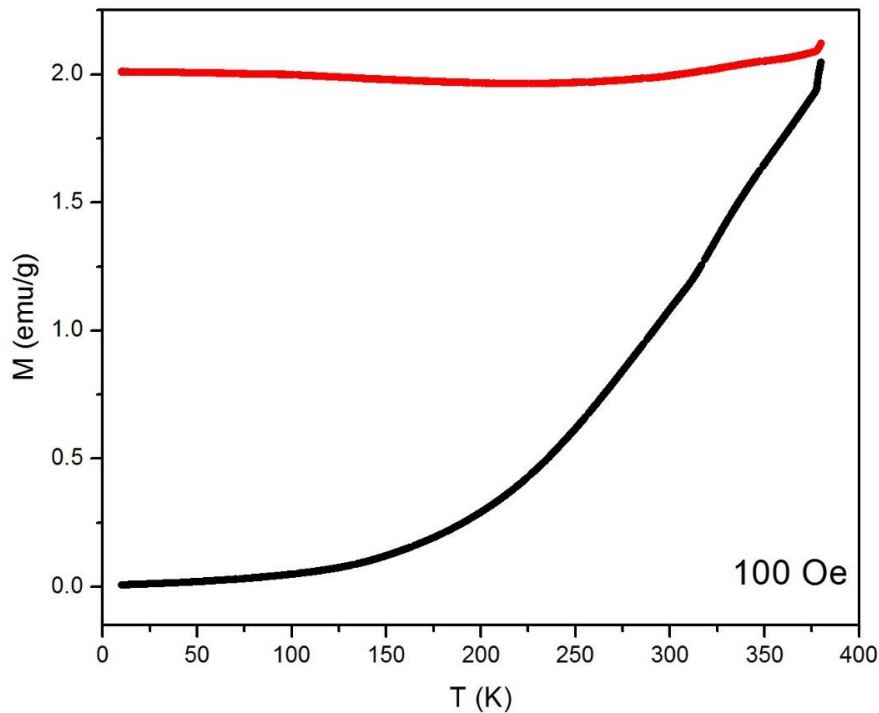


Fig.6. ZFC-FC curves of CZ5050.

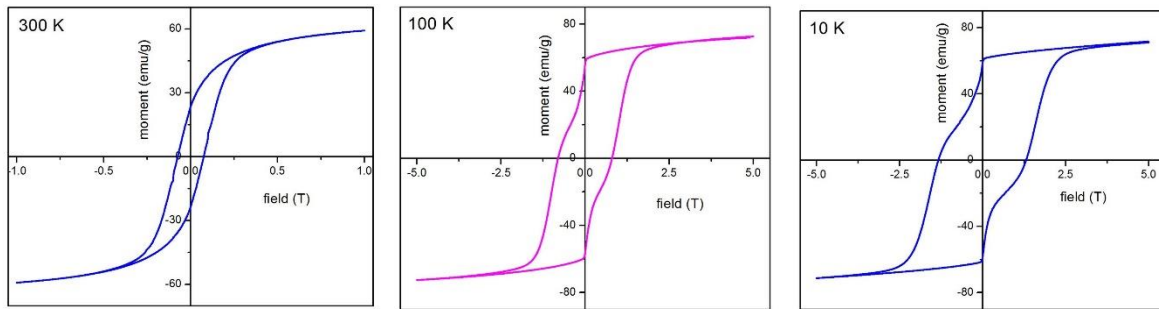
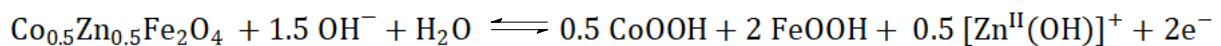


Fig.7. M-H curves of CZ5050 at 300, 100 and 10 K, respectively.

5.3.4. Electrochemical performance study

The cyclic voltammograms (CV) of CZ5050 electrode at scan rates of 10, 20, 50, 100 and 200 mV/s in the potential range of ± 0.3 V with reference to the saturated calomel electrode are illustrated in Fig.8. From the CV curves of CZ5050, it is apparent that they do not follow the behaviour of ideal electrical double layer capacitor [79,80]. The nonconformity from the usual shape of the CV curves can be credited to the pseudocapacitive behavior of CZ5050 originating from the transfer of charges between electrode and electrolyte through electrosorption and intercalation processes. Moreover, there is absence of any redox peaks in the cathodic or anodic cycles of the CV curves of CZ5050. For CZ5050, the pseudocapacitance takes place through interconversion of $\text{Co}^{2+}/\text{Co}^{3+}$ states accompanied by concurrent insertion/ deintercalation of OH^- ions following the under mentioned equation:



The values of specific capacitance (CS) have been calculated from the CV plot using the formula: $C_s = \frac{i}{mv}$, where m is the mass of the active electrode material, v is the potential sweep rate and i is the current response that can be obtained by integrating the area of the curve $i = \int_{V_a}^{V_c} \frac{i(V)dV}{V_c - V_a}$, where V_a and V_c represent the anodic and cathodic voltages, respectively [81, 82]. CS values for CZ5050 at scan rates of 10, 20, 50, 100 and 200 mV/s are 85.5, 56,

25, 20 and 17 F/g, respectively. At high values of scan rates, atoms of the electrode are surrounded by ions escalating obstruction in the charge transfer process leading to the drop of capacitance [83]. Further, the area of the CV curves upsurges with the scan rate, without altering the shape of the curves, reflecting good electrochemical response of the sample [61].

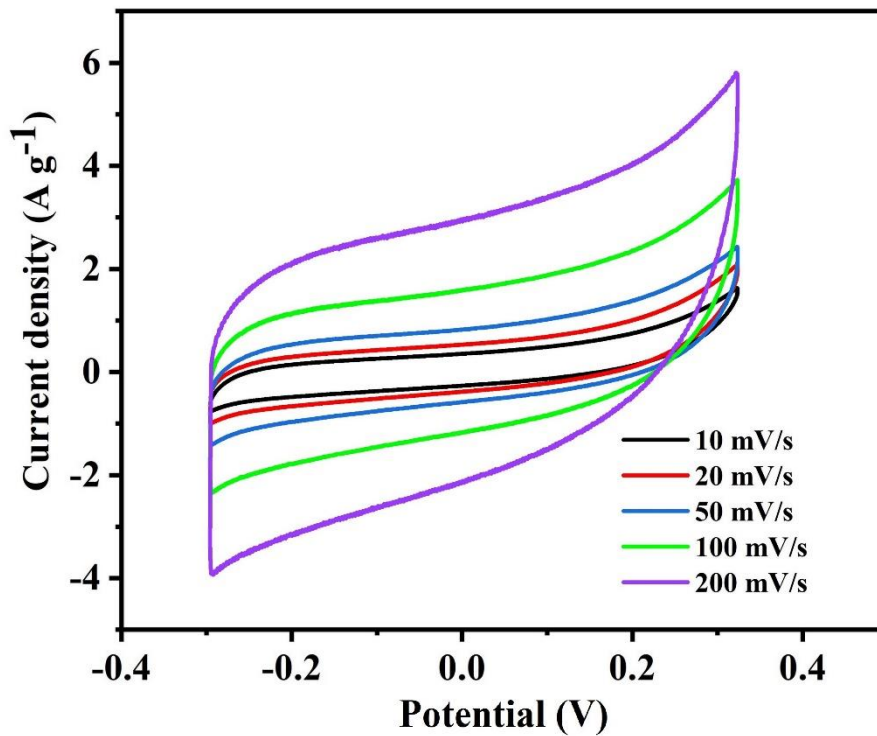


Fig. 4. CV plots of CZ5050

5.4. Conclusion

The structural, magnetic, optical properties of nanosized $\text{Co}_{0.5}\text{Zn}_{0.5}\text{Fe}_2\text{O}_4$ have been judiciously studied by PXRD, FESEM, HRTEM, UV-vis DRS and dc magnetic methods. The particle size from PXRD and crystallite size from TEM studies match well with each other revealing that CZ5050 is well-crystalline in nature. The sample exhibits wide distribution in particle size along with strong interparticle interactions. The dc magnetic studies reveal that CZ5050 is magnetically well-ordered at room temperature and also possess strong interparticle interactions within the ensemble of nanoparticles. The values of saturation magnetization of the samples are lower than bulk CoFe_2O_4 due to presence of surface spin canting. The values of coercivity at 10 K are significantly higher than at room temperature

signifying increase in anisotropy at 10 K. This boost in anisotropy energy has been instigated by the combined effect of surface anisotropy and interparticle interactions. CZ5050 exhibits good electrochemical performance due to its nano size, morphology and lower band gap energy and can act as a supercapacitor.

References

1. L. Khanna, N.K. Verma, S.K. Tripathi, *J Alloys Compd* 752 (2018) 332-353.
2. Thomas Dippong, E. A. Levei, O. Cadar, *Nanomaterials* 11 (2021) 1560.
3. P. Chand, S. Vaish, P. Kumar, *Physica B Condens. Matter* 524 (2017) 53 – 63.
4. J. Jeevanandam, A. Barhoum, Y. S. Chan, A. Dufresne, M. K. Danquah, *Beilstein J. Nanotechnol.* 9 (2018) 1050–1074.
5. M.C. Dimri, H. Khanduri, P. Agarwal, V. Garg, A. Mere, R. Stern, *AIP Conf. Proc.* 2265 (2020) 030517.
6. S. Sharma, N. Choudhary, M. K. Verma, N. D. Sharma, D. Singh, *Ceram. Int.* 43 (2017) 11083 – 11089.
7. Karla R. Sanchez-Lievanos, James L. Stair, Kathryn E. Knowles, *Inorg. Chem.* 60 (2021) 4291–4305.
8. Jongnam Park, Jin Joo, Soon Gu Kwon, Youngjin Jang, Taeghwan Hyeon, *Angew. Chem. Int. Ed.* 46 (2007) 4630 – 4660.
9. S. Dey, R. Mondal, S. K. Dey, S. Majumder, P. Dasgupta, A. Poddar, V. R. Reddy, S. Kumar, *J. Appl. Phys.* 118 (2015) 103905.
10. S. Chakraverty, B. Ghosh, S. Kumar, A. Frydman, *Appl. Phys. Lett.* 88 (2006) 042501.
11. Md. J. N. Isfahani, M. Myndyk, D. Menzel, A. Feldhoff, J. Amighian, V. Šepelák, *J. Magn. Magn. Mater.* 321 (2009) 152–156.
12. L. S. Ganapathe, M. A. Mohamed, R. M. Yunus, D. D. Berhanuddin, *Magnetochemistry* 6 (2020) 68
13. B. Jansi Rani, M. Ravina, B. Saravanakumar, G. Ravi, V. Ganesh, S. Ravichandran, R. Yuvakkumar, *Nano-Struct. Nano-Objects* 14 (2018) 84 – 91.
14. M. Bini, M. Ambrosetti, D. Spada, *Appl. Sci.* 11 (2021) 11713.
15. N. Akhlaghi, G. Najafpour-Darzi, *J Ind Eng Chem.* 103 (2021) 292 – 304.
16. Y. Zhang, W. Zhang, C. Yu, Z. Liu, X. Yu, F. Meng, *Ceram. Int.* 47 (2021) 10063 – 10071.

17. M.A. S. Amulya, H. P. Nagaswarupa, M.R. Anil Kumar, C.R. Ravikumar, K. B. Kusuma, S.C. Prashantha, *J. Phys. Chem. Solids*, 148 (2021) 109756.
18. S. M. Ansari, B. B. Sinha, K.R. Pai, S.K. Bhat, Y-R Ma, D. Sen, Y. D. Kolekar, C.V. Ramana, *Appl. Surf. Sci.* 459 (2018) 788–801.
19. B. H. Liu, J. Ding, Z. L. Dong, C. B. Boothroyd, J. H. Yin, J. B. Yi, *Phys. Rev. B* 74 (2006) 184427.
20. S. Jauhar, J. Kaur, A. Goyal, S. Singhal, *RSC Adv.* 6 (2016) 97694 – 97719.
21. R.K. Panda, D. Behera, *J. Alloys Compd.* 587 (2014) 481–486.
22. M J Akhtar, M Nadeem, S Javaid, M Atif, *J. Phys.: Condens. Matter* 21 (2009) 405303.
23. S. Dey, R. Mondal, S. Majumder, P. Dasgupta, A. Poddar, S. Banerjee, S. Kumar, *Materials Today: Proceedings* 5 (2018) 9855 – 9859.
24. M. Bohra, S. Prasad, N. Kumar, D. S. Misra, S. C. Sahoo, N. Venkataramani, R. Krishnan, *Appl. Phys. Lett.*, 88 (2006) 262506.
25. S. S. Jadhav, S. E. Shirsath, S. M. Patange, K. M. Jadhav, *J. Appl. Phys.* 108 (2010) 093920.
26. D. S. Nikam, S. V. Jadhav, V. M. Khot, R. A. Bohara, C. K. Hong, S. S. Mali, S. H. Pawar, *RSC Adv.* 5 (2015) 2338.
27. V. Mamei, A. Musinu, A. Ardu, G. Ennas, D. Peddis, D. Niznansky, C. Sangregorio, C. Innocenti, Nguyen T. K. Thanh, C. Cannas, *Nanoscale*, 8 (2016) 10124.
28. M. Schmidt, H. L. Andersen, C. Granados-Miralles, M. Saura-Múzquiz, M. Stingaciu, M. Christensen, *Dalton Trans.* 45 (2016) 6439.
29. X. Huang, J. Zhang, W. Wang, T. Sang, B. Song, H. Zhu, W. Rao, C. Wong, *J. Magn. Mater.* 405 (2016) 36–41.
30. R.N. Bhowmik, R. Ranganathan, *J. Magn. Mater.* 248 (2002) 101–111.

31. R.V. Upadhyay, H. Parmar, P. Acharya, A. Banerjee, Solid State Commun. 163 (2013) 50–54.
32. G. A. Petitt, D. W. Forester, Phys. Rev. B4 (1971) 11.
33. K. Sarkar, R. Mondal, S. Dey, S. Majumder, S. Kumar, J. Magn. Magn. Mater. 487 (2019) 165303.
34. S. Dey, A. Roy, J. Ghose, R. N. Bhowmik, R. Ranganathan, J. Appl. Phys. 90 (2001) 4138.
35. I. Sharifi, H. Shokrollahi, J. Magn. Magn. Mater. 324(2012) 2397–2403.
36. R.N. Bhowmik, R. Ranganathan, J. Magn. Magn. Mater. 248 (2002) 101–111.
37. H. Parmar, P. Acharya, R.V. Upadhyay, V. Siruguri, S. Rayaprol, Solid State Commun. 153(2013) 60–65.
38. R.V. Upadhyay, H. Parmar, P. Acharya, A. Banerjee, Solid StateCommun. 163 (2013) 50–54.
39. G.A. Petitt, D.W. Forester, Mossbauer study of cobalt-zinc ferrites, Phys. Rev. B 4(1971) 11.
40. S. Dey, A. Roy, J. Ghose, R.N. Bhowmik, R. Ranganathan, J. Appl. Phys. 90 (2001) 4138.
41. I. Sharifi, H. Shokrollahi, J. Magn.Magn. Mater. 334 (2013) 36–40
42. A. Ramakrishna, N. Murali, Tulu Wegayehu Mammo, K. Samatha, V. Veeraiah,Phys. B: Condens. Matter. 534 (2018)134–140.
43. T.R. Tatarchuk, N.D. Paliychuk, M. Bououdina, B. Al-Najar, M. Pacia, W. Macyk,A. Shyichuk, J. Alloy. Compd. 731 (2018) 1256–1266.
44. D.M. Jnaneshwara, D.N. Avadhani, B.D. Prasad, B.M. Nagabhushana,H. Nagabhushana, S.C. Sharma, S.C. Prashantha, C. Shivakumara, J. Alloy.Comp. 587 (2014) 50–58.

45. A. Manikandan, L. John Kennedy, M. Bououdina, J. Judith Vijaya, J. Magn. Magn. Mater. 349 (2014) 249–258.
46. L. Cervera and C. G. Polo, in Book of Abstracts of Jornada Doctoral de Jovenes Investigadores en Magnetism, 17 October 2019 (The Spanish Magnetism Club and the Spanish Chapter of the IEEE Magnetics Society Annual Joint Meeting, 2019) p. 18.
47. C. Hou, H. Yu, Q. Zhang, Y. Li, and H. Wang, J. Alloys Compd. 491 (2010)431.
48. Yi-Wei Liu, Jing Zhang, Lu-Shun Gu, Li-Xi Wang, Qi-Tu Zhang, Rare Met. 41 (2022) 3228–3232.
49. M. Zhu, X. Zhang, Y. Zhou, C. Zhuo, J. Huang and S. Li, RSC Adv. 5 (2015) 39270 – 39277.
50. W. Chen, R. B. Rakhi, L. Hu, X. Xie, Y. Cui and H. N. Alshareef, Nano Lett. 11 (2011) 5165–5172.
51. T-Y. Wei, C-H. Chen, H-C. Chien, S-Y. Lu and C-C. Hu, Adv. Mater. 22 (2010) 347 – 351.
52. C. Z. Yuan, B. Gao, L. F. Shen, S. D. Yang, L. Hao, X. J. Lu, F. Zhang, L. J. Zhang and X. G. Zhang, Nanoscale 3 (2011) 529 – 545.
53. Z. Chen, Y. Qin, D. Weng, Q. Xiao, Y. Peng, X. Wang, H. Li, F. Wei and Y. Lu, Adv. Funct. Mater. 19 (2009) 3420 – 3426.
54. W. Sugimoto, H. Iwata, Y. Yasunaga, Y. Murakami and Y. Takasu, Angew. Chem., Int. Ed. 42 (2003) 4092–4096.
55. M. Zhu, Y. Wang, D. Meng, X. Qin and G. Diao, J. Phys. Chem. C 116 (2012) 276–16285.
56. Z. Chen, V. Augustyn, X. Jia, Q. Xiao, B. Dunn and Y. Lu, ACS Nano 6 (2012) 4319 – 4327.


57. A. K. Singh, D. Sarkar, G. Khan and K. Mandal, *ACS Appl. Mater. Interfaces* 6 (2014) 4684–4692.
58. S. Chen, J. Zhu, X. Wu, Q. F. Han and X. Wang, *ACS Nano* 4 (2010) 2822–2830.
59. G. Srabanti, P. Kar, N. Bhandary, S. Basu, S. Sardar, T. Maiyalagan, D. Majumder, S. K. Bhattacharya, A. Bhaumik, P. Lemmens and S. K. Pala, *Catal. Sci. Technol.* 6 (2016) 1417 – 1429.
60. M-S. Balogun, Y. Huang, W. Qiu, H. Yang, H. Ji and Y. Tong, *Materials Today* 20 (2017) 425 – 451.
61. L. Li, H. Bi, S. Gai, F. He, P. Gao, Y. Dai, X. Zhang, D. Yang, M. Zhang and P. Yang, *Sci. Rep.* 7 (2017) 43116-1 – 43116-12.
62. S. Majumder, S. Dey, K. Bagani, S. K. Dey, S. Banerjee and S. Kumar, *Dalton Trans.* 44 (2015) 7190 – 7202.
63. W. Zhang, B. Quan, C. Lee, S-K. Park, X. Li, E. Choi, G. Diao and Y. Piao, *ACS Appl. Mater. Interfaces* 7 (2015) 2404 – 2414.
64. Z. Wang, W. Jia, M. Jiang, C. Chen and Y. Li, *Nano Res.* 9 (2016) 2026 – 2033.
65. V.S. Kumbhar, A.D. Jagadale, N.M. Shinde and C.D. Lokhande, *Appl. Surf. Sci.* 259 (2012) 39 – 43.
66. B. Wang, P. Guo, H. Bi, Q. Li, G. Zhang, R. Wang, J. Liu. and X. S. Zhao, *Int. J. Electrochem. Sci.* 8 (2013) 8966 – 8977.
67. L. Lutterotti, MAUDWEB, Version 1.9992 (2004).
68. P.E. Werner, L. Eriksson, M.J. Westdahl, *J. Appl. Crystallogr.* 18 (1985) 367 – 370.
69. A. Boultif, D. Louer, *J. Appl. Crystallogr.* 37 (2004) 724 – 731.
70. A. Altomare, C. Giacovazzo, A. Guagliardi, A.G.G. Moliterni, R. Rizzi, E.J. Werner, J. *Appl. Crystallogr.* 33 (2000) 1180 – 1186.
-

71. A. Altomare, R. Caliendo, M. Camalli, C. Cuocci, C. Giacobazzi, A.G.G. Moliterni, R. Rizzi, *J. Appl. Crystallogr.* 37 (2004) 1025 – 1028.
72. T. Lopez, E. Sanchez, P. Bosch, Y. Meas and R. Gomez, *Mater. Chem. Phys.* 32 (1992) 141-152.
73. A. Manikandan, L.J. Kennedy, M. Bououdina, J. J. Vijaya, *J. Magn. Mater.* 349 (2014) 249-258.
74. M. Sundararajan, L. John Kennedy, J. Judith Vijaya, Udaya Aruldoss, *Spectrochim. Acta A Mol. Biomol. Spectrosc.* 140 (2015) 421–430.
75. Sumayya M. Ansari, Bhavesh B. Sinha, Kalpana R. Pai, Suresh K. Bhat, Yuan-Ron Ma, Debasis Sen, Yesh D. Kolekar, C.V. Ramana, *Appl. Surf. Sci.* 459 (2018) 788–801
76. C.R. Lin, Y.M. Chu, S.C. Wang, *Mater. Lett.* 60 (2006) 447–450.
77. T. Bala, C.R. Sankar, M. Baidakova, V. Osipov, T. Enoki, P.A. Joy, B.L.V. Prasad, M. Sastry, *Langmuir.* 21 (2005) 10638–10643.
78. S. Bhattacharyya, J.P. Salvetat, R. Fleurier, A. Husmann, T. Cacciaguerra, M.L. Saboungi, *Chem. Commun.* (2005) 4818–4820.
79. L. Guan, L. Yu and G. Z. Chen, *Electrochim. Acta* 206 (2016) 464 – 478.
80. Y. Wang, Y. Song and Y. Xia, *Chem. Soc. Rev.* 45 (2016) 5925 – 5950.
81. Z. Fan, J. Yan, T. Wei, L. Zhi, G. Ning, T. Li and F. Wei, *Adv. Funct. Mater.* 21 (2011) 2366 – 2375.
82. D. Majumdar, N. Baugh and S. K. Bhattacharya, *Colloids and Surfaces A: Physicochem. Eng. Aspects* 512 (2013) 158–170.
83. R.S. Hastak, P. Sivaraman, D. D. Potphode, K. Shashidhara and A.B. Samui, *Electrochim. Acta* 59 (2012) 296 – 303.



Chapter 6

*Influences of morphology, cation distribution
and surface spin canting on magnetic and
hyperfine properties of mechanically activated
and subsequently heat treated nanosized
 $\text{Co}_{0.8}\text{Zn}_{0.2}\text{Fe}_2\text{O}_4$ exhibiting excellent catalytic
activity*



6.1. Introduction

In past two decades, nanocrystalline magnetic materials are in the limelight partly owing to their exceptional physicochemical properties in comparison to their bulk counterparts and mainly for their versatile technological applications. [1-4]. Ferrites, in their bulk phase, possess equilibrium cation distribution and their physical properties are exclusively determined by chemical composition and synthesis procedure adopted [5,6]. In case of nanosized counterparts of any bulk ferrite, cation redistribution takes place resulting in non-equilibrium cation distribution [5-7]. Apart from this, the finite size effect and surface spin canting reduce the magnetization of nanometric ferrites significantly compared to their bulk counterparts [7]. The physical properties of nanometric ferrites are strongly reigned on morphology (shape and size), cation distribution, surface spin alignment. These characteristic features of nanosized ferrites can be easily modified by choosing synthesis procedure judiciously [2,8]. The nanostructured ferrites are extensively used for fabrication of magnetic storage device, magnetic resonance imaging agents, gas and electrochemical sensors, and electrodes of supercapacitors [9-12]. Additionally, their application encompasses the fields of industrial wastewater treatment, catalysis, photocatalytic dye degradation, medical science (hyperthermia treatment, targeted drug delivery etc.) [1,2,13-15]. It is noteworthy that the basic requirement for each kind of applications is discrete. Mechanically activated nanosized ferrites like Co-Zn, Ni-Zn, Mn-Zn etc., displaying high saturation magnetization and high coercivity at room temperature have evolved as promising candidates for applications in magnetic storage device [16-18]. In contrary, the nanostructured superparamagnetic ferrites viz., Fe_3O_4 , CoFe_2O_4 , ZnFe_2O_4 , MnFe_2O_4 , NiFe_2O_4 , CuFe_2O_4 etc., prepared by chemical method displaying moderate saturation magnetization and no coercivity at room temperature are preferred for catalysis, photocatalytic degradation of dyes and removal of heavy metals from polluted water discharged by industries due to their high surface to volume ratio,

presence of active site, stability, reusability and ease of separation simply with the help of magnetic field [15,19-23]. In particular, CoFe_2O_4 with inverse spinel structure exhibits many interesting physical properties like high coercivity [24,25], high magnetic anisotropy [24], moderate saturation magnetization [25], high chemical stability [26] and electrical conductivity [27]. On the other hand, ZnFe_2O_4 is antiferromagnetic in bulk [28] and shows ferrimagnetic nature in nanometric domain and in the form of thin films [29,30]. Substitution of non-magnetic Zn^{2+} ions in nanosized CoFe_2O_4 is expected to modify the exchange interactions in tetrahedral (A) and octahedral [B] sites of the spinel lattice and consequently alter magnetic properties of the so formed mixed Co-Zn ferrites [31,32]. According to literature, mostly the structural, morphological, magnetic, and dielectric properties of mixed $\text{Co}_{1-x}\text{Zn}_x\text{Fe}_2\text{O}_4$ ferrite series with $x = 0 - 1$ prepared by chemical method have been investigated in abundance [31-40]. Interestingly, some research groups have come up with rare features like cluster glass phase [36-38], mixed magnetic phase [39], superparamagnetic clusters [40] etc. However, the magnetic and hyperfine properties of nanosized $\text{Co}_{0.8}\text{Zn}_{0.2}\text{Fe}_2\text{O}_4$ ferrites have not been investigated in detail [41-43]. Notably, there are few reports on the influence of morphology in governing the physical properties of Co-Zn ferrites synthesized by mechanochemical methods [16,40,43,44]. To the best of our knowledge, there is no report on structural, magnetic, hyperfine properties and application potential of Co-Zn ferrites prepared by chemical route followed by high energy ball milling (mechanical activation) and subsequent heat treatment. Further, it will be highly interesting to examine the role of morphology in ascertaining the magnetic and hyperfine properties of such systems. In this background, thorough study on structural, magnetic, hyperfine properties and catalytic activity of mechanically activated and subsequently heat treated nanosized $\text{Co}_{0.8}\text{Zn}_{0.2}\text{Fe}_2\text{O}_4$ ferrite with different sizes seems propitious.

At room temperature (300 K), $\text{Co}_{0.9}\text{Zn}_{0.1}\text{Fe}_2\text{O}_4$ nanoparticles prepared by flow rate controlled coprecipitation method exhibit saturation magnetization (M_{SAT}) and coercivity (H_{C}) of 48 emu g^{-1} and 1775 Oe , respectively, while its counterpart synthesized by conventional coprecipitation method gives values of M_{SAT} and H_{C} as 54.1 emu g^{-1} and 223 Oe , respectively [45,46]. The superparamagnetic $\text{Co}_{0.8}\text{Zn}_{0.2}\text{Fe}_2\text{O}_4$ nanoparticles synthesized by hydrolysis method (particle size $\sim 3.5 \text{ nm}$) have $M_{\text{SAT}} \sim 89.7 \text{ emu g}^{-1}$ at 300 K, which is considerably higher than that of its counterpart produced by combustion method (particle size $\sim 37 \text{ nm}$; $M_{\text{SAT}} \sim 70 \text{ emu g}^{-1}$ and $H_{\text{C}} \sim 70 \text{ Oe}$ at 300 K) [43,47]. $\text{Co}_{0.8}\text{Zn}_{0.2}\text{Fe}_2\text{O}_4$ nanofibres prepared by electrospinning via sol-gel and subsequent heat treatment show gradual increase in M_{SAT} while H_{C} first increases followed by steady decrease with increase in annealing temperature [48]. $\text{Co}_{0.8}\text{Zn}_{0.2}\text{Fe}_2\text{O}_4$ thin films synthesized by electron beam deposition technique exhibit reduction in M_{SAT} , H_{C} and anisotropy constant (K) with increase in annealing temperature [41]. Significant enhancement in M_{SAT} has been observed for superparamagnetic $\text{Co}_{0.6}\text{Zn}_{0.4}\text{Fe}_2\text{O}_4$ nanoparticles synthesized by modified hydrothermal method [49]. The nanometric $\text{Co}_{0.5}\text{Zn}_{0.5}\text{Fe}_2\text{O}_4$ ferrite could not be obtained directly through ball milling alone but it required to be subsequently heat treated for having the spinel phase [50]. The values of magnetic parameters viz., M_{SAT} , H_{C} , blocking temperature (T_{B}) and K of $\text{Co}_{0.3}\text{Zn}_{0.7}\text{Fe}_2\text{O}_4$ nanoparticles synthesized by mechanical milling are substantially higher as compared to its counterparts prepared by chemical routes [51]. Nanosized $\text{Co}_{0.2}\text{Zn}_{0.8}\text{Fe}_2\text{O}_4$ formed by mechanical milling of its counterpart prepared by chemical coprecipitation method (precursor) displays higher saturation magnetization (44 emu g^{-1}) in comparison to its precursor (32 emu g^{-1}) [52]. $\text{Co}_{1-x}\text{Zn}_x\text{Fe}_2\text{O}_4$ ($x = 0-1$) nanoparticles synthesized separately by thermal decomposition of carboxylates, sol-gel auto-combustion and coprecipitation technique show decrease in the values of M_{SAT} , H_{C} and K with increase of Zn^{2+} concentration [53-55]. Nanosized $\text{Co}_{1-x}\text{Zn}_x\text{Fe}_2\text{O}_4$ ($x = 0-0.3$) ferrites synthesized by sol/gel method

(particles size = 11–28 nm) show appreciable increase in M_{SAT} from 60.92 emu/g ($x=0$) to 74.67 emu/g ($x=0.3$) with increasing Zn^{2+} content [56]. It has been found that $Co_{1-x}Zn_xFe_2O_4$ ($x = 0.5, 0.6, \text{ and } 0.7$) nanoparticles (average particle size $\sim 3\text{--}23$ nm) synthesized by co-precipitation method followed by a thermal treatment exhibit variation in T_B with modification of particle size and Zn^{2+} content [44]. Thus, it is apparent from the results of previous studies that magnetic parameters of nanometric $Co_{1-x}Zn_xFe_2O_4$ ferrites strongly depend on the choice of synthesis method, morphology, and relative ratio of Zn^{2+} and Co^{2+} ions in those samples.

In recent years, nanosized magnetic spinel ferrites have attracted special attention because of their application in green catalysis owing to their eco-friendly, benign nature and ease of separation from reaction mixture [14,57]. They possess admirable features such as high surface to volume ratio, low toxicity, thermal stability and capability of surface modification [58], which are beneficial for having good catalytic activity [57,58]. Most importantly, the ferrite nanoparticles can be easily recovered after the catalytic reaction which avoids the loss of catalyst associated with traditional filtering and centrifugation techniques [59]. Further, the recyclability of these samples are usually better than other conventional catalyst in same reaction [57]. Among the nanostructured ferrites, $Co_{1-x}Zn_xFe_2O_4$ systems display excellent catalytic activity [57,60]. It may also be noted that core-shell magnetic nanoparticles have gained special attention owing to their extensive use as catalyst [60]. The 9-substituted aryl-1,8-dioxooctahydroxanthenes could be synthesized using $CuFe_2O_4$ as catalyst with excellent yield and short reaction time [61]. The nanosized $NiFe_2O_4$ acts as a very good catalyst in the chemoselective oxidation of thiols to disulfides and sulfides to sulfoxides [62]. Recently, coumarin (2H-1-benzopyran-2-one) and its derivatives have raised a stir in biomedical field due to their anti-cancer, anti-inflammatory, anti-viral and anti-microbial properties [63]. Besides, the presence of amide group in coumarin-3-

carboxamide improves the biological activity of these compounds [63]. Nanosized Ni-NiO composite was used as a Lewis acid for coumarin-3-carboxamide synthesis [64]. Based on these studies, we were motivated to explore the catalytic activity of nanosized $\text{Co}_{0.8}\text{Zn}_{0.2}\text{Fe}_2\text{O}_4$ in the multicomponent reaction for the synthesis of coumarin-3-carboxamide.

To the best of our knowledge, there is no report on the structural, magnetic (except at 300 K), hyperfine properties and catalytic activity of nanosized $\text{Co}_{0.8}\text{Zn}_{0.2}\text{Fe}_2\text{O}_4$. In this context, we have prepared $\text{Co}_{0.8}\text{Zn}_{0.2}\text{Fe}_2\text{O}_4$ nanoparticles by coprecipitation method followed by ball milling and subsequent thermal treatment at three different temperatures with the aim to understand the evolution of structural and magnetic properties of the samples with change in morphology. We have characterized the samples by using powder x-ray diffraction (PXRD), scanning electron microscopy (SEM), transmission electron microscopy (TEM), dc magnetic and Mössbauer spectroscopic techniques. We have presented a thorough interpretation of the results obtained from dc magnetic and Mössbauer studies in order to reveal the role of morphology, cation redistribution and surface spin canting in shaping the magnetic and hyperfine properties of the samples. In this paper, we have shown that (i) the particle size, cation distribution and surface spin disorder cause significant changes in magnetic and hyperfine properties of mechanically activated $\text{Co}_{0.8}\text{Zn}_{0.2}\text{Fe}_2\text{O}_4$ samples obtained after heat treatment at three different temperatures, (ii) out of three, the sample annealed at 500 °C and having the smallest particle size (23 nm) exhibits exchange bias effect while others do not and (iii) among the three samples, the sample with smallest particle size exhibits best catalytic response towards formation of coumarin-3-carboxamide via a multi component reaction.

6.2. Experimental

6.2.1. Synthesis of $\text{Co}_{0.8}\text{Zn}_{0.2}\text{Fe}_2\text{O}_4$ nanoparticles and characterization techniques

The $\text{Co}_{0.8}\text{Zn}_{0.2}\text{Fe}_2\text{O}_4$ nanoparticles (precursor) were synthesized by chemical coprecipitation method following standard method [65], then it was subjected to ball milling to prepare the intermediate specimen [51] and finally the intermediate specimen was thermally treated to obtain the desired samples. The precursor has been synthesized by chemical co-precipitation technique by putting the constituents in the appropriate stoichiometric ratio. Reagents having purity more than 99% have been acquired from the Sigma-Aldrich and employed without additional decontamination. The aqueous solution of 40 mM $\text{CoCl}_2 \cdot 6\text{H}_2\text{O}$; 10 mM $\text{ZnSO}_4 \cdot 7\text{H}_2\text{O}$ and 0.1 M $\text{Fe}(\text{NO}_3)_3 \cdot 9\text{H}_2\text{O}$ were readied and stirred together on magnetic stirrer. The mixture was transferred in a burette and then dropped at a precise flow rate of 10mL/m into a solution of NaOH (pH~11) and moved dynamically on a magnetic stirrer. The pH of the solution was supervised during the process and was preserved at ~11 by putting NaOH solution as per requirement. The precipitate so obtained was permitted to settle down. Later, the precipitate was accumulated by centrifugation. Lastly, the specimen was desiccated in vacuum at normal conditions and separated by a magnet. Further it was calcined at 600°C for 10 hours to attain phase properly. This precursor was subjected to high energy ball milling (Fritsch Planetary Mono Mill “pulverisette6”) for 10 hours using tungsten carbide balls and vials, keeping ball to mass ratio 20:1 and setting the speed of the rotor at 350 rpm. The intermediate specimen so obtained after ball milling was annealed for 3 hours at temperatures of 500, 700 and 900 °C. Finally, three samples were obtained by heat treatment of the intermediate specimen at 500, 700 and 900 °C and those are designated as CZ1, CZ2 and CZ3, respectively.

The powder X-ray diffraction (PXRD) pattern of the sample has been attained by a Bruker D8 Advanced Diffractometer using $\text{CuK}\alpha$ ($\lambda = 1.54184 \text{ \AA}$) radiation. For this, the X-

ray generator was fixed at 40 kV and 40 mA. The diffraction images were attained at normal conditions (25°C) with step size 0.01991 and a counting time of 3s/step over the range of $2\theta=20^{\circ}-80^{\circ}$. The particle size and morphology of the sample were examined by field emission scanning and high-resolution transmission electron microscopic techniques (FESEM, Inspect F50 and HRTEM, Jeol 2100). Before subjecting the sample to TEM investigation, it was methodically crumpled in a mortar, disseminated in ethyl alcohol, set on a Cu-grid by means of spin-coater and desiccated in vacuum. The dc magnetization as a function of temperature and versus magnetic field was recorded using vibrating sample magnetometer (Cryogenics made). The $M(T)$ data were attained under zero field cooled (ZFC) and field cooled (FC) mode, respectively. The substance was cooled from 300 to 10 K without external magnetic field in zero field cooled mode and in the existence of magnetic field for field cooled mode. In the temperature range of 10 to 300 K, $M(T)$ data were attained in the presence of external magnetic field. In the field cooled mode, same field value was maintained while the cooling and measurement. The hysteresis loop data were attained at 300, 100 and 10 K were recorded under ZFC mode. The 300 K Mössbauer spectra of the samples were recorded in transmission geometry using constant acceleration drive (CMTE-250) with a 5 mCi⁵⁷Co source in Rh matrix. The 10 K Mössbauer spectrum was recorded with the help of JANIS SVT-400 MOSS cryostat system. The Mössbauer spectrum of the sample at 10 K in presence of an external magnetic field of 5T applied parallel to the γ -ray direction was recorded by using a superconducting magnet (JANIS SuperOptiMag) and a 40 mCi ⁵⁷Co source. The velocity calibration was performed by using a natural iron foil, and the values of isomer shifts were estimated with reference to standard α -Fe at 300 K.

6.2.2. Reaction methodology for the synthesis of coumarin-3-carboxamide using CZ1, CZ2 and CZ3 NPs as catalyst

The multicomponent catalysis reactions were carried out in a 25 ml round bottomed (RB) flask fitted with a condenser, oil bath and a stirring bar according to the following procedure. 2-hydroxybenzaldehyde (**1**) (1.0 mmol), required secondary amine (**2**) (1.2 mmol), diethylmalonate (DEM) (**3**) (1.0 mmol), and the nanoparticles (CZ1/CZ2/CZ3) (6.5 mg/mmol of **1**) were first taken in the RB flask and mixed with 6 ml of ethanol. The reaction mixture was then settled to the desired temperature in an oil bath and refluxed for 5 hours with continuous stirring. Then the reaction mixture was allowed to stand and cool down at room temperature. The used nanoparticle catalyst was recovered magnetically from the reaction mixture. Now, 15 ml of distilled water was added to the resulting reaction mixture and the desired organic products were extracted using 5 ml of dichloromethane three times. All the collected organic layers (dichloromethane part) were combined and dried over anhydrous sodium sulphate followed by evaporation in vacuo. The desired coumarin-3-carboxamide thus obtained was either purified by crystallization or by column chromatography followed by crystallization (whenever required). Melting points of the desired amides were recorded on a K f ler block and NMR spectra of same were recorded using Bruker ADVANCE 300 spectrometer. The catalytic activity of all the three samples (CZ1, CZ2, CZ3) have been examined.

6.3. Results**6.3.1. Structural and morphological study**

The presence of all the characteristic peaks corresponding to spinel phase in the powder x-ray diffraction patterns (PXRDs) of CZ1, CZ2 and CZ3 (Fig.1) suggests that the samples are spinel ferrites. The intense peaks with slight broadening and no extra phases in the PXRDs indicate the formation of well-crystalline and pure nanoparticles. Rietveld

refinement of the samples using MAUD2.33 [66] has been carried out considering CoFe_2O_4 [67] and ZnFe_2O_4 [68] as model systems. The refinement yields very low residue (Fig.1). It can be seen from Fig.1 that the experimental PXRDs almost completely overlap with those obtained theoretically using Rietveld refinement. The refinement parameters are listed in Table 1. The results of fitting (Fig.1) confirm that the samples are single phase cubic spinel with $Fd\bar{3}m$ symmetry. The values of lattice parameter are smaller as compared to bulk $\text{Co}_{0.8}\text{Zn}_{0.2}\text{Fe}_2\text{O}_4$ ($\sim 8.40 \text{ \AA}$) [43]. As these samples are prepared by heat treatment of mechanically activated intermediate specimen, therefore, the lattice strain induced by ball milling also contributes to the lowering of lattice volume of these samples compared to their bulk counterpart [39,51].

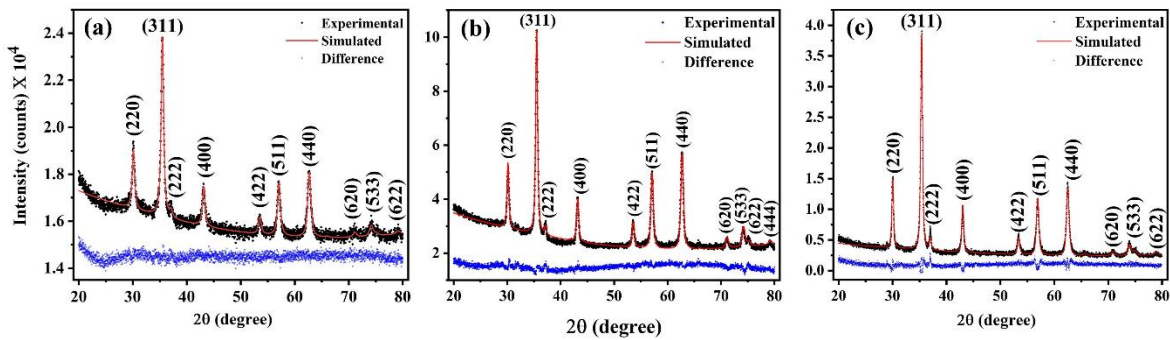


Fig.1. PXRD pattern of the sample (a) CZ1, (b) CZ2 and (c) CZ3 obtained after MAUD analysis. The experimental data and the simulated pattern are represented by black dots and continuous red line, respectively. The difference between the experimental and simulated curve is plotted at the bottom with continuous blue line.

In order to investigate the structural and microstructural properties of the samples in more detail, Rietveld refinement of the PXRD data of the present samples have been done by GSAS program [69] with EXPGUI interface [70]. The procedure implemented for this analysis is described in our previous works [51,71]. As per the results of Rietveld refinement, the experimental data and simulated curves have converged with good accord (Fig.2). Table 2 depicts the values of the structural and microstructural parameters of the samples. The

asymmetric units, surroundings of the metal and oxygen ions, bond angles and lengths for sample CZ1 are shown in Fig.3. The fractional coordinates and cation occupancies have been provided in Table 3. The lattice parameter of the samples increases upon heat treatment. Thus, it is apparent that the lattice volume contraction of the samples with respect to bulk $\text{Co}_{0.8}\text{Zn}_{0.2}\text{Fe}_2\text{O}_4$ is owing to lattice strain induced by high energy ball milling and cation redistribution among the (A) and [B] sites of the spinel lattice, which gradually reduces with heat treatment [39,51].

Table 1 Crystal data and refinement parameters of the CZ1, CZ2, CZ3 obtained from MAUD

Parameters	CZ1	CZ2	CZ3
Crystal System	cubic	cubic	cubic
Space group	$\text{Fd}\bar{3}\text{m}$	$\text{Fd}\bar{3}\text{m}$	$\text{Fd}\bar{3}\text{m}$
Crystallite size (nm)	23 (± 0.33)	34 (± 0.31)	42 (± 0.37)
Microstrain	$1.39 (\pm 0.02) \times 10^{-3}$	$1.46 (\pm 0.02) \times 10^{-3}$	$2.08 (\pm 0.02) \times 10^{-3}$
Lattice parameter (a(Å))	8.3809 (± 0.0005)	8.3752 (± 0.0004)	8.4022 (± 0.0004)
Density (g cm $^{-3}$)	5.2249 (± 0.05)	5.305 (± 0.02)	5.2544 (± 0.01)
R _{wp}	1.2	1.5	1.8
R _{exp}	1.3	1.6	1.4
GOF	1.1	1.2	1.5

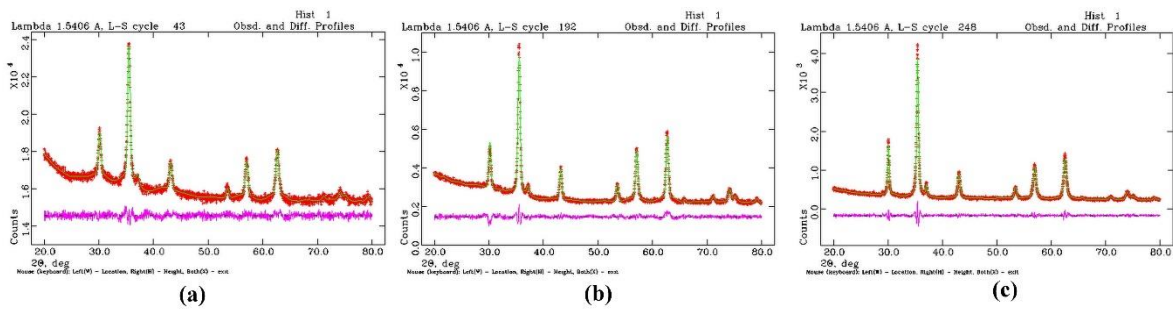


Fig.2 Indexed powder PXRD pattern of the sample (red dots) (a) CZ1 (b) CZ2 (c) CZ3 and the simulated Rietveld refinement plot (continuous green line) obtained by fitting the experimental powder PXRD pattern using GSAS program.

Table 2 Structural and microstructural parameters along with metal-oxygen (M-O) bond angles and bond lengths obtained from Rietveld analysis of PXRD of the samples by GSAS program

Parameters	CZ1	CZ2	CZ3
Formula weight	471.8	471.8	471.8
Crystal System	Fd $\bar{3}$ m	Fd $\bar{3}$ m	Fd $\bar{3}$ m
Lattice parameter (Å)	8.3833 (± 0.0012)	8.3720 (± 0.0014)	8.3961 (± 0.0011)
Density (g cm ⁻³)	5.319	5.332	5.256
Volume (Å ³)	589.176 (17)	587.733 (10)	596.318 (9)
Metal-Oxygen bond length (Å)	1.906 (A-site) 2.045 (B-site)	1.903 (A-site) 2.044 (B-site)	1.904 (A-site) 2.058 (B-site)
Metal-Oxygen bond angle	109.47° (A-site) 92.97° (B-site)	109.47° (A-site) 92.92° (B-site)	109.47° (A-site) 92.66° (B-site)

Table 3 Fractional coordinates and occupancy of different ions obtained from the Rietveld refinement by GSAS program

Ions	x	y	z	Occupancy (± 0.003)
Zn (A)	0.125000	0.125000	0.125000	0.2000
Co (A)	0.125000	0.125000	0.125000	0.3400
Fe (B)	0.125000	0.125000	0.125000	0.4600
Co (B)	0.500000	0.500000	0.500000	0.2300
Fe (B)	0.500000	0.500000	0.500000	0.7700
O	0.25624 (4)	0.25624 (4)	0.25624 (4)	1.0000

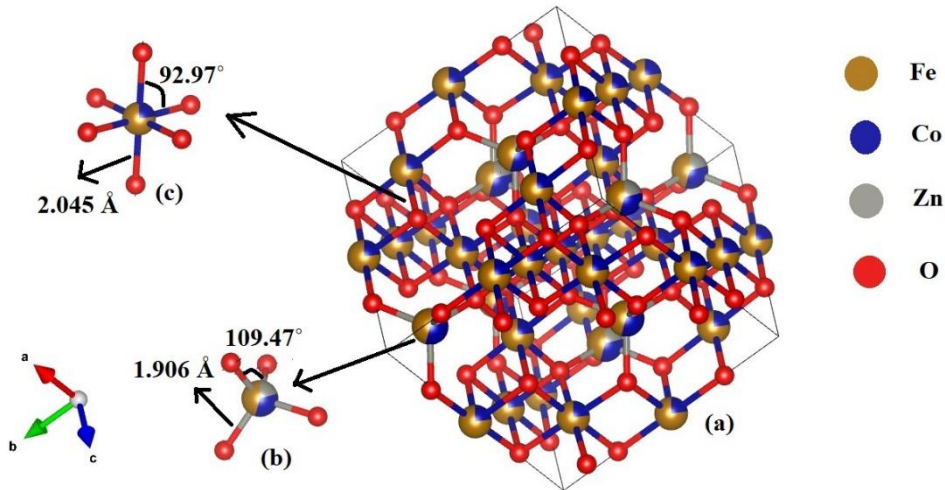


Fig. 3 (a) Unit cell of the sample, (b) tetrahedral (A) site and (c) octahedral [B] site bond angles and bond lengths of sample CZ1.

Fig.4 presents TEM image showing the particle size distribution of CZ1 (Fig.4(a)), CZ2 (Fig.4(b)) and CZ3 (Fig.4(c)) along with particle size histogram of the samples in the inset of corresponding figures. On careful examination of the TEM images, it is found that the nanoparticles are of assorted size and arbitrary shape along with strong affinity of agglomeration. The selected area electron diffraction (SAED) patterns of CZ1 (Fig.5(a)), CZ2 (Fig.5(b)) and CZ3 (Fig.5(c)) along with the high-resolution TEM (HRTEM) micrograph (in the inset) are displayed in Fig.5. The SAED pattern of all three samples represents typical features shown by a polycrystalline sample. It consists of diffused concentric rings with a bright central spot that represents the undiffracted electrons. Intense bright spots in the rings of the SAED image (Fig.4) and distinct lattice fringes in the HRTEM images (inset of Fig.5) of the samples together with indicate that they possess good crystalline character [72]. The ‘d’ values obtained from the TEM study are in consonance with the ones obtained from XRD analysis. The elemental composition (EDX spectrum) of all the samples is shown in Fig.6. The atomic percentages of Co, Zn, and Fe in the present samples are ~ 20.27 , 5.15 , 46.4 , which confirms that the samples are in proper stoichiometry.

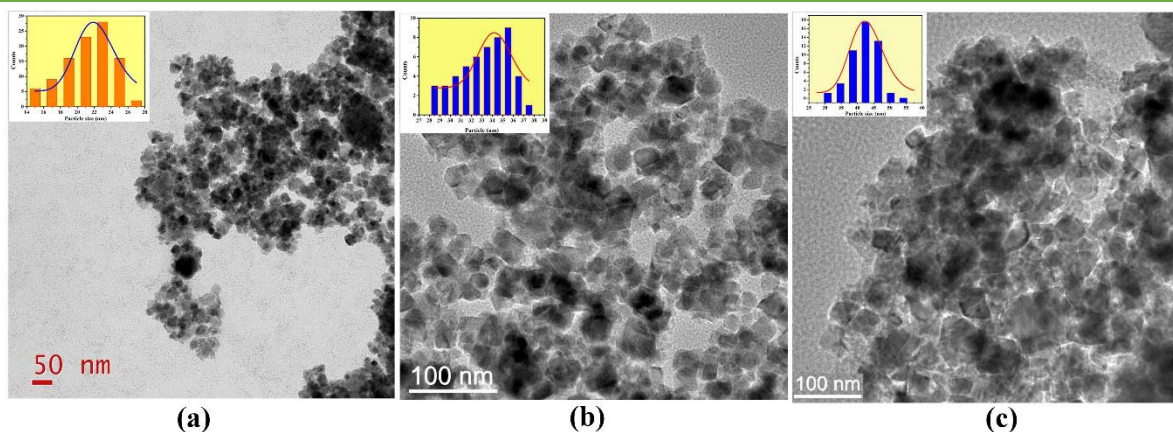


Fig.4 TEM morphographs showing particle distribution of (a) CZ1, (b) CZ2 and (c) CZ3, and particle size histogram of CZ1, CZ2 and CZ3 in the inset, respectively.

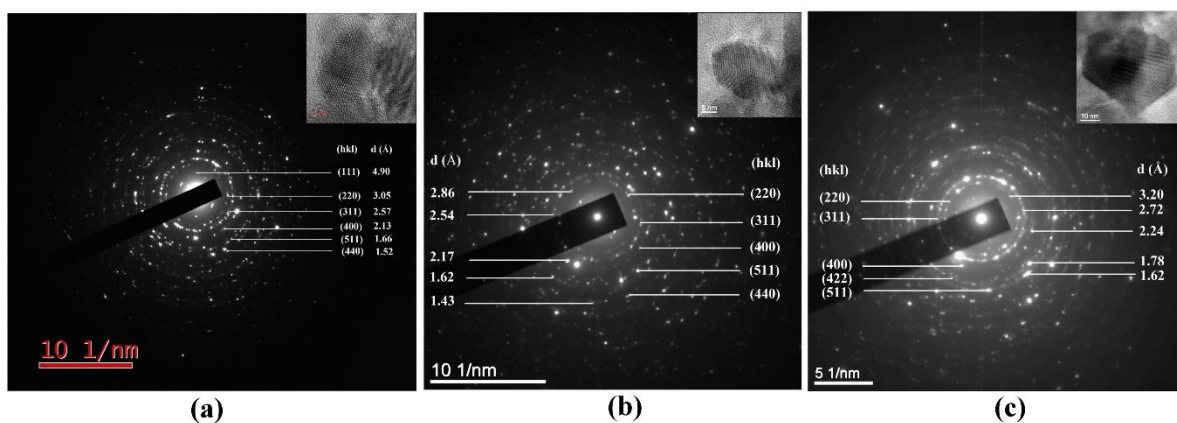


Fig.5 SAED pattern of (a) CZ1, (b) CZ2 and (c) CZ3, and single particle HRTEM of CZ1, CZ2 and CZ3 in the inset, respectively.

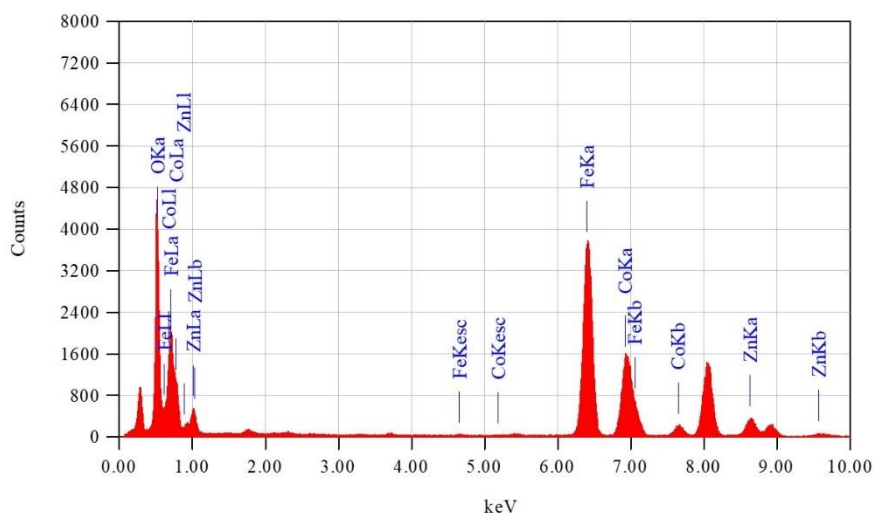


Fig.6 EDX spectrum of the sample

6.3.2. Magnetic and Hyperfine study

The ZFC-FC magnetization curves of all three samples are presented in Fig.7. Primarily, the ZFC curves show a gradual decrease in magnetization value as the samples are being cooled from 300 K and this reduction in magnetization almost ceases below 150 K (Fig.7). In addition to these observations, no visible hump of a typical superparamagnetic sample can be traced up to 300 K. The nature of the curves from 300 K to 150 K points that some particles in the samples are attaining blocked state gradually while most of the constituent particles in the sample possess high anisotropy energy and are in magnetically ordered state at room temperature [65]. This suggests that the particles in the samples are of variable size as also seen from TEM micrographs. Below 150 K, the ZFC curves of the samples show a saturating nature up to 5 K revealing that the constituent particles no longer act as single domain superparamagnetic (SPM) system. Such behavior points towards the presence of strong interparticle interactions among the constituent particles [73] causing a change in the regime of magnetic properties. When interactions act, it is difficult to define a single particle anisotropy barrier and the system approaches towards a frozen or collective state [73]. The FC magnetization curves of the samples stagger in the temperature range of 300 – 150 K followed by a slight increase in magnetization up to 5 K (Fig.7) indicating interparticle interaction induced increase in anisotropy of the nanoparticle systems [74]. So, this also provides support in favor of our proposition from ZFC study that there exists strong interparticle interaction in the samples due to which the particles in the samples exhibit collective magnetic excitation at low temperature. In order to gather more information regarding the magnetic nature of these samples, we have recorded their hysteresis loops.

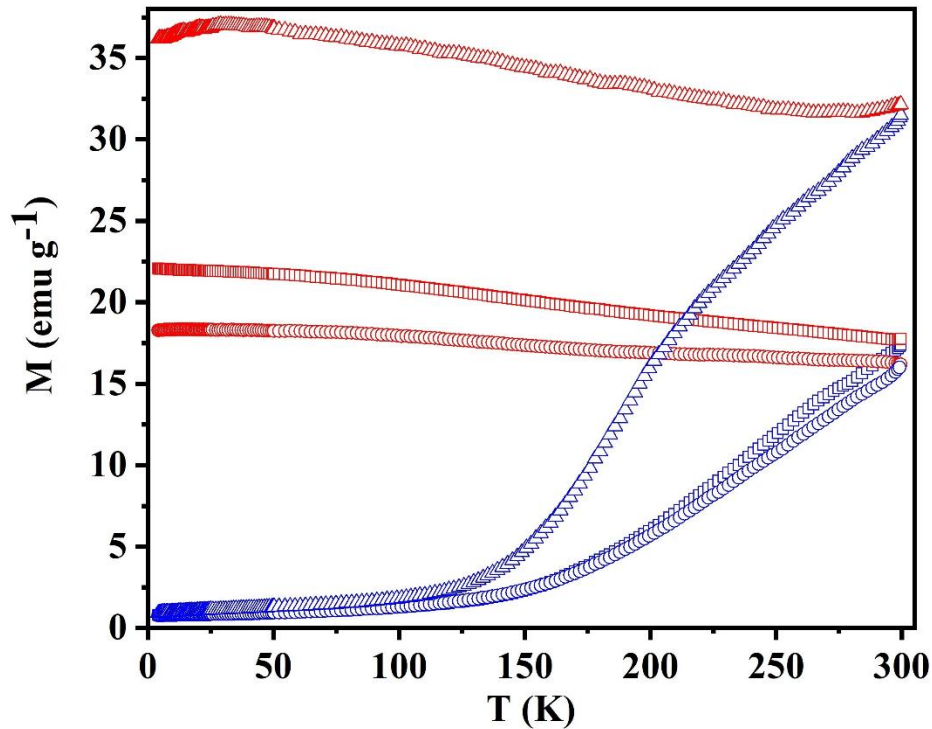


Fig.7. ZFC-FC magnetization curves of CZ1 (circle), CZ2 (square) and CZ3 (triangle) at 500 Oe.

Table 4 Values of crystallite size obtained from PXRD, particle size obtained from TEM, saturation magnetization (M_{SAT}), coercivity (H_C) and effective anisotropy constant (K_E)

Sl. No.	Sample	Crystallite Size (nm)	Particle size (nm)	M_{SAT} (emu/g)		H_C (Oe)		$K_E \times 10^6$ (erg/cm ³) Or $K_E \times 10^5$ (J/m ³)	
				300 K (± 0.01)	10 K (± 0.01)	300 K	10 K	300 K	10 K
1.	CZ1	23	23	75.22	100.39	530	13000	1.4	1.54
2.	CZ2	34	34	81.07	110.54	460	10000	1.48	2.01
3.	CZ3	42	42	82.89	126.01	420	9000	1.57	3.01

The magnetization versus field (M-H) loops has been recorded at 300 and 10 K at ± 1 T field for CZ1, CZ2 and CZ3. The samples exhibit clear hysteresis at 300 K indicating magnetic ordering at room temperature (Fig.8(a)), which corroborates the findings of ZFC study. At 10 K, samples exhibit very large coercivity values and ± 1 T field was unable to saturate any of the moments (Fig.9). So, in order to draw a proper inference of the

magnetization properties at 10 K, we have recorded M-H loops at high field of ± 7 T (Fig.8(b)). Complete saturation of all the moments still could not be achieved at such high field most probably due to presence of some surface disorder in the form of canted spins as reported in literature [51]. In addition, the M-H loop of CZ1 is not symmetrical about origin but is slightly shifted along negative field axis. The non-saturation of moments and shift of hysteresis loops are typical features of canted magnetic systems [75]. This proposition will further be testified by infield Mössbauer spectroscopic study. There are aberrations in the M-H loops at 10 K (Fig.8(b)) whenever there is field reversal. This may be attributed to the reorientation of the surface spins [24]. The parameters obtained from M-H loop study are listed in Table 4. The values of saturation magnetization (M_{SAT}) rise with the increase in particle size at both 300 and 10 K following development in magnetization of the samples with heat treatment. The M_{SAT} values at 300 K for all three samples were slightly less than that of bulk sample of same composition [34] implying that there is enhancement in magnetization of the present samples because of the incorporation of strain induced anisotropy as they were subjected to mechanical milling [16,40,43,51,52]. It has been found that the value of M_{SAT} increases with increment of particle size upon heat treatment (Table 4). This can be attributed to the reduction of spin canting due to betterment of crystalline quality caused by heat treatment. There is a sharp increase in the M_{SAT} values of the samples at 10 K as compared to those at 300 K pointing towards attainment of a frozen state at low temperature as observed from ZFC-FC study [30]. All the samples exhibit very high coercivity values at 10 K (Table 4), even larger than that of bulk cobalt ferrite (~ 5 kOe at 5 K [24]). Table 5 compares the values of room temperature (300 K) magnetic parameters like M_{SAT} and H_C for nanosized $Co_{0.8}Zn_{0.2}Fe_2O_4$ ferrites synthesized by different techniques with that of the present samples. It seems that magnetic parameters are influenced by the choice of synthesis procedure.

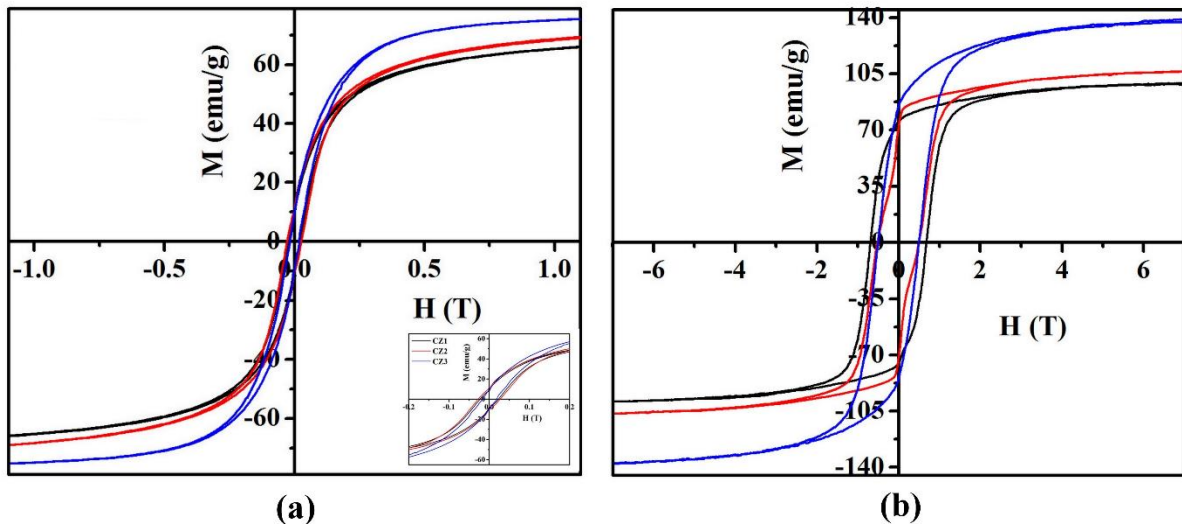


Fig.8 M-H (hysteresis) loop of CZ1 (black line), CZ2 (red line) and CZ3 (blue line) at (a) 300 K between ± 1 T and (b) 10 K shown between ± 7 T.

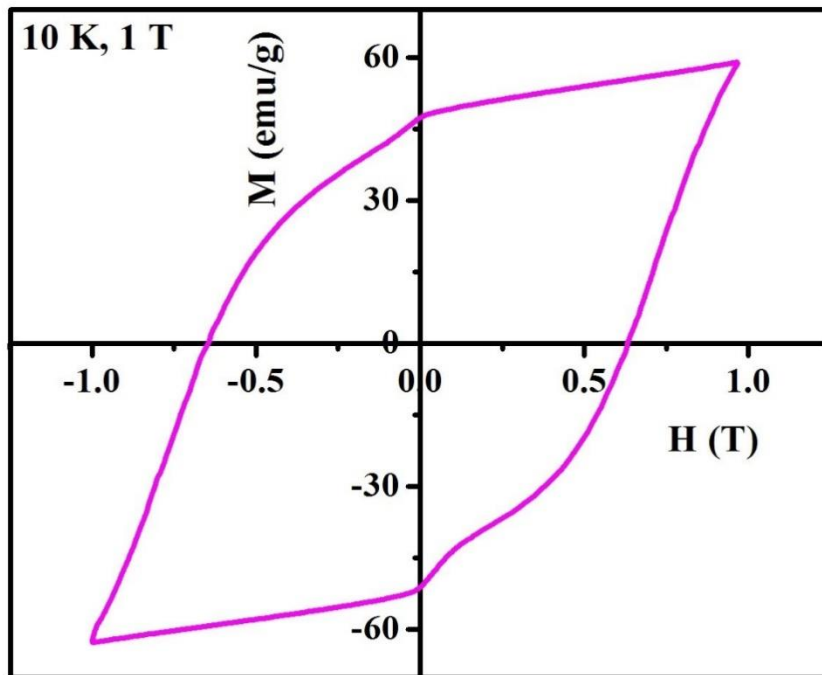


Fig.9 M-H curve of CZ1 at 10 K between ± 1 T

Table 5 Table for comparison of room temperature (300 K) magnetic parameters of nanosized $\text{Co}_{0.8}\text{Zn}_{0.2}\text{Fe}_2\text{O}_4$ ferrite synthesized by various procedures.

Sl .No.	Synthesis procedure	Morphology	Particle size (nm)	M_{SAT} (emu/g)	H_c (Oe)	Reference
1.	Electron beam deposition technique	Thin films	19.83 (300) 21.36 (400) 24.54 (500)	155.02 153.93 153.28	123.89 109.50 106.49	[41]
2.	Combustion method	Nanopowders	37	70	270	[43]
3.	Electrospinning via sol-gel and subsequent heat treatment	Nanofibres	20.5 (550) 35.3 (650) 44.2 (750) 56.5 (850) 61.9 (950)	16.6 46.7 66.1 75.4 87.2	314.3 363.9 527.7 494.1 446.4	[48]
4.	Thermal decomposition of carboxylates	Nanopowders	7.2 (300) 18.9 (600) 67.4 (1000)	43.04 75.2 84.92	510 482 149	[53]
5.	Sol-gel auto-combustion	Nanoparticles	43.93	55.947	306.16	[54]
6.	Sol/gel (citratemethod)	Nanoparticles	22.1	72.17	220	[56]
7.	Sonochemical method	Nanoparticles	8.1	27.5	206	[76]
8.	Sol-gel auto combustion using gelatin fuel	Nanoparticles	52	56.7	319	[77]
9.	Flow rate controlled chemical co-precipitation route	Nanopowders	14	80	-	[78]
10.	Wet chemical method	Nanoparticles	30-50	74		[79]
11.	Reverse micelle technique	Nanoparticles	6.6	31.3	22.5	[80]
12.	Combustion method	Nanoparticles	33	78	400	[81]
13.	Coprecipitation followed by ball milling and heat treatment	Nanoparticles	23 34 42	75.22 81.07 82.89	530 460 420	Present samples

Several authors have observed the phenomenon of exchange bias (EB) in single phase ferrite systems earlier and attributed it to the combined effect of interparticle interactions and canted spin structure [82-84]. Moreover, Coppola et al., have studied the magnetic behavior of Co-Zn system in detail and indicated about the possibility of EB phase in such system owing to anisotropy evolution instigated by chemical composition [85]. The results of ZFC-FC and M-H study of the present system along with the literature survey motivated us to investigate the hysteretic behavior of the samples in more detail. At first, the samples were subjected to a damped oscillating magnetic field to ensure zero magnetization state of the samples as described by Dakua et. al., [86]. Then the samples were field cooled at a static field of 5 T from 300 K to 10 K and M-H loops were measured at 10 K under ± 5 T field. A huge shift along the -ve field axis was seen in the M-H loop of CZ1 after the procedure whereas the loop remained symmetric about the origin for other two samples. Despite the occurrence of pronounced EB effect in single phase ferrimagnetic particles [82-84], some of the authors have pointed that EB can also be seen sometimes due to minor loop [86] and experimental artifacts [86]. In general, a minor loop displays open loop and non-saturation [84]. But in case of CZ1, the M-H loop obtained after field cooling at 5 T showed equal values of saturation magnetization field (at ± 5 T) and a disappearance of the hysteresis after ± 3 T (Fig.10). So, it is confirmed that the M-H loop for CZ1 is not a minor loop. Further, in order to check any influence of experimental artifacts on the emergence of EB effect in CZ1, p-type and n-type M-H loops were measured following procedure adopted by several other groups to check the same [87]. Magnetization values for both the measurements remained same for CZ1, only the shift for p-type loop was along negative field axis (Fig.10(a)) and for n-type along positive field axis (Fig.10(b)) with almost same shift value. These results eliminate the possibility of having any effect of experimental artifacts on the observed EB effect. Since XRD could not detect any impurity phase in CZ1, the possibility of EB effect

due to any impurity can be ruled out. A necessary condition for the occurrence of EB is presence of a bilayer like antiferromagnetic (or spin glass)/ferromagnetic (or ferrimagnetic) in which the antiferromagnetic (or spin glass) layer having a large magnetic anisotropy can exert a pinning action on the ferromagnetic (or ferrimagnetic) phase during magnetic reversal in M-H experiment [83]. Since our sample is single phase spinel ferrite, the canted surface spins freeze progressively on lowering the temperature creating a magnetically disordered shell that exerts strong pinning action around magnetically well-ordered core. This may be the possible reason behind appearance of EB. In order to validate this idea of the core-shell structure, we have carried out in-field Mössbauer spectroscopic study whose results have been summarized in paragraph below.

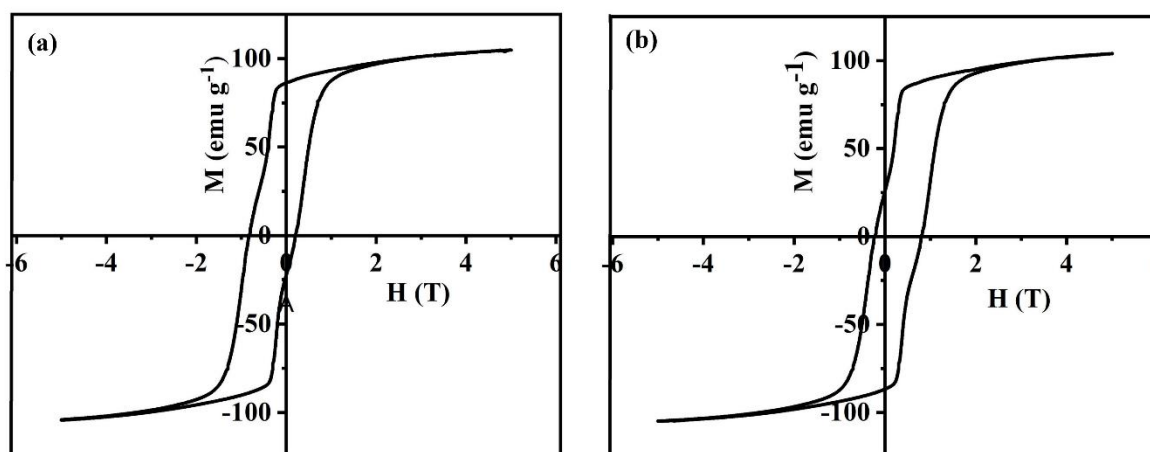


Fig.10. (a) p-type and (b) n-type M–H loops of CZ2 at 10 K between ± 5 T field.

We have recorded the room temperature (300 K) Mössbauer spectra of CZ1, CZ2 and CZ3. In all three cases, a very broad asymmetric sextet (Fig.11) with small splitting in both the 1st and 6th lines of the sextet has been observed. The splitting of 1st and 6th lines of the Mössbauer spectra of the samples insisted us to fit them by two sextets. We have used the Recoil program [88] for this purpose. It can be seen from Fig.11 that all the spectra are being well fitted with two well-resolved sextets indicating that the samples are magnetically ordered at room temperature. There is no signature of SPM doublet in the 300 K spectra of

the samples further indicating the existence of magnetic ordering at this temperature. The presence of magnetic ordering in the 300 K spectra of all the three samples can be ascribed to the influence of interparticle interaction within the nanoparticle system, which is able to suppress the SPM relaxation. The fitting parameters are presented in Table 6. It may be noted that the width of the spectrum is showing decreasing trend while the hyperfine field is increasing as particle size increases. This is a usual phenomenon for nanosized magnetic systems.

For a system of interacting particles, energy of a particle ‘p’ can be written as

$$E_p = KV \sin^2 \theta - \sum_{i,j} J_{ij} \vec{S}_i \cdot \vec{S}_j \quad (1)$$

where K is the effective anisotropy constant, V is average volume of the particle, θ is the angle between magnetization direction and easy direction of magnetization, \vec{S}_i and \vec{S}_j represent surface spins belonging to particle ‘p’ and its neighboring particle ‘q’, respectively, and J_{ij} is the exchange coupling constant [89]. Using mean field approximation, equation (1) becomes

$$E_p = KV \sin^2 \theta - \vec{M}_p \cdot \langle \sum_q J_{pq} \vec{M}_q \rangle \quad (2)$$

where \vec{M}_p and \vec{M}_q represent sublattice magnetization vectors of particles ‘p’ and ‘q’, respectively, and J_{pq} is the effective exchange coupling constant [89]. If the first term is predominant, SPM flipping of magnetic moment of the individual particles takes place between easy directions close to $\theta = 0$ and π [89]. However, if the interactions are significant then the energy at the two minima will differ and the effective internal field may influence the magnetic dynamics of the particle system in a way similar to application of external magnetic field on a ferrimagnetic system. This would suppress the SPM relaxation giving rise to magnetically split sextets [89] as has been observed in the present case for all the samples.

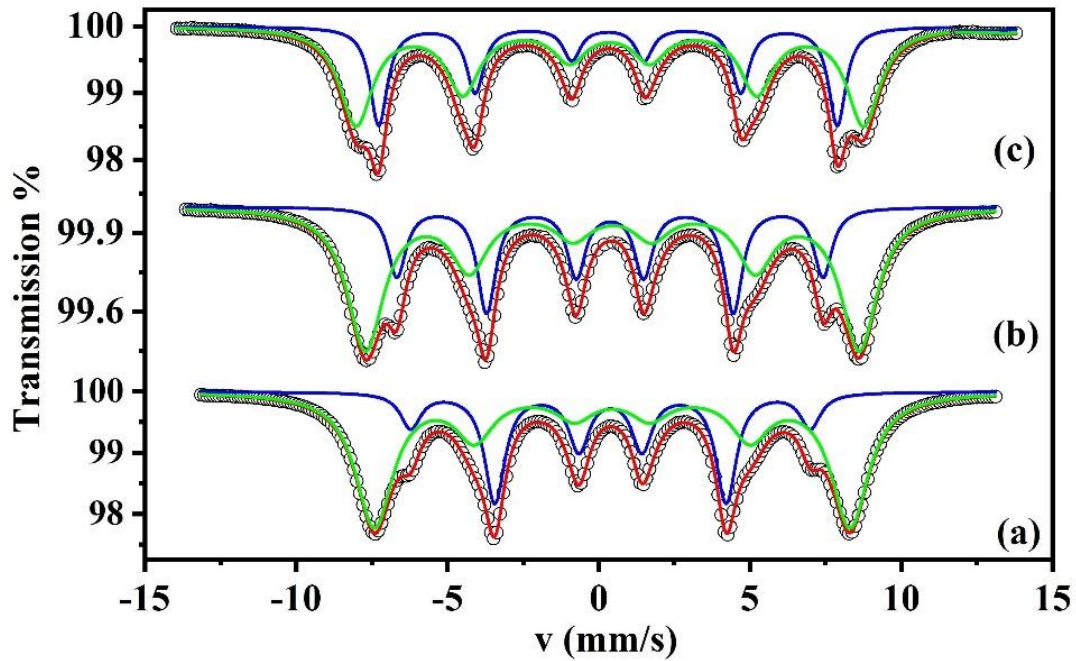


Fig.11. Mössbauer spectra of CZ1 at 300 K (without field) fitted by Lorentzian site analysis method of the Recoil program

Table 6 Hyperfine parameters obtained by fitting the Mössbauer spectra of CZ1, CZ2 and CZ3 at 300 K.

Sample	Spectra	IS (± 0.02) (mm s ⁻¹)	HMF (± 0.1) (T)	Width (± 0.03) (mm s ⁻¹)	Area (± 0.3) (%)
CZ1	Site 1	0.39	40.96	0.39	34.8
	Site 2	0.45	48.74	0.75	65.2
CZ2	Site 1	0.37	43.67	0.35	34.3
	Site 2	0.45	50.59	0.72	65.7
CZ3	Site 1	0.3	47.00	0.33	35.4
	Site 2	0.36	51.99	0.65	65.6

It may be noted that spin canting effect and cation distribution in the ferrite system can be conveniently studied using infield Mössbauer spectroscopic technique [39,51]. So, we

have recorded the low temperature (5 K) infield (in presence of 5 T external magnetic field applied parallel to γ -ray direction) (Fig.12(a),(b),(c)) and without field Mössbauer spectra (Fig.12(d),(e),(f)) of all three samples. Samples CZ1 and CZ2 both display weak 2nd and 5th lines in their respective spectra while only CZ1 displays slightly asymmetric and comparatively broadened (though relaxation has been suppressed at this temperature) lines. The former feature is an indicator of presence of canted spins in both CZ1 and CZ2 [90], and the latter points that for CZ1, the iron nuclei in it are surrounded by environment with slightly different hyperfine interactions [90]. The absence of 2nd and 5th lines in the infield Mössbauer spectrum of CZ3 rules out the presence of any canted spins in this sample. At first, we have tried to fit all the infield Mössbauer spectra by two sextets using the “Lorentzian site analysis” method of the Recoil program [88]. The two-sextet component fitting for CZ2 and CZ3 yielded very good matching (Fig.12(b) and (c)) between the experimental and calculated spectra. In case of CZ1, the goodness of fit using two sextets was not of desired standard. So, we opted for fitting using four sextets and obtained a very good matching between the experimental and calculated spectra with acceptable goodness of fitting parameters. To check the validity of the procedure adopted to fit the infield Mössbauer spectra of the samples, we have fitted the 5K without field Mössbauer spectrum of CZ1 by four sextets while those of CZ2, CZ3 with two sextets, restricting the proportion of Fe³⁺ ions at (A) and [B] sites as obtained from the infield Mössbauer spectra. It can be seen from Fig.12(d), (e) and (f) that each of the three experimental spectra has fitted well with their corresponding calculated spectra, which in turn substantiates the suitability of the methodology adopted for fitting the infield Mössbauer spectra. The values of refined hyperfine parameters for both infield and without field Mössbauer study are enlisted in Table 7. The values of all the hyperfine parameters (Table 7) obtained for infield and without field Mössbauer study are in consonance with each other. The results of low temperature Mössbauer study of the samples

ascertain the ferrimagnetic nature of the samples at 5 K. According to the fitting, for CZ2, (A) and [B] sites acquire ~ 26% and 74% of the total spectral area, respectively, along with presence of moderate canting of magnetic moments at [B] site. For CZ3, (A) and [B] sites occupy ~ 28 % and 72 % of the total spectral area, respectively, with no canting of magnetic moments. The above-mentioned findings reveal that both CZ2 and CZ3 are ferrimagnetic in nature. However, CZ2 is a canted ferrimagnetic system ($\theta_A=5.1^\circ$ and $\theta_B=26.1^\circ$) whereas CZ3 is purely ferrimagnetic without having any canting of its magnetic moments. The ratio of Fe^{3+} ions at (A) and [B] sites (Table 7) indicates that Fe^{3+} ions have migrated from (A) to [B] site. In case of Co-Zn ferrites, the Zn^{2+} ions usually occupy (A) site of the spinel lattice while for accomplishing the migration of Fe^{3+} ions from (A) to [B] site, Co^{2+} ions move from [B] to (A) site [39,51]. Thus, the cation distributions for CZ2 and CZ3 can be written as:

$$(Co_{0.28}^{2+}Zn_{0.20}^{2+}Fe_{0.52}^{3+})_A[Co_{0.52}^{2+}Fe_{1.48}^{3+}]_BO_4 \quad \text{and} \quad (Co_{0.24}^{2+}Zn_{0.20}^{2+}Fe_{0.56}^{3+})_A[Co_{0.56}^{2+}Fe_{1.44}^{3+}]_BO_4,$$

respectively. For CZ1, the pair of sextets having high values of canting angles depict the shell region and the other pair with moderate values of canting angle represent the core region. Since PXRD and HRTEM analysis have revealed that the particles in CZ1 are well-crystalline, so the presence of prominent 2nd and 5th lines can be attributed to large spin canting at the nanoparticle surface/grain boundaries. There will be more broken exchange bonds for the sample with lower particle size because of their high surface to volume ratio compared to that of the sample having larger particles [90]. Therefore, for the present case, there will be more broken exchange bonds in CZ1 as it is lowest in size while its amount decreases significantly in CZ2 and completely vanishes for CZ3. It is noteworthy that the constituent particles of CZ3 are largest sized amongst these three samples. Thus, the presence of canted magnetic moments in CZ1 and CZ2 can be attributed to the presence of broken exchange bonds in the surface regions of the samples. The contribution of Fe^{3+} ions in the

core and shell region for CZ1 is 68% and 32% of the spectral area, respectively. So, the particles in CZ1 are composed of ferrimagnetically aligned core with slight canting ($\theta_A=11.48^\circ$ and $\theta_B=23.07^\circ$) and magnetically disordered shell. The cation distribution (calculated as per the ratio of Fe^{3+} ions at (A) and [B] site in core and shell region (Table 7)) in the core region: $(\text{Co}_{0.27}^{2+}\text{Zn}_{0.20}^{2+}\text{Fe}_{0.53}^{3+})_A[\text{Co}_{0.53}^{2+}\text{Fe}_{1.47}^{3+}]_B\text{O}_4$ and that in the shell region is $(\text{Co}_{0.43}^{2+}\text{Zn}_{0.20}^{2+}\text{Fe}_{0.37}^{3+})_A[\text{Co}_{0.37}^{2+}\text{Fe}_{1.63}^{3+}]_B\text{O}_4$. It appears that the core region possesses almost equilibrium cation distribution whereas in the shell region, $\sim 26\%$ of Fe^{3+} ions have migrated from [B] to (A) site in lieu of Co^{2+} ions. This may lead to an additional increase in anisotropy of the disordered surface layer as compared to the ferrimagnetic core. This layering of ferrimagnetically ordered core and magnetically disordered shell has formed the base for strong pinning action on the core during field reversal (during MH measurements) and possibly resulted in appearance of EB effect in CZ1. Such behavior has been observed in nanosized ferrimagnetic systems earlier also [84,91]. The appearance of asymmetric and broadened lines in the Mössbauer spectra of CZ1 are due to the presence of chemical inhomogeneity within the constituent nanoparticles of the sample [92].

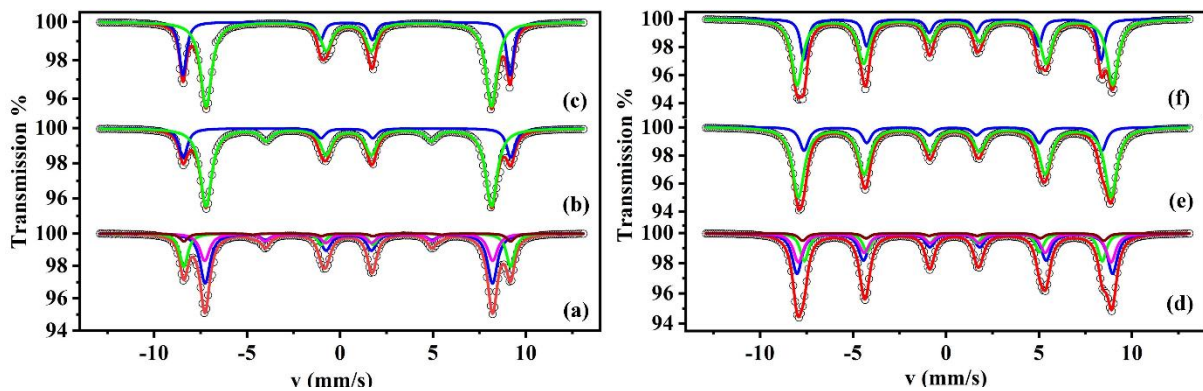


Fig.12 Mössbauer spectra at 5 K with 5 T external magnetic field of (a) CZ1, (b) CZ2 and (c) CZ3, and 5 K without field of (d) CZ1, (e) CZ2 and (f) CZ3 fitted by Lorentzian site analysis method of the Recoil program

Table 7 Values of zero field and infield Mössbauer parameters of the samples at 5 K determined by Lorentzian profile fitting

Sample	Temperature /Field	Site	Width (mm s ⁻¹) (±0.03)	IS (mm s ⁻¹) (±0.03)	B _{eff} ^a (T) (±0.14)	B _{hf} (T) (±0.14)	A ₂₃	θ ^b (deg) (±0.02)	Area (%) (±0.2)
CZ1	5 K /5 T	[Fe ³⁺ _A] _C	0.25	0.39	54.49	49.68 ^c	0.09	11.48	18.03
		[Fe ³⁺ _B] _C	0.30	0.47	47.93	52.63 ^c	0.35	23.07	49.06
		[Fe ³⁺ _A] _S	0.25	0.39	54.50	50.22 ^c	0.50	28.36	6.21
		[Fe ³⁺ _B] _S	0.30	0.47	48.02	52.15 ^c	0.80	34.91	26.69
	5 K /0 T	[Fe ³⁺ _A] _C	0.25	0.39	-	49.68	-	-	17.69
		[Fe ³⁺ _B] _C	0.30	0.47	-	52.63	-	-	49.46
		[Fe ³⁺ _A] _S	0.25	0.39	-	50.22	-	-	5.94
		[Fe ³⁺ _B] _S	0.30	0.47	-	52.15	-	-	26.89
CZ2	5 K /5 T	[Fe ³⁺ _A]	0.28	0.39	57.34	52.36 ^c	0.02	5.73	26.19
		[Fe ³⁺ _B]	0.38	0.49	49.96	54.49 ^c	0.43	26.1	73.81
	5 K /0 T	[Fe ³⁺ _A]	0.28	0.39	-	52.36	-	-	26.18
		[Fe ³⁺ _B]	0.38	0.49	-	54.49	-	-	73.82
CZ3	5 K /5 T	[Fe ³⁺ _A]	0.24	0.36	60.06	55.06 ^c	0.0	0.0	28.2
		[Fe ³⁺ _B]	0.40	0.48	52.32	57.32 ^c	0.0	0.0	71.8
		[Fe ³⁺ _A]	0.24	0.36	-	55.06	-	-	28.2
	5 K /0 T	[Fe ³⁺ _B]	0.40	0.48	-	57.32	-	-	71.8

‘C’ denotes the core region and ‘S’ denotes the shell region.

^a Observed HMF (BHF) is the vector sum of the internal HMF and the external applied magnetic field.

^b The average canting angle estimated from the ratio of the intensities of lines 2 and 3 from each subspectra, I₂/I₃ (A₂₃) according to $\theta = \arccos[(4 - I_2/I_3)/(4 + I_2/I_3)]^{1/2}$, where I₂/I₃=A₂₃.

^c Estimated according to the relationship of B_{eff}, B_{hf} and applied field.

In order to testify the validity of the cation distribution as estimated above, we have calculated the theoretical magnetic moment per formula unit (m_{th}) of the samples considering the ratio of Fe³⁺ ions at (A) and [B] sites and canting angles obtained from infield Mössbauer spectroscopic study at 5 K [51] and compared it with the experimental M_{SAT} values of the samples (in Bohr magneton) obtained from M-H study at 10 K (m_{exp}). The ‘m_{th}’ is given by the relation: $m = m_B \cos \theta_B - m_A \cos \theta_A$, where m_B and m_A are the magnetic moments of [B] and (A) sites and θ_A and θ_B are (A) and [B] site canting angles [51]. We have calculated the ‘m_{th}’ for CZ1 considering the core-shell structure as obtained above. The values of ‘m_{th}’ value for CZ1, CZ2 and CZ3 have been calculated using the ratio of Fe³⁺ ions at (A) and [B] sites and canting angles (see Table 6). The values of m_{th} for CZ1, CZ2 and CZ3 are 4.63, 4.62 and 5.36 μ_B, respectively. The values of m_{exp} for CZ1, CZ2 and CZ3 are 4.24, 4.66 and 5.32

μ_B , respectively. The m_{th} and m_{exp} values for CZ2 and CZ3 match well. However, there is a slight discrepancy in the two values for CZ1 is due to presence of chemical inhomogeneity in this sample. The results strongly validate the reliability of the cation distribution obtained from infield Mössbauer spectroscopic study.

6.3.3. Study of catalytic activity of $Co_{0.8}Zn_{0.2}Fe_2O_4$ nanoparticles.

6.3.3.1 Catalysis reaction

The structural and morphological analysis of the CZ1, CZ2 and CZ3 nanoparticles inspire us to investigate their role as a heterogeneous catalyst in the synthesis of coumarin-3-carboxamides by multi component reaction. In this study, synthesis of N, N-dimethyl-2-oxo-2H-chromene-3-carboxamide (**4**) by using 2-hydroxybenzaldehyde (**1**), N, N-dimethylamine (**2**), DEM (**3**) as substrates and $Co_{0.8}Zn_{0.2}Fe_2O_4$ nanoparticles as catalyst was chosen as the representative multicomponent catalysis reaction to standardize the reaction conditions (Scheme1, Fig.13). The effects of various solvents, molar ratio of catalyst/substrate, temperature, and the reaction times on the yield of the product have been summarized in Table 8.

In order to study the solvent effect, catalytic multicomponent organic reactions were carried out in water, ethanol, acetonitrile, chloroform, toluene and THF solvent and it was found that the highest yield of the desired amide (82%) was obtained in ethanol at 80 °C after 5 h (Table 8; entry 4). In water and all other organic solvents, the nanoparticle catalyst exhibited either zero or much lower reactivity in the conversion of substrates into desired product. Therefore, the green solvent ethanol is the most effective solvent in the present catalytic multicomponent organic reaction. The effect of molar ratio of the nanoparticle catalyst to substrate (**1**) on the yield of amide was also examined (Table 8, entries: 3, 4 and 6) and experimental outcomes revealed that the use of 6.5 mg catalyst/mmol of **1** is sufficient to obtain maximum yield of coumarin-3-carboxamides. A blank experiment (Table 8, entry 3)

was also carried out in absence of the CZ1 nanoparticles catalyst under the same experimental conditions which resulted in negligible yield of the desired product. This observation confirms high catalytic activity of the nanoparticles in the reaction for synthesizing coumarin-3-carboxamide (4).

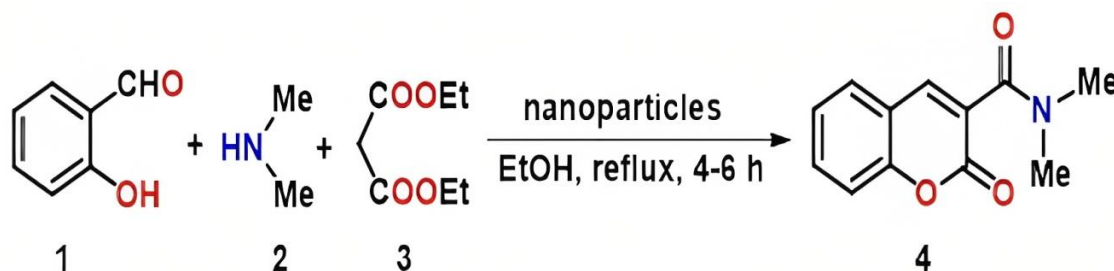


Fig.13 $\text{Co}_{0.8}\text{Zn}_{0.2}\text{Fe}_2\text{O}_4$ nanoparticles catalyzed multicomponent reaction of 2-hydroxybenzaldehyde, secondary amine and diethylmalonate (DEM).

Table 8 Standardization of multicomponent reaction conditions^a

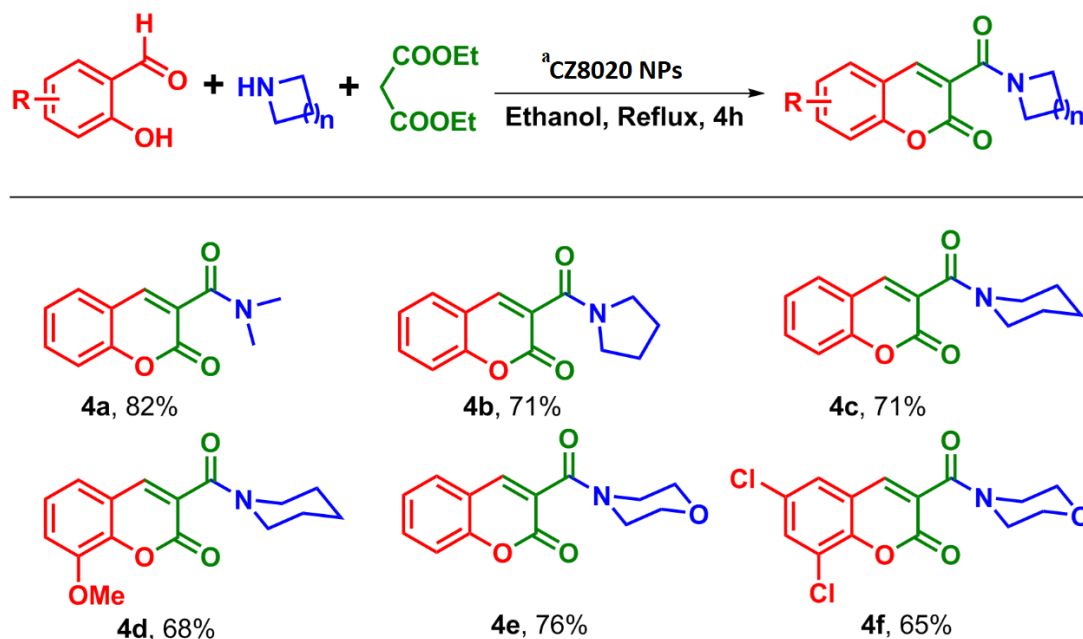
Entry	Amt. of NP catalyst(mg)	Solvent	T(°C) (±0.1)	Reaction time(h)	Yield(%) ^[b] (±0.5)
1	0	H ₂ O	30	3	-
2	6.5	H ₂ O	80	3	-
3	0	Ethanol	80	5	-
4	6.5	Ethanol	80	5	82
5	6.5	Ethanol	30	5	-
6	10	Ethanol	80	5	80
7	6.5	Ethanol	90	5	82
8	6.5	Toluene	80	5	62
9	6.5	CHCl ₃	60	5	49
10	6.5	CH ₃ CN	80	5	70
11	6.5	THF	70	5	32

^a Reaction condition: 2-hydroxybenzaldehyde (**1**) (1.0 mmol), required secondary amine (**2**) (1.2 mmol), diethylmalonate (DEM) (**3**) (1.0 mmol), and the NP CZ1 (in mg/mmol of **1**), solvent, heat. ^bYield of isolated pure desired product.

We have compared the catalytic activity of the three nanoparticle catalysts CZ1, CZ2, CZ3 under identical reaction conditions and found that sample CZ1 is the most efficient catalyst (Table 9; entry 1). This is probably due to its smallest particle size, high surface area and presence of crystalline disorder in its shell region. We have also examined the catalytic activity of the nanoparticles in the reaction of various other aldehydes and amine substrates in presence of DEM to get different chromene-3-carboxamides (**4**) and the results have been enlisted in the Table 10. The optimized reaction conditions as obtained during first screening experiment were applied in case of all other catalytic multicomponent organic reactions. The details of the yields, melting points and spectral data of the products are summarized in Table 11. In general, the outcomes of present study indicate that the samples act as an excellent catalyst in the synthesis of chromene-3-carboxamides (**4**) by the reaction of aldehydes and amines in presence of DEM. A brief comparative study on the synthesis of some other coumarin derivatives by different synthesis procedures using various nanoparticles and other catalysts has been summarized in Table 12. It suggests that the yield (%) of the coumarin derivatives depend upon the synthesis procedure followed and type of the catalyst used.

Table 9 Comparison of catalytic activity of $\text{Co}_{0.8}\text{Zn}_{0.2}\text{Fe}_2\text{O}_4$ nanoparticles

Entry	Nanoparticles	Amount (mg)	Yield (%) (± 0.5)
1	CZ1	6.5	82
2	CZ1	2.0	68
3	CZ2	6.5	77
4	CZ3	6.5	73

Table 10 Scope of products for the multi-component reaction of salicylaldehyde, secondary amine and DEM^aCo_{0.8}Zn_{0.2}Fe₂O₄ nanoparticles**Table 11** Yields, melting points and spectral data of the different chromene-3-carboxamides

Entry	Amide	Yield (%)	Morphology	Melting point (°C)	Spectral Analysis
4a	<i>N,N</i> -Dimethyl-2-oxo-2H-chromene-3-carboxamide	74	colorless crystalline solid	152–154	¹ H NMR (300 MHz, CDCl ₃): δ 7.91 (s, 1H), 7.52–7.61 (m, 2H), 7.29–7.37 (m, 2H), 3.12 (s, 3H, CH ₃), 3.01 (s, 3H, CH ₃)
4b	<i>N,N</i> -Tetramethylene-2-oxo-2H-chromene-3-carboxamide	68	colorless crystalline solid	144–146	¹ H NMR (300 MHz, CDCl ₃): δ 7.97 (s, 1H), 7.53–7.62 (m, 2H), 7.29–7.37 (m, 2H), 3.64 (t, <i>J</i> = 6.0 Hz, 2H), 3.46 (t, <i>J</i> = 6.0

					Hz, 2H), 1.91–2.00 (m, 4H)
4c	<i>N,N</i> -Pentamethylene-2-oxo-2 <i>H</i> -chromene-3-carboxamide	70	colorless crystalline solid	154–156	¹ H NMR (300MHz, CDCl ₃): δ7.86 (s, 1H), 7.51–7.59 (m, 2H), 7.28–7.36 (m, 2H), 3.71 (br s, 2H), 3.33 (br s, 2H), 1.62–1.69 (m, 6H)
4d	8-Methoxy- <i>N,N</i> -pentamethylene-2-oxo-2 <i>H</i> -chromene-3-carboxamide	58	colorless crystalline solid	186–188	¹ H NMR (400 MHz, CDCl ₃): δ7.84 (s, 1H), 7.23 (t, <i>J</i> = 7.8 Hz), 7.08–7.12 (m, 2H), 3.96 (s, 3H, OCH ₃), 3.69 (br s, 2H), 3.31 (t, <i>J</i> = 4.8 Hz, 2H), 1.59–1.67 (m, 6H)
4e	<i>N,N</i> -(3-oxapentamethylene)-2-oxo-2 <i>H</i> -chromene-3-carboxamide	71	colorless crystalline solid	138–140	¹ H NMR (400 MHz, CDCl ₃): δ7.96 (s, 1H), 7.54–7.62 (m, 2H), 7.31–7.37 (m, 2H), 3.79 (s, 4H), 3.72 (t, <i>J</i> = 4.4 Hz, 2H), 3.40 (t, <i>J</i> = 4.4 Hz, 2H)
4f	6,8-Dichloro- <i>N,N</i> -(3-oxapentamethylene)-2-oxo-2 <i>H</i> -chromene-3-carboxamide	68	colorless crystalline solid	222–224	¹ H NMR (300 MHz, CDCl ₃): δ7.88 (s, 1H), 7.67 (d, <i>J</i> = 2.1 Hz, 1H), 7.46 (d, <i>J</i> = 2.1 Hz, 1H), 3.81 (s, 4H), 3.74 (t, <i>J</i> = 4.5 Hz, 2H), 3.39 (t, <i>J</i> = 4.5 Hz, 2H)

Table 12 Table for comparison of the results of preparation of some coumarin derivatives using different catalysts.

Entry	Product	Reaction type	Catalyst used	% of catalyst	Yield (%)	Ref .
1.	3-substituted coumarins	Knoevenagel condensation under solvent-free conditions with ultrasound irradiation	MgFe ₂ O ₄ nanoparticles	4 mol%	96	[66]
2a	Benzylaminocoumarins	On-pot three component coupling reaction	CuO nanoparticles	20 mol%	92	[67]
2b			NiO nanoparticles	15	30	
2c			MgO nanoparticles	15	45	
2d			Fe ₃ O ₄ nanoparticles	15	40	
2e			ZnO nanoparticles	15	92	
3	Coumarin-3-carbamides	A three-component reaction	Ni-NiO nanoparticles	5 mg	72	[57]
4	Some coumarin derivatives	Von-Pechmann condensation	SnCl ₂ .2H ₂ O	10 mol%	60	[68]
5	Some coumarin derivatives	Pechmann condensation	Mesoporous Zirconium phosphate	15 wt%	57	[69]
6	Some coumarin derivatives	Knoevenagel condensation	ZnO (in methanol)	8.2 mg	74	[70]
7	Some coumarin derivatives	Pechmann condensation	Preyssler	1 mol%	79	[71]
8	Some coumarin derivatives	Pechmann condensation	TiCl ₄	-	60	[72]
9	Some coumarin derivatives	Knoevenagel condensation	Ionic liquid	-	95	[73]

10	Some coumarin derivatives	Pechmann condensation	ZrOCl ₂ .8H ₂ O/SiO ₂	10 mol%	98	[74]
11	Pyrano[2,3-h]coumarin derivatives	One-pot three component reaction	K ₂ CO ₃	-	95	[75]
12	Coumarin-3-carbamides	Multi component reaction	CZ1 CZ2 CZ3	6.5 mg	82 77 73	Present samples

It is a worthy attempt to draw a reasonable and plausible mechanistic pathway for a multicomponent organic reaction in order to get a deep insight about the catalytic activity of Co_{0.8}Zn_{0.2}Fe₂O₄ nanoparticles. In presence of a secondary amine (**2**), the reaction of 2-hydroxybenzaldehyde (**1**) and DEM (**3**) to obtain coumarin derivative (**9**) is a common organic reaction [93]. This organic reaction generally follows the path in which nucleophilic attack by malonate ion (produced in the medium from DEM) to **1** or iminium ion (produced by the condensation of **1** and amine) takes place in the first step followed by ring cyclization with subsequent loss of amine. In the present study, it was a general observation that on mixing of reagents (**1**, **2**, **3**) and nanoparticle catalyst the mixture immediately turns yellowish red. This observation clearly indicates the formation of iminium ion by condensation of **1** and **2**. Moreover, a trace amount of **9** has also been identified in our case. Therefore, on the basis these two findings it can reasonably be concluded that the present catalytic organic reaction follows the same path as described above. A general reaction mechanism is pictorially depicted in Fig.14. Further, the coumarin derivative (**9**) subsequently undergoes nucleophilic attack by the free amine (**2**) at its ester carbon and finally produce the desired chromene-3-carboxamides (**4**) by the removal of EtO⁻. Subsequently, steps of the above mentioned reaction mechanism reveal that the Co_{0.8}Zn_{0.2}Fe₂O₄ nanoparticles perform as an effective catalyst due to following reasons: (i) they facilitate the formation of malonate ion, (ii) they

activate the iminium ion for the nucleophilic attack by malonate ion, (iii) they facilitate the nucleophilic attack at the ester carbon(*) over the competitive 4-position of coumarin derivative (**9**) at the final step. This is very crucial to achieve the desired product, chromene-3-carboxamides (**4**) with good yield. In the present case, we have obtained the desired product (**4**) with 82% yield.

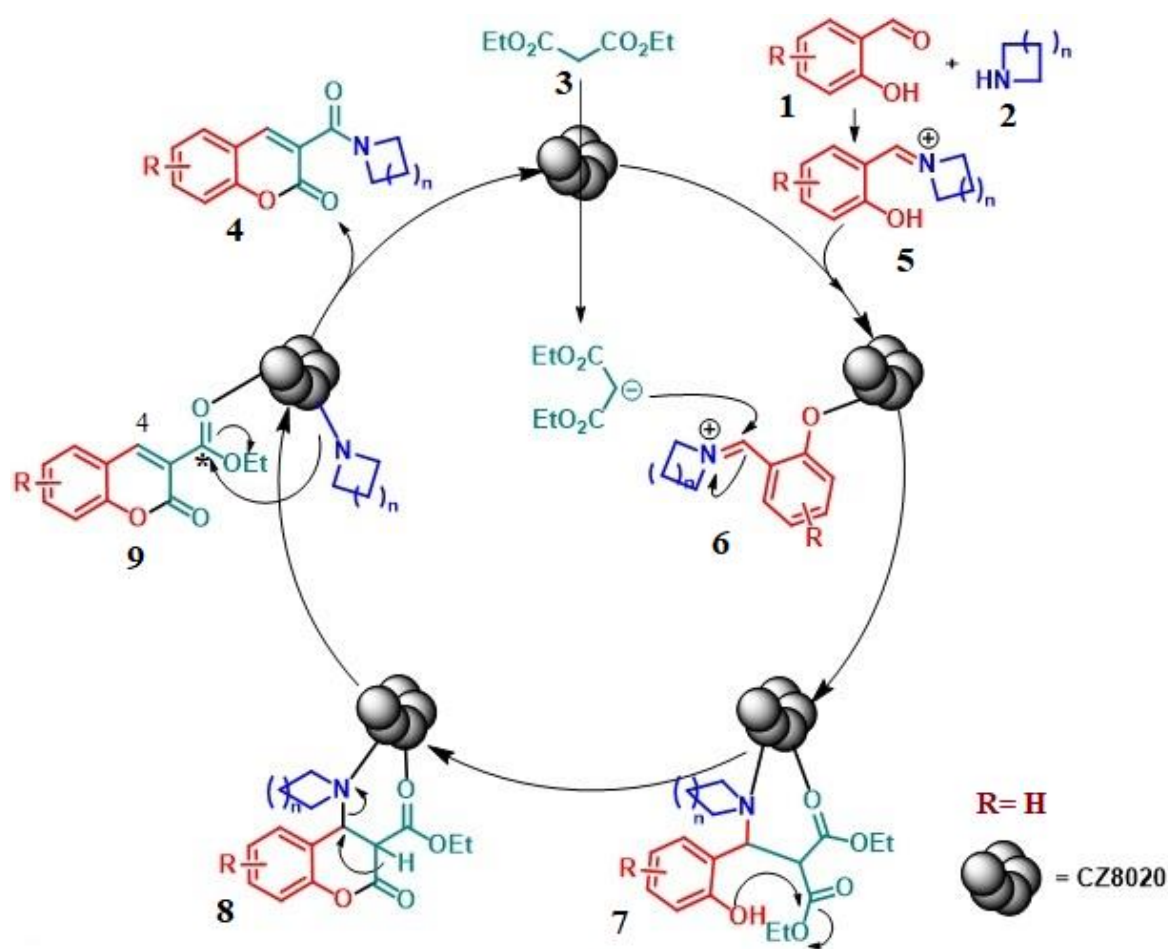


Fig.14. Reaction mechanism of $\text{Co}_{0.8}\text{Zn}_{0.2}\text{Fe}_2\text{O}_4$ (CZ8020) nanoparticles catalyzed multicomponent organic reaction

6.3.3.2 Reusability of the catalyst

In catalysis and green chemistry, the recovery and recycling of the catalyst are very important. The magnetic, non-toxic and benign nature of the present nanoparticle catalysts have made the recovery and reusability of the catalyst effortless and economic. In all the

cases, we have recovered nanoparticle catalyst from the reaction mixture using a common laboratory magnet. In the above-mentioned representative catalysis reaction, 95% (w/w) of the nanoparticle catalyst was recovered after the first catalytic cycle. The separated nano-catalyst has been used in another catalytic cycle after washing with ethanol and dichloromethane. We have recycled the catalyst for eight catalytic cycles and found a slight decrease in catalytic activity of it. The catalytic activity of nano-catalyst in terms of product yield and recovery of the catalyst are demonstrated in Fig.15. We have recorded the PXRD pattern (Fig.16) and FESEM micrograph (Fig.17) of the catalyst isolated after the eight cycles of catalytic reaction. The recovered catalyst has retained its both spinel ferrite structure and morphology after eight cycles of reaction. Thus, the samples are easily recoverable and reusable as catalyst in formation of chromene-3-carboxamides.

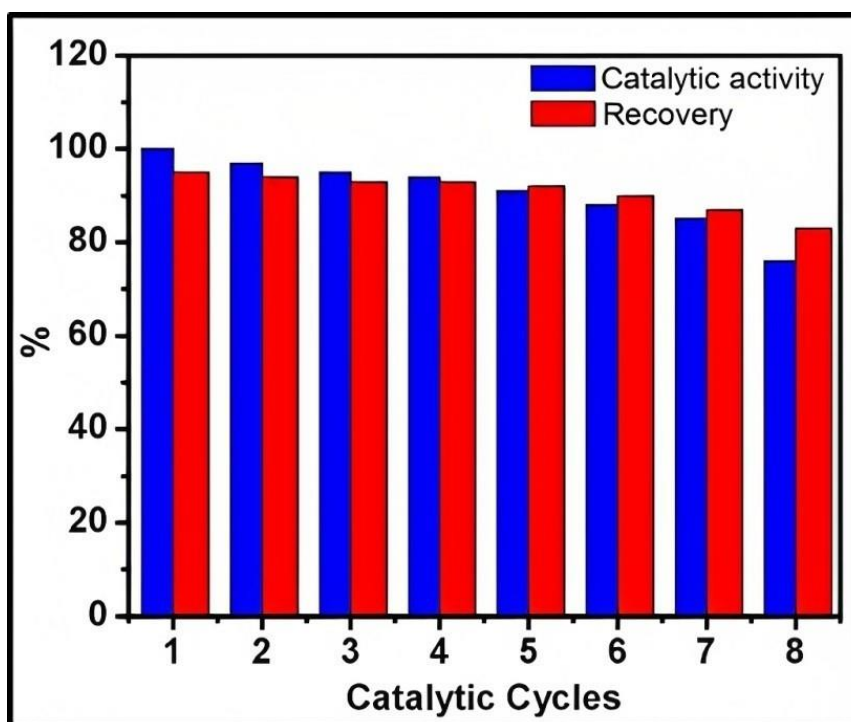


Fig.15 Recovery and catalytic activity of the catalyst

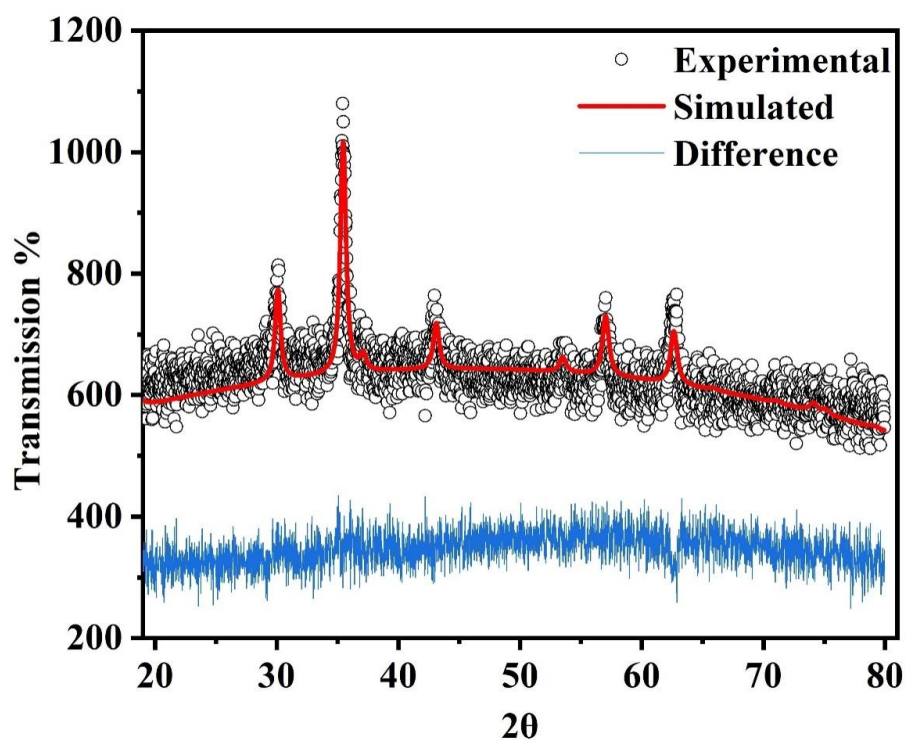


Fig.16 PXRD of the catalyst after eight cycles

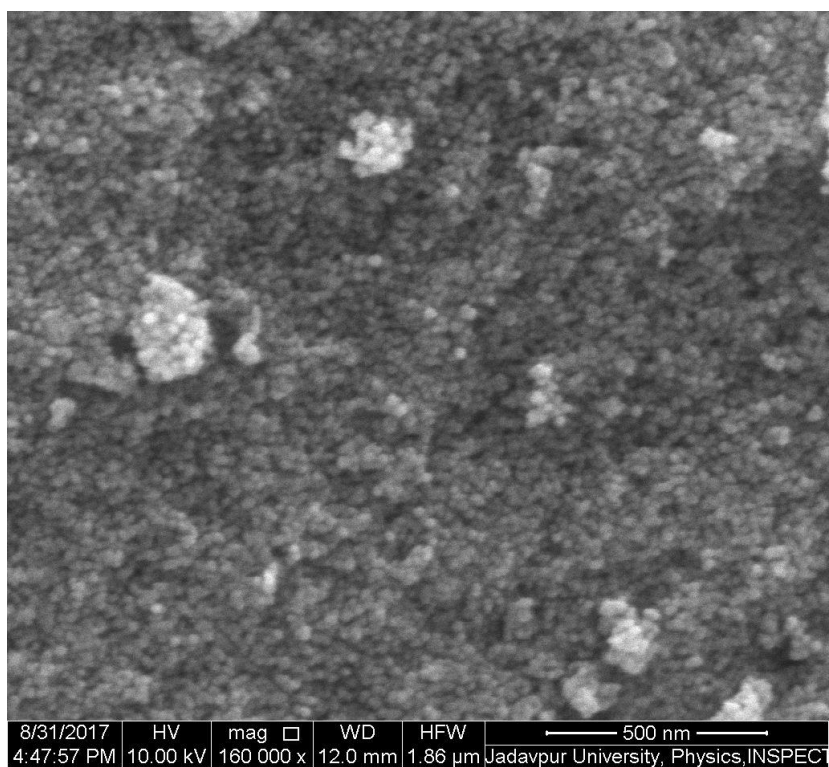


Fig.17 FESEM of the catalyst after eight cycles

6.4. Discussion

The PXRD, FESEM, EDS and HRTEM studies together with have uncovered some characteristics common to all three samples and those are as follows: (i) samples are well crystalline, single phase spinel ferrites with structural parameters close to those of bulk $\text{Co}_{0.8}\text{Zn}_{0.2}\text{Fe}_2\text{O}_4$ but with large lattice strain and (ii) the constituent nanoparticles of the samples are mostly non-spherical in shape and exhibit broad size distribution with agglomeration. According to the study on magnetic and hyperfine properties, all three samples show: (i) magnetic ordering at room temperature with M_{SAT} , H_C close to that of their bulk counterpart, (ii) signature of interparticle interactions, (iii) enhancement in magnetic parameters (M_{SAT} , H_C and K) especially the H_C at low temperature compared to their counterparts synthesized by chemical methods, (iv) non-equilibrium cation distribution and (v) CZ1 has shown EB effect in hysteresis loop, spin canted core-shell structure and chemical inhomogeneity while other two do not. It is well known that ball milling introduces surface defects, disorders, non-equilibrium cation distribution in nanometric ferrites [16,40,43,51,52,90,91]. Moreover, the constituent particles of such samples sometimes exhibit core-shell structure [16,40,43,51,52,90,91]. The high values of microstrain obtained by analyzing of PXRD data, surface defects found in the HRTEM images and the site exchange of Fe^{3+} ions from [B] to (A) sites in lieu of migration of Co^{2+} ions from (A) to [B] sites as has been detected by infield Mössbauer study in conjugation with Rietveld refinement of PXRD data are direct consequences of mechanical milling. Out of three samples, CZ1 has been heat treated at lowest temperature (500 °C), therefore, the effect of ball milling will be more pronounced in it. Thus, the core-shell structure and chemical inhomogeneity of CZ1 are exclusively due to mechanical milling whose dominating effect has not been overruled by heat treatment at 500 °C. Upon subsequent annealing, the system tries to attain equilibrium cation distribution along with enhancement of crystallinity, magnetic parameters and

reduction of spin canting effect [40,43]. The lattice parameter increases and approaches to the value of the bulk $\text{Co}_{0.8}\text{Zn}_{0.2}\text{Fe}_2\text{O}_4$ with the increase in temperature of heat treatment. This points towards development of good crystalline character in the samples. There is an increase in the size of the particles in the samples with increase in temperature of heat treatment [40,43]. It may, therefore, be inferred that the magnetic parameters of the samples get enhanced with increase in particle size due to reduction of superparamagnetic flipping of magnetic moments owing to finite size effect and reduction of spin canting effect caused by good crystallinity [39,51].

The values of M_{SAT} and H_C of nanosized $\text{Co}_{0.8}\text{Zn}_{0.2}\text{Fe}_2\text{O}_4$ prepared by different chemical routes are listed in Table 5. By comparing the values of magnetic parameters of our samples (Table 4) with those listed in Table 5, it appears that the magnetic parameters of CZ1, CZ2 and CZ3 are the best among all the samples. All three samples show significant values of H_C at room temperature (Table 5) and thus, suggest presence of magnetic ordering at 300 K. There is a huge enhancement in the H_C values at 10 K (see Table 4), even greater than that of bulk CoFe_2O_4 [24]. Such high values of H_C at 10 K may be due to an increase in effective anisotropy of the system caused by upliftment of crystalline, shape and strain induced anisotropy energies [24]. The values of coercivity at 10 K vary in the order $\text{CZ1} > \text{CZ2} > \text{CZ3}$. This kind of variation in H_C values has been observed earlier beyond a certain particle size and can be explained from the theory of domain structure [50,94]. It is well known that for an isolated spherical magnetic nanoparticle (in the absence of an external magnetic field), there exists a critical diameter (D_C) below which it can be considered single domain [94]. The formula for calculating D_C can be written as:

$$D_C = 9w_p / 2\pi M_S^2 \quad (3)$$

, where w_p is the energy density of the magnetic domain wall. The expression for w_p is given by $w_p = \left(\frac{2k_B T_C K_E}{a} \right)^{1/2}$, where k_B is the Boltzmann constant, T_C the Curie temperature, K_E is the anisotropy constant and a is the lattice constant [94]. Although the shape of the constituent nanoparticles in the samples deviate from spherical shape and presence of interparticle interactions is evident from TEM images in the present samples, we have tried to calculate approximate value of D_C . At first, the value of w_p has been calculated by taking $K_E = 1.4 \times 10^6$ erg/cm³ (Table 4), $k_B = 1.38 \times 10^{-16}$ erg/K, $a = 8.38 \times 10^{-8}$ cm (Table 1) and $T_C = 623.15$ K [43] and found to be 1.7 erg/cm². Finally, by putting $M_s = 945.24$ G (obtained from value of M_{SAT} for CZ1 at 300 K) and the calculated value of w_p in Eq. (5), we have obtained the theoretical value of D_C for our system as ~ 27 nm. So, from the value of D_C it seems that CZ1 is single domain, whereas CZ2 and CZ3 are multidomain. Since a maximum value is observed in coercive field near D_C , it can be assumed that CZ1 having particle size closest to D_C may exhibit highest value of H_C among the three samples. Further, with the increase in particle size, the value of H_C is decreasing as expected.

It has been reported earlier that presence of large microstrain caused by mechanical strain, departure from spherical shape and crystalline quality are primary factors for the enhancement of anisotropy energy (K_E) in mechanically activated nanosized ferrites compared to the samples prepared by chemical methods [39,51,90]. Such an increase in K_E gets manifested in the form of an increase in blocking temperature (T_B), magnetic ordering, M_{SAT} and H_C generally. The effective anisotropy of a polycrystalline magnetic material can be calculated using the ‘law of approach’ to saturation [24]. The magnetization $M(H)$ is given by the equation:

$$M(H) = M_s \left(1 - \frac{a}{H} - \frac{b}{H^2} - \dots \right) \quad (4)$$

where M_s and H are applied field and saturation magnetization, respectively, and a , b are constants. The $\frac{b}{H^2}$ term represents the magnetic anisotropy and coefficient 'b' is related to K_E as follows:

$$b = 4 \frac{K_E^2}{15M_s^2} = 4 \left(\frac{K_{Sh}^2 + K_{St}^2 + K_{Sf}^2 + \frac{2}{7}K_1^2}{15M_s^2} \right) \quad (5)$$

where K_{Sh} , K_{St} , K_{Sf} and K_1 are the shape, stress, surface and magnetocrystalline anisotropy, respectively. The parameters 'b' and M_s have been obtained from the intercept and slope of the linear fit of M_s versus H^2 curves, respectively, and the linear fitted regions of these curves are displayed in Fig.18. The values of K_E so obtained have been summarized in Table 4. In the present case, it can be ascertained that the K_E of the samples have significantly enhanced due to the increase in shape, crystalline and strain induced anisotropy of the samples and this leads to overall enhancement of magnetic parameters of the samples with respect to their counterparts synthesized by chemical methods. Now, for the present group of samples with increase of heat treatment temperature, betterment of the crystalline character and increase in particle size has been noticed, whereas, the microstrain and crystalline disorder at the surface caused by ball milling get subsequently reduced. Thus, the increase of crystalline anisotropy energy overrules the decrease of strain induced anisotropy energy and as a whole, the K_E of the system increases in the order $(K_E)_{CZ3} > (K_E)_{CZ2} > (K_E)_{CZ1}$. This leads to the overall betterment of magnetic parameters of the samples as particle size increases.

The conventional EB effect, as first observed by Meiklejohn and Bean in Co-CoO nanoparticles system, is generally referred to as the shifting of hysteresis loop along field axis owing to the exchange coupling between antiferromagnetic/ferromagnetic (AFM/FM) phases, when AFM/FM is cooled through the Néel temperature (T_N) of the AFM component [95,96]. Apart from these nanocomposite systems, some single-phase materials have also shown EB effect due to the exchange coupling at the interface of different magnetic orders present

within them [82-84]. Based on in-field Mössbauer spectroscopic study, we may describe the sample CZ1 as being constituted of two different magnetic phases; a slightly canted core region surrounded by a completely disordered shell with different chemical environments. At room temperature, the moments at the shell region are thermally fluctuating while the core moments tend to align them (giving rise to a split relaxed sextet in 300 K Mössbauer spectrum). With the lowering of temperature, there is a progressive freezing of the spins in the shell region according to the distribution of their energy barriers and associated interparticle interactions. After a certain temperature (~ 150 K as seen from ZFC curves for present samples), the freezing of shell region spins in a glass-like state is complete then the coupling between the magnetically ordered core and magnetically disordered shell region is established [83]. During the FC process, the spins of these frozen glassy state attain a specific orientation and attempt to lock the core spins in this alignment after removal of the field. During M-H experiment as the applied magnetic field is reversed, the frozen shell layer (due to its higher anisotropy) applies a torque on the strongly pinned core spins resulting in the offset of the entire hysteresis loop [97]. Generally, EB is found to be influenced by the thickness of the interface, strength of magnetic spin coupling at the interface, anisotropy of AFM phase, Zeeman energy etc. [84,97]. Most importantly, the competition between the interfacial exchange energy and Zeeman energy determines the emergence and stability of the observed EB effect [84,97]. The essential condition for attaining EB is that interfacial energy must be greater than the Zeeman energy [97]. In general, there is an increase in interfacial exchange energy density due to increase in the number of frozen spins and exchange coupled spins at the interface [84,97] whereas Zeeman energy, being a volume term, increases with an increase in core thickness [84,97]. With subsequent heat treatment, there is a decrease in surface spin disorder and increase in crystallinity of the samples, which in turn diminishes the favorable conditions for formation of core-shell structure. Thus, the persistence of core-shell

structure in CZ1 promoted the appearance of EB in CZ1 whereas reduction in surface spin disorder and betterment of crystalline character ruled out the possibility of occurrence of EB in CZ2 and CZ3. Moreover, there exists a critical size for the emergence and stability of EB in spheroidal nanoparticles [83]. So it seems that, among the three samples, only CZ1 possesses the critical particle size necessary for the emergence of EB.

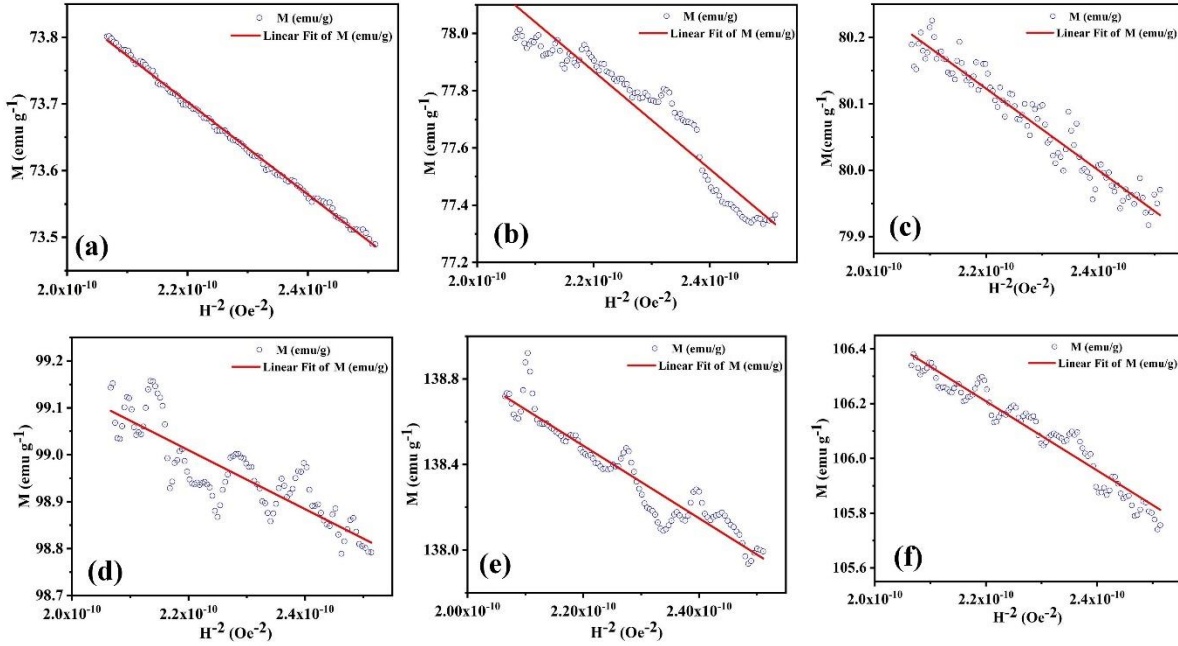


Fig.18 Linear fit of M versus H^{-2} curves of (a) CZ1, (b) CZ2, (c) CZ3 at 300 K and (d) CZ1, (e) CZ2, (f) CZ3 at 10K for estimating values of parameters ‘b’ and M_s for K_E calculation

6.5. Conclusion

We have thoroughly characterized the three samples viz., CZ1, CZ2, CZ3 having sizes 23, 34 and 42 nm, respectively, synthesized by coprecipitation method followed by high energy ball milling and subsequent thermal treatment using PXRD, HRTEM, EDS and Mössbauer spectroscopic studies. The dc magnetic and hyperfine properties of the samples have also been examined. The PXRD and HRTEM studies revealed that constituent nanoparticles of all three samples are well crystalline, possess large microstrain, are assorted in shape and size with visible agglomeration. All these effects are direct consequences of the synthesis procedure undertaken to obtain the present samples. The ball milling has induced

higher values of microstrain and broad particle size distribution while subsequent thermal treatment resulted in good crystallinity along with gradual reduction of microstrain, controlled modification of particle size and narrowing of particle size distribution. The EDS studies have revealed that the samples are in proper stoichiometric ratio. Further, we have estimated the cation distribution of the samples using the results of PXRD and Mössbauer spectroscopy study in conjugation and accuracy of the cation distribution so obtained has been checked and validated through theoretical analysis of dc magnetic data. The M-T measurements pointed towards presence of interparticle interactions within the nanoparticle system that induced collective freezing of moments at low temperature. All three samples displayed coercivity at 300 K indicating that the nanoparticle systems are magnetically well ordered at room temperature. The very high values of coercivity at 10 K are supposedly due to an increase in effective anisotropy of the nanoparticle system owing to combined effect of interparticle interactions and surface spin disorder. The results of Mössbauer spectroscopic study indicates the presence of core-shell structure and chemical inhomogeneity in CZ1. The core-shell structure along with chemical inhomogeneity in CZ1 and irrefutable presence of interparticle interactions in the nanoparticle assembly resulted in an increase of the anisotropy of the disordered shell layer which applied strong pinning action on the core leading to emergence of exchange bias in it. All three samples can be used in magnetic storage devices. The samples exhibited very good catalytic activity in the multicomponent reaction for the synthesis of coumarin-3-carboxamide together with excellent recovery and recyclability. In conclusion, we have shown that (i) morphology, particle size distribution, crystalline quality, cation redistribution, interparticle interactions, anisotropy energy, surface spin disorder and presence of different magnetic phases due to spin canting effect are the key factors in shaping magnetic and hyperfine properties of nanometric $\text{Co}_{0.8}\text{Zn}_{0.2}\text{Fe}_2\text{O}_4$ samples (ii) CZ1 sample having particle size below the critical diameter exhibits exchange bias effect owing to its

core-shell magnetic structure while others do not, (iii) the accuracy of the cation distribution of the present samples as determined from the results of PXRD and Mössbauer spectroscopy study in conjugation has been established by theoretical analysis of dc magnetic data indicating that cation distribution of ferrite samples can be estimated without using costly equipment like x-ray photoelectron spectrometer, (iv) CZ1 exhibits best catalytic response towards formation of coumarin-3-carboxamide via a multi component reaction due to its high surface to volume ratio among all three samples and (v) the samples are suitable for application in magnetic storage device and green catalysis.

References

1. L. Khanna, N.K. Verma, S.K. Tripathi, *J Alloys Compd* 752 (2018) 332-353.
2. Thomas Dippong, E. A. Levei, O. Cadar, *Nanomaterials* 11 (2021) 1560.
3. P. Chand, S. Vaish, P. Kumar, *Physica B Condens. Matter* 524 (2017) 53 – 63.
4. J. Jeevanandam, A. Barhoum, Y. S. Chan, A. Dufresne, M. K. Danquah, *Beilstein J. Nanotechnol.* 9 (2018) 1050–1074.
5. M.C. Dimri, H. Khanduri, P. Agarwal, V. Garg, A. Mere, R. Stern, *AIP Conf. Proc.* 2265 (2020) 030517.
6. S. Sharma, N. Choudhary, M. K. Verma, N. D. Sharma, D. Singh, *Ceram. Int.* 43 (2017) 11083 – 11089.
7. Karla R. Sanchez-Lievanos, James L. Stair, Kathryn E. Knowles, *Inorg. Chem.* 60 (2021) 4291–4305.
8. Jongnam Park, Jin Joo, Soon Gu Kwon, Youngjin Jang, Taeghwan Hyeon, *Angew. Chem. Int. Ed.* 46 (2007) 4630 – 4660.
9. P. Kharbanda, T. Madaan, I. Sharma, S. Vashishtha, P. Kumar, A. Chauhan, S. Mittal, J. S. Bangruwa, V. Verma, *Heliyon* 5 (2019) 1 – 14.
10. Ç.E. Demirci, P.K. Manna, Y. Wroczynskyj, S. Aktürk, J. van Lierop, *J. Magn. Magn. Mater.* 458 (2018) 253–260.
11. Andris Šutka, Kārlis A. Gross, *Sens. Actuators B Chem.* 222 (2016) 95–105.
12. S. Majumder, B. Saha, S. Dey, R. Mondal, S. Kumar, S. Banerjee, *RSC Adv.* 6 (2016) 59907.
13. S. K. Dutta, M. Akhter, J.Ahmed, Md. K. Amin, P. K. Dhar, *Biointerface Res. Appl. Chem.* 12 (2022) 4399 – 4416.
14. M. Amiri, K. Eskandari, M. Salavati-Niasari, *Adv. Colloid Interface Sci.* 271 (2019) 101982.
15. L. S. Ganapathe, M. A. Mohamed, R. M. Yunus, D. D. Berhanuddin, *Magnetochemistry* 6 (2020) 68
16. S. Dey, R. Mondal, S. K. Dey, S. Majumder, P. Dasgupta, A. Poddar, V. R. Reddy, S. Kumar, *J. Appl. Phys.* 118 (2015) 103905.

17. S. Chakraverty, B. Ghosh, S. Kumar, A. Frydman, Appl. Phys. Lett. 88 (2006) 042501.
18. Md. J. N. Isfahani, M. Myndyk, D. Menzel, A. Feldhoff, J. Amighian, V. Šepelák, J. Magn. Magn. Mater. 321 (2009) 152–156.
19. B. Jansi Rani, M. Ravina, B. Saravanakumar, G. Ravi, V. Ganesh, S. Ravichandran, R. Yuvakkumar, Nano-Struct. Nano-Objects 14 (2018) 84 – 91.
20. M. Bini, M. Ambrosetti, D. Spada, Appl. Sci. 11 (2021) 11713.
21. N. Akhlaghi, G. Najafpour-Darzi, J Ind Eng Chem. 103 (2021) 292 – 304.
22. Y. Zhang, W. Zhang, C. Yu, Z. Liu, X. Yu, F. Meng, Ceram. Int. 47 (2021) 10063 – 10071.
23. M.A. S. Amulya, H. P. Nagaswarupa, M.R. Anil Kumar, C.R. Ravikumar, K. B. Kusuma, S.C. Prashantha, J. Phys. Chem. Solids, 148 (2021) 109756.
24. S. M. Ansari, B. B. Sinha, K.R. Pai, S.K. Bhat, Y-R Ma, D. Sen, Y. D. Kolekar, C.V. Ramana, Appl. Surf. Sci. 459 (2018) 788–801.
25. B. H. Liu, J. Ding, Z. L. Dong, C. B. Boothroyd, J. H. Yin, J. B. Yi, Phys. Rev. B 74 (2006) 184427.
26. S. Jauhar, J. Kaur, A. Goyal, S. Singhal, RSC Adv. 6 (2016) 97694 – 97719.
27. R.K. Panda, D. Behera, J. Alloys Compd. 587 (2014) 481–486.
28. M J Akhtar, M Nadeem, S Javaid, M Atif, J. Phys.: Condens. Matter 21 (2009) 405303.
29. S. Dey, R. Mondal, S. Majumder, P. Dasgupta, A. Poddar, S. Banerjee, S. Kumar, Materials Today: Proceedings 5 (2018) 9855 – 9859.
30. M. Bohra, S. Prasad, N. Kumar, D. S. Misra, S. C. Sahoo, N. Venkataramani, R. Krishnan, Appl. Phys. Lett., 88 (2006) 262506.
31. S. S. Jadhav, S. E. Shirsath, S. M. Patange, K. M. Jadhav, J. Appl. Phys. 108 (2010) 093920.

-
32. D. S. Nikam, S. V. Jadhav, V. M. Khot, R. A. Bohara, C. K. Hong, S. S. Mali, S. H. Pawar, *RSC Adv.* 5 (2015) 2338.
33. V. Marneli, A. Musinu, A. Ardu, G. Ennas, D. Peddis, D. Niznansky, C. Sangregorio, C. Innocenti, Nguyen T. K. Thanh, C. Cannas, *Nanoscale*, 8 (2016) 10124.
34. M. Schmidt, H. L. Andersen, C. Granados-Miralles, M. Saura-Múzquiz, M. Stingaciu, M. Christensen, *Dalton Trans.* 45 (2016) 6439.
35. X. Huang, J. Zhang, W. Wang, T. Sang, B. Song, H. Zhu, W. Rao, C. Wong, J. Magn. Mater. 405 (2016) 36–41.
36. R.N. Bhowmik, R. Ranganathan, *J. Magn. Magn. Mater.* 248 (2002) 101–111.
37. R.V. Upadhyay, H. Parmar, P. Acharya, A. Banerjee, *Solid State Commun.* 163 (2013) 50–54.
38. G. A. Petitt, D. W. Forester, *Phys. Rev. B* 4 (1971) 11.
39. K. Sarkar, R. Mondal, S. Dey, S. Majumder, S. Kumar, *J. Magn. Magn. Mater.* 487 (2019) 165303.
40. S. Dey, A. Roy, J. Ghose, R. N. Bhowmik, R. Ranganathan, *J. Appl. Phys.* 90 (2001) 4138.
41. S. Anjum, J. Fayyaz, R. Khurram, R. Zia, *J Supercond Nov Magn* 31 (2018) 4095 – 4106.
42. L. R. Gonsalves, S. C. Mojumdar, V. M. S. Verenkar, *J Therm Anal Calorim* 104 (2011) 869–873.
43. M.H. Yousefi, S. Manouchehri, A. Arab, M. Mozaffari, Gh. R. Amiri, J. Amighian, *Mater. Res. Bull.* 45 (2010) 1792–1795.
44. M. Veverka, P.Veverka, Z.Jiráček, O.Kaman, K.Knížek, M.Maryško, E.Pollert, K. Závěta, *J. Magn. Magn. Mater.* 322 (2010) 2386–2389
45. S. Urcia-Romero, O. Perales-Pérez, O. N. C. Uwakweh, C. Osorio, H. A. Radovan, J. Appl. Phys. 109 (2011) 07B512.
-

-
46. R. Arulmurugan, G. Vaidyanathan, S. Sendhilnathan, B. Jeyadevan, *Physica B* 363, 225 (2005).
47. G. V. Duong, N. Hanh, D. V. Linh, R. Groessinger, P. Weinberger, E. Schafner, M. Zehetbauer, *J. Magn. Magn. Mater.* 311 (2007) 46.
48. Dai Jian-Feng, Lu Rui-E, Fu Bi, Gao Kun, Zhang Liang-Liang, *Chin. Phys. B* 23 (2014) 037505.
49. Wei Wang Ri Chen, Xiruo Zhao, Yajun Zhang, Jinliang Zhao, Feng Li, *J. Am. Ceram. Soc.* (2013) 1 – 7.
50. S. B. Waje, M. Hashim, W. D. W. Yusoff, Z. Abbas, *J. Magn. Magn. Mater.* 322 (2010) 686–691
51. R. Mondal, S. Dey, K. Sarkar, P. Dasgupta, S. Kumar, *Mater. Res. Bull.* 102 (2018) 160–171
52. S. Dey, R. Mondal, S. K. Dey, S. Majumder, P. Dasgupta, A. Poddar, V. R. Reddy, S. Kumar, *J. Appl. Phys.* 118 (2015) 103905.
53. M. Stefanescu, M. Bozdog, C. Muntean, O. Stefanescu, T. Vlase, *J. Magn. Magn. Mater.* 393 (2015) 92–98.
54. A.V. Raut, R.S. Barkule, D. R. Shengule, K. M. Jadhav, *J. Magn. Magn. Mater.* 358-359 (2014) 87–92.
55. C. Gómez-Polo, V. Recarte, L. Cervera, J.J. Beato-López, J. López-García, J.A. Rodríguez-Velamazán, M.D. Ugarte, E.C. Mendonça, J.G.S. Duque, *J. Magn. Magn. Mater.* 465 (2018) 211–219.
56. M. Ben Ali, K.El Maalam, H.El Moussaoui, O. Mounkachi, M. Hamedoun, R. Masrour, E.K. Hlil, A. Benyoussef, *J. Magn. Magn. Mater.* 398 (2016) 20–25
57. Boris I. Kharisov, H.V. Rasika Dias, Oxana V. Kharissov, *Arab. J. Chem.* 12 (2019) 1234–1246.
-

-
58. M. Kazemi, M. Ghobadi, A. Mirzaie, *Nanotechnol Rev* 7 (2018) 43–68
59. An-Hui Lu, E. L. Salabas, F. Schüth, *Angew Chem Int Ed* 46 (2007) 1222–44.
60. S. K. Sharma, *Complex Magnetic Nanostructures*, Springer, Switzerland, 2017.
61. Y L N Murthya, B S Diwakar, B Govindh, K Nagalakshmi, I V K Viswanath, R. Singh, J. Chem. Sci. 124 (2012) 639–645.
62. A. M. Kulkarni, U. V. Desai, K. S. Pandit, M. A. Kulkarni, P. P. Wadgaonkar, *RSC Adv.* 4 (2014) 36702.
63. S. Shaabani, A. Shaabani, S. Weng Ng, *ACS Comb. Sci.* 16 (2014) 176–183.
64. N. Sepay, C. Guha, A. Kool A. K. Mallik, *RSC Adv.* 5 (2015) 70718-70725.
65. S. Dey, S. K. Dey, S. Majumder, A. Poddar, P. Dasgupta, S. Banerjee, S. Kumar, *Physica B* 448 (2014) 247–252.
66. L. Lutterotti, MAUDWEB, Version 1.9992 (2004).
67. T.A.S. Ferreira, J.C. Waerenborgh, M.H.R.M. Mendonça, M.R. Nunes, F.M. Costa, *Solid State Sci.* 5 (2003) 383–392.
68. P. F. Teh, S. S. Pramana, C. Kim, C-M Chen, C-H Chuang, Y. Sharma, J. Cabana, S. Madhavi, *J. Phys. Chem. C* 2013, 117, 24213–24223.
69. A.C. Larson, R.B. Von Dreele, “General structure analysis system (GSAS),” Los Alamos National Laboratory, Rep. LAUR (2000) 86–748.
70. B.H. Toby, EXPGUI, a graphical user interface for GSAS, *J. Appl. Crystallogr.* 34 (2001) 210–213.
71. S. Dey, S.K. Dey, B. Ghosh, V.R. Reddy, S. Kumar, *Mater. Chem. Phys.* 138 (2013) 833–842.
72. B. Fultz, J. Howe, *Transmission Electron Microscopy and Diffractometry of Materials*, Springer-Verlag Berlin Heidelberg 2008.
73. J. L. Dormann, D. Fiorani, J. Magn. Mater. 140-144 (1995) 415-418.
-


-
74. J. L. Dormann, *Magnetic Properties of Fine Particles*, Elsevier Science Publishers B.V. (1992).
75. R. H. Kodama, A. E. Berkowitz, *Phys. Rev. B* 59 (1999) 6321 – 6336.
76. S. Manjura Hoque, C. Srivastava, N. Srivastava, N. Venkateshan, K. Chattopadhyay, *J Mater Sci* 48 (2013) 812–818.
77. M. A. Gabal, N. H. Al-Zahrani, Y. M. Al Angari, A. Saaed, *IEEE Trans. Magn.* 54 (2018) 2400112.
78. M. Kubisztal, I. Herok, M. Karolus, K. Prusik, G. Haneczok, *Acta Phys. Pol. A* 131 (2017) 1236.
79. P. B. Pandya, H. H. Joshi, R. G. Kulkarni, *J. Mater. Sci.* 26 (1991) 5509 – 5512.
80. C. Singh, S. Jauhar, V. Kumar, J. Singh, S. Singhal *Mater. Chem. Phys.* 156 (2015) 188 – 197.
81. A. Franco, F. C. e Silva, *J. Appl. Phys.* 113 (2013) 17B513.
82. D. Peddis, F. Orrù, A. Ardu, C. Cannas, A. Musinu, G. Piccaluga, *Chem. Mater.* 24 (2012) 1062–1071.
83. C. Martínez-Boubeta, K. Simeonidis, M. Angelakeris, N. Pazos-Pérez, M. Giersig, A. Delimitis, L. Nalbandian, V. Alexandrakis, D. Niarchos, *Phys. Rev. B* 74 (2006) 054430.
84. R. Mohan, M. P. Ghosh, S. Mukherjee, *J. Magn. Mater.* 458 (2018) 193–199.
85. P. Coppola, F. G. da Silva, G. Gomide, F. L. O. Paula, A. F. C. Campos, R. Perzynski, C. Kern, J. Depeyrot, R. Aquino, *J Nanopart Res* 18 (2016) 138.
86. H. R. Dakua, *AIP Advances* 10 (2020) 035324.
87. B. M. Wang, Y. Liu, P. Ren, B. Xia, K. B. Ruan, J. B. Yi, J. Ding, X. G. Li, L. Wang, *Phys. Rev. Lett.* 106 (2011) 077203.
88. K. Lagarec, D.G. Rancourt, *Recoil-Mössbauer Spectral Analysis Software for Window*, University of Ottawa Press, Ottawa, 1998.
-

-
89. L.T. Kuhn, K. Lefmann, C.R.H. Bahl, S.N. Ancona, P.A. Lindgård, C. Frandsen, D.E. Madsen, S. Mørup, *Phys. Rev. B* 74 (2006) 184406.
90. S. Dey, S. K. Dey, B. Ghosh, P. Dasgupta, A. Poddar, V. R. Reddy, S. Kumar, *J. Appl. Phys.* 114 (2013) 093901.
91. V. Šepelák, D. Baabe, D. Mienert, F.J. Litterst, K.D. Becker, *Scripta Mater.* 48 (2003) 961–966.
92. N. N. Greenwood, T. C. Gibb, *Mössbauer Spectroscopy* (1971) Springer Dordrecht.
93. M. M. Zeydi, S. J. Kalantarian, Z. Kazeminejad, *J. Iran. Chem. Soc.* 17 (2020) 3031 – 3094.
94. C. Caizer, M. Stefanescu, *Physica B* 327 (2003) 129–134.
95. W.H. Meiklejohn, C.P. Bean, *Phys. Rev.* 102 (1956) 1413.
96. W.H. Meiklejohn, C.P. Bean, *Phys. Rev.* 105 (1957) 904.
97. R. Mohan, M. P. Ghosh, S. Mukherjee, *Mater. Res. Express* 6 (2019) 056105.



Chapter 7

Study on structural, magnetic, hyperfine and optical properties and dye-degradation of self-assembled $\text{Co}_{0.5}\text{Zn}_{0.5}\text{Fe}_2\text{O}_4$ microspheres



7.1. Introduction

Ferrite nanoparticles are omnipresent due to their applicability in a wide range of disciplines encompassing ferrofluids, catalysis, biotechnology/biomedicine, hyperthermia, magnetic data storage and environmental remediation [1]. In most of the envisioned applications, the particles are found to perform best when their size is below a critical value, typically around 10–20 nm [1]. Then each particle consists of a single magnetic domain and behaves like a giant paramagnetic atom with a fast response to applied magnetic fields with negligible remanence and coercivity i.e., displays superparamagnetism. These prodigious features render superparamagnetic nanoparticles very fascinating for a broad range of biomedical applications as there is almost negligible risk of forming agglomerates at room temperature. Nevertheless, an inherent problem associated with particles in this size range is their intrinsic instability over long time periods. These nanoparticles are forced to form agglomerates to lessen the energy associated with their high surface area to volume ratio. Furthermore, bare metallic nanoparticles are highly active chemically and are easily oxidized in air, resulting generally in loss of magnetism and dispersibility [1]. Simply increasing the nanocrystal size would reduce instability related to high surface area but will induce a transition from superparamagnetic to ferromagnetic phase [1,2]. But if these nanocrystals are modified to form hierarchical, self-assembled structures then it would be possible to combine the size-dependent properties of individual nanoparticles along with a possibility to tune their collective properties arising due to interaction between subunits [2]. So, the process of self-aggregation has an advantage of retaining the superparamagnetic characteristics along with inhibiting the instability problem.

The trend of fabrication of self-assembled nano/microstructures using nanoparticles, nanorods, nanofibers etc., as building blocks have become a hot topic in recent research fields [3-7]. These structures formed by self-assembly provide new opportunities for optimizing,

tuning and enhancing the properties and performance of materials [3-7]. Colloidal nanoclusters of Fe_3O_4 (size ranging from 30 nm to 100 nm) composed of single magnetite crystals of 10 nm size were found to be highly advantageous as carrier in targeted drug delivery as compared to their separated individual nanodots [2]. ZnFe_2O_4 nanoparticles of size 15-20 nm assembled to form two different morphologies viz., rod like structure of diameter ~ 60 nm and flower like structure of diameter ~ 200 nm, which led to increase in their specific surface area and consequently their photocatalytic activity [7]. Self-assembled 3D suprastructures formed by Fe_3O_4 nanocrystals displayed increased cellular uptake by tumour cells as compared to individual nanocrystals constituting them [8]. Self-assembled superstructures of Fe_3O_4 and CoFe_2O_4 comprising nanoparticles with low magnetocrystalline anisotropy-to-dipolar energy ratio could be utilized in applications requiring long-term mechanical stability [9]. CoFe_2O_4 superstructures with higher magnetocrystalline anisotropy-to-dipolar ratios which can sustain permanent super-antiferromagnetic at room temperature, are recognized as promising candidates for use in a variety of applications [9]. Ferrite composite microspheres have shown enhancement in magnetic microwave absorption properties at low frequency owing to control in microsphere morphologies [10]. Self-assembled submicron spheres containing CuFe_2O_4 nanoparticles displayed superparamagnetic character and performed well as photocatalyst in degradation of methyl orange under visible and UV radiation [11]. Self-assembled hierarchical zinc ferrite nanospheres showed anti-proliferative behavior against the human breast cancer cell lines in invitro cytotoxicity study [12]. Self-assembled $\text{CuFe}_2\text{O}_4/\text{MoS}_2$ composite shows high absorption capabilities, thin thickness, and wide absorption bandwidth, thus, emerging as a promising candidate in the field of high-efficiency electromagnetic wave absorbing materials [13]. Self-assembled ZnFe_2O_4 microspheres with diameter ranging from 284-346 nm displays superparamagnetic behavior at room temperature [14]. Thus, the results from previous studies

establish that the hierarchical structures formed by self-assembly of ferrite nanoparticles show multifunctional behavior.

Zinc substituted cobalt ferrites have excelled over other ferrites not only because of their interesting magnetic features but also their broad scope of applications [15]. On varying the concentration of Zn^{2+} ions in nanosized $\text{Co}_{1-x}\text{Zn}_x\text{Fe}_2\text{O}_4$ ferrites, there is development of diverse magnetic behavior owing to modification in sublattice exchange interactions within the spinel lattice [16-21]. Nanometric $\text{Co}_{0.2}\text{Zn}_{0.8}\text{Fe}_2\text{O}_4$, $\text{Co}_{0.3}\text{Zn}_{0.7}\text{Fe}_2\text{O}_4$, $\text{Co}_{0.4}\text{Zn}_{0.6}\text{Fe}_2\text{O}_4$, $\text{Co}_{0.5}\text{Zn}_{0.5}\text{Fe}_2\text{O}_4$ and $\text{Co}_{0.6}\text{Zn}_{0.4}\text{Fe}_2\text{O}_4$ ferrites have shown presence of magnetic clusters in an infinite magnetic framework, cluster-paramagnetic phase, cluster glass phase, dual magnetic phase, non-collinear spin structure and superparamagnetic clusters[22-28].Doping of nonmagnetic Zn^{2+} ions in nanometric CoFe_2O_4 at a ratio of $X=0.5$ results in highest value of saturation magnetization due to increase in inter-sublattice A-O-B (JAB) exchange interactions between tetrahedral (A) site and octahedral [B] site of the spinel lattice [29-32].Nanosized $\text{Co}_{0.5}\text{Zn}_{0.5}\text{Fe}_2\text{O}_4$ has been found to be an optimum composition displaying superior magnetic properties in the series of [33].Nanometric $\text{Co}_x\text{Zn}_{1-x}\text{Fe}_2\text{O}_4$ has shown maximum saturation magnetization value for the as-prepared sample at $x = 0.5$ [34].Nanosized $\text{Co}_{0.5}\text{Zn}_{0.5}\text{Fe}_2\text{O}_4$ ferrite has proved to be potentially used as an excellent microwave absorber in the C-band [35].It has been found from literature survey that on tuning the shape and size of $\text{Co}_{1-x}\text{Zn}_x\text{Fe}_2\text{O}_4$ ferrites through different synthesis procedure, there is evolution in their magnetic properties and application potential as well [15-21]. So, choice of synthesis procedure is of particular importance in determining properties of $\text{Co}_{1-x}\text{Zn}_x\text{Fe}_2\text{O}_4$ ferrites and their effectiveness in technological applications [36-38]. Chemical methods assisted by surfactants have paved a unique way to develop size- and shape-tailored magnetic nanocrystals by judiciously regulating the growth processes in liquid media [39,40]. These methods may be either single-step or more complex multiple-step

solution-phase routes. The former is convenient, cheaper, and non-time consuming while the latter is only beneficial for obtaining better size distribution [41]. In recent times, one-step and facile hydrothermal/solvothermal method has appeared as a panacea to produce both nanosized and micro sized ferrites by simply varying the reaction conditions [2,39-41]. We have prepared self-assembled $\text{Co}_{0.3}\text{Zn}_{0.7}\text{Fe}_2\text{O}_4$ microspheres using solvothermal technique and found that these microspheres display enhancement in magnetic properties and electrochemical performance in comparison to their nanosized counterpart [42]. We have also synthesized nanosized $\text{Co}_{0.3}\text{Zn}_{0.7}\text{Fe}_2\text{O}_4$ by hydrothermal method and they acted as efficient catalyst in photodegradation of Congo Red dye under UV irradiation [43].

Now-a-days, water pollution through industrial effluents have become a major area of concern [44]. These pollutants render water unsuitable for human use. So, the scientific community has been trying to develop substances which can absorb these pollutants from the water bodies and make them fit for usage. In this regard, nano ferrites have played an important role in the removal of toxic contaminants from water [45]. Among these toxic pollutants, dyes have carcinogenic effects, are very stable and extremely difficult to degrade [44-46]. Thus, dye degradation happens to be a challenging problem for researchers. There are several techniques for dye removal viz., electrochemical degradation, coagulation, aerobic and anaerobic microbial degradation, ozonation, adsorption, precipitation, and photocatalytic degradation [47-49]. Among all these procedures, photocatalytic degradation is one of the simplest and cost-saving techniques [50-52]. Literature study shows that ferrite nanoparticles have shown excellent catalytic activity in the photodegradation of industrial dyes [53,54].

Recently, we have performed a detailed study on structural, microstructural, magnetic, and hyperfine properties of the $\text{Co}_{0.5}\text{Zn}_{0.5}\text{Fe}_2\text{O}_4$ nanoparticle system and found to our very interest that these nanosized ferrites displayed mixed magnetic phase in room temperature [55]. So, it will be interesting to examine the magnetic character of self-assembled spheres

composed of $\text{Co}_{0.5}\text{Zn}_{0.5}\text{Fe}_2\text{O}_4$ nanoparticles. Further, it will help us to compare the structural, magnetic, hyperfine, and photocatalytic properties of both $\text{Co}_{0.5}\text{Zn}_{0.5}\text{Fe}_2\text{O}_4$ nanoparticles and microspheres. In this background, we have synthesised $\text{Co}_{0.5}\text{Zn}_{0.5}\text{Fe}_2\text{O}_4$ microspheres by simple solvothermal technique and studied their crystal structure, morphology, optical band structure and colloidal stability in detail. Moreover, we have digged into the effect of the formation of microspheres by nanoparticle self-assembly on the evolution of magnetic and hyperfine properties. The catalytic efficiency of the sample in degradation of an industrial dye viz., Congo Red has also been tested thoroughly under dark as well as light conditions.

7.2. Experimental Methods

7.2.1. Synthesis Procedure of $\text{Co}_{0.5}\text{Zn}_{0.5}\text{Fe}_2\text{O}_4$ Microspheres

Sigma-Aldrich make $\text{CoCl}_2 \cdot 6\text{H}_2\text{O}$, $\text{ZnCl}_2 \cdot 4\text{H}_2\text{O}$, and $\text{FeCl}_3 \cdot 6\text{H}_2\text{O}$ of extremely high purity ($\sim 99.99\%$) were used without further purification. Sodium acetate (NaAc), ethylene glycol (EG) and polyethylene glycol (PEG, MW = 4000) of analytical purity were procured from Merck India. $\text{Co}_{0.5}\text{Zn}_{0.5}\text{Fe}_2\text{O}_4$ microspheres (CZ50) were synthesized by a facile solvothermal method [42]. For this purpose, 10 mM $\text{FeCl}_3 \cdot 6\text{H}_2\text{O}$, 2.5 mM $\text{CoCl}_2 \cdot 6\text{H}_2\text{O}$ and 2.5 mM $\text{ZnSO}_4 \cdot 6\text{H}_2\text{O}$ were mixed into 80 ml of EG by continuous magnetic stirring. Following that, 7.2 g of NaAc along with 2 g of surfactant PEG-4000 were added to the above mixture at room temperature and stirred for 2 h giving rise to a homogeneous brown solution. After this, the solution was poured into a stainless-steel autoclave of 100 ml capacity and heated at 190°C for 18 h in a hydrothermal oven. The autoclave was left to cool down naturally and then removed from the oven. Then the contents of the autoclave (thick black precipitate) were collected and later cleaned numerous times with deionized water and ethanol through centrifugation in order to remove organic and inorganic leftovers. Finally, the precipitate was dried in vacuum at 60°C for 7 h to obtain a fine powder of CZ50.

7.2.2. Characterization Techniques

The powder x-ray diffraction (PXRD) pattern of CZ50 over the 2θ range of $20\text{--}80^\circ$ was recorded using a Bruker D8 Advance diffractometer. Field-emission scanning electron microscopy (FESEM, FEI INSPECT F50) and transmission electron microscopy (JEOL JEM 2100) were employed to unravel the morphological features of the sample. The selected area electron diffraction (SAED) pattern was recorded using a JEOL JEM 2100 instrument. Bruker EDS system attached with HRTEM equipment was used to examine the constituent elements in CZ50. The UV-Vis and Photoluminescence spectra were obtained using a JASCO V650 spectrophotometer. Zeta potential and size distribution of the sample were measured using a Zetasizer Nano ZS (Malvern Instruments, UK). The magnetic property of CZ50 was explored by a Cryogenic vibrating sample magnetometer (VSM). The room temperature Mössbauer spectrum of the sample was recorded by utilising a constant acceleration drive (CMTE-250) equipped with a $10\text{mCi } ^{57}\text{Co}$ source embedded in the Rh matrix. The low temperature Mössbauer spectrum was recorded using a JANIS SVT-400 MOSS cryostat system both in the presence of a 5 T external field and without field.

7.2.3. Photocatalytic experiment

The photocatalytic degradation potential of CZ50 was tested considering Congo Red (CR) as a representative pollutant dye. For aforesaid purpose, 15 mg of CR dye was dissolved in 1 L of deionized (DI) water to prepare the stock solution. Then, required amount of CZ50 was added to 20 ml of CR stock solution at room temperature. This mixture was sonicated vigorously for 30 min in dark to achieve adsorption-desorption equilibrium between CR dye solution and CZ50. Then this mixture was kept in undisturbed state before subjecting the mixture to dark conditions and visible and UV light irradiation, respectively. The mixture was incessantly stirred by ultrasonication to avoid agglomeration within the samples throughout visible and UV irradiation. Aliquots of certain amount were withdrawn from the reaction

medium at different time intervals. The catalyst was separated from the solution by centrifugation. The change of absorbance of the characteristic peaks of CR dye degradation was inspected by collecting UV-Vis spectra of the leftover filtrate. The best performance in terms of catalytic activity was found to be for 8 mg of catalyst. For both dark and light mediated degradation, 8 mg of CZ50 was added in 20 ml of the stock solution and above procedure was conducted. The recyclability of the catalyst was also examined by magnetic extraction of the catalyst from the solution and repeating the above said procedure.

7.3. Results

7.3.1. Structural, Microstructural, and Morphological Study

Fig. 1 shows the PXRD pattern of CZ50, which exhibit strong and well-defined reflection peak positions matching well with those from the standard JCPDS patterns (JCPDS card no 89-1012 and 22-1086 for zinc ferrite and cobalt ferrite) and devoid of any characteristic impure phases. DICVOL06 and TREOR90 of the FullProf package and NTREOR of the EXPO2009 package were utilized for indexing the PXRD pattern adopting the procedure described in our previous work [42]. The sample crystallized in $Fd\bar{3}m$ space group, which was determined by FINDSPACE of the EXPO2009 package [56]. MAUD2.33 software package [57] was employed to get detailed information about the structural parameters and constituent phase of the sample. The fitted PXRD pattern has been presented in Fig. 1 and the refinement parameters have been listed in Table 1. The results indicate that CZ50 is a single-phase cubic spinel ferrite, crystallized in the $Fd\bar{3}m$ space group. Furthermore, GSAS software [58] was employed to extract precise information on crystal structure of the sample considering the standard methodology reported previously [17,59] and the results are presented in Fig. 2 and, Tables 2 and 3. The experimentally obtained PXRD data are in good agreement with the fitted patterns. The values of lattice parameter obtained for CZ50 are in good accord when compared with other Co-Zn ferrite systems

[21,22,29,30,31,60,61]. This clearly rules out the chances of occurrence of any impurity phases in the sample. The structural formula of CZ50: $(\text{Zn}^{2+}_{0.33}\text{Fe}^{3+}_{0.67})_{\text{A}}[\text{Zn}^{2+}_{0.17}\text{Co}^{2+}_{0.50}\text{Fe}^{3+}_{1.33}]_{\text{B}}\text{O}_4$. In order to fit the PXRD data using GSAS software, we have tried fitting by inserting Co^{2+} ions at (A) site, but the refinement parameters viz., R_p , R_{wp} , and GOF appeared unacceptable. Hence, it can be ascertained that Co^{2+} ions have not occupied (A) site of the spinel lattice.

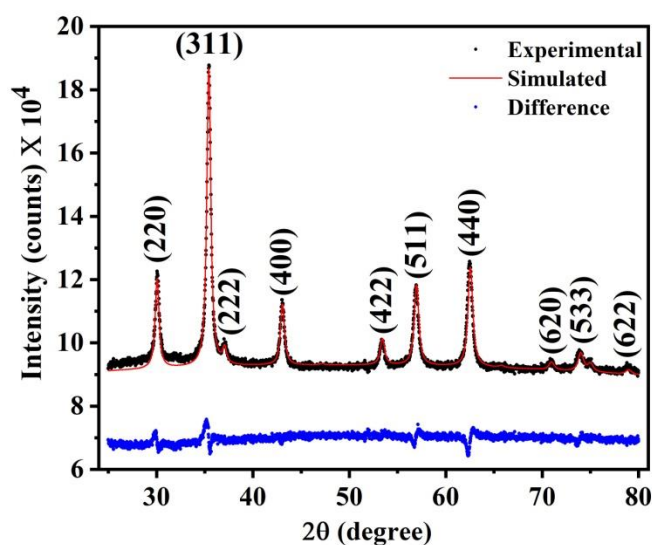


Fig.1. PXRD pattern of the sample obtained after MAUD analysis. The experimental data and the simulated pattern are represented by black dots and continuous red line, respectively. The difference between the experimental and simulated curve is plotted at the bottom with continuous blue line.

Table 1 Crystal data and refinement parameters of the sample obtained from MAUD

Parameters	CZ50
Crystal System	cubic
Space group	Fd-3m
Crystallite size (nm)	25
Microstrain	1.6×10^{-4}
Lattice parameter ($a(\text{\AA})$)	8.397
Density (g cm^{-3})	5.28
R_{wp}	0.13
R_{exp}	0.15
GOF	1.17

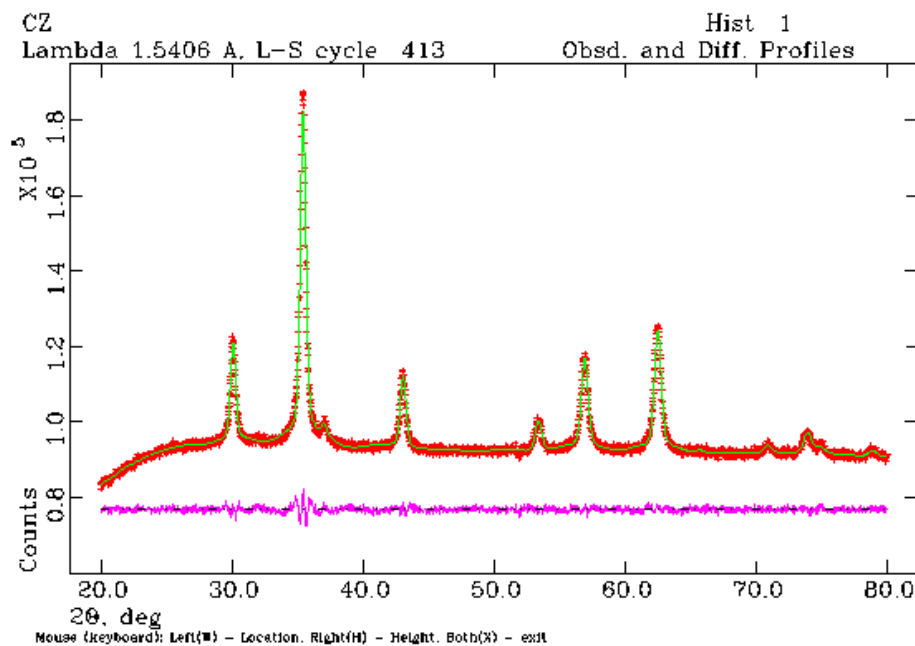


Fig.2. Indexed powder PXRD pattern of the sample (red dots) and the simulated Rietveld refinement plot (continuous green line) obtained by fitting the experimental powder PXRD pattern using GSAS program. The respective residue is plotted at the bottom (pink line).

Table 2 Structural and microstructural parameters along with metal-oxygen (M-O) bond angles and bond lengths obtained from Rietveld analysis of PXRD of the samples by GSAS program

Parameters	CZ5050
Formula weight	475.72
Crystal System	Fd $\bar{3}$ m
Lattice parameter (\AA)	8.41(4)
Density (g cm^{-3})	5.311
Volume (\AA^3)	594.959 (8)
Metal-Oxygen bond length (\AA)	1.891 (A-site) 2.063 (B-site)
Metal-Oxygen bond angle	109.47° (A-site) 92.27° (B-site)

Table 3 Fractional coordinates and occupancy of different ions obtained from the Rietveld refinement by GSAS program

Ions	x	y	Z	Occupancy (± 0.003)
Zn (A)	0.125000	0.125000	0.125000	0.3300
Fe (A)	0.125000	0.125000	0.125000	0.6700
Zn (A)	0.500000	0.500000	0.500000	0.0850
Co (B)	0.500000	0.500000	0.500000	0.2500
Fe (B)	0.500000	0.500000	0.500000	0.6650
O	0.25482 (3)	0.25482 (3)	0.25482 (3)	1.0000

The FESEM micrograph (Fig.3(a)) displays mesoporous clusters of $\text{Co}_{0.5}\text{Zn}_{0.5}\text{Fe}_2\text{O}_4$ nanoparticles with average diameter of ~ 140 nm (inset of Fig. 3(a)). The particle size distribution and high-resolution TEM (HRTEM) images along with the SAED pattern are shown in Fig.3(b), (c), (d) respectively. The TEM study suggests that CZ50 is mostly monodisperse with average diameter of ~ 137 nm. Careful examination of HRTEM image has revealed that CZ50 is composed of $\text{Co}_{0.5}\text{Zn}_{0.5}\text{Fe}_2\text{O}_4$ nanoparticles of ~ 27 nm size (Fig. 3(b)), agreeing well with the value of crystallite size (~ 25 nm) obtained from the Rietveld refinement of the PXRD data. Owing to the difficulty in accurate distinction of constituent particles of CZ50 there is a slight mismatch in the crystallite size and the particle size. Presence of clear lattice fringes in the HRTEM micrograph (inset of Fig.3(b)) and bright Debye–Scherrer ring in the selected area diffraction (SAED) pattern (Fig.3(d)) indicate good crystallinity of the sample. The crystallographic ‘d’ values obtained from the radius of the rings corresponding to different lattice spacings of the SAED pattern corroborate with those acquired from the PXRD study. The distinct peaks originating from the constituent elements (Co, Zn, Fe, and O) were clearly observed in the EDS spectra of the sample (Fig. 4). The atomic percentage of Co, Zn, and Fe in CZ50 obtained from the EDS spectrum is 6.9:6.4:12.4, which confirm that the samples are in proper stoichiometry.

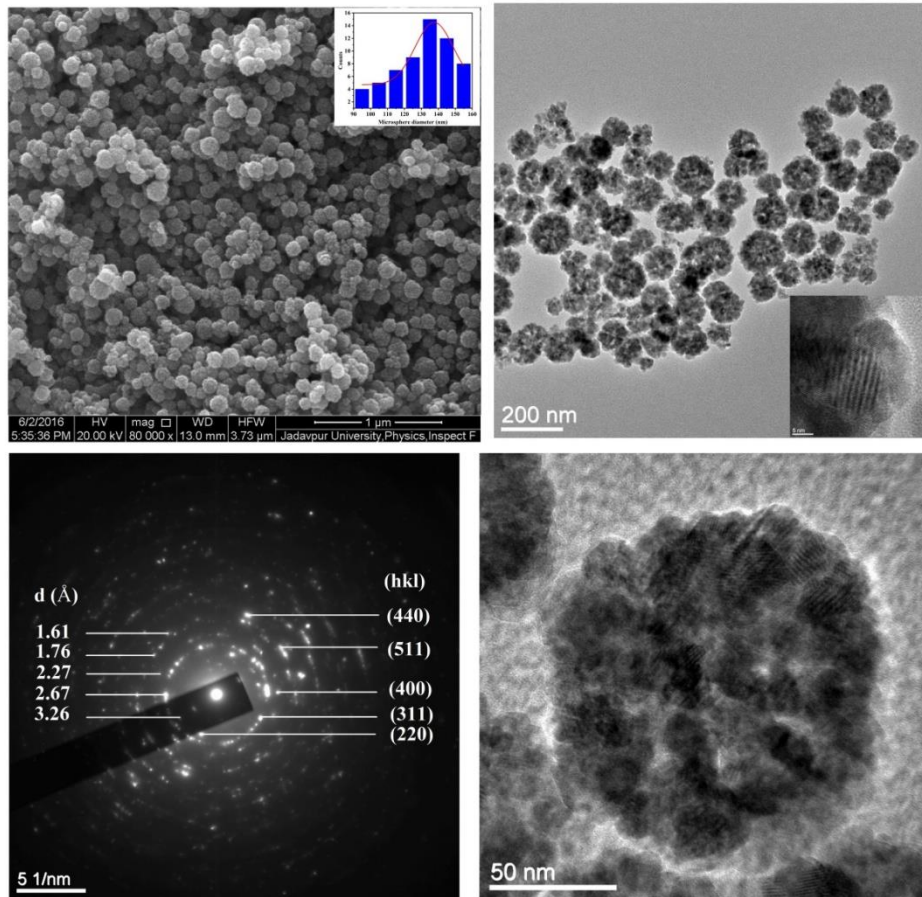


Fig.3 (a) FESEM morphographs with particle size histogram in the inset (b) TEM micrograph showing size distribution along with HRTEM showing lattice fringes in the inset (c) single particle HRTEM image showing particle distribution and (d) SAED pattern of the sample.

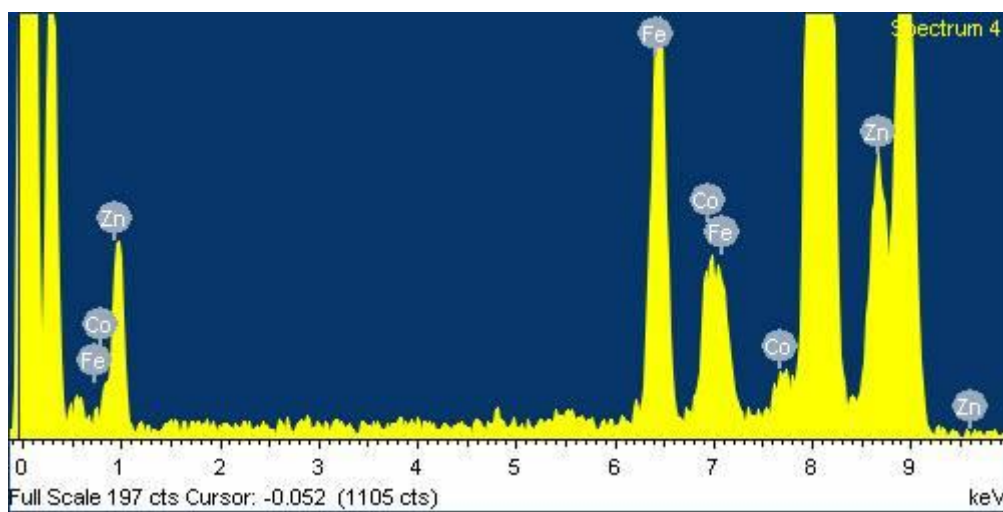


Fig.4 EDX spectrum of the sample

7.3.2. UV-Vis and PL study

UV–Vis spectrum of the sample was recorded to investigate the optical properties and determine the band gap of the sample. The spectrum of CZ50 is presented in Fig.5 (a) and it displays an absorption hump at around 405 nm, which can be attributed to the d-orbital transitions of Fe^{3+} [62]. Crystallite size, dopant concentration, and structural parameters of the sample are determining factors of band gap of samples [42]. Moreover, both direct and indirect transitions are possible in ferrites [63]. The Kubelka–Munk function has been employed to calculate the absorption coefficient $(\alpha) = F(R) \frac{(1-R)^2}{2R}$, where $F(R)$ is Kubelka–Munk function and R , the reflectance [64]. Further, the band gap values have been calculated using Tauc relation as follows $\alpha h\nu = A(h\nu - E_g)^n$, where $n = \frac{1}{2}$ and 2 for direct and indirect transitions, respectively [64]. The plots of $(\alpha h\nu)^2$ versus $h\nu$ and $(\alpha h\nu)^{1/2}$ versus $h\nu$ are presented in Fig. 6 (a) and (b), respectively. The estimated direct and indirect band gaps of CZ50 are 3.25 and 2.3 eV, respectively. Band gap value of undoped cobalt ferrite is 2.56 eV [64]. The value of direct band gap of the sample has increased as compared to bulk cobalt ferrite. Since the microspheres are composed of nanoparticles, so it seems that band gap of the sample has increased due to quantum confinement phenomenon [65].

The photoluminescence (PL) spectrum was recorded to investigate the recombination (or) efficiency of photogenerated charge carrier, energetic position of sub band gap and defects [66]. The sample was excited at a wavelength of 350 nm and the recorded emission spectrum is presented in Fig. 5 (b). The PL peak falls in the visible range of 415-450 nm (violet emission) and can be attributed to radiating defects related to the interface traps existing at the grain boundaries [64]. Thus, emission characteristics in the sample are governed by defect-controlled processes.

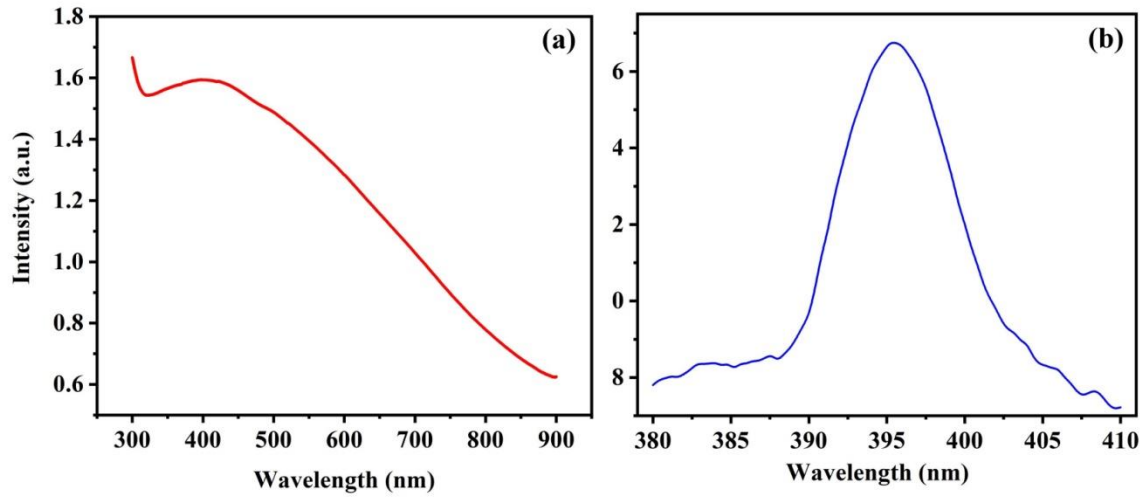


Fig.5. (a) UV-Vis spectrum of the sample and (b) PL spectrum of the sample excited at a wavelength of 350 nm

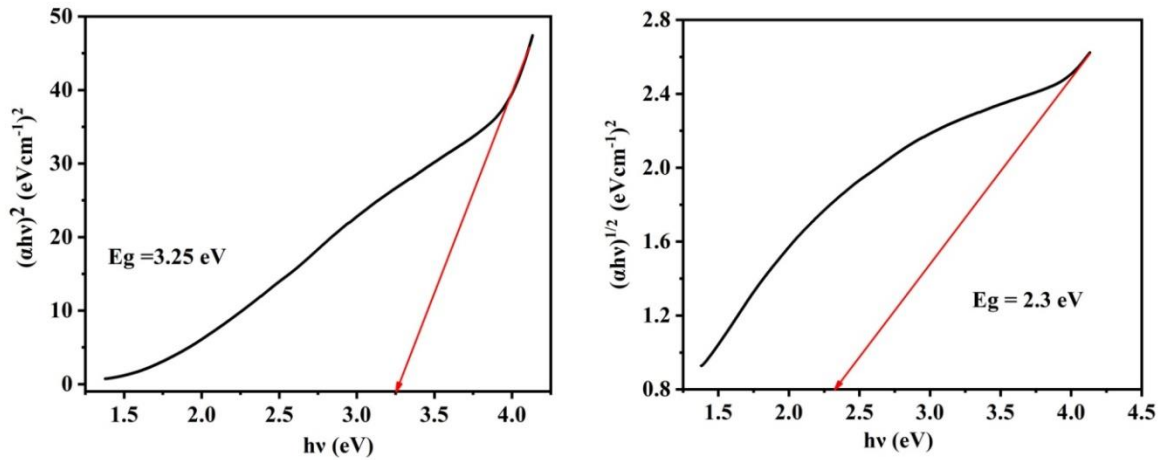


Fig.6. Plots of (a) $(\alpha h\nu)^2$ versus $h\nu$ and (b) $(\alpha h\nu)^{1/2}$ versus $h\nu$

7.3.3. DLS and Zeta potential study

DLS is one of the most popular methods to determine the hydrodynamic diameter on an ensemble average [67]. The results of DLS are expressed in terms of Z-average and polydispersity index. For an ensemble of particles with discrete size distribution, Z-average is the averaged hydrodynamic diameter determined by DLS [67]. The results of DLS for CZ50

are summarized in Fig. 7 (a). The Z-average for CZ50 is ~ 330 nm. From SEM & TEM study, the ‘true diameter’ of the microspheres is ~ 140 nm. The microspheres have been prepared using CH_3COONa and PEG-4000 as binding agents and they form a layer on the microsphere surface. This layer is responsible for the difference in the diameter from TEM and DLS study [67]. It has been found that the diameter of magnesium ferrite microspheres prepared by molten salt route obtained through SEM and DLS are consistent (650 ± 50) nm [68]. Xie et al., have observed that the organic PEG_{6000} layer on Fe_3O_4 nanoparticles was not visible in TEM but could be characterized by DLS study [69]. So, it is apparent that the organic layer on the microspheres cannot be detected in TEM as it is burnt out in high energy electron beam of TEM. But DLS technique cannot differentiate between inorganic and organic layer [70] and so gives an overall diameter. Moreover, for an ensemble of particles with a range of sizes (bimodal distribution), the calculated Z-average carries extraneous size information [67]. The value of polydispersity index (0.285) reveals that there is a moderate distribution in the diameters of the microspheres.

Zeta potential measurements help us in determining the charge of nanoparticles in different environments and to understand their dispersion stability [70]. Presence of positive or negative charge on the surface of nanoparticles can be identified by a positive or negative zeta potential, respectively, and are directly proportional to the value of zeta potential [70]. The results of zeta potential measurements for CZ50 are summarized in Fig. 7 (b). The value of zeta potential for CZ50 is 1.05 mV, asserting that the surficial charge of the microspheres is positive. Generally, higher zeta potentials indicate stable nanoparticle systems [62]. CZ50 appears to be less stable in the dispersion media due to low electrostatic repulsive forces between the microspheres [40]. It has been found that upon incorporation of zinc in cobalt ferrite, there is an increase in agglomeration behavior [62].

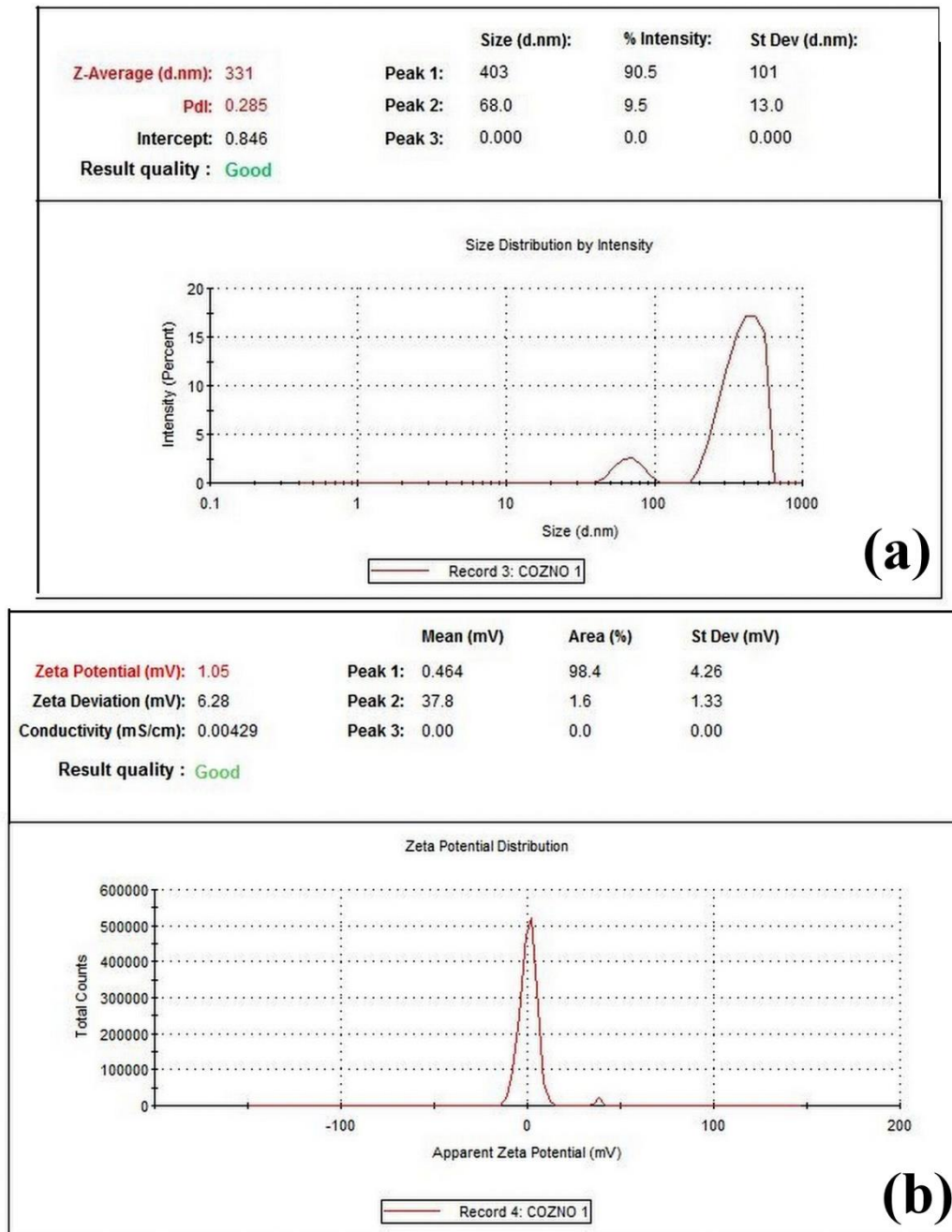


Fig.7. (a) DLS measurement and (b) Zeta potential measurement results for the sample

7.3.4. FTIR Study

The FTIR spectrum of a substance is always exclusive and characteristic. Thus, FTIR spectroscopy is a swift and relatively low-priced technique for characterizing compounds [71-74]. The FTIR spectrum of CZ50 recorded in the wavenumber range of 400 to 4000 cm^{-1} is displayed in Fig.8. It may be noted that ferrites show two broad bands at ~ 590 and 405

cm^{-1} owing to stretching vibration of (A) and [B] site metal–oxygen (M–O) bonds, respectively [75]. In case of present sample, absorption bands appear at 560 and 424 cm^{-1} , respectively for (A) and [B] site vibrations. So, it can be ascertained that the sample is a cubic spinel ferrite. The part of the FTIR spectrum from wavenumber range of 900 to 4000 cm^{-1} is separately shown in the inset of Fig. 8 since the peaks in this part are not distinguishable in the total spectrum. The inset of Fig. 8 shows vibrations at 1100, 1343, 1560, 1688, 2910, 3009, 3358 cm^{-1} . It is pertinent to mention that the microspheres have been synthesized by using PEG-4000 as the binding agent. The FTIR spectrum of PEG-4000 displays principal peaks at wave numbers of 1074.39, 1240.27, 1528.64, 1641.48, 2946.36, 3275.24 and 3421.83 cm^{-1} corresponding to C–N vibrations, –C–O stretching, N–H bending vibration for secondary amines, C=C stretching of α,β -unsaturated ring, C–H stretching, O–H stretching and N–H amide ben-ding, respectively [77]. So, the results from DLS study corroborate with that of FTIR study.

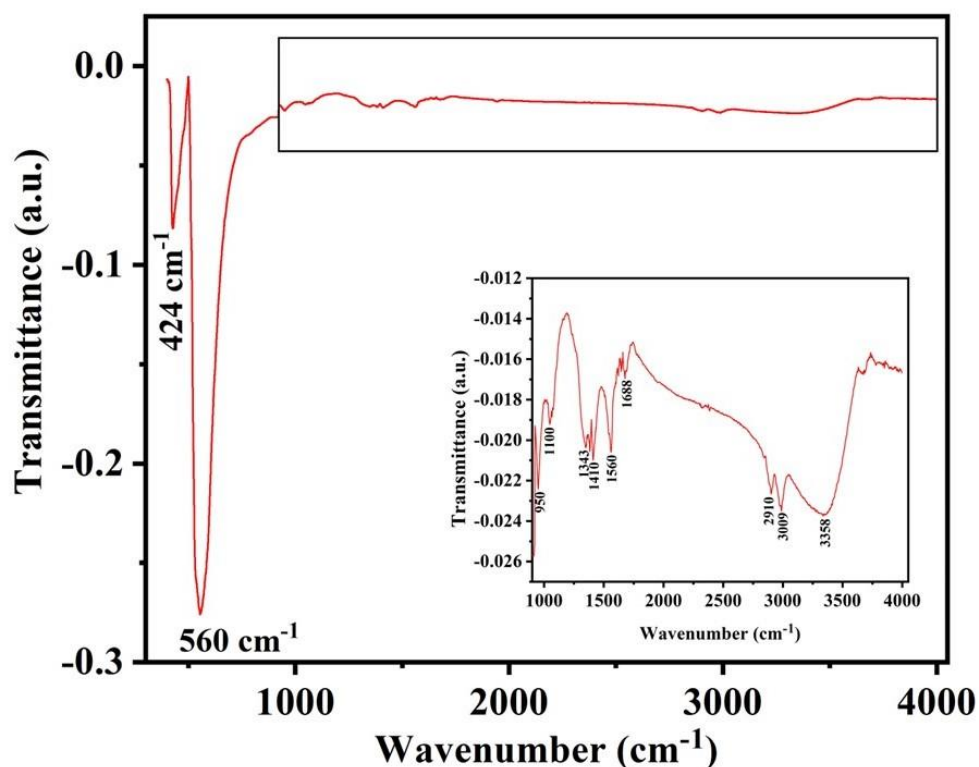


Fig.8. FTIR spectrum of CZ50

7.3.5. Magnetic and hyperfine study

The magnetization versus temperature curves of the sample were recorded in the temperature range of 5 – 300 K following standard zero-field cooled (ZFC) and field cooled (FC) magnetization protocol [55] at external magnetic fields of 100 and 500 Oe (Fig.9 (a) and (b)). The ZFC magnetization curve decreases with decreasing temperature from 300 to 100 K. Below 100 K, the magnetization value decreases very slowly upto 25 K and then drops suddenly below 25 K. The ZFC curve shows two distinct features viz., a sharp drop in magnetization at freezing temperature $T_f=25$ K and a small shoulder at $T_s=100$ K. The position of T_f is almost field independent and ZFC magnetization remains almost constant between T_s and T_f . The FC magnetization initially decreases monotonically with decreasing temperature in the range from 300 K to 250 K at 100 Oe which corresponds to non-interacting regions and then shows constant value from 250 K to 100 K (showing temperature independence), and slightly increases below 100 K upto 5 K. This may be a consequence of finite-size interaction effects which occur from dipolar interactions and interparticle coupling interactions [77].

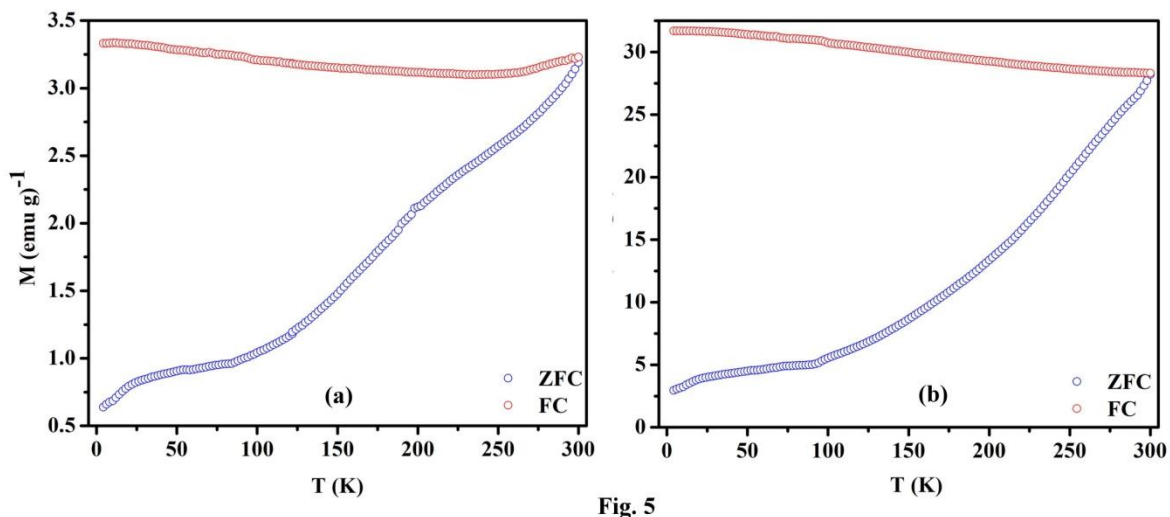


Fig.9. ZFC-FC magnetization curves of the sample at (a) 100 Oe and (b) 500 Oe. The FC and ZFC magnetization are represented by red and the blue lines, respectively.

The variations of magnetization (M) as a function of the external magnetic field (H) at 300, 100 and 5 K in the field range of ± 5 T are shown in Fig. 10. The saturation magnetizations (M_{SAT}) of the sample have been calculated from the M versus $1/H$ plot using the law of approach to saturation. The values of M_{SAT} and coercivity (H_C) at 300, 100 and 5 K are listed in Table 4. The values of M_{SAT} increase gradually with the decrease in temperature due to development of magnetic ordering [55]. There is a steep increase in the value of H_C at 5 K, which may be attributed to the freezing of spins [55].

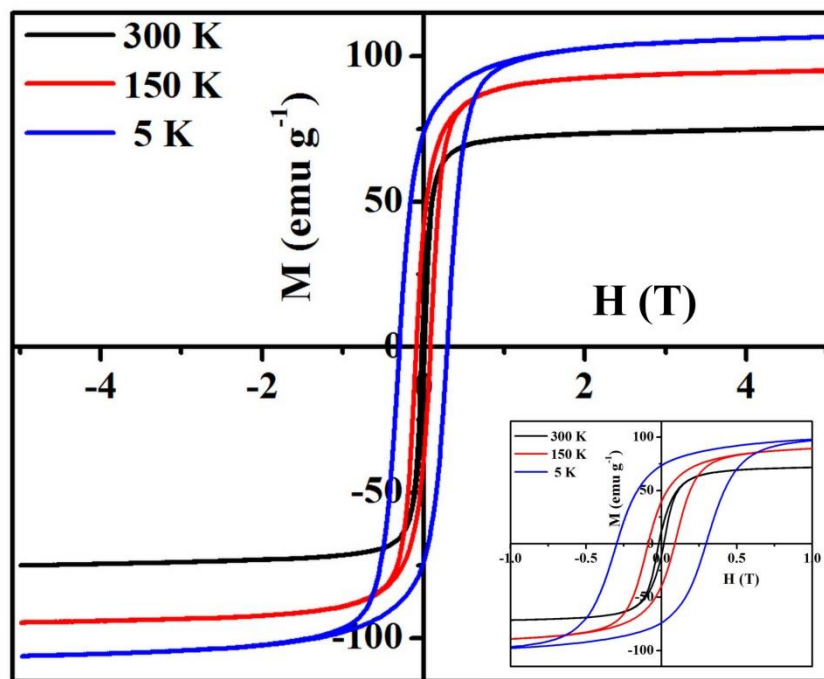


Fig.10. M-H (hysteresis) loop of the sample at (a) 300 K, (b) 150 K and (c) 5 K shown between ± 5 T. The M-H loops are shown in the inset between ± 1.0 T for shake of clarity

Table 4 Values of crystallite size obtained from PXRD, saturation magnetization (M_{SAT}) and coercivity (H_C)

Sl.No	T (K)	M_{SAT} (emu/g)	H_C (Oe)
1.	300	77.7	165
2.	150	97.3	895
3.	5	109.7	2963

^{57}Fe Mössbauer spectroscopy is a trustworthy tool to determine the valency of iron ions and investigate the hyperfine interactions of the magnetic systems. Fig.11 shows the fitted room temperature (300 K) Mössbauer spectrum of CZ50 and the fitting parameters obtained using “Lorentzian site analysis” method of the Recoil program [78] are listed in Table 5. The spectrum exhibits a diffused sextet arising due to the collective behaviour of ensemble of magnetic nanoparticles which have aggregated to form the microspheres. The 300 K Mössbauer spectrum has been fitted with two hyperfine split sextets and a doublet. The values of the isomer shift (IS) indicate towards existence of only the high-spin Fe^{3+} ions in the sample [79]. The simultaneous occurrence of both the sextets and a doublet (90 % and 10 %, respectively) ascertains the samples consist of both superparamagnetic and magnetically well-ordered particles at room temperature [55]. Although CZ50 is an aggregation of large numbers of individual nanoparticles, SPM relaxation characteristic of single nanoparticle could not be absolutely wiped out from their aggregate. Aggregation of nanoparticles to form microspheres resulted in interparticle coupling interactions within the nanoparticle ensemble. So, anisotropy energy barrier cannot be defined for individual particle and CZ50 microspheres display collective magnetic state.

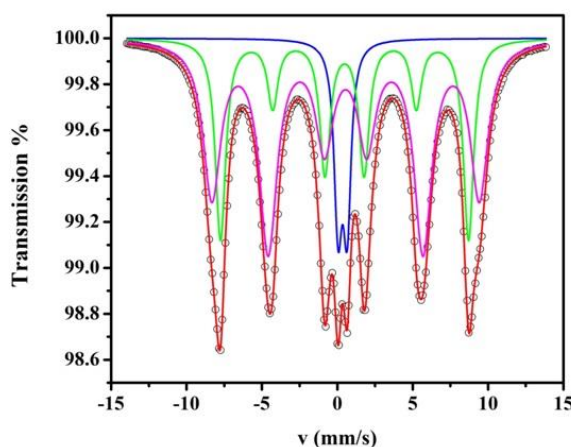


Fig.11. Mössbauer spectra of CZ5050 at 300 K (without field) fitted by Lorentzian site analysis method of the Recoil program

Table 5 Hyperfine parameters obtained by fitting the Mössbauer spectra at 300 K.

Spectra	IS (± 0.02) (mm s ⁻¹)	2 ε (± 0.03) (mm s ⁻¹)	HMF (± 0.1) (T)	Width (± 0.03) (mm s ⁻¹)	Area (± 0.3) (%)
[Fe ³⁺ _A]	0.48	0.0	51.0	0.40	30.0
[Fe ³⁺ _B]	0.55	0.0	55.0	0.70	60.0
Doublet	0.35	0.6	-	0.30	10.0

Infield Mössbauer spectroscopy is one of the most useful techniques for probing the cation distribution and the spin disorder [80]. In order to determine the cation distribution and the relative occupancy of Fe³⁺ ions at tetrahedral (A) and octahedral [B] sites of the spinel lattice, Mössbauer spectra were recorded at 5 K and while subjecting the sample to 5 T external magnetic field (applied parallel to gamma rays) as well. The infield spectrum has been fitted using the “Lorentzian site analysis” method of the Recoil program by considering a pair of sextets assigned to the (A) and [B] site iron ions. The fitted spectrum is displayed in Fig. 12 (a) and the hyperfine parameters are enlisted in Table 6. The feeble intensities of the 2nd and 5th lines in the spectrum suggest that some of the surface spins are canted [79]. There is presence of canted spins in the [B] site of the spinel lattice with canting angle of 17° (see Table 6), which has been estimated using standard formulae [81,82]. The relative ratio of Fe³⁺ ions among (A) and [B] sites (as determined from the areal intensity of the sextets corresponding to the (A) and [B] sites) is 0.5, whereas equilibrium ratio should be 0.33 [79]. Hence, it is apparent that Fe³⁺ ions have migrated from [B] to (A) sites. It may be noted that Co²⁺ has a strong tendency of occupying the [B] site owing to its favourable atomic radius and charge distribution in the octahedral crystal field, thus the estimated structural formula of CZ50 stands as (Zn²⁺_{0.33}Fe³⁺_{0.67})_A[Zn²⁺_{0.17}Co²⁺_{0.50}Fe³⁺_{1.33}]_BO₄. The 5 K without field Mössbauer spectrum has been fitted using the ratio of Fe³⁺ ions among (A) and [B] sites as obtained by fitting the infield pattern. The 5 K without field spectrum (Fig.12 (b)) has fitted with the experimental data very well and the values of the hyperfine parameters are enlisted in Table 6. This validates the observations of the infield study. Thus, it is evident from the

Mössbauer study that CZ50 is ferrimagnetically ordered at 5 K, substantial migration of iron ions from [B] to (A) site has occurred and canting of surface spins has taken place.

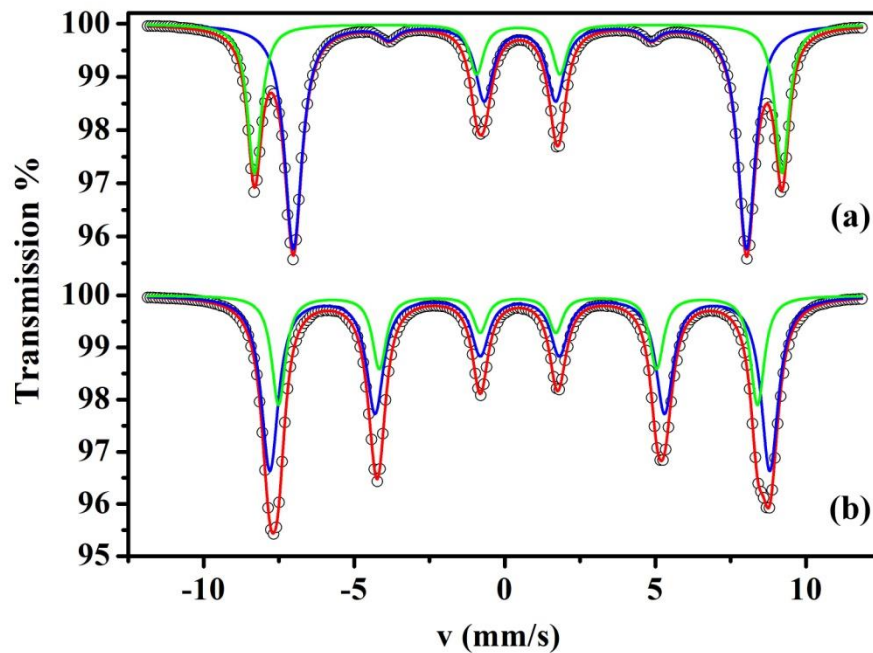


Fig.12. Mössbauer spectra at 5 K with 5 T external magnetic field and 5 K without field of the sample fitted by Lorentzian site analysis method of the Recoil program

Table 6 Values of infield and zero field Mössbauer parameters of the samples at 5 K determined by Lorentzian profile fitting

Temperature	Site	Width	IS	2ε	B _{eff} ^a	B _{hf}	A ₂₃	θ ^b	Area
/Field		(mm s ⁻¹)	(mm s ⁻¹)	(mm s ⁻¹)	(T)	(T)		(Degree)	(%)
		(±0.03)	(±0.03)	(±0.03)	(±0.3)	(±0.2)		(±0.02)	(±0.2)
5 K /5 T	[Fe ³⁺ _A]	0.26	0.44	0.0	54.3	49.3 ^c	0.00	0.00	34
	[Fe ³⁺ _B]	0.33	0.50	0.0	46.7	51.5 ^c	0.17	17.0	66
5 K /0 T	[Fe ³⁺ _A]	0.26	0.44	0.0	-	49.3	-	-	34
	[Fe ³⁺ _B]	0.33	0.50	0.0	-	51.5	-	-	66

^a Observed HMF (BHF) is the vector sum of the internal HMF and the external applied magnetic field.

^b The average canting angle estimated from the ratio of the intensities of lines 2 and 3 from each subspectra, $I_2/I_3(A_{23})$ according to $\theta = \arccos[(4 - I_2/I_3)/(4 + I_2/I_3)]^{1/2}$, where $I_2/I_3 = A_{23}$.

^c Estimated according to the relationship of B_{eff}, B_{hf} and applied field.

7.3.6. Photocatalytic study

CZ50 microspheres were used as photocatalyst for degradation of Congo Red (CR) dye. In order to find the best conditions for dye degradation, different parameters like effect of initial dye concentration, irradiation time and dark, visible and UV light irradiation were investigated in detail. CR is a structurally stable anionic dye possessing absorption bands at 343 nm and 496 nm owing to the $p-p^*$ transition of the aromatic ring and to the $n-p^*$ transition of the lone pair present in the N atom of the chromophoric $-NLN-$ azo moiety, respectively [83]. The degradation of the CR dye was monitored by observing the decrease in the intensity of the absorption band at 496 nm, indicating cleavage of the $-NLN-$ bond [83].

7.3.6.1. Critical catalyst study

The effect of catalyst amount was studied by adding 2 – 20 mg of catalyst in 20 ml of the as prepared stock solution. Initially, upon increasing the catalyst dosage from 2 – 10 mg, enhancement of degradation efficiency occurs as was observed from the reduction in the absorbance intensity of the characteristic peak of CR dye (Fig. 13). This may be due to an increase in the number of active reaction sites and reactive radicals [84]. Further, as the catalyst amount was increased to 20 mg, a decrease in the efficiency of dye degradation occurred. This may be possibly due to agglomeration of the catalyst, which subsequently minimized the active sites required for catalysis [85]. From Fig. 13, it appears that 8 mg is the best amount of catalyst for achieving the finest result.

7.3.6.2. Dark degradation study

Dark catalysis has become a potential method for effective degradation of industrial dyes [86]. This process neither requires photon energy nor any external energy as compared to photo degradation and heterogenous-Fenton catalysis [86]. So, the degradation efficiency of CR dye in dark condition was studied by mingling 8 mg of CZ50 microspheres with 20 ml of CR standard solution.

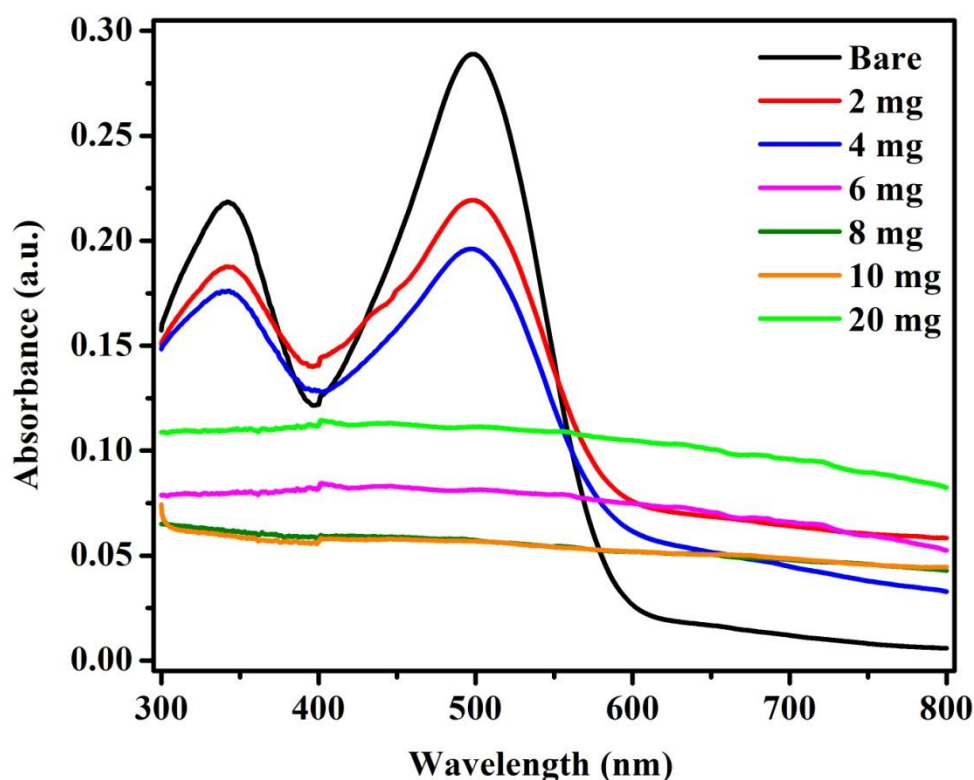


Fig.13. Critical catalyst study for degradation of Congo red dye

The absorption spectra of the solutions found after separation by a magnet and purification of the aliquot part obtained from the CR solution broken down by CZ50 after 30, 60, 90, 120, 150, 180 and 210 min under dark conditions are presented in Fig. 14(a). It may be noted that there is a gradual decline in the intensity of the absorption peak of CR with increasing reaction time indicating degradation of CR dye (Fig. 14(a)). The empirically obtained degradation percentage of CR by CZ50 at subsequent times is shown in Fig. 14(b). The degradation percentage was calculated using the formula $\{(C_0 - C_t)/C_0\} \times 100 \%$, where C_0 and C_t corresponds to the concentration of CR initially and after degradation for time 't' [43]. It can be seen from the curves that maximum degradation occurs within first 15-30 minutes. The degradation efficiency under dark conditions is 70 %. A few research groups have studied the dark catalysis of CR dye [84,85,87], but CZ50 displays higher degradation efficiency under dark conditions as compared to all of them. CZ50 was synthesized using organic compounds like ethylene glycol and polyethylene glycol; some traces of these remain

on the surface of the catalyst. All these compounds consist of a number of OH groups attached to the carbon atom. The presence of these organic residues results in high electron density and thus acts as reductive sites [88]. They would facilitate the formation of reactive oxygen species which result in the degradation of CR dye even in dark conditions.

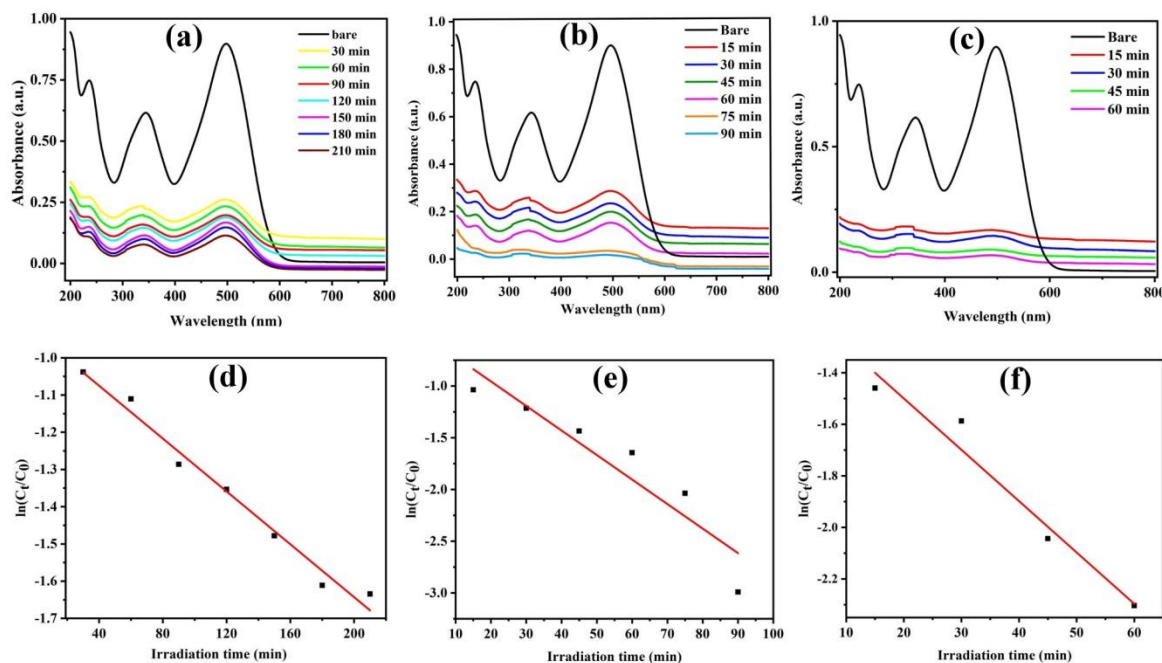


Fig. 14. The UV- Vis absorption spectra showing the degradation of CR dye for different time intervals in the presence of 8 mg catalyst under (a) dark (b) visible (c) UV light and plot of $\ln(C_t/C_0)$ versus irradiation time for degradation of CR dye by CZ50 under (d) dark (e) visible (f) UV light conditions.

7.3.6.3. Photodegradation study

Under dark conditions, the dye could not be completely degraded even after 210 minutes. Therefore, we have also examined the efficiency of the catalyst under visible and UV light conditions. Fig. 14 (c) and (e) show the respective absorption spectra of CR dye solution catalyzed by CZ50 under visible and UV light irradiation with time. The degradation

efficiency under visible and UV light conditions are 80 and 90 %, respectively (Fig.14 (d) and (f)). The CR dye got degraded totally within 90 min under visible light and within 60 min under UV light irradiation. The degradation efficiency of the catalyst increased in the present cases as compared to that under dark conditions. This may be due to inclusion of extra energy in the catalyst system, which results in easier bridging of energy band gap by electrons on the photocatalyst surface. The ejected electron creates a hole in the valence band, which on reaction with water molecules produces reactive oxygen species, thus causing dye degradation.

7.3.6.4. Degradation kinetics study

The dye degradation process usually follows the first order kinetic model [56]. So, the kinetics of the degradation in the present case were explored by plotting the $\ln \frac{C_t}{C_0}$ vs time (t) curves of CR dye degraded by CZ50 under dark, visible and UV light conditions (Fig.15), where C_0 and C_t represent initial concentration of dye and concentration of dye at time 't', respectively. The reaction rate constant (k) can be calculated from the slope of this curve. The values of 'k' and correlation coefficient (R^2) are listed in Table 7. The fitted line approves with the experimental data and this suggests that the degradation follows pseudo first-order kinetic model [43]. The testified values of 'k' for photodegradation of CR with diverse initial concentrations by means of CoFe_2O_4 as catalyst varies from $5-7 \times 10^{-3} \text{ min}^{-1}$ [44]. The values of 'k' for CZ50 are slightly less than CoFe_2O_4 under dark conditions but much greater under light conditions. Thus, CZ50 can aid as an effective catalyst for elimination of Congo Red from the solution medium.

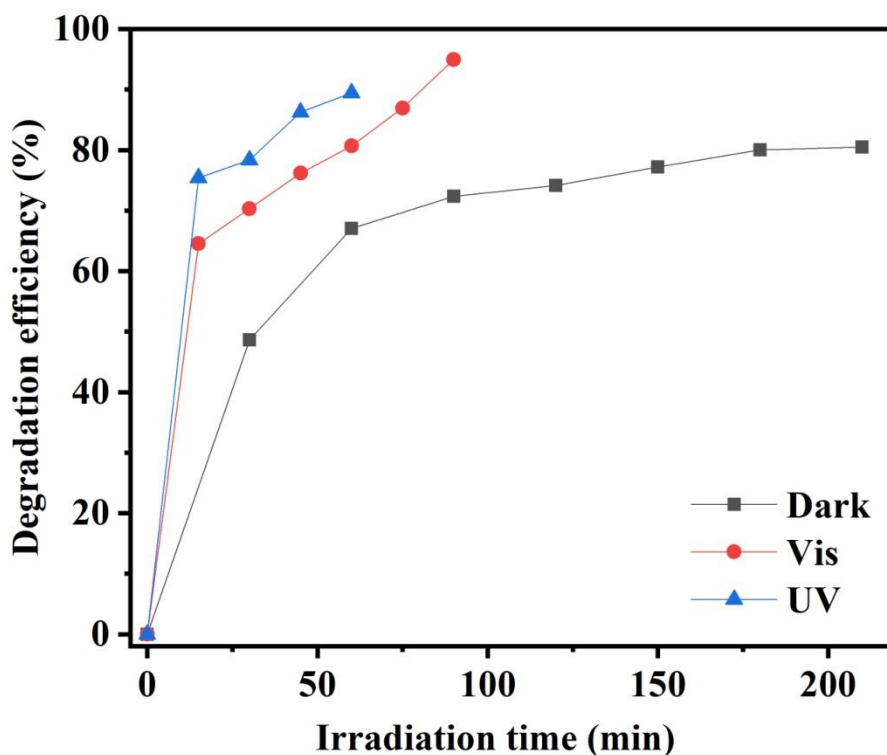


Fig.15. Degradation percentage versus time plot for degradation of CR dye by CZ50

Table 7 Fitting parameters calculated from pseudo-first-order kinetics model

Conditions	Rate constant, k (min^{-1})	Correlation coefficient (R^2)
Dark	3.0×10^{-3}	0.98
Visible light	2.4×10^{-2}	0.95
UV light	2.0×10^{-2}	0.94

7.3.6.5. Resuability test

The reusability of CZ50 as a photocatalyst was investigated under UV light conditions only as CR dye got degraded substantially in short span of time when exposed to UV light as compared to dark and visible light conditions. In this regard, the catalyst-CR dye mixture was subjected to UV light conditions for required time and all relevant procedures were followed subsequently as already mentioned in the previous part of the text. Prior to each cycle, the catalyst was magnetically separated from the mixture, washed properly with deionized water

and dried in vacuum at 100 °C. Almost 90, 85 and 81% of CR dye was photodegraded during the first, second and third cycle of the catalytic experiment, respectively (Fig.16). So, there is trivial change in the catalytic degradation efficiency of CZ50 upon recycling. Moreover, we have captured the FESEM micrograph (Fig.17) of the catalyst separated after three cycles of photocatalytic reaction. The recovered catalyst has retained its morphology after three cycles of photocatalytic reaction. Thus, CZ50 can be reused as an effective photocatalyst for degradation of CR dye under UV light exposure for several times.

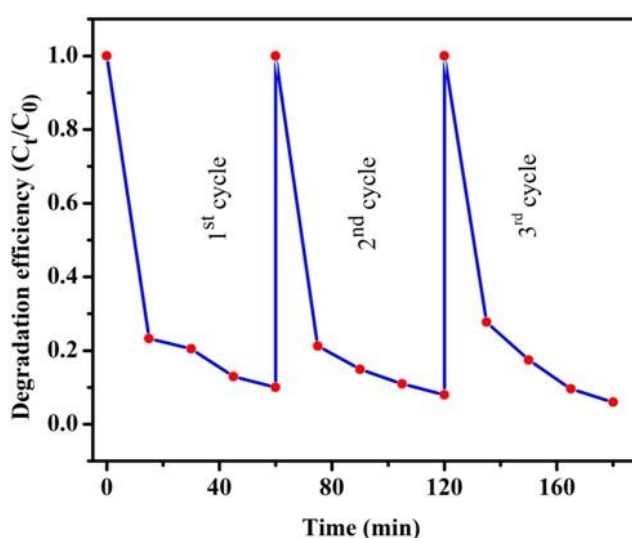


Fig.16. Recyclability test for degradation of CR dye by CZ50

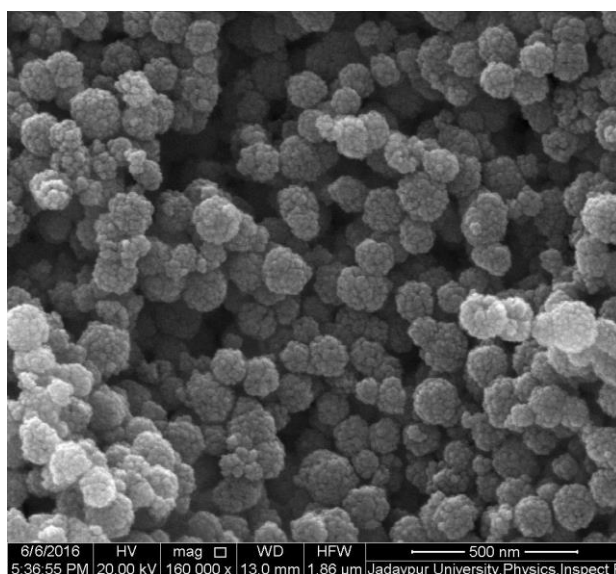


Fig.17. FESEM of CZ50 after three cycles of photocatalytic reaction.

7.4. Discussion

The structural and morphological characterization through PXRD, FESEM and TEM reveals following facts about CZ50. The microspheres are of diameter ~ 140 nm and composed of particles of crystallite size ~ 25 nm. The microspheres have crystallized in cubic spinel phase with values of lattice parameter ~ 8.397 Å and 8.41 Å, respectively, obtained by analyzing PXRD data using MAUD2.33 and GSAS software. The theoretical value of lattice parameter (a_{av}) for $Co_{0.5}Zn_{0.5}Fe_2O_4$ system can be calculated by considering the weighted average of the lattice parameters of pure $CoFe_2O_4$ and $ZnFe_2O_4$ i.e., using the relation $a_{av} = 0.5 a_c + 0.5 a_z$, where $a_c = 8.391$ Å and $a_z = 8.440$ Å are the lattice parameters of $CoFe_2O_4$ (JCPDS ICDD card no. 22-1086) and $ZnFe_2O_4$ (JCPDS ICDD card no. 82-1049), respectively. The calculated value of a_{av} is ~ 8.41 Å. The values of lattice parameter obtained from PXRD and calculated theoretically are in good accord. Thus, the results obtained from PXRD analysis are trustworthy. Existence of clear lattice fringes in the HRTEM micrograph and distinct rings in the SAED pattern together ascertain good crystallinity of the sample.

The cation distribution of CZ50 deduced from PXRD and infield Mössbauer spectroscopic studies are in good consonance. We have also calculated the theoretical value of magnetic moment per formula unit using the cation distribution obtained from the above studies and compared them with their experimental values obtained from dc magnetic studies. The theoretical magnetic moment per formula unit (m_{th}) of ferrites can be written as $m_{th} = m_B \cos \theta_B - m_A \cos \theta_A$ where, m_B and m_A are the magnetic moments associated with [B] and (A) sublattice of the spinel structure, respectively, θ_A and θ_B are the (A) and [B] site canting angles, respectively. Taking into account the canting angles for CZ50 as mentioned in Table 6, we have calculated the value of m_{th} as $4.44 \mu_B$. The experimental magnetic moment per formula unit (m_{exp}) obtained from the value of M_{SAT} of 5 K M-H curve is $4.67 \mu_B$. The values

of m_{th} and m_{exp} are in good conformity. So, the deduced cation distribution for the present sample is reliable.

The dc magnetic measurements and Mössbauer spectroscopic studies unravel some fascinating magnetic phenomena like spin glass-like freezing and collective magnetic excitations in the sample. The Mössbauer study divulges that CZ50 is in collective state at 300 K. According to the findings of ZFC-FC studies, CZ50 exhibits spin glass-like behavior below $T_f = 25$ K. Thus, it may be asserted that CZ50 exhibits mixed magnetic phase i.e., the system is in collective magnetic state above T_f and spin glass-like freezing of magnetic moments happens at T_f . In the collective state, it is not possible to outline the anisotropy energy of individual particles instead the anisotropy energy of the assembly needs to be considered. The anisotropy energy of the assemblage shows multiminima in phase space as for spin glass phase [89]. This is primarily manifested by a sudden fall in ZFC magnetization at T_f . In the present case, no superparamagnetic blocking has been observed. CZ50 has been formed by self-assembly of nanoparticles having varied shape and sizes. So, it is inevitable that strong interparticle interactions will exist within the ensemble. It has been reported earlier that blocked state gets suppressed and a transition from superparamagnetic to collective state takes place under the influence of interactions [89]. The blocking temperature of the system decreases with interaction and if strength of interaction is above a critical value the temperature of appearance of collective state increases. Since the sample under investigation is an assemblage of magnetic nanoparticles, hence interparticle interactions overpower the characteristic blocked state of each particle.

The 5 K Mössbauer spectroscopic study (both in field and without field) reveal that CZ50 comprises of particles displaying ferrimagnetic phase and no sign of relaxation is noticeable at this temperature. Additionally, the sample exhibits spin canting. On the other hand, the ZFC-FC study on CZ50 point towards existence of a spin glass-like freezing in the

sample below 50 K which evidently objects the outcomes of Mössbauer spectroscopic study carried out at 5K. This discrepancy amongst the two measurements can be addressed by bearing in mind the fact that Mössbauer spectroscopy investigates the local fluctuations of hyperfine magnetic field whereas dc magnetization records the overall magnetic moment of the sample as a whole [90]. The presence of both (A) and [B] site sextets in the Mössbauer spectra of CZ50 at 5 K reveals that either the sample as a whole is ferrimagnetic or there are portions (clusters) inside the constituent particles of CZ50 that are in ferrimagnetic state. Thus, in view of the results of Mössbauer spectroscopic study and dc magnetic measurements collectively, it can be ascertained that ferrimagnetically ordered clusters exist within the grains of the sample. With the reduction in temperature, the interaction between conflicting sublattice interactions and frustrations produce freezing of local magnetic moment of these clusters in haphazard way and the system all together freezes in a spin glass like phase [90].

The sample exhibits a sudden rise in the value of coercivity at 5 K as compared to 300 and 100 K in its M-H study and spin canting in its 5 K infield Mössbauer spectroscopic study. Kodama and Berkowitz elaborated that the coercivity of nanosized ferrites would increase only when there is presence of broken exchange bonds in the near-surface layers [91]. It may be noted that CZ50 has been synthesized by using PEG-4000 as binding agent. Moreover, the results of DLS and FTIR studies have indicated the presence of an organic layer of PEG-4000 on the outer surface of the microspheres. It is well-known that variation in coordination of surface cations result in a distribution of net exchange field [ref]. Moreover, the exchange interactions are mediated by an intervening oxygen ion. If organic molecules are bonded to the surface, then these oxygen ions are missing on the surface resulting in broken exchange bonds. These broken exchange bonds additionally reduce overall coordination of surface cations and enforce the phenomena of surface spin disorder.

Consequently, there is an additional increase in the coercivity of the sample at 5 K induced by boost in anisotropy energy following freezing of the disordered spins.

7.5. Conclusion

In summary, $\text{Co}_{0.5}\text{Zn}_{0.5}\text{Fe}_2\text{O}_4$ microspheres were synthesized by facile solvothermal method and characterized by powder X-ray diffraction, scanning and transmission electron microscopic, UV-Vis, photoluminescence, dynamic light scattering, dc magnetic and Mössbauer spectroscopic techniques. These microspheres are single-phase cubic spinel ferrite crystallized in the $\text{Fd}\bar{3}\text{m}$ symmetry and possess monodispersity in size. The FESEM and TEM micrographs display mesoporous clusters of $\text{Co}_{0.5}\text{Zn}_{0.5}\text{Fe}_2\text{O}_4$ nanoparticles. The sample displays both direct and indirect band gaps of 3.25 and 2.3 eV, respectively. The PL spectrum displays hump in the range of 415-450 nm indicating defects related to the interface traps existing at the grain boundaries. The hydrodynamic diameter of the microspheres is ~ 330 nm, which is much greater than the true diameter due to the presence of carbonaceous binding agents on the microspheres surface. The M-T studies have suggested presence of dipolar and interparticle coupling interactions within the nanoparticles. The sample exhibits increase in coercivity values at low temperature owing to the freezing of surface spins. The room temperature Mössbauer spectrum exhibits a diffused sextet along with a doublet and can be attributed to the collective behaviour of ensemble of magnetic nanoparticles which have aggregated to form the microspheres. The low temperature Mössbauer study ascertains that the microspheres are ferrimagnetically ordered at 5 K, substantial migration of Fe^{3+} ions have occurred from [B] to (A) site of the spinel lattice and surface spin canting has taken place. The sample has successfully degraded Congo Red dye under dark conditions due to the presence of organic residues on the microsphere surface. In addition, the sample can serve as a very efficient photocatalyst for removal of Congo Red dye.

References

1. An-Hui Lu, E. L. Salabas, F. Schüth, *Angew. Chem. Int. Ed.* 46 (2007) 1222 – 1244.
2. J. Ge, Y. Hu, M. Biasini, Ward P. Beyermann, Y. Yin, *Angew. Chem.* 119 (2007) 4420 – 4423
3. Y-M Hao, S-Yun Lou, Shao-Min Zhou, Rui-Jian Yuan, Gong-Yu Zhu, Ning Li, *Nanoscale Research Letters* 7 (2012) 100.
4. X. Zeng, J. Yuan, L. Zhang, *J Phys Chem C* 112 (2008) 3503-3508.
5. K. Barick, M. Aslam, V. Dravid, D. Bahadur, *J Phys Chem C* 112 (2008) 15163-15170.
6. Z. Liu, Q. Zhang, G. Shi, Y. Li, H. Wang, *J Magn. Magn Mater* 323 (2011) 1022-1026.
7. M. Dhiman, R. Sharma, V. Kumar, S. Singhal, *Ceramics International* 42 (2016) 12594-12605.
8. A. Nicolas-Boluda, Z. Yang, I. Dobryden, F. Carn, N. Winckelmans, C. Péchoux, P. Bonville, S. Bals, P. Martin Claesson, F. Gazeau, M. Paule Pileni, *Adv. Funct. Mater.* (2020) 2004274.
9. V. Håkonsen, G. Singh, José A. De Toro, Peter S. Normile, E. Wahlström, J. He, Z. Zhang, *Adv. Sci.* 8 (2021) 2002683.
10. M. Huang, X. Yu, L. Wang, J. Liu, W. You, M. Wang, R. Che, *Small Structures* 2 (2021) 2100033.
11. A. R. Abbasian, S. Sadat Hosseini, M. Shayesteh, M. Shafiee Afarani, M. Rafigh Esmaeilzaei, *Int. J. Nano Dimens.* 11 (2020) 130-144.
12. J. Panda, K. Ghorui, R. Sarkar, B. Tudu, *Appl. Phys. A* 128 (2022) 128.
13. J. Liu, Z. Jia, W. Zhou, X. Liu, C. Zhang, B. Xu, G. Wu, *Chem. Engg. J* 429 (2022) 132253.
14. M. Shaterian, A. Rezvani, A. R. Abbasian, *Mater. Res. Express* 6 (2020) 12505.

15. P. Annie Vinosha, A. Manikandan, A. Sherley Judith Ceicilia, A. Dinesh, G. Francisco Nirmala, A. Christy Preetha, Y. Slimani, M.A. Almessiere, A. Baykal, B. Xavier, Ceram. Int. 47 (2021) 10512–10535.
16. S. Dey, R. Mondal, S.K. Dey, S. Majumder, P. Dasgupta, A. Poddar, V.R. Reddy, S. Kumar, J. Appl. Phys. 118 (2015).
17. R. Mondal, S. Dey, K. Sarkar, P. Dasgupta, S. Kumar, Mater. Res. Bull. 102 (2018) 160–171.
18. V. Mameli, A. Musinu, A. Ardu, G. Ennas, D. Peddis, D. Niznansky, C. Sangregorio, C. Innocenti, T.K. Nguyen, Nanoscale 8 (2016) 10124.
19. M. Schmidt, H.L. Andersen, C. Granados-Miralles, M. Saura-Múzquiz, M. Stingaciu, M. Christensen, Dalton Trans. 45 (2016) 6439.
20. M. Veverka, P. Veverka, Z. Jiráček, O. Kaman, K. Knížek, M. Maryško, E. Pollert, K. Závěta, J. Magn. Magn. Mater. 322 (2010) 2386–2389.
21. D.S. Nikam, S.V. Jadhav, V.M. Khot, R.A. Bohara, C.K. Hong, S.S. Malib, S.H. Pawar, RSC Adv. 5 (2015) 2338.
22. I. Sharifi, H. Shokrollahi, J. Magn. Magn. Mater. 324 (2012) 2397–2403.
23. R.N. Bhowmik, R. Ranganathan, J. Magn. Magn. Mater. 248 (2002) 101–111.
24. H. Parmar, P. Acharya, R.V. Upadhyay, V. Siruguri, S. Rayaprol, Solid State Commun. 153 (2013) 60–65.
25. R.V. Upadhyay, H. Parmar, P. Acharya, A. Banerjee, Solid State Commun. 163 (2013) 50–54.
26. G.A. Petitt, D.W. Forester, Mossbauer study of cobalt-zinc ferrites, Phys. Rev. B 4 (1971) 11.
27. S. Dey, A. Roy, J. Ghose, R.N. Bhowmik, R. Ranganathan, J. Appl. Phys. 90 (2001) 4138.
28. I. Sharifi, H. Shokrollahi, J. Magn. Magn. Mater. 334 (2013) 36–40

29. A. Ramakrishna, N. Murali, Tulu Wegayehu Mammo, K. Samatha, V. Veeraiah, *Phys. B: Condens. Matter.* 534 (2018) 134–140.
30. T.R. Tatarchuk, N.D. Paliychuk, M. Bououdina, B. Al-Najar, M. Pacia, W. Macyk, A. Shyichuk, *J. Alloy. Compd.* 731 (2018) 1256–1266.
31. D.M. Jnaneshwara, D.N. Avadhani, B.D. Prasad, B.M. Nagabhushana, H. Nagabhushana, S.C. Sharma, S.C. Prashantha, C. Shivakumara, *J. Alloy. Compd.* 587 (2014) 50–58.
32. A. Manikandan, L. John Kennedy, M. Bououdina, J. Judith Vijaya, *J. Magn. Mater.* 349 (2014) 249–258.
33. L. Cervera and C. G. Polo, in *Book of Abstracts of Jornada Doctoral de Jovenes Investigadores en Magnetism*, 17 October 2019 (The Spanish Magnetism Club and the Spanish Chapter of the IEEE Magnetics Society Annual Joint Meeting, 2019) p. 18.
34. C. Hou, H. Yu, Q. Zhang, Y. Li, and H. Wang, *J. Alloys Compd.* 491 (2010) 431.
35. Yi-Wei Liu, Jing Zhang, Lu-Shun Gu, Li-Xi Wang, Qi-Tu Zhang, *Rare Met.* 41 (2022) 3228–3232.
36. S. BawaWaje, M. Hashim, W. DaudWanYusoff, Z. Abbas, *J. Mag. Mater.* 322(2010) 686–691.
37. M. Schmidt, H. L. Andersen, C. Granados-Miralles, M. Saura Múzquiz, M. Stingaciu, M. Christensen, *Dalton Trans.* 45 (2016) 6439
38. V. Mameli, A. Musinu, A. Ardu, G. Ennas, D. Peddis, D. Niznansky, C. Sangregorio, C. Innocenti, Nguyen T. K. Thanh, C. Cannas, *Nanoscale* 8(2016) 10124.
39. H. Deng, X. Li, Q. Peng, X. Wang, J. Chen, Y. Li, *Angew. Chem. Int. Ed.* 44 (2005) 2782–2785.
40. M. Penchal Reddy, A.M.A. Mohamed, *Microporous Mesoporous Mater.* 215 (2015) 37–45.
41. A. Kostopoulou, A. Lappas, *Nanotechnol. Rev.* 4 (6) (2015) 595–624.

-
42. R. Mondal, K. Sarkar, S. Dey, D. Majumdar, S. K. Bhattacharya, P. Sen, S. Kumar, ACS Omega 4 (2019) 12632–12646.
43. R. Mondal, K. Sarkar, S. Dey, S. Bhattacharjee, C. K. Ghosh, S. Kumar, AIP Conf. Proc. 1942 (2018) 050072
44. N.Ali, A. Said, F. Ali, F.Raziq, Z. Ali, M. Bilal, L. Reinert, T. Begum, H. M. N. Iqbal, Photocatalytic Degradation of Congo Red Dye from Aqueous Environment Using Cobalt Ferrite Nanostructures: Development, Characterization, and Photocatalytic Performance, Water Air Soil Pollut 231 (2020) 50
45. D. Chahar, S. Taneja, S. Bisht, S. Kesarwani, P. Thakur, A. Thakur, P.B. Sharma, Photocatalytic activity of cobalt substituted zinc ferrite for the degradation of methylene blue dye under visible light irradiation, J. Alloys Compd. 851 (2021) 156878
46. B. Mandal, J. Panda, P. K. Paul, R. Sarkar, B. Tudu, MnFe_2O_4 decorated reduced graphene oxide heterostructures: Nanophotocatalyst for methylene blue dye degradation, Vacuum 173 (2020) 109150.
47. B.K. Körbahti, K. Artut, C. Gec, A. Özer, Electrochemical Decolorization of Textile Dyes and Removal of Metal Ions from Textile Dye and Metal Ion Binary Mixtures, Chem. Eng. J. 173 (2011) 677 – 688
48. N.F. Cardoso, E.C. Lima, I.S. Pinto, C.V. Amavisca, B. Royer, R.B. Pinto, W.S. Alencar, S.F.P. Pereira, Application of cupuassu shell as biosorbent for the removal of textile dyes from aqueous solution, J. Environ. Manag. 92 (2011) 1237 – 1247.
49. A. El Nemr, O. Abdelwahab, A. El-sikaily, A. Khaled, Removal of direct blue-86 from aqueous solution by new activated carbon developed from orange peel, J. Hazard Mater. 161 (2009) 102 – 110
-

-
50. M. Reza, D. Khaki, M. Saleh, A. Aziz, A. Raman, W. Mohd, A. Wan, Application of doped photocatalysts for organic pollutant degradation - a review, *J. Environ. Manag.* 198 (2017) 78-94
 51. P. Taylor, C. Sahoo, A.K. Gupta, I.M.S. Pillai, Heterogeneous photocatalysis of real textile wastewater : evaluation of reaction kinetics and characterization, *J. Environ. Sci. Health A* 47 (2012) 2109
 52. B. Boutra, M. Trari, Solar photodegradation of a textile azo dye using synthesized ZnO/Bentonite, *Water Sci. Technol.* 75 (2016) 1-11
 53. F. Ajormal, F. Moradnia, S. T. Fardood, A. Ramazani, Zinc Ferrite Nanoparticles in Photo-Degradation of Dye: Mini-Review, *Chem. Rev.* 2 (2020) 90-102.
 54. E. Casbeer, V. K. Sharma, X-Z Li, Synthesis and photocatalytic activity of ferrites under visible light: A review, *Sep. Purif. Technol.* 87 (2012) 1–14
 55. K. Sarkar, R. Mondal, S. Dey, S. Majumder, S. Kumar, *J. Magn. Magn. Mater.* 487 (2019) 165303.
 56. A. Altomare, R. Caliandro, M. Camalli, C. Cuocci, C. Giacovazzo, A. G. G. Moliterni, R. Rizzi, Automatic structure determination from powder data with EXPO2004, *J. Appl. Crystallogr.* 37 (2004) 1025–1028.
 57. L. Lutterotti, MAUDWEB; version 1.9992, Università degli Studi di Trento, 2004.
 58. B. H. Toby, EXPGUI, a graphical user interface for GSAS, *J. Appl. Crystallogr.* 34 (2001) 210 – 213.
 59. R. Mondal, S. Dey, S. Majumder, A. Poddar, P. Dasgupta, S. Kumar, *J. Magn. Magn. Mater.* 448 (2018) 135–145.
 60. Yi-Wei Liu, Jing Zhang, Lu-Shun Gu, Li-Xi Wang, Qi-Tu Zhang, *Rare Met.* 41 (2022) 3228–3232.

61. R. Singh Yadav, I. Kuřitka, J. Havlica, M. Hnatko, C. Alexander, J. Masilko, L. Kalina, M. Hajdúchová, J. Rusnak, V. Enev, J. Magn. Magn. Mater. 447 (2018) 48–57.
62. M. S. A. Darwish, H. Kim, H. Lee, C. Ryu, J. Y. Lee, J. Yoon, Nanomaterials 9 (2019) 1176.
63. A.-H. El Foulani, A. Aamouche, F. Mohseni, J.S. Amaral, D.M. Tobaldi, R.C. Pullar, J. Alloys Compd. 774 (2019) 1250
64. M. Sundararajan, L. John Kennedy, J. Judith Vijaya, Udaya Aruldoss, Spectrochim. Acta A Mol. Biomol. Spectrosc. 140 (2015) 421–430
65. G. Fan, J. Tong, F. Li, Ind. Eng. Chem. Res. 51 (2012) 13639–13647
66. M. Sundararajan, V. Sailaja, L. J. Kennedy, J. J. Vijaya, Ceram. Int. 43 (2017) 540-548
67. J. Lim, S. P. Yeap, H. X. Che, S. C. Low, Characterization of magnetic nanoparticle by dynamic light scattering, Nanoscale Res. Lett. 8 (2013) 381
68. Z. Lou, M. He, R. Wang, W. Qin, D. Zhao, and C. Chen, Inorg. Chem. 53 (2014) 2053–2057.
69. J. Xie, C. Xu, N. Kohler, Y. Hou, and S. Sun, Adv. Mater. 19 (2007) 3163–3166.
70. A. B. Salunkhe, V. M. Khot, JuanM. Ruso, S.I. Patil, J. Magn. Magn. Mater. 419 (2016) 533-542
71. S. Sahoo, C.K. Chakraborti, P.K. Behera, Asian J. Pharm. Clin. Res. 5(2012) 125-130.
72. S. Sahoo, C.K. Chakraborti, P.K. Behera, Int. J. PharmTech. Res. 4 (2012) 382-391.
73. S. Sahoo, C.K. Chakraborti, S.C. Mishra, S. Naik, Drug Invention Today 3 (2011) 78- 82.
74. P.F. Builders, O.O. Kunle,M.U. Adikwu, Int. J. Pharm. 356 (2008) 174–180.
75. R.D. Waldron, Phys. Rev. 99 (1955) 1727–1735.
76. F. C. Kenechukwu, E. C. Ibezim, A. A. Attama,M. A. Momoh, J. D. N. Ogbonna, P. O. Nnamani, S. A. Chime, C. E. Umeyor and E. M. Uronnachi, Afr. J. Biotechnol. 12 (2013) 6661-6671.

-
77. S. M. Ansari, R. D. Bhor, K. R. Pai, S. Mazumder, D. Sen, Y. D. Kolekar, C. V. Ramana, ACS Biomater. Sci. Eng. 2 (2016) 2139–2152
78. K. Lagarec, D.G. Rancourt, Recoil-Mössbauer Spectral Analysis Software for Window, University of Ottawa Press: Ottawa, 1998.
79. C. E. Johnson, J. A. Johnson, H. Y. Hah, M. Cole, S. Gray, V. Kolesnichenko, P. Kucheryavy, G. Goloverda, Hyperfine Interact. 237 (2016) 27
80. E. Kuzmann, Z. Homonnay, Z. Klencsár, and R. Szalay, Molecules 26(2021) 1062.
81. S. Dey, S.K. Dey, B. Ghosh, P. Dasgupta, A. Poddar, V. R. Reddy, S. Kumar, Role of inhomogeneous cation distribution in magnetic enhancement of nanosized $\text{Ni}_{0.35}\text{Zn}_{0.65}\text{Fe}_2\text{O}_4$: A structural, magnetic, and hyperfine study. J. Appl. Phys. 114 (2013) 093901.
82. C. N. Chinnasamy, A. Narayanasamy, N. Ponpandian, K. Chattopadhyay, H. Guerault, J. M. Greneche, J. Phys.: Condens. Matter 12 (2000) 7795–7805.
83. S.S. M. Bhat, N. G. Sundaram, RSC Adv. 3 (2013) 14371-14378.
84. F. Moradnia, S. T. Fardood, A. Ramazani, S. Osali, I. Abdolmaleki, Micro Nano Lett. 15 (2020) 674–677.
85. C. M. Magdalane, G. M. A. Priyadharsini, K. Kaviyarasu, A. I. Jothi, G. G. Simiyon, Surf. Interfaces 25 (2021) 101296.
86. S. Jayaraman, A. R. Warriar, J. Mol. Liq. 301 (2020) 112360
87. S. T. Fardood, F. Moradnia, S. Moradi, R. Forootan, F. Y. Zare, M. Heidari, Nanochem Res 4 (2019) 140-147
88. A.F. Cabreraa, C.E. R. Torresa, S.G. Marchettib, S.J. Stewarta, J. Environ. Chem. Eng. 8 (2020) 104274
89. J. L. Dormann, D. Fiorani, and E. Tronc, Adv. Chem. Phys. 98 (1997) 283.
-

90. B. Ghosh, S. Kumar, A. Poddar, C. Mazumdar, S. Banerjee, V. R. Reddy, A. Gupta, Spin glasslike behavior and magnetic enhancement in nanosized Ni–Zn ferrite system, J. Appl. Phys. 108 (2010) 034307. DOI: 10.1063/1.3456174
91. R. H. Kodama and A. E. Berkowitz, Phys. Rev. B 59 (1999) 6321.



Chapter 8

Conclusions and Future Scope of the Work



8.1 Conclusions

The present thesis comprises of the details on synthesis technique and characterization of both nano- and micro-sized $\text{Co}_{0.5}\text{Zn}_{0.5}\text{Fe}_2\text{O}_4$, solid and hollow ZnFe_2O_4 microspheres and nanosized $\text{Co}_{0.8}\text{Zn}_{0.2}\text{Fe}_2\text{O}_4$ ferrites. Moreover, it also deals with exploration of their application potential in the field of magnetic storage device, catalysis and photocatalysis. These samples have shown some fascinating properties, which are incredible both from basic science and industrial application viewpoint. The development of superior magnetic quality in the samples like existence of stable magnetic ordering at room temperature and high saturation magnetization in nanosize regime are the primary requirements for their application in the arena of magnetic storage devices, hyperthermia, biomedicine etc. The nanoparticles possessing superparamagnetic (SPM) character are most suited for application in biomedical field owing to negligible interparticle interactions. But lowering of magnetization due to finite size and spin canting effect restricts their potential in the various application fields. Thus, the need of the hour is to overcome the shortcomings of SPM nanoparticles along with retention of their beneficial characteristics. Keeping this mind, efforts have been made to fabricate ferrite microspheres through self-assembly of nanoparticles such that their size is similar to that of protein molecules and they possess high saturation magnetization. In this context, the principal objectives of the thesis work are upgradation of basic magnetic features such as saturation magnetization, coercivity, anisotropy energy and magnetic ordering temperature of nanosized ferrites remarkably. In this attempt, strain anisotropy has been produced in the nanoparticle ensemble by mechanical milling and reduction of spin canting by heat treatment. Moreover, doping of nonmagnetic Zn^{2+} ions in nanosized Fe_3O_4 and CoFe_2O_4 , respectively, results in arousal of some interesting magnetic properties like superparamagnetism, collective magnetic state, spin canting effect, spin glass like behavior, ferrimagnetism etc. owing to the change in

superexchange interactions. Hence, cation redistribution caused either by mechanical activation or magnetic dilution can obliterate the undesirable effects of spin canting and superparamagnetism in nanosized ferrites in a constructive manner. Furthermore, there is a significant boost in anisotropy energy of the system due to lattice strain caused by mechanical milling. On the other hand, the magnetic properties of self-assembled microspheres composed of SPM $\text{Co}_{0.5}\text{Zn}_{0.5}\text{Fe}_2\text{O}_4$ nanoparticles have been analyzed in detail and they have shown collective magnetic behavior at room temperature. They have proved to excellent photocatalyst in the removal of an azo dye. The main conclusions of the thesis work are as follows:

[1] The first work of the thesis is a detailed study on the effects of mechanical activation caused by high energy ball milling on the structural, magnetic and hyperfine properties of nanosized $\text{Co}_{0.5}\text{Zn}_{0.5}\text{Fe}_2\text{O}_4$ having three different particle sizes 63 (M1), 25 (M2) and 17 nm (M3) synthesized by chemical coprecipitation method. Characterization techniques like powder x-ray diffraction, high resolution transmission electron microscopy, dc magnetic measurements and Mössbauer spectroscopic techniques have been employed to examine M1, M2 and M3 thoroughly. All the three samples are cubic spinel ferrites with $Fd\bar{3}m$ symmetry. The lattice parameters of M1, M2 and M3 are 8.395, 8.391 and 8.375 Å, respectively. The particles constituting all the three samples possess both superparamagnetic and ferrimagnetic phases at room temperature. The values of blocking temperature of M1, M2 and M3 are 204, 210 and 220 K, respectively. The values of saturation magnetization of M1, M2 and M3 at 300 and 10 K are 56.8, 55.3, 51.5 emu g⁻¹ and 115.68, 113.84, 109.65 emu g⁻¹, respectively. The values of coercivity for M1, M2 and M3 at 10 K are 1395, 2190 and 1950 Oe, respectively. The theory of magnetic domains has been exploited to explicate the trend in coercivity. The cation distribution of M2 is $(\text{Zn}^{2+}_{0.48}\text{Fe}^{3+}_{0.52})_{\text{A}}[\text{Co}^{2+}_{0.5}\text{Zn}^{2+}_{0.02}\text{Fe}^{3+}_{1.48}]_{\text{B}}\text{O}_4$. The effects of mechanical activation on cation

redistribution and magnetic property of M2 have been investigated by infield Mössbauer spectroscopic measurements and verified by theoretical analysis of experimental results of Rietveld refinement of powder x-ray diffraction data in conjugation with dc magnetic study. The sample M2 is basically ferrimagnetic in nature possessing a slightly canted core surrounded by a disordered shell. It exhibits excellent memory effect in its dc magnetization measurement. The sample is capable of encoding, preserving and recalling binary numbers through magnetic field change. This property of the sample may be used to design magnetic coding and sensing devices.

[2] Herein, we have compared the structural, morphological, magnetic and hyperfine properties of ZnFe_2O_4 solid (ZFMS) and hollow (ZFMH) microspheres synthesized by simple solvothermal technique. ZFMS, having diameter ~ 314 nm and formed by self-assembly of nanoparticles, displays superparamagnetic character predominantly along with collective magnetic excitations at room temperature. ZFMH of diameter ~ 375 nm exhibits single crystal like dotted selected area electron diffraction pattern and is magnetically well-ordered at room temperature. The values of saturation magnetization of ZFMS and ZFMH at 300, 100 and 10 K are 41.5, 64, 85.7 and 77, 84.5, 90.75 emu/g, respectively. Further, ZFMH has been found to be nonstoichiometric and possess cation vacancy from both X-ray photoelectron spectroscopic and Mössbauer studies. The cation distribution of the ZFMS and ZFMH are $(\text{Zn}_{0.44}\text{Fe}_{0.56})[\text{Zn}_{0.56}\text{Fe}_{1.44}]\text{O}_4$ and $(\text{Fe}^{3+}_{0.925}\text{Zn}^{2+}_{0.075})[\text{Fe}^{2+}_{0.31}\text{Fe}^{3+}_{1.46}\Phi_{0.23}]\text{O}_4$, respectively, where Φ corresponds to vacancy. ZFMH displays Verway transition due to the presence Fe^{2+} ions caused by cation vacancy in ZFMH while ZFMS does not.

[3] Herein, we report the electrochemical study of nanosized $\text{Co}_{0.5}\text{Zn}_{0.5}\text{Fe}_2\text{O}_4$ synthesized by hydrothermal method. Structural and microstructural characterization has been carried out by powder x-ray diffraction (PXRD), field emission scanning and transmission electron microscopic techniques. UV-vis diffuse reflectance spectroscopy has

been performed to analyze the optical property of the sample. dc magnetic measurements have been done to investigate the magnetic character of the sample. The PXRD study suggests that the sample has crystallized as a single-phase cubic spinel ferrite with $Fd\bar{3}m$ symmetry. The average particle size is ~ 19 nm. The band gap of the sample is 1.75 eV. The sample exhibits maximum specific capacitance of 85.5 F/g at 10 mV/s scan rate. The dc magnetic studies ascertain that the sample is magnetically ordered at room temperature and possess strong interparticle interactions within the assemblage of nanoparticles. The pseudocapacitive behavior of the sample can be established from the non-rectangular shape of cyclic voltammetry curves. The sample can act as a supercapacitor.

[4] Here, we have shown that the particle size, cation redistribution, interparticle interactions, surface spin disorder and strain induced anisotropy play a pivotal role in shaping the magnetic and hyperfine properties of nanosized $\text{Co}_{0.8}\text{Zn}_{0.2}\text{Fe}_2\text{O}_4$ samples prepared by coprecipitation method followed by high energy ball milling and subsequent thermal treatment. Three samples with different particle size viz., 23 nm (CZ1), 34 nm (CZ2) and 42 nm (CZ3) are characterized by powder x-ray diffraction, transmission electron microscopy and energy dispersive x-ray spectroscopy studies. The samples are well-crystalline, single-phase spinel with appropriate stoichiometry, assorted size and shape. All three samples are magnetically ordered at 300 K with M_{SAT} and H_C values 75.22, 81.07, 82.89 emu g^{-1} , respectively, and 530, 460, 420 Oe, respectively. The values of coercivity at 10 K are remarkably high. Cation distribution of CZ1, CZ2 and CZ3 as estimated by taking into account the results of infield Mössbauer spectroscopic study and powder x-ray diffraction in conjugation are: $(\text{Co}_{0.27}^{2+}\text{Zn}_{0.20}^{2+}\text{Fe}_{0.53}^{3+})_{\text{A}}[\text{Co}_{0.53}^{2+}\text{Fe}_{1.47}^{3+}]_{\text{B}}\text{O}_4$ (core region of CZ1), $(\text{Co}_{0.43}^{2+}\text{Zn}_{0.20}^{2+}\text{Fe}_{0.37}^{3+})_{\text{A}}[\text{Co}_{0.37}^{2+}\text{Fe}_{1.63}^{3+}]_{\text{B}}\text{O}_4$ (shell region of CZ1), $(\text{Co}_{0.28}^{2+}\text{Zn}_{0.20}^{2+}\text{Fe}_{0.52}^{3+})_{\text{A}}[\text{Co}_{0.52}^{2+}\text{Fe}_{1.48}^{3+}]_{\text{B}}\text{O}_4$ and $(\text{Co}_{0.24}^{2+}\text{Zn}_{0.20}^{2+}\text{Fe}_{0.56}^{3+})_{\text{A}}[\text{Co}_{0.56}^{2+}\text{Fe}_{1.44}^{3+}]_{\text{B}}\text{O}_4$, respectively. Further, this result has been validated theoretically. Owing to the core-shell

structure (ferrimagnetically ordered core surrounded by a disordered shell), sample CZ1 having particle size below calculated critical diameter (~ 27 nm) exhibits exchange bias effect. All three samples display excellent catalytic activity in the multicomponent reaction for the synthesis of coumarin-3-carboxamide. CZ1 shows best catalytic activity owing to its high surface to volume ratio.

[5] It has been shown that $\text{Co}_{0.5}\text{Zn}_{0.5}\text{Fe}_2\text{O}_4$ microspheres (~ 140 nm) are comprised of closely packed nanoparticles (~ 27 nm) and successfully synthesized by template-free solvothermal technique. Powder x-ray diffraction and electron microscopic techniques were utilised to methodically examine the structural and microstructural properties of these microspheres. The optical properties of the microspheres were explored using UV-Vis, Fourier Transform Infrared spectroscopic and photoluminescence measurements. The FTIR spectrum divulges that the microspheres are cubic spinel ferrite. The results revealed that $\text{Co}_{0.5}\text{Zn}_{0.5}\text{Fe}_2\text{O}_4$ microspheres possess both direct and indirect transitions and display violet emissions in their PL spectra. The colloidal stability of the microspheres was analysed by dynamic light scattering and zeta potential measurements. The outcomes indicate that the hydrodynamic size of the microspheres is much larger as compared to their true diameter and they possess positive surface charge. The dc magnetic and Mössbauer spectroscopic studies together confirm that the sample is ferrimagnetic in nature and migration of iron ions have occurred from [B] to (A) sites causing cation redistribution. The estimated cation distribution is as follows: $(\text{Zn}^{2+}_{0.33}\text{Fe}^{3+}_{0.67})_{\text{A}}[\text{Zn}^{2+}_{0.17}\text{Co}^{2+}_{0.50}\text{Fe}^{3+}_{1.33}]_{\text{B}}\text{O}_4$. The cation distribution of the microspheres has been testified by comparing the theoretical and experimental values of magnetic moment per formula unit and found to be reliable. The sample acts as an efficient catalyst in the degradation of Congo Red dye in dark conditions. It also displays very high photodegradation efficiency under both visible and UV light conditions.

8.2 Future scope of the work

In this thesis, nano- and micro-sized $\text{Co}_{0.5}\text{Zn}_{0.5}\text{Fe}_2\text{O}_4$, solid and hollow ZnFe_2O_4 microspheres and nanosized $\text{Co}_{0.8}\text{Zn}_{0.2}\text{Fe}_2\text{O}_4$ ferrites have been prepared through different synthesis methods. Their structural, microstructural, optical, magnetic and hyperfine properties have been characterized thoroughly. In addition, their application potential in the fields of magnetic data storage devices, catalysis and photocatalyst for dye degradation have been investigated in detail. Hierarchical ferrite microspheres synthesized by implementing simple synthesis procedures have displayed possibility for application in drug delivery system, catalysis, biomedical fields etc. They have also revealed fascinating properties different from nanoparticle counterparts. Thus, it can be ascertained that the role of synthesis procedure in tuning the physico-chemical properties of these ferrites is significant. On the basis of the revelations from the works in the present thesis, following works can be planned as future prospect.

In recent times, several research groups have fabricated nano/microstructured (spheres, cube, rods, flower-like structures etc.) ferrites with ferrite nanoparticles as their primary constituent. There is a growing interest in development of one-step facile methods of synthesizing different nano/microstructured ferrites of varied chemical composition. Alongside, magnetic core-non-magnetic shell type nano and microstructures display improved magnetic and optical properties with their plausible applications in hyperthermia as heat intermediaries, drug delivery system as drug carriers, magnetic resonance imaging (MRI) as contrast agents, photo-magnetic nano device, magneto-optical recording industry etc.

Hollow nano/microstructured ferrites are in the limelight due to their widespread applicability in the field of drug delivery. Efforts are being made to produce hollow ferrites with desirable size, shape, shell thickness by modifying the reaction parameters. In addition,

these hollow ferrite nano/microspheres have proved themselves as excellent absorber of As (V) Cr (VI) from wastewater. They can even degrade diverse pollutants like benzene and other harmful dyes under both dark and visible light irradiation owing to their physical characteristics like high surface area, highly porous structure and high saturation magnetization. Recently, studies have shown that the hollow nanoparticles and microspheres can be used not only as a cheap, efficient, and environmentally beneficial anode material for lithium-ion batteries but also in a plethora of industrial areas such as catalyst, supercapacitors, sensors etc. due to their huge specific capacity, reversibility, recoverability and retentivity.

The motto of the research is to tune the dimension and morphology of ferrites by engaging diverse synthesis routes as such variations can help in increasing their photocatalytic degradation efficiency. It has been noted that combination of other photocatalysts with ferrites in different ratios has enhanced their overall photocatalytic activity owing to broadening of band-gap in the resultant composite. This results in arousal of a greater number of reactive species to degrade a vast range of contaminants. Recently, the scientific community is engrossed in developing mixed ternary transition metal ferrites to investigate their potential as electrode material for supercapacitors and found them highly efficient with distinct redox behavior and high value of specific capacitance.

In this framework, it seems prudent to fabricate nano/microstructured ferrite with controlled shape, size and chemical composition by employing varied combinations of facile and environmentally benign synthesis procedures. The influence of morphology on the magnetic and hyperfine properties of these ferrites can be studied in detail. Moreover, there is a room to investigate the potential of these ferrites in diverse technological fields such as hyperthermia, drug delivery, magnetic resonance imaging, magneto-optical recording

industry, microwave absorber, wastewater pollutant absorber, anode material for lithium-ion batteries, catalyst, supercapacitors, sensors and photocatalyst.



List of Publications



LIST OF PUBLICATIONS

Publications related to thesis work

- [1] **K. Sarkar**, R. Mondal, S. Dey, S. Majumder and S. Kumar, Presence of mixed magnetic phase in mechanically milled nanosized $\text{Co}_{0.5}\text{Zn}_{0.5}\text{Fe}_2\text{O}_4$: A study on structural, magnetic and hyperfine properties, *Journal of magnetism and magnetic material*, 487 (2019) 165303-1 – 165303-11.
- [2] **K. Sarkar**, R. Mondal, S. Dey and S. Kumar, Cation vacancy and magnetic properties of ZnFe_2O_4 microspheres, *Physica B: Condensed Matter*, 583 (2020) 412015-1 – 412015-12.
- [3] **K. Sarkar**, R. Mondal, D. Majumdar, S. K. Bhattacharya and S. Kumar Electrochemical Study of Nanosized $\text{Co}_{0.5}\text{Zn}_{0.5}\text{Fe}_2\text{O}_4$ Synthesized by Hydrothermal Method, *Proceedings of DAE SSPS* (2021) 198-199.
- [4] **K. Sarkar**, M. Dutta, R. Mondal, S. Dey, S. Majumder, N. Sepay, U.C. Halder and S. Kumar, Influences of morphology, cation distribution and surface spin canting on magnetic and hyperfine properties of mechanically activated and subsequently heat treated nanosized $\text{Co}_{0.8}\text{Zn}_{0.2}\text{Fe}_2\text{O}_4$ exhibiting excellent catalytic activity, *Materials Today Communications* (under Review).
- [5] **K. Sarkar**, M. Dutta, R. Mondal and S. Kumar, Study on structural, magnetic, hyperfine, optical properties and dye-degradation of self-assembled $\text{Co}_{0.5}\text{Zn}_{0.5}\text{Fe}_2\text{O}_4$ microspheres, *Physica B: Condensed Matter* (under review)

Publications not related to thesis work

- [1] R. Mondal, S. Dey, **K. Sarkar**, P. Dasgupta, and S. Kumar, Influence of high energy ball milling on structural parameters, cation distribution and magnetic enhancement of nanosized $\text{Co}_{0.3}\text{Zn}_{0.7}\text{Fe}_2\text{O}_4$, *Materials Research Bulletin*, 102 (2018) 160–171.
- [2] R. Mondal, **K. Sarkar**, S. Dey, D. Majumdar, S. K. Bhattacharya, P. Sen and S. Kumar, Magnetic, pseudocapacitive, and H_2O_2 -electrosensing properties of self-assembled superparamagnetic $\text{Co}_{0.3}\text{Zn}_{0.7}\text{Fe}_2\text{O}_4$ with enhanced saturation magnetization, *ACS Omega*, 4 (2019) 12632–12646.
- [3] R. Mondal, **K. Sarkar**, S. Dey, S. Bhattacharya, C.K. Ghosh and S. Kumar, Study on photocatalytic activity of nanosized $\text{Co}_{0.3}\text{Zn}_{0.7}\text{Fe}_2\text{O}_4$ synthesized by hydrothermal method, *AIP Conference Proceedings*, 1942 (1) (2018) 050072-1 – 050072-4.



*Seminar, Symposium, Conferences
and Awards*



Conference/Seminar attended

- [1] Presented a paper as poster and as oral presentation in **65th DAE Solid State Physics Symposium** at Bhabha Atomic Research Centre, Mumbai during December 15th – 19th Dec, 2021.
- [2] Presented a paper as poster in National Conference on **Recent Developments in Nanoscience & Nanotechnology (NCRDNN – 2019)** at Jadavpur University, Kolkata during January 29th – 31st, 2019.
- [3] Presented a paper as poster in **6th International Conference on Advanced nanomaterials and Nanotechnology (ICANN – 2017)** at IIT Guwahati, Assam during December 18th – 21st 2017.
- [4] Presented a paper as poster in **4th International Symposium on Semiconductor Materials and Devices (ISSMD 4)** at Jadavpur University, Kolkata during March 8th – 10th, 2017.
- [5] Participated in two days seminar on **Twists and Turns in Physics Research: Special Emphasis on Condensed Matter and Biophysics (TTPR – 2017)** at Jadavpur University, Kolkata during February 21st – 22nd, 2017.
- [6] Participated in one day seminar on **Some recent trends in research in Physics -** Department of Physics, Jadavpur University, Kolkata, 2016.

Award

- [1] Best poster award in **65th DAE Solid State Physics Symposium** at Bhabha Atomic Research Centre, Mumbai during December 15th – 19th Dec, 2021.



Appendix

*Reprints of the published papers
related to the thesis*





Research articles

Presence of mixed magnetic phase in mechanically milled nanosized $\text{Co}_{0.5}\text{Zn}_{0.5}\text{Fe}_2\text{O}_4$: A study on structural, magnetic and hyperfine properties

K. Sarkar^a, R. Mondal^a, S. Dey^b, S. Majumder^a, S. Kumar^{a,*}^a Department of Physics, Jadavpur University, Kolkata 700032, India^b Swami Vivekananda Institute of Science & Technology, Sonarpur, Kolkata 700 145, India

ARTICLE INFO

Keywords:

Nanostructures

Magnetic property

Mössbauer spectroscopy

Rietveld refinement

Magnetic coding

ABSTRACT

In this paper, we have presented a detailed study on the effects of mechanical activation caused by high energy ball milling on the structural, magnetic and hyperfine properties of nanosized $\text{Co}_{0.5}\text{Zn}_{0.5}\text{Fe}_2\text{O}_4$ having three different particle sizes 63 (M1), 25 (M2) and 17 nm (M3) synthesized by chemical coprecipitation method. Characterization techniques like powder x-ray diffraction, high resolution transmission electron microscopy, dc magnetic measurements and Mössbauer spectroscopic techniques have been employed to examine M1, M2 and M3 thoroughly. All the three samples are cubic spinel ferrites with $Fd\bar{3}m$ symmetry. The lattice parameters of M1, M2 and M3 are 8.395, 8.391 and 8.375 Å, respectively. The particles constituting all the three samples possess both superparamagnetic and ferrimagnetic phases at room temperature. The values of blocking temperature of M1, M2 and M3 are 204, 210 and 220 K, respectively. The values of saturation magnetization of M1, M2 and M3 at 300 and 10 K are 56.8, 55.3, 51.5 emu g^{-1} and 115.68, 113.84, 109.65 emu g^{-1} , respectively. The values of coercivity for M1, M2 and M3 at 10 K are 1395, 2190 and 1950 Oe, respectively. The theory of magnetic domains has been exploited to explicate the trend in coercivity. The cation distribution of M2 is $(\text{Zn}_{0.48}\text{Fe}_{0.52})_A(\text{Co}_{0.5}\text{Zn}_{0.02}\text{Fe}_{1.48})_B\text{O}_4$. The effects of mechanical activation on cation redistribution and magnetic property of M2 have been investigated by in-field Mössbauer spectroscopic measurements and verified by theoretical analysis of experimental results of Rietveld refinement of powder x-ray diffraction data in conjugation with dc magnetic study. The sample M2 is basically ferrimagnetic in nature possessing a slightly canted core surrounded by a disordered shell. It exhibits excellent memory effect in its dc magnetization measurement. The sample is capable of encoding, preserving and recalling binary numbers through magnetic field change. This property of the sample may be used to design magnetic coding and sensing devices.

1. Introduction

In recent times, nanosized spinel ferrites are in the limelight not only because of their application in hyperthermia [1], drug delivery [2], magnetic storage devices [3], sensors (electrochemical and gas sensing) [4,5], high frequency electronic devices [6,7] along with their use as contrast agent in magnetic resonance imaging [8] and active component in ferrofluid technology [9] but also pertaining to their distinctive physicochemical features as compared to their bulk counterparts [10,11]. The arousal of extraordinary properties in these spinel ferrites when reduced to nanoscale is due to increase in the surface to volume ratio, spin canting at the surface, cation redistribution between two interstitial sites of the spinel lattice and finite size effect [12,13]. On curbing down to the nanometric regime, stunning magnetic behaviors like superparamagnetism, high saturation magnetization, spin

glass like freezing and several unique electrical properties like high electrical resistivity and high permeability crop up [11,14–18]. These properties have shown variations following the synthesis procedure adopted, composition, size and shape of the fabricated nanoparticles [3,19–24]. So, tailoring of these parameters can enable us to control the properties of the nanosized ferrites and render them suitable for various technological applications.

Nanosized $\text{Co}_{1-x}\text{Zn}_x\text{Fe}_2\text{O}_4$ ferrites have been studied comprehensively in recent years due to their phenomenal magnetic, electrical and photocatalytic properties [13,18–22,25–27]. Bulk ZnFe_2O_4 is a non-toxic and soft-magnetic normal spinel whereas bulk CoFe_2O_4 is a comparatively toxic and hard-magnetic inverse spinel [28]. Replacement of Co^{2+} ions by Zn^{2+} ions through proper synthesis procedure produces non-toxic nanosized $\text{Co}_{1-x}\text{Zn}_x\text{Fe}_2\text{O}_4$ ferrites and helps in optimizing their magnetic behavior, which leads to development of

* Corresponding author.

E-mail address: kumars@phys.jdpu.ac.in (S. Kumar).<https://doi.org/10.1016/j.jmmm.2019.165303>

Received 20 November 2018; Received in revised form 8 April 2019; Accepted 12 May 2019

Available online 13 May 2019

0304-8853/© 2019 Elsevier B.V. All rights reserved.

diverse magnetic orders owing to variation in sublattice exchange interactions within the spinel lattice [12,13,20–22,29]. Doping of non-magnetic Zn^{2+} ions in nanometric CoFe_2O_4 at a ratio of $X = 0.5$ gives rise to maximum value of saturation magnetization due to increase in inter-sublattice A-O-B (J_{AB}) exchange interactions between tetrahedral (A) site and octahedral [B] site of the spinel lattice [30–33]. Above this ratio ($X > 0.5$), magnetization starts to decrease due to movement of Fe^{3+} ions from [B] site to (A) site in lieu of Zn^{2+} ions which preferentially occupy (A) site when $X < 0.5$. As per literature review, magnetization of nanometric $\text{Co}_{1-x}\text{Zn}_x\text{Fe}_2\text{O}_4$ increases systematically in the region $0.1 \leq X \leq 0.5$ [34]. For $X > 0.5$, non-magnetic Zn^{2+} ions tends to occupy octahedral [B] site which results in weakening of the long range J_{AB} interactions and strengthening of the short range B-O-B (J_{BB}) and A-O-A (J_{AA}) interactions, simultaneously [34]. Thus, thorough investigation of magnetic properties of $\text{Co}_{0.5}\text{Zn}_{0.5}\text{Fe}_2\text{O}_4$ appears to be promising.

According to literature survey, most of the studies on nanosized $\text{Co}_{1-x}\text{Zn}_x\text{Fe}_2\text{O}_4$ ferrites till date involve investigation of structural, magnetic and electrical properties of entire series of this system [20–22,29,31–33,35–37]. Very few groups have studied the properties of a particular composition of $\text{Co}_{1-x}\text{Zn}_x\text{Fe}_2\text{O}_4$ in detail and some of them have come out with exceptional results, which otherwise get overshadowed when studied in series. Presence of nanosized magnetic clusters in an infinite magnetic framework, cluster-paramagnetic phase, cluster glass phase, mixed magnetic phase, non-collinear spin structure and superparamagnetic clusters have been recognized in nanosized $\text{Co}_{0.2}\text{Zn}_{0.8}\text{Fe}_2\text{O}_4$, $\text{Co}_{0.3}\text{Zn}_{0.7}\text{Fe}_2\text{O}_4$, $\text{Co}_{0.4}\text{Zn}_{0.6}\text{Fe}_2\text{O}_4$, $\text{Co}_{0.5}\text{Zn}_{0.5}\text{Fe}_2\text{O}_4$ and $\text{Co}_{0.6}\text{Zn}_{0.4}\text{Fe}_2\text{O}_4$ ferrites [34,38–43]. The nanometric $\text{Co}_{0.5}\text{Zn}_{0.5}\text{Fe}_2\text{O}_4$ has attracted special attention due to rare presence of mixed magnetic phase in this system [34,43].

The synthesis procedure of nanosized spinel ferrites is of particular importance in determining their properties and their effectiveness in technological applications [19,25–27]. In this regard, chemical coprecipitation method has emerged as an efficient synthesis technique because of low cost precursors, moderate preparation time, modest heating and large scale production of nanometric ferrites, all of which are industrially important [19,21,22,36,37,44]. But, these nanometric ferrites are vulnerable to reduction of magnetization and magnetic ordering temperature due to the undesirable effects of surface spin canting and superparamagnetism related to finite size effect [45–49]. Heat treatment can increase magnetization and blocking temperature of nanosized ferrites [22,42] but is associated with the drawback of increase in particle size [46]. Interestingly, nanosized ferrites have displayed enhancement in magnetic parameters on mechanical milling due to cation rearrangement among the two interstitial sites of spinel lattice and escalation of stress anisotropy energy induced by the mechanical strain generated in the process [3,12,13,45,46,50,51]. So, synthesis of nanosized spinel ferrites by chemical coprecipitation method followed by mechanical treatment through high energy ball milling seems to be an appropriate technique to produce nanosized spinel ferrites of superior magnetic quality without compromising on the industrial demand of miniaturization.

In this background, we have employed the method of chemical coprecipitation to synthesize nanosized $\text{Co}_{0.5}\text{Zn}_{0.5}\text{Fe}_2\text{O}_4$ and ball milled it for duration of three, six and nine hours to obtain samples M1, M2 and M3, respectively, with the aim to examine the changes that have arisen in the structural, microstructural, magnetic and hyperfine properties of the samples as they undergo milling for different duration. The structural and microstructural characteristics have been inspected through powder x-ray diffraction and transmission electron microscopic techniques. The in-field and without field Mössbauer spectroscopic technique along with dc magnetic measurements have been utilized to delve into the variations that have emerged in magnetic and hyperfine properties of the samples. Moreover, the dependence of magnetic properties on the structural changes induced by high energy ball milling has been investigated thoroughly on sample M2.

2. Experimental

$\text{Co}_{0.5}\text{Zn}_{0.5}\text{Fe}_2\text{O}_4$ nanoparticles were synthesized by chemical coprecipitation method followed by ball milling for three, six and nine hours to obtain samples M1 (~63 nm), M2 (~25 nm) and M3 (~17 nm). All Sigma-Aldrich made (purity > 99.99%) reagents viz., $\text{CoCl}_2 \cdot 6\text{H}_2\text{O}$, $\text{ZnSO}_4 \cdot 7\text{H}_2\text{O}$ and $\text{Fe}(\text{NO}_3)_3 \cdot 9\text{H}_2\text{O}$ (precursors of the reaction) were taken in proper stoichiometric ratio and mixed in distilled water following addition of 10 M NaOH solution to attain a pH of ~12 under constant stirring. Afterward, the solution was continuously stirred for 9–10 h and then the precipitate was washed in ethanol and collected by centrifugation. This precipitate was sintered at 700°C for 8 h to obtain fine black powder. Further, this powder was annealed at 1000°C for 12 h to attain better crystallinity. The so obtained sample shows average particle size of ~90 nm (Fig. S1, see supplementary file). In general, the particle size of Co-Zn ferrites obtained from coprecipitation method ranges around 10–20 nm [12,13,22,52], but in the present case the average particle size is much larger due to the heat treatment of the sample obtained from coprecipitation method. The heat treated sample was ball milled in a Fritsch Planetary Mono Mill Pulverisette 6 ball mill at a rotational speed of 330 rpm with ball to mass ratio 20:1 using tungsten carbide balls and vials. The detailed procedure followed for synthesis of the samples and the methodologies of ball milling experiment are also presented in our previous work [47]. Bruker D8 Advanced diffractometer, FEI Inspect F50 FESEM, JEOL 2100 HRTEM equipped with Bruker EDS system, Wissel made Mössbauer spectrometer equipped with Janis SuperOptimag superconducting magnet and Superconducting quantum interference device (SQUID) magnetometer (Quantum Design, SVSM, USA) were used for structural, morphological, hyperfine and magnetic characterization of the samples, respectively, by adopting standard measurement protocol illustrated in our earlier work [13]. The Mössbauer data of the samples were analyzed by Recoil program [53].

3. Results

3.1. Structural characterization

The observed reflections in the powder x-ray diffraction (PXRD) patterns of M1, M2 and M3 are in good conformity with the miller indices of cubic spinel structure of $Fd\bar{3}m$ space group and match well with JCPDS ICDD card numbers 22-1086 and 82-1049 for Co and Zn ferrite, respectively. The PXRD patterns of the samples M1, M2 and M3 have been indexed by Rietveld based software packages Fullprof2k [54,55]. MAUD2.33 package [56] has been used to analyze the phase purity and determine the microstructural parameters of the samples as this software can determine quantitative abundance of different phases in a composite (multiphase) material by structural refinement along with meaningful extraction of microstructural parameters by peak shift and broadening analysis of PXRD profile [57] whereas most of the Rietveld programs (Fullprof, EXPO etc.) are not capable of implementing this procedure. The outcomes are summarized in Fig. S2 and Table S1 (see supplementary file). Further, GSAS software [58] has been used for extracting precise information on crystal structure of the samples taking into account the standard methodology reported earlier [3,13] and the results are presented in Fig. 1, Fig. S3 (see supplementary file) and Tables 1 and 2. For Rietveld refinement by GSAS software, the initial positions of tetrahedral (A) site metal ions, octahedral [B] site metal ions, and O atoms have been assigned in the special Wyckoff positions 8(b), 16(c), and 32(e), respectively, and refinement was carried out for the position coordinates of the oxygen atom, lattice parameters, background coefficients, cation occupancies and profile parameters. In the final stages of refinement, the preferred orientation correction was performed using the generalized spherical harmonic (order 14) model. The refinement of 63 parameters viz., 3 coordinates, 1 lattice parameter, 36 background points, 15 profile parameters, 7 orientation distribution

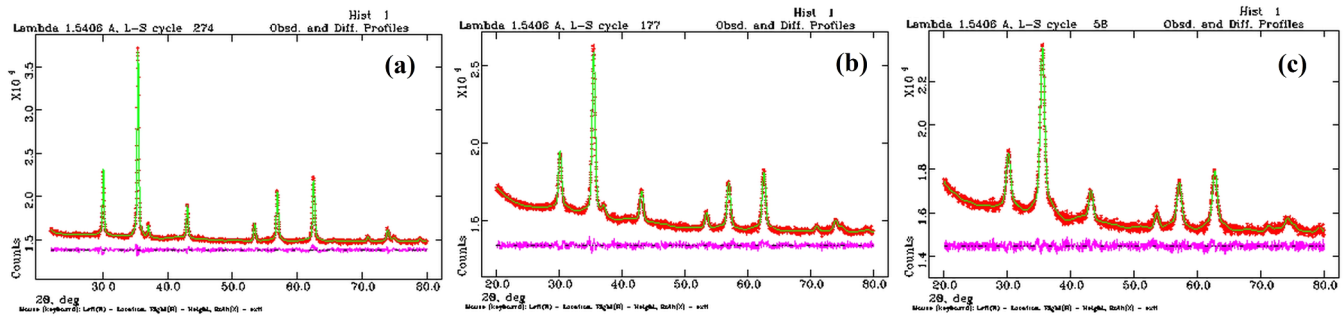


Fig. 1. Indexed powder PXRD pattern of the sample (red dots) and the simulated Rietveld refinement plot (continuous green line) obtained by fitting the experimental powder PXRD pattern using GSAS program. The respective residue is plotted at the bottom (pink line). (For interpretation of the references to colour in this figure legend, the reader is referred to the web version of this article.)

Table 1

Structural and microstructural parameters along with metal–oxygen (M–O) bond angles and bond lengths of M1, M2 and M3 obtained from Rietveld analysis of PXRD pattern of the sample by GSAS program.

Parameters	M1	M2	M3
Formula weight	475.7	475.7	475.7
Crystal System	F d - 3 m	F d - 3 m	F d - 3 m
Lattice parameter (Å)	8.396 (2)	8.390 (6)	8.378 (10)
Density (g cm ⁻³)	5.338	5.331	5.373
Volume (Å ³)	591.89 (4)	592.76 (13)	588.12 (2)
Metal–Oxygen bond length (Å)	1.835 (A-site) 2.089 (B-site)	1.836 (A-site) 2.090 (B-site)	1.831 (A-site) 2.085 (B-site)
Metal–Oxygen bond angle (Å)	109.47° (A-site) 89.45° (B-site)	109.47° (A-site) 89.45° (B-site)	109.47° (A-site) 89.45° (B-site)

Table 2

Fractional coordinates and occupancy of different ions obtained from the Rietveld refinement of PXRD pattern of M2 by GSAS program.

Ions	x	y	z	Occupancy (± 0.003)
Zn (A)	0.125000	0.125000	0.125000	0.4800
Fe (A)	0.125000	0.125000	0.125000	0.5200
Co (B)	0.500000	0.500000	0.500000	0.2500
Zn (B)	0.500000	0.500000	0.500000	0.0100
Fe (B)	0.500000	0.500000	0.500000	0.7400
O	0.251194 (3)	0.251194 (3)	0.251194 (3)	1.0000

function coefficients and 1 scale factor were performed. The experimentally recorded PXRD patterns of the samples are in good agreement with the corresponding simulated patterns. The values of lattice parameter obtained for M1, M2 and M3 are in good agreement with those for nanometric Co–Zn ferrites reported earlier [19,29–32,34,50]. This clearly discards the possibility of presence of any probable impurity phase in the samples. The results of fitting reveal that the samples are single phase nanometric spinel ferrites of *Fd3m* symmetry. The structural formula of M1 is $(\text{Zn}_{0.5}^{2+}\text{Fe}_{0.5}^{3+})_{\text{A}}[\text{Co}_{0.5}^{2+}\text{Fe}_{1.5}^{3+}]_{\text{B}}\text{O}_4$, M2 is $(\text{Zn}_{0.48}^{2+}\text{Fe}_{0.52}^{3+})_{\text{A}}[\text{Co}_{0.5}^{2+}\text{Zn}_{0.02}^{2+}\text{Fe}_{1.48}^{3+}]_{\text{B}}\text{O}_4$, and M3 is $(\text{Zn}_{0.46}^{2+}\text{Fe}_{0.54}^{3+})_{\text{A}}[\text{Co}_{0.5}^{2+}\text{Zn}_{0.04}^{2+}\text{Fe}_{1.46}^{3+}]_{\text{B}}\text{O}_4$. It may be noted that in our attempt to fit the PXRD data by placing Co^{2+} ions at (A) site, the values of refinement parameters (R_p , R_{wp} , and GOF) turned out to be undesirable. Thus, Co^{2+} ions have probably not occupied (A) site of the spinel lattice.

3.2. Electron microscopic investigation

Transmission electron microscopic (TEM) images representing the distribution of particle size in M1, M2 and M3 (Fig. 2) reveal that the constituent particles in all three samples are of variable shape and size along with a strong tendency of aggregate formation, which increases

with the diminution of particle size and vary following the sequence $\text{M3} > \text{M2} > \text{M1}$. Such agglomeration is a common trait in case of ferrites because of strong interparticle interaction [59]. All the three samples exhibit clear lattice fringes in their high resolution TEM micrograph (Fig. 2). The distribution of particle size for M1, M2 and M3 has been examined by taking diameters (considering particles as nearly spherical) of nearly hundred nanoparticles into consideration and represented in the form of histograms. The polydisperse nature of the samples is clear from their respective histograms. The fitting of histograms with the log normal function (Fig. S4, see supplementary file) yields average particle sizes of M1, M2 and M3 as ~ 63, 25 and 17 nm with values of standard deviation (σ) as 0.15, 0.24 and 0.08, respectively. The value of ' σ ' quantifies the amount of dispersion in data values and so in the present case gives an idea about the polydispersity of the samples, which is directly related to the blocking temperature distribution.

The presence of bright distinct rings in the selected area diffraction (SAED) pattern of sample M2 (Fig. S5, see supplementary file) and matching of 'd' values obtained from PXRD study with those obtained by evaluating the SAED pattern together with assure about the crystallinity of the nanoparticles. The EDX survey spectrum of M2 (Fig. S6, see supplementary file) in the energy range of 0–16 keV displays only peaks for the constituent elements (Co, Zn and Fe) with no signature of any impurity phase. The ratio of Co, Zn and Fe is 16.14:16.16:64.71, which assure that the sample is in appropriate stoichiometry.

3.3. Magnetic and hyperfine study

The curves of zero field cooled (ZFC) and field cooled (FC) magnetization versus temperature (range of 5–350 K) of samples M1 (Fig. 3(a)), M2 (Fig. 3(b)) and M3 (Fig. 3(c)) under an external applied magnetic field of 100 Oe primarily exhibiting phase transition from superparamagnetic to magnetically well-ordered state with the decrease in temperature are shown in Fig. 3. It is well known that the distribution of blocking temperatures is closely related to the anisotropy energy barrier distribution of the system and thus, with the particle size distribution [60]. If the particle size distribution is uniform, the half-width of the ZFC versus temperature (T) curve is expected to be narrower [60]. The TEM study indicates the polydisperse nature of all three samples which in turn resulted in an increase in the half-width of the ZFC vs T curve. In such case, the maximum of the ZFC curve (T_{max}) corresponds to the blocking of particles with average volume [61,62] and can be written as $T_{\text{max}} = \beta T_B$ [63], where β is proportionality constant that depends on the type of size distribution and T_B is defined as the temperature at which 50% of the nanoparticles are in blocked state and rest 50% are in superparamagnetic state. To account for the polydisperse nature of the samples, it would be better to determine T_B from the derivative of the difference in ZFC magnetization (M_{ZFC}) and FC magnetization (M_{FC}) with respect to temperature [22,60]. We have plotted the $(d(M_{\text{ZFC}} - M_{\text{FC}}))/dT$ versus T curve (Fig. 4) and estimated

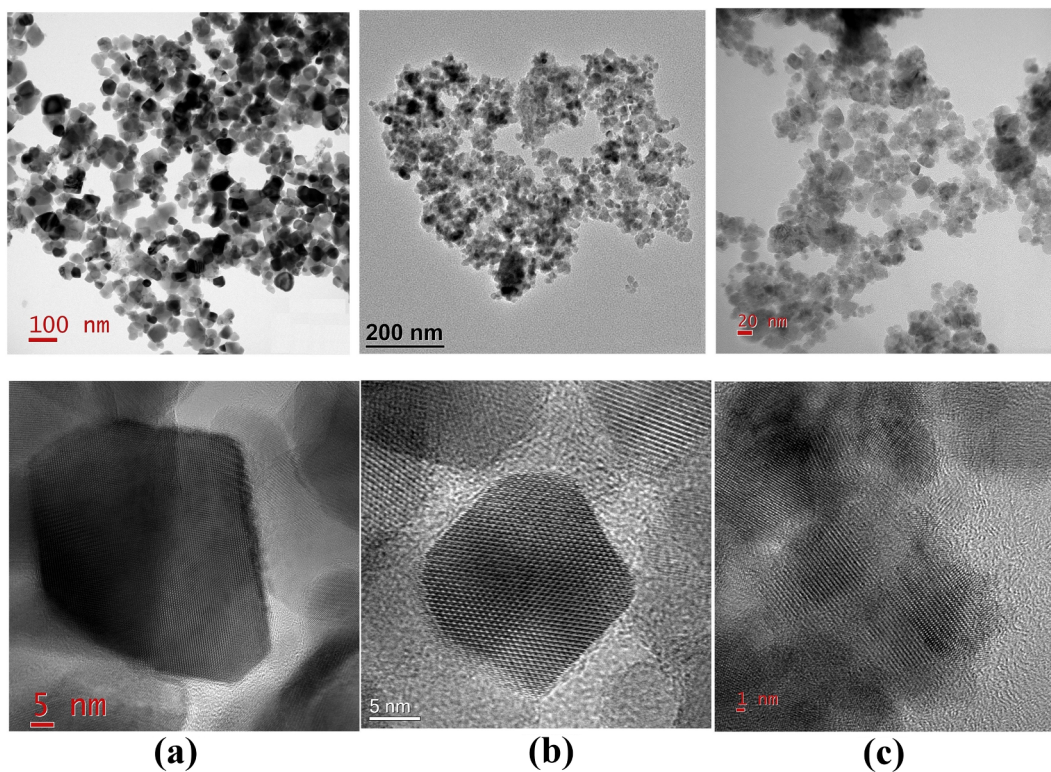


Fig. 2. TEM micrographs showing particle distribution and lattice fringes of (a) M1 (b) M2 (c) M3.

the value of T_B for each sample. The values of T_{max} , T_B and T_{irr} (temperature corresponding to the blocking of the largest particle) are enlisted in Table 3. The values of β for all three samples lies in the range 1.5–2.5 as should be for a nanoparticle assembly following log-normal distribution [64]. Further, the variations in values of T_B , T_{max} and T_{irr} i.e., $T_B < T_{max} < T_{irr}$ points out that the samples are polydisperse, thus, corroborating with the TEM study.

A second phase change transpires at about 50 K which is seen as a cusp in the ZFC curves of all the samples suggesting a spin glass like random freezing of moments resulting from strong magnetic interaction within the constituent particles of the samples [15,16,65]. This temperature is usually termed as the freezing temperature (T_f) of the system. In order to gain insight of the observed phase transition at low temperature, we have plotted the dM_{ZFC}/dT versus T curves for all three samples. The dM_{ZFC}/dT versus T curves for M1, M2 and M3 (Fig. 5) exhibit a maximum at ~ 20 K and the change in derivative begins at ~ 50 K which marks the inception of spin glass like behavior in their ZFC curve. Further, it is expected that FC curve will increase monotonically with reduction in temperature due to decreasing thermal

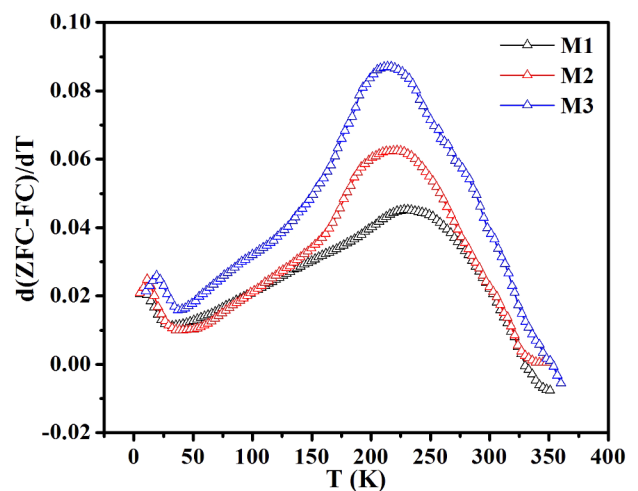


Fig. 4. $d(ZFC-FC)/dT$ versus T curves for M1, M2 and M3.

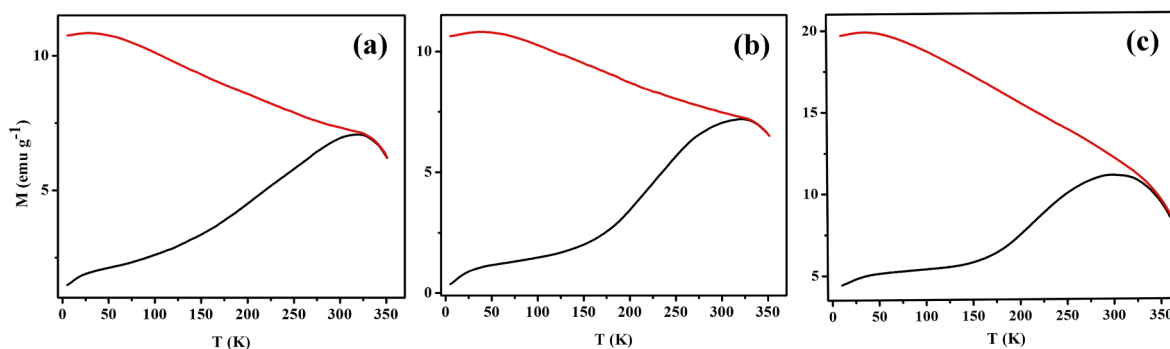


Fig. 3. ZFC-FC magnetization curves of (a) M1 (b) M2 and (c) M3 at 100 Oe. The FC and ZFC magnetization is represented by red and the black lines, respectively. (For interpretation of the references to colour in this figure legend, the reader is referred to the web version of this article.)

Table 3

Values of crystallite size obtained from PXRD, particle size obtained from TEM, blocking temperature (T_B), temperature corresponding to the maximum in ZFC curve (T_{max}), irreversibility temperature (T_{irr}), saturation magnetization (M_{SAT}) and coercivity (H_C).

Sl. No	Sample	Crystallite size (nm)	Particle size (nm)	T_B	T_{max}	T_{irr}	M_{SAT} (emu g ⁻¹)	H_C (Oe)
1.	M1	63	63	220	330	348	56.8 (300 K) 115.68 (10 K)	30 (300 K) 1395 (10 K)
2.	M2	25	25	210	318	345	55.3 (300 K) 113.84 (10 K)	20 (300 K) 2190 (10 K)
3.	M3	17	17	204	310	340	51.5 (300 K) 109.65 (10 K)	0 (300 K) 1950 (10 K)

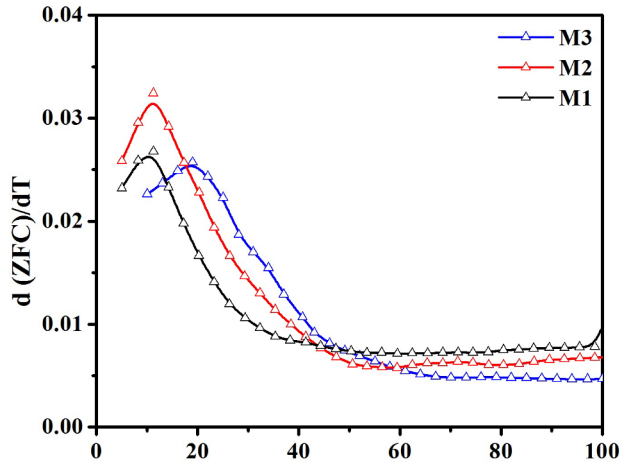


Fig. 5. $d(ZFC)/dT$ versus T curves for M1, M2 and M3.

fluctuations for typical superparamagnetic system [59]. But in this case, the FC curves of all three samples exhibit a slow fall in magnetization on decreasing the temperature below T_f of the ZFC curve. Usually if there is a combined interplay of interparticle interactions and spin glass like freezing, a flat region develops in the FC curve at very low temperatures. So, this unexpected behavior in magnetization of the FC curve below 50 K, in the present case, can be due to the random freezing of canted surface spin arrangement in the sample reinforced due to higher non-magnetic Zn^{2+} concentration in it, which can be further confirmed from in-field Mössbauer spectroscopic study. We have further performed M-H (variation of magnetization with field change) loop measurements to validate the findings of ZFC-FC study. The M-H loops of M1, M2 and M3 at 300 and 10 K in the field range -1 to $+1$ T are shown in Fig. 6. M1 and M2 exhibit a small hysteresis in their M-H loops at room temperature but M3 does not. So, M3 is mostly superparamagnetic but M1 and M2 clearly exhibit mixed magnetic phases. However, all the three samples exhibit clear hysteresis loops at 10 K.

The values of saturation magnetization (M_{SAT}) at 300 and 10 K for the three samples have been estimated by plotting M versus $1/H$ curve using the law of approach to saturation. The values of M_{SAT} and coercivity (H_C) are provided in Table 3. The steep increase in the values of M_{SAT} and H_C at low temperature suggest development of magnetic ordering with the decrease in temperature, which may be due to freezing of surface canted spins.

⁵⁷Fe Mössbauer spectroscopy has been employed to determine the valency of iron ions and probe the hyperfine interactions to further delve into the observations arrived from the dc magnetic studies. The room temperature (300 K) Mössbauer data of M1, M2 and M3 have been analyzed by Recoil program [53] and the fitted spectra are presented in Fig. 7. The values of hyperfine parameters are listed in Table S2 (see supplementary file). The values of isomer shift (IS) indicate presence of only Fe^{3+} ions in all three samples [3,12,13,45,46]. M1 exhibits a clear hyperfine sextet (76.9%) and a feeble doublet (23.1%). In the spectrum of M2, a less intense sextet (69.9%) as compared to M1 along with a superparamagnetic doublet (30.1%) has been found. M3 displays a prominent doublet (49.73%) along with a poorly defined sextet (50.26%) in its room temperature Mössbauer spectrum. The intensity of the hyperfine sextet gradually diminishes with decreasing particle size. The doublet has large line width while the sextet is diffused in nature (Fig. 7). The pattern of evolution of the Mössbauer spectra with increase of particle size can be elucidated by the theory of superparamagnetic relaxations [14,15,28,59,65]. The dependence of the relaxation time (τ) of superparamagnetic nanoparticles on particle volume (V), temperature (T) and anisotropy energy constant (K) is given by Neel-Brown equation $\tau = \tau(0)\exp\left(\frac{KV}{kT}\right)$ [28] (k is the Boltzmann constant), which suggests that τ decreases with the reduction in particle size. If $\tau < \tau_m$ (time of measurement), total moment during the time of measurement becomes zero giving rise to a doublet [59]. On the contrary for $\tau > \tau_m$, a narrow hyperfine split sextet emerges [59]. But, the presence of an admixture of a relaxed sextet with a superparamagnetic doublet for all three samples indicates that the samples consist of both superparamagnetic ($\tau < \tau_m$) and magnetically well-ordered ($\tau > \tau_m$) particles. The results of dc magnetic

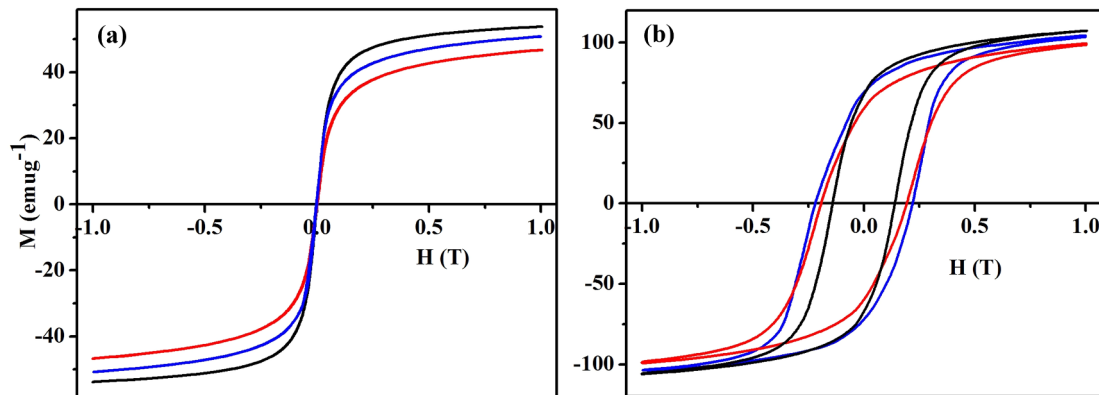


Fig. 6. M-H (hysteresis) loop of M1 (black line), M2 (blue line) and M3 (red line) at (a) 300 and (b) 10 K shown between ± 1 T. (For interpretation of the references to colour in this figure legend, the reader is referred to the web version of this article.)

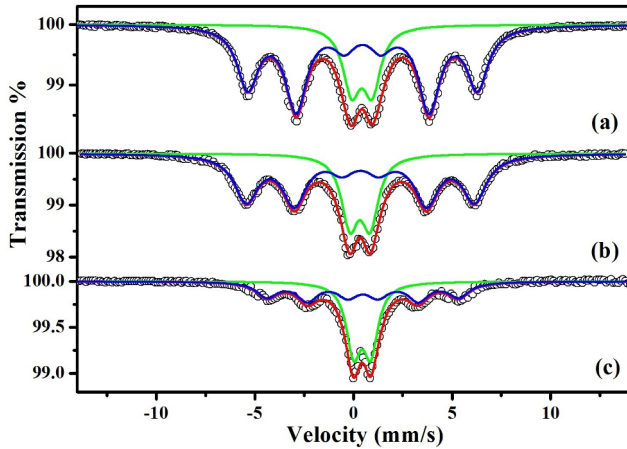


Fig. 7. Mössbauer spectrum of (a) M1, (b) M2 and (c) M3 at 300 K.

measurements and room temperature Mössbauer spectroscopic measurements, together with, suggest that at room temperature particles in all the samples exhibit mixed magnetic state composed of superparamagnetic and magnetically ordered phases.

Low temperature (5 K) infield and without field Mössbauer spectroscopic data have been recorded to determine the spin configuration of M2, estimate the ratio of Fe^{3+} ions at (A) and [B] sites of the spinel lattice and explicate the magnetic behavior of M2 thoroughly. The infield Mössbauer spectrum was recorded in presence of 5 T magnetic field applied parallel to the γ -ray direction. The ferrimagnetic nature of M2 can be affirmed from the appearance of a split in the 1st and the 6th line of the infield Mössbauer spectrum of the sample [3,12,13,45–47,59]. Further, the occurrence of 2nd and 5th lines in the infield Mössbauer spectrum of M2 clearly suggests the presence of canted spins in the sample [3,12,13,45–47,59]. Although two-component fitting is capable of extracting the information on the global canting of the system but it is unable to extort the local hyperfine character embedded in the Mössbauer spectrum [3,12]. So, the infield Mössbauer spectrum recorded at 5 K has been fitted by four sextets using “Lorentzian site analysis” of Recoil program to acquire quantitative information on the distribution of cations and spin canting effect at the core and surface regions of the sample [12]. The refined values of the hyperfine parameters and the precise values of canting angles have been depicted in Table 4. The pair of sextet with lower hyperfine field (HMF), higher isomer shift (IS) and higher canting angles corresponds to the canted surface region. The core is also not perfectly aligned and possesses canted spins. The simulated and experimental spectra corroborate with each other (Fig. 8) and the values of refinement parameters are good enough. Presence of only Fe^{3+} ions in the sample can be ascertained from the values of IS [28]. The proportion of the intensity of the

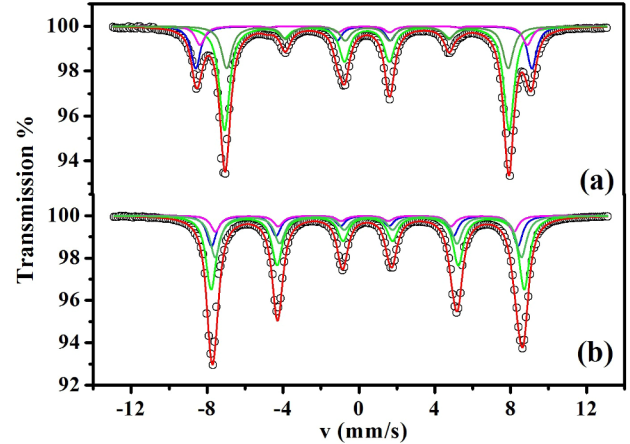


Fig. 8. Mössbauer spectra of M2 at (a) 5 K with 5 T external magnetic field and (b) 5 K fitted by Lorentzian site analysis method of the Recoil program.

sextets corresponding to (A) and [B] site of M2 for both core and shell is 0.35 which is greater than its bulk counterpart with equilibrium cation distribution (0.33). This suggests that the sample is chemically homogeneous and Fe^{3+} ions have migrated from [B] site to (A) site in M2. The ratio of Fe^{3+} at (A) and [B] sites obtained from the infield Mössbauer spectrum corroborates with the one obtained from Rietveld refinement of PXRD pattern. Thus, the four-component fitting assuming the core-shell model in case of M2 is capable of divulging the hyperfine character of the system accurately.

The without field Mössbauer spectrum of M2 at 5 K has been fitted with “Lorentzian profile” using four sextets by restricting the ratio of iron ions in (A) and [B] sites to that obtained from the infield spectrum to verify the results acquired from infield Mössbauer measurements [3,13]. The experimentally obtained and fitted spectra have matched with an excellent concord (Fig. 8). Presence of a well-defined sextet in the without field Mössbauer spectrum of M2 suggests that superparamagnetic relaxation has completely vanished at 5 K [3,13]. Table 4 contains the fitted values of hyperfine parameters of both the without field and infield Mössbauer study, and they agree very well with each other. Thus, taking into account the outcomes of the room temperature Mössbauer study, infield and without field Mössbauer spectrum of M2 at 5 K and dc magnetic measurements, it can be inferred that particles in M2 possess core-shell structure with a slightly canted core surrounded by a disordered shell and they exhibit superparamagnetic behavior at room temperature owing to their nanometric size.

3.4. Study of memory effect

From literature survey, it is well-established that magnetic

Table 4

Values of zero field and infield Mössbauer parameters of the sample at 5 K determined by Lorentzian profile fitting.

Temperature/Field	Site	Width (mm s^{-1})	IS (mm s^{-1})	2ϵ (mm s^{-1})	B_{eff}^a (T)	B_{hf} (T)	A_{23}	θ^b (degree)	Area (%)
5 K/5 T	[Fe_A^{3+}] _c	0.28	0.31	–	54.94	50.07 ^c	0.1	12.75	17.9
	[Fe_A^{3+}] _s	0.31	0.47	–	46.5	51.17 ^c	0.3	21.93	50.69
	[Fe_B^{3+}] _s	0.28	0.30	–	53.5	48.76 ^c	0.2	17.97	8.14
	[Fe_B^{3+}] _c	0.31	0.50	–	46.0	50.06 ^c	0.9	37.31	23.25
5 K/0 T	[Fe_A^{3+}] _c	0.28	0.31	–	–	50.07	–	–	17.55
	[Fe_A^{3+}] _s	0.31	0.47	–	–	51.17	–	–	46.80
	[Fe_B^{3+}] _s	0.28	0.30	–	–	48.76	–	–	9.29
	[Fe_B^{3+}] _c	0.31	0.50	–	–	50.06	–	–	26.33

^c ‘C’ denotes the core region and ‘S’ denotes the shell region.

^a Observed HMF (BHF) is the vector sum of the internal HMF and the external applied magnetic field.

^b The average canting angle estimated from the ratio of the intensities of lines 2 and 3 from each subspectra, I_2/I_3 (A_{23}) according to $\theta = \arccos[(4 - I_2/I_3)/(4 + I_2/I_3)]^{1/2}$. Where $I_2/I_3 = A_{23}$.

^c Estimated according to the relationship of B_{eff} , B_{hf} and applied field.

nanoparticles can keep a track of field changes in their dc magnetization measurement as a function of temperature [66–69]. The origin of this effect can be accredited to the presence of either spin glass like state in the system or due to broad particle size distribution in the nanoparticle assembly [66,67]. In the present case, all the three samples consist of both superparamagnetic (single domain) and magnetically well-ordered (multidomain) particles with broad size distribution. Further, the constituent particles in all three samples possess strong interparticle interactions which result in spin glass like phase at low temperature. Thus, it can be predicted that the samples under investigation may exhibit memory effect in both low and high temperature regions.

In order to testify the above argument, we have carried out a memory protocol experiment on sample M2 following the procedure described herein. At first, the magnetization versus temperature ($M(T)$) data of M2 was recorded as the sample underwent cooling from 300 K to 250 K with application of 100 Oe external magnetic field. Then, the field was switched off after 250 K temperature was attained and the system was held in this state for one hour. Post that, the 100 Oe field was reinstated and $M(T)$ data was recorded for temperature decrease from 250 to 70 K. The field was raised to 200 Oe after the system reached 70 K and kept in this condition for one hour. Thereafter, the field was reduced to 100 Oe and $M(T)$ data was recorded from 70 to 25 K under 100 Oe field. The field was turned off and the system was arrested in this state for one hour. Again, 100 Oe field was restored and $M(T)$ data was taken from 25 to 5 K. After reaching 5 K, the system was heated from 5 to 300 K under 100 Oe magnetic field and $M(T)$ data was recorded. Both cooling and heating rates were fixed at 2 K/min throughout the experiment. Fig. 9 depicts the outcomes of the memory experiment. It clearly reveals that the system remembers the changes made in the values of applied magnetic field during the experiment and can track such changes, thus displaying “memory effect”. So, it seems that the nanoparticle assembly can encode a rapid rise or fall in the applied field during cooling process which can be successfully decoded in the heating cycle.

4. Discussions

The results of Rietveld refinement of the PXRD pattern of M1, M2 and M3 using MAUD2.33 has revealed that all three samples are single phase nanometric spinel ferrite possessing $Fd\bar{3}m$ symmetry having chemical composition $\text{Co}_{0.5}\text{Zn}_{0.5}\text{Fe}_2\text{O}_4$. It is possible to estimate the value of lattice parameter (a_{es}) of $\text{Co}_{0.5}\text{Zn}_{0.5}\text{Fe}_2\text{O}_4$ system by taking the

weighted average of the lattice parameters of pure CoFe_2O_4 and ZnFe_2O_4 i.e., using the relation $a_{\text{es}} = 0.5 a_1 + 0.5 a_2$, where $a_1 = 8.391 \text{ \AA}$ and $a_2 = 8.440 \text{ \AA}$ are the lattice parameters of CoFe_2O_4 (JCPDS ICDD card no. 22–1086) and ZnFe_2O_4 (JCPDS ICDD card no. 82–1049), respectively. The obtained value of a_{es} is $\sim 8.41 \text{ \AA}$, which is in good agreement with those of the present samples. The values of microstrain (Table S1, see supplementary file) vary in the order $M3 (63 \text{ nm}) > M2 (25 \text{ nm}) > M1 (17 \text{ nm})$ i.e., microstrain increases upon increase in milling time which is a common phenomenon in mechanically milled ferrites [3]. In the present case, the values of lattice parameter (Table 1 and Table S1, see supplementary file) change following the sequence $M3 < M2 < M1$ i.e., decreases with the increase in milling time. It is well known that mechanical milling promotes changes in structural and microstructural properties due to cation redistribution which, in turn, affect the magnetic properties of these compounds [3,12,13,45,46,50,51]. In this light, we have studied the effects of mechanical activation through ball milling on bonding properties, cation distribution and size reduction of all three samples. In this regard, we have calculated the theoretical values of lattice parameter (a), tetrahedral (d_{AO}) and octahedral (d_{BO}) bond lengths, and oxygen positional parameter (u) using the formulae described in detail in following works [3,29,70–74] taking into consideration the Shannon effective ionic radii [75] and compared those values with the ones obtained experimentally. All the calculations have been executed using the cation distribution obtained collectively from the Rietveld refinement of PXRD data and infield Mössbauer spectroscopy. The experimental results and theoretical calculations are in consonance (Table S3, see supplementary file). This validates that the outcomes of analysis of the PXRD data are reliable and the cation distribution of M2 is trustworthy. As can be seen from Table S3 (see supplementary file), the values of ‘ a ’ for all three samples are slightly reduced in comparison to bulk $\text{Co}_{0.5}\text{Zn}_{0.5}\text{Fe}_2\text{O}_4$ [76]. Further, the values of d_{AO} have reduced and d_{BO} increased in all three cases in contrast to bulk. It is a well known fact that by comparing the value of u , one can map out the possibility of cation migration in spinel ferrites [70]. We have also observed that the value of u for the bulk $\text{Co}_{0.5}\text{Zn}_{0.5}\text{Fe}_2\text{O}_4$ [77] is different from all three samples indicating cation redistribution as has been estimated from infield Mössbauer spectroscopic study. So, we can conclude that, in the present case, structural parameters have changed noticeably upon scaling down to nanometric size as a result of incorporation of mechanical strain by ball milling.

Furthermore, we have calculated the theoretical value of magnetic moment per formula unit (m) adopting the procedure described in our earlier works [3,13]. Since the cation distribution for both core and shell of M2 is $(\text{Zn}_{0.48}^{2+}\text{Fe}_{0.52}^{3+})_{\text{A}}[\text{Co}_{0.25}^{2+}\text{Zn}_{0.02}^{2+}\text{Fe}_{1.48}^{3+}]_{\text{B}}\text{O}_4$, we have calculated the theoretical value of m using this formula and taking canting angles from Table 4. The values of the magnetic moment for the core region (m_{CR}) and surface region (m_{SR}) are 5.72 and 4.606 μ_{B} , respectively. From the results of Mössbauer spectroscopic study, it has been found that the core and the shell regions cover 68.6% and 31.4% of the total volume of each particle, respectively. Considering this fact, we have calculated the value of m of the sample using the formula $m = 0.686 \times m_{\text{CR}} + 0.314 \times m_{\text{SR}}$ and obtained value of m is 5.37 μ_{B} . The experimental value of m for M2 in Bohr magneton (μ_{B}) obtained by using M-H data at 10 K is 5.32 μ_{B} . The experimental and theoretical values of ‘ m ’ are very close to each other which indicate that the structural formula used for the calculation of magnetic moments has been precisely determined and the particles in the sample possess almost ferrimagnetically aligned core with small canting along with magnetically disordered shell.

The results of TEM, dc magnetic and Mössbauer studies together with bring about following main issues about all three samples: (i) existence of mixed magnetic phases at room temperature, (ii) presence of overall ferrimagnetic ordering along with surface spin canting, and (iii) random spin glass like freezing of magnetic moments at low temperature. The possible reasons for such observations have been

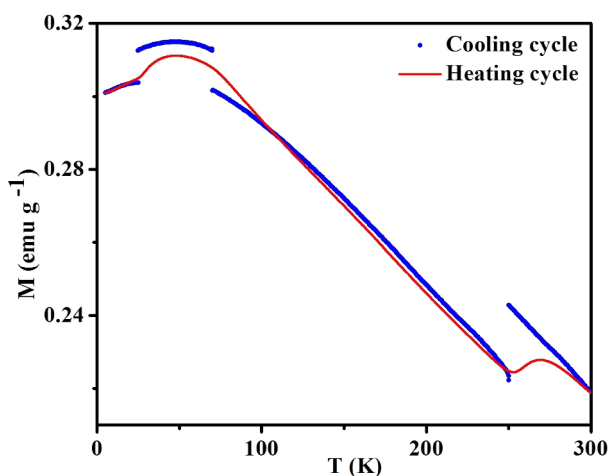


Fig. 9. Memory effect in the dc magnetization of M2 (red line and blue dots represent the magnetization data for the heating and the cooling cycles, respectively). (For interpretation of the references to colour in this figure legend, the reader is referred to the web version of this article.)

discussed thoroughly with supporting references in the rest part of this text. The morphological study of M1, M2 and M3 using TEM indicates that constituent particles of all three samples have variable shape and size, possess interparticle interactions and surface disorder. These features have induced two different phase transitions in the ZFC versus T curves of M1, M2 and M3; transition from superparamagnetic to blocked state below blocking temperature (T_B) and a random spin glass like freezing below T_f ($< T_B$). According to the outcomes of Mössbauer spectroscopic studies at room temperature (~ 300 K), majority of the particles in the milled samples are in superparamagnetic state (single domain) and a small fraction (multi domain) exhibit collective magnetic excitations. Further, due to the presence of strong interparticle interactions within the samples, the particles in the samples undergo transition from collective state to spin glass like state, which has been indicated by the appearance of a sharp cusp in the ZFC versus T curve [65]. Hence, the observed behaviour of the ZFC versus T curves is a result of a complex combination of individual blocking phenomena, interparticle interaction and collective freezing of magnetic moments.

Further, the low temperature in-field Mössbauer spectroscopic studies also bring forth the core-shell structure of the nanoparticles in M2 with a core having slightly canted spins surrounded by a shell with disordered spin alignment. The effect of these disordered spins at the surface gets more prominent below a certain particle size when the surface to volume ratio is high. Thus for the nanoparticle assembly in M2, these disordered surface spins get randomly frozen as the temperature is lowered and it has been manifested by fall in magnetization of the FC curve at very low temperatures. Thus, the dc magnetic and in-field Mössbauer studies together suggest that the freezing of disordered spins of the core-shell structure is responsible for the unexpected and topological magnetic behavior of the FC curves of the present samples at low temperature.

The constituent particles of all three samples M1, M2 and M3 are polydisperse in nature as has been observed from TEM analysis. Further, the room temperature Mössbauer spectra of all three samples possess an admixture of a superparamagnetic doublet and a diffused sextet. So, it is clear that all the samples consist of both single domain and multi domain particles. It is well known that for uniaxial single domain particles, anisotropy energy constant (K) can be calculated using the formula $KV = 25 k_B T_B$, where V is the particle volume, k_B is the Boltzmann constant and T_B is the blocking temperature of the particle. So, in the present case, it will not be appropriate to use the above formula for calculation of K. But still then, we have used the above formula and found the values of K for M1, M2 and M3 as 3.07×10^2 , 4.4×10^3 , 1.41×10^4 J/m³, which are unusually small as compared to other nanosized Co-Zn systems [13,52,78]. So, we have employed a formula for the calculation of K, which does not take the particle size of the samples into consideration; instead the values of M_{SAT} , H_C and density of the nanoparticles (ρ) are used and can be written as $K = \mu_0 M_{SAT} \frac{H_a}{2} \rho$, where H_a is the anisotropy field and $\frac{H_a}{2}$ corresponds to the maximum value of H_C [78]. The values of K obtained using this formula are 8.6×10^4 , 1.3×10^5 , 1.1×10^5 J/m³ for M1, M2 and M3, respectively. The calculations have been done taking into consideration the estimated values of M_{SAT} and H_C provided in Table 3, and values of ρ present in Table 1. These values of K for M1, M2 and M3 are very close to that of pure cobalt ferrite ($\sim 2 \times 10^5$ J/m³). It can be clearly seen that there is a difference of almost two orders in the values of K for M1 and M2 obtained using formulae $KV = 25 k_B T_B$ and $K = \mu_0 M_{SAT} \frac{H_a}{2} \rho$ as both consist of mainly multi domain particles, whereas for M1 the difference is of one order as most of the constituent particles of M1 are single domain (superparamagnetic). Thus, the values of K obtained using $K = \mu_0 M_{SAT} \frac{H_a}{2} \rho$ formula is trustworthy. All the three samples exhibit high values of K due to enhancement of both magnetocrystalline and strain induced anisotropy caused by mechanical strain produced through high energy ball milling [13]. We have compared the lattice parameter of the present samples with bulk $Co_{0.5}Zn_{0.5}Fe_2O_4$ in

Table S3 (see supplementary file) and observed that there is a contraction in lattice parameter for the present samples. This contraction has contributed to the increase in magnetocrystalline anisotropy energy. Further, an increase in microstrain with increasing milling time has been observed for the present samples. Thus, strain induced anisotropy and magnetocrystalline anisotropy together have lead to the enhancement of K.

The values of M_{SAT} of M1, M2 and M3, both at 300 and 10 K, falls off gradually with the decrement in particle size i.e., M1 (63 nm) > M2 (25 nm) > M3 (17 nm). This reduction can be ascribed to the occurrence of spin canting at the nanoparticle surface introduced by high energy ball milling resulting in magnetic disorder [3,12,13,59]. With the minimization in particle size upon mechanical milling, surface effects become more prominent and thus, canted spins at the surface can cause a reduction in effective magnetization of the system [63,79]. Table 5 compares the values of room temperature (300 K) magnetic parameters like M_{SAT} and H_C for nanosized $Co_{0.5}Zn_{0.5}Fe_2O_4$ ferrites synthesized by different techniques with that of the present samples. It suggests that the value of M_{SAT} of $Co_{0.5}Zn_{0.5}Fe_2O_4$ ferrite depends upon the synthesis procedure and particle size. Further, the values of M_{SAT} of the present samples M1, M2 and M3 at 10 K, $Co_{0.5}Zn_{0.5}Fe_2O_4$ synthesized by coprecipitation followed by heat treatment with particle size 15 and 22 nm at 4.5 K [22] and $Co_{0.5}Zn_{0.5}Fe_2O_4$ synthesized by low temperature solution combustion method having particle size 12 nm at 20 K [32] are 115.68, 113.84, 109.65, 112.5, 125 and 100 emu g⁻¹, respectively. There is a sheer rise in the values of M_{SAT} at low temperature (10 K) as compared to room temperature (300 K). This behavior has been detected in ferrimagnetic nanoparticles and assigned to the freezing of surface spins [57,63,79,80].

Samples M1 and M2 exhibit small coercivity at room temperature (300 K) but M3 does not as it is almost purely superparamagnetic possessing very few larger sized particles as has been predicted from room temperature Mössbauer spectroscopic study. The small coercivity at 300 K displayed by M1 and M2 are due to increased magnetocrystalline anisotropy of the samples caused by ball milling [12]. At 10 K, the coercive field varies following the order M2 > M3 > M1. Waje et al., and Iqbal et al., have obtained similar changes in coercivity (H_C) beyond a certain particle size [18,85]. This pattern of variation in H_C can be explained from the magnetic domain theory as has been illustrated in our earlier work [3]. Although for strongly interacting particles, it is problematic to obtain parameters related to non-interacting independent particles, we have calculated the critical diameter (D_C) of a particle approximately by using the formula $D_C = 9E_p/2\pi M_S$, where $E_p = \sqrt{\frac{2k_B T_C K}{a}}$ is the energy density of the magnetic domain wall and M_S is the saturation magnetization, considering it to be nearly spherical [3]. We have first estimated the value of E_p by taking Boltzmann constant k_B , magnetocrystalline anisotropy $K = 1.1 \times 10^5$ J/m³, lattice constant $a = 8.40$ Å, saturation magnetization $M_S = 647.17$ Gauss and Curie temperature $T_C = 420$ K as has been obtained from Veverka et al., considering the fact that sample M3 has particle size nearly equal to one of their samples having same chemical composition [22]. The calculated value of D_C for nanosized $Co_{0.5}Zn_{0.5}Fe_2O_4$ is ~ 27 nm. Thus, particles in M1 (63 nm) are multi domain whereas M2 (25 nm) and M3 (17 nm) can be considered as single domain. Among three samples, the particle size of M2 is closest to the value of D_C . It is well known that the value of H_C increases with the decrement in particle size in multi domain region then attains a maximum value at D_C and again decreases in single domain regime with diminution of particle size [11,87]. In the present case, the highest value of H_C has been obtained for M2 which consists of particles with diameter closer to the critical diameter while value of H_C decreases for both M3 with particle size much smaller than D_C and M1 with particle size larger than D_C . In larger particles, reversal of magnetization occurs by magnetic domain wall motion, whereas in a fine particle, entire spin needs to be rotated for magnetization reversal [3]. It is easier to rotate the domain wall in comparison to rotation of all

Table 5Table for comparison of room temperature (300 K) magnetic parameters of nanosized $\text{Co}_{0.5}\text{Zn}_{0.5}\text{Fe}_2\text{O}_4$ ferrite synthesized by various procedures.

Sl. No	Synthesis procedure	Particle size (nm)	Magnetisation M_s (emu g^{-1})	Coercivity H_c (Oe)	Reference
1.	Co-precipitation followed by heat treatment	7	–	> 250	[22]
		15	–	250	
		22	–	< 250	
2.	Wet chemical coprecipitation	7.26	75.80208	0	[29]
3.	Sol-gel auto combustion	29.01	90.13	176.24	[30]
4.	Coprecipitation	51	82	75.4	[31]
5.	Low temperature solution combustion	12	~ 63	~ 100	[32]
6.	Microwave combustion	45.81	65.20	66.36	[33]
7.	Chemical coprecipitation method	9.8	49.55	22	[34]
8.	Starch-assisted sol-gel auto-combustion method and ball milled	75.7	76.70	73.56	[50]
		69.4	82.47	196.31	
9.	Sol-gel auto-combustion method and ball milled	21.68	21.38	9.56	[51]
		18.99	61.38	79.7	
10.	Coprecipitation	5.8	15.5	–	[81]
11.	Precipitation Combustion	17.0	14.7	10	[82]
		24.0	3.65	50	
12.	Sol-gel Hydrothermal	23.1	73.6	314	[83]
		11.2	56.7	1464	
13.	High-temperature thermal decomposition	9.4	78.7	21	[84]
14.	Chemical coprecipitation	21	19.32	96.88	[85]
15.	Microwave combustion	35.68	73.80	~ 300	[86]
16.	Chemical coprecipitation Followed by high energy ball milling for 3 h (M1) 6 h (M2) 9 h (M3)	63	56.8	30	Present samples
		25	55.3	20	
		17	51.5	0	

the spins [11,87]. Thus, higher value of H_c for M2 and M3 as compared to M1 is justified.

The superposition of a doublet and a sextet in the room temperature Mössbauer spectrum of all three samples suggest that some of the particles are very small and single domain in nature, hence, they exhibit superparamagnetic behavior while rest of the particles are larger in size and they display ferrimagnetic behavior. It infers that the particles in the samples are not monodispersed. The outcomes of the low temperature (5 K) Mössbauer spectroscopic study (both in-field and without field) reveal that M2 constitutes of particles having ferrimagnetic phase and no signature of relaxation is visible at this temperature. However, the sample exhibits spin canting. On contrary, the dc magnetization study on M2 indicates presence of a cluster glass like state in the sample below 50 K which apparently disapproves the results of Mössbauer spectroscopic study performed at 5 K. This disparity between the two measurements can be accounted by considering the fact that Mössbauer spectroscopy probes the local fluctuations of hyperfine magnetic field whereas dc magnetization records the effective magnetic moment of the sample as a whole [65]. The presence of both (A) and [B] site sextets in the Mössbauer spectra of M2 at 5 K reveals that M2 is either ferrimagnetic in nature or there are regions (clusters) inside the particles of M2 which are in ferrimagnetic state. Thus, considering the results of Mössbauer spectroscopic study and dc magnetic measurements together, it can be concluded that there are ferrimagnetically ordered clusters inside the grains of the sample and with decreasing temperature the interplay between opposing sublattice interactions and frustrations result in freezing of local magnetic moment of these clusters in random orientation and the system en masse stabilizes in a spin glass like state [65].

The sample M2 has exhibited excellent memory effect in its dc magnetization measurements in both high temperature and low temperature regimes. The presence of strong interactions within the nanoparticle assembly and polydisperse nature of the sample have together given rise to the memory effect in M2. The presence of a stable spin glass phase in the sample is responsible for the origin of memory effect at low temperature region. The ensemble of nanoparticles can memorize the field change in its cooling cycle and can recall it accurately during the heating cycle. Hence, binary numbers 0 and 1 can be coded by defining 'H decrease' as "0" and 'H increase' as "1" in the cooling cycle of the dc magnetization measurement and decoded if

heating is done under constant magnetic field keeping both heating and cooling rates same.

5. Conclusion

The structural, microstructural, magnetic and hyperfine properties of nanosized $\text{Co}_{0.5}\text{Zn}_{0.5}\text{Fe}_2\text{O}_4$ having three different particle sizes have been carefully examined by PXRD, HRTEM, dc magnetic and Mössbauer spectroscopic techniques. The particle size from PXRD and crystallite size from TEM studies match well with each other revealing that M1, M2 and M3 are well-crystalline in nature. All the three samples have a wide distribution in particle size and possess strong interparticle interactions. The dc magnetic and room temperature Mössbauer spectroscopic studies together reveal that M1, M2 and M3 exhibit mixed magnetic behavior possessing both superparamagnetic and magnetically well-ordered phases at room temperature along with spin glass like freezing at low temperature invoked by the strong interparticle interactions within the ensemble of nanoparticles and random freezing of disordered surface spins at low temperature. The values of saturation magnetization of the samples are slightly lower than its equivalents due to presence of spin canting caused by milling. The values of coercivity at 10 K are much higher than at room temperature indicating absence of any relaxations within the samples at 10 K. The cation distribution of M2 obtained using in-field Mössbauer spectroscopic and PXRD studies has been testified by a trustworthy method of comparison of the experimentally obtained value of magnetic moment per formula unit with that of its theoretically calculated value. The sample M2 can keep a memory of field changes in its dc magnetic measurements, i.e., displays "memory effect" and may be technologically applicable for fabrication of sensors capable of detecting field changes and in encoding and decoding binary numbers. In summary, we can conclude that the magnetic structure of nanosized ferrites can be moderated suitably through mechanical activation to produce samples which can meet industrial demand of manufacturing miniature devices having superior magnetic quality.

Acknowledgements

K. Sarkar (Ref. No: 20/12/2015(ii)EU-V) gratefully acknowledges UGC, New Delhi for junior research fellowship. R. Mondal (IVR No.

201400001001) acknowledges Department of Science and Technology (DST), Govt. of India for providing INSPIRE fellowship. We gratefully acknowledge the support received from the UGC-DAE CSR, Indore Center for infield Mössbauer measurement and UGC-DAE CSR, Kolkata Center in connection to dc magnetic measurements. We sincerely thank Prof. V. R. Reddy of UGC-DAE CSR, Indore Center and Prof. Souvik Chatterjee of UGC-DAE CSR, Kolkata Center for their help and co-operation regarding infield Mössbauer spectroscopic study and magnetic measurements, respectively. The UPE program of UGC and the PURSE program of DST, Govt. of India are also acknowledged.

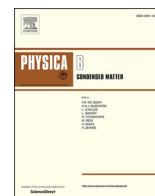
Appendix A. Supplementary data

Supplementary data to this article can be found online at <https://doi.org/10.1016/j.jmmm.2019.165303>.

References

- [1] Ç.E. Demirci, P.K. Manna, Y. Wroczynski, S. Aktürk, J. van Lierop, Lanthanum ion substituted cobalt ferrite nanoparticles and their hyperthermia efficiency, *J. Magn. Mater.* 458 (2018) 253–260, <https://doi.org/10.1016/j.jmmm.2018.03.024>.
- [2] L. Khanna, N.K. Verma, S.K. Tripathi, Burgeoning tool of biomedical applications – Superparamagnetic nanoparticles, *J. Alloy. Compd.* 752 (2018) 332–353, <https://doi.org/10.1016/j.jallcom.2018.04.093>.
- [3] R. Mondal, S. Dey, S. Majumder, A. Poddar, P. Dasgupta, S. Kumar, Study on magnetic and hyperfine properties of mechanically milled $\text{Ni}_{0.4}\text{Zn}_{0.6}\text{Fe}_2\text{O}_4$ nanoparticles, *J. Magn. Mater.* 448 (2018) 135–145, <https://doi.org/10.1016/j.jmmm.2017.07.031>.
- [4] S. Majumder, B. Saha, S. Dey, R. Mondal, S. Kumar, S. Banerjee, A highly sensitive non-enzymatic hydrogen peroxide and hydrazine electrochemical sensor based on 3D micro-snowflake architectures of α - Fe_2O_3 , *RSC Adv.* 6 (2016) 59907, <https://doi.org/10.1039/c6ra10470c>.
- [5] P. Guo, L. Cui, Y. Wang, M. Lv, B. Wang, X.S. Zhao, Facile synthesis of ZnFe_2O_4 nanoparticles with tunable magnetic and sensing properties, *Langmuir* 29 (2013) 8997–9003, <https://doi.org/10.1021/la401627x>.
- [6] A.B. Gadkari, T.J. Shinde, P.N. Vasambekar, Ferrite gas sensors, *IEEE Sens. J.* 11 (2011) 849, <https://doi.org/10.1109/JSEN.2010.2068285>.
- [7] R. Sharma, P. Thakur, M. Kumar, P. Sharma, V. Sharma, Nanomaterials for high frequency device and photocatalytic applications: Mg-Zn-Ni ferrites, *J. Alloy. Compd.* 746 (2018) 532–539, <https://doi.org/10.1016/j.jallcom.2018.02.287>.
- [8] D. Lam Tran, V. Hong Le, H. Linh Pham, T. My Nhung Hoang, T. Quy Nguyen, T. Tai Luong, P. Thu Ha, X. Phuc Nguyen, Biomedical and environmental applications of magnetic nanoparticles, *Adv. Nat. Sci.: Nanosci. Nanotechnol.* 1 (2010) 5, <https://doi.org/10.1088/2043-6262/1/4/045013>.
- [9] S. Mornet, S. Vasseur, F. Grasset, E. Duguet, Magnetic nanoparticle design for medical diagnosis and therapy, *J. Mater. Chem.* 14 (2004) 2161–2175, <https://doi.org/10.1039/b402025a>.
- [10] L. Wu, A. Mendoza-Garcia, Q. Li, S. Sun, Organic phase syntheses of magnetic nanoparticles and their applications, *Chem. Rev.* 116 (2016) 10473–10512, <https://doi.org/10.1021/acs.chemrev.5b00687>.
- [11] Lu An-Hui, E.L. Salabas, F. Schüth, Magnetic nanoparticles: synthesis, protection, functionalization, and application, *Angew. Chem. Int. Ed.* 46 (2007) 1222–1244, <https://doi.org/10.1002/anie.200602866>.
- [12] S. Dey, R. Mondal, S.K. Dey, S. Majumder, P. Dasgupta, A. Poddar, V.R. Reddy, S. Kumar, Tuning magnetization, blocking temperature, cation distribution of nanosized $\text{Co}_{0.2}\text{Zn}_{0.8}\text{Fe}_2\text{O}_4$ by mechanical activation, *J. Appl. Phys.* 118 (2015) 103905, <https://doi.org/10.1063/1.4930801>.
- [13] R. Mondal, S. Dey, K. Sarkar, P. Dasgupta, S. Kumar, Influence of high energy ball milling on structural parameters, cation distribution and magnetic enhancement of nanosized $\text{Co}_{0.3}\text{Zn}_{0.7}\text{Fe}_2\text{O}_4$, *Mater. Res. Bull.* 102 (2018) 160–171, <https://doi.org/10.1016/j.materresbull.2018.02.016>.
- [14] G. Balaji, N.S. Gajbhiye, G. Wilde, J. Weissmüller, Magnetic properties of MnFe_2O_4 nanoparticles, *J. Magn. Magn. Mater.* 242–245 (2002) 617–620.
- [15] R.D. Zysler, D. Fiorani, A.M. Testa, Investigation of magnetic properties of interacting Fe_2O_3 nanoparticles, *J. Magn. Magn. Mater.* 224 (2001) 5–11.
- [16] J.L. Dormann, R. Cherkaoui, L. Spinu, M. Noguès, F. Lucari, F. D'Orazio, D. Fiorani, A. Garcia, E. Tronc, J.P. Jolivet, From pure superparamagnetic regime to glass collective state of magnetic moments in $\gamma\text{-Fe}_2\text{O}_3$ nanoparticle assemblies, *J. Magn. Magn. Mater.* 187 (1998) L139–L144.
- [17] A.N. Hapishah, M. Hashim, M.M. Syazwan, I.R. Idza, N. Rodziah, I. Ismayadi, Phase, microstructure and magnetic evaluation in yttrium iron garnet (YIG) synthesized via mechanical alloying, *J. Mater. Sci.: Mater. Electron.* 28 (2017) 15270–15278, <https://doi.org/10.1007/s10854-017-7407-3>.
- [18] S.B. Waje, M. Hashim, W.D. Wan Yusoff, Z. Abbas, Sintering temperature dependence of room temperature magnetic and dielectric properties of $\text{Co}_{0.5}\text{Zn}_{0.5}\text{Fe}_2\text{O}_4$ prepared using mechanically alloyed nanoparticles, *J. Magn. Magn. Mater.* 322 (2010) 686–691, <https://doi.org/10.1016/j.jmmm.2009.10.041>.
- [19] Yi-Wei Liu, Jing Zhang, Lu-Shun Gu, Li-Xi Wang, Qi-Tu Zhang, Preparation and electromagnetic properties of nanosized $\text{Co}_0.5\text{Zn}_{0.5}\text{Fe}_2\text{O}_4$ ferrite, *Rare Met. Doi: 10.1007/s12598-015-0670-7*.
- [20] V. Mameli, A. Musinu, A. Ardu, G. Ennas, D. Peddis, D. Niznansky, C. Sangregorio, C. Innocenti, T.K. Nguyen, C. Cannas Thanh, Studying the effect of Zn-substitution on the magnetic and hyperthermic properties of cobalt ferrite nanoparticles, *Nanoscale* 8 (2016) 10124, <https://doi.org/10.1039/c6nr01303a>.
- [21] M. Schmidt, H.L. Andersen, C. Granados-Miralles, M. Saura-Múzquiz, M. Stingaciu, M. Christensen, Tuning the size and magnetic properties of $\text{Zn}_x\text{Co}_{1-x}\text{Fe}_2\text{O}_4$ nanocrystallites, *Dalton Trans.* 45 (2016) 6439, <https://doi.org/10.1039/c5dt04701c>.
- [22] M. Veverka, P. Veverka, Z. Jiráček, O. Kaman, K. Knížek, M. Maryško, E. Pollert, K. Závěta, Synthesis and magnetic properties of $\text{Co}_{1-x}\text{Zn}_x\text{Fe}_2\text{O}_4$ nanoparticles as materials for magnetic fluid hyperthermia, *J. Magn. Magn. Mater.* 322 (2010) 2386–2389, <https://doi.org/10.1016/j.jmmm.2010.02.042>.
- [23] M. Penchal Reddy, A.M.A. Mohamed, One-pot solvothermal synthesis and performance of mesoporous magnetic ferrite MFe_2O_4 nanospheres, *Microporous Mesoporous Mater.* 215 (2015) 37–45, <https://doi.org/10.1016/j.micromeso.2015.05.024>.
- [24] Z. Jia, D. Ren, R. Zhu, Synthesis, characterization and magnetic properties of CoFe_2O_4 nanorods, *Mater. Lett.* 66 (2012) 128–131, <https://doi.org/10.1016/j.matlet.2011.08.056>.
- [25] R.A. Bohara, N.D. Thorat, A.K. Chaurasia, S.H. Pawar, Cancer cell extinction through a magnetic fluid hyperthermia treatment produced by superparamagnetic Co-Zn ferrite nanoparticles, *RSC Adv.* 5 (2015) 47225, <https://doi.org/10.1039/c5ra04553c>.
- [26] X. Huang, J. Zhang, W. Wang, T. Sang, B. Song, H. Zhu, W. Rao, C. Wong, Effect of pH value on electromagnetic loss properties of Co-Zn ferrite prepared via coprecipitation method, *J. Magn. Magn. Mater.* 405 (2016) 36–41, <https://doi.org/10.1016/j.jmmm.2015.12.051>.
- [27] M. Sundararajan, V. Sailaja, L. John Kennedy, J. Judith Vijaya, Photocatalytic degradation of rhodamine B under visible light using nanostructured zinc doped cobalt ferrite: kinetics and mechanism, *Ceram. Int.* 43 (2017) 540–548, <https://doi.org/10.1016/j.ceramint.2016.09.191>.
- [28] B.D. Culity, Introduction to Magnetic Materials, Addison-Wesley, New York, 1972.
- [29] D.S. Nikam, S.V. Jadhav, V.M. Khot, R.A. Bohara, C.K. Hong, S.S. Malib, S.H. Pawar, Cation distribution, structural, morphological and magnetic properties of $\text{Co}_{1-x}\text{Zn}_x\text{Fe}_2\text{O}_4$ ($x = 0-1$) nanoparticles, *RSC Adv.* 5 (2015) 2338, <https://doi.org/10.1039/c4ra08342c>.
- [30] A. Ramakrishna, N. Murali, Tulu Wegayehu Mammo, K. Samatha, V. Veeraiah, Structural and DC electrical resistivity, magnetic properties of $\text{Co}_{0.5}\text{Mn}_{0.5}\text{Fe}_2\text{O}_4$ ($M = \text{Ni, Zn, and Mg}$) ferrite nanoparticles, *Phys. B: Condens. Matter.* 534 (2018) 134–140, <https://doi.org/10.1016/j.physb.2018.01.033>.
- [31] T.R. Tatarchuk, N.D. Paliychuk, M. Bououdina, B. Al-Najar, M. Pacia, W. Macyk, A. Shyichuk, Effect of cobalt substitution on structural, elastic, magnetic and optical properties of zinc ferrite nanoparticles, *J. Alloy. Compd.* 731 (2018) 1256–1266, <https://doi.org/10.1016/j.jallcom.2017.10.103>.
- [32] D.M. Jnaneshwara, D.N. Avadhani, B.D. Prasad, B.M. Nagabhushana, H. Nagabhushana, S.C. Sharma, S.C. Prashantha, C. Shivakumara, Effect of zinc substitution on the nanocobalt ferrite powders for nanoelectronic devices, *J. Alloy. Compd.* 587 (2014) 50–58, <https://doi.org/10.1016/j.jallcom.2013.10.146>.
- [33] A. Manikandan, L. John Kennedy, M. Bououdina, J. Judith Vijaya, Synthesis, optical and magnetic properties of pure and Co-doped ZnFe_2O_4 nanoparticles by microwave combustion method, *J. Magn. Magn. Mater.* 349 (2014) 249–258, <https://doi.org/10.1016/j.jmmm.2013.09.013>.
- [34] I. Sharifi, H. Shokrollahi, Nanostructural, magnetic and Mössbauer studies of nanosized $\text{Co}_{1-x}\text{Zn}_x\text{Fe}_2\text{O}_4$ synthesized by co-precipitation, *J. Magn. Magn. Mater.* 324 (2012) 2397–2403, <https://doi.org/10.1016/j.jmmm.2012.03.008>.
- [35] G. Barrera, M. Coisson, F. Celegato, S. Raghuvanshi, F. Mazaleyrat, S.N. Kane, P. Tiberto, Cation distribution effect on static and dynamic magnetic properties of $\text{Co}_{1-x}\text{Zn}_x\text{Fe}_2\text{O}_4$ ferrite powders, *J. Magn. Magn. Mater.* 456 (2018) 372–380, <https://doi.org/10.1016/j.jmmm.2018.02.072>.
- [36] P. Coppola, F.G. da Silva, G. Gornide, F.L.O. Paula, A.F.C. Campos, R. Perzynski, C. Kern, J. Depuyot, R. Aquino, Hydrothermal synthesis of mixed zinc-cobalt ferrite nanoparticles: structural and magnetic properties, *J. Nanopart. Res.* 18 (2016) 138, <https://doi.org/10.1007/s11051-016-3430-1>.
- [37] T.R. Tatarchuk, M. Bououdina, N.D. Paliychuk, I.P. Yaremiy, V.V. Moklyak, Structural characterization and antistructure modeling of cobalt substituted zinc ferrites, *J. Alloy. Compd.* 694 (2017) 777–791, <https://doi.org/10.1016/j.jallcom.2016.10.067>.
- [38] R.N. Bhowmik, R. Ranganathan, Anomaly in cluster glass behaviour of $\text{Co}_{0.2}\text{Zn}_{0.8}\text{Fe}_2\text{O}_4$ spinel oxide, *J. Magn. Magn. Mater.* 248 (2002) 101–111.
- [39] H. Parmar, P. Acharya, R.V. Upadhyay, V. Siruguri, S. Rayaprol, Low temperature magnetic ground state in bulk $\text{Co}_{0.3}\text{Zn}_{0.7}\text{Fe}_2\text{O}_4$ spinel ferrite system: neutron diffraction, magnetization and ac-susceptibility studies, *Solid State Commun.* 153 (2013) 60–65, <https://doi.org/10.1016/j.ssc.2012.09.021>.
- [40] R.V. Upadhyay, H. Parmar, P. Acharya, A. Banerjee, Progressive freezing of finite cluster in locally canted spin $\text{Co}_{0.3}\text{Zn}_{0.7}\text{Fe}_2\text{O}_4$ spinel ferrite system, *Solid State Commun.* 163 (2013) 50–54, <https://doi.org/10.1016/j.ssc.2013.02.020>.
- [41] G.A. Petitt, D.W. Forester, Mossbauer study of cobalt-zinc ferrites, *Phys. Rev. B* 4 (1971) 11.
- [42] S. Dey, A. Roy, J. Ghose, R.N. Bhowmik, R. Ranganathan, Size dependent magnetic phase of nanocrystalline $\text{Co}_{0.2}\text{Zn}_{0.8}\text{Fe}_2\text{O}_4$, *J. Appl. Phys.* 90 (2001) 4138, <https://doi.org/10.1063/1.1401798>.
- [43] I. Sharifi, H. Shokrollahi, Structural, magnetic and Mössbauer evaluation of Mn substituted Co-Zn ferrite nanoparticles synthesized by co-precipitation, *J. Magn. Magn. Mater.* 334 (2013) 36–40, <https://doi.org/10.1016/j.jmmm.2013.01.021>.
- [44] W. Sacchi Petemele, V. Monge Fuentes, M. Luiza Fascineli, J. Rodrigues da Silva, R. Carvalho Silva, Ca. Madeira Lucci, R. Bentes de Azevedo, Experimental investigation of the coprecipitation method: an approach to obtain magnetite and

- maghemite nanoparticles with improved properties, *J. Nanomater.* (2014), <https://doi.org/10.1155/2014/682985>.
- [45] S. Dey, S.K. Dey, B. Ghosh, P. Dasgupta, A. Poddar, V.R. Reddy, S. Kumar, Role of inhomogeneous cation distribution in magnetic enhancement of nanosized $\text{Ni}_{0.35}\text{Zn}_{0.65}\text{Fe}_2\text{O}_4$: a structural, magnetic, and hyperfine study, *J. Appl. Phys.* 114 (2013), <https://doi.org/10.1063/1.4819809> 093901.
- [46] S. Dey, S.K. Dey, K. Bagani, S. Majumder, A. Roychowdhury, S. Banerjee, V.R. Reddy, D. Das, S. Kumar, Overcoming inherent magnetic instability, preventing spin canting and magnetic coding in an assembly of ferrimagnetic nanoparticles, *Appl. Phys. Lett.* 105 (2014) 063110, <https://doi.org/10.1063/1.4893028>.
- [47] S. Dey, S.K. Dey, S. Majumder, A. Poddar, P. Dasgupta, S. Banerjee, S. Kumar, Superparamagnetic behavior of nanosized $\text{Co}_{0.2}\text{Zn}_{0.8}\text{Fe}_2\text{O}_4$ synthesized by a flow rate controlled chemical coprecipitation method, *Phys. B* 448 (2014) 247–252, <https://doi.org/10.1016/j.physb.2014.03.073>.
- [48] R.N. Bhowmik, R. Ranganathan, R. Nagarajan, S. Biswatosh Ghosh, S. Kumar, Role of strain-induced anisotropy on magnetic enhancement in mechanically alloyed $\text{Co}_{0.2}\text{Zn}_{0.8}\text{Fe}_2\text{O}_4$ nanoparticle, *Phys. Rev. B* 72 (2005) 094405. [10.1103/PhysRevB.72.094405](https://doi.org/10.1103/PhysRevB.72.094405).
- [49] R.N. Bhowmik, R. Ranganathan, Magnetic enhancement of $\text{Co}_{0.2}\text{Zn}_{0.8}\text{Fe}_2\text{O}_4$ spinel oxide by mechanical milling, *Phys. Rev. B* 68 (2003) 134433. [10.1103/PhysRevB.68.134433](https://doi.org/10.1103/PhysRevB.68.134433).
- [50] R. Singh Yadav, I. Kuřitka, J. Havlica, M. Hnatko, C. Alexander, J. Masilko, L. Kalina, M. Hajdúchová, J. Rusnak, V. Enev, Structural, magnetic, elastic, dielectric and electrical properties of hotpress sintered $\text{Co}_{1-x}\text{Zn}_x\text{Fe}_2\text{O}_4$ ($x = 0.0, 0.5$) spinel ferrite nanoparticles, *J. Magn. Magn. Mater.* 447 (2018) 48–57, <https://doi.org/10.1016/j.jmmm.2017.09.033>.
- [51] R. Singh Yadav, J. Havlica, M. Hnatko, P. Šajgalík, C. Alexander, M. Palou, E. Bartoničková, M. Boháč, F. Frajkorová, J. Masilko, M. Zmrzlý, L. Kalina, M. Hajdúchová, V. Enev, Magnetic properties of $\text{Co}_{1-x}\text{Zn}_x\text{Fe}_2\text{O}_4$ spinel ferrite nanoparticles synthesized by starch-assisted sol–gel auto combustion method and its ball milling, *J. Magn. Magn. Mater.* 378 (2015) 190–199, <https://doi.org/10.1016/j.jmmm.2014.11.027>.
- [52] C. Gómez-Polo, V. Recarte, L. Cervera, J.J. Beato-López, J. López-García, J.A. Rodríguez-Velamazán, M.D. Ugarte, E.C. Mendonça, J.G.S. Duque, Tailoring the structural and magnetic properties of Co–Zn nanosized ferrites for hyperthermia applications, *J. Magn. Magn. Mater.* 465 (2018) 211–219, <https://doi.org/10.1016/j.jmmm.2018.05.051>.
- [53] K. Lagarec, D.G. Rancourt, Recoil-Mössbauer Spectral Analysis Software for Window, University of Ottawa Press, Ottawa, 1998.
- [54] A. Boulfif, D. Louer, Powder pattern indexing with the dichotomy method, *J. Appl. Crystallogr.* 37 (2004) 724–731.
- [55] P.E. Werner, L. Eriksson, M.J. Westdahl, TREOR, a semi-exhaustive trial-and-error powder indexing program for all symmetries, *J. Appl. Crystallogr.* 18 (1985) 367–370.
- [56] L. Lutterotti, MAUDWEB, Version 1.9992 (2004).
- [57] D. Balzar, N.C. Popa, Analyzing microstructure by Rietveld refinement, *Rigaku J.* 22 (2015) 16–25.
- [58] B.H. Toby, EXPGUI, a graphical user interface for GSAS, *J. Appl. Crystallogr.* 34 (2001) 210–213.
- [59] S. Dey, S.K. Dey, B. Ghosh, V.R. Reddy, S. Kumar, Structural, microstructural, magnetic and hyperfine characterization of nanosized $\text{Ni}_{0.5}\text{Zn}_{0.5}\text{Fe}_2\text{O}_4$ synthesized by high energy ball-milling method, *Mater. Chem. Phys.* 138 (2013) 833–842, <https://doi.org/10.1016/j.matchemphys.2012.12.067>.
- [60] J.J. Lu, H.Y. Deng, H.L. Huang, Thermal relaxation of interacting fine magnetic particles-field-cooled and zero-field-cooled magnetization variation, *J. Magn. Magn. Mater.* 209 (2000) 37–41.
- [61] A.H. Morrish, *The Principles of Magnetism*, John Wiley & Sons, New York, 1965.
- [62] L. Néel, *Ann. Geophys.* 5 (1949) 99.
- [63] D. Peddis, M.V. Mansilla, S. Mørup, C. Cannas, A. Musinu, G. Piccaluga, F. D'Orazio, F. Lucari, D. Fiorani, Spin-canting and magnetic anisotropy in ultrasmall CoFe_2O_4 nanoparticles, *J. Phys. Chem. B* 112 (2008) 8507–8513.
- [64] J.L. Gittleman, B. Abels, S. Bozowski, *Phys. Rev. B* 9 (1974) 3891.
- [65] B. Ghosh, S. Kumar, A. Poddar, C. Mazumdar, S. Banerjee, V.R. Reddy, A. Gupta, Spin glasslike behavior and magnetic enhancement in nanosized Ni–Zn ferrite system, *J. Appl. Phys.* 108 (2010) 034307, <https://doi.org/10.1063/1.3456174>.
- [66] S. Chakraverty, B. Ghosh, S. Kumar, A. Frydman, Magnetic coding in systems of nanomagnetic particles, *Appl. Phys. Lett.* 88 (2006) 042501, <https://doi.org/10.1063/1.2166203>.
- [67] Y. Sun, M.B. Salamon, K. Garnier, R.S. Averback, Memory effects in an interacting magnetic nanoparticle system, *Phys. Rev. Lett.* 91 (2003) 167206, <https://doi.org/10.1103/PhysRevLett.91.167206>.
- [68] M. Sasaki, P.E. Jönsson, H. Takayama, H. Mamiya, Aging and memory effects in superparamagnets and superspin glasses, *Phys. Rev. B* 71 (2005) 104405, <https://doi.org/10.1103/PhysRevB.71.104405>.
- [69] M. Östh, D. Hérisson, P. Nordblad, J.A. De Toro, J.M. Riveiro, Ageing and memory effects in a mechanically alloyed nanoparticle system, *J. Magn. Magn. Mater.* 313 (2007) 373, <https://doi.org/10.1016/j.jmmm.2007.02.006>.
- [70] M. Satalkar, S.N. Kane, On the study of structural properties and cation distribution of $\text{Zn}_{0.75-x}\text{Ni}_x\text{Mg}_{0.15}\text{Cu}_{0.1}\text{Fe}_2\text{O}_4$ nano ferrite: effect of Ni addition, *J. Phys.: Conf. Ser.* 755 (2016), <https://doi.org/10.1088/1742-6596/755/1/012050> 012050-1 – 012050-10.
- [71] O.M. Hemeda, Structural and magnetic properties of $\text{Co}_{0.6}\text{Zn}_{0.4}\text{Mn}_x\text{Fe}_{2-x}\text{O}_4$, *Turk. J. Phys.* 28 (2004) 121–132.
- [72] S.P. Dalawai, T.J. Shinde, A.B. Gadkari, P.N. Vasambekar, Structural properties of Cd–Co ferrites, *Bull. Mater. Sci.* 36 (2013) 919–922.
- [73] J.A. Gomes, M.H. Sousa, F.A. Tourinho, J. Mestnik-Filho, R. Itri, J. Depeyrot, Rietveld structure refinement of the cation distribution in ferrite fine particles studied by X-ray powder diffraction, *J. Magn. Magn. Mater.* 289 (2005) 184–187, <https://doi.org/10.1016/j.jmmm.2004.11.053>.
- [74] L. Kumar, P. Kumar, A. Narayan, M. Kar, Rietveld analysis of XRD patterns of different sizes of nanocrystalline cobalt ferrite, *Int Nano Lett.* 3 (2013) 8, <https://doi.org/10.1186/2228-5326-3-8>.
- [75] R.D. Shannon, Revised effective ionic radii and systematic studies of interatomic distances in halides and chalcogenides, *Acta Crystallogr. A* 32 (1976) 751–767.
- [76] D.N. Bhosale, S.S. Suryavanshi, S.R. Sawant, A.M. Sankpal, S.V. Kakatkar, S.A. Patil, B.V. Khasbaddar, Bulk magnetic studies on $\text{Co}_x\text{Zn}_{1-x}\text{Fe}_2\text{O}_4$ substituted with Al and Gd_2O_3 , *J. Magn. Magn. Mater.* 124 (1993) 298–300.
- [77] M. Veverka, Z. Jiráč, O. Kaman, K. Knížek, M. Maryško, E. Pollert, K. Závěta, A. Lančok, M. Dlouhá, S. Vratislav, Distribution of cations in nanosize and bulk Co–Zn ferrites, *Nanotechnology* 22 (2011), <https://doi.org/10.1088/0957-4484/22/34/345701>.
- [78] V. Pilati, R.C. Gomes, G. Gomide, P. Coppola, F.G. Silva, F.L.O. Paula, R. Perzynski, G.F. Goya, R. Aquino, J. Depeyrot, Core/shell nanoparticles of non-stoichiometric Zn–Mn and Zn–Co ferrites as thermosensitive heat sources for magnetic fluid hyperthermia, *J. Phys. Chem. C* 122 (2018) 3028–3038, <https://doi.org/10.1021/acs.jpcc.7b11014>.
- [79] R. Aquino, J. Depeyrot, M.H. Sousa, F.A. Tourinho, E. Dubois, R. Perzynski, Magnetization temperature dependence and freezing of surface spins in magnetic fluids based on ferrite nanoparticles, *Phys. Rev. B* 72 (2005) 184435, <https://doi.org/10.1103/PhysRevB.72.184435>.
- [80] E. De Biasi, R.D. Zysler, C.A. Ramos, H. Romero, Magnetization enhancement at low temperature due to surface ordering in Fe–Ni–B amorphous nanoparticles, *Phys. B* 320 (2002) 203–205.
- [81] H. Bhargava, K.T. Vasudevan, N. Lakshmi, K. Venugopalan, Bulk magnetic properties of nanosized spinel ferrites, *Int. J. Res. Eng. Technol.* 05 (2016) 401–404.
- [82] H. Fakhr Nabavi, M. Aliofkhaezai, M. Hasanpoor, Combustion and coprecipitation synthesis of Co–Zn ferrite nanoparticles: comparison of structure and magnetic properties, *Int. J. Appl. Ceram. Technol.* (13(6), 2016), pp. 1112–1118. DOI:10.1111/jjac.12580.
- [83] H.Y. He, Comparison study on magnetic property of $\text{Co}_{0.5}\text{Zn}_{0.5}\text{Fe}_2\text{O}_4$ powders by template-assisted sol–gel and hydrothermal methods, *J. Mater. Sci.: Mater. Electron.* 23 (2012) 995–1000, <https://doi.org/10.1007/s10854-011-0535-2>.
- [84] S. Lee, C. Sung Kim, Thermal properties of $\text{Co}_{0.5}\text{Zn}_{0.5}\text{Fe}_2\text{O}_4$ nanoparticles for hyperthermia Applications, *J. Korean Phys. Soc.* 66 (2015) 104–107, <https://doi.org/10.3938/jkps.66.104>.
- [85] J. Iqbal, M. Rajpoot, T. Jan, I. Ahmad, Annealing induced enhancement in magnetic properties of $\text{Co}_{0.5}\text{Zn}_{0.5}\text{Fe}_2\text{O}_4$ nanoparticles, *J. Supercond. Nov. Magn.* 27 (2014) 1743–1749, <https://doi.org/10.1007/s10948-014-2505-4>.
- [86] M. Sundararajan, L. John Kennedy, J. Judith Vijaya, Synthesis and characterization of cobalt substituted zinc ferrite nanoparticles by microwave combustion method, *J. Nanosci. Nanotechnol.* 15 (2015) 6719–6728, <https://doi.org/10.1166/jnn.2015.10347>.
- [87] C. Kittel, Physical theory of ferromagnetic domains, *Rev. Mod. Phys.* 21 (1949) 541–583.

Cation vacancy and magnetic properties of ZnFe_2O_4 microspheresK. Sarkar^a, R. Mondal^{a,b}, S. Dey^c, S. Kumar^{a,*}^a Department of Physics, Jadavpur University, Kolkata, 700032, India^b Department of Electronics, Barrackpore Rastraguru Surendranath College, Barrackpore, West Bengal, 700120, India^c Swami Vivekananda Institute of Science & Technology, Sonarpur, Kolkata, 700 145, India

ARTICLE INFO

Keywords:

ZnFe_2O_4 microsphere
Verway transition
Magnetic property
Cation distribution
Mössbauer spectroscopy

ABSTRACT

In this report, we have compared the structural, morphological, magnetic and hyperfine properties of ZnFe_2O_4 solid (ZFMS) and hollow (ZFMH) microspheres synthesized by simple solvothermal technique. ZFMS, having diameter ~ 314 nm and formed by self-assembly of nanoparticles, displays superparamagnetic character predominantly along with collective magnetic excitations at room temperature. ZFMH of diameter ~ 375 nm exhibits single crystal like dotted selected area electron diffraction pattern and is magnetically well-ordered at room temperature. The values of saturation magnetization of ZFMS and ZFMH at 300, 100 and 10 K are 41.5, 64, 85.7 and 77, 84.5, 90.75 emu/g, respectively. According to x-ray photoelectron and Mössbauer spectroscopic studies the cation distribution of the ZFMS and ZFMH are $(\text{Zn}_{0.44}\text{Fe}_{0.56})[\text{Zn}_{0.56}\text{Fe}_{1.44}]\text{O}_4$ and $(\text{Fe}^{3+}_{0.925}\text{Zn}^{2+}_{0.075})[\text{Fe}^{2+}_{0.31}\text{Fe}^{3+}_{1.46}\Phi_{0.23}]\text{O}_4$, respectively, where Φ corresponds to vacancy. ZFMH displays Verway transition due to the presence Fe^{2+} ions caused by cation vacancy in ZFMH while ZFMS does not.

1. Introduction

In recent times, the fabrication of self-assembled heterostructured magnetic materials have attracted immense attention of material scientists as their properties can be potentially tuned by building increasingly complex structures [1] leading to interesting functional features and wide variety of applications as well [1,2]. Fabrication of assembly of nanoparticles to form microspheres in the size range of protein molecules has extensive applications in the field of drug delivery [3–6]. Superparamagnetic ferrite nanoparticles display good dispersibility in solvent [7,8] as interparticle interactions within the nanoparticles is weak and thus, they do not agglomerate. These characteristics render them apposite for biomedical applications [9,10]. But low magnetization resulting from finite size effect and spin canting hinders their application potential in many areas [11,12]. In order to attain high saturation magnetization while retaining the superparamagnetic character of the nanoparticles, a novel way of fabricating self-assembled heterostructures has been developed [1,2,13]. Among these heterostructures, microspheres have displayed highest value of saturation magnetization [14]. Further, self-assembled ferrite microspheres generally possess smooth and highly porous surface [15,16]. So, it seems obvious that nanoparticle-assembled ferrite microspheres will fare very well in magnetically guided site-specific drug delivery, magnetic

hyperthermia and catalysis [17]. Apart from their application potential, these ferrite microspheres give rise to astonishing magnetic behavior like enhanced saturation magnetization and reduced coercive field at low temperature compared to those of their constituent nanoparticles [17–19]. These magnetic properties are very interesting from scientific view point and at the same time crucial for application in various fields. Since the microspheres are formed by self-assembly of nanoparticles, modulations of size and shape in the nanoscale regime can direct the evolution of their magnetic properties in unexpected ways [20,21]. These modulations can be controlled by tuning different parameters of synthesis procedure of the nanocrystals. So, in order to obtain function specific nano/micro structures, choice of proper synthesis procedure is very important.

ZnFe_2O_4 is an important member of the ferrite family owing to its fascinating magnetic, electrical, electrochemical and sensing properties [22–31]. Although electrochemical and sensing properties of ZnFe_2O_4 nano and microstructures have been explored in great detail [27,30,32,33], there are only few studies on its magnetic behavior [15,16,23,24,26,29,34–37]. Among them, Guo et al., have showed that ZnFe_2O_4 solid microspheres (diameter ~ 450 nm) composed of small nanosheets synthesized by solvothermal method exhibit superparamagnetic behavior [23], Rahimi et al., have found that ZnFe_2O_4 hollow nanospheres (diameter ~ 127 nm) synthesized by solvothermal method using

* Corresponding author.

E-mail address: kumars@phys.jdvu.ac.in (S. Kumar).<https://doi.org/10.1016/j.physb.2020.412015>

Received 31 August 2019; Received in revised form 3 January 2020; Accepted 13 January 2020

Available online 14 January 2020

0921-4526/© 2020 Elsevier B.V. All rights reserved.

ultrasonic waves show ferromagnetic behavior [26], Xu et al., have observed antiferromagnetic behavior in the ZnFe_2O_4 hollow spheres (diameter ranging from 70 to 100 nm) synthesized by surfactant assisted hydrothermal approach [34], Guo et al., have obtained weak ferromagnetic character in solvothermally synthesized ZnFe_2O_4 solid and hollow colloidal nanocrystal assemblies (diameter ranging from 100 to 300 nm) [35], Chen et al., have synthesized ZnFe_2O_4 nanocubes (mean edge length ~ 50 nm) by simple hydrothermal technique and found them to be ferromagnetic with enhanced saturation magnetization and coercivity [36], Kmita et al., have synthesized ZnFe_2O_4 nanorods (mean length ~ 20 nm and thickness ~ 5 nm) by coprecipitation method and found them to be superparamagnetic [37]. From these studies, we can conclude that morphology and synthesis procedure are responsible in determining the magnetic behavior of the materials. Moreover, the observed diversity in the magnetic behavior of ZnFe_2O_4 motivates us to explore its magnetic behavior in more detail.

It is well known that the magnetic properties of ferrites are strongly dependent on the distribution of cations among tetrahedral (A) and octahedral [B] sites of the spinel lattice [38]. Different synthesis procedures give rise to different morphologies causing cation redistribution among these two sites and consequently, magnetic properties get altered [39–41]. Surfactant-assisted chemical methods have paved a novel way to develop size- and shape-tailored magnetic nanocrystals by carefully regulating the growth processes in liquid media [15,16]. These methods may be either single-step or more complex multiple-step solution-phase routes. The former is convenient, cheaper, and non-time consuming while the latter is only advantageous for obtaining better size distribution [17]. In the literature, study on the structural, magnetic, electrical and electrochemical properties of solid and hollow microspheres of Fe_3O_4 synthesized by solvothermal method at 200°C using NaAc + PEG and NH_4Ac , respectively [15,42], CoFe_2O_4 synthesized by solvothermal method at 200°C using NaAc + PEG and urea + oleylamine, respectively [15,43], NiFe_2O_4 synthesized by solvothermal method at 180°C using NaAc + PEG and at 200°C using NH_4Ac , respectively [16,44], MnFe_2O_4 synthesized by solvothermal method at 180°C using NaAc + PEG and NH_4Ac + PEG, respectively [15,16,45], MgFe_2O_4 synthesized by solvothermal method at 180°C using NaAc + PEG and at 200°C using urea + PEG, respectively [46,47], and ZnFe_2O_4 synthesized by solvothermal method at 200°C and 180°C using NaAc + PEG, respectively [15,48], have been found. Thus, it is apparent that one-step solvothermal method has emerged as an efficient technique to synthesize monodisperse spherical magnetic microspheres with large surface area, high magnetic saturation and good dispersive property in liquid media. Hence, it would be feasible to use this technique in developing ferrite microspheres with desirable properties.

In this backdrop, we have synthesized solid and hollow microspheres of ZnFe_2O_4 by one-step solvothermal method with the endeavor to thoroughly study their magnetic properties. The phase of the samples has been characterized by powder x-ray diffraction. The morphology, elemental composition and valance state of the constituent elements have been investigated by field emission scanning electron microscopic, transmission electron microscopic, energy dispersive x-ray spectroscopic and x-ray photoelectron spectroscopic techniques. The dc magnetic and Mössbauer spectroscopic techniques have been employed to probe the magnetic and hyperfine properties of the microspheres.

2. Experimental

2.1. Materials

Analytical grade $\text{FeCl}_3 \cdot 6\text{H}_2\text{O}$, $\text{ZnSO}_4 \cdot 7\text{H}_2\text{O}$, anhydrous ZnCl_2 , NaAc, NH_4Ac and PEG-4000 were purchased from Sigma Aldrich and used without further purification. Ethylene glycol (EG) procured from Merck India (99.9%) was used as the solvent.

2.2. Synthesis procedures

In the preparation of ZnFe_2O_4 solid microspheres (ZFMS), 5 mmol $\text{FeCl}_3 \cdot 6\text{H}_2\text{O}$ and 2.5 mmol $\text{ZnSO}_4 \cdot 7\text{H}_2\text{O}$ (precursors of the reaction) were mixed in 40 ml of EG under continuous magnetic stirring. After that 3.6 g NaAc $\cdot 3\text{H}_2\text{O}$ (stabilization agent) and 1 g PEG-4000 (structure-directing agent) were added into this mixture. The entire mixture was stirred for 5–6 h at room temperature following which it was transferred in a 100 ml Teflon pot. The pot was enclosed in a stainless steel autoclave and solvothermally heated in an oven for 20 h at 180°C . The oven was allowed to cool naturally to room temperature after which the so obtained precipitate was washed several times by ethanol and deionized water in an ultracentrifuge. The resulting product was dried in a vacuum oven at 60°C for 6 h and finally a fine black coloured powder was obtained.

Similarly, ZnFe_2O_4 hollow microspheres (ZFMH) were synthesized by mixing 5 mmol $\text{FeCl}_3 \cdot 6\text{H}_2\text{O}$ and 2.5 mmol anhydrous ZnCl_2 (precursors of the reaction) in 40 ml of EG under continuous magnetic stirring. Then 50 mmol of NH_4Ac was added to the solution and the mixture was stirred for 5–6 h. After that, the mixture was autoclaved at 170°C for 17 h in an oven. The black precipitate obtained from the above procedure was washed several times with ethanol and deionized water, and collected by centrifugation. The so obtained product was vacuum dried at 60°C for 6 h. The final sample was a fine black powder.

2.3. Characterization

Structural and microstructural studies on the as-synthesized samples were carried out using powder x-ray diffraction (PXRD), field emission scanning electron microscopic (FESEM) and transmission electron microscopic (TEM) techniques. XRD measurements were performed using a Bruker D8 Advanced diffractometer with $\text{Cu K}\alpha$ irradiation in the 2θ range of 20 – 80° . FESEM micrographs were recorded in a FEI INSPECT F50 system. TEM micrographs along with elemental study were collected using a JEOL 2100 HRTEM equipped with Bruker EDS system. X-ray photoelectron spectroscopy (XPS) was performed using XPS, Omicron, serial no 0571. Magnetic measurements viz., magnetization versus temperature (in zero-field cooling and field cooling modes) and variation of magnetization with field (hysteresis loops) were performed using a Cryogenic make vibrating sample magnetometer. The room temperature (300 K) and low temperature (5 K) Mössbauer spectra of both the samples were recorded in transmission geometry with constant acceleration drive (CMTE-250) using a 10 mCi ^{57}Co source. JANIS SVT-400 MOSS cryostat system was employed to obtain the 5 K Mössbauer spectrum. The 5 K Mössbauer spectrum in presence of a 5 T external magnetic field applied parallel to the γ -ray direction was recorded in presence of a superconducting magnet (JANIS Super-OptiMag) and a 40 mCi ^{57}Co source. Calibration of the Mössbauer spectrometer was done using a natural iron sample.

3. Results

3.1. Structural and morphological study

The PXRD patterns of ZFMS and ZFMH are shown in Fig. 1. The peak positions of both the samples are consistent with those of the cubic spinel structure of ZnFe_2O_4 nanoparticles (ICDD card no: 82–1049). The patterns have been indexed by TREOR90 of Fullprof2k package [49]. The space group has been determined using FINDSPACE of EXPO2009 package [50]. The peaks of ZFMS are slightly broader as compared to ZFMH indicating that the crystallite size of the former is smaller. The patterns have been fitted by Rietveld based MAUD2.33 software [51] from which the crystallite size of ZFMS and ZFMH has been deduced as ~ 25 nm and 80 nm, respectively. The experimental and simulated patterns are in well accord. The values of refinement, structural and microstructural parameters have been enlisted in Table 1. Thus, both

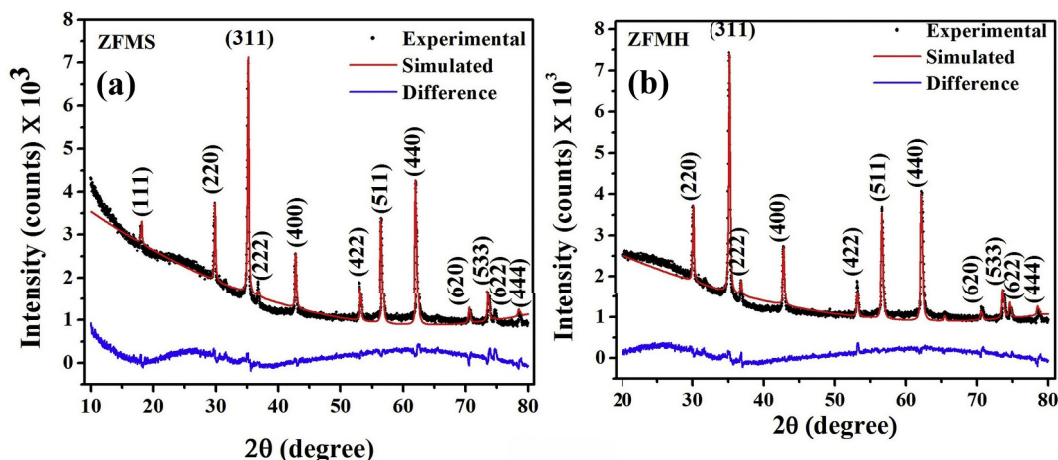


Fig. 1. Indexed powder PXRD pattern of (a) ZFMS and (b) ZFMH (black dots) and the simulated Rietveld refinement plot (continuous red line) obtained by fitting the experimental powder PXRD pattern using MAUD2.33 software. The respective residue is plotted at the bottom (blue line). (For interpretation of the references to colour in this figure legend, the reader is referred to the Web version of this article.)

Table 1

Crystal data and refinement parameters of ZFMS and ZFMH obtained from MAUD2.33

Parameters	ZFMS	ZFMH
Crystal System	cubic	cubic
Space group	$Fd\bar{3}m$	$Fd\bar{3}m$
Crystallite size (nm)	25	80
Microstrain	8.27×10^{-4}	2.76×10^{-4}
Lattice parameter (a(Å))	8.487	8.432
Density (g cm ⁻³)	5.098	5.198
R _{wp}	1.97	1.95
R _{exp}	1.41	1.42
GOF	1.29	1.10

ZFMS and ZFMH have crystallized in $Fd\bar{3}m$ space group of cubic spinel lattice and devoid of any additional impurity phases.

The FESEM micrograph (Fig. 2 (a)) of ZFMS displays microspheres of average diameter ~ 314 nm, which have been formed by self-assembly of nanoparticles. The spheres are almost uniformly sized and their surface is slightly rough due to the aggregation of nanoparticles. In the FESEM micrograph of ZFMH, the spheres are almost regular in size with some broken spheres confirming their hollow interior (Fig. 2 (b)). In contrast to ZFMS, the surface of ZFMH is smooth due to continuous overlapping of subsequent layers of smaller nanoparticles during their

formation following Kirkendall effect [52]. The morphology of ZFMS and ZFMH has been further investigated by TEM study. The average diameter of ZFMS as has been obtained from the TEM micrograph (Fig. 3 (a)) is ~ 310 nm. The spheres seen in the TEM micrograph of ZFMS are almost completely dark with clear sign of agglomeration as presented in the inset of (Fig. 3 (a)). The sharp contrast between the outer black margin and the bright center of the microspheres in the TEM micrograph of ZFMH (Fig. 3 (b)) confirms hollow structure formation. Typical TEM image of a single hollow microsphere has been presented in the inset of Fig. 3 (b). It is clear that the shell of the hollow microspheres is smooth. Although some of the individual particles can be identified in the hollow region but their boundaries are not distinct. So, it is not possible to estimate the appropriate particle size of individual nanoparticles which have aggregated to form the spheres. The average diameter and shell thickness of ZFMH are ~ 375 and 50 nm, respectively.

The selected area electron diffraction (SAED) pattern of ZFMS (Fig. S1) shows some bright rings composed of evenly distributed bright spots indicating polycrystalline nature of the sample. The equally spaced bright spots in the SAED pattern of ZFMH (Fig. 4 (a)) arise from the clear lattice fringes and suggest good crystalline character of the sample. The SAED patterns of both the samples have been fitted by CrysTBox software [53]. The crystallographic 'd' values obtained from SAED for both the samples are in good agreement with those obtained from PXRD study. The energy dispersive x-ray (EDAX) spectra of both ZFMS (Fig. S2) and ZFMH (Fig. 4 (b)) suggest presence of Fe, Zn and O atoms

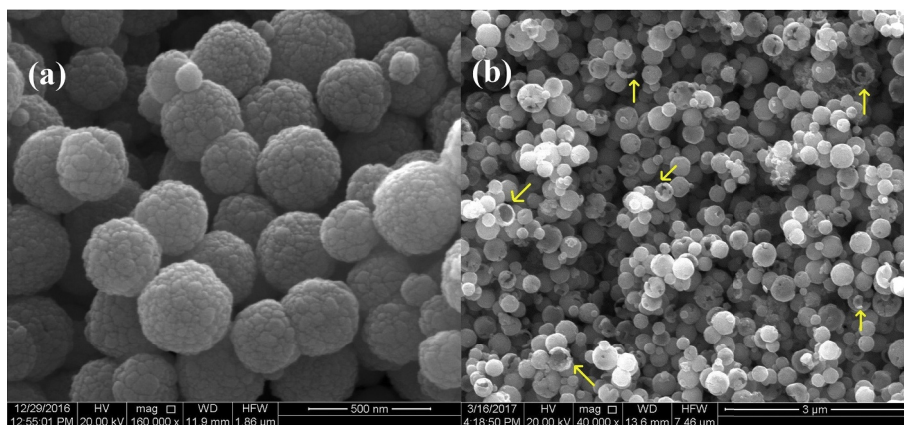


Fig. 2. FESEM micrographs showing particle distribution of (a) ZFMS and (b) ZFMH (some of the broken hollow spheres have been marked by yellow arrows). (For interpretation of the references to colour in this figure legend, the reader is referred to the Web version of this article.)

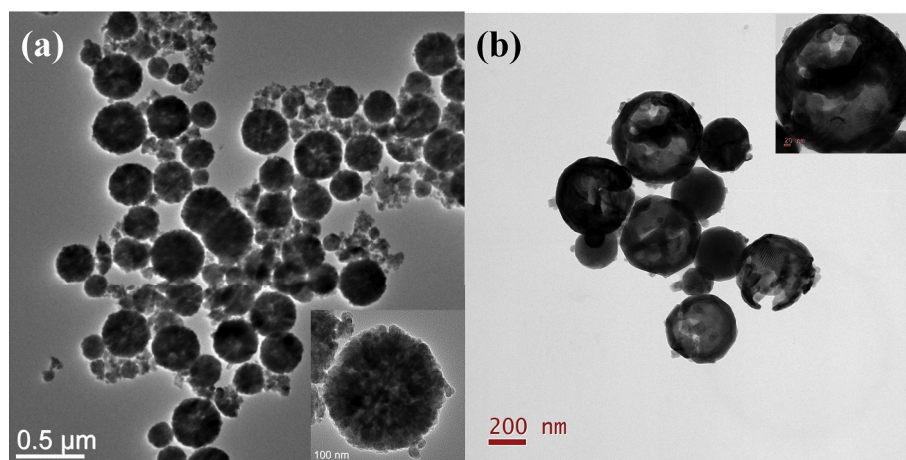


Fig. 3. TEM micrographs showing particle distribution of (a) ZFMS and (b) ZFMH along with single particle at the inset of respective picture.

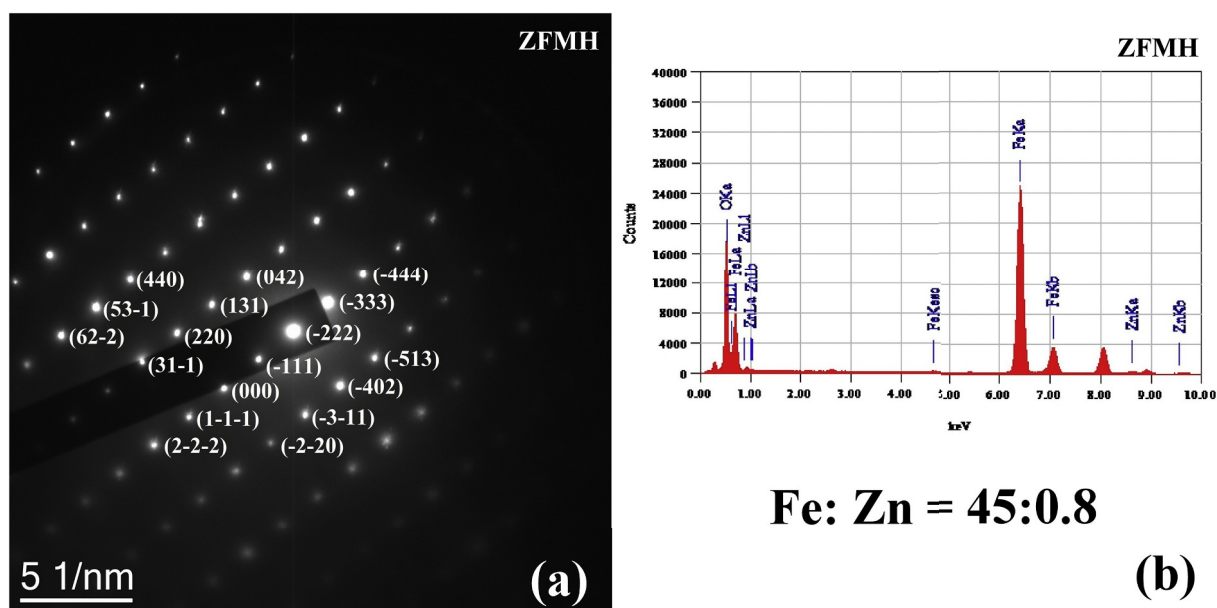


Fig. 4. (a) Indexed SAED pattern and (b) EDAX analysis of ZFMH.

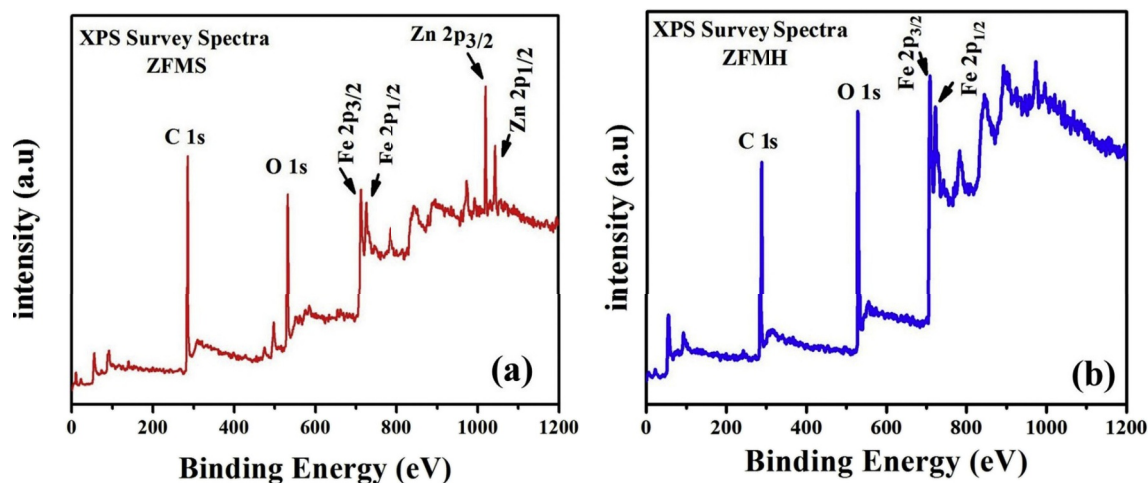


Fig. 5. XPS survey spectra of (a) ZFMS and (b) ZFMH.

only with no signature of any contamination. The metal cations Fe and Zn are in the ratio $\sim 26:12$ in ZFMS, which shows that ZFMS is in proper stoichiometry. The atomic ratio of Fe:Zn is $\sim 45:0.8$, indicating that ZFMH is nonstoichiometric in nature.

3.2. X-ray photoelectron spectroscopic study

The x-ray photoelectron spectroscopy (XPS) is a widely used technique for characterizing ferrites [54–58]. We have recorded the XPS spectra of ZFMS and ZFMH to probe the chemical composition and valance state of the constituent elements of the samples. Fig. 5 (a) and (b) show the XPS survey spectra of ZFMS and ZFMH, respectively. The adventitious C 1s peak in these spectra has been observed as the specimen for XPS study is prepared by pasting sample powder over a carbon coated adhesive tape. Peaks due to O 1s, Fe 2p_{3/2} and Fe 2p_{1/2} are observed in the survey spectra of both ZFMS and ZFMH. However, the peaks corresponding to Zn 2p_{3/2} and Zn 2p_{1/2} states are observed only in case of ZFMS. Thus, the absence of the peaks pertaining to Zn 2p states in the survey spectrum of ZFMH indicates that the sample may be devoid of Zn. The high-resolution Fe 2p spectra of ZFMS and ZFMH are presented in Fig. 6 (a). In the Fe 2p XPS spectra, two peaks with binding energies (BEs) 710.1 eV and 723.5 eV for ZFMS and 709.7 eV and 722.8 eV for ZFMH can be attributed to Fe 2p_{3/2} and Fe 2p_{1/2}, respectively. Thus, Fe 2p peaks of ZFMH have been slightly shifted toward lower BEs with respect to ZFMS and this indicates towards the possibility of presence of Fe²⁺ ions in ZFMH [59]. The high-resolution Fe 2p_{3/2} XPS spectra of ZFMS and ZFMH (Fig. 6 (b) and (c)) are deconvoluted into two and three sub-peaks, respectively. The peaks at 709.2 eV and 710.9 eV (Fig. 6 (b)) can be assigned to Fe³⁺ (A) and [B] sites of ZnFe₂O₄, respectively. The area ratio corresponding to peaks due to Fe³⁺ ions at (A) and [B] sites (Fe³⁺_A:

Fe³⁺_B) is 1:2.56. The peak at 707.9 eV for ZFMH (Fig. 6 (c)) can be assigned to the Fe²⁺ 2p_{3/2} peak at (B) site [60] while The peaks located at 709.2 and 710.4 eV correspond to Fe³⁺ (A) and [B] sites, respectively [54,55]. The area ratio of the peaks corresponding to Fe²⁺ and Fe³⁺ ions (Fe²⁺: Fe³⁺) is 1:8 whereas, the area ratio Fe³⁺_A: Fe³⁺_B ratio is 1:1.25. Moreover, Fe 3p peaks in XPS spectra of ZFMS and ZFMH (Fig. 6 (d)) are found at the BEs of 55.3 and 54.8 eV, respectively. The high-resolution Zn 2p XPS spectrum of ZFMS consist of two peaks which can be allocated to Zn 2p_{3/2} and Zn 2p_{1/2} states. The Zn 2p_{3/2} peak for ZFMS (Fig. 7 (a)) is fitted with two sub-peaks centered at 1021.7 and 1022.3 eV assigned for Zn²⁺ at (A) and [B] sites, respectively. The area ratio of the peaks corresponding to Zn²⁺ at (A) and [B] sites (Zn²⁺_A: Zn²⁺_B) of ZnFe₂O₄ is 1:1.26. The peak at BE 1045.1 eV can be assigned to Zn 2p_{1/2} state [56]. In the high resolution Zn 2p XPS spectrum of ZFMH (Fig. 7 (b)) two insignificant peaks due to Zn 2p_{3/2} and Zn 2p_{1/2} are noticed, which suggests that trace amount of Zn in +2 oxidation state is present in ZFMH. The O 1s XPS spectra of ZFMS and ZFMH are shown in Fig. 8 (a) and (b). The broad and asymmetric peak in O 1s XPS spectrum of ZFMS is deconvoluted into three sub-peaks whereas O 1s XPS spectrum of ZFMH is fitted with two sub-peaks. It may be noted that in ZFMS both metallic iron and zinc are present. Hence, the signature of oxygen containing Zn and Fe species is expected in O 1s XPS spectrum of ZFMS. Further, the area ratio of the peaks located at 530.1 and 530.6 eV is 1:1.9, which is close to the ratio of Zn²⁺ and Fe³⁺ (1:2) in ZFMS. Thus, the peaks at BEs 530.1 and 530.6 eV can be assigned to O²⁻ ions in Zn–O, Fe–O frameworks of ZnFe₂O₄, respectively. Only a single peak located at 530 eV is observed in the O 1s XPS spectra of ZFMH which can be assigned to O²⁻ in Fe–O framework. No peak due to O²⁻ ions in Zn–O framework has been observed in O 1s XPS spectrum of ZFMH as only a trace amount of Zn²⁺ is present in this sample. The peaks with BEs 532.1

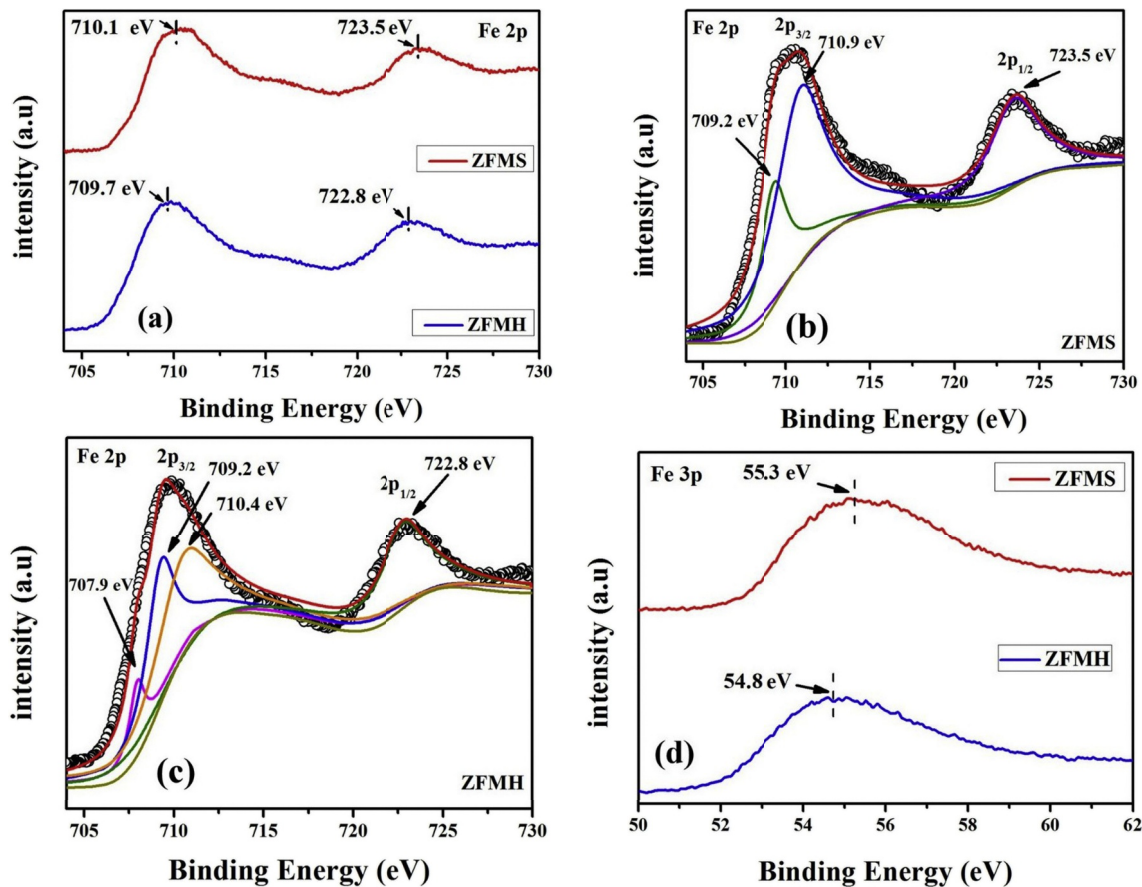


Fig. 6. Core level XPS spectrum corresponding to the (a) Fe 2p peak of ZFMS and ZFMH, (b) fitted Fe 2p peak of ZFMS, (c) fitted Fe 2p peak of ZFMH and (d) Fe 3p peak of ZFMS and ZFMH.

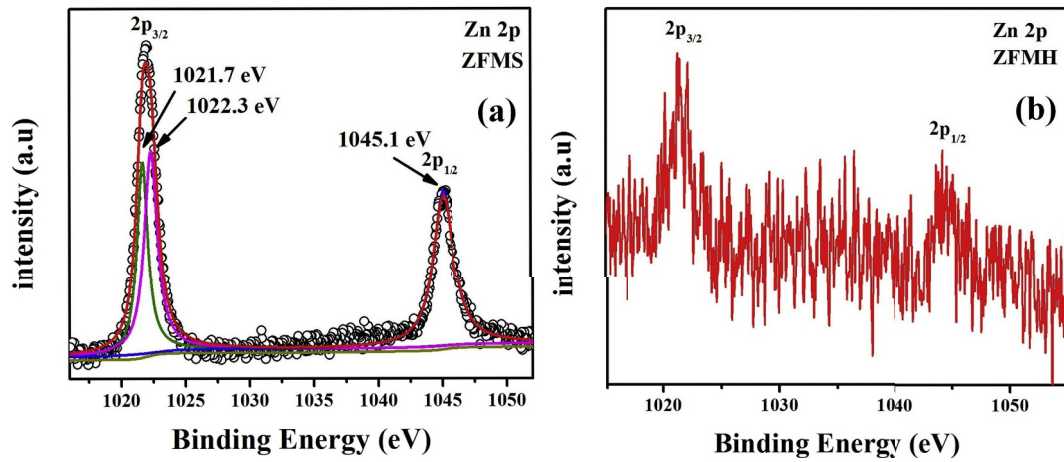


Fig. 7. Core level XPS spectrum corresponding to the Zn 2p peak of (a) ZFMS and (b) ZFMH.

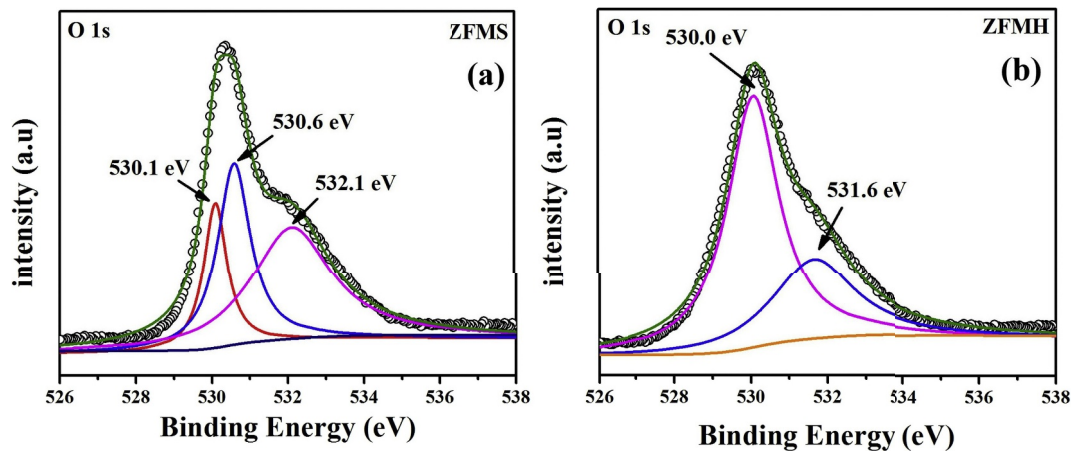


Fig. 8. Core level XPS spectrum corresponding to the O 1s peak of (a) ZFMS and (b) ZFMH.

eV for ZFMS and 531.6 eV for ZFMH can be assigned to the surface absorbed oxygen containing species (possibly water molecules) [55,57, 58].

3.3. Magnetic and hyperfine study

Fig. 9 (a) and (b) show the thermal dependence of magnetization for

ZFMS and ZFMH at a field of 100 Oe. The magnetic moment of the zero field cooled (ZFC) curve of ZFMS remains almost constant between 300 and 200 K, below which it decreases gradually with decreasing temperature up to 25 K; under 25 K the moment falls sharply indicating a spin glass like random freezing [41]. The field cooled (FC) curve follows the trend of a typical superparamagnetic substance [61] and increases simultaneously with decreasing temperature; further below 25 K it

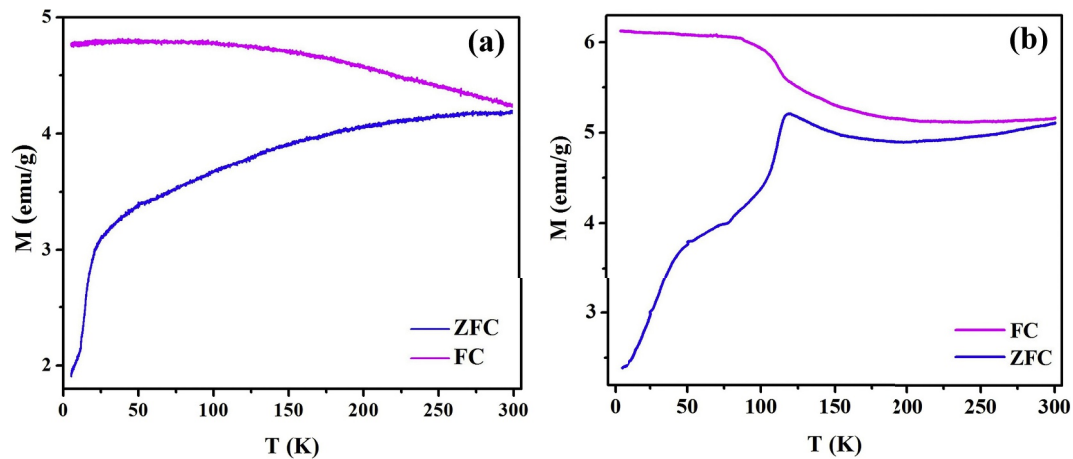


Fig. 9. ZFC-FC magnetization curves of (a) ZFMS and (b) ZFMH at 100 Oe. The FC and ZFC magnetization is represented by pink and the blue lines, respectively. (For interpretation of the references to colour in this figure legend, the reader is referred to the Web version of this article.)

becomes almost constant. The ZFC and FC curves do not coincide up to 300 K (highest measurement temperature). The temperature dependence of magnetization for ZFMS suggests that the nanoparticles constituting the microsphere are superparamagnetic in nature and they possess a broad particle size distribution which results in a wide range of blocking temperatures. But due to aggregate formation, their magnetic behavior has been overshadowed and thus, they exhibit collective magnetic excitations at room temperature, which can be further confirmed from Mössbauer spectroscopy. Further, due to the randomness in distribution of anisotropy energy, spins freeze randomly with the decrease in temperature and lead to the formation of spin glasslike state [62]. The ZFC and FC curves of ZFMH display a completely different behavior from ZFMS. The ZFC and FC curves are slightly bifurcated from 300 K with almost no temperature dependence up to 150 K. The ZFC curve exhibits a distinct peak at ~ 120 K and at the same temperature; the FC magnetization curve takes a sudden leap after which it tends to be constant. Below 120 K, the magnetic moment of ZFC curve decreases sharply with decreasing temperature, while FC curve remains almost constant with negligible dependence on temperature. This behavior of the ZFC-FC curves is reminiscent of the Verway transition [63]. Some of the works on MFe_2O_4 ($\text{M} = \text{Mn}^{2+}, \text{Zn}^{2+}, \text{Co}^{2+}, \text{Ni}^{2+}$ etc.) have ruled out the occurrence of Verway transition in them [64,65]. But, in the present case, we have found a signature of Verway transition in the ZFC-FC curves of ZFMH at 100 Oe. We have also recorded the ZFC-FC curves of ZFMH at 500 Oe (Fig. S3) and found similar trend as in 100 Oe curves, which reinforces the proposition of Verway transition in the present case.

We have further recorded the curves of field dependence on magnetization ($M-H$) at 300, 100 and 10 K in the field range of ± 1 T for both ZFMS and ZFMH (Fig. 10). The $M-H$ loop for ZFMS does not show any hysteresis (H_C) at 300 K supporting its superparamagnetic behavior. The 100 K $M-H$ loop shows slight coercivity and high saturation magnetization (M_{SAT}) as compared to 300 K $M-H$ curve indicating development of magnetic ordering at this temperature. The $M-H$ curve for ZFMH shows small value of H_C at 300 K suggesting presence of magnetic ordering at this temperature. The values of M_{SAT} for ZFMS and ZFMH have been estimated by using the law of approach to saturation. The values of M_{SAT} and H_C are presented in Table 2. We have compared the values of saturation magnetization at 300 K of the present samples with that of other ZnFe_2O_4 solid and hollow microspheres available in literature, and enlisted them in Table 3. It seems that reaction parameters strongly influence the formation of microspheres and consequently their magnetic properties.

The room temperature (300 K) Mössbauer spectra (Fig. 11 (a) and (b)) show a strong superparamagnetic doublet along with diffused sextets for ZFMS and well-defined sextet with a clearly split left most line for ZFMH. Both the spectra have been fitted with “Lorentzian site

Table 2

Values of saturation magnetization (M_{SAT}) and coercivity (H_C) for ZFMS and ZFMH.

Sample	Temperature (K)	M_{SAT} (emu/g)	H_C (Oe)
ZFMS	300	41.5	0
	100	64.0	55
	10	85.7	170
ZFMH	300	77.0	90
	100	84.5	100
	10	90.75	190

analysis” of Recoil program [66]. The 300 K Mössbauer spectrum of ZFMS has been fitted with a doublet and two sextets whereas that of ZFMH has been fitted with two sextets. The fitting of both the samples is good enough and the values of hyperfine parameters are trustworthy. The results have been summarized in Table 4. The doublet is a signature of superparamagnetic character of the nanoparticles constituting ZFMS, whereas the diffused sextets are a result of collective magnetic excitation caused by nanoparticle aggregation. ZFMS has been formed by self assembly of nanoparticles of variable size and assorted shape. So, ZFMS consist of both superparamagnetic and magnetically well-ordered particles, which give rise to an admixture of a doublet and two diffused sextets. The doublet is predominant indicating that most of the constituent particles are superparamagnetic. The ZFC-FC study has also given clear indication in regard of superparamagnetic character of the constituent particles. But, due to variation in the size of the nanoparticles, there is a wide range of distribution in blocking temperature. Since ZFMH is nonstoichiometric with very few Zn^{2+} ions and has shown Verway transition in its ZFC-FC study, so we have fitted the 300 K Mössbauer spectrum of ZFMH with two sextets; one pertaining to the Fe^{3+} ions at tetrahedral site and the other to Fe ions which generally exhibit an exchange of type $\text{Fe}^{2+} \leftrightarrow \text{Fe}^{3+}$ [67]. The values of hyperfine magnetic field (HMF) obtained from fitting for (A) and [B] sites are 57.58 and 51.39 T, respectively. The higher HMF value for (A) site corresponds to the contribution from about half of the Fe^{3+} ions present in the sample and the lower value of HMF for [B] site comes from Fe ions involving $\text{Fe}^{2+} \leftrightarrow \text{Fe}^{3+}$ exchange [67]. The presence of clear sextet in the Mössbauer spectrum of ZFMH suggests that the sample is magnetically well ordered at this temperature, which also corroborates the ZFC-FC study.

Fig. 12 presents the simulated and experimental infield and without field Mössbauer spectrum of ZFMS (Fig. 12 (a) & (b)) and ZFMH (Fig. 12 (c) & (d)). The split 1st and 6th lines in infield spectrum of both ZFMS and ZFMH are a signature of their ferromagnetic character [40,61,62]. The existence of 2nd and 5th lines in the infield spectrum of ZFMS is clear indicator of presence of spin canting in the sample [40,68,69]. We have fitted the infield spectra with two sextets by using “Lorentzian site

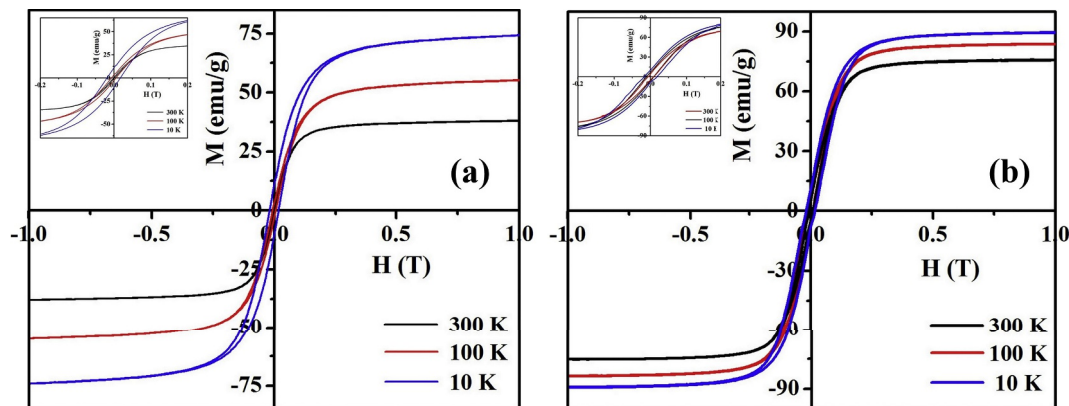
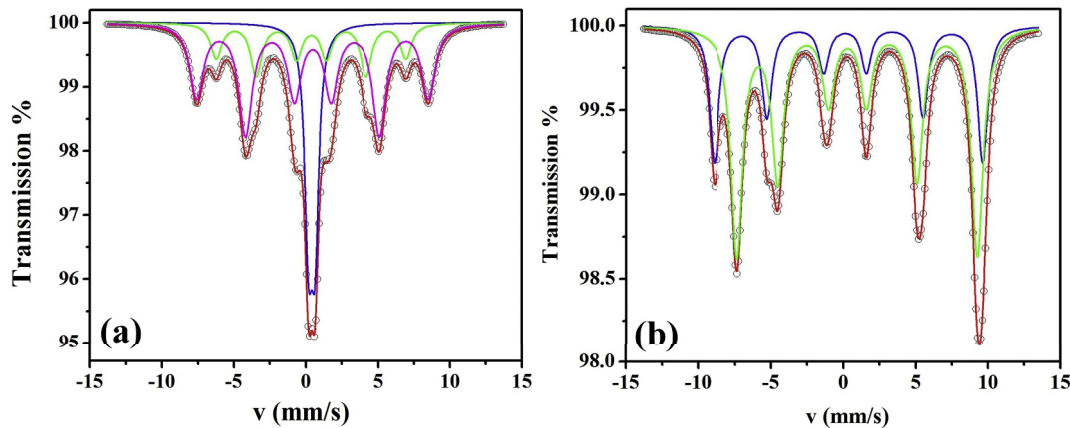


Fig. 10. $M-H$ (hysteresis) loop of (a) ZFMS and (b) ZFMH at 300 (black line), 100 K (red line) and 10 K (blue line) shown between ± 1 T. (For interpretation of the references to colour in this figure legend, the reader is referred to the Web version of this article.)

Table 3Comparison of the room temperature (300 K) saturation magnetization M_{SAT} values of $ZnFe_2O_4$ microspheres with literature values.

Sl No.	Synthesis procedure	Type of microsphere	Surfactant, reaction temperature (°C) & time (hours)	Diameter of microsphere (nm)	M_{SAT} (emu/g)	Reference
1.	Solvothermal	solid	NaAc + PEG, 200 & 8-72	200–800	60	[15]
2.	Solvothermal	solid	NaAc, 200 & 12	450 (with particle sizes) 11.6 nm 16.2 nm 20.5 nm	49.5 53.8 61.3	[23]
3.	Solvothermal	hollow	NaAc + PEG, 180 & 16	100–210	32	[16]
4.	Solvothermal	hollow	NH_4Ac , 170–200 & 24-48	200–450	80.2	[24]
5.	Solvothermal	hollow	NH_4Ac , 210 & 48	127	76.2	[26]
6.	Solvothermal	hollow	PEG-600, 200 & 24	400	83.4	[29]
7.	Hydrothermal	hollow	SDS + TMAOH, 180 & 48	70–100	47.7	[34]
8.	Solvothermal	solid	NaAc + PEG, 180 & 20	314	41.5	ZFMS (present study)
9.	Solvothermal	hollow	NH_4Ac , 170 & 17	375	77	ZFMH (present study)

**Fig. 11.** Mössbauer spectrum of (a) ZFMS and (b) ZFMH at 300 K.**Table 4**

Hyperfine parameters obtained by fitting the Mössbauer spectra of ZFMS and ZFMH at 300 K.

Sample	Spectra	Site	IS (± 0.02) (mm s ⁻¹)	QS (± 0.07) (mm s ⁻¹)	HMF (± 0.1) (T)	Width (± 0.03) (mm s ⁻¹)	Area (± 0.3) (%)
ZFMS	Sextet	$[Fe^{3+}_A]$	0.37	0.0	41.0	0.45	21.36
		$[Fe^{3+}_B]$	0.47	0.0	50.0	0.55	54.76
	Doublet	–	0.39	0.45	–	0.30	23.87
ZFMH	Sextet	$[Fe^{3+}_A]$	0.29	0.10	57.58	0.40	33.33
		$[Fe_B]$	0.69	0.33	51.39	0.48	66.67

analysis” of Recoil program and tried to obtain the precise values of canting angles along with other hyperfine parameters. The results have been summarized in Table 5. The values of isomer shift (IS) assure about the presence of only Fe^{3+} ions in the sample [40,68,69]. The goodness of the fitting suggests that the two component fitting is capable of divulging the hyperfine character of this system precisely. The ratio of Fe^{3+} ions in (A) to [B] site (Fe^{3+}_A/Fe^{3+}_B) of ZFMS is 0.39, whereas in ideal case no Fe^{3+} ion should have been present in tetrahedral (A) site. This affirms that Fe^{3+} ions have migrated from [B] to (A) site in ZFMS. So, as per the ratio of Fe^{3+}_A/Fe^{3+}_B obtained from infield spectrum, we propose a cation distribution for ZFMS as: $(Zn_{0.44}Fe_{0.56})[Zn_{0.56}Fe_{1.44}]O_4$. The infield Mössbauer spectrum of ZFMH discards the presence of spin canting in the sample. We have found from EDS study that ZFMH is nonstoichiometric in nature and it has also shown Verway transition in its ZFC-FC curves. It is well known that the latter is only possible if both Fe^{2+} and Fe^{3+} ions are simultaneously present at [B] site of the spinel lattice [70,71]. So, we have fitted the infield Mössbauer spectrum of ZFMH by three sextets, where 1st and 2nd correspond to Fe^{3+} ions at (A) and [B] site, and 3rd to the Fe^{2+} ions at [B] site. The goodness of fitting

and the values of isomer shift obtained from the fitting suggest that our proposition of presence of both Fe^{2+} and Fe^{3+} ions in the [B] site is correct. The values of hyperfine parameters have been included in Table 5. The proportion of intensity of Fe^{2+} ions in [B] site and the value of Fe^{3+}_A/Fe^{3+}_B obtained from the infield Mössbauer spectrum suggest that there is a vacancy of cations in the [B] site. So to account for the nonstoichiometry of ZFMH and the speculated cation vacancy at [B] site, we have deduced the following possible cation distribution for ZFMH from the ratio of intensities of Fe^{3+} at (A) to [B] sites and Fe^{2+} to Fe^{3+} ions in the infield Mössbauer spectrum: $(Fe^{3+}_xZn^{2+}_{1-x})[Fe^{2+}_{1-3x}Fe^{3+}_{1+2x}\Phi_x]O_4$, where Φ corresponds to vacancies that have appeared in the lattice to account for charge balance [72]. The formula can be written as: $(Fe^{3+}_{0.925}Zn^{2+}_{0.075})[Fe^{2+}_{0.31}Fe^{3+}_{1.46}\Phi_{0.23}]O_4$. The ratio of Fe:Zn from the so obtained cation distribution is in good agreement with the ratio of the same estimated from EDS study. Further, the Verway transition in ZFMH can now be clearly asserted to the possible charge orbital ordering established due to the simultaneous presence of Fe^{2+} and Fe^{3+} ions in the [B] site.

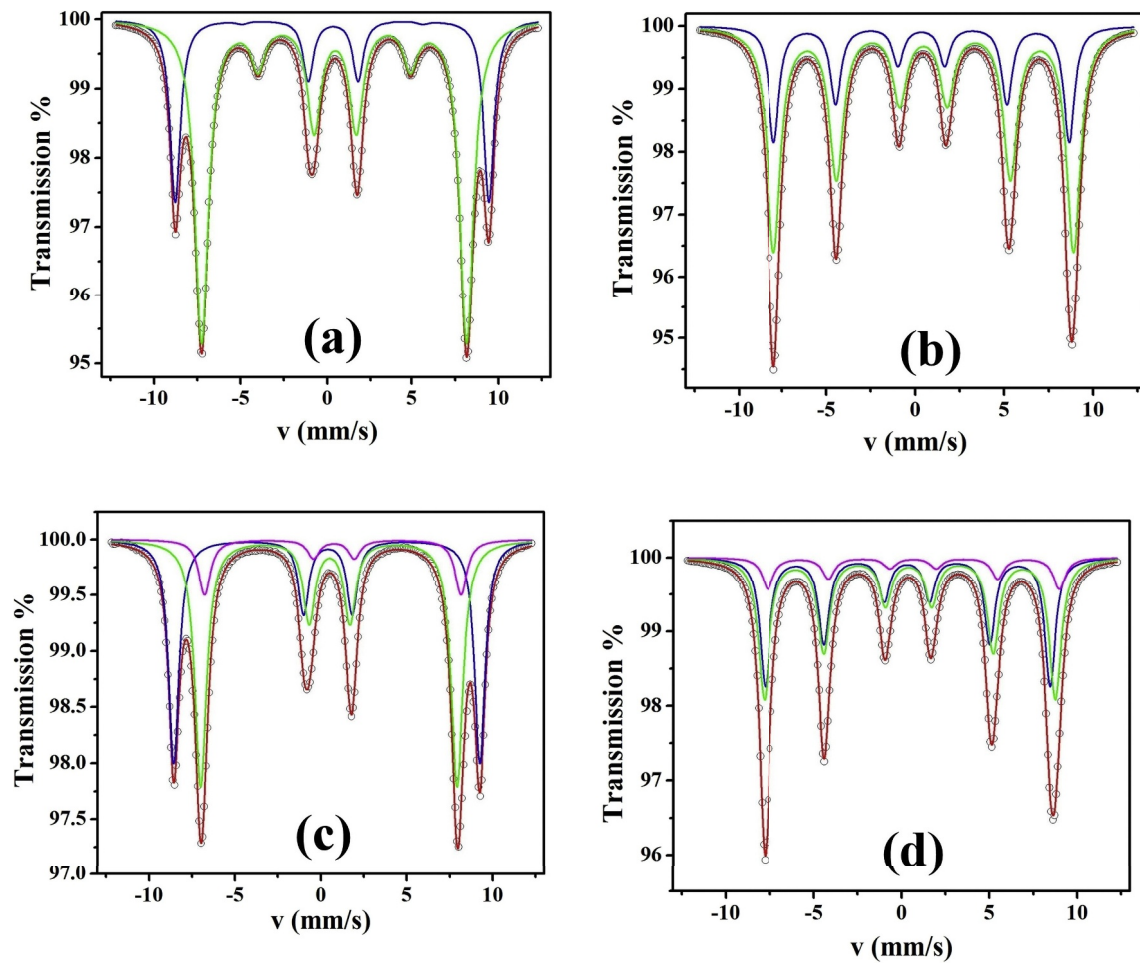


Fig. 12. Fitted Mössbauer spectra of ZFMS at (a) 5 K with 5 T external magnetic field, (b) 5 K without field and ZFMH at (c) 5 K under 5 T external magnetic field, (d) 5 K without field by using Lorentzian site analysis method of the Recoil program.

Table 5

Values of zero field and infield Mössbauer parameters of the sample at 5 K determined by Lorentzian profile fitting.

Sample	Temperature/Field	Site	Width (mm s ⁻¹) (±0.03)	IS (mm s ⁻¹) (±0.03)	2e (mm s ⁻¹) (±0.03)	B _{eff} ^a (T) (±0.14)	B _{hf} (T) (±0.14)	A ₂₃	θ ^b (Degree) (±0.02)	Area (%) (±0.2)
ZFMS	5 K/5T	[Fe ³⁺ _A]	0.35	0.35	0.00	56.5	51.57	0.05	9.04	28.12
		[Fe ³⁺ _B]	0.47	0.47	0.00	47.8	52.35	0.41	25.54	71.87
	5 K/0 T	[Fe ³⁺ _A]	0.35	0.35	0.00	–	51.57	–	–	28.12
		[Fe ³⁺ _B]	0.47	0.47	0.00	–	52.35	–	–	71.87
ZFMH	5 K/5T	[Fe ³⁺ _A]	0.35	0.36	0.00	55.44	50.43	0.0	0.0	39.50
		[Fe ³⁺ _B]	0.40	0.47	0.01	46.50	51.50	0.0	0.0	49.35
		[Fe ²⁺ _B]	0.40	0.70	0.00	46.50	51.50	0.0	0.0	11.11
	5 K/0 T	[Fe ³⁺ _A]	0.35	0.36	0.00	–	50.43	–	–	39.50
		[Fe ³⁺ _B]	0.40	0.47	0.01	–	51.50	–	–	49.35
		[Fe ²⁺ _B]	0.40	0.70	0.00	–	51.50	–	–	11.11

^a Estimated according to the relationship of B_{eff}, B_{hf} and applied field.

^b Observed HMF (BHF) is the vector sum of the internal HMF and the external applied magnetic field.

^c The average canting angle estimated from the ratio of the intensities of lines 2 and 3 from each subspectra, I₂/I₃ (A₂₃) according to $\theta = \arccos [(4 - I_2/I_3)/(4 + I_2/I_3)]^{1/2}$. Where I₂/I₃ = A₂₃.

4. Discussion

The structural and morphological characterization through PXRD, FESEM and TEM reveals following facts about ZFMS and ZFMH. ZFMS of diameter ~314 nm are composed of particles of crystallite size ~25 nm. They have crystallized in cubic spinel phase with lattice parameter ~8.487 Å. ZFMH has a hollow interior and an outer shell formed by continuous overlapping of layers of nanoparticles whose boundaries are

indistinguishable. The smallest region of regular crystalline structure in ZFMH is of ~80 nm and it has also crystallized in cubic spinel phase. The value of lattice parameter for ZFMH is ~8.432 Å. The lattice parameter for bulk ZnFe₂O₄ is ~8.440 Å (ICDD card no: 82-1049). So, the lattice parameters of ZFMS and ZFMH are in good agreement with that of bulk ZnFe₂O₄, which suggests that the results of PXRD analysis are reliable. We have found that the crystallite size of ZFMH is quite large and clear boundaries of single particles are not separable in the TEM micrographs.

Further, each bright single spot in the SAED pattern corresponds to a single large crystallite. The clear hyperfine split sextets in the 300 K Mössbauer spectrum of ZFMH also clearly indicates that the particles constituting it are larger in size, bear excellent crystalline character and consequently, are magnetically well-ordered.

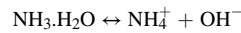
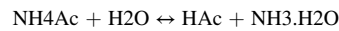
The cation distribution proposed for ZFMS and ZFMH on the basis of valance state and the occupancy of iron ions at tetrahedral (A) and octahedral [B] sites of ZnFe_2O_4 obtained from the results of Mössbauer spectroscopic study can be verified by taking into account the valance state and ratio of metal ions determined through XPS study. In case of ZFMS, the value of $\text{Fe}^{3+}_\text{A}/\text{Fe}^{3+}_\text{B}$ determined from Mössbauer spectroscopic study is 0.39, which is same as that obtained from XPS study. Further, for ZFMS, the area ratio of Zn^{2+} at (A) and [B] sites ($\text{Zn}^{2+}_\text{A}/\text{Zn}^{2+}_\text{B}$) is 0.79 while the value of the same for cation distribution proposed for ZFMS on the basis of Mössbauer spectroscopic study is 0.786. Thus, the results of Mössbauer spectroscopic and XPS studies corroborate with each other and together with confirm that the cation distribution for ZFMS is $(\text{Zn}_{0.44}\text{Fe}_{0.56})[\text{Zn}_{0.56}\text{Fe}_{1.44}]\text{O}_4$. It may be noted that in ZnFe_2O_4 Zn^{2+} ions preferably occupy the (A) site [24]. However, in this case the Zn^{2+} ions have migrated from (A) to [B] sites by replacing equal amount of Fe^{3+} ions of [B] sites and pushing them to the (A) sites. Now, the cation distribution $(\text{Fe}^{3+}_{0.925}\text{Zn}^{2+}_{0.075})[\text{Fe}^{2+}_{0.31}\text{Fe}^{3+}_{1.46}\text{O}_{0.23}]\text{O}_4$ for ZFMH has been determined using the ratio of $\text{Fe}^{3+}_\text{A}/\text{Fe}^{3+}_\text{B}$ and $\text{Fe}^{2+}/\text{Fe}^{3+}$ as obtained from Mössbauer spectroscopic study keeping in mind the charge balance condition. Again, both XPS and Mössbauer spectroscopic studies confirm the presence of Fe^{2+} ion in [B] sites of ZFMH. According to the Mössbauer spectroscopic study the values of $\text{Fe}^{3+}_\text{A}/\text{Fe}^{3+}_\text{B}$ and $\text{Fe}^{2+}/\text{Fe}^{3+}$ for ZFMH are 0.81 and 0.125, respectively, while the corresponding values obtained from the analysis of Fe 2p_{3/2} XPS spectra are 0.80 and 0.125, respectively. Thus, the results of Mössbauer and XPS studies match well for ZFMH. The XPS study also indicates that very small amount of Zn is present in ZFMH. According to EDS study the ratio of Fe:Zn is $\sim 45:0.8$. Thus, ZFMH should be non-stoichiometric in nature and cation vacancy is inhabitable in it to maintain charge balance. Therefore, the perfect matching of occupancy of Fe^{3+} and Fe^{2+} ions at tetrahedral (A) and octahedral [B] sites for ZFMH suggests that the proposed cation distribution is correct and there is cation vacancy in this sample.

In order to test the accuracy of the cation distribution of ZFMS and ZFMH deduced from infield Mössbauer spectroscopic studies, we have calculated the theoretical value of magnetic moment per formula unit using the same and compared them with their experimental values obtained from dc magnetic studies. The theoretical magnetic moment per formula unit (m_th) of ferrites can be written as $m_\text{th} = m_\text{B}\cos\theta_\text{B} - m_\text{A}\cos\theta_\text{A}$ where, m_B and m_A are the magnetic moments associated with [B] and (A) sublattice of the spinel structure, respectively, θ_A and θ_B are the (A) and [B] site canting angles, respectively. Taking into consideration the values of θ_A and θ_B for ZFMS, we have found the value of m_th as 3.73 μ_B . The experimental magnetic moment per formula unit (m_exp) obtained from the value of M_SAT of 10 K M – H curve is 3.70 μ_B . The value of m_th and m_exp for ZFMH are 3.915 and 3.917 μ_B , respectively. The values of m_th and m_exp for both ZFMS and ZFMH are in excellent agreement. So, the deduced cation distribution of both ZFMS and ZFMH are trustworthy.

The dc magnetic measurements and Mössbauer spectroscopic studies give rise to some interesting magnetic phenomena such as superparamagnetism, spin glasslike freezing and collective magnetic excitations in ZFMS while most importantly Verway transition in ZFMH. ZFMS have been formed by aggregation of nanoparticles of assorted shape and sizes. As a result, they display broad superparamagnetic hump in their ZFC curve at higher temperatures with a distribution of blocking temperatures. On lowering the temperature, the spins freeze in random orientations due to competing sublattice interactions along with frustrations and the entire system stabilizes in a spin glasslike state. The room temperature Mössbauer spectroscopic studies of ZFMS reveal mixed magnetic phase possessing a superparamagnetic doublet along

with diffused sextets. This result complies with the dc magnetic observations that the sample consists of nanoparticles with a broad particle size distribution consisting both superparamagnetic and magnetically well-ordered particles. There is an anomaly between the results of low temperature Mössbauer spectroscopic studies and the dc magnetic measurement. The 5 K zero field and infield Mössbauer spectrum assure ferrimagnetic ordering within the sample whereas ZFC curve displays spin glasslike behavior at about same temperature. The difference arises from the fact that Mössbauer spectroscopy probes fluctuations of magnetic moment in the locality of Fe^{3+} ions whereas dc magnetic study records the magnetization as a whole.

ZFMH displays Verway transition in its dc magnetic studies. It is well known that Verway transition has been observed in magnetite at ~ 124 K [70,71]. Below this temperature, a first-order metal insulator transition takes places as a result of charge ordering between Fe^{3+} and Fe^{2+} ions at [B] site of the spinel lattice [70]. From literature survey, it is apparent that Verway transition is very prone to impurities and disappears with a little perturbation [73]. So, it is one of the most intriguing topics to researchers. Recently, Yeo et al., have found Verway transition in Gd doped magnetite nanoparticles and suggested that charge- orbital ordering has mainly instigated the transition [74]. In the present case, we have found from EDS study that ZFMH is nonstoichiometric in nature with very few Zn^{2+} ions in the system. The XPS study also corroborates this fact. From the results of XPS and low temperature Mössbauer spectroscopic studies we have found that apart from Fe^{3+} ions, Fe^{2+} ions are also present in ZFMH. These Fe^{2+} ions are the product of redox reaction of ethylene glycol (solvent) and Fe^{3+} ions [75]. Further, NH_4Ac was used as hollowing agent in the synthesis of ZFMH. NH_4Ac is a weak-acid-weak-base salt that can be hydrolysed at high temperature in the presence of a trace amount of water coming from $\text{FeCl}_3\cdot 6\text{H}_2\text{O}$ as follows:



Zinc has a tendency to form a very stable zinc amine complex. It seems that the Zn^{2+} ions at (A) site may have been replaced by Fe^{3+} ions from [B] site of the spinel lattice. Those misplaced Zn^{2+} ions have not migrated to [B] site following their strong chemical affinity towards (A) site; instead they may have formed the amine complex and remained in the solution, which was separated out during ultracentrifugation. As a result, a vacancy of Zn^{2+} ions has occurred in the lattice. Moreover, Verway transition is also sensitive to the nature of surface atoms [74] and no surface spin canting has been observed for ZFMH from its infield Mössbauer spectroscopic study. Thus, it seems that presence of considerable amount of Fe^{2+} ions at [B] site in addition to Fe^{3+} ions resulting in charge-orbital ordering and absence of any surface spin canting leading to more symmetric coordination have together contributed to the occurrence of Verway transition in ZFMH.

5. Conclusion

The ZnFe_2O_4 solid and hollow microspheres, which have been synthesized by one-step solvothermal technique, display unique magnetic and hyperfine properties. The presence of collective magnetic excitations in the solid microspheres has been attributed to its nanoparticle self-assembled structure, which possesses both superparamagnetic and magnetically well-ordered particles. The appearance of Verway transition in the hollow microspheres has been mostly instigated by the charge orbital ordering between Fe^{3+} and Fe^{2+} ions in the [B] site of the spinel lattice. Presence of spin canting has been detected in the solid microspheres from its low temperature infield Mössbauer spectroscopic studies, whereas a possible cation vacancy along with existence of Fe^{2+} ions at [B] site of the spinel lattice has been found in the hollow microspheres. The cation distribution of both the microspheres has been testified by comparing the theoretical and experimental values of

magnetic moment per formula unit and found to be reliable.

CRedit authorship contribution statement

K. Sarkar: Conceptualization, Methodology, Data curation, Software, Writing - original draft, Visualization, Investigation. **R. Mondal:** Data curation, Writing - review & editing. **S. Dey:** Software, Visualization, Investigation. **S. Kumar:** Conceptualization, Supervision.

Acknowledgements

K. Sarkar (Ref. No: 20/12/2015(ii)EU-V) gratefully acknowledges UGC, New Delhi for senior research fellowship. We gratefully acknowledge the support received from the UGC-DAE CSR, Indore Center for in-field Mössbauer measurement and UGC-DAE CSR, Kolkata Center in connection to dc magnetic measurements. We sincerely thank Prof. V. R. Reddy of UGC-DAE CSR, Indore Center for his help and cooperation regarding in-field Mössbauer spectroscopic measurements. The UPE program of UGC and the PURSE program of DST, Govt. of India are also acknowledged.

Appendix A. Supplementary data

Supplementary data to this article can be found online at <https://doi.org/10.1016/j.physb.2020.412015>.

References

- [1] M.A. Boles, M. Engel, D.V. Talapin, Self-assembly of colloidal nanocrystals: from intricate structures to functional materials, *Chem. Rev.* 116 (2016) 11220–11289.
- [2] S. Singamaneni, V.N. Bliznyuk, C. Binek, E.Y. Tsymlar, Magnetic nanoparticles: recent advances in synthesis, self-assembly and applications, *J. Mater. Chem.* 21 (2011) 16819.
- [3] M. Rad-Malekshahi, L. Lempink, M. Amidi, W.E. Hennink, E. Mastrobattista, Biomedical applications of self-assembling peptides, *Bioconjug. Chem.* 27 (2016) 3–18.
- [4] K.M.Z. Hossain, U. Patel, I. Ahmed, Development of microspheres for biomedical applications: a review, *Prog. Biomater.* 4 (2015) 1–19.
- [5] R. Mellors, I. Benzeval, R. Eissenthal, J. Hubble, Preparation of self-assembled microspheres and their potential for drug delivery, *Pharm. Dev. Technol.* 15 (1) (2010) 105–111.
- [6] L. Zhang, J.M. Chan, F.X. Gu, June-Wha Rhee, A.Z. Wang, A.F. Radovic-Moreno, F. Alexis, R. Langer, O.C. Farokhzad, Self-assembled LipidPolymer hybrid nanoparticles: a robust drug delivery platform, *ACS Nano* 2 (2008) 1696–1702.
- [7] B.I. Kharisov, H.V. Rasika Dias, O.V. Kharisova, A. Vázquez, Y. Peña, I. Gómez, Solubilization, dispersion and stabilization of magnetic nanoparticles in water and non-aqueous solvents: recent trends, *RSC Adv.* 4 (2014) 45354–45381.
- [8] C. Pereira, A.M. Pereira, C. Fernandes, M. Rocha, R. Mendes, M.P. Fernández-García, A. Guedes, P.B. Tavares, J.-M. Grenèche, J.P. Araújo, C. Freire, Superparamagnetic MFe_2O_4 ($\text{M} = \text{Fe}, \text{Co}, \text{Mn}$) nanoparticles: tuning the particle size and magnetic properties through a novel one-step coprecipitation route, *Chem. Mater.* 24 (2012) 1496–1504.
- [9] T. Neuberger, B. Schöpf, H. Hofmann, M. Hofmann, B. von Rechenberg, Superparamagnetic nanoparticles for biomedical applications: possibilities and limitations of a new drug delivery system, *J. Magn. Magn. Mater.* 293 (2005) 483–496.
- [10] D.K. Kim, Y. Zhang, W. Voit, K.V. Rao, J. Kehr, B. Bjelke, M. Muhammed, Superparamagnetic iron oxide nanoparticles for bio-medical applications, *Scr. Mater.* 44 (2001) 1713–1717.
- [11] N. Bao, L. Shen, Yu-Hsiang A. Wang, J. Ma, D. Mazumdar, A. Gupta, Controlled growth of monodisperse self-supported superparamagnetic nanostructures of spherical and rod-like CoFe_2O_4 nanocrystals, *J. Am. Chem. Soc.* 131 (2009) 12900–12901.
- [12] H.L. Yuan, Y.Q. Wang, S.M. Zhou, L.S. Liu, X.L. Chen, S.Y. Lou, R.J. Yuan, Y. M. Hao, N. Li, Low-temperature preparation of superparamagnetic CoFe_2O_4 microspheres with high saturation magnetization, *Nanoscale Res. Lett.* 5 (2010) 1817–1821.
- [13] R. Mondal, K. Sarkar, S. Dey, D. Majumdar, S.K. Bhattacharya, P. Sen, S. Kumar, Magnetic, pseudocapacitive, and H_2O_2 -electrosensing properties of self-assembled superparamagnetic $\text{Co}_{0.3}\text{Zn}_{0.7}\text{Fe}_2\text{O}_4$ with enhanced saturation magnetization, *ACS Omega* 4 (2019) 12632–12646.
- [14] S. Majumder, S. Dey, K. Bagani, S.K. Dey, S. Banerjee, S. Kumar, A comparative study on the structural, optical and magnetic properties of Fe_3O_4 and $\text{Fe}_3\text{O}_4/\text{SiO}_2$ core-shell microspheres along with an assessment of their potentiality as electrochemical double layer capacitors, *Dalton Trans.* 44 (2015) 7190.
- [15] H. Deng, X. Li, Q. Peng, X. Wang, J. Chen, Y. Li, Monodisperse magnetic single-crystal ferrite microspheres, *Angew. Chem. Int. Ed.* 44 (2005) 2782–2785.
- [16] M. Penchal Reddy, A.M.A. Mohamed, One-pot solvothermal synthesis and performance of mesoporous magnetic ferrite MFe_2O_4 nanospheres, *Microporous Mesoporous Mater.* 215 (2015) 37–45.
- [17] A. Kostopoulou, A. Lappas, Colloidal magnetic nanocrystal clusters: variable length-scale interaction mechanisms, synergetic functionalities and technological advantages, *Nanotechnol. Rev.* 4 (6) (2015) 595–624.
- [18] A. Kostopoulou, K. Brintakis, M. Vasilakaki, K.N. Trohidou, A.P. Douvalis, A. Lascialfari, L. Manna, A. Lappas, Assembly-mediated interplay of dipolar interactions and surface spin disorder in colloidal maghemite nanoclusters, *Nanoscale* 6 (2014) 3764.
- [19] L. Lartigue, P. Hugouenq, D. Alloyeau, S.P. Clarke, M. Levy, J.-C. Bacri, R. Bazzi, D.F. Brougham, C. Wilhelm, F. Gazeau, Cooperative organization in iron oxide multi-core nanoparticles potentiates their efficiency as heating mediators and MRI contrast agents, *ACS Nano* 6 (2012) 10935–10949.
- [20] G.F. Goya, T.S. Berquó, F.C. Fonseca, M.P. Morales, Static and dynamic magnetic properties of spherical magnetite nanoparticles, *J. Appl. Phys.* 94 (2003) 3520.
- [21] A. Espinosa, A. Muñoz-Noval, M. García-Hernández, A. Serrano, J. Jiménez de la, A. Figuerola, A. Quarta, T. Pellegrino, C. Wilhelm, M.A. García, Magnetic properties of iron oxide nanoparticles prepared by seeded-growth route, *J. Nano Res.* 15 (2013) 1514.
- [22] C. Yao, Q. Zeng, G.F. Goya, T. Torres, J. Liu, H. Wu, M. Ge, Y. Zeng, Y. Wang, J. Z. Jiang, ZnFe_2O_4 nanocrystals: synthesis and magnetic properties, *J. Phys. Chem. C* 111 (2007) 12274–12278.
- [23] P. Guo, L. Cui, Y. Wang, M. Lv, B. Wang, X.S. Zhao, Facile synthesis of ZnFe_2O_4 nanoparticles with tunable magnetic and sensing properties, *Langmuir* 29 (2013) 8997–9003.
- [24] A. Yan, X. Liu, R. Yi, R. Shi, N. Zhang, G. Qiu, Selective synthesis and properties of monodisperse Zn ferrite hollow nanospheres and nanosheets, *J. Phys. Chem. C* 112 (2008) 8558–8563.
- [25] Z. Li, X. Lai, H. Wang, D. Mao, C. Xing, D. Wang, General synthesis of homogeneous hollow core-shell ferrite microspheres, *J. Phys. Chem. C* 113 (2009) 2792–2797.
- [26] R. Rahimi, H. Kerdari, M. Rabbani, M. Shafiee, Synthesis, characterization and adsorbing properties of hollow $\text{Zn-Fe}_2\text{O}_4$ nanospheres on removal of Congo red from aqueous solution, *Desalination* 280 (2011) 412–418.
- [27] Yu Meng, Ying Huang, Ke Wang, Xiaopeng Han, Mingyue Wang, Yade Zhu, Liu Liu, Complete hollow ZnFe_2O_4 nanospheres with huge internal space synthesized by a simple solvothermal method as anode for lithium ion batteries, *Appl. Surf. Sci.* 462 (2018) 955–962.
- [28] D. Yang, K. Wei, Q. Liu, Y. Yang, X. Guo, H. Rong, M.-L. Cheng, G. Wang, Follic acid functionalized magnetic ZnFe_2O_4 hollow microsphere core/mesoporous silica shell composite particles: synthesis and application in drug release, *Mater. Sci. Eng. C* 33 (2013) 2879–2884.
- [29] W. Jiang, Z. Cao, R. Gu, X. Ye, C. Jiang, X. Gong, A simple route to synthesize ZnFe_2O_4 hollow spheres and their magnetorheological characteristics, *Smart Mater. Struct.* 18 (2009) 125013.
- [30] Y. Qu, D. Zhang, X. Wang, H. Qiu, T. Zhang, M. Zhang, G. Tian, H. Yue, S. Feng, G. Chen, Porous ZnFe_2O_4 nanospheres as anode materials for Li-ion battery with high performance, *J. Alloy. Comp.* 721 (2017) 697–704.
- [31] X. Zhou, J. Liu, C. Wang, P. Sun, X. Hu, X. Li, K. Shimanoe, N. Yamazoe, G. Lu, Highly sensitive acetone gas sensor based on porous ZnFe_2O_4 nanospheres, *Sens. Actuators B* 206 (2015) 577–583.
- [32] X. Guo, X. Lu, X. Fang, Y. Mao, Z. Wang, L. Chen, X. Xu, H. Yang, Y. Liu, A facile bubble-assisted synthesis of porous Zn ferrite hollow microsphere and their excellent performance as an anode in lithium ion battery, *Electrochem. Commun.* 12 (2010) 847–850.
- [33] L. Yao, X. Hou, S. Hu, Q. Ru, X. Tang, L. Zhao, D. Sun, Lithium storage in hollow spherical ZnFe_2O_4 as anode materials for lithium ion batteries, *J. Solid State Electrochem.* 17 (2013) 2055–2060.
- [34] X.-J. Xu, L.-H. Zhou, Q.-G. Zhai, C.-Z. Lu, Synthesis, properties, and formation mechanism of zinc ferrite hollow spheres, *J. Am. Ceram. Soc.* 90 (2007) 1959–1962.
- [35] P. Guo, M. Lv, G. Han, C. Wen, Q. Wang, H. Li, X.S. Zhao, Solvothermal synthesis of hierarchical colloidal nanocrystal assemblies of ZnFe_2O_4 and their application in water treatment, *Materials* 9 (2016) 806.
- [36] Z.P. Chen, W.Q. Fang, B. Zhang, H.G. Yang, High-yield synthesis and magnetic properties of ZnFe_2O_4 single crystal nanocubes in aqueous solution, *J. Alloy. Comp.* 550 (2013) 348–352.
- [37] A. Kmita, D. Lachowicz, J. Żukrowski, M. Gajewska, W. Szczerba, J. Kuciakowski, S. Zapotoczny, M. Sikora, One-step synthesis of long term stable superparamagnetic colloid of zinc ferrite nanorods in water, *Materials* 12 (2019) 1048.
- [38] B.D. Cullity, C.D. Graham, Introduction to Magnetic Materials, IEEE Press, 2009.
- [39] S. Dey, S.K. Dey, B. Ghosh, P. Dasgupta, A. Poddar, V.R. Reddy, S. Kumar, Role of inhomogeneous cation distribution in magnetic enhancement of nanosized $\text{Ni}_{0.35}\text{Zn}_{0.65}\text{Fe}_2\text{O}_4$: a structural, magnetic, and hyperfine study, *J. Appl. Phys.* 114 (2013) 093901.
- [40] S. Dey, R. Mondal, S.K. Dey, S. Majumder, P. Dasgupta, A. Poddar, V.R. Reddy, S. Kumar, Tuning magnetization, blocking temperature, cation distribution of nanosized $\text{Co}_{0.2}\text{Zn}_{0.8}\text{Fe}_2\text{O}_4$ by mechanical activation, *J. Appl. Phys.* 118 (2015) 103905.
- [41] B. Ghosh, S. Kumar, A. Poddar, C. Mazumdar, S. Banerjee, V.R. Reddy, A. Gupta, Spin glasslike behavior and magnetic enhancement in nanosized Ni–Zn ferrite system, *J. Appl. Phys.* 108 (2010), 034307.
- [42] P. Hu, L. Yu, A. Zuo, C. Guo, F. Yuan, Fabrication of monodisperse magnetite hollow spheres, *J. Phys. Chem. C* 113 (2009) 900–906.

- [43] Y. Wang, D. Su1, A. Ung, J-ho Ahn, G. Wang, Hollow CoFe_2O_4 nanospheres as a high capacity anode material for lithium ion batteries, *Nanotechnology* 23 (2012), 055402, 6pp.
- [44] D. Mandal, M. Alam, K. Mandal, NiFe_2O_4 nano-hollow spheres with improved magnetic and dielectric properties, *Physica B* 554 (2019) 51–56.
- [45] W. Zhang, X. Hou, Z. Lin, L. Yao, X. Wang, Y. Gao, S. Hu, Hollow microspheres and nanoparticles MnFe_2O_4 as superior anode materials for lithium ion batteries, *J. Mater. Sci. Mater. Electron.* 26 (2015) 9535–9545.
- [46] M.P. Reddy, X.B. Zhou, Q. Huang, R.R. Reddy, Synthesis and characterization of ultrafine and porous structure of magnesium ferrite nanospheres, *Int. J. Nano Stud. Technol.* 3 (6) (2014) 72–77.
- [47] Y. Yin, N. Huo, W. Liu, Z. Shi, Q. Wang, Y. Ding, J. Zhang, S. Yang, Hollow spheres of MgFe_2O_4 as anode material for lithium-ion batteries, *Scr. Mater.* 110 (2016) 92–95.
- [48] M.P. Reddy, X. Zhou, D. Shiyu, Q. Huang, Fabrication, characterization, and magnetic behavior of porous ZnFe_2O_4 hollow microspheres, *Int. Nano Lett.* 5 (2015) 53–59.
- [49] P.E. Werner, L. Eriksson, M. Westdahl, TREOR, A semi-exhaustive trial-and-error powder indexing program for all symmetries, *J. Appl. Crystallogr.* 18 (1985) 367–370.
- [50] A. Altomare, R. Caliendo, M. Camalli, C. Cuocci, I. da Silva, C. Giacovazzo, A. Grazia G. Moliterni, R. Spagna, Space-group determination from powder diffraction data: a probabilistic approach, *J. Appl. Crystallogr.* 37 (2004) 957–966.
- [51] L. Lutterotti, MAUDWEB, 2004, p. 9992, Ver.
- [52] Y. Yin, R.M. Rioux, C.K. Erdonmez, S. Hughes, G.A. Somorjai, A. Paul Alivisatos, formation of hollow nanocrystals through the nanoscale kirkendall effect, *Science* 304 (2004) 711–714.
- [53] M. Klinger, More features, more tools, more CrysTBox, *J. Appl. Crystallogr.* 50 (2017) 1226–1234.
- [54] M. Wen, Q. Li, Y. Li, Magnetic, electronic and structural properties of $\text{Zn}_x\text{Fe}_{3-x}\text{O}_4$, *J. Electron. Spectrosc. Relat. Phenom.* 153 (2006) 65–70.
- [55] Z.P. Chen, W.Q. Fang, B. Zhang, H.G. Yang, High-yield synthesis and magnetic properties of ZnFe_2O_4 single crystal nanocubes in aqueous solution, *J. Alloy. Comp.* 550 (2013) 348–352.
- [56] J. Wu, N. Li, J. Xu, Y. Jiang, Z.-G. Ye, Z. Xie, L. Zheng, Partially inverse spinel ZnFe_2O_4 with high saturation magnetization via a molten salt route, *Appl. Phys. Lett.* 99 (2011) 202505.
- [57] S. Majumder, M. Sardar, B. Satpati, S. Kumar, S. Banerjee, Magnetization enhancement of Fe_3O_4 by attaching onto graphene oxide: an interfacial effect, *J. Phys. Chem. C* 122 (2018) 21356–21365.
- [58] M. Wang, Z. Ai, L. Zhang, Generalized preparation of porous nanocrystalline ZnFe_2O_4 superstructures from zinc ferrioxalate precursor and its superparamagnetic property, *J. Phys. Chem. C* 112 (2008) 13163–13170.
- [59] G. Chen, J.J. Peng, C. Song, F. Zeng, F. Pan, Interplay between chemical state, electric properties, and ferromagnetism in Fe-doped ZnO films, *J. Appl. Phys.* 113 (2013) 104503.
- [60] J.F. Moulder, W.E. Stickle, P.E. Sobol, K.D. Bomben, *Handbook of X-Ray Photoelectron Spectroscopy*, Perkin Elmer Corporation, 1992.
- [61] S. Dey, S.K. Dey, B. Ghosh, V.R. Reddy, S. Kumar, Structural, microstructural, magnetic and hyperfine characterization of nanosized $\text{Ni}_{0.5}\text{Zn}_{0.5}\text{Fe}_2\text{O}_4$ synthesized by high energy ball-milling method, *Mater. Chem. Phys.* 138 (2013) 833–842.
- [62] J.L. Dormann, D. Fiorani, E. Tronc, Magnetic Relaxation in Fine-particle Systems, in: *Advances in Chemical Physics*, XCVIII, John Wiley & Sons, 1997, pp. 283–494.
- [63] A. Mitra, J. Mohapatra, S.S. Meena, C.V. Tomy, M. Aslam, Verwey transition in ultrasmall-sized octahedral Fe_3O_4 nanoparticles, *J. Phys. Chem. C* 118 (2014) 19356–19362.
- [64] J. Liu, Y. Bin, M. Matsuo, Magnetic behavior of Zn-doped Fe_3O_4 nanoparticles estimated in terms of crystal domain size, *J. Phys. Chem. C* 116 (2012) 134–143.
- [65] F.L. Deepak, M. Bañobre-López, E. Carbó-Argibay, M. Fátima Cerqueira, Y. Piñeiro-Redondo, J. Rivas, C.M. Thompson, S. Kamali, C. Rodríguez-Abreu, K. Kovnir, Y. V. Kolen'ko, A systematic study of the structural and magnetic properties of Mn-, Co-, and Ni-doped colloidal magnetite nanoparticles, *J. Phys. Chem. C* 119 (2015) 11947–11957.
- [66] K. Lagarec, D.G. Rancourt, Recoil-Mössbauer Spectral Analysis Software for Window, University of Ottawa Press, Ottawa, 1998.
- [67] R. Bauminger, S.G. Cohen, A. Marinov, S. Oper, K. Segal, Study of the low-temperature transition in magnetite and the internal fields acting on iron nuclei in some spinel ferrites, using mossbauer absorption, *Phys. Rev.* 122 (1961) 1447–1450.
- [68] K. Sarkar, R. Mondal, S. Dey, S. Majumder, S. Kumar, Presence of mixed magnetic phase in mechanically milled nanosized $\text{Co}_{0.5}\text{Zn}_{0.5}\text{Fe}_2\text{O}_4$: a study on structural, magnetic and hyperfine properties, *J. Magn. Magn. Mater.* 487 (2019) 165303.
- [69] R. Mondal, S. Dey, K. Sarkar, P. Dasgupta, S. Kumar, Influence of high energy ball milling on structural parameters, cation distribution and magnetic enhancement of nanosized $\text{Co}_{0.3}\text{Zn}_{0.7}\text{Fe}_2\text{O}_4$, *Mater. Res. Bull.* 102 (2018) 160–171.
- [70] E.J.W. Verwey, Electronic conduction of magnetite (Fe_3O_4) and its transition point at low temperatures, *Nature* 144 (1939) 327–328.
- [71] Mark S. Senn, Jon P. Wright, J. Paul Attfield, Charge order and three-site distortions in the Verwey structure of magnetite, *Nature* 481 (2012) 173–176.
- [72] C.A. Gorski, M.M. Scherer, Determination of nanoparticulate magnetite stoichiometry by Mössbauer spectroscopy, acidic dissolution, and powder X-ray diffraction: a critical review, *Am. Mineral.* 95 (2010) 1017–1026.
- [73] V.A.M. Brabers, F. Walz, H. Kronmüller, The formation mechanism of iron oxide nanoparticles within the microwave-assisted solvothermal synthesis and its correlation with the structural and magnetic properties, *Phys. Rev. B* 58 (1998) 14163–14166.
- [74] S. Yeo, H. Choi, C.S. Kim, G.T. Lee, J.H. Seo, H.J. Chad, J.C. Park, Survival of Verwey transition in gadolinium-doped ultrasmall magnetite nanoparticles, *Nanoscale* 9 (2017) 13976.
- [75] Z. Kozakova, I. Kuritka, N.E. Kazantseva, V. Babayan, M. Pastorek, M. Machovsky, P. Bazant, P. Saha, The formation mechanism of iron oxide nanoparticles within the microwave-assisted solvothermal synthesis and its correlation with the structural and magnetic properties, *Dalton Trans.* 44 (2015) 21099.

Electrochemical Study of Nanosized $\text{Co}_{0.5}\text{Zn}_{0.5}\text{Fe}_2\text{O}_4$ Synthesized by Hydrothermal Method

K. Sarkar^{1,*}, R. Mondal², D. Majumdar³, S. K. Bhattacharya⁴ and S. Kumar¹

¹Department of Physics, Jadavpur University, Kolkata-700032, India, ²Department of Electronics, Barrackpore Rashtraguru Surendranath College, Kolkata-700120, ³Department of Chemistry, Chandernagore College, Chandannagar, West Bengal 712136, ⁴Department of Chemistry, Jadavpur University, Kolkata 700032

*Corresponding author: koyelsarkar9@gmail.com

Abstract

Herein, we report the electrochemical study of nanosized $\text{Co}_{0.5}\text{Zn}_{0.5}\text{Fe}_2\text{O}_4$ synthesized by hydrothermal method. Structural and microstructural characterization has been carried out by powder x-ray diffraction (PXRD) and transmission electron microscopic techniques. UV-vis diffuse reflectance spectroscopy has been performed to analyze the optical property of the sample. The PXRD study suggests that the sample has crystallized as a single-phase cubic spinel ferrite with $\text{Fd}\bar{3}\text{m}$ symmetry. The average particle size is ~ 19 nm. The band gap of the sample is 1.75 eV. The sample exhibits maximum specific capacitance of 85.5 F/g at 10 mV/s scan rate. The pseudocapacitive behavior of the sample can be ascertained from the non-rectangular shape of cyclic voltammetry curves. The sample can act as a supercapacitor.

Introduction

In the fast-growing world, development of energy storage devices is gaining special attention in order to sustainably harness the depleting energy resources. Supercapacitors are emerging as the most promising next-generation energy storage devices due to their high-power density and longer cycling life [1]. The supercapacitor performance is mainly governed by the surface morphology and electrical properties of electrodes [1]. Nanosized ferrites are appearing as potential candidates for supercapacitor application owing to their high surface to volume ratio, low price, environmental benignity and large abundance [1]. But, electrochemical properties of mixed ferrites have not been explored abundantly [1]. In this regard, investigation of electrochemical properties of nanosized $\text{Co}_{0.5}\text{Zn}_{0.5}\text{Fe}_2\text{O}_4$ and accessing their application as supercapacitor appears promising.

Experimental

The nanosized $\text{Co}_{0.5}\text{Zn}_{0.5}\text{Fe}_2\text{O}_4$ (CZ5050) has been synthesized by hydrothermal method maintaining proper stoichiometric ratio following the procedure described in our earlier work [2].

The powder X-ray diffraction (PXRD) data and high-resolution transmission electron micrograph were recorded using Bruker D8 Advanced Diffractometer and Jeol2100 HRTEM, respectively. The diffuse reflectance spectroscopy (DRS) spectrum of the sample was recorded by a PerkinElmer UV-vis spectrometer (Lambda 35). The working electrode for cyclic voltametric measurements was fabricated by adopting the procedure described in our earlier work

[1] and measurements were carried out using a potentiostat instrument (Digi-ivy, model No. DY2300).

Results and Discussion

Structural and microstructural characterization

The PXRD pattern of CZ5050 (Fig. 1) match well with JCPDS ICDD card numbers 22-1086 and 82-1049 for Co and Zn ferrite, respectively. The data has been refined using MAUD2.33 package [3] and the values of structural, microstructural and refinement parameters are presented in Table 1.

Table 1. Crystal data and refinement parameters

Parameters	CZ5050
Crystallite size (nm)	17
Microstrain	3.76×10^{-3}
Lattice parameter (a(Å))	8.372
Density (g cm ⁻³)	5.304
Rwp	0.008
Rexp	0.005
GOF	1.21

The TEM micrograph of CZ5050, given in Fig. 2, suggest that the constituent particles are non-spherical in shape and possess a size distribution. The average particle size of CZ5050 obtained by fitting with lognormal distribution function is 19 nm, which is slightly greater than the crystallite size due to strong tendency of agglomeration.

Study of Optical Properties

The UV-vis diffuse reflectance spectrum (DRS) of CZ5050 shown in Fig. 3 displays an absorption edge

at around 705 nm. The band gap of CZ5050 is 1.75 eV (shown in inset of Fig.3), as estimated from the intercept of the $(\alpha h\nu)^2$ versus $h\nu$ plot (Kubelka–Munk plot), where α is the absorption coefficient [4].

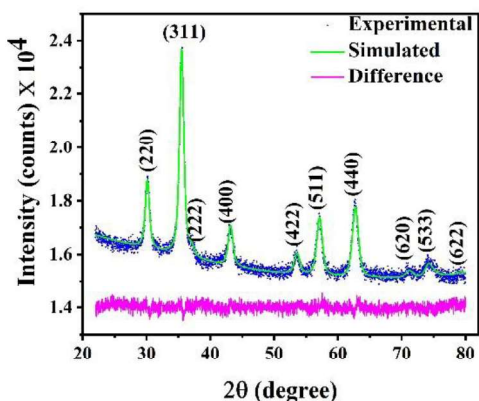


Fig. 1. PXRD pattern of CZ5050

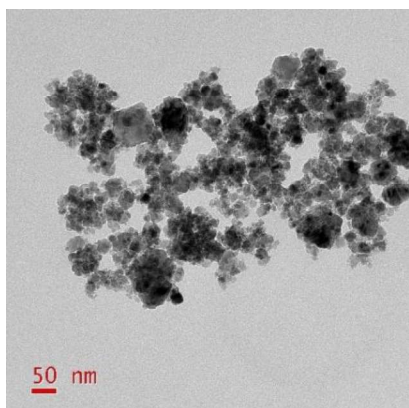


Fig. 2. TEM micrograph of CZ5050

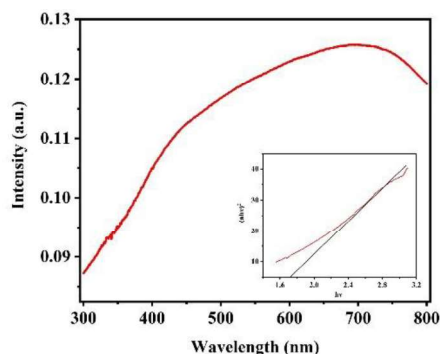


Fig. 3. UV-DRS spectrum of CZ5050 and $(\alpha h\nu)^2$ versus $h\nu$ plot (inset)

Electrochemical performance study

The cyclic voltammograms (CV) of CZ5050 electrode at scan rates of 10, 20, 50, 100 and 200 mV/s in the potential range of ± 0.3 V with reference to the saturated calomel electrode are illustrated in Fig. 4.

The deviation from the rectangular shape of the CV curves can be ascribed to the pseudocapacitive behavior of CZ5050 originating from the transfer of charges between electrode and electrolyte through electrosorption and intercalation processes. The values of specific capacitance (C_s) have been calculated from the CV plot using formula described elsewhere [1]. C_s values for CZ5050 at scan rates of 10, 20, 50, 100 and 200 mV/s are 85.5, 56, 25, 20 and 17 F/g, respectively. At higher scan rates, ions get attached to the atoms of the electrode escalating obstruction in the charge transfer process leading to the drop of capacitance. Further, the area of the CV curves increases with the sweep rate, keeping the shape of the curves unaltered, reflecting good electrochemical response of the sample [1].

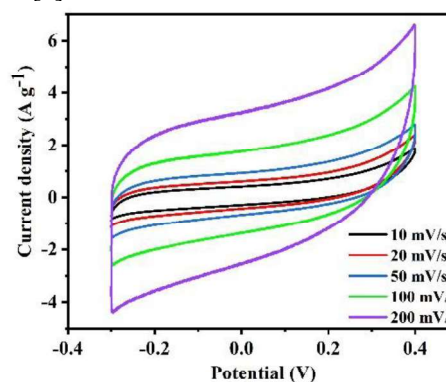


Fig. 4. CV plots of CZ5050

Conclusion

The PXRD and TEM suggest that CZ5050 is a well crystalline, single phase spinel ferrite with average particle size ~ 19 nm. CZ5050 exhibits good electrochemical performance due to its nano size, morphology and lower band gap energy and can act as a supercapacitor.

Acknowledgement

The UPE program of UGC and the PURSE program of DST, Govt. of India, are acknowledged. D.M. acknowledges Chandernagore College, Hooghly, WB, India, for permitting honorary research work.

References

1. R. Mondal, K. Sarkar, S. Dey, D. Majumdar, S. K. Bhattacharya, P. Sen, and S. Kumar, *ACS Omega* **4**, 12632–12646 (2019).
2. R. Mondal, K. Sarkar, S. Dey, S. Bhattacharjee, C. K. Ghosh, and S. Kumar, *AIP Conference Proceedings* **1942**, 050072 (2018).
3. L. Lutterotti, MAUDWEB, Version 1.9992 (2004).
4. A. Manikandan, L.J. Kennedy, M. Bououdina, J. J. Vijaya, *J. Magn. Mater.* **349**, 249-258 (2014).

9%

SIMILARITY INDEX

PRIMARY SOURCES

- 1

R. Mondal, S. Dey, K. Sarkar, P. Dasgupta, S. Kumar. "Influence of high energy ball milling on structural parameters, cation distribution and magnetic enhancement of nanosized $\text{Co}_{0.3}\text{Zn}_{0.7}\text{Fe}_2\text{O}_4$ ", Materials Research Bulletin, 2018
Crossref

300 words — 1%
- 2

Rituparna Mondal, Koyel Sarkar, Subhrajyoti Dey, Dipanwita Majumdar, Swapan Kumar Bhattacharya, Pintu Sen, Sanjay Kumar. " Magnetic, Pseudocapacitive, and H₂O₂-Electrosensing Properties of Self-Assembled Superparamagnetic Co Zn Fe O with Enhanced Saturation Magnetization ", ACS Omega, 2019
Crossref

291 words — 1%
- 3

pubs.rsc.org
Internet

188 words — 1%
- 4

aip.scitation.org
Internet

175 words — 1%
- 5

R. Mondal, S. Dey, S. Majumder, A. Poddar, P. Dasgupta, S. Kumar. "Study on magnetic and hyperfine properties of mechanically milled $\text{Ni}_{0.4}\text{Zn}_{0.6}\text{Fe}_2\text{O}_4$ nanoparticles", Journal of Magnetism and Magnetic Materials, 2018
Crossref

151 words — < 1%

-
- 6 Dey, S., S.K. Dey, B. Ghosh, V.R. Reddy, and S. Kumar. "Structural, microstructural, magnetic and hyperfine characterization of nanosized Ni_{0.5}Zn_{0.5}Fe₂O₄ synthesized by high energy ball-milling method", Materials Chemistry and Physics, 2013. 147 words — < 1%
Crossref
-
- 7 www.mdpi.com 117 words — < 1%
Internet
-
- 8 ftp.aip.org 108 words — < 1%
Internet
-
- 9 Animesh Halder, Achinta Sannigrahi, Nayan De, Krishnananda Chattopadhyay, Sanat Karmakar. "Kinetoplastid membrane protein 11 induces pores in anionic phospholipid membranes: Effect of cholesterol", Langmuir, 2020 103 words — < 1%
Crossref
-
- 10 Sumit Majumder, Manas Sardar, Biswarup Satpati, Sanjay Kumar, Sangam Banerjee. " Magnetization Enhancement of Fe O by Attaching onto Graphene Oxide: An Interfacial Effect ", The Journal of Physical Chemistry C, 2018 77 words — < 1%
Crossref
-
- 11 J. L. Dormann. "Magnetic Relaxation in Fine-Particle Systems", Advances in Chemical Physics, 01/01/1997 63 words — < 1%
Crossref
-
- 12 www.ncbi.nlm.nih.gov 59 words — < 1%
Internet
-
- 13 S. Chakraverty. "Magnetic coding in systems of nanomagnetic particles", Applied Physics Letters, 2006 56 words — < 1%

- 14 S. Dey, R. Mondal, S. Majumder, P. Dasgupta, A. Poddar, S. Banerjee, S. Kumar. "Superparamagnetic behavior of nanosized ZnFe₂O₄", Materials Today: Proceedings, 2018

56 words — < 1%

Crossref

- 15 iopscience.iop.org

Internet

52 words — < 1%

- 16 V. Karthik, G. Dhivya Dharshini, P. Senthil Kumar, S. Kiruthika, Gayathri Rangasamy, Selvakumar Periyasamy, B. Senthil Rathi. "Ferrite-Supported Nanocomposite Polymers for Emerging Organic and Inorganic Pollutants Removal from Wastewater: A Review", Industrial & Engineering Chemistry Research, 2023

51 words — < 1%

Crossref

- 17 R. Mondal, K. Sarkar, S. Dey, S. Bhattacharjee, C. K. Ghosh, S. Kumar. "Study on photocatalytic activity of nanosized Co_{0.3}Zn_{0.7}Fe₂O₄ synthesized by hydrothermal method", AIP Publishing, 2018

47 words — < 1%

Crossref

- 18 onlinelibrary.wiley.com

Internet

43 words — < 1%

- 19 Qureshi, Anjum. "Modification of organometallics dispersed polymers and pure polymers by ion irradiation.", Maharaja Sayajirao University of Baroda (India),

40 words — < 1%

ProQuest

- 20 Peizhi Guo, Lijun Cui, Yiqian Wang, Meng Lv, Baoyan Wang, X. S. Zhao. " Facile Synthesis of ZnFe O Nanoparticles with Tunable Magnetic and Sensing Properties ", Langmuir, 2013

35 words — < 1%

Crossref

21 S. Dey, S.K. Dey, B. Ghosh, V.R. Reddy, S. Kumar. "Structural, microstructural, magnetic and hyperfine characterization of nanosized Ni_{0.5}Zn_{0.5}Fe₂O₄ synthesized by high energy ball-milling method", Materials Chemistry and Physics, 2013

32 words — < 1%

Crossref

22 [epdf.tips](#)
Internet

32 words — < 1%

23 [www.science.gov](#)
Internet

32 words — < 1%

24 Sumayya M. Ansari, Bhavesh B. Sinha, Kalpana R. Pai, Suresh K. Bhat, Yuan-Ron Ma, Debasis Sen, Yesh D. Kolekar, C.V. Ramana. "Controlled surface/interface structure and spin enabled superior properties and biocompatibility of cobalt ferrite nanoparticles", Applied Surface Science, 2018

30 words — < 1%

Crossref

25 Zhong, Tianyu. "Trapping Ferrofluid Patterns: Insights into Hierarchies of Order from Self-Organization of Magnetic Nanoparticles", McGill University (Canada)

29 words — < 1%

ProQuest

26 Mathew, D.S.. "An overview of the structure and magnetism of spinel ferrite nanoparticles and their synthesis in microemulsions", Chemical Engineering Journal, 20070501

26 words — < 1%

Crossref

27 Noémie Elgrishi, Kelley J. Rountree, Brian D. McCarthy, Eric S. Rountree, Thomas T. Eisenhart,

25 words — < 1%

Jillian L. Dempsey. "A Practical Beginner's Guide to Cyclic Voltammetry", Journal of Chemical Education, 2017

Crossref

28 rc.library.uta.edu 23 words — < 1%
Internet

29 S Mukherjee, S Kumar, D Das. "A novel shape transformation of Fe-MgO nanocomposites: microstructural, magnetic and hyperfine investigations", Journal of Physics D: Applied Physics, 2007 22 words — < 1%
Crossref

30 Byong Yong Yu, Seung-Yeop Kwak. "Self-assembled mesoporous Co and Ni-ferrite spherical clusters consisting of spinel nanocrystals prepared using a template-free approach", Dalton Transactions, 2011 19 words — < 1%
Crossref

31 O. Dehghani Dastjerdi, H. Shokrollahi, S. Mirshekari. "A review of synthesis, characterization, and magnetic properties of soft spinel ferrites", Inorganic Chemistry Communications, 2023 19 words — < 1%
Crossref

32 archive.org 19 words — < 1%
Internet

33 nopr.niscpr.res.in 19 words — < 1%
Internet

34 Davide Peddis, Federica Orrù, Andrea Ardu, Carla Cannas, Anna Musinu, Giorgio Piccaluga. "Interparticle Interactions and Magnetic Anisotropy in Cobalt Ferrite Nanoparticles: Influence of Molecular Coating", Chemistry of Materials, 2012 18 words — < 1%
Crossref

35 L. C. Bartel. "Theory of Strain-Induced Anisotropy and the Rotation of the Magnetization in Cubic Single Crystals", Journal of Applied Physics, 1969 18 words — < 1%
Crossref

36 Patel, Narendra P.. "Hyperfine interaction studies in germanium based dilute magnetic semiconducting alloys.", Maharaja Sayajirao University of Baroda (India), ProQuest 18 words — < 1%

37 K. Gupta, P. T. Das, T. K. Nath, A. K. Meikap, P. C. Jana. "A facile route for the synthesis of nanotubular composite of polyaniline with cobalt and its superparamagnetism below blocking temperature", Polymer Composites, 2015 17 words — < 1%
Crossref

38 M. Sundararajan, L. John Kennedy, Udaya Aruldoss, Sk. Khadeer Pasha, J. Judith Vijaya, Steve Dunn. "Microwave combustion synthesis of zinc substituted nanocrystalline spinel cobalt ferrite: Structural and magnetic studies", Materials Science in Semiconductor Processing, 2015 17 words — < 1%
Crossref

39 Thakur, Shyam Singh, Abhilash Pathania, Preeti Thakur, Atul Thakur, and Jen-Hwa Hsu. "Improved structural, electrical and magnetic properties of Mn-Zn-Cd nanoferrites", Ceramics International, 2015. 17 words — < 1%
Crossref

40 lib.buet.ac.bd:8080 17 words — < 1%
Internet

41 S. Dey, S. K. Dey, K. Bagani, S. Majumder, A. Roychowdhury, S. Banerjee, V. R. Reddy, D. Das, 15 words — < 1%

S. Kumar. "Overcoming inherent magnetic instability, preventing spin canting and magnetic coding in an assembly of ferrimagnetic nanoparticles", Applied Physics Letters, 2014

Crossref

42 Sundararaju Meenakshiah Pillai, Karthik. "Copper electrodeposition on ruthenium-tantalum and corrosion of plasma treated copper in post etch cleaning solution", Proquest, 2013.

ProQuest

43 chem.libretexts.org 15 words — < 1%

Internet

44 electrochemsci.org 15 words — < 1%

Internet

45 www.coursehero.com 15 words — < 1%

Internet

46 www.mpboardsolutions.com 15 words — < 1%

Internet

47 Chen, Ming, Leng-Leng Shao, Jia-Jia Li, Wei-Jie Pei, Meng-Ke Chen, and Xia-Hui Xie. "One-step hydrothermal synthesis of hydrophilic Fe₃O₄/carbon composites and their application in removing toxic chemicals", RSC Advances, 2016.

Crossref

48 Narendra Kumar, Sunita Kumbhat. "Essentials in Nanoscience and Nanotechnology", Wiley, 2016

Crossref

49 Ofelia Rodríguez Alzueta. "2'-Methoxyacethopenone as DNA Photosensitiser 14 words — < 1%

50 Qilun Wang, Huawei Wang, Hao Cao, Ching-Wei Tung et al. "Atomic metal-non-metal catalytic pair drives efficient hydrogen oxidation catalysis in fuel cells", Nature Catalysis, 2023

Crossref

14 words — < 1%

51 Sahu, Gay. "Investigating the Electron Transport and Light Scattering Enhancement in Radial Core-Shell Metal-Metal Oxide Novel 3D Nanoarchitectures for Dye Sensitized Solar Cells", Proquest, 2014.

ProQuest

14 words — < 1%

52 Yanyue Liu, Dongfang Guo, Kai Wu, Jinhang Guo, Zijiong Li. " Simultaneous enhanced electrochemical and photoelectrochemical properties of -Fe O /graphene by hydrogen annealing ", Materials Research Express, 2020

Crossref

14 words — < 1%

53 pubs.aip.org

Internet

14 words — < 1%

54 www.azonano.com

Internet

14 words — < 1%

55 www.freepatentsonline.com

Internet

14 words — < 1%